

# Measurement of W bosons in p-Pb at 8.16 TeV and of charmonia in Pb-Pb at 5.02 TeV with the CMS detector at the LHC

Mesure des bosons W en p-Pb à 8.16 TeV et  
des charmonia en Pb-Pb à 5.02 TeV avec le  
déTECTeur CMS au LHC

Thèse de doctorat de l'Université Paris-Saclay  
préparée à l'École Polytechnique

École doctorale n°576  
Particules, Hadrons, Énergie, Noyau, Instrumentation, Imagerie,  
Cosmos et Simulation (PHENIICS)  
Spécialité de doctorat: Physique hadronique

Thèse présentée et soutenue à l'École Polytechnique, le 8 octobre 2018, par

**André Govinda Ståhl Leiton**

Composition du Jury :

Sophie Henrot-Versillé	LAL, Orsay	Présidente du Jury
Lydia Roos	LPNHE, Paris	Rapporteuse
Boris Hippolyte	IPHC, Strasbourg	Rapporteur
Albert de Roeck	University of Antwerp	Examinateur
Begoña de la Cruz Martínez	CIEMAT, Madrid	Examinatrice
Carlos A. Salgado	Universidade de Santiago de Compostela	Examinateur
Raphaël Granier de Cassagnac	LLR, Palaiseau	Directeur de thèse



## TABLE OF CONTENTS

<b>Table of Contents</b>	<b>iii</b>
	<b>Page</b>
<b>Introduction</b>	<b>1</b>
<b>1 High energy nuclear physics</b>	<b>3</b>
1.1 The strong interaction . . . . .	3
1.1.1 The standard model . . . . .	3
1.1.2 Quantum chromodynamics . . . . .	5
1.1.3 Parton distribution functions . . . . .	10
1.1.4 QCD phase diagram . . . . .	14
1.2 Relativistic heavy-ion collisions . . . . .	14
1.2.1 History of heavy-ion accelerators . . . . .	15
1.2.2 Geometry of nucleus-nucleus collisions . . . . .	17
1.2.3 Evolution of heavy-ion collisions . . . . .	20
1.2.4 Experimental probes of the QGP . . . . .	21
<b>2 Experimental setup</b>	<b>35</b>
2.1 The Large Hadron Collider . . . . .	35
2.1.1 Accelerator complex . . . . .	36
2.1.2 Detectors . . . . .	37
2.1.3 Luminosity . . . . .	39
2.1.4 LHC schedule . . . . .	39
2.1.5 Heavy-ion schemes in 2015-2016 . . . . .	40
2.2 The Compact Muon Solenoid . . . . .	41
2.2.1 Subdetectors . . . . .	45
2.2.2 Trigger system . . . . .	53
2.2.3 Reconstruction . . . . .	60

---

**TABLE OF CONTENTS**


---

<b>3 W-boson production in proton-lead collisions</b>	<b>65</b>
3.1 Introduction . . . . .	65
3.1.1 A brief history of the weak theory . . . . .	66
3.1.2 The modern electroweak theory . . . . .	69
3.1.3 Production of W bosons in p-Pb and decay into muons . . . . .	71
3.1.4 Nuclear PDFs . . . . .	74
3.1.5 Experimental results at LHC . . . . .	80
3.2 Analysis . . . . .	84
3.2.1 Dataset . . . . .	85
3.2.2 Next-to-leading order simulations . . . . .	86
3.2.3 Event selection . . . . .	89
3.2.4 Correction for weak-boson transverse momentum . . . . .	92
3.2.5 Corrections for missing transverse momentum . . . . .	95
3.2.6 Signal efficiency . . . . .	107
3.2.7 Signal extraction . . . . .	114
3.2.8 Observables . . . . .	123
3.2.9 Systematic uncertainties . . . . .	126
3.3 Results . . . . .	137
3.3.1 W-boson production in p-Pb at 8.16 TeV . . . . .	137
3.3.2 Comparison with theoretical models . . . . .	139
<b>4 Charmonium production in lead-lead collisions</b>	<b>145</b>
4.1 Introduction . . . . .	145
4.1.1 Spectrum of charmonium states . . . . .	145
4.1.2 Hadroproduction of charmonia . . . . .	147
4.1.3 Charmonia in heavy-ion collisions . . . . .	152
4.2 Analysis . . . . .	158
4.2.1 Dataset . . . . .	160
4.2.2 Charmonium simulations . . . . .	161
4.2.3 Event selection . . . . .	162
4.2.4 Extraction of prompt and nonprompt $J/\psi$ mesons . . . . .	168
4.2.5 Extraction of prompt $\psi(2S)/J/\psi$ ratio . . . . .	180
4.2.6 Charmonium acceptance and efficiency . . . . .	187
4.2.7 Systematic uncertainties of $J/\psi$ -meson yields . . . . .	194
4.2.8 Systematic uncertainties on the $\psi(2S)/J/\psi$ ratio . . . . .	200

---

TABLE OF CONTENTS

4.3 Results . . . . .	204
4.3.1 Nonprompt fraction of $J/\psi$ mesons . . . . .	204
4.3.2 Cross section of prompt and nonprompt $J/\psi$ mesons . . . . .	205
4.3.3 Nuclear modification factor of $J/\psi$ mesons . . . . .	207
4.3.4 Double ratio of prompt $\psi(2S)/J/\psi$ yields . . . . .	211
4.3.5 Discussion . . . . .	213
<b>Conclusion</b>	<b>217</b>
<b>A Résumé en français</b>	<b>219</b>
<b>B Results of the fits for the W boson analysis</b>	<b>231</b>
<b>C Analysis bins used in the charmonia analyses</b>	<b>235</b>
<b>Bibliography</b>	<b>241</b>
<b>List of Tables</b>	<b>267</b>
<b>List of Figures</b>	<b>271</b>



## INTRODUCTION

The progress made by the scientific community over the last century has pushed the boundaries of our understanding of the subatomic world and led to the formulation of one the most successful theories of physics, corresponding to the Standard Model (SM) of particle physics. Even though the SM framework is able to describe, with great accuracy, the interactions and properties of most known particles, some fundamental phenomena still need to be clarified, such as the phase states of matter or the evolution of particles in a nuclear environment.

Under normal circumstances, the main constituents of matter, called partons (i.e. quarks and gluons), are confined by the strong nuclear force into hadrons. However, at high enough temperatures or densities, matter undergoes a phase transition to a state where quarks and gluons become asymptotically free, known as the Quark Gluon Plasma (QGP). Such extreme state of matter is believed to have prevailed during the first microseconds of the creation of the universe and to be part of the core of neutron stars. To recreate the QGP in the laboratory, heavy ions are collided in accelerator facilities at high energies. The QGP can be probed in heavy-ion experiments by measuring different observables, such as the production yield of particles that interact strongly with the QGP medium (e.g. quarkonia, jets, ...). In addition, the environment present in a nucleus can also affect the production of particles produced in heavy-ion collisions, even in the absence of QGP. The measurement of electroweak particles that do not interact with the QGP medium (photons, Z and W bosons) allows to study the nuclear modification of Parton Distribution Functions (PDF). The PDFs of nuclei are crucial inputs to theory predictions for heavy-ion colliders and their precise determination with experimental data is indispensable for calculations of the initial stage of nucleus-nucleus reactions.

Three analyses are presented in this thesis. All of them use data recorded by the Compact Muon Solenoid [1] apparatus at the Large Hadron Collider [2]. The first one measure the production of W bosons in p-Pb collisions at a center-of-mass energy per nucleon pair of  $\sqrt{s_{\text{NN}}} = 8.16 \text{ TeV}$ , with the goal to provide precise experimental constrains to the nuclear modifications of the quark PDFs. I am the *contact person* of this analysis

## TABLE OF CONTENTS

---

and have conducted all the work except the tag-and-probe and the weak boson  $p_T$  corrections. I presented the preliminary results at the Quark Matter [3] and ICHEP [4] conferences in 2018. The work is expected to be published in a peer-reviewed journal in the near future [5]. The second and third analyses probe quark deconfinement in the QGP by measuring the  $J/\psi$  and  $\psi(2S)$  (i.e. charmonium) production in Pb-Pb collisions at  $\sqrt{s_{NN}} = 5.02 \text{ TeV}$ . My main contributions to the  $J/\psi$  and  $\psi(2S)$  analyses include the optimization of the muon kinematic selection, the signal extraction and the systematic uncertainties associated to the fitting. The results of the  $\psi(2S)$  and  $J/\psi$  analyses have been published in PRL [6] and EPJC [7], respectively, and I presented them at the Hot Quarks 2016 [8] and EPS-HEP 2017 [9] conferences.

The manuscript is organised as follows. The general concepts of the strong interactions and heavy-ion collisions are introduced in Chapter 1. A brief description of the main probes of the QGP concludes the chapter. Chapter 2 describes the experimental apparatus, where the operational conditions of the Large Hadron Collider and characteristics of the Compact Muon Solenoid detector are detailed. The chapter also describes the trigger and reconstruction algorithms employed to select and process the data. Chapter 3 presents in details the generated samples, the event selections, the corrections to the missing transverse momentum, the estimation of the muon efficiency, the signal extraction, the systematic uncertainties and the results of the W-boson analysis, accompanied by a short introduction on electroweak physics. The charmonium analysis in Pb-Pb collisions is exposed in Chapter 4. The chapter contains details on the charmonium samples, the event selection, the  $J/\psi$  efficiency estimation, the extraction of the  $J/\psi$  yields and the  $\psi(2S)/J/\psi$  ratios, the systematic uncertainties and the results, including a brief introduction to the physics of charmonia in heavy-ion collisions.

## HIGH ENERGY NUCLEAR PHYSICS

This chapter introduces some key concepts of high energy nuclear physics common to the analysis of the production of W bosons and charmonia in heavy-ion collisions. The quantum field theory of the strong interactions is described in Section 1.1. The state of hot dense hadronic matter, known as the quark-gluon plasma, and the study of its properties in heavy-ion collisions are reviewed in Section 1.2.

### 1.1 The strong interaction

The strong interaction is one of the three fundamental interactions described by the standard model of particle physics introduced in Section 1.1.1. Its underlying theory is Quantum Chromodynamics (QCD) presented in Section 1.1.2. It binds quarks and gluons in hadrons, which are distributed inside the hadron as described by PDFs (Section 1.1.3). Depending on the temperature and density of the system, it is expected to exhibit a complex phase diagram (Section 1.1.4).

#### 1.1.1 The standard model

The Standard Model (SM) is a theoretical framework that describes the properties of elementary particles and their interactions. The SM was developed during the 20th century through the collaborative effort of many physicists. According to the SM, the most elementary particles are fermions and bosons. Fermions are particles with half-

integer spin which behave according to Fermi-Dirac statistics formulated by Enrico Fermi [10] and Paul Dirac [11] in 1926. As a consequence, fermions are restricted by the Pauli exclusion principle [12] which dictates that two or more fermions with the same quantum numbers cannot occupy the same quantum state.

In addition, fermions can be classified as leptons or quarks. There are six leptons arranged in three "generations": the electron ( $e^-$ ) and the electron neutrino ( $\nu_e$ ), the muon ( $\mu^-$ ) and the muon neutrino ( $\nu_\mu$ ), and the tau ( $\tau^-$ ) and the tau neutrino ( $\nu_\tau$ ). The neutrinos are electrically neutral and almost massless, while the other leptons have negative electric charge ( $-1$ ) and sizeable masses. In the case of quarks, there are six "flavours" paired also in three generations of increasing mass. The up and down quarks belong to the first generation, while the heavier quarks are included in the second generation (charm and strange quarks) and third generation (top and bottom quarks). The up (u), charm (c) and top (t) quarks have positive electric charge ( $+2/3$ ) while the down (d), strange (s) and bottom (b) quarks have negative electric charge ( $-1/3$ ). Each quark also carry another quantum number called colour charge that can have three different values labelled as red, green and blue. Moreover, each fermion has an associated antiparticle with the same mass but with opposite charges. The positron ( $e^+$ ) is the antiparticle of the electron, while the name of the rest of antiparticles simply starts with the prefix "anti" (e.g. anti-quarks  $\bar{q}$ , anti-neutrinos  $\bar{\nu}$  or anti-leptons  $\ell^+$ ).

The interactions between fermions are described in the SM by three fundamental forces: the electromagnetic force, the strong nuclear force and the weak nuclear force. The gravitational force is currently not included in the SM but the effect of gravity at the quantum level is too small to be observed. In the SM, each fundamental force is mediated by the exchange of bosons, which are integer spin particles that follows the Bose-Einstein statistics proposed in 1924 by Sateyndra Bose [13] and Albert Einstein [14].

The electromagnetic and the weak nuclear forces are described in the SM by the electroweak theory. The electromagnetic interactions between particles with electric charge are mediated by photons which are massless and chargeless spin one particles. On the other hand, the weak interactions can act on all fermions but the strength of the weak force is roughly  $10^{-4}$  times weaker than the electromagnetic force and  $10^{-6}$  times weaker than the strong nuclear force<sup>1</sup>. The weak interactions are mediated by three massive vector bosons: the electrically charged  $W^\pm$  bosons<sup>2</sup> and the electrically neutral Z boson. Processes involving neutrinos or the change of quark flavour are only

---

<sup>1</sup>The strength of the interactions is determined for two up quarks separated by a distance of  $3 \times 10^{-17}$  m.

<sup>2</sup>Since the W bosons are used to probe the nuclear PDF, the theory of the weak interaction is further described, together with the analysis in p-Pb collisions, in Chapter 3.

possible through the weak interactions. Last, the strong nuclear force is responsible for the interactions between colour charged particles (i.e. quarks) described by the theory of Quantum Chromodynamics (QCD). The strong interactions are mediated by spin one bosons called gluons which carry colour and anti-colour charge. Unlike the photon, gluons can interact with each other leading to a strong attraction that confines the quarks in colourless configurations known as hadrons. Hadrons composed of three (anti-)quarks are called (anti-)baryons while those made of a quark and an anti-quark are called mesons. Exotic hadrons containing four and five quarks have been recently observed by the Belle [15] and LHCb [16] collaborations, respectively.

The generation of mass of the elementary particles is explained in the SM by the Brout-Englert-Higgs (BEH) mechanism [17, 18]. The weak bosons and the fermions acquire their mass by interacting with the Higgs field. The stronger a particle couples to the Higgs field, the more massive it becomes. The quantum excitation of the Higgs field corresponds to a scalar boson, the so-called Higgs boson. The BEH mechanism was experimentally confirmed after the CMS [19] and ATLAS [20] collaborations announced the discovery of the Higgs boson in 2012. The basic properties of leptons, quarks and bosons of the SM are summarised in Table 1.1.

### 1.1.2 Quantum chromodynamics

The development of new experimental techniques, such as the synchrocyclotron and the bubble chamber, led to the discovery of many hadronic resonances starting from the late 1940s. In an attempt to organise these new hadrons, Murray Gell-Mann [22] and Yuval Ne’eman [23] proposed in 1961 the Eightfold Way classification. The Eightfold Way scheme managed to sort the hadrons into representations of the SU(3) group leading to the creation of the quark model. The quark model, developed in 1964 by Gell-Mann [24] and George Zweig [25], considered the hadrons as composite objects made of valence quarks and anti-quarks. Even though the quark model was successful at describing the properties of most hadrons known at the time, it had problems explaining the structure of the  $\Omega^-$  baryon. The  $\Omega^-$  baryon is made of three strange quarks with parallel spins but such configuration was forbidden by the Pauli exclusion principle. To solve the spin-statistics paradox, Oscar Greenberg [26] proposed that each quark also carried a 3-valued quantum number named the colour charge. The description of the strong interactions using the concept of colour charges was formally developed in the theory of QCD by Harald Fritzsch, Heinrich Leutwyler and Murray Gell-Mann [27] in 1973.

	Name	Symbol	Mass	Charge	Spin	Interactions
Quarks	1 <sup>st</sup> Up	u	2.2 MeV/c <sup>2</sup>	2/3	1/2	All
	Down	d	4.7 MeV/c <sup>2</sup>	-1/3	1/2	All
	2 <sup>nd</sup> Charm	c	1.275 GeV/c <sup>2</sup>	2/3	1/2	All
	Strange	s	95 MeV/c <sup>2</sup>	-1/3	1/2	All
	3 <sup>rd</sup> Top	t	173.0 GeV/c <sup>2</sup>	2/3	1/2	All
	Bottom	b	4.18 GeV/c <sup>2</sup>	-1/3	1/2	All
Leptons	1 <sup>st</sup> Electron	e <sup>-</sup>	511 keV/c <sup>2</sup>	-1	1/2	Electroweak
	Electron neutrino	$\nu_e$	< 2 eV/c <sup>2</sup>	0	1/2	Weak
	2 <sup>nd</sup> Muon	$\mu^-$	106 MeV/c <sup>2</sup>	-1	1/2	Electroweak
	Muon neutrino	$\nu_\mu$	< 2 eV/c <sup>2</sup>	0	1/2	Weak
	3 <sup>rd</sup> Tau	$\tau^-$	1.78 GeV/c <sup>2</sup>	-1	1/2	Electroweak
Bosons	Tau neutrino	$\nu_\tau$	< 2 eV/c <sup>2</sup>	0	1/2	Weak
	Photon	$\gamma$	< 10 <sup>-18</sup> eV/c <sup>2</sup>	0	1	Electromagnetic
	Gluon	g	0	0	1	Strong
	W boson	$W^\pm$	80.4 GeV/c <sup>2</sup>	$\pm 1$	1	Electroweak
	Z boson	Z	91.2 GeV/c <sup>2</sup>	0	1	Electroweak
	Higgs boson	H	125.2 GeV/c <sup>2</sup>	0	0	BEH mechanism

Table 1.1: Basic properties of quarks, leptons and bosons from the SM. The table includes the mass, electric charge, spin and type of interactions of each particle. The values are taken from Ref. [21].

Quantum Chromodynamics is a non-abelian quantum field theory with gauge symmetry group SU(3), that describes the strong interactions between colour charged particles. The primary objects of QCD are the quarks which carry one colour charge (e.g. green) and the gluons which carry a colour and an anti-colour charge (e.g. red-antiblue). There are eight different gluons which form an octet representation of SU(3)<sup>3</sup>. The Lagrangian of QCD is:

$$L_{QCD} = \sum_f \bar{q}_{f,i} \left( i \gamma^\mu D_\mu^{i,j} - m_f \delta^{a,b} \right) q_{f,j} - \frac{1}{4} F_{\mu,\nu}^a F_a^{\mu,\nu} \quad (1.1)$$

where  $\gamma^\mu$  are the Dirac  $\gamma$ -matrices. The  $q_{f,i}$  represents the Dirac spinor of a quark with flavour  $f$ , mass  $m_f$  and colour index  $i$  running from  $i = 1$  to 3. The QCD gauge covariant derivative  $D_\mu^{i,j}$  and the gluon field strength tensor  $F_{\mu,\nu}^a$  are given by:

<sup>3</sup>The fully symmetric colour-anticolour combination is colourless and thus, can not mediate colour.

$$D_\mu^{i,j} = \delta^{i,j} \partial_\mu - i \frac{g_s}{2} \lambda_a^{i,j} G_\mu^a \quad (1.2)$$

$$F_{\mu,\nu}^a = \partial_\mu G_\nu^a - \partial_\nu G_\mu^a + g_s f_{bc}^a G_\mu^b G_\nu^c$$

where  $g_s$  is the strong gauge coupling constant,  $f_{bc}^a$  are the SU(3) structure constants,  $\lambda_a^{i,j}$  are the Gell-Mann matrices, and  $G_\mu^a$  is the vector field of a gluon with index  $a$  that runs from 1 to 8.

Expanding the terms in Eq. (1.1), one can derive three different types of vertices representing the interaction between quarks and gluons, and the gluon self-interactions as shown in Figure 1.1.

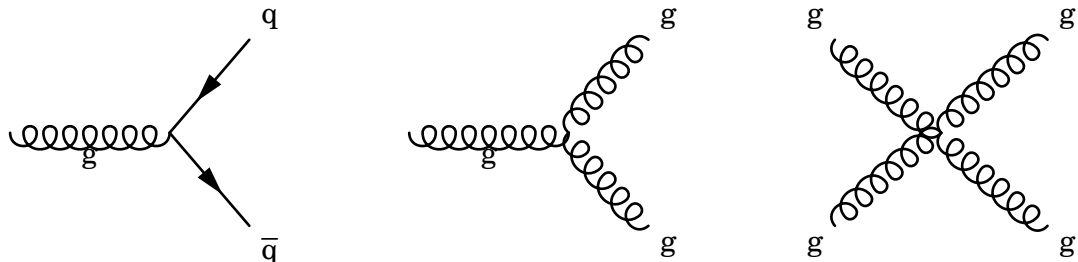


Figure 1.1: Feynman diagrams of the QCD vertices for quark-gluon coupling (left), triple-gluon self-coupling (middle) and quadri-gluon self-coupling (right).

### 1.1.2.1 Running coupling constant

In quantum field theory, physical quantities are calculated by performing a perturbative expansion of the theory in terms of its coupling constant. The first order of the expansion is called the leading order (LO). At higher orders, some of the terms contain loops (infinite integrals) which diverge due to high momentum particles in the loop. The ultraviolet (UV) divergences can be removed from the perturbation series by renormalising the Lagrangian.

The renormalisation procedure consists in replacing the bare parameters of the Lagrangian by finite renormalised parameters, and then treat the divergences by applying a regularisation scheme. There are many regularisation schemes but one of the most often used is Minimal Subtraction (MS) based on dimensional regularisation. The MS scheme consists in solving the loop integrals in  $d$  arbitrary spacetime dimensions introducing a scale  $\mu$  in the process [28]. In order to keep the physical observables independent of the renormalisation scale, the dependence of the renormalised parameters on the scale  $\mu$  is fixed by renormalisation group equations (RGE) [28].

In the case of QCD, the strength of the strong interactions is parametrised by the strong coupling constant  $\alpha_s = 4\pi g_s^2$ . The UV divergences in perturbative QCD (pQCD) appear from loop diagrams like those shown in Figure 1.2.

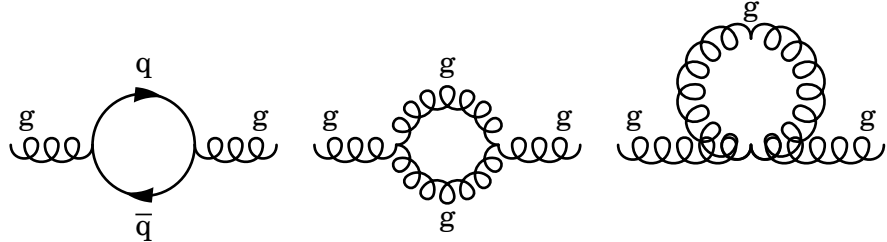


Figure 1.2: Feynman diagrams of 1-loop contributions to pQCD.

The renormalised strong coupling constant  $\alpha_s(\mu^2)$  satisfies the following RGE [21]:

$$\mu^2 \frac{d\alpha_s(\mu^2)}{d\mu^2} = \beta(\alpha_s) = -\alpha_s^2 (\beta_0 + \beta_1 \alpha_s + \dots) \quad (1.3)$$

where  $\beta_0 = 7/(4\pi)$  and  $\beta_1 = 13/(8\pi^2)$  are the 1-loop and the 2-loop coefficients of the  $\beta$ -function, respectively [21]. In the one-loop approximation,  $\alpha_s(\mu^2)$  can be expressed as:

$$\alpha_s(\mu^2) = \frac{1}{\beta_0 \ln\left(\frac{\mu^2}{\Lambda_{\text{QCD}}^2}\right)} \quad (1.4)$$

where  $\Lambda_{\text{QCD}} \approx 255 \text{ MeV}$  [29]<sup>4</sup> is the QCD Landau pole (i.e. the scale at which the coupling becomes infinite). The factorisation scale  $\mu$  is generally associated to the energy scale  $Q$  of a given process. This means that  $\alpha_s(\mu^2)$  is not really a constant but depends on the energy scale, so it is also known as the QCD running coupling constant. Figure 1.3 presents the latest results on the measurement of  $\alpha_s(Q^2)$  as a function of the energy scale  $Q$  [21].

### 1.1.2.2 Asymptotic freedom

One important consequence of the non-abelian nature of QCD is the asymptotic freedom of colour charged particles discovered in 1973 by David Gross and Frank Wilczek [30], and also by David Politzer [31]. As can be observed in Figure 1.3, the strength of the strong nuclear force gets asymptotically reduced as the energy scale is increased. Perturbative

<sup>4</sup>Derived for 2 quark flavours in the modified minimal subtraction  $\overline{\text{MS}}$  scheme (variation of the MS scheme where the renormalisation scale  $\mu$  is rescaled by  $e^{\gamma_E}/4\pi$ , with  $\gamma_E$  the Euler-Mascheroni constant).

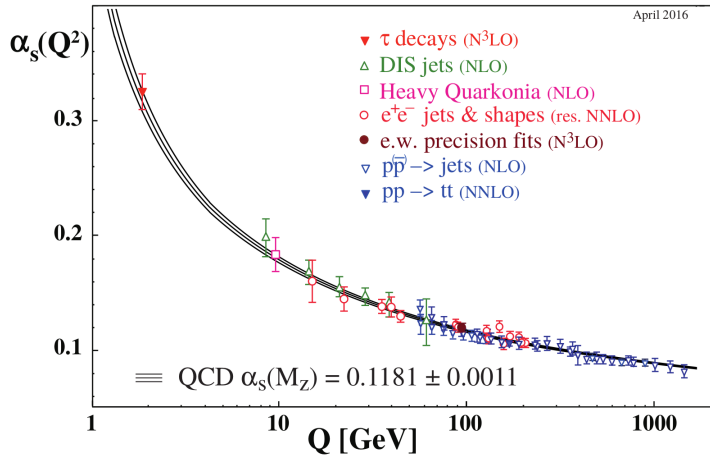


Figure 1.3: Summary of measurements of  $\alpha_s$  as a function of the energy scale  $Q$ . Figure taken from Ref. [21].

QCD can then be fully applied in the asymptotic free regime since the strong coupling constant is small.

Considering the inverse relation between the wavelength of particles and their momentum (the de Broglie hypothesis [32]), asymptotic freedom implies that the strong nuclear interactions between quarks gets weaker at larger momentum or at shorter distances. This phenomenon can be understood qualitatively as derived from the interaction with the QCD vacuum. The presence of virtual quark-antiquark pairs from the vacuum acts as colour dipoles reducing (screening) the strength of the colour charge field. In addition, virtual gluons can couple to other gluons increasing (anti-screening) the net effect of the colour charge seen at larger distances. Thus, there is an interplay between quark-antiquark colour screening and gluon colour anti-screening, where the later effect dominates in QCD.

### 1.1.2.3 Colour confinement

The fact that quarks and gluons have never been observed isolated in normal conditions is due to another phenomenon of QCD called colour confinement. The intensity of the strong nuclear force increases when the energy scale is reduced or the distance is increased as seen in Figure 1.3. The large strong interactions between colour charged particles force the quarks and gluons to be confined in hadrons. The divergent behaviour of  $\alpha_s$  at the Landau pole shown in Eq. (1.4), is a consequence of the inability of pQCD to describe the low energy regime, which becomes non-perturbative.

The strong nuclear force can be described qualitatively as a string. When a quark

and anti-quark gets separated, the gluon string that mediates their strong interaction elongates, increasing the energy. The string eventually breaks when it becomes more energetically favourable to create a light quark-antiquark pair, splitting the original meson into two mesons as shown in Figure 1.4. This leads to a process called hadronisation where quarks and gluons produce a cascade of hadrons<sup>5</sup>. The presence of colour charged particles in high energy collisions can be measured experimentally using jets derived by clustering the final state hadrons in narrow cones.

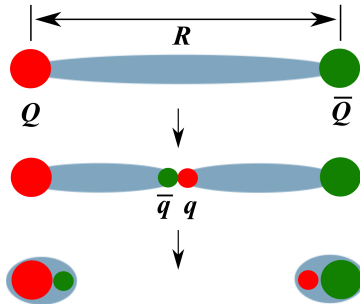


Figure 1.4: Sketch of the gluon string breaking between a quark  $Q$  and an anti-quark  $\bar{Q}$  due to  $q\bar{q}$  pair creation. Figure taken from Ref. [33].

### 1.1.3 Parton distribution functions

The production of particles in hadronic collisions depends on the evolution of the partons (i.e. quarks and gluons) inside the hadrons and the parton momentum transfer during the hard scattering. Since the strong coupling constant decreases with increasing momentum scales, partons can be considered asymptotically free within the hadron during collisions involving large momentum transfers. In this case, each parton carries a fraction of the total momentum of the hadron, represented by the quantity called Bjorken  $x$  [34] (labelled simply as  $x$ ), given by:

$$p_{\text{parton}} = x p_{\text{proton}} \quad (1.5)$$

The net quantum properties of hadrons, such as the electric or colour charge, are derived from the valence quarks. The interaction between valence quarks is mediated by the exchange of gluons. Gluons can also produce virtual quark-antiquark pairs and other gluons through self interactions. The virtual quarks produced inside the hadrons

---

<sup>5</sup>In the case of baryons, a di-quark is located at one end of the string and a quark on the other end, and the string can eventually break producing a baryon and a meson.

are called sea quarks. The gluons and sea quarks do not contribute to the net quantum numbers of the hadron but they can contribute to its mass and they also play a key role in the interaction of hadrons with other particles.

A convenient way of studying the partonic content of hadrons is through the parton distribution functions. The PDF of a hadron represents the probability that a parton carries a given fraction  $x$  of the total momentum of the hadron.

According to the QCD factorisation theorem [35], the cross section of a given hard scattering process in hadronic collisions can be split in a partonic cross section times the PDFs of each incoming hadron. On one hand, the partonic cross section can be derived using perturbative QCD and does not depend on the colliding hadrons. On the other hand, the PDFs can not be calculated from first principles due to the non-perturbative nature of QCD, but they can be determined from global fits to experimental data since the PDFs are independent of the initial scattering process (i.e. universal). The hadronic cross section in a given final state can be expressed at LO, using the factorisation theorem, as:

$$\sigma_{h_1, h_2} = \sum_{f_1, f_2=(q, \bar{q}, g)} \int_0^1 dx_1 dx_2 f_1^{h_1}(x_1, Q^2) f_2^{h_2}(x_2, Q^2) \hat{\sigma}_{f_1 f_2} \quad (1.6)$$

where  $Q$  is the momentum scale,  $f^{h_1}(x, Q^2)$  is the PDF of a given incoming hadron  $h_1$ , and  $\hat{\sigma}_{f_1 f_2}$  represents the partonic cross section of the scattering process between partons  $f_1$  and  $f_2$ .

The  $Q$  dependence of the PDFs is described by the parton evolution equations developed by Dokshitzer, Gribov, Lipatov, Altarelli and Parisi (DGLAP) [36, 37, 38]. In the DGLAP formalism, the PDFs can be expressed in terms of kernels  $P_{q_1 q_2}$  (called splitting functions), and the evolution equations of the parton densities can be written as:

$$\begin{aligned} \frac{d}{dt} q_i(x, t) &= \frac{\alpha_s(Q)}{2\pi} [q_i \circledast P_{qq} + g \circledast P_{qg}] \\ \frac{d}{dt} g(x, t) &= \frac{\alpha_s(Q)}{2\pi} \left[ \sum_i (q_i + \bar{q}_i) \circledast P_{gq} + g \circledast P_{gg} \right] \\ [q \circledast P] &= \int_x^1 dy \frac{q(y, t)}{y} \times P\left(\frac{x}{y}\right) \end{aligned} \quad (1.7)$$

where  $t = \log(Q^2/\mu_F^2)$ ,  $\mu_F$  is the factorisation scale (energy scale that separates the PDFs from the partonic cross sections), and  $P_{q_1 q_2}$  represents the probability that a parton of type  $q_1$  emits a parton of type  $q_2$ . In other words, the DGLAP evolution equations state that the PDF of a given parton  $q$  at an  $x$  value is determined from the contribution

of all the partons at higher momentum fraction considering their probability of decaying into the parton  $q$ .

From the definition of the PDFs, one can also formulate a set of structure functions defined as:

$$F_2^p(x) = \sum_q e_q^2 f(x, Q^2) x \quad (1.8)$$

where  $e_q$  is the electric charge of a given quark flavour  $q$ . The structure functions were extensively measured in deep-inelastic scattering (DIS) collisions at the Hadron-Elektron-Ring-Anlage (HERA) accelerator. The DIS process consists in the inelastic scattering of electrons off protons as presented in Figure 1.5. In the DIS process, the momentum transferred from the electron to the proton is defined as  $Q^2 = -q^2 = -(k - k')^2$  and the corresponding Bjorken  $x$  fraction is  $x = Q^2 / (2p \cdot q)$ , where all 4-momenta are defined in the figure.

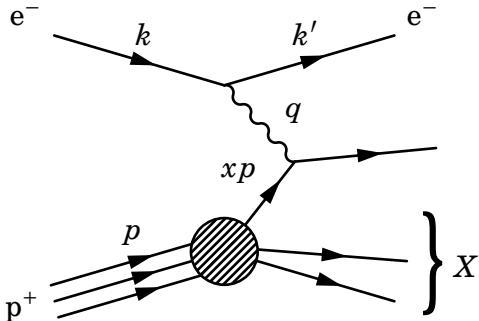


Figure 1.5: Feynman diagram of deep inelastic scattering of electrons against protons.

The measurements of the  $F_2$  structure function performed by the ZEUS collaboration [39] at HERA are shown in Figure 1.6. Even though DIS experiments were not able to probe the gluons directly, the DIS data showed that valence quarks only carry half of the proton momentum, the other half being carried by the gluons.

Another important process used to constrain PDFs is the Drell-Yan (DY) process or the production of W bosons. In the DY process, a quark from one hadron and an anti-quark from another hadron annihilate into a virtual photon ( $\gamma^*$ ) or a Z boson, which then decays to a particle-antiparticle pair as shown in Figure 1.7. The measurement of DY production can be used to constrain the quark PDFs in a wide range of momentum fraction  $x$  depending on the invariant mass of the dilepton pair. In addition, the measurement of the production of positive and negative charged W bosons in hadronic collisions is used to

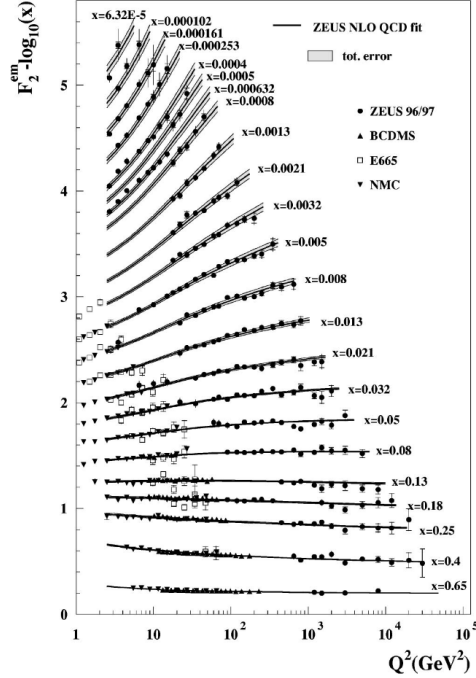


Figure 1.6: Next-to-leading order QCD fits to the ZEUS  $F_2$  structure function data from 1996, 1997 and proton fixed-target at HERA. The error bands of the fit represent the total experimental uncertainty from both correlated and uncorrelated sources. Figure taken from Ref. [39].

disentangle the flavour dependence of the quark PDFs. More details about the W boson production will be provided in Chapter 3, since the present thesis reports a measurement of W bosons in p-Pb collisions that provide strong constraints on nuclear PDF.

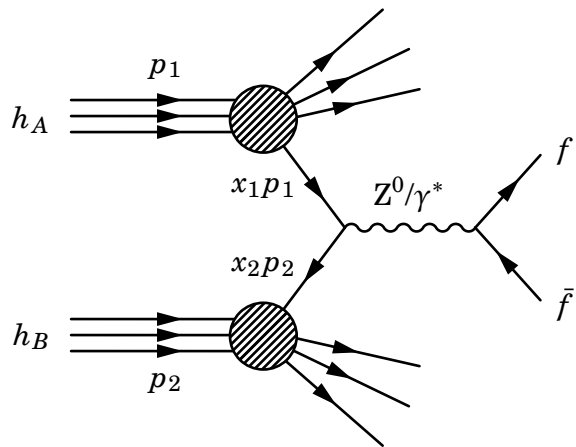


Figure 1.7: Feynman diagram of the Drell-Yan process.

### 1.1.4 QCD phase diagram

The first attempt to describe the temperature evolution of matter at high energies was performed by Rolf Hagedorn in 1965 [40]. Hagedorn considered matter at high energies as a gas made of hadrons and he employed a thermodynamical bootstrap approach to describe the hadron gas. After studying the mass spectrum of all the hadron species measured at the time, Hagedorn realised that the density of hadron species grows exponentially until it diverges at a temperature of  $T_H \approx 158$  MeV, known as the Hagedorn temperature. Years later, with the advent of QCD, it was understood that the Hagedorn temperature described a transition from a hadron gas to a state of matter where quarks and gluons are asymptotically free called the quark-gluon plasma.

The description of the QCD phase transition turned out to be complicated because the critical temperature is close to the QCD scale  $\Lambda_{\text{QCD}} \approx 255$  MeV [29], where perturbative calculations are no longer reliable. An alternative method to study the non-perturbative regime of QCD consists of solving numerically the QCD field equations on a discrete space-time grid using a method called lattice QCD. Nowadays, lattice QCD is able to describe the evolution of matter at finite temperatures and low densities [41, 42]. A sketch of the QCD phase diagram in terms of the temperature  $T$  and the baryon chemical potential<sup>6</sup>  $\mu_B$  is shown in Figure 1.8.

Normal nuclear matter exists in nature at low temperatures and relatively high  $\mu_B$  (900 MeV). At higher  $\mu_B$ , matter undergoes a phase transition to a degenerate gas of fermions, known as neutron gas, which is present in neutron stars. It is theorised that at even higher  $\mu_B$ , matter could reach a state of colour superconductivity where quarks bind together into Cooper pairs [44]. On the other hand, matter present at the beginning of the universe or produced in TeV-scale particle collisions has very low baryon chemical potential. Matter is described at low temperatures as a hadron gas and it becomes a QGP when the temperature exceeds some critical value. At low  $\mu_B$ , the phase transition between the hadron gas and the QGP has been established, using lattice QCD, to be a crossover where the two states coexist [45, 46].

## 1.2 Relativistic heavy-ion collisions

Heavy-ion colliders have become essential tools to explore the fundamental properties of matter. Collisions of nuclei are used to probe the phase transitions of QCD and to recreate

---

<sup>6</sup>The baryon chemical potential can be viewed as a measure of the excess of matter over anti-matter and it is proportional to the baryon density.

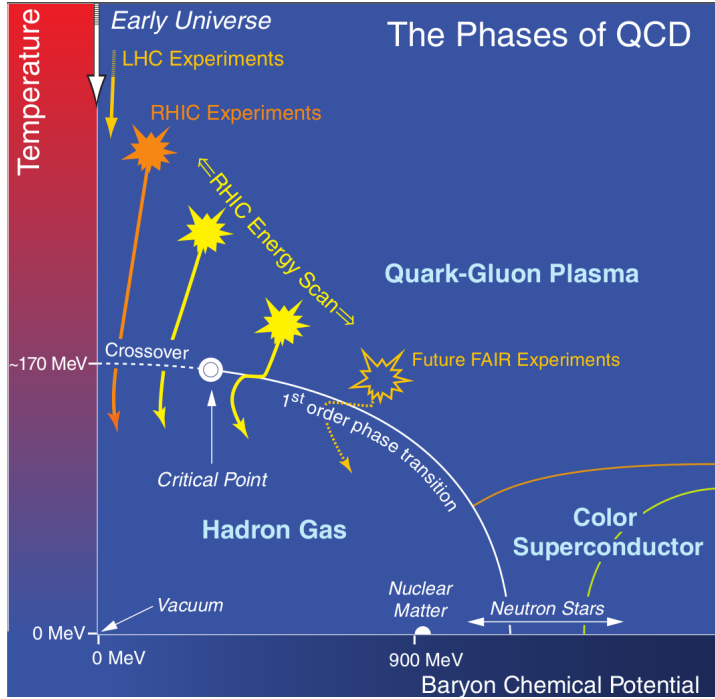


Figure 1.8: Sketch of the QCD phase diagram for nuclear matter. The solid lines show the phase boundaries and the solid circle represents the critical point. Figure taken from Ref. [43].

the QGP in the laboratory. The QGP is believed to have existed at the beginning of the universe and to be part of the core of some astrophysical objects such as neutron stars. The study of the QGP allows to test QCD in the most extreme regimes and provides an insight on the evolution of the universe. Some of the primary research goals of the heavy-ion physics programme is to understand the formation and properties of the QGP, and how does matter interact with the nuclear medium. Nowadays, the experimental study of ultra-relativistic (i.e. at energies above  $\sqrt{s_{\text{NN}}} > 10 \text{ GeV}$ ) heavy-ion collisions is performed at the Brookhaven National Laboratory (BNL) and at the European Organization for Nuclear Research (CERN).

### 1.2.1 History of heavy-ion accelerators

The interest in probing the QCD phase diagram in the laboratory arose in the 1970s after Werner Scheid, Hans Müller and Walter Greiner predicted that nuclear matter could be compressed in heavy-ion collisions at nucleus-nucleus energies larger than 100 MeV/nucleon [47]. The shock compression mechanism could reach matter densities up to five times higher than the density of atomic nuclei ( $\rho_0 = 0.16 \text{ baryon/fm}^3$ ) [47].

Coinciding in time, the Lawrence Berkeley National Laboratory (LBNL) decided to transform their proton synchrotron accelerator Bevatron into a heavy-ion experiment called Bevalac. Heavy ions were produced in the Bevalac using the heavy-ion linear accelerator SuperHILAC and then sent to the Bevatron, where the ions were further accelerated against a fixed target with energies of up to 2.6 GeV/nucleon [48]. The goal at the time was to investigate the equation of state (EoS) of hadronic matter at high densities. The understanding of the relation between the pressure and the energy density of dense matter was a key element needed to describe the dynamics of astrophysical objects such as neutron stars [49, 50].

The successful creation of compressed nuclear matter at the Bevatron motivated the construction of several heavy-ion accelerators at higher energies. The first one was the Alternating Gradient Synchrotron (AGS) particle accelerator at the Brookhaven National Laboratory (BNL). The AGS became the first facility in 1960 to accelerate protons to an energy of 33 GeV, which allowed to discover the muon neutrino in 1962 and to observe the CP violation of the weak interactions in kaon decays in 1964. An electrostatic accelerator called the Tandem Van de Graaf was built in 1970 to provide beams of ions to the AGS. The relativistic heavy-ion programme started at AGS in 1986 and lasted for 12 years during which several experiments were performed (e.g. E802, E858, E866, E896 and E917). The AGS accelerated silicon beams at 14.6 GeV/nucleon and gold beams at 11.1 GeV/nucleon, and collided them against different types of fixed targets (e.g. aluminium and gold).

In parallel, CERN built the Super Proton Synchrotron (SPS) in 1976. To study the QGP, CERN added an Electron-Cyclotron Resonance (ECR) ion source in 1986 which initially accelerated ions of oxygen and sulphur at 200 GeV/nucleon. A subsequent upgrade of the ion injector in 1994 allowed to accelerate up to an energy of 158 GeV/nucleon the Pb ions, which were collided against fixed targets located in two experimental halls: one in the SPS north area (NA) and the other in the SPS west area (WA). Several fixed target experiments were built at the SPS between 1986 and 2005. After years of analysing the Pb-Pb and Pb-Au fixed target collision data from SPS, CERN announced in 2000 that the combined results of the experiments NA44, NA45, NA49, NA50, NA52, WA97/NA57 and WA98, provided a first evidence of the creation of a new state of matter consistent with the QGP [51].

In the meantime, the first nucleus-nucleus collider, known as the Relativistic Heavy Ion Collider (RHIC), started operations at the BNL in 2000. Two beams of Au are pre-accelerated at the AGS to an energy of 8.86 GeV/nucleon and then sent to RHIC where

the Au beams were first collided at  $\sqrt{s_{\text{NN}}} = 130 \text{ GeV}$ , and later at 200 GeV. Other collision systems explored at RHIC include: p-p, p-Au, d-Au, Cu-Cu, Cu-Au and U-U [52]. There were four detectors at RHIC called BRAHMS, PHENIX, STAR, and PHOBOS. Currently, only the STAR and PHENIX collaborations are still active, while PHOBOS ceased operations in 2005 and BRAHMS in 2006. After four years of meticulously studying the system produced in Au-Au collisions with the four detectors, RHIC finally announced in 2005 the discovery of a strongly coupled QGP. Contrary to the expected gaseous behaviour, the QGP observed at RHIC turned out to resemble more a liquid with very little viscosity [53, 54, 55, 56].

Currently, the largest heavy-ion collider is the Large Hadron Collider (LHC) at CERN, whose construction finished in 2008. The SPS is used as injector to the LHC, accelerating the Pb beams to energies of 1.38 TeV. The first nucleus-nucleus collisions at LHC took place in 2010 using Pb beams at 2.76 TeV. Since then, the LHC has collided different configurations involving ions, including p-Pb at 2.76 TeV (2013), Pb-Pb at 5.02 TeV (2015), p-Pb at 8.16 TeV (2016), Xe-Xe at 5.44 TeV (2017), and at the end of 2018 LHC is planning to provide a larger set of Pb-Pb collisions at 5.02 TeV. There are four large experiments at the LHC called ALICE, CMS, ATLAS and LHCb. The four experiments are nowadays participating in the heavy-ion programme at LHC. Due to the large beam energies, the LHC is an ideal collider to study the QGP at very high temperatures, where one expects smaller QGP formation times and larger hot medium densities, compared to RHIC.

### 1.2.2 Geometry of nucleus-nucleus collisions

The number of particles produced in a nucleus-nucleus collision depends on the geometry of the collision. Since nuclei are extended objects made of nucleons (i.e. protons and neutrons), the number of nucleon-nucleon (NN) interactions increases the more head-on or central is the collision. The nucleons that participate in the collision are called participants while those that do not participate are referred to as spectators. The overlap region of the collision depends on the impact parameter  $\vec{b}$ , which is the transverse distance between the centres of the two colliding nuclei as shown in Figure 1.9.

The formation and characteristics of the QGP in nucleus-nucleus collisions depends on the number of colliding nucleons. To study the dynamics of the nuclear medium, the heavy-ion collisions are classified based on their centrality. The centrality  $c$  is defined as the fraction of the total nucleus-nucleus inelastic cross section  $\sigma_{\text{AB}}^{\text{inel}}$  determined within the area defined by the impact parameter  $b$ , and it is expressed as:

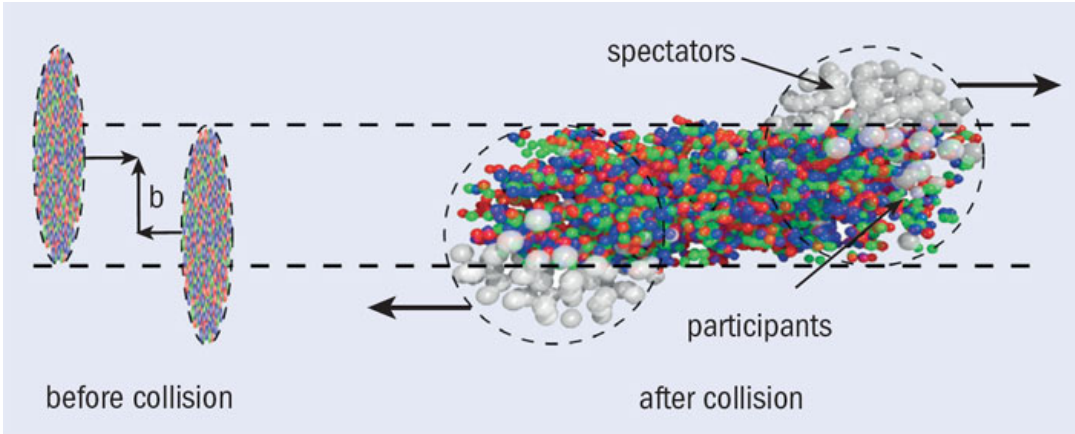


Figure 1.9: Illustration of two nucleus with impact parameter  $b$  before (left) and after (right) colliding. Figure taken from Ref. [43].

$$c = \frac{\pi b^2}{\sigma_{AB}^{inel}} \quad (1.9)$$

The collision centrality can be related to the number of participants  $N_{part}$  and the number of binary nucleon-nucleon collisions  $N_{coll}$  using a Glauber model. The Glauber model, developed in the 1950s by Roy Glauber, describes the collision between two nuclei as a superposition of independent NN interactions [57].

There are two ways of implementing the Glauber model, the optical and the Monte Carlo approaches. In the optical approach, the physical observables are computed using the optical limit which assumes a continuous nucleon density distribution. On the other hand, in the Monte Carlo approach, the two nuclei are simulated by distributing the nucleons according to their nuclear density profile, and then the nucleus-nucleus collisions are modelled, at random impact parameters, by computing the individual NN collisions [57].

An example of a heavy-ion collision described by the optical Glauber model geometry is shown in Figure 1.10. It represents the collision between a nucleus A with  $A$  nucleons and a nucleus B with  $B$  nucleons.

The tube located at a distance  $\vec{s}$  from the center of the nucleus A overlaps the tube located at a distance  $\vec{b} - \vec{s}$  from the center of the nucleus B. In this case, the nuclear overlap function  $T_{AB}(b)$  is defined as:

$$T_{AB}(b) = \int d\vec{s}^2 T_A(\vec{s}) T_B(\vec{b} - \vec{s}) \quad (1.10)$$

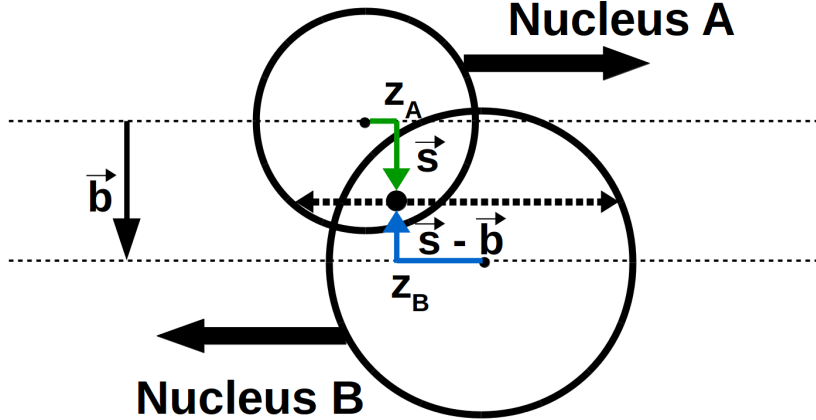


Figure 1.10: Schematic representation of the optical Glauber model geometry.

where  $T_A$  and  $T_B$  are the nuclear thickness functions of the nucleus A and B, respectively.

The nuclear thickness function is given by  $T(\vec{r}) = \int dz \rho(\vec{r}, z)$ , where  $\rho$  is the nuclear density distribution of a given nucleus, which is generally parametrised with a Wood-Saxon density profile [57]:

$$\rho(r) = \frac{\rho_0}{1 + \exp\left(\frac{r-r_0}{a}\right)} \quad (1.11)$$

where  $r$  is the distance to the center of the nucleus,  $a$  represents the width of the edge region of the nucleus called the skin depth,  $r_0$  is the mean radius of the nucleus and  $\rho_0$  is the nuclear density at the center of the nucleus. The average number of binary NN collisions  $\langle N_{\text{coll}} \rangle$  for a given impact parameter  $b$  is defined as:

$$\langle N_{\text{coll}}(b) \rangle = AB \cdot \langle T_{AB}(b) \rangle \cdot \sigma_{nn}^{\text{inel}} \quad (1.12)$$

where  $\sigma_{nn}^{\text{inel}}$  is the inelastic nucleon-nucleon cross section and  $\langle T_{AB}(b) \rangle$  is the average nuclear overlap function. Hence, the Glauber model provides a quantitative description of the geometry of the nuclear collision and can be used to estimate the variables ( $N_{\text{part}}$ ,  $N_{\text{coll}}$  and  $T_{AB}$ ) for a given centrality class.

Experimentally, the impact parameter of the collision can not be determined directly. However, the distribution of the number of soft particles scales with  $N_{\text{part}}$ . As a result, one can classify the events in different centrality classes by binning the measured distribution of charged particles, so that each bin contains the same fraction of the total integral. The mean parameters  $\langle N_{\text{part}} \rangle$  and  $\langle N_{\text{coll}} \rangle$ , can be then derived, for each

centrality class, by simulating the charged-particle distribution using a MC Glauber model. In addition, the collision centrality can sometimes be also inferred from the number of spectators determined from the measurement of the transverse energy in the forward region.

### 1.2.3 Evolution of heavy-ion collisions

The evolution of a nucleus-nucleus collision undergoes several steps, starting from the collision of the nuclei to the final production of hadrons. Figure 1.11 illustrates the main processes that occur during a heavy-ion collision associated to the production of the QGP.

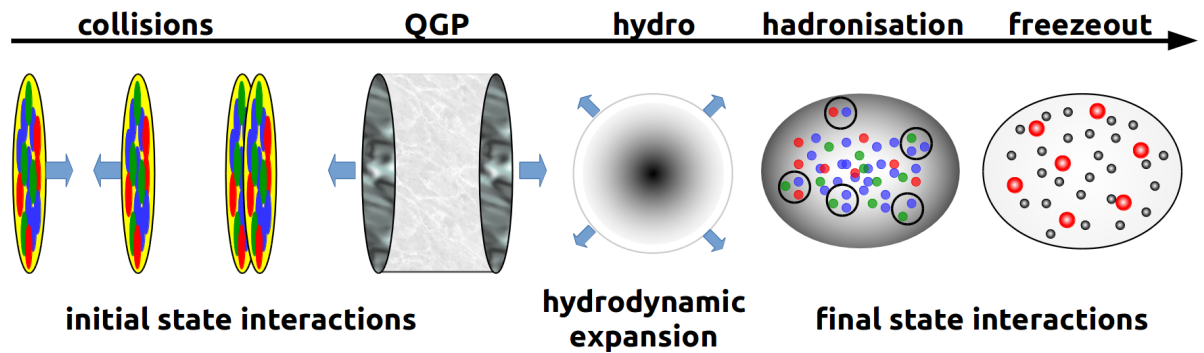


Figure 1.11: Sketch of the evolution of a relativistic heavy-ion collision.

1. Initial stage: At high energies, the two nuclei are Lorentz contracted along the axis of motion while approaching each other at almost the speed of light. As a consequence, the nucleons of each nuclei are also contracted increasing the number of gluons until it reaches the gluon saturation scale. The initial conditions can be described in various ways, depending on the physics to be addressed: the Glauber model or the effective theory called the Colour Glass Condensate are often used. When the two nuclei collide, the partons inside the geometrical overlap region of the two nuclei undergo parton-parton interactions.
2. QGP formation: The parton-parton interactions quickly start producing new particles increasing the density of the system until a phase transition is reached forming the QGP.

3. Hydrodynamical expansion: After the QGP is produced, the system evolves as a nearly-perfect fluid. It first expands longitudinally along the beam direction and then it expands in all directions until the QGP cools down back to the critical temperature.
4. Hadronisation: The medium undergoes a second phase transition back to a hadronic gas where the partons recombine into hadrons. In this phase, the system keeps expanding via hadron-hadron interactions until the average path length of the hadrons is as large as the size of the system.
5. Freeze-out: The hadron gas experience first a chemical freeze-out when the inelastic collisions between hadrons cease, fixing the composition of the particles. Subsequently, the system reaches a kinetic freeze-out when the elastic scatterings between hadrons also stop, fixing the kinematic distributions of the particles. Subsequently, the particles escape the medium and are reconstructed in the detector.

#### 1.2.4 Experimental probes of the QGP

The QGP can not be directly measured experimentally, since once it is created it only exists for a very short amount of time. Nonetheless, the QGP can be studied indirectly by measuring how the particles and the system produced in the collision are modified by the presence of the QGP. There are many experimental *signatures* that have been used to assess the different properties of the QGP, such as the enhancement of the strange quark production, suppression of the quarkonium yields, attenuation of the energy of jets, anisotropies in the azimuthal distribution of particles, among others. The production mechanism of each experimental probe depends on the momentum scale of the process. Signatures produced in processes involving large momentum transfer are called hard probes while those produced at low momentum scales are called soft probes.

The majority of the particles produced in heavy-ion collisions are soft and constitutes the bulk of the system. Soft probes are used to study the thermal and hydrodynamical evolution of the medium. The production yields of soft particles scale with  $N_{\text{part}}$ . The strange hadron yields and the elliptic flow are two examples of soft probes. On the other hand, hard probes are produced from the parton-parton hard scatterings during the initial stage of the collision. Hard probes are ideal tools to study the structure of

the system since they are produced early in a well-controlled manner<sup>7</sup> and often living through the QGP. The number of hard particles produced in the medium scales with  $N_{\text{coll}}$ . Some important hard probes used to study the nuclear medium includes the electroweak bosons, quarkonia and jets. The following subsections present a brief description on some of the soft and hard probes of the QGP.

#### 1.2.4.1 Elliptic flow

When the QGP is formed, it undergoes a collective expansion due to the large pressure gradient produced by the multiple partonic interactions during the heavy-ion collision. This collective expansion is known as flow. The magnitude of the flow tends to grow with the number of parton-parton interactions and it depends on the initial conditions of the collision. In a nucleus-nucleus collision the particles develop a strong radial flow and if the collision is non-central ( $b \neq 0$ ) then the spatial anisotropy of the overlap region leads to an additional anisotropic flow as shown in Figure 1.12.

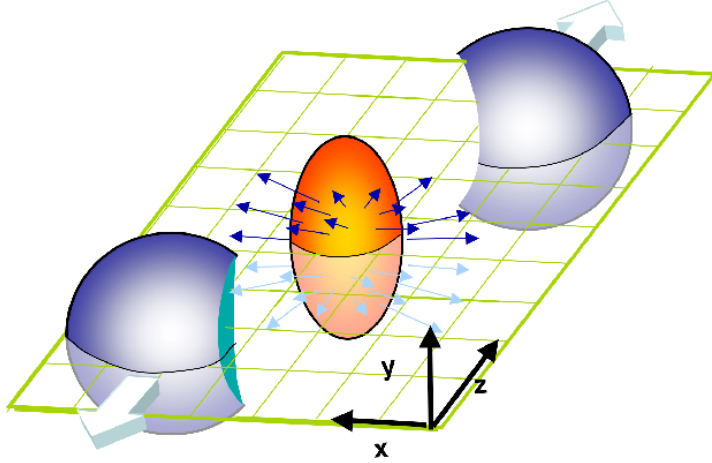


Figure 1.12: Sketch of the elliptic flow produced in non-central heavy-ion collisions. Figure taken from Ref. [58].

Experimentally, the anisotropic flow can be determined from the Fourier decomposition of the particle azimuthal angle  $\phi$  distribution with respect to the reaction plane  $\psi_{RP}$  [59]:

$$\frac{d^3N}{d^3\vec{p}} = \frac{1}{2\pi} \frac{d^2N}{p_T dp_T dy} \left( 1 + 2 \sum_{n=1}^{\infty} v_n \cos[n(\phi - \psi_{RP})] \right) \quad (1.13)$$

<sup>7</sup>The production cross section of hard probes can be computed using the QCD factorisation theorem.

where the Fourier coefficient  $v_2$  measures the strength of the elliptic flow and the reaction plane is derived from the direction of the beam ( $z$ -axis) and the impact parameter ( $x$ -axis) as presented in Figure 1.12.

An alternative way to derive the flow coefficients is by computing the Fourier decomposition of the two-particle azimuthal distribution defined as [59]:

$$v_n \{2\}^2 = c_n \{2\} = \langle \cos[n(\phi_1 - \phi_2)] \rangle \quad (1.14)$$

where  $c_n \{2\}$  is called the two-particle cumulant and the brackets represent the average over all particles and events. The advantage of using particle correlations is that the Fourier coefficients do not depend on the reaction plane determination, but non-flow contributions (e.g. resonance decays or back-to-back jets) can affect the measurements. Correlating more than two particles, such as four-particle correlations, can reduce the impact of the non-flow effects.

The elliptic flow of the medium is sensitive to the equation of states of the QGP [59] and bulk viscosity [60]. Furthermore, relativistic hydrodynamic calculations [61] predict that the elliptic flow of hadrons can approximately be expressed as  $v_2 \propto (p_T - \beta \cdot m_T)$ , where  $\beta$  is the average flow velocity and  $m_T$  is the transverse mass of the hadron, which is defined as  $m_T^2 = m^2 + p_T^2$ . As a consequence, the elliptic flow is expected to show a mass ordering where the more massive hadrons would have lower  $v_2$  values compared to the lighter hadrons.

The low  $p_T$ -dependence of the elliptic flow of strange hadrons measured at RHIC in Au-Au collisions at  $\sqrt{s_{NN}} = 200 \text{ GeV}$  is presented in Figure 1.13. The measurement of the elliptic flow of  $\pi^\pm$  mesons,  $K_s^0$  mesons, anti-protons and  $\Lambda$  baryons (with masses of 140, 498, 938 and 1116 MeV, respectively), shows the expected mass ordering pattern. Moreover, the good agreement between the RHIC results and the predictions using relativistic hydrodynamics assuming that the fluid flow is non-viscous, supported the conclusion that the QGP behaves as a nearly ideal fluid [62].

At the start of the LHC, the CMS collaboration performed a measurement of the two-particle angular correlations in p-p collisions producing high number of particles (referred as high-multiplicity collisions). Figure 1.14 presents the two-particle  $\Delta\eta$ - $\Delta\phi$  correlation function measured by the CMS collaboration in p-p collisions at  $\sqrt{s} = 7 \text{ TeV}$  [63], where  $\Delta\phi$  is the azimuthal angle difference between the two particles and  $\Delta\eta$  is the difference in their pseudorapidity. The results show a long-range structure ( $2.0 < \Delta\eta < 4.8$ ) of near-side ( $\Delta\phi \sim 0$ ) two-particle correlations, often called "ridge". The structure is seen for particles with  $1 \text{ GeV}/c < p_T < 3 \text{ GeV}/c$ , produced in high-multiplicity ( $N > 110$ ) p-p

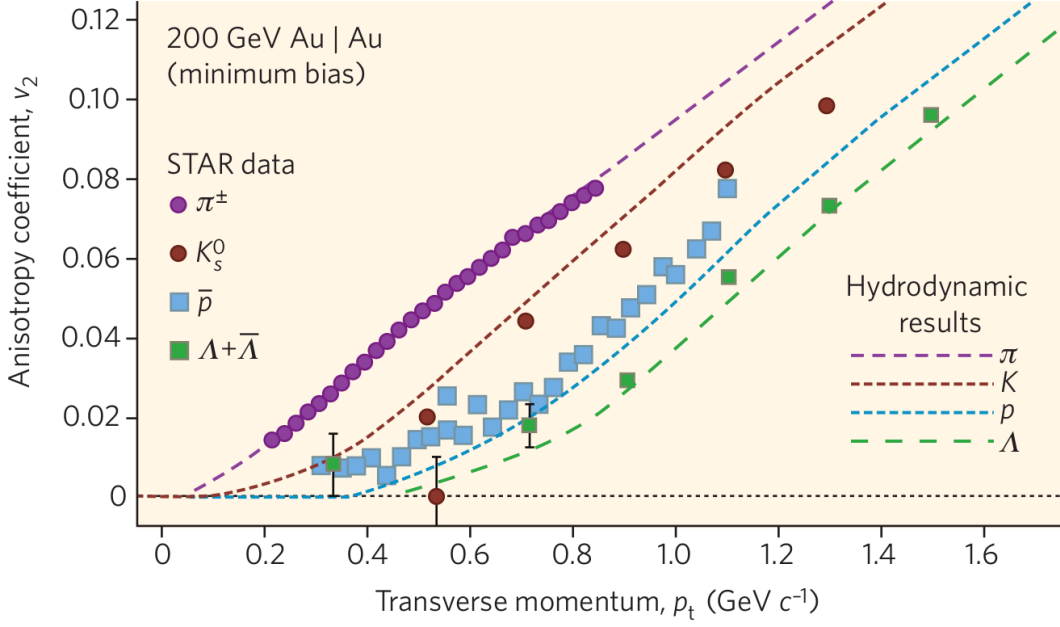


Figure 1.13: Elliptic flow distribution of as a function of transverse momentum for  $\pi^\pm$  mesons,  $K_s^0$  mesons, antiprotons and  $\Lambda$  baryons measured by STAR collaboration in Au-Au collisions at  $\sqrt{s_{\text{NN}}} = 200 \text{ GeV}$ . The results are compared with relativistic hydrodynamic calculations. Figure taken from Ref. [62].

collisions. A similar ridge-like structure had already been observed at RHIC in heavy-ion collisions [64], which was understood as a result of the hydrodynamic expansion of the QGP, but the phenomenon found in p-p collisions was completely unexpected at the time and it is still not fully understood yet.

#### 1.2.4.2 Strangeness enhancement

Strange quarks belong to the second generation of quarks and are roughly 20-40 times more massive than up and down quarks. The number of strange quarks involved in a decay can be quantified through the quantum number called strangeness, which can take values of  $+1$ ,  $-1$  and  $0$ , for strange quarks, strange anti-quarks, and the other quarks, respectively. Strangeness is conserved in strong and electromagnetic interactions, while it is not conserved in weak decays. In hadronic collisions, strange quark-antiquark pairs ( $s\bar{s}$ ) are produced in parton-parton interactions via gluon fusion ( $gg \rightarrow s\bar{s}$ ) or quark annihilation ( $q\bar{q} \rightarrow s\bar{s}$ ), and through gluon splitting ( $g \rightarrow s\bar{s}$ ) during the evolution of the system. The production of strange hadrons in proton-proton collisions is suppressed relative to hadrons made of light quarks (i.e. pions), due to the higher mass of the strange

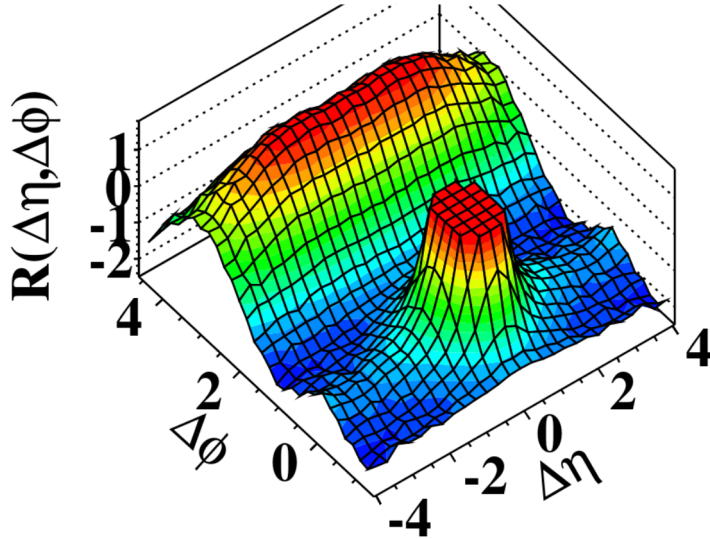


Figure 1.14: 3D display of the  $\Delta\eta$ - $\Delta\phi$  correlation function between two charged particles with  $1 \text{ GeV}/c < p_T < 3 \text{ GeV}/c$ , measured by the CMS collaboration in high multiplicity ( $N \geq 110$ ) p-p collisions at  $\sqrt{s} = 7 \text{ TeV}$ . Figure taken from Ref. [63].

quark.

In heavy-ion collisions, where the QGP is formed, it was proposed by Johann Rafelski and Rolf Hagedorn [65] in 1980, that the enhancement of strangeness could serve as a signature of the QGP. Due to the large gluon density and energy present in the hot medium, the gluon fusion becomes the dominant production mode of strange-quark pairs in the QGP. When the temperature of the QGP decreases and the partons hadronise, the production of hadrons containing strange (anti-)quarks is enhanced relative to the production of pions. Moreover, at high collision energies, the strange quarks can also bind to charm and bottom quarks during hadronisation, producing many exotic hadrons (e.g. strange D<sub>s</sub> or B<sub>s</sub> mesons) that would otherwise be rarely seen without the presence of the QGP. In summary, one expects an overall increase of strange-quark pair production, leading to an enhancement of the production of strange hadrons in central heavy-ion collisions compared to proton-proton collisions [66].

The enhancement of strange hadrons has been observed at SPS [67, 68] and RHIC [69]. The production yields in heavy-ion collisions of strange hadrons measured at RHIC and SPS are shown in Figure 1.15. The results show a clear enhancement of the production of strange baryons in heavy-ion collisions relative to p-p (at RHIC) or p-Be (at SPS) collisions, increasing for higher  $N_{\text{part}}$  (more central collisions) and strangeness content. This strangeness enhancement can be described using a thermal model based on a grand

canonical ensemble approach, suggesting the presence of a hot medium [66].

Recently, the ALICE collaboration published in [70] the observation of enhanced production of strange hadrons in high-multiplicity proton-proton collisions at  $\sqrt{s} = 7 \text{ TeV}$ , as presented in the right plot of Figure 1.15. The results at LHC show that the enhancement of the strangeness production increases as a function of charged-particle multiplicity from high-multiplicity p-p to p-Pb to Pb-Pb collisions. Therefore, further studies of the mechanism of strangeness production at high multiplicities are necessary to understand the evolution of small systems.

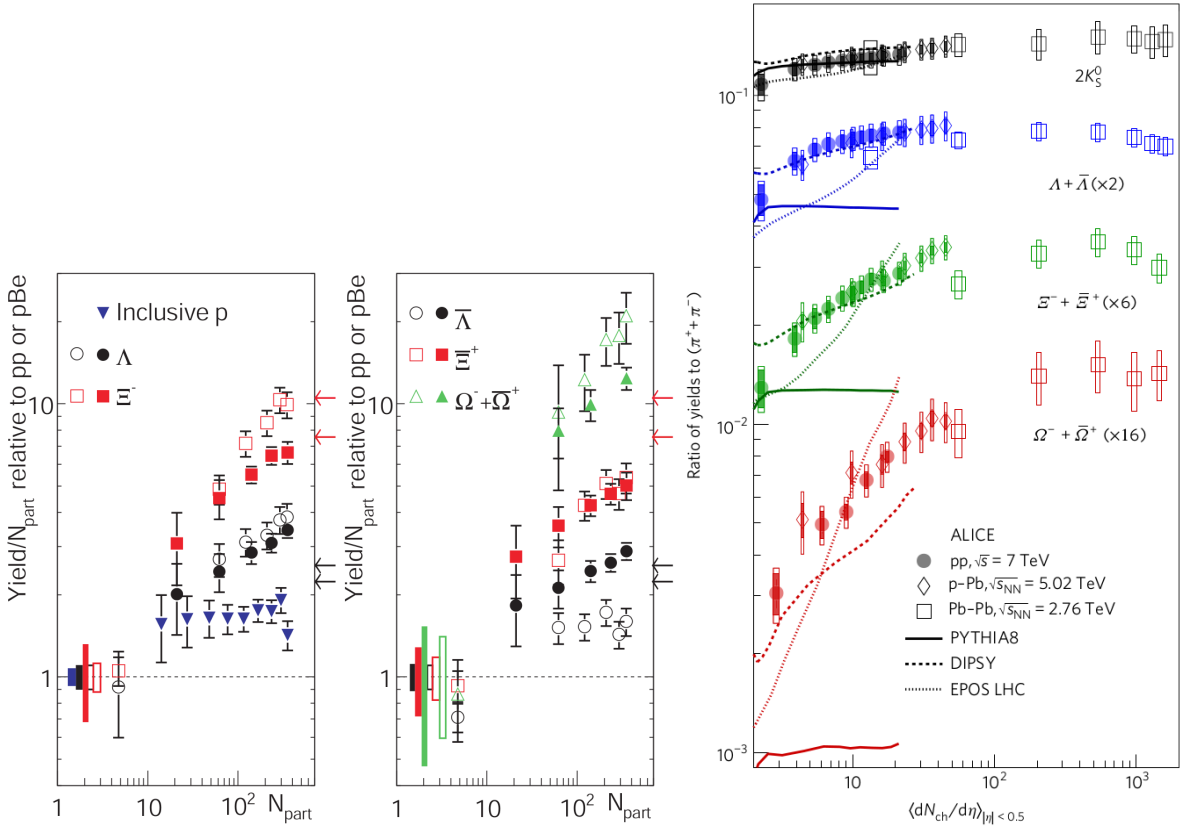


Figure 1.15: Left: Distribution of the yield of inclusive protons and strange baryons, measured by the STAR collaboration in Au-Au collisions at  $\sqrt{s_{\text{NN}}} = 200 \text{ GeV}$  (solid symbols) and by the NA57 collaboration in Pb-Pb collisions at  $\sqrt{s_{\text{NN}}} = 17.3 \text{ GeV}$  (empty symbols), relative to the corresponding yield in  $\text{p-p}$  (at RHIC) or  $\text{p-Be}$  (at SPS) collisions scaled by  $N_{\text{part}}$ . Figure from Ref. [69]. Right: Distribution of the  $p_{\text{T}}$ -integrated yield ratios of strange hadrons to pions as a function of the average charged-particle multiplicity measured in  $|\eta| < 0.5$  by the ALICE collaboration in  $\text{p-p}$ ,  $\text{p-Pb}$  and  $\text{Pb-Pb}$  collisions at  $\sqrt{s} = 7 \text{ TeV}$ ,  $\sqrt{s_{\text{NN}}} = 5.02 \text{ TeV}$  and  $\sqrt{s_{\text{NN}}} = 2.76 \text{ TeV}$ , respectively. Figure from Ref. [70].

### 1.2.4.3 Jet quenching

Energetic partons are produced in the hard scattering at the beginning of the collision. These scattered partons fragment into other colour-charged particles, which then create an ensemble of hadrons during the hadronisation process. The baryons and mesons produced at the end of the collision tend to move along the same direction as the original fragmented parton, forming a localised spray of particles called jet. The jets can be reconstructed by clustering hadrons and other particles around a given direction using a jet sequential recombination algorithm (e.g. anti- $k_t$  [71]).

In heavy-ion collisions, the hard partons lose energy when they traverse the hot medium either by multiple scattering with the medium constituents or by medium-induced gluon radiation. As a consequence, the energy of the jets is attenuated and the jets are considered quenched by the medium. The phenomenon of jet quenching in the QGP was first proposed in 1982 by James Bjorken. Bjorken suggested in [72] that the observation of events with two jets, where one of the jets escapes the QGP without losing energy while the other jet is fully quenched as shown in Figure 1.16, could be used as a probe to determine the presence of the QGP.

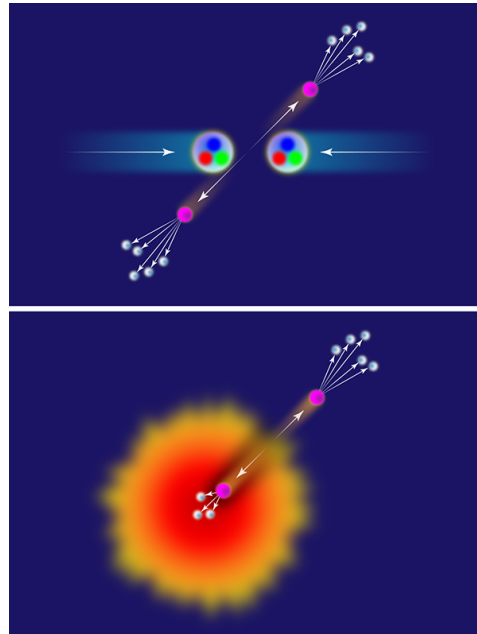


Figure 1.16: Sketch of the production mechanism of two jets in proton-proton (top) and heavy-ions (bottom) collisions. Figure taken from Ref. [73].

In order to quantify how the hot nuclear medium modifies the production of a given particle, one can measure the nuclear modification factor  $R_{AA}$  defined as:

$$R_{AA} = \frac{N_{AA}}{\langle N_{coll} \rangle N_{pp}} \quad (1.15)$$

where  $N_{AA}$  is the yield of particles measured per nucleus-nucleus collision,  $N_{pp}$  is the same yield measured per p-p collision, and  $\langle N_{coll} \rangle$  is the average number of binary nucleon-nucleon collisions. Proton-proton collisions are used as a reference since most of the events do not produce a QGP, even though it is not excluded that a hot medium could be formed in the most rare and violent p-p collisions.

The first direct observation of jet quenching was determined at RHIC, where the production of hadrons were found to be suppressed in central Au-Au collisions compared to p-p collisions. Figure 1.17 shows the nuclear modification factor of direct photons<sup>8</sup>, pions,  $\eta$  mesons, and charged hadrons measured at RHIC in central Au-Au collisions at  $\sqrt{s_{NN}} = 200$  GeV. The results show a strong suppression ( $R_{AA} \sim 0.2$ ) of the production of hadrons consistent with parton energy loss in the QGP<sup>9</sup>. In addition, the  $R_{AA}$  of direct photons is found to be consistent with unity (expected since photons do not interact strongly), which serves as a sanity check of the  $N_{coll}$  scaling.

In the case of LHC, an enhanced dijet asymmetry was observed in Pb-Pb collisions compared to proton-proton collisions. The dijet asymmetry is quantified by measuring the jet energy imbalance between the two highest transverse energy jets with an azimuthal angle separation of  $\Delta\phi = |\phi_1 - \phi_2| > \pi/2$ . The jet energy imbalance  $A_J$  is derived as:

$$A_J = \frac{E_{T1} - E_{T2}}{E_{T1} + E_{T2}} \quad (1.16)$$

where  $E_{T1}$  is the transverse energy of the most energetic jet among the pair of jets. Figure 1.18 presents the results, published by the ATLAS collaboration [76], of the dijet asymmetry distribution and the azimuthal angle between the two jets in different bins of centrality. The dijet asymmetry measured in Pb-Pb collisions at  $\sqrt{s_{NN}} = 2.76$  TeV are compared to the measurements from p-p collisions at  $\sqrt{s} = 7$  TeV and the simulated results derived using events from the Heavy Ion Jet INteraction Generator (HIJING) superimposed with PYTHIA events. The LHC results show a significant dijet energy imbalance in Pb-Pb collisions which increases with the centrality of the collision. The missing jet energy was later found in the form of low-momentum particles emitted at larger angles [77]. This dijet asymmetry is not seen in p-p collisions evidencing the strong jet energy loss present in the QGP.

---

<sup>8</sup>Photons not originating from the decay of hadrons.

<sup>9</sup>At low  $p_T$ , extra thermal photons can be created by the medium providing insights on its average temperature [74].

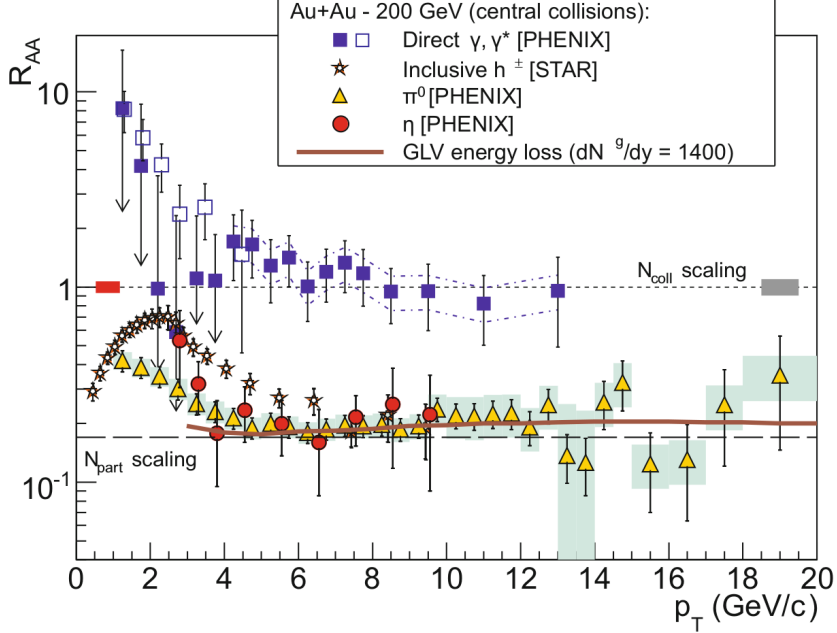


Figure 1.17: Distribution of the nuclear modification factor  $R_{AA}$  of direct photons, pions,  $\eta$  mesons and charged hadrons, measured at RHIC in central Au-Au collisions at  $\sqrt{s_{NN}} = 200 \text{ GeV}$  as a function of  $p_T$ . Theoretical predictions of radiative parton energy loss are also included. Figure taken from Ref. [75].

#### 1.2.4.4 Quarkonium production

Quarkonia ( $Q\bar{Q}$ ) are mesons composed of a heavy quark and its own anti-quark. Quarkonia can be classified as charmonia or bottomonia if they are made of charm quarks or bottom quarks, respectively. The first excited state of charmonia is called  $J/\psi$  meson while for bottomonia is called  $\Upsilon(1S)$  meson. The properties of quarkonia are non-perturbative but since the mass of the heavy quarks is comparable to the mass of the quarkonia, the quarks move inside the quarkonia much slower than the speed of light. As a result, the properties of quarkonia can be computed using an effective non-relativistic model. For instance, one way to describe the binding of the quarks is by using a Cornell potential [78] given by:

$$V_{Q\bar{Q}}(r) = -\frac{a}{r} + br \quad (1.17)$$

where  $r$  is the binding radius of the quarkonium,  $a$  is the coulombic interaction coupling, and  $b$  is the string tension. By solving the Schrödinger equation for the  $Q\bar{Q}$  potential, one finds several higher excited states of charmonia (e.g.  $\psi(2S)$ ) and bottomonia

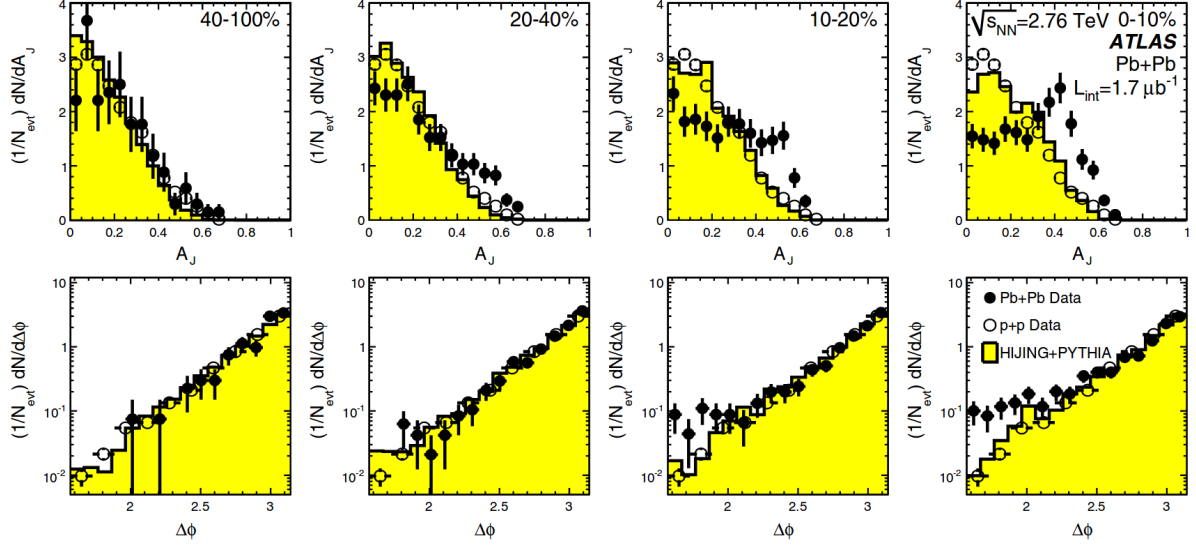


Figure 1.18: Dijet asymmetry measured by the ATLAS collaboration in lead-lead collisions at  $\sqrt{s_{NN}} = 2.76$  TeV (points) and proton-proton collisions at  $\sqrt{s} = 7$  TeV (open circles). The top panel shows the dijet asymmetry distributions and unquenched HIJING with superimposed PYTHIA dijets (solid yellow histograms), as a function of collision centrality. The bottom panel shows the distribution of the azimuthal angle between the two jets  $\Delta\phi$ , for data and HIJING+PYTHIA, also as a function of centrality. Figure taken from Ref. [76].

(e.g.  $\Upsilon(2S)$  and  $\Upsilon(3S)$ ), with lower binding energies and larger radius (i.e.  $r_{\Upsilon(1S)} < r_{\Upsilon(2S)} < r_{\Upsilon(3S)}$ ).

One of the first signatures suggested to probe the QGP was the suppression of  $J/\psi$  meson production. In 1986, Tetsuo Matsui and Helmut Satz [79] proposed that the  $J/\psi$  meson binding potential gets screened in the QGP due to the interactions with the free colour charged constituents of the hot medium. The Debye colour screening potential increases with the temperature of the medium until the binding potential can no longer hold the quarks together, and the quarkonium "melts". The binding potential of quarkonium states gets weaker for larger binding radius. As a result, the higher excited states of quarkonium are expected to be more dissociated at a given temperature compared to the ground state, leading to a sequential suppression of quarkonia.

The sequential suppression of bottomonium states has been observed at the LHC. Figure 1.19 shows the invariant mass distribution of dimuons measured by the CMS collaboration in Pb-Pb collisions at  $\sqrt{s_{NN}} = 5.02$  TeV [80]. The result is compared to the invariant mass distribution obtained by adding the bottomonium mass peaks extracted

from p-p collisions at  $\sqrt{s} = 5.02$  TeV on top of the Pb-Pb background and normalised to the  $\Upsilon(1S)$  mass peak in Pb-Pb. The comparison shows a clear suppression pattern where the  $\Upsilon(3S)$  meson is completely melted while part of the  $\Upsilon(2S)$  mass peak still survives. In the case of the  $\Upsilon(1S)$  meson, the feed-down contributions from excited state decays of  $\chi_b(nP) \rightarrow \Upsilon(1S)$  and  $\nu(nS) \rightarrow \Upsilon(1S)$ , can reach values up to 40% as measured by the LHCb collaboration for  $p_T^\Upsilon > 6$  GeV/c [81]. As a result, it is not clear if the observed suppression of the  $\Upsilon(1S)$  meson is due to deconfinement in the QGP or the dissociation of the excited states that decays to the  $\Upsilon(1S)$  meson.

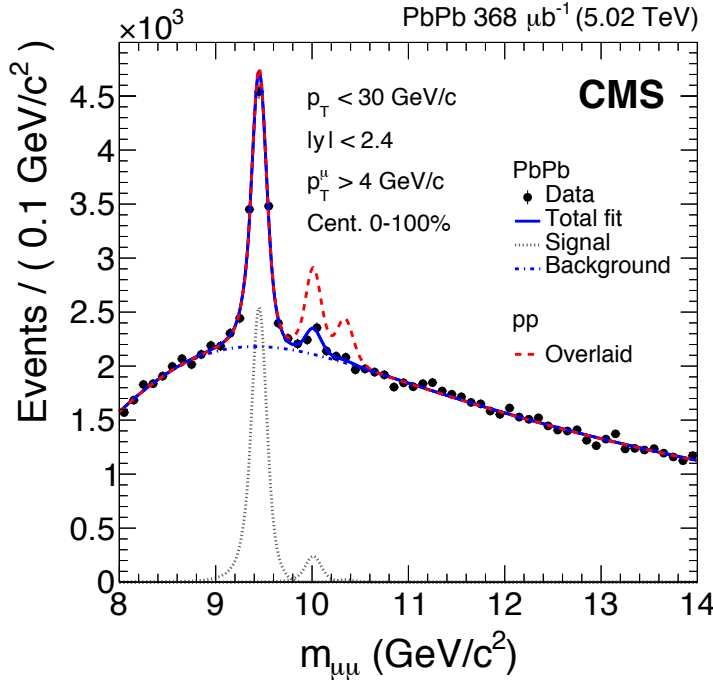


Figure 1.19: Dimuon invariant mass distribution measured by the CMS collaboration in Pb-Pb collisions at  $\sqrt{s_{NN}} = 5.02$  TeV. The total fit (solid blue line), the background component (dot-dashed blue line) and the individual  $\Upsilon(1S)$ ,  $\Upsilon(2S)$  and  $\Upsilon(3S)$  mass peaks (dotted gray lines) are shown. The dashed red line represents the p-p signal shapes added on top of the Pb-Pb background and normalised to the  $\Upsilon(1S)$  mass peak in Pb-Pb. Figure taken from Ref. [80].

The first evidence of  $J/\psi$ -meson anomalous suppression (i.e. beyond nuclear effects) was observed in Pb-Pb collisions at 158 GeV/nucleon by the NA50 collaboration at SPS [82]. The results at SPS showed that the  $J/\psi$ -meson cross section measured in peripheral collisions was consistent with the expectations from nuclear absorption while in central collisions it was more suppressed [83]. The measurement of the  $J/\psi$ -meson production in Au-Au collisions at  $\sqrt{s_{NN}} = 200$  GeV at RHIC [84] showed a similar level of

suppression at mid-rapidity ( $|y| < 0.35$ ) compared to SPS, despite the higher energy density at RHIC. In addition, the production of  $J/\psi$  mesons at forward rapidity ( $1.2 < |y| < 2.2$ ) was found to be more suppressed than at mid-rapidity.

To understand the measurements of  $J/\psi$ -meson production at SPS and RHIC, two explanations were proposed. The first one suggested that, apart from the anomalous suppression, the  $J/\psi$  meson production could also be enhanced at RHIC energies. According to [85], the  $J/\psi$  mesons could be regenerated in the most central collisions from the combination of initially uncorrelated charm quarks (i.e. not produced in the same hard scattering). The number of directly produced  $c\bar{c}$  pairs in central nucleus-nucleus collisions is expected to be small at SPS energies, but it can reach values around 10 (200) charm-quark pairs at RHIC (LHC) energies [86, 87]. The second explanation proposed that the production of  $J/\psi$  mesons at RHIC was mainly affected by an interplay between initial state effects (e.g. nuclear PDFs or CGC) and the dissociation of the excited states (e.g.  $\chi_c$  and  $\psi(2S)$ ) that contributes to the feed-down of the  $J/\psi$  meson.

The measurements of the  $J/\psi$ -meson production have also been performed at the LHC [88]. The results of the  $J/\psi$ -meson nuclear modification factor measured by the ALICE collaboration in the 0% – 20% most central Pb-Pb collisions at  $\sqrt{s_{NN}} = 2.76 \text{ TeV}$  are compared in Figure 1.20 to the results measured by the PHENIX collaboration in the 0% – 20% most central Au-Au collisions at  $\sqrt{s_{NN}} = 200 \text{ GeV}$ . The  $J/\psi R_{AA}$  measured at the LHC is larger than the one measured at RHIC at low  $J/\psi$  meson  $p_T$ , which can so far only be explained by the presence of regeneration.

#### 1.2.4.5 Electroweak boson production

Electroweak particles, such as W bosons and Z bosons, are produced in the parton-parton hard scattering and they do not interact strongly with the nuclear medium produced in the heavy-ion collisions. As a result, electroweak bosons are good probes of the initial stage of the proton-nucleus (p-A) and nucleus-nucleus (A-A) collisions, but they do not probe the QGP. The dominant production mode of electroweak bosons in heavy-ion collisions is via the annihilation of a light quark and anti-quark. The large momentum scales involved in the production of weak bosons allow to derive precise calculations of their partonic cross sections using pQCD.

The production yields of electroweak bosons in p-A or A-A collisions are affected by the mix of protons and neutrons in the colliding nucleus (isospin effect), and the depletion (shadowing) or enhancement (anti-shadowing) of the PDFs in the nucleus. Thus, the measurement of the electroweak boson production in heavy-ion collisions can be used

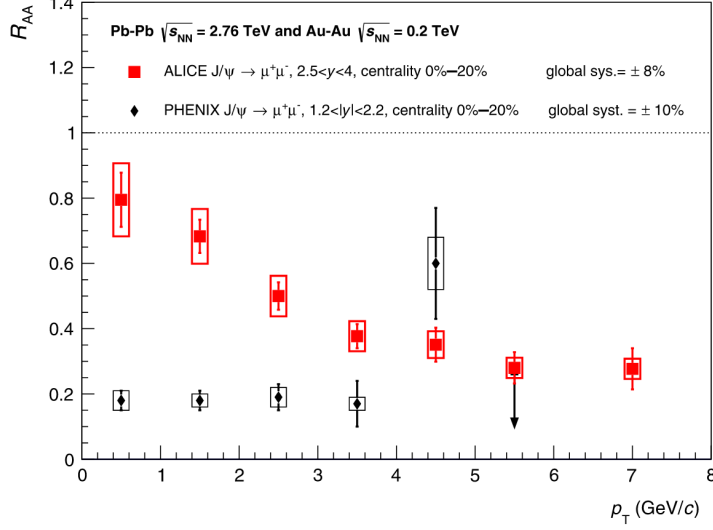


Figure 1.20: Nuclear modification factor of  $\text{J}/\psi$  meson as a function of transverse momentum measured by the ALICE collaboration in the 0% – 20% most central Pb-Pb collisions at  $\sqrt{s_{\text{NN}}} = 2.76$  TeV compared to results from the PHENIX collaboration measured in the 0% – 20% most central Au-Au collisions at  $\sqrt{s_{\text{NN}}} = 200$  GeV. Figure taken from Ref. [88].

to set constraints to the global fits of the nuclear PDFs. In the case of A-A collisions, the measurement of the nuclear modification factor of Z bosons at the LHC in Pb-Pb collisions at  $\sqrt{s_{\text{NN}}} = 2.76$  TeV [89], presented in Figure 1.21, shows that the production of weak bosons is not modified by the hot nuclear medium and can then be used as a *standard candle* to check, at first order, the binary scaling ( $R_{\text{AA}} = 1$ ) and indirectly determine the centrality of the collision.

## Summary

Our understanding of the QGP has expanded substantially since the last 20 years. The first evidence of its existence was found at SPS, after studying the suppression of  $\text{J}/\psi$  mesons and the strangeness enhancement in Pb-Pb collisions. Years after, the first observation of the QGP was claimed at RHIC, supported by a vast amount of experimental signatures such as jet quenching, charmonium suppression, strangeness enhancement and collectivity. The QGP found at RHIC turns out to behave as a nearly perfect dense fluid. The QGP was later also observed at the LHC, which has provided further knowledge on the properties of the QGP at TeV energies. In addition, the LHC experiments have also observed hints of the formation of a collective medium in small systems such as

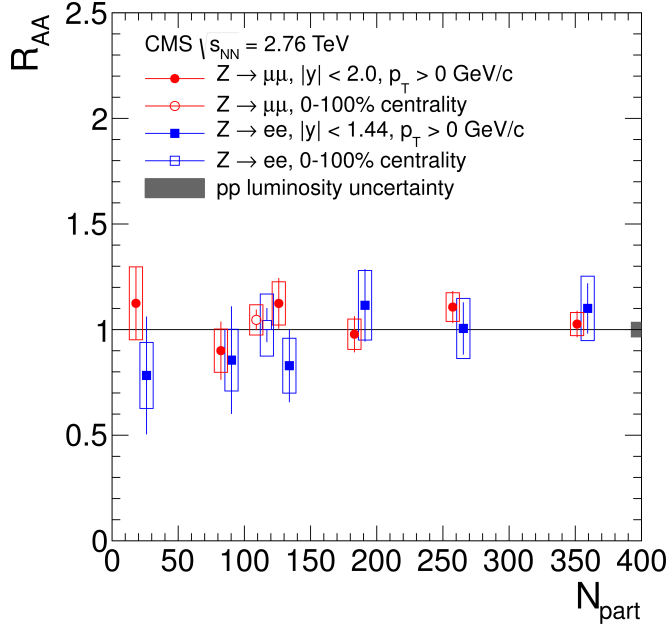


Figure 1.21: Nuclear modification factor  $R_{AA}$  of  $Z \rightarrow e^+e^-$  (blue squares) and  $Z \rightarrow \mu^+\mu^-$  (red circles) events as a function of  $N_{part}$  measured by the CMS collaboration in Pb-Pb collisions at  $\sqrt{s_{NN}} = 2.76$  TeV. The open points represent the centrality-integrated  $R_{AA}$  and the vertical lines (boxes) correspond to statistical (systematic) uncertainties. Figure taken from Ref. [89].

high-multiplicity p-p collisions, which is currently thoroughly investigated as it could correspond to small droplets of QGP.

The production of  $J/\psi$  mesons in heavy-ion collisions has shown a rich phenomenology and will be the main topic of Chapter 4, where the analysis of charmonia in Pb-Pb collisions will be presented. These results provide new insights on the production of non-prompt  $J/\psi$  mesons (i.e. from b-hadron decays) and  $\psi(2S)$  mesons, extending the coverage to higher charmonium  $p_T$  ranges.

Electroweak bosons are sensitive probes of the initial state of the collision and the measurement of their production in heavy-ion collisions can be used to constrain the nuclear PDFs, which are crucial theoretical inputs for a better description of the QGP formation. In Chapter 3, this thesis reports the first measurement of significant nuclear modification of W-boson production.

## EXPERIMENTAL SETUP

This chapter provides a brief overview of the experimental setup employed to acquire the data used in this thesis. The data is derived from high energy collisions of protons and lead ions recorded by the Compact Muon Solenoid (CMS) detector. The Large Hadron Collider (LHC) and the settings of the particle collisions are described in Section 2.1. The main features of the CMS detector and its components are detailed in Section 2.2.

### 2.1 The Large Hadron Collider

The Large Hadron Collider is currently the largest and highest-energy particle accelerator in the world. It is installed in an underground tunnel of 26.7 km in circumference, located as deep as 175 m underground beneath the border between France and Switzerland. The construction of the LHC was handled by CERN and took almost 30 years. The LHC is designed to accelerate and collide beams of protons or heavy ions (e.g Pb nuclei). Before being injected into the LHC, particles are accelerated through a chain of accelerators housed at CERN. Each accelerator boosts the energy of the particles and transfers them to the next machine. The accelerator complex for the LHC is presented in Section 2.1.1 and a short description of the LHC detectors is given in Section 2.1.2. The concept of luminosity is introduced in Section 2.1.3, and brief overview of the LHC schedule and heavy-ion schemes used during 2015-2016, are presented in Section 2.1.4 and Section 2.1.5, respectively.

### 2.1.1 Accelerator complex

There are two main injection chains for the LHC, one optimised for protons and the other for Pb nuclei ( $Pb^{82+}$ ). Figure 2.1 shows a schematic diagram of the LHC injection chains for protons and Pb ions represented with red and blue arrows, respectively.

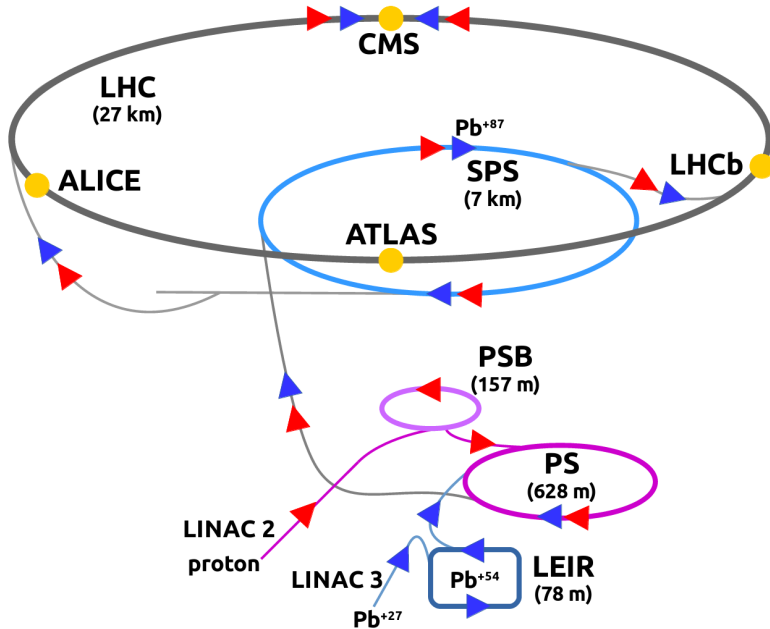


Figure 2.1: Schematic diagram of the LHC injection chain for protons and Pb nuclei. The proton and Pb ion trajectories are indicated with red and blue arrows, accordingly. The location of each LHC detector is also included.

Protons are extracted from a gas of hydrogen atoms by stripping off their electrons in a duoplasmatron, and are initially accelerated to an energy of 50 MeV with radio-frequency (RF) cavities in the linear accelerator Linac-2. Afterwards, they are sent to the Proton Synchrotron Booster (PSB), which is composed of four superimposed synchrotron rings that group the protons into bunches and accelerate them to 1.4 GeV. Six proton bunches from the PSB are sequentially fed into the Proton Synchrotron (PS), where they are accelerated to 25 GeV and further split into 72 bunches separated in time by 25 ns. The proton beam is further accelerated to 450 GeV in the Super Proton Synchrotron (SPS) and alternately injected in the two LHC beam pipes, one beam pipe in the clockwise direction and the other in the counter-clockwise direction. Conventional electromagnets are used to keep the particles circulating in the PSB, PS and SPS accelerators.

The heavy-ion accelerator chain was initially designed in the 1990s for the SPS fixed-

target experiments and then upgraded in the 2000s for the LHC. The Electron Cyclotron Resonance Ion Source (ECRIS) is used to produce heavy ions. In the case of lead, a beam of  $\text{Pb}^{27+}$  ions with an energy of 2.5 keV/nucleon is extracted from the ECRIS every 200  $\mu\text{s}$ , and then accelerated to 250 keV/nucleon with a 100 MHz RF quadrupole (RFQ). The ion beam is sent afterwards to the linear accelerator Linac-3, which accelerates the Pb ions to 4.2 MeV/nucleon and transfers them to the Low Energy Ion Ring (LEIR). The  $\text{Pb}^{27+}$  ions are passed through a 0.3  $\mu\text{m}$ -thick carbon foil in the Linac-3–LEIR transfer line, stripping them to  $\text{Pb}^{54+}$  ions. The LEIR accelerates the  $\text{Pb}^{54+}$  ions to 72 MeV/nucleon and packs them in bunches using electron cooling. Every 3.6 s, the LEIR feeds two bunches into the PS ring and up to 16 bunches are accumulated, forming a batch, before being transferred to the SPS. The PS batch is compressed to a time interval of 100 ns, and accelerated to 5.9 GeV/nucleon. When the  $\text{Pb}^{54+}$  ions are sent to the SPS, they are fully stripped ( $\text{Pb}^{82+}$  ions) through an aluminium foil. The SPS accelerates up to twelve  $\text{Pb}^{82+}$  ion batches from the PS to 176.4 GeV/nucleon and then injects them into the LHC.

The LHC consists of eight straight sections called insertion regions (IR), connected by eight arc sections as shown in Figure 2.2. The size and trajectory of the particle beams are controlled, in each arc section of the LHC, with a series of superconducting magnets made of Niobium-Titanium which are kept at a temperature of 1.9 K with superfluid Helium-4. Dipole magnets are used to bend the trajectory of particles, while quadrupole magnets focus the beam. Moreover, each particle beam is accelerated in IR4 with eight RF superconducting cavities operated at 400 MHz. The LHC beam dumping system, employed to safely stop the particle beams, is located at IR6. In addition, to protect the LHC from beam losses and absorb the beam halo, a collimation system is installed at IR3 and IR7, dedicated for beam momentum and betatron cleaning, respectively. The other four insertion regions house each of the four main LHC detectors, where the beams are collided in their corresponding interaction point (IP).

### 2.1.2 Detectors

The four main detectors installed in the LHC ring are:

- A Large Ion Collider Experiment (ALICE) [91]: a particle detector located at IP2, specialised on the measurement of the properties of nuclear matter at high energy densities. The main interest of the ALICE collaboration is the study of the QGP and the different aspects of heavy-ion physics. The ALICE detector is divided in three sets of subdetectors: the global event detectors are used to characterise

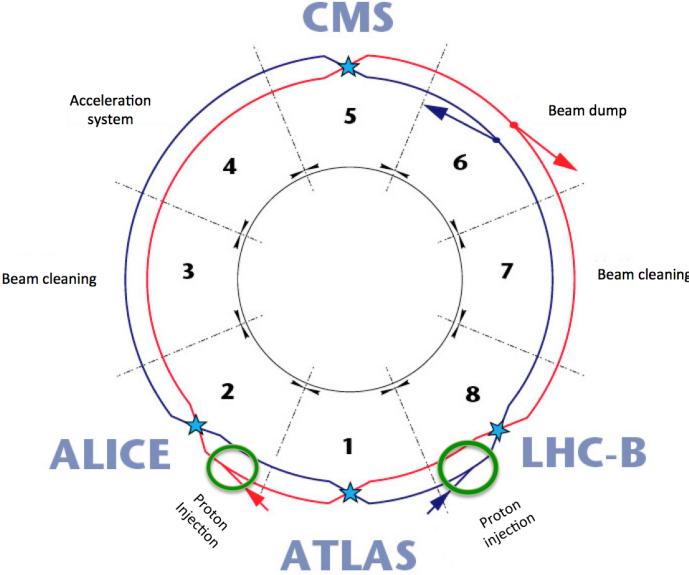


Figure 2.2: Schematic diagram of the LHC layout. Figure taken from Ref. [90].

the geometry of the collisions, the central barrel detectors can track charged particles down to low momentum and identify hadrons and electrons, and the muon spectrometer can reconstruct muons in the forward region.

- A Toroidal LHC ApparatuS (ATLAS) [92]: a general-purpose particle detector located at IP1, optimised for particle collisions at the highest rates and energies achieved in the LHC. It consists of a toroidal magnetic system, an inner tracker, an electromagnetic and hadronic calorimeter, and a muon spectrometer. It is able to measure the energy of electromagnetic particles and hadrons, determine the momentum of charged particles, reconstruct jets, and identify muons with high precision. The ATLAS collaboration is involved in different physic areas including the discovery of the Higgs boson, searches for physics beyond the SM, precision measurements of electroweak and top-quark properties, and heavy-ion physics.
- Compact Muon Solenoid (CMS) [1]: a multi-purpose particle detector located at IP5. It has a similar design as the ATLAS detector covering the same physics areas. The CMS detector and its inner components are detailed in Section 2.2.
- LHCb [93]: a single-arm forward spectrometer located at IP8, designed to precisely measure the decays of hadrons containing bottom quarks. It is able to distinguish

between the interaction point and the b-hadron decay vertex, perform particle identification, measure the energy of electrons, photons and hadrons, and reconstruct the trajectories of charged particles. The research programme of the LHCb experiment nowadays covers heavy-flavour, QCD, electroweak and heavy-ion physics. LHCb can also operate in fixed-target mode by injecting a small amount of a noble gas (e.g. helium) around its collision region inside the beam pipe.

### 2.1.3 Luminosity

The performance of the LHC can be characterised based on its delivered luminosity. The higher the luminosity of the collider, the more particle interactions occur when the beams are collided. The number of interactions per unit time  $dN/dt$ , produced in a given reaction, is proportional to the cross section  $\sigma_r$  of the corresponding process, as defined in:

$$\frac{dN}{dt} = \mathcal{L}\sigma_r \quad (2.1)$$

where  $\mathcal{L}$  represents the instantaneous luminosity of the particle collisions. In the case of circular beam profiles, the instantaneous luminosity depends on several factors:

$$\mathcal{L} = \frac{k_b N_{b,1} N_{b,2} f_{rev} \gamma}{4\pi\epsilon_n \beta^*} F \quad (2.2)$$

where  $\gamma$  is the Lorentz gamma factor,  $k_b$  is the number of bunches collided,  $N_{b,1}$  and  $N_{b,2}$  are the number of particles per bunch in the two beams,  $f_{rev} = 11245$  Hz is the revolution frequency at the LHC,  $\epsilon_n$  is the normalised transverse beam emittance,  $\beta^*$  is the beta-function defined at the interaction point, and  $F$  is a geometric reduction factor due to the angle at which the two beams collide. The integrated luminosity is derived by integrating the instantaneous luminosity over a given period of time.

### 2.1.4 LHC schedule

The LHC started operations in 2008, and delivered collision data during its first running period (labelled as Run-1) until 2013, followed by a long shut-down (LS1) period of 2 years dedicated to upgrade the machine. The second period of LHC operations (Run-2) started on 2015 and will conclude at the end of 2018. During Run-1, the LHC performed proton-proton (p-p) collisions at a center-of-mass (CM) energy of  $\sqrt{s} = 0.9$  TeV and  $\sqrt{s} = 2.36$  TeV

in 2009, and p-p collisions at  $\sqrt{s} = 7\text{TeV}$  and lead-lead (Pb-Pb) collisions at a nucleon-nucleon CM energy of  $\sqrt{s_{\text{NN}}} = 2.76\text{TeV}$  between 2010 and 2011. In addition, the LHC collided protons at  $\sqrt{s} = 8\text{TeV}$  in 2012, and proton-lead (p-Pb) at  $\sqrt{s_{\text{NN}}} = 5.02\text{TeV}$  in 2013. Afterwards, the Run-2 period started with p-p collisions at  $\sqrt{s} = 13\text{TeV}$  in 2015, followed by p-p collisions at  $\sqrt{s} = 5.02\text{TeV}$  and Pb-Pb collisions at  $\sqrt{s_{\text{NN}}} = 5.02\text{TeV}$  in 2015, p-Pb collisions at  $\sqrt{s_{\text{NN}}} = 8.16\text{TeV}$  in 2016, p-p collisions at  $\sqrt{s} = 5.02\text{TeV}$  and Xenon-Xenon collisions at  $\sqrt{s_{\text{NN}}} = 5.16\text{TeV}$  in 2017, and will finish with Pb-Pb collisions at  $\sqrt{s_{\text{NN}}} = 5.02\text{TeV}$  at the end of 2018.

### 2.1.5 Heavy-ion schemes in 2015-2016

The LHC heavy-ion physics programme began in 2010, and has since then provided data from p-Pb and Pb-Pb collisions at various beam energies. The results presented in this thesis are based on heavy-ion data taken between 2015 and 2016. The charmonium analysis, detailed in Chapter 4, uses data from p-p and Pb-Pb collisions at  $\sqrt{s_{\text{NN}}} = 5.02\text{TeV}$  taken in 2015, while the W-boson analysis, described in Chapter 3, utilises p-Pb collision data recorded in 2016.

In 2015, the LHC programme dedicated to heavy-ion physics took place during four weeks between November and December. The first week was dedicated to p-p collisions at  $\sqrt{s} = 5.02\text{TeV}$  to create a reference sample for the Pb-Pb collision data. Each proton beam was accelerated to 2.51 TeV. The number of proton bunches were initially 44 and was sequentially increased during the week to a maximum of 1825 bunches. The subsequent week, the LHC beam settings were modified to collide two beams of  $\text{Pb}^{82+}$  ions at  $\sqrt{s_{\text{NN}}} = 5.02\text{TeV}$ . The LHC started accelerating ten Pb bunches to 2.51 TeV/nucleon, and then progressively increased the number of Pb bunches until it reached 518 at the end of the Pb-Pb data taking. The Pb beam lifetime was shorter than for protons due to the large ultraperipheral electromagnetic interactions between Pb ions, requiring to refill the beams more often. All experiments took Pb-Pb collision data, including LHCb for the first time [94]. The integrated luminosity of the Pb-Pb collision data is shown in the left plot of Figure 2.3.

The following year, asymmetric collisions of  $\text{Pb}^{82+}$  nuclei with protons were performed between November 7th and December 4th. Several beam configurations were implemented in 2016 to fulfil the interests of each experiment: ALICE requested p-Pb data at  $\sqrt{s_{\text{NN}}} = 5.02\text{TeV}$ , CMS and ATLAS asked for p-Pb data at  $\sqrt{s_{\text{NN}}} = 8.16\text{TeV}$  with an integrated luminosity of at least  $\mathcal{L} = 100 \text{ nb}^{-1}$ , and LHCb requested p-Pb collisions at  $\sqrt{s_{\text{NN}}} = 8.16\text{TeV}$  complemented with a reversal of the beam direction. After careful plan-

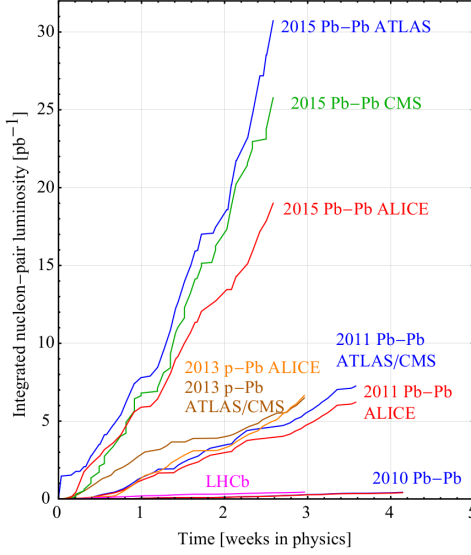


Figure 2.3: Integrated nucleon-pair luminosity delivered by the LHC to each experiment during Pb-Pb collisions at  $\sqrt{s_{NN}} = 5.02\text{ TeV}$ . The integrated luminosity of p-Pb collisions at  $\sqrt{s_{NN}} = 5.02\text{ TeV}$  and Pb-Pb collisions at  $\sqrt{s_{NN}} = 2.76\text{ TeV}$  are included for comparison. Figure taken from Ref. [94].

ning, the first ten days were dedicated to p-Pb collisions at  $\sqrt{s_{NN}} = 5.02\text{ TeV}$  optimised for ALICE. Afterwards, the LHC spent two weeks on p-Pb collisions at  $\sqrt{s_{NN}} = 8.16\text{ TeV}$ . At the beginning of the p-Pb collisions at  $\sqrt{s_{NN}} = 8.16\text{ TeV}$ , the proton beam was composed of 702 bunches at 6.5 TeV moving in the clockwise direction, while the Pb beam was made of 548 bunches at 2.56 TeV/nucleon moving in the anti-clockwise direction, around the LHC rings. The LHC then proceeded to reverse the beam directions after the integrated luminosity accumulated in CMS and ATLAS reached half of the requested value ( $\sim 60\text{ nb}^{-1}$ ), and kept colliding 540 Pb bunches with 684 proton bunches during the last nine days. At the end of the heavy-ion data taking period, the LHC managed to deliver a total integrated luminosity of  $\mathcal{L} = 188\text{ nb}^{-1}$  of p-Pb data to the CMS experiment as shown in Figure 2.4. The beam settings used by LHC during the heavy-ion collision programme performed in 2015 and 2016 are summarised in Table 2.1.

## 2.2 The Compact Muon Solenoid

The CMS [1] is a multi-purpose particle detector housed in an underground cavern at IP5 of the LHC. The CMS experiment is integrated, at the time of writing this thesis, by an international collaboration of over 5600 members from around 215 institutes from

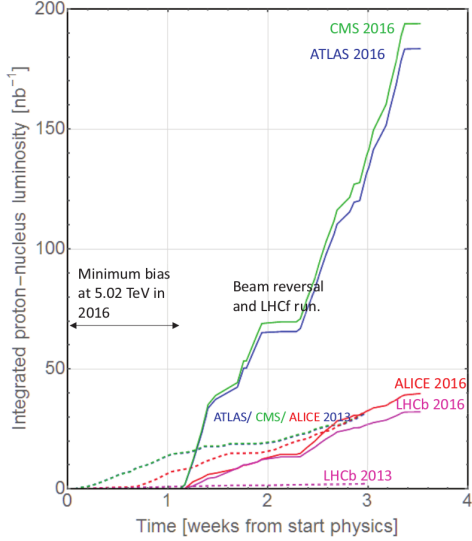


Figure 2.4: Integrated proton-nucleus luminosity delivered by the LHC to each experiment during p-Pb collisions at  $\sqrt{s_{NN}} = 8.16 \text{ TeV}$  (solid lines). The integrated luminosity of p-Pb collisions at  $\sqrt{s_{NN}} = 5.02 \text{ TeV}$  (dashed lines) is included for comparison. Figure taken from Ref. [95].

Variable	p-p 2015	Pb-Pb 2015	p-Pb 2016
Fill no.	4647	4720	5562
Collision energy $\sqrt{s_{NN}}$ [TeV]	5.02	5.02	8.16
Pb beam energy $E_{\text{Pb}}$ [TeV/nucleon]	-	2.51	2.56
Beam energy $E_p$ [TeV/proton]	2.56	6.37	6.5
Pb ions per bunch $N_b^{\text{Pb}}$ [ $10^8$ ]	-	2.0	2.1
Protons per bunch $N_b^p$ [ $10^{10}$ ]	10.1	-	2.7
No. of Pb bunches $k_b^{\text{Pb}}$	-	518	540
No. of proton bunches $k_b^p$	1825	-	684
No. of colliding bunches $k_c$	1813	491	513
$\beta^*$ [m]	4	0.8	0.6
Crossing angle [ $\mu\text{rad}$ ]	170	145	140
Pb beam emittance $\epsilon_n^{\text{Pb}}(x, y)$ [ $\mu\text{m}$ ]	-	2.1	1.6
Pb bunch length $\sigma_z^{\text{Pb}}$ [m]	-	0.09	0.9
CMS peak lumi. $\mathcal{L}^{\text{peak}}$ [ $10^{27} \text{ cm}^{-2} \text{ s}^{-1}$ ]	$3.4 \times 10^5$	3	869
CMS integrated lumi. $\mathcal{L}_{\text{int}}$ [ $\text{nb}^{-1}$ ]	28820	0.6	188

Table 2.1: LHC beam parameters during the highest luminosity physics fills. The luminosity values are averages for CMS. Information extracted from Ref. [96].

## 2.2. THE COMPACT MUON SOLENOID

46 countries. The CMS is composed of a central barrel in the mid-rapidity region closed by two endcap disks, one on each side of the IP, forming a hermetic cylindrical detector. The CMS detector consists of four main subdetector systems: the silicon tracker, the Electromagnetic CALorimeter (ECAL), the Hadronic CALorimeter (HCAL) and the muon chambers. A superconducting solenoid magnet placed in the barrel section generates a magnetic field of 3.8 T. The tracking system, the ECAL and the HCAL, are located within the solenoid volume, while the muon system is placed between the layers of the flux-return yoke, which confines the magnetic flux. A sectional view of the CMS detector including the number of channels per subdetector, in its 2015-2016 configuration, is shown in Figure 2.5.

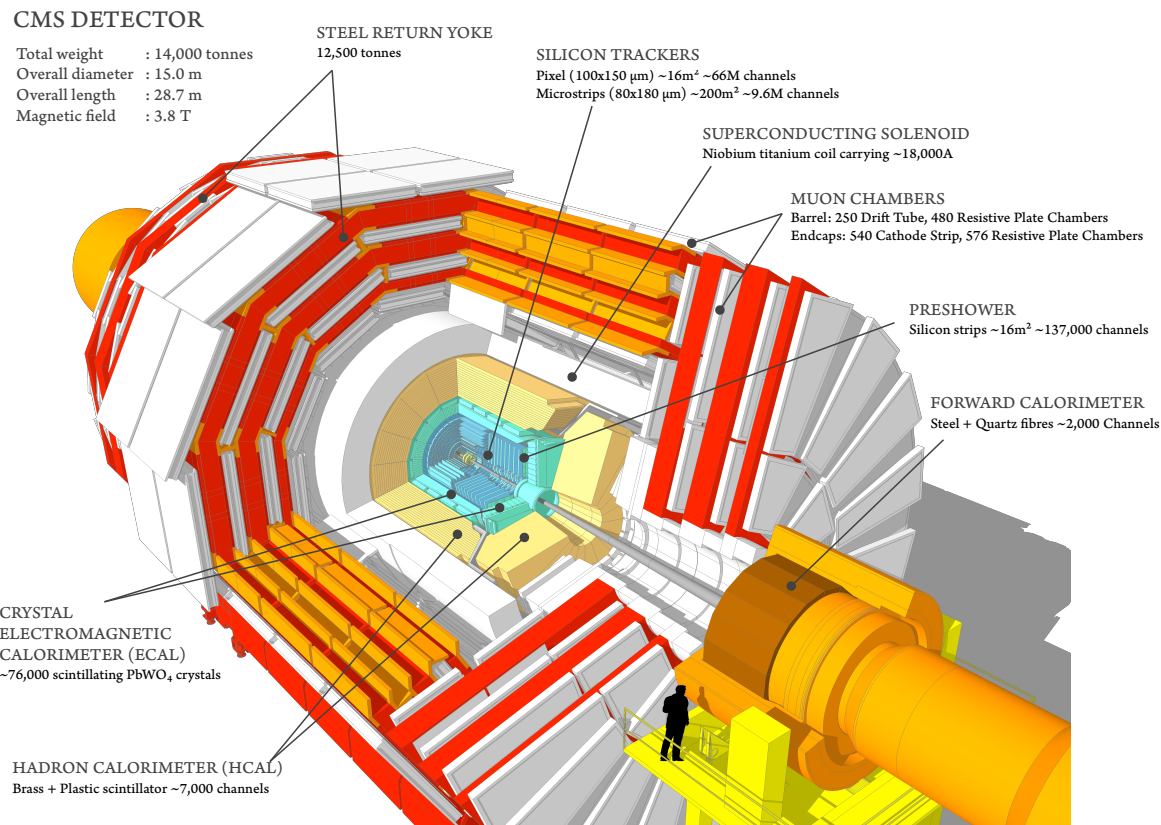


Figure 2.5: Cutaway view of the CMS detector in its configuration used during 2015 and 2016. Labels and basic details of each subdetector are included. [97]

One of the main components of the CMS detector is its superconducting solenoid magnet of 6 m internal diameter and 12.5 m length. The magnet produces a uniform magnetic field of 3.8 T in the central region by supplying an electric current of 18.1 kA

through a four-layer winding coil made of NbTi wire. To be able to sustain the large electric currents, the solenoid coil is thermally insulated within a vacuum volume and operated in superconducting mode at a temperature of 4.6 K with a thermal-siphon cooling system fed with liquid helium. The flux of the magnetic field outside the barrel is returned through a massive steel yoke of 10000 tons divided in five barrel wheels and four endcap disks at each end. In case there is a major system fault or the magnet suffers a superconducting-to-resistive transition (quench), the electric power source is immediately disconnected and the stored magnetic energy is quickly discharged through a 30 mΩ dump resistor placed outdoors.

The coordinate system of the CMS detector is centred at the interaction point. It is oriented in such a way that the  $x$ -axis points radially inward to the centre of the LHC ring while the  $y$ -axis points upward perpendicular to the LHC plane. The  $z$ -axis is defined parallel to the beam. By convention, the positive  $z$ -direction is defined along the counter-clockwise beam direction. For asymmetric collisions, such as p-Pb, it is later reversed (if necessary) to match the proton-going direction, so that the "forward" (low Bjorken- $x$ ) physics corresponds to the "forward" ( $\eta > 0$ ) part of the detector (see Section 3.2.1).

The trajectory of particles measured at CMS is described in the coordinate system displayed in Figure 2.6. The polar angle  $\theta$  is measured from the  $z$ -axis while the azimuthal angle  $\phi$  is measured from the  $x$ -axis in the  $x$ - $y$  plane, called the transverse plane. The radial coordinate  $r$  is also measured in the transverse plane. The polar angle is replaced by the pseudorapidity  $\eta$  which, for massless particles, matches the rapidity and is Lorentz invariant under longitudinal boosts. The pseudorapidity is zero in the transverse plane and approaches infinity towards the  $z$ -axis, according to:

$$\eta = -\ln \left[ \tan \left( \frac{\theta}{2} \right) \right] \quad (2.3)$$

The details of the original configuration of the CMS detector can be found in Ref. [1]. After Run-1 was over, CMS underwent several improvements as part of the planned upgrades for the LS1 shut-down period (2013-2014). The systems upgraded during LS1 include the muon endcap stations, the hadron calorimeter, and the L1 trigger. In the case of the muon system, an additional disk of muon detectors was installed on the outermost part of each endcap section providing a fourth measurement in the forward region [98]. Moreover, the photosensors of the forward (outer-barrel) hadron calorimeter were replaced with multi-anode photomultiplier tubes (silicon photomultipliers), and the corresponding readout electronics were upgraded to handle the new sensors [99]. And

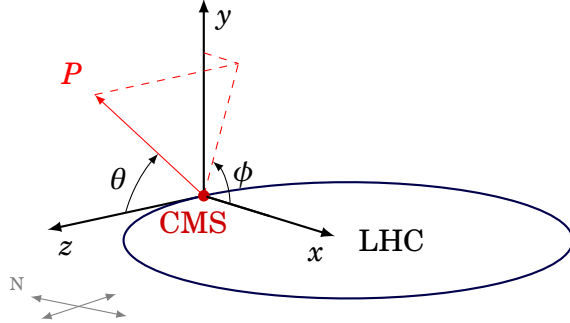


Figure 2.6: Schematic diagram of the coordinate system used in the CMS experiment.

finally, the framework and electronics of the L1 trigger system were completely changed to sustain the increasing interaction rate of the LHC beam collisions [100].

### 2.2.1 Subdetectors

The CMS detector [1] is composed of several subdetectors which provide a precise measurement of the trajectory and energy of the particles emitted from the LHC collisions. The superconducting solenoid volume contains the inner tracker close to the beam line followed radially outwards by the electromagnetic and hadronic calorimeters. The muon chambers are installed outside of the solenoid, interspersed with layers of the flux-return yoke. An electromagnetic preshower is installed in the endcaps complementing the ECAL to improve the identification of photons and electrons.

#### 2.2.1.1 Tracker

The CMS tracking system is designed to measure the trajectory of charged particles and reconstruct the 3D vertex position of the primary interaction and the secondary decays. It is completely surrounded by the volume of the solenoid magnet in the barrel region, and has a diameter of 2.5 m and a length of 5.8 m, centred on the interaction point. The CMS tracker is made of a pixel detector and a silicon strip tracker. A schematic cross section of the CMS tracker is presented in Figure 2.7.

The pixel detector is made of 1440 pixel modules installed in the tracker section closest to the interaction region. It covers the pseudorapidity range  $|\eta| < 2.5$  with three Barrel Pixel (BPix) layers and two Forward Pixel (FPix) disks. The BPix layers are placed at a radii of 4.4 cm, 7.3 cm and 10.2 cm from the beam axis, while the FPix disks are located, on each side of the IP, at a longitudinal distance of  $z = \pm 34.5$  cm and  $z = \pm 46.5$  cm. The BPix (FPix) detectors contain 48 (18) million silicon pixels, each with a cell size of

## CHAPTER 2. EXPERIMENTAL SETUP

---

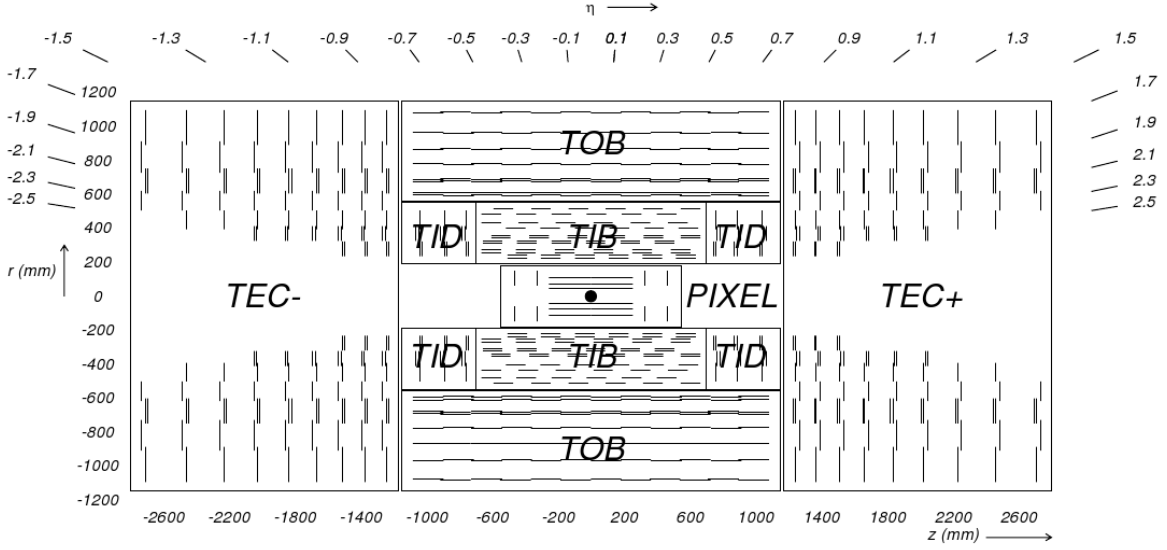


Figure 2.7: View of the CMS tracker in the  $r$ - $z$  plane. Each line represents a detector module. Figure taken from Ref. [1].

$100 \times 150 \mu\text{m}^2$ . The arrangement of the pixel detector modules in the barrel (forward) region provides, over the full tracker coverage, three tracking hits per track and a position resolution of 15-20 (15)  $\mu\text{m}$  in the  $z$ -coordinate.

The silicon-strip tracker contains 9.3 million strips divided in 24244 silicon sensors, covering the region between the pixel detector and the ECAL. In the barrel region, the strip tracker is composed of the Tracker Inner Barrel (TIB), made of four concentric cylinders placed at a radius between 25.5 cm and 49.8 cm, and the Tracker Outer Barrel (TOB), which consists of a wheel-like structure containing six cylinders with an inner (outer) radius of 55.5 (116) cm. The pseudorapidity coverage of the strip tracker is extended up to  $|\eta| = 2.5$  with three Tracker Inner Disks (TID) and nine Tracker EndCap (TEC) disks, installed on each endcap section along  $80 \text{ cm} < |z| < 90 \text{ cm}$  and  $124 \text{ cm} < |z| < 282 \text{ cm}$ , accordingly. The strip detector modules used in the TIB, TID and inner four TEC rings are made of one 320  $\mu\text{m}$ -thick sensor, while those used in the TOB and outer five TEC rings are made of two 500  $\mu\text{m}$ -thick sensors. The strip pitch varies between 80-120  $\mu\text{m}$ , 100-141  $\mu\text{m}$ , 122-183  $\mu\text{m}$ , and 97-184  $\mu\text{m}$ , in the TIB, TID, TOB and TEC, respectively. The strip tracker can achieve a position resolution in the TIB (TOB) of 23-35 (35-53)  $\mu\text{m}$  in the transverse plane and 230 (530)  $\mu\text{m}$  in the  $z$ -coordinate.

### 2.2.1.2 Electromagnetic calorimeter

The ECAL of CMS is a hermetic homogeneous calorimeter composed of 75848 lead-tungstate ( $\text{PbWO}_4$ ) crystals. The ECAL is designed to fully absorb and measure the energy of electrons and photons. The  $\text{PbWO}_4$  material was chosen for its small Molière radius (2.2 cm), a short radiation length (0.89 cm), and a high density ( $8.28 \text{ g cm}^{-3}$ ). When a high-energy electron or photon interacts with the nuclei of the ECAL crystals, it generates a cascade of electromagnetic particles ( $e^-$ ,  $e^+$  and  $\gamma$ ) and induces the emission of blue scintillation light ( $\lambda \approx 420 \text{ nm}$ ), which is then measured in photodetectors. The total amount of scintillation light produced is proportional to the energy deposited in the crystals by the electrons and photons. In order to cope with the running conditions of the LHC, the crystals are designed to have a fast response (25 ns), and be optically transparent and radiation-hard.

The ECAL is installed between the silicon-strip tracker and the HCAL. It is divided in a cylindrical-barrel section (EB) and two endcap rings (EE), one on each side of the IP. The EB is made of 61200 crystals of 23 cm long, covering the pseudorapidity range  $|\eta| < 1.48$  with a granularity of 170-fold in  $\eta$  and 360-fold in  $\phi$ . The crystals are grouped in modules of either 400 or 500 units, and four modules are assembled in so-called supermodules. The EB has a total of 36 supermodules, each covering  $20^\circ$  in  $\phi$  with 1700 crystals. The scintillation light is measured in the EB with Avalanche PhotoDiodes (APD), mounted in pairs on the back of each crystal. Each APD is operated, with a high-voltage power supply system, at gain 50 and a voltage between 340-430 V. The schematic layout and geometric view of the ECAL are shown in Figure 2.8.

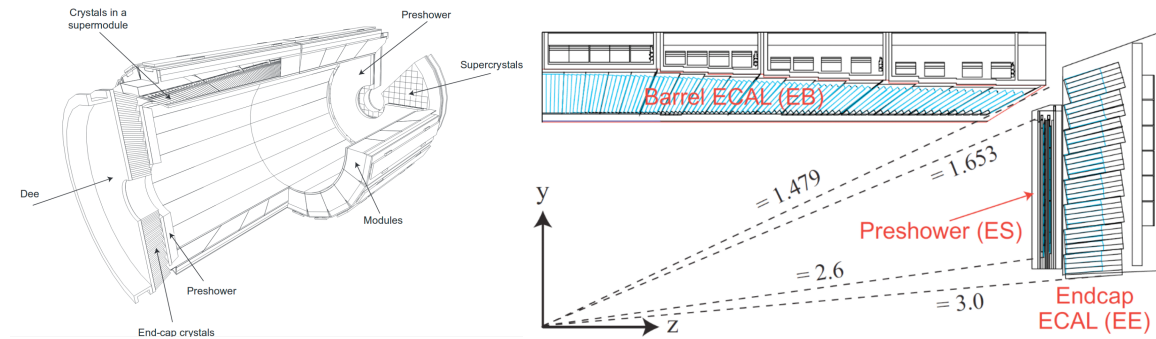


Figure 2.8: Schematic layout [1] (left) of the CMS electromagnetic calorimeter, and its corresponding one-quarter geometric view [101] (right).

The EE rings are installed at  $z = \pm 3.15 \text{ m}$ , extending the coverage of the ECAL up to  $|\eta| = 3.0$ . The EE consists of 14648 crystals of 22 cm long, assembled in units of  $5 \times 5$

crystals known as SuperCrystals (SC). Each EE ring is divided in two halves, each containing 156 SCs. A single-stage photomultiplier called Vacuum PhotoTriodes (VPT), attached to the back of each EE crystal, is used to measure the scintillation photons. The VPT has a diameter of 25 mm, a quantum efficiency of 22% at a wavelength of 430 nm, and a gain of 10.2 at zero magnetic field.

An additional calorimeter called the Preshower detector is installed in the endcap rings between the tracker and the EE. The Preshower is an electromagnetic sampling calorimeter of 20 cm thickness, optimised to identify photons from neutral pion decays. It is composed of two layers of lead absorbers interleaved with 4300 silicon sensors organised in 32 strips. Each silicon sensor has a thickness of 320  $\mu\text{m}$  and an active area of  $63 \times 63 \text{ mm}^2$ . Incoming photons and electrons initiate an electromagnetic shower when they interact with the lead absorbers. The energy deposited in the absorbers and the transverse profile of the shower are measured in the silicon strips.

The response of the crystals and the signal amplification of the APDs depend on the operating temperature. As a result, a water flow cooling system is installed to keep the crystals and sensors at a stable temperature of  $18.00 \pm 0.05^\circ\text{C}$ . Moreover, the transparency of the crystals to scintillation light is affected by the radiation dose due to the formation of colour centres which absorb part of the light. The variation of the crystal transparency is monitored using laser pulses introduced into the crystals at a frequency of 80 Hz. The laser monitoring system uses two blue lasers ( $\lambda \approx 440 \text{ nm}$ ) to track the radiation-induced transparency variations, which are then corrected for by recalibrating the detector.

The energy resolution of the ECAL is affected by several sources, such as the fluctuations in the shower, crystal non-uniformities, calibration errors, and noise in the photodetectors. The relative energy resolution of the ECAL is parametrised as a function of the measured energy  $E$  via:

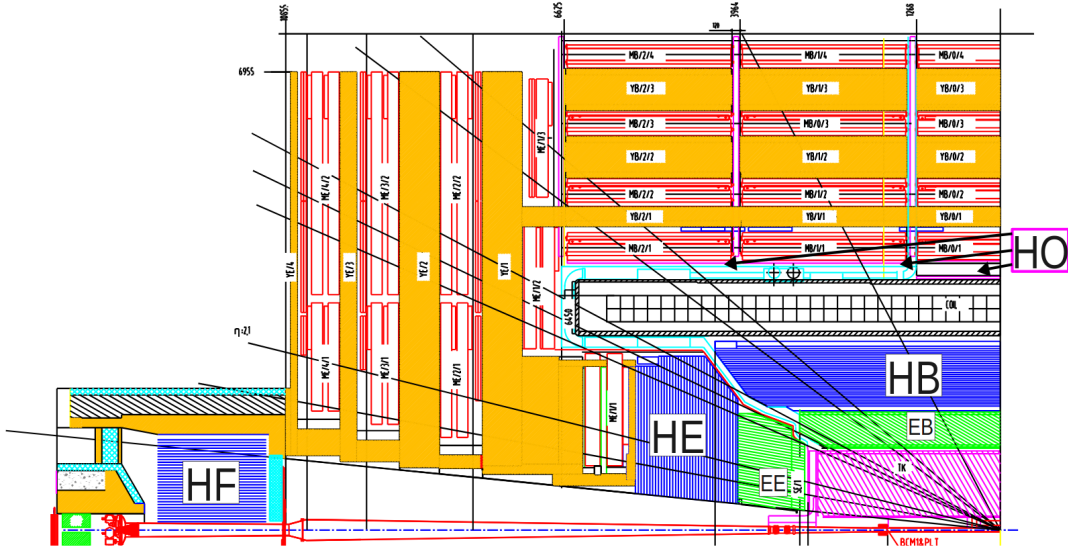
$$\left(\frac{\sigma_E}{E}\right)^2 = \left(\frac{2.8\%}{\sqrt{E/\text{GeV}}}\right)^2 + \left(\frac{12\%}{E/\text{GeV}}\right)^2 + (0.3\%) \quad (2.4)$$

### 2.2.1.3 Hadronic calorimeter

The HCAL is a hermetic sampling calorimeter made of 70000 plastic-scintillator tiles interleaved with absorber plates. The goal of the HCAL is to completely absorb and measure the energy of hadrons. When a hadron hits an absorber plate, it induces a shower of particles through the successive absorber layers. The secondary particles

## 2.2. THE COMPACT MUON SOLENOID

produced in the cascade pass through the plastic tiles, located in between the absorbers, leading to the emission of scintillator light at a peak wavelength of  $\sim 440\text{ nm}$ . Photons generated on each tile are collected with WaveLength-Shifting (WLS) fibres fabricated in a double-clad configuration with a diameter of 0.94 mm. The WLS fibres shift the scintillator light to the green spectrum (515 nm) and pass it to fibre-optic waveguides, which then transfer the light to a phototransducer. The scintillator tiles are grouped in trays that are  $5^\circ$  wide in  $\phi$ . A geometric view of CMS, highlighting the different components of the HCAL, is presented in Figure 2.9.



trays. The HO has 2730 scintillator tiles of 10 mm thick organised in 422 trays, offering the same  $\Delta\eta \times \Delta\phi$  granularity as the HB. The HO uses a multipixel Geiger-mode APD, known as Silicon PhotoMultiplier (SiPM), to detect photons.

The coverage of the HCAL is extended in the forward region to  $|\eta| = 3$  with the Hadron-Endcap (HE) calorimeter and up to  $|\eta| = 5.2$  with the Hadron-Forward (HF) calorimeter. The HE is located in the endcap rings and its absorber is made of two 79 mm-thick plates of cartridge brass separated by 9 mm. The HE contains 20916 plastic tiles and has a  $\Delta\eta \times \Delta\phi$  granularity of  $0.17 \times 0.17$ . The HE also uses HPDs to measure the scintillator light.

The HF is divided in 36 wedges that are  $20^\circ$  wide in  $\phi$ , and its front face is located at  $z = \pm 11.2\text{ m}$ , on each side of the IP. Since the HF experience a large energy deposit from the beam collisions, its design has been optimised to handle high levels of radiation. The HF absorber consists of a 1.7 m-depth cylindrical structure made of 5 mm-thick steel-grooved plates, while the HF active medium is composed of quartz fibres of polymer hard-cladding and fused-silica core. The signal consists of Cherenkov light generated when energetic charged particles from the shower traverse the quartz fibres. The Cherenkov light is measured by multi-anode PhotoMultiplier Tubes (PMT) shielded behind 40 cm of steel. The HF fibres are inserted in the absorber grooves along the beam line in two longitudinal segments. Long fibres are inserted over the full absorber depth while short fibres starts at a depth of 22 cm from the front face covering the back of the absorber. Since most of the energy of electrons and photons is deposited in the first 22 cm while hadrons are able to penetrate more in the HF absorber, the difference in energy measured in the long and short fibres is used to estimate the electromagnetic and hadronic components of the shower.

#### 2.2.1.4 Muon detectors

The CMS muon tracking system measures the momentum and charge of muons, and provides trigger for muons in the fiducial region  $|\eta| < 2.4$ . It is divided in four stations corresponding to four concentric cylinders in the barrel region and to four disks on each endcap section. Figure 2.10 shows a geometric view of one quadrant of the CMS muon system. The dense material of the calorimeters and the solenoid magnet absorbs most of the hadrons, electrons and photons, while energetic muons are able to reach the muon stations loosing only a small fraction of their energy. Muons are detected in CMS using three type of gaseous technologies: Drift Tubes (DT), Cathode Strip Chambers (CSC) and Resistive Plate Chambers (RPC).

## 2.2. THE COMPACT MUON SOLENOID

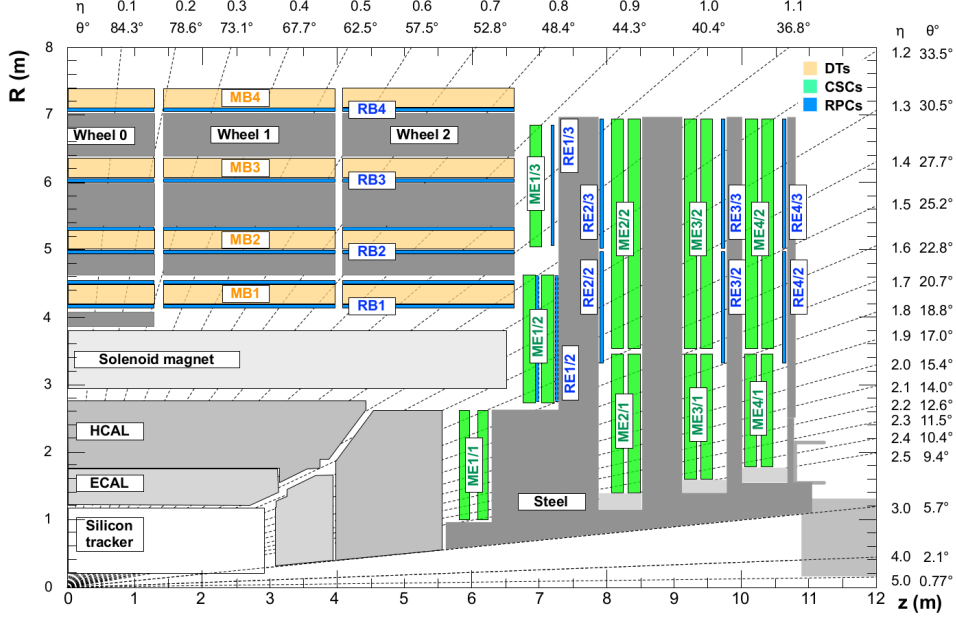


Figure 2.10: Geometric view of one quadrant the CMS detector in the  $r$ - $z$  plane. Each chamber of the muon system is shown in blue (RPC), green (CSC) and orange (DT). Figure taken from Ref. [102].

The DT detectors are used in the barrel region of the muon system ( $|\eta| < 1.2$ ). A DT consists of a 50  $\mu\text{m}$ -diameter anode wire placed inside a rectangular tube connected to two cathode strips and filled with a gas mixture of 85% of argon and 15% of CO<sub>2</sub>. The layout of a DT cell is displayed on the left of Figure 2.11. When a charged particle passes through a DT, it ionises the gas releasing electrons that are then detected in the anode wire. The DT system is composed of 172000 anode wires of 2.4 m length. There are four DT chambers in each of the five barrel wheels and twelve azimuthal sectors. In total, the fourth station contains 70 DT chambers and the first three stations contain 60 DT chambers each. Four layers, each containing up to 60 DTs, are grouped in units called SuperLayers (SL). The DT chambers of the three inner stations (outermost station) are made of three (two) SLs. The first and third SL, as shown on the right of Figure 2.11, have their anode wires installed parallel to the  $z$ -axis to measure the bending in the transverse plane, while the anode wires of the second SL are placed orthogonal to the beam line to measure the position in the  $z$ -coordinate. The SLs of the fourth station only have anode wires parallel to the  $z$ -axis. The SLs measure the position and angle of the track segments with a precision of 1.5 mm and 20 mrad, respectively.

Instead of DTs, the two endcap sections use 540 CSCs covering a pseudorapidity range  $0.9 < |\eta| < 2.4$ . The CSC system is designed to cope with the higher rate of particles

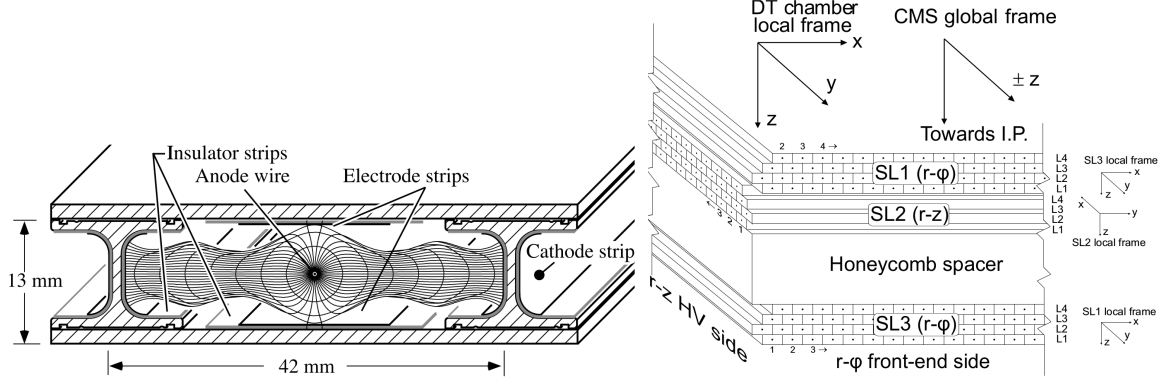


Figure 2.11: Schematic layout of a DT cell (left) and a DT chamber (right). Figures taken from [103].

and the large non-uniform magnetic field present in the forward region. A CSC is made of six anode wire planes crossed with seven copper cathode strips within a gas mixture of 40% Ar, 50% CO<sub>2</sub>, and 10% CF<sub>4</sub>, forming a multiwire proportional chamber. The CSCs are operated at 3.6 kV with a gas gain of  $7 \times 10^4$ , and are organised in chambers installed perpendicular to the beam pipe. The CSC chambers are trapezoidal and cover either 10° or 20° in  $\phi$ , and they overlap providing contiguous coverage in  $\phi$ . The cathode strips are milled in panels along constant  $\Delta\phi$ -width and provide measurements in the transverse plane, while the anode wires are placed azimuthally and measure the pseudorapidity of muons. The CSC system has a total of 266112 cathode-strip and 210816 anode-wire read-out channels. A schematic layout of a CSC is shown in Figure 2.12.

To allow fast muon triggering, the barrel and endcap regions are complemented with RPC detectors. A RPC module consists of an anode plate parallel to a cathode plate, as shown in Figure 2.13. The RPC plates are separated by a gap filled with a gas mixture of 96.2% C<sub>2</sub>H<sub>2</sub>F<sub>4</sub>, 3.5% *i*C<sub>4</sub>H<sub>10</sub> and 0.3% SF<sub>6</sub>, and operated in avalanche mode with read-out strips in between. There are 480 (576) RPC chambers in the barrel (endcap) region. Each RPC chamber consists of two or three modules of up to 96 strips each. Each RPC strip covers 0.31° in  $\phi$ . The RPC chambers are organised in six coaxial cylinders in the barrel region and four rings in the endcaps, covering the pseudorapidity region up to  $|\eta| = 1.9$ . The innermost ring span 20° in  $\phi$  while the other rings span 10°. The RPC modules are optimised for fast muon triggering by detecting ionising events faster than the time interval between two bunch crossings (25 ns). They provide a good timing resolution but with a coarser spatial granularity compared to DTs and CSCs. The RPCs also allow to resolve ambiguities between tracks made from multiple hits in the muon chambers.

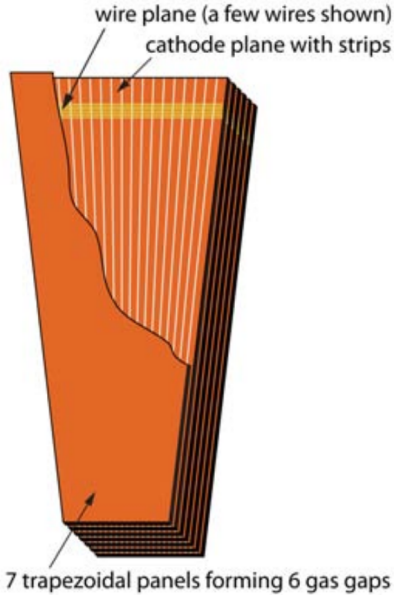


Figure 2.12: Schematic layout of a CSC. Figure taken from [1].

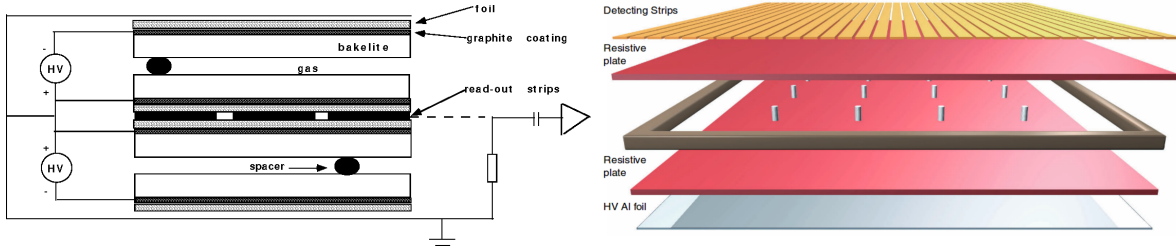


Figure 2.13: Cross section view (left) [104] and exploded view (right) [105] of a RPC module.

## 2.2.2 Trigger system

At LHC design conditions, the two beams cross each IP every 25 ns, equivalent to a frequency of 40 MHz. Once a collision is recorded by CMS, all detector channels are read out and the data is sent to the CERN main computing farm, known as the Tier-0, to be further processed with the CMS SoftWare (CMSSW). However, the Tier-0 processing rate is limited by its CPU performance and storage capacity. As a result, the input rate of data transferred to the Tier-0 has to be kept below 1 kHz to avoid overflowing the computing centre.

To reach this goal, CMS has implemented a two-level trigger system designed to select events of interest for physics analysis. The first level, known as the Level-1 (L1) trigger, lowers the collision rate to an output rate of 100 kHz by filtering events using custom

hardware. The next trigger level, called the High Level Trigger (HLT), is performed in a cluster of computers located in the CMS experimental cavern. The HLT software algorithms further reduce the data rate down the limit required by the Tier-0.

### 2.2.2.1 Level-1 trigger

The L1 trigger system [106] is designed to handle the large collision rate of the LHC. To accomplish this goal, the L1 trigger is made of custom hardware modules optimised to process the events with a latency of less than 4  $\mu$ s. The L1 trigger is divided in two parts: the calorimeter and muon triggers.

The data from each subdetector are organised in units called Trigger Primitives (TP). The calorimeter TP are derived from the Trigger Towers (TT), each corresponding to a region of  $0.087 \times 0.087$  in  $\eta\phi$  (represents  $5 \times 5$  crystals in the ECAL). While for muons, a TP corresponds to a segment in either the DT or CSC systems. The information of the inner tracker is not used in the L1 trigger since the tracker data can not be currently read out within a bunch crossing time of 25 ns. As a result, the L1 calorimeter trigger cannot discriminate between electrons and photons. The output of the L1 muon and calorimeter triggers is combined in the L1 Global Trigger (GT), which then takes the final decision to either reject or accept the event.

The L1 trigger decision is determined according to a set of user-defined L1 trigger conditions. The L1 criteria are organised in a menu made of different algorithms which are programmed by the users and hard-coded in the firmware of a Field-Programmable Gate Array (FPGA). Some typical conditions used to define the L1 algorithms include setting a minimum  $p_T$  threshold or  $\eta$  range on the L1 objects, or requiring events to have a given amount of L1 candidates. If an event passes the conditions of at least one of the L1 algorithms, the whole CMS detector is read out and the data is then sent to the HLT computers. The L1 menu is updated several times during data taking, to adapt to the changes in the LHC beam conditions and physics requirements.

In order to reduce the contribution from cosmic muons and also suppress pre-firing from the calorimeters caused by particles interacting in the photomultipliers, the events processed by the L1 trigger are required to be associated to a bunch crossing. The Beam Pick-up Timing eXperiment (BPTX) detectors, installed at a distance of  $z = \pm 175$  m on each side of the IP, are used to select valid bunch crossings by checking for a coincidence of the signals on each side.

The L1 system underwent, between 2014 and 2015, an extensive upgrade that included a complete replacement of the electronics and the data acquisition system. The

previous L1 trigger, used during LHC Run-1 and 2015, is referred in this manuscript as the legacy L1 trigger, while the L1 trigger deployed before the pPb collision run in 2016, is called the upgraded L1 trigger.

**Legacy L1 trigger.** The legacy L1 trigger [106] was used in CMS until the end of 2015, covering the entire LHC Run-1 and beginning of Run-2 data taking periods. The events from p-p and Pb-Pb collisions at  $\sqrt{s_{\text{NN}}} = 5.02 \text{ TeV}$ , in particular the data used for the charmonium analysis reported in Chapter 4, were selected using the legacy L1 trigger. Figure 2.14 shows a diagram of the legacy L1 trigger system.

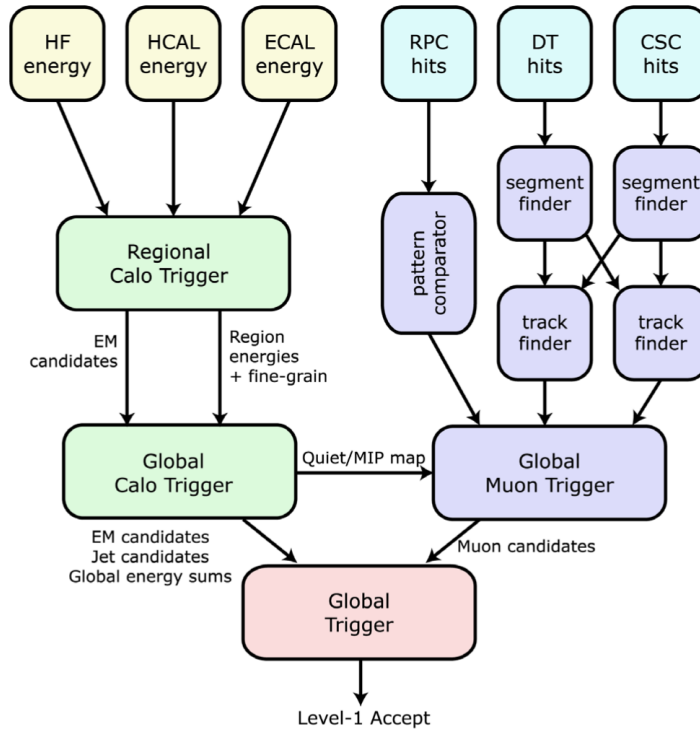


Figure 2.14: Diagram of the legacy L1 trigger of CMS. Figure taken from Ref. [107].

In the legacy L1 trigger, the transverse energy  $E_T$  values are read out from each ECAL, HF and HCAL TT, and then sent to the Regional Calorimeter Trigger (RCT). The RCT processes the raw data and produces 72 electron-photon ( $e/\gamma$ ) candidates (identified as energy clusters mainly deposited in the ECAL), computes the  $E_T$  in the HF region and derives 396  $E_T$  sums of  $4 \times 4$  TT regions. The Global Calorimeter Trigger (GCT) then receives the objects from the RCT and reconstructs jets and hadronic tau decays based on the regional  $E_T$  sums, sorts the  $e/\gamma$  candidates according to their  $E_T$ , and computes global

quantities such as the total  $E_T$ . Eight  $e/\gamma$  candidates, eight jets, four tau candidates, the HF  $E_T$ , and the global quantities are then sent to the GT.

The legacy L1 muon trigger follows a detector-based design. The DT and CSC hit measurements are used by the front-end trigger electronics to reconstruct track segments in each muon station. Regional track finders (TF), one for each muon subsystem, sort the track segments and identify muons using pattern recognition algorithms. The hardware modules of the DT (CSC) TFs consist of 72 (12) Versa Module Eurocard (VME) boards. The muon momentum is estimated based on the bending of the track along the magnetic field. The position of each muon detector hit is converted to  $\eta\text{-}\phi$  coordinates using lookup tables derived from simulation. To cover the overlap region between the CSC and DT muon systems, the information of their TFs is combined. The RPC hits are directly sent to a pattern comparator trigger (PACT), which finds muon candidates by comparing the RPC measurements to predefined patterns. Each muon TF determines the  $\eta\text{-}\phi$  position and the  $p_T$  of the muon candidates, and also assigns a quality value based on the position and number of muon stations used to form the muon track.

On every bunch crossing, the CSC and DT TFs transfer, each one, four muon candidates to the Global Muon Trigger (GMT), while the RPC trigger sends eight muon candidates. The GMT then proceeds to merge the muon tracks if they have been identified by several muon subsystems, and assigns a three-bit quality code to the muon tracks depending on the information provided by each TF. All muon candidates are ranked in the GMT based on their quality code, and those with the same quality are then ranked based on their  $p_T$ . The four highest ranked candidates are then transferred to the GT. The quality bits assigned to the L1 muon candidates are:

- **Bits 0 to 4:** Represent empty, halo or very low quality muon tracks. Not used for physics.
- **Bit 5:** Muon candidate found by the DT or CSC TFs, but not confirmed by the RPC PACT.
- **Bit 6:** Muon candidate found by the RPC PACT, but not confirmed by the DT or CSC TFs.
- **Bit 7:** Muon candidate detected by the DT or CSC TFs, and also by the RPC PACT.

Finally, legacy GT takes the final L1 decision based on the information provided by the GMT and the GCT. It is able to evaluate up to 128 L1 algorithms.

**Upgraded L1 trigger.** The upgraded L1 trigger system [100], deployed in CMS at the beginning of 2016, was used during the data taking period of p-Pb collisions at

$\sqrt{s_{\text{NN}}} = 8.16 \text{ TeV}$ , and thus for the W-boson analysis reported in Chapter 3. A diagram of the upgraded L1 trigger system is shown in Figure 2.15.

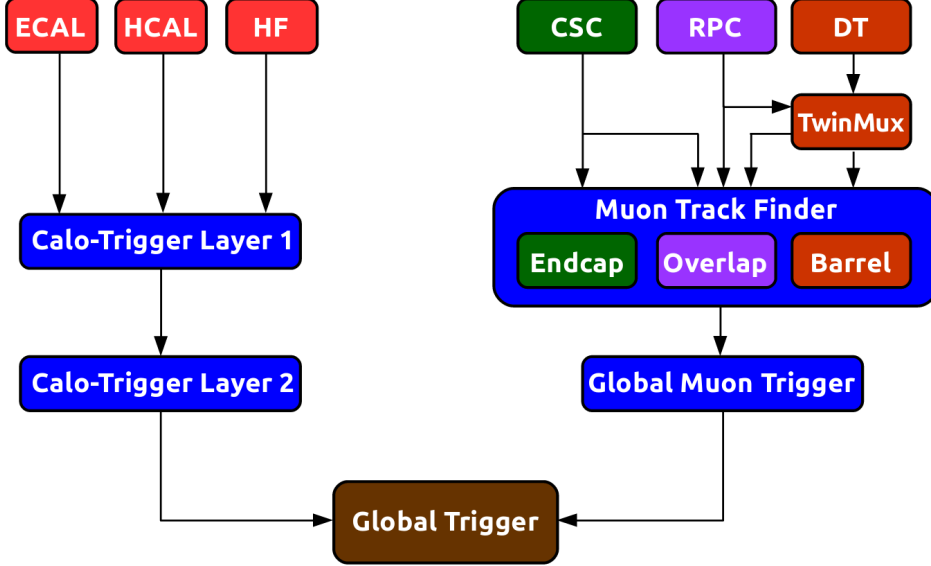


Figure 2.15: Diagram of the CMS L1 trigger used in 2016.

The electronic system of the upgraded L1 trigger consists of Xilinx Virtex-7 FPGAs mounted on Advanced Mezzanine Cards (AMC), designed according to the micro Telecommunications Computing Architecture ( $\mu$ TCA) standard. Compared to the VME standard employed in its predecessor, the  $\mu$ TCA standard provides higher scalability, flexibility and bandwidth. The communication links between the L1 boards were upgraded from copper serial links (limited to 1.2 Gb/s in the legacy L1 trigger) to high speed optical serial links capable of handling a bandwidth of up to 10 Gb/s.

The upgraded L1 calorimeter [108] trigger is divided in two separate processing layers and its architecture follows a time-multiplexed trigger design (the data is splitted in bunch-crossing intervals instead of detector regions). The first layer (Layer-1) collects data from the calorimeter TTs with 36 trigger processor cards and then distributes all data for a given bunch crossing to one of the nine multi-purpose FPGAs of the second layer (Layer-2). The Layer-2 uses the TT data to reconstruct  $e/\gamma$  candidates, jets, and taus (decaying to hadrons), and compute global energy quantities. Lookup tables are used to perform the shape pattern recognition and the energy calibration.

In the case of the L1 muon trigger [109], its architecture is upgraded following a regional approach. The data from the different muon subsystems are combined at an earlier stage than in the legacy trigger, and L1 muon tracks are reconstructed in three

regions: barrel ( $|\eta| < 0.8$ ), overlap ( $0.8 < |\eta| < 1.25$ ), and endcap ( $1.25 < |\eta| < 2.4$ ). The Endcap-Muon TF (EMTF) is designed to process the information from the CSC and RPC modules, however it only received data from the CSC system during 2016 since the RPC concentrator card was still being commissioned. The Barrel-Muon TF (BMTF) builds muon candidates using RPC hits and DT segments reconstructed in the central region. The transition area ( $|\eta| \approx 1.04$ ) between the endcap and barrel sections is covered with the Overlap-Muon TF (OMTF), which takes into account the data from the three muon subsystems. The DT and RPC segments from the barrel region are collected by an intermediate layer called the TwinMux system, which concentrates data and distributes it to the BMTF and OMTF.

The upgraded GMT, referred as  $\mu$ GMT, receives up to 36 L1 muon candidates from each L1 muon TF. The  $\mu$ GMT sorts the muon tracks, removes duplicate muons found by different TFs and ranks the muon candidates by their  $p_T$  and track quality. The eight highest ranked L1 muon candidates are then sent to the GT. The information from the  $\mu$ GMT and the Layer-2 is used by the upgraded GT to evaluate up to 512 L1 algorithms and determine the final L1 decision.

### 2.2.2.2 High level trigger

The HLT is executed on a processor farm composed of an array of multi-core computers running a Linux-based operating system known as Scientific Linux. During 2016, approximately 20000 cores were employed to run the HLT [110]. The HLT software is organised in readout, builder and filter units. The readout unit extracts the information from all CMS subsystems once an event passes the L1 trigger. The builder unit assembles the raw data provided by the readout unit to build detector segments, hits and clusters. The assembled data are subsequently sent to the filter unit which performs the reconstruction of physics objects and selects events for data analysis. The logic of the HLT reconstruction framework is similar to what is used in offline reconstruction but optimised to handle high input data rates ( $\leq 100\text{kHz}$ ).

The structure of the HLT algorithms is organised in a set of processing steps, called HLT path, that runs the reconstruction and selection of events. Each HLT path consists of a sequence of processing units that runs in a predefined order and selects events based on user-defined conditions, such as requiring the presence of muons with  $p_T$  larger than a given threshold. Once an event has been accepted by the HLT, the CMS data is kept temporarily on disk and eventually sent to the Tier-0 computing facility for further offline processing. The HLT output rate is constrained by the size of the event data and

the Tier-0 processing power. The average data size of an event in p-p collisions is around 500 kb, while in central Pb-Pb collisions it can reach values as large as 3 Mb due to the higher particle multiplicity.

For the analyses presented in this manuscript, the data was triggered requiring the presence of identified muons. The reconstruction of muon candidates in the HLT is performed in two steps. The first one, referred as the Level-2 (L2), reconstructs muon tracks using data from the muon system only, while the next step, known as the Level-3 (L3), combines the information from both the inner tracker and the muon stations.

**HLT L2 muon reconstruction.** The L2 muon algorithm starts by performing a local reconstruction of the muon detectors to determine the hits on each muon chamber. The CSC and DT hits are then combined to form segments, which are only kept if found near a L1 muon candidate. The muon segments are then recursively fitted with a Kalman Filter (KF) technique [111] to build the L2 muon tracks. Duplicate tracks are filtered by removing L2 muon tracks that share hits. The KF fit is constrained to the position of the IP to improve the  $p_T$  resolution of L2 muon candidates.

**HLT L3 muon reconstruction.** The L3 muon reconstruction improves the momentum resolution by combining the measurements from the inner tracker and the muon chambers. The reconstruction of all tracks in the inner tracker (hereafter called tracker tracks) cannot be done at HLT due to timing constrains. Instead, a regional tracking is performed by only reconstructing tracker tracks close to the L2 muon candidates using three different seeding algorithms. In the first case, the seeds are defined by extrapolating the parameters (position and  $p_T$ ) of the L2 muon tracks to the outer surface of the inner tracker. The second seeding procedure takes the extrapolated L2 muon tracks and updates their parameters with the hit information from the outermost layers of the silicon-strip tracker. And the third seeding algorithm uses segments from two pixel hits measured in consecutive layers found in a narrow  $\eta$ - $\phi$  region around each L2 muon track. Each seed is then used to build the tracker tracks with a KF fit. The reconstructed tracker and L2 muon tracks are propagated to a common surface, and then matched by comparing their goodness-of-fit  $\chi^2$ . If a L2 muon track and a tracker track are matched, the hits of both tracks are then combined and refitted to form the L3 muon track.

### 2.2.3 Reconstruction

The aim of the CMS event reconstruction algorithms is to build and identify the physics objects generated during the collision by processing the raw data recorded by the CMS detector. The reconstruction algorithms are implemented in the CMS software framework. Once an event is selected by the HLT, the detector information is then transferred to the Tier-0 computing centre and processed with CMSSW. The reconstruction software starts by building the hits, segments and clusters, measured in each of the CMS subdetectors. Afterwards, it processes the detector information to form physics objects such as charged-particle tracks, muons, electrons, photons and jets. Global event quantities, like the missing transverse momentum ( $p_T^{\text{miss}}$ ), are computed by combining the information from the different reconstructed objects. Only the reconstruction of muons and the  $p_T^{\text{miss}}$  are described hereafter, since they are the only objects used in the W-boson and charmonium analyses presented in Chapter 3 and Chapter 4, respectively.

#### 2.2.3.1 Muon reconstruction

Muon candidates are reconstructed in CMS using the information from the inner tracker and the muon system. Tracks formed in the muon system only are called *standalone-muon* tracks, while those built in the inner tracker and matched to a hit in the muon system are referred to as *tracker-muon* tracks. *Global-muon* tracks are reconstructed by matching a tracker track with a standalone-muon track [112]. The three different types of muon tracks used in CMS are displayed in Figure 2.16.

**Standalone muons.** The standalone muon reconstruction starts with the formation of segments made from a linear interpolation of the position of hits measured in the DT or CSC layers. Each track segment has an associated state vector representing its position, direction and  $p_T$ . The state vector of the segments built in the innermost muon station is used to seed the muon track fit.

In the barrel region, tracks are built by fitting the DT segments with a KF algorithm [111], starting from the innermost muon chamber. Moreover, since the magnetic field in the endcap sections is not uniform, the hits of the CSC segments are used directly to perform the KF fit. The RPC hits are also included in the KF. In the case that no hits are found between muon layers, the state vector of the muon track is propagated to the next layer taking into account the magnetic field and the interaction of muons with the CMS detector material.

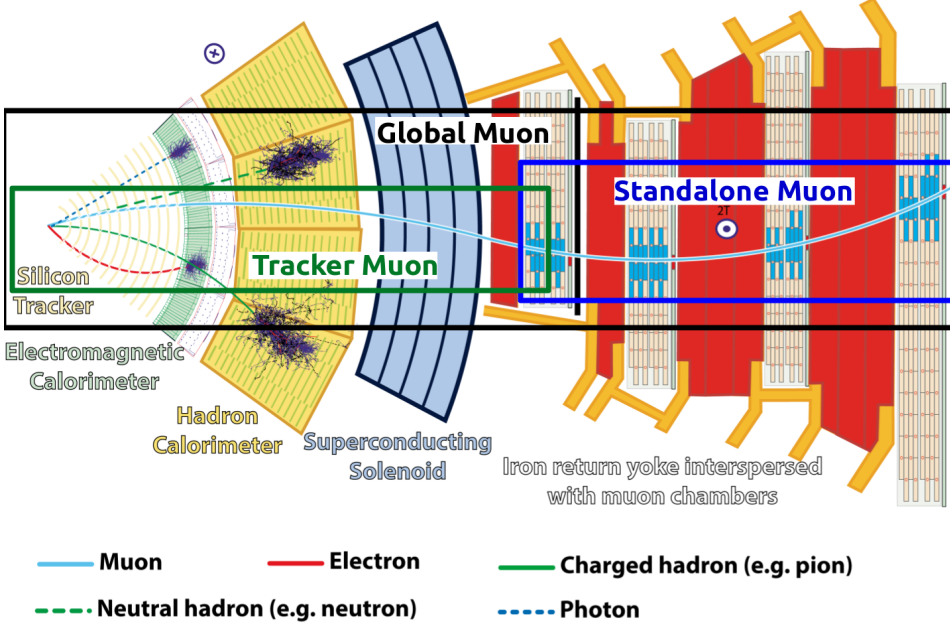


Figure 2.16: Cross section view of the CMS detector showing how particles interact in the CMS. The different types of muon tracks are indicated by boxes. Figure taken from Ref. [113].

The track building procedure is iterated while progressing towards the outer muon chambers. The  $\chi^2$  value between the detector hits and the position of the track projected onto the muon chambers is computed in each step. The hits with large  $\chi^2$  values are excluded from the KF fit and the parameters of the track are updated accordingly. The track fit algorithm stops when it reaches the last muon station. Subsequently, the KF algorithm is performed backwards working from the outermost to the innermost muon chambers, completing the standalone-muon track. Finally, the standalone-muon tracks are extrapolated to the closest approach to the beam line and their position is required to be close to the IP.

**Global muons.** The global muon reconstruction improves the momentum measurement by including the information from the inner tracker. The global muon tracking begins by propagating the standalone-muon tracks to the outer surface of the silicon-strip tracker, and a tracker layer consistent with the position of the propagated standalone muon then defines a common surface.

Tracker-track segments are built from pairs (triplets), made of two (three) hits reconstructed in adjacent inner-tracker layers. These segments are then employed to seed

an iterative KF combinatorial track finder. The sophisticated tracking procedure runs ten different iterations. The first two iterations reconstruct low- $p_T$  and high- $p_T$  tracks seeded with pixel-hit triplets. The third iteration uses pixel-hit triplets to reconstruct tracks from secondary vertices displaced, within a radial distance  $R < 5$  cm, from the primary vertex. The next iteration is meant to recover tracks with one or two missing hits by seeding with pixel-hit pairs instead. The fifth iteration builds displaced tracks ( $R < 7$  cm) seeded by triplets from pixel and strip hits. The following two iterations reconstruct very displaced tracks ( $R < 60$  cm) seeded by strip-hit triplets. The eighth iteration aims to find tracks within the core of high- $p_T$  jets seeded by pairs of pixel and strip hits. And the last two iterations build tracks seeded with hits and segments from the muon chambers, to improve the muon reconstruction efficiency. The hits associated to tracks formed in a given iteration are excluded in the subsequent iterations to avoid duplicating tracks. The rate of mis-reconstructed tracks is kept low in each step by applying a set of quality criteria on the goodness-of-fit  $\chi^2$  and the number of hits used, and by requiring the tracks to be consistent with a charged-particle trajectory originating from the primary vertex.

The tracker track and the propagated standalone-muon track are matched in the common surface according to their  $p_T$ , position and direction measured in the common plane, and the hits from both tracks are then refitted to derive the ultimate global-muon candidate. If multiple global-muon tracks are found for the same standalone muon, the track with the best  $\chi^2$  fit value is kept.

**Tracker muons.** The tracker-muon candidates are built by propagating all tracker tracks with  $p_T > 0.5$  GeV/c and total momentum  $p > 2.5$  GeV/c, outward to the innermost muon station. The propagated track is then considered a tracker-muon track if it matches, along the transverse plane, at least one hit reconstructed in the inner muon chambers.

**Tracking in Pb-Pb collisions.** A modified version of the tracker-track reconstruction was employed during Pb-Pb collisions at  $\sqrt{s_{\text{NN}}} = 5.02$  TeV, to cope with the large number of charged particles produced in central heavy-ion collisions. The tracking algorithm used to build the tracker tracks consists of seven iterations and is called Regional Iterative tracking (RegIt). Instead of using all pixel hits reconstructed in the inner tracker, RegIt performs a regional track reconstruction using only those hits found in a  $\eta$ - $\phi$  area around each standalone-muon track. The RegIt iterations follow the same logic as the standard tracking, excluding the three iterations corresponding to low- $p_T$ , very displaced, and

high- $p_T$  jet tracks. In each iteration, tracks made with RegIt are required to have a  $p_T > 0.8$  GeV/c and at least eight hits, which is a tighter criteria compared to the standard track reconstruction.

### 2.2.3.2 Missing transverse momentum reconstruction

Since neutrinos cannot be detected, their presence is inferred from the overall particle momentum imbalance in the transverse plane, known as missing transverse momentum ( $p_T^{\text{miss}}$ ). The  $p_T^{\text{miss}}$  is defined as the magnitude of  $\vec{p}_T^{\text{miss}}$ , which represents the negative vector sum of the transverse momentum of all particles identified by CMS in an event, as described in:

$$\begin{aligned}\vec{p}_T^{\text{miss}} &= - \sum_{\text{particles}} \vec{p}_T \\ p_T^{\text{miss}} &= \left| \vec{p}_T^{\text{miss}} \right|\end{aligned}\tag{2.5}$$

The Particle-Flow (PF) algorithm [114] is used to identify the particles produced in a given event. The PF algorithm is optimised to reconstruct stable particles by taking into account the information from all CMS subdetectors. The algorithm determines the momentum of the reconstructed objects and classifies them in five categories: electron, muon, photon, charged hadron and neutral hadron, as shown in Figure 2.16. The transverse momentum of all PF particles is used to compute the  $p_T^{\text{miss}}$ . The performance of the  $p_T^{\text{miss}}$  reconstruction in p-p collision data has been documented in [115, 116].



## W-BOSON PRODUCTION IN PROTON-LEAD COLLISIONS

This chapter reports the measurement of the production of W bosons in proton-lead collisions at a nucleon-nucleon center-of-mass energy  $\sqrt{s_{\text{NN}}} = 8.16 \text{ TeV}$  with the CMS detector. A brief introduction to the theory of electroweak interactions and the W-boson production in p-Pb collisions is presented in Section 3.1. This section concludes with a overview of the latest measurements of weak-boson production in heavy-ion collisions at the LHC. The W-boson analysis is then described in detailed in Section 3.2. In Section 3.3, the results of the W-boson analysis are presented and compared to theoretical calculations based on PDFs.

### 3.1 Introduction

This section provides a short introduction to the W-boson analysis. It starts with a brief historical overview of the weak theory (Section 3.1.1) and continues with a short description of the modern theory of electroweak interactions (Section 3.1.2). The process of interest in this analysis,  $p\text{Pb} \rightarrow W \rightarrow \mu\nu_\mu$ , is detailed in Section 3.1.3. Section 3.1.4 introduces the nuclear PDFs and describes the most recent nuclear PDF sets. Finally, Section 3.1.5 presents some of the latest results on weak boson production in heavy-ion collisions at the LHC.

### 3.1.1 A brief history of the weak theory

In the early 20th century, quantum mechanics was the standard framework of atomic physics but several processes such as the  $\beta$  decay, discovered by Ernest Rutherford in 1899 [117], were not fully understood yet. At the time, the  $\beta$  decay was characterized by the process  $A_i \rightarrow A_f + e^-$ , where an initial nucleus  $A_i$  decays into another nucleus  $A_f$  emitting an electron during the process. In order to conserve energy, the electron is required to have a fixed kinetic energy, but James Chadwick observed in 1914 that the  $\beta$  rays produced a continuous energy spectrum [118, 119] in disagreement with what was expected. Another puzzle was the apparently wrong statistics of the  $^{14}\text{N}^{7+}$  ion ( $A = 14$  and electric charge 7), which was thought at the time to be composed of 14 protons and 7 electrons (behaving as a fermion), but was experimentally proven to have spin 1. As a way to solve the problem of the continuous  $\beta$  decay spectrum and the statistics problem of nitrogen, Wolfgang Pauli proposed in 1930 the existence of a new particle [120, 121]. Pauli named his particle initially the neutron, but was later renamed to neutrino by Enrico Fermi after the discovery of a new heavy neutral particle by Chadwick in 1932 [122], that ended up solving the  $^{14}\text{N}^{7+}$  statistics problem by explaining the nitrogen nucleus as made of 7 protons and 7 neutrons (even number of fermions). Pauli described the neutrino as a neutral fermion with mass close to zero and spin 1/2 capable of penetrating matter deeper than photons [120].

Enrico Fermi, after attending the 7th Solvay conference, where the discovery of the neutron and the neutrino hypothesis were presented, proposed a new theory to explain the  $\beta$  decay [123]. Fermi's theory defined the  $\beta$  decay as a process in which the neutron decays to a proton, emitting an electron and a neutrino. Fermi formulated his theory using an analogous approach as in Quantum Electrodynamics (QED), by proposing the following Lagrangian for  $\beta$  decay [124]:

$$L_\beta = G_F (\bar{u}_p \gamma_\mu u_n) (\bar{u}_e \gamma^\mu u_\nu) \quad (3.1)$$

where  $u$  is the Dirac spinor of each particle,  $\gamma_\mu$  is the Dirac matrix and  $G_F$  is the Fermi coupling constant. Fermi's theory of weak interactions assumed the same conservation rules as QED, including the symmetry under reflection in space [124]. A system that is invariant under reflections conserves a quantity called parity.

In the upcoming years, the physicists Tsung Dao Lee and Chen Ning Yang started to suspect that the weak interactions could violate parity conservation, after not finding any experimental evidence of its conservation so far [125]. In an attempt to test the

conservation of parity in weak interactions, Lee and Yang proposed in 1956 to study the  $\beta$  decays of Cobalt ( $^{60}\text{Co}$ ) and measure the projection of the momentum of electrons along the spin axis of the Cobalt nucleus [125]. If the decay process conserves parity then electrons would be produced in both directions: parallel and anti-parallel to the magnetic field. The experiment to test the conservation of parity was realized by Chien-Shiung Wu in 1957. The results of Wu's research showed that electrons were preferentially produced in the opposite direction to the Cobalt spin [126], which meant that parity was not conserved in weak interactions, and even maximally violated.

Apart from parity, one can also associate a helicity to particles. The particle's helicity is considered right-handed if the projection of the spin on the particle momentum is aligned, and left-handed otherwise. In 1958, Goldhaber, Grodzins and Sunyar measured the neutrino helicity at Brookhaven National Laboratory (BNL) and discovered that neutrinos were always left-handed and anti-neutrinos were right-handed [127]. As a consequence of the discovery of parity violation and the neutrino helicity, Robert Marshak and George Sudarshan modified Fermi's weak theory and introduced an axial vector term, giving rise to the V-A (vector-axial) theory of weak interactions [128]. Even though parity (P) and charge conjugation (C) (transforms particles into their anti-particles) were violated separately, it was then assumed that the combined CP operation was still conserved by the weak interaction.

The assumption of the conservation of CP did not last long. An experiment performed at BNL by James Christenson, James Cronin, Val Fitch and René Turlay [129] in 1964 concluded that a small proportion of long-lived  $K_L$  meson ( $\text{CP} = -1$ ) was able to decay to two pions ( $\text{CP} = +1$ ) violating CP in the process. To explain the CP violation in weak theory, Makoto Kobayashi and Toshihide Maskawa [130] extended in 1973 the formulation of the Cabibbo angle to include three generations of quarks and a CP-violating phase term. The Cabibbo angle was originally computed by Nicola Cabibbo [131] to explain the different amplitudes observed between the up, down and strange quark transitions. The charm quark was not yet discovered but was strongly hypothesized, through the Glashow-Iliopoulos-Maiani (GIM) mechanism [132]. The Cabibbo, Kobayashi and Maskawa (CKM) matrix supposed the existence of the charm, bottom and top quarks, discovered later in 1974 [133, 134], 1977 [135] and 1995 [136], respectively.

Following Paul Dirac's formulation of QED [137], Sheldon Glashow [138], Steven Weinberg [139] and Abdus Salam [140] managed in 1968 to build a gauge-invariant unified theory of the electromagnetic and weak interactions. In order to make the electroweak theory symmetric under local phase transformations, it required the presence

of four spin-1 massless bosons: two charged particles called  $W^\pm$  bosons and two neutral particles corresponding to the Z boson and photon. But since the weak interactions are short ranged, they have to be mediated by massive bosons. The addition of mass to the bosons was realized after introducing the spontaneous local breaking of the underlying SU(2) symmetry through the Higgs mechanism [17, 18]. In the following years, Gerardus t’Hooft and Martinus Veltman managed to renormalise the electroweak theory [141, 142], allowing to calculate more precisely the theoretical masses of the weak bosons.

The Z boson was then missing, but a single event was found in the Gargamelle experiment [143], exhibiting a flavour-changing neutral current that could only be mediated by a virtual Z boson ( $\nu_\mu + e^- \rightarrow \nu_\mu + e^-$ ). The experimental study of weak bosons required the development of new particle acceleration technologies. In 1976, Carlo Rubbia, Peter McIntyre and David Cline suggested to transform CERN’s circular proton accelerator, the SPS, into a proton-antiproton collider (Sp $\bar{p}$ S) [144]. The upgrade to Sp $\bar{p}$ S was made possible thanks to the stochastic cooling technology invented by Simon van der Meer [145] in 1972, which allowed to cool down and collect anti-protons. Several experiments were built in the Underground Area (UA) to study the proton-antiproton collisions at the Sp $\bar{p}$ S. The UA1 and UA2 collaborations observed on-shell W bosons [146, 147] in 1983, via reporting the observation of electrons with large transverse energy and the presence of missing momentum in p $\bar{p}$  collisions at  $\sqrt{s} = 540\text{ GeV}$ . And few months later, both collaborations also reported the observation of on-shell Z bosons in the dilepton decay channel [148, 149].

After the major success of the Sp $\bar{p}$ S project, CERN constructed in 1983 a new lepton circular collider called the Large Electron-Positron (LEP) collider [150]. LEP was designed to accelerate electrons and positrons to an energy of half the Z-boson mass ( $45\text{ GeV}/c^2$ ), in order to perform precision measurements of the Z-boson line-shape. Precise measurements of the W-boson mass [151] were later performed by the experiments in the Fermi National Accelerator Laboratory (FNAL). The FNAL experiments analysed data collected between 1983 and 2011 from the Tevatron [152], a proton-antiproton synchrotron collider that operated at energies up to  $\sqrt{s} = 1.96\text{ TeV}$ .

The successful programs of LEP and Tevatron produced the most precise measurements of the properties of the electroweak theory, but there was still a missing piece to complete the picture, the Higgs boson. The discovery of the Higgs boson was finally achieved in 2012 by the CMS [19] and ATLAS [20] collaborations at the Large Hadron Collider (LHC).

### 3.1.2 The modern electroweak theory

The interactions between elementary particles mediated by the weak and electromagnetic forces are described in the Standard Model using the electroweak theory developed by Glashow, Weinberg and Salam [138, 139, 140]. The unification of these two fundamental forces of nature is accomplished mathematically using a non-abelian  $SU(2) \times U(1)_Y$  gauge theory. The electroweak theory requires four massless gauge bosons: three bosons with weak isospin (called  $W_1$ ,  $W_2$  and  $W_3$ ) from  $SU(2)$  and one boson (named  $B$ ) with weak hypercharge from  $U(1)_Y$ .

Since weak bosons have mass, a full description of the electroweak interactions requires the inclusion of massive vector bosons. The problem is that one can not naively add a mass term of the form  $m^2 W^\mu W_\mu$  into the electroweak Lagrangian since this would break gauge invariance making the theory divergent. Thus, this issue is instead solved by spontaneously breaking the  $SU(2) \times U(1)_Y$  electroweak symmetry into a  $U(1)_{\text{EM}}$  symmetry using the Higgs mechanism [17, 18]. The overall idea is that the electroweak gauge bosons couple to a scalar field called the Higgs field which is present in all space. When this field induces a spontaneous breaking of the gauge symmetry, it is split into one dynamic part corresponding to the Higgs boson, and another constant part called the vacuum expectation value (VEV). The symmetry breaking of  $SU(2) \times U(1)_Y$  to  $U(1)_{\text{EM}}$  generates three massless Goldstone bosons. The Goldstone bosons are then absorbed by the electroweak gauge bosons producing the  $W^+$ ,  $W^-$  and  $Z$  bosons with masses proportional to the VEV, while the photon remains massless. The  $W^\pm$ ,  $Z$  and  $\gamma$  bosons are correlated with the  $W_1$ ,  $W_2$ ,  $W_3$  and  $B$  gauge bosons in the following way:

$$\begin{aligned} W^\pm &= \frac{1}{\sqrt{2}} (W_1 \pm W_2) \\ \begin{pmatrix} Z \\ \gamma \end{pmatrix} &= \begin{pmatrix} \cos \theta_W & \sin \theta_W \\ -\sin \theta_W & \cos \theta_W \end{pmatrix} \begin{pmatrix} B \\ W_3 \end{pmatrix} \end{aligned} \tag{3.2}$$

where  $\theta_W$  represents the weak mixing angle. In addition, quarks and leptons acquire mass through the Yukawa interaction with the Higgs field. Since the quark weak eigenstates are not the same as their mass eigenstates, weak interactions can induce a transition from an up-like quark ( $u$ ,  $c$ ,  $t$ ) to a down-like quark ( $d$ ,  $s$ ,  $b$ ). The strength of the quark-flavour mixing in weak decays is parametrised by the CKM matrix  $V_{\text{CKM}}$  via:

$$\begin{pmatrix} d' \\ s' \\ b' \end{pmatrix} = \begin{pmatrix} V_{ud} & V_{us} & V_{ub} \\ V_{cd} & V_{cs} & V_{cb} \\ V_{td} & V_{ts} & V_{tb} \end{pmatrix} \begin{pmatrix} d \\ s \\ b \end{pmatrix} \quad (3.3)$$

where  $(d', s', b')$  are the down-like quark weak eigenstates and  $(d, s, b)$  are the corresponding mass eigenstates. The latest values of the magnitude of the CKM matrix elements are [21]:

$$\begin{pmatrix} |V_{ud}| & |V_{us}| & |V_{ub}| \\ |V_{cd}| & |V_{cs}| & |V_{cb}| \\ |V_{td}| & |V_{ts}| & |V_{tb}| \end{pmatrix} = \begin{pmatrix} 0.97420 & 0.2243 & 0.00394 \\ 0.218 & 0.997 & 0.0422 \\ 0.0081 & 0.0394 & 1.019 \end{pmatrix} \quad (3.4)$$

The Lagrangian of the electroweak theory includes several components that describe the interactions between the fermions, electroweak bosons and the Higgs boson. In the case of the Z boson, the term of the Lagrangian that represents the interactions between fermions and neutral-charged electroweak bosons is:

$$L_{NC} = \alpha_{em} \theta_W \sum_{\text{fermions}} \bar{f} \gamma^\mu A_\mu f + \frac{g}{\cos \theta_W} \sum_{\text{fermions}} \bar{f} \gamma^\mu \frac{(g_v^f - g_a^f \gamma^5)}{2} Z_\mu f \quad (3.5)$$

where  $g$  is the coupling constant of  $SU(2)_L$ ,  $f$  is the Dirac spinors of fermions,  $A_\mu$  is the electromagnetic field, and  $g_v^f$  ( $g_a^f$ ) is the fermion vector (axial) weak coupling constants. Eq. (3.5) specifies that the Z bosons and photons conserve flavour, always decaying into a fermion and its corresponding anti-fermion. While photons do not distinguish the helicity of particles, the Z-boson couplings are different for left- and right-handed fermions.

Furthermore, the component of the Lagrangian that represents the interaction between W bosons and fermions is given by:

$$L_{CC} = \frac{g}{2\sqrt{2}} \left( (\bar{u}, \bar{c}, \bar{t})_R W_\mu^+ \gamma^\mu V^{\text{CKM}} \begin{pmatrix} d_L \\ s_L \\ b_L \end{pmatrix} + (\bar{\nu}_e, \bar{\nu}_\mu, \bar{\nu}_\tau)_R W_\mu^+ \gamma^\mu \begin{pmatrix} e_L^- \\ \mu_L^- \\ \tau_L^- \end{pmatrix} \right) \quad (3.6)$$

where  $f_L$  correspond to left-handed fermions and  $\bar{f}_R$  represents right-handed anti-fermions. Thus, W bosons only couple to right-handed anti-fermions and left-handed fermions organized in pairs of lepton-neutrino or quark-antiquark, where the electric charge of the particles differs by one unit. Since the top-quark mass ( $173 \text{ GeV}/c^2$ ) is larger than the W-boson mass ( $80 \text{ GeV}/c^2$ ), the W boson can not decay to a virtual top quark.

Figure 3.1 shows the possible decays of weak bosons to fermions. The measured values of the mass, width and couplings of weak vector bosons are summarized in Table 3.1.

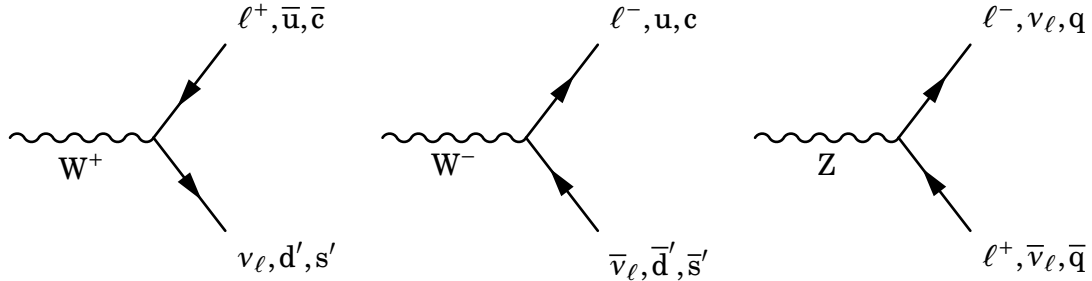


Figure 3.1: Feynman diagrams of the decay modes of  $W^+$  (left),  $W^-$  (middle) and  $Z$  (right) bosons to fermions.

Variable	Description	Value
$M_W$	$W$ boson mass	$80.379 \pm 0.012 \text{ GeV}/c^2$
$\Gamma_W$	$W$ boson width	$2.085 \pm 0.042 \text{ GeV}/c^2$
$\text{BR}(W \rightarrow \ell\nu)$	Branching fraction of $W$ boson leptonic decays	$(10.86 \pm 0.09)\%$
$\text{BR}(W \rightarrow q\bar{q}')$	Branching fraction of $W$ boson hadronic decays	$(67.41 \pm 0.27)\%$
$M_Z$	$Z$ boson mass	$91.1876 \pm 0.0021 \text{ GeV}/c^2$
$\Gamma_Z$	$Z$ boson width	$2.4952 \pm 0.0023 \text{ GeV}/c^2$
$\text{BR}(Z \rightarrow \ell^+\ell^-)$	Fraction of $Z$ boson charged-lepton decays	$(3.3658 \pm 0.0023)\%$
$\text{BR}(Z \rightarrow \nu\bar{\nu})$	Fraction of $Z$ boson neutrino decays	$(20.000 \pm 0.055)\%$
$\text{BR}(Z \rightarrow q\bar{q})$	Fraction of $Z$ boson hadronic decays	$(69.911 \pm 0.056)\%$

Table 3.1: Experimental values of the mass, width and branching fractions of weak bosons extracted from the PDG [21].

### 3.1.3 Production of $W$ bosons in p-Pb and decay into muons

In this thesis, the inclusive production of  $W$  bosons is measured in p-Pb collisions through the muonic decay channel, which is represented by the process  $p\text{Pb} \rightarrow W + X \rightarrow \mu + \nu_\mu + X$ . Since the mass of the  $W$  boson is large ( $M_W = 80.385 \text{ GeV}$ ), the  $W$  bosons are formed during the initial hard scatterings between the partons from the incoming proton and those from the nucleons bound in the Pb ion.

The cross section for the inclusive production of  $W$  bosons in p-Pb collisions can be expressed, assuming that the QCD factorisation holds for a nucleus, as:

$$\sigma[p\text{Pb} \rightarrow W + X] = \sum_{a,i,j} \int dx_p dP_{\text{Pb}}^a f_i^p(x_p, Q^2) \cdot f_j^{a/\text{Pb}}(x_{\text{Pb}}, Q^2) \hat{\sigma}[i + j \rightarrow W + X] \quad (3.7)$$

where  $f_j^{a/\text{Pb}}$  is the PDF of a parton  $j$  from a nucleon  $a$  bound in the Pb ion,  $f_i^p$  is the PDF of a parton  $i$  from the incoming proton and  $\hat{\sigma}$  is the partonic cross section. The partonic cross section is evaluated using pQCD by expanding it in terms of  $\alpha_s$ , as given by:

$$\hat{\sigma} = \sum_i (\alpha_s^i \cdot \hat{\sigma}^i) = \hat{\sigma}^{\text{LO}} + \alpha_s \hat{\sigma}^{\text{NLO}} + \dots \quad (3.8)$$

In practice, the expansion of the partonic cross section is truncated at a given order (e.g. NLO). At leading order, the production of W bosons in proton-nucleon collisions is accomplished through the process of quark-antiquark annihilation ( $q + \bar{q} \rightarrow W$ ), as shown in Figure 3.2. On the other hand, the NLO cross section includes contributions from the processes shown in Figure 3.3.

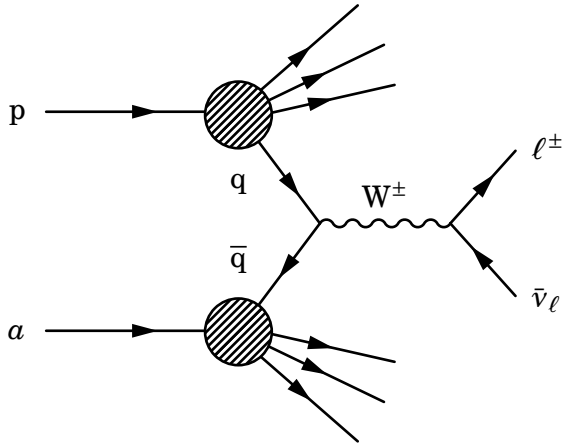


Figure 3.2: Leading order Feynman diagram of W boson production to final state leptons, from a collision between an incoming proton ( $p$ ) and a bound nucleon ( $a$ ) in a Pb nucleus.

The total partonic cross section at LO for  $p\text{Pb} \rightarrow W \rightarrow \mu\nu_\mu$  can be computed using electroweak theory and is given by [21]:

$$\hat{\sigma}^{\text{LO}}[ij \rightarrow W \rightarrow \mu\nu_\mu](Q^2) = \frac{|V_{ij}^{\text{CKM}}|^2}{N_c} \frac{8G_F^2 M_W^4}{16\sqrt{2}\pi} \left( \frac{Q^2}{(Q^2 - M_W^2)^2 + Q^2 \Gamma_W^2} \right) \quad (3.9)$$

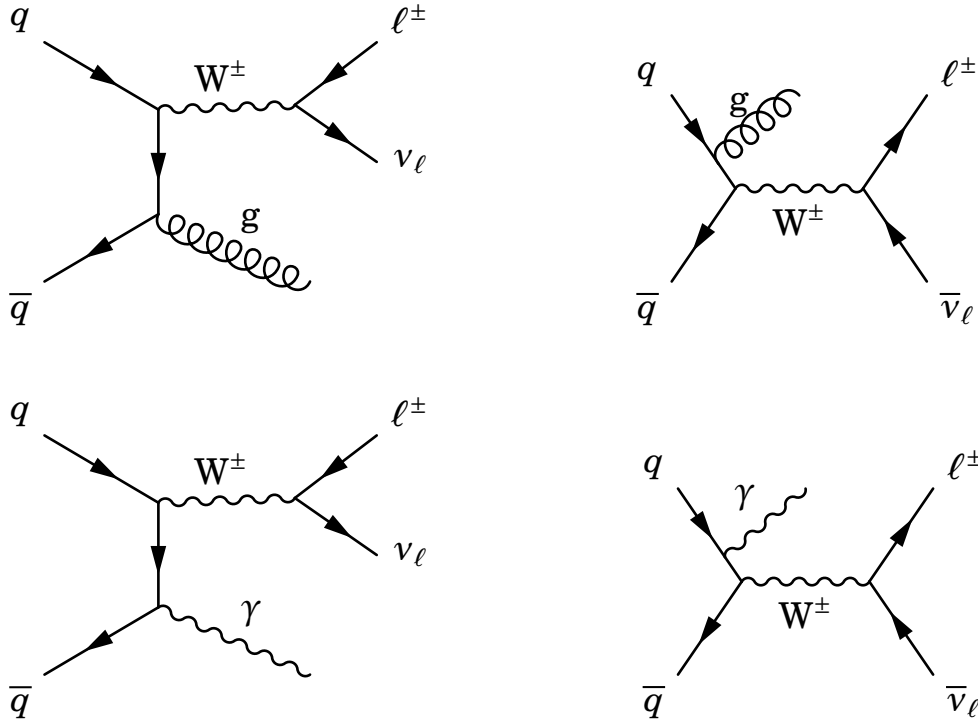


Figure 3.3: Next-to-leading order Feynman diagrams of W boson partonic production to final state leptons.

where  $M_W$  is the mass of the W boson,  $\Gamma_W$  is the width of the W boson,  $N_c = 3$  is the number of colour charges of quarks, and  $|V_{ij}^{\text{CKM}}|$  is the magnitude of the CKM matrix element associated to the interaction between the quarks i and j.

In pPb collisions, the W bosons are mainly produced from interactions between the valence quarks and sea anti-quarks of the proton and nucleons. The dominant production mode of  $W^+$  bosons corresponds to up quark and down anti-quark annihilation ( $u\bar{d} \rightarrow W^+$ ), while for  $W^-$  bosons is the annihilation of down quarks with up anti-quarks ( $d\bar{u} \rightarrow W^-$ ). The next relevant contributions come from  $c\bar{s}$  and  $s\bar{c}$ , while the other quark-antiquark contributions are suppressed according to the off-diagonal CKM matrix elements. Thus, the inclusive W boson cross section measured in p-Pb data is mostly sensitive to the proton and nuclear PDFs of light quarks and anti-quarks.

In addition, the direction of the outgoing muons and anti-muons is different with respect to the scattered quarks. In weak interactions, the  $W^+$  boson couples to left-handed neutrinos while the  $W^-$  boson couples to right-handed anti-neutrinos. As a consequence, in order to conserve helicity, the anti-muons are preferentially produced in the same direction as the  $W^+$  boson while muons are preferentially produced in the opposite

direction, as shown in Figure 3.4.

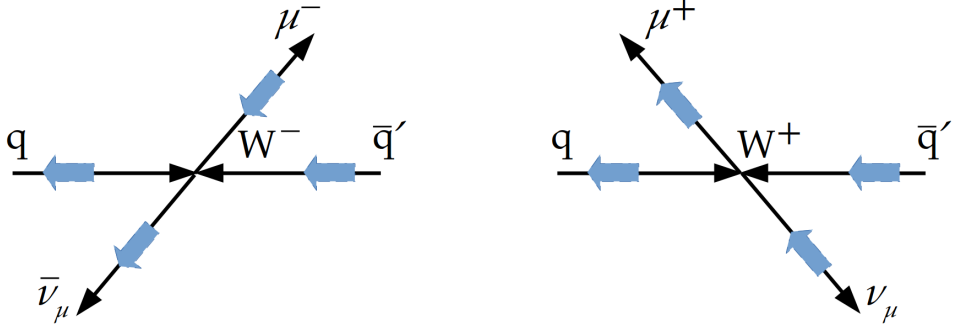


Figure 3.4: Schematic diagram of the production of  $W^-$  (left) and  $W^+$  (right) bosons to muonic decays. The black arrows represent the particle direction of motion whereas the blue arrows correspond to its spin. The spin of the  $W^\pm$  boson points in the direction of the anti-quark.

At LO, the rapidity of  $W$  bosons ( $y_W$ ) is related to the Bjorken- $x$  of the proton and Pb nucleon via:

$$x_p = \frac{M_W}{\sqrt{s_{NN}}} e^{y_W} , \quad x_{Pb} = \frac{M_W}{\sqrt{s_{NN}}} e^{-y_W} \quad (3.10)$$

And since the  $W$ -boson rapidity is correlated to the muon  $\eta$ , then the pseudorapidity distribution of muons arising from  $W$ -boson decays in p-Pb collisions is sensitive to different  $x$  regions of the light quark nuclear PDF that are described in the next section.

### 3.1.4 Nuclear PDFs

The parton distribution functions, introduced in Section 1.1.3, can not be determined from first principles due to the non-perturbative behaviour of the strong interactions. Nevertheless, their dependence on the parton momentum fraction  $x$  can be derived by fitting observables (e.g. structure functions or asymmetries) to experimental data from different processes since PDFs do not depend on the initial hard scattering. The  $Q^2$  dependence of the PDFs is determined using the DGLAP evolution equations. The most common processes used to constrain the PDFs correspond to Drell-Yan (DY), deep-inelastic scattering (DIS), vector boson and jet production, which have been measured by various experiments, including data from HERA, SLAC and LHC.

There are several proton PDF global fits currently available. In this thesis we use the NLO CT14 PDF sets published in 2016 [153] by the collaboration of theorists and experimentalists on QCD (CTEQ). The global fits of CT14 PDFs include data of vector

bosons and jets from LHC p-p collisions at 7 TeV and 8 TeV, charm quark DIS production from HERA, and electron charge asymmetry from Tevatron. The  $x$ -dependence of the CT14 PDF is parametrised at low  $Q^2$  by [153]:

$$xf_a(x, Q^2) = x^{c_1}(1-x)^{c_2} P_a(x) \quad (3.11)$$

where  $f_a$  is the PDF of a parton  $a$ ,  $c_i$  are parameters and  $P_a$  is a polynomial function. In total, the CT14 proton PDFs are described by 26 parameters including: 8 parameters for the valence quarks, 5 parameters for the gluon and 13 parameters for the sea quarks [153].

Figure 3.5 presents the CT14 proton PDF results at  $Q = 2\text{ GeV}$  and  $Q = 100\text{ GeV}$ . One can observe that the light valence quarks carry most of the momentum of the proton while the gluons and sea quarks are mainly distributed at low  $x$ . When the energy is increased, the distribution of partons gets significantly enhanced at low  $x$ , dominated by gluons.

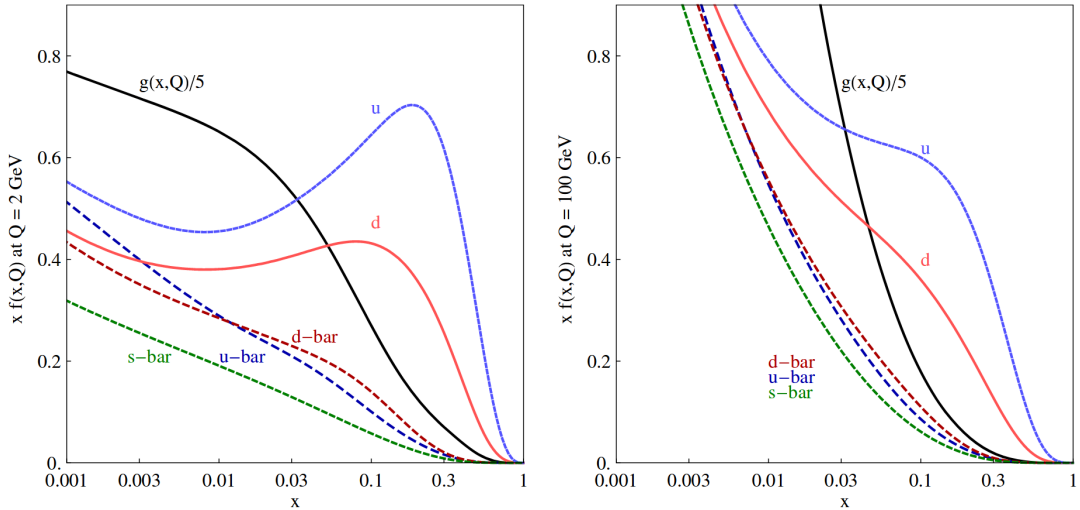


Figure 3.5: Results of the CT14 proton PDFs at NNLO derived at  $Q = 2\text{ GeV}$  (left) and  $Q = 100\text{ GeV}$  (right). Figures taken from Ref. [153].

In heavy-ion collisions, the PDFs of the protons and neutrons bound in the nucleus are modified by the presence of the nuclear environment. The PDFs of nuclei were initially analysed in charged-lepton DIS experiments using nuclear targets by measuring the nuclear structure function per nucleon ( $F_2^A$ ) for a heavy-ion target (A) relative to the one for deuterium ( $F_2^D$ )<sup>1</sup> ( $R_{F_2}^A = F_2^A/F_2^D$ ).

<sup>1</sup>Deuterium is approximately considered to be composed of a free proton and a free neutron.

The European Muon Collaboration (EMC) measured at CERN the structure function of muon DIS from iron and deuterium targets, and published in 1983 the first observation of a depletion of the DIS cross section from iron relative to the one from deuterium in the high  $x$ -region  $0.3 < x < 0.65$  [154], which was named the EMC region. Afterwards, further DIS measurements at CERN and SLAC found a suppression of the nuclear structure function compared to deuterium in the low- $x$  region  $x < 0.1$  and an enhancement in the intermediate  $x$ -region  $0.1 < x < 0.3$ , which are referred as the shadowing and anti-shadowing regions [155]. Moreover, the measurements at SLAC using data at higher  $x$  observed an increase of  $R_{F_2}^A$  while approaching  $x = 1$ , which was expected from the motion of nucleons inside the nuclei, called Fermi motion. Figure 3.6 presents an illustration of the different regions of nuclear modifications found experimentally.

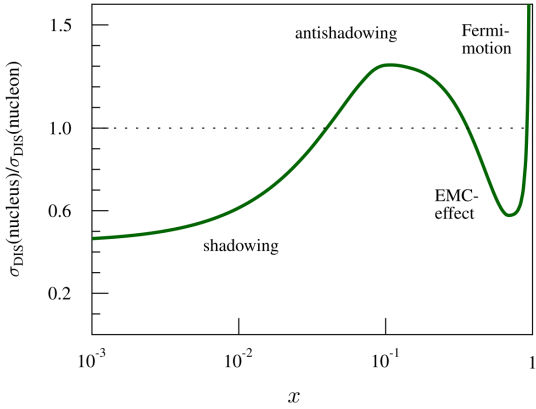


Figure 3.6: Illustration of the different nuclear PDF effects. Figure taken from Ref. [156].

The different nuclear modifications can be qualitatively described as follows:

- **Shadowing:** corresponds to the suppression seen in  $x \lesssim 0.1$ , and it arises from the multiple interactions between the scattered partons and the ones from the different nucleons. The multiple parton scatterings shifts the momentum transfer  $x$  of the partons towards higher values, effectively reducing the parton densities at low  $x$ .
- **Anti-shadowing:** corresponds to an enhancement in  $0.1 \lesssim x \lesssim 0.3$ , and it can be understood as a consequence of the multiple parton scatterings that occur in the nucleus.
- **EMC effect:** corresponds to the suppression in  $0.3 \lesssim x \lesssim 0.7$ . Some models have been proposed to explain this phenomenon which consider modifications of the nu-

cleon structure due to the nuclear medium and also due to short-range correlations between nucleons.

- **Fermi-motion effect:** corresponds to a enhancement in  $x > 0.7$ , and it is due to the motion of nucleons inside the nucleus.

The first global fit to describe leading-order nuclear effects was the EKS98 nPDF [157], which employed the nuclear DIS data measured at CERN and Fermilab, and the DY dimuon data from Fermilab proton-nucleus collisions. The pion data collected by RHIC was later included in subsequent global nPDF fits, such as EPS08 [158], EPS09 [159] and DSSZ12 [160], which provided constrains to the gluon nPDF.

The nPDFs or the nuclear modification are defined for protons bound in a nucleus. The bound neutron nPDFs are derived from the bound proton PDFs using isospin symmetry (i.e. by exchanging the up and down quark PDFs). The full nPDFs for a nucleus of  $Z$  protons and  $A - Z$  neutrons can be derived using the bound proton nPDFs  $f^{p/A}$  and the bound neutron nPDFs  $f^{n/A}$ , according to:

$$f^A = \frac{Z}{A} f^{p/Pb} + \frac{A-Z}{A} f^{n/Pb} \quad (3.12)$$

From now on, we will focus on the latest nuclear PDF sets: the EPPS16 and nCTEQ15 nPDFs, which are used in this thesis.

**EPPS16 nPDF.** The EPPS16 nuclear PDFs were published in 2017 by Eskola, Paakkinen, Paukkunen and Salgado [161]. By including new data and additional parameters, they replace the previous EPS09 set [159].

The EPPS16 global fits includes the same data sets as EPS09 (charged-lepton-nucleus DIS data from SLAC, DY dilepton production from EMC proton-nucleus collisions, and inclusive pion production from RHIC deuteron-nucleus collisions), as well as the CHORUS neutrino-nucleus DIS data, low-mass DY production from RHIC pion-nucleus collisions, and the results using dijet and electroweak boson production in LHC pPb collisions at  $\sqrt{s_{NN}} = 5.02\text{ TeV}$ . The addition of the new LHC, RHIC and CHORUS data into the global fit is not in tension with the previous EPS09 data sets, reassuring the validity of the universality of the nuclear PDFs. Moreover, the inclusion of the CMS measurements of the dijet pseudorapidity spectra in pPb collisions at  $\sqrt{s_{NN}} = 5.02\text{ TeV}$  [162] highly constrained the gluon nPDF. On the other hand, the LHC measurements of the electroweak boson production in pPb data did not significantly constrain the nPDF fits, mostly due to the limited statistical precision. Nevertheless, the results of the W-boson production

from the CMS collaboration suggested possible differences in the modifications of the quark nPDFs. These measurements of the electroweak boson production in heavy-ion collisions at LHC will be presented in the next subsection.

The EPPS16 includes five additional parameters compared to EPS09, to account for possible flavour dependence of the quark nuclear modifications seen at LHC. The nuclear PDFs are parametrised in EPPS16 as:

$$f_i^{p/A}(x, Q^2) = R_i^A(x, Q^2) f_i^p(x, Q^2) \quad (3.13)$$

where  $f_i^{p/A}$  represents the bound proton nPDF of parton  $i$  in a nucleus A,  $f_i^p$  is the free proton PDF of parton  $i$  and  $R_i^A$  is the corresponding nuclear correction factor. The EPPS16 nuclear modifications are derived using the NLO CT14 PDF as the free proton baseline. The parameters of  $R_i^A$  are determined in three regions: the shadowing region  $x \rightarrow 0$ , the anti-shadowing maximum point  $x_a$  and the EMC minimum point  $x_e$  (see Figure 3.6). The dependence on the number of nucleons  $A$  is parametrised along the three  $x$  regions in the following way:

$$R_i^A(x, Q_0^2) = R_i^{A_{\text{ref}}}(x, Q_0^2) \left( \frac{A}{A_{\text{ref}}} \right)^{\gamma_i [R_i^{A_{\text{ref}}}(x, Q_0^2) - 1]} \quad (3.14)$$

where  $Q_0$  is a parametrisation scale fixed at the charm pole mass (1.3 GeV),  $\gamma_i$  is a positive parameter and  $A_{\text{ref}} = 12$ . The  $Q^2$  dependence above  $Q_0^2$  is determined by solving the DGLAP parton evolution equations. The EPPS16 nuclear modifications are parametrised in total by 20 parameters.

The EPPS16 nuclear correction factors for Pb ions  $R^{\text{Pb}}$  extracted from the global PDF fit are shown in Figure 3.7. The EPPS16 results are compared against a baseline derived by performing the EPPS16 fits on the reduced dataset used in EPS09. The inclusion of these CHORUS, RHIC p-A and LHC data improves the uncertainties of the gluon  $R^A$  at high  $x$  and the strange-quark  $R^{\text{Pb}}$  at low  $x$ .

**nCTEQ15 nPDF.** The nCTEQ15 nuclear PDFs, published by Kovarik *et al.* in 2016 [163], were derived using the CTEQ framework. The nCTEQ15 nPDF global fits make use of the charged-lepton DIS data, DY dilepton data and RHIC inclusive pion data. In contrast with EPPS16, where the nuclear modification factor  $R_i^{p/A}$  is fitted, the nCTEQ15 global analysis parametrises the nuclear PDF  $f_i^{p/A}$  directly (i.e. no free proton PDF is used as baseline). The nCTEQ nPDFs are parametrised as:

### 3.1. INTRODUCTION

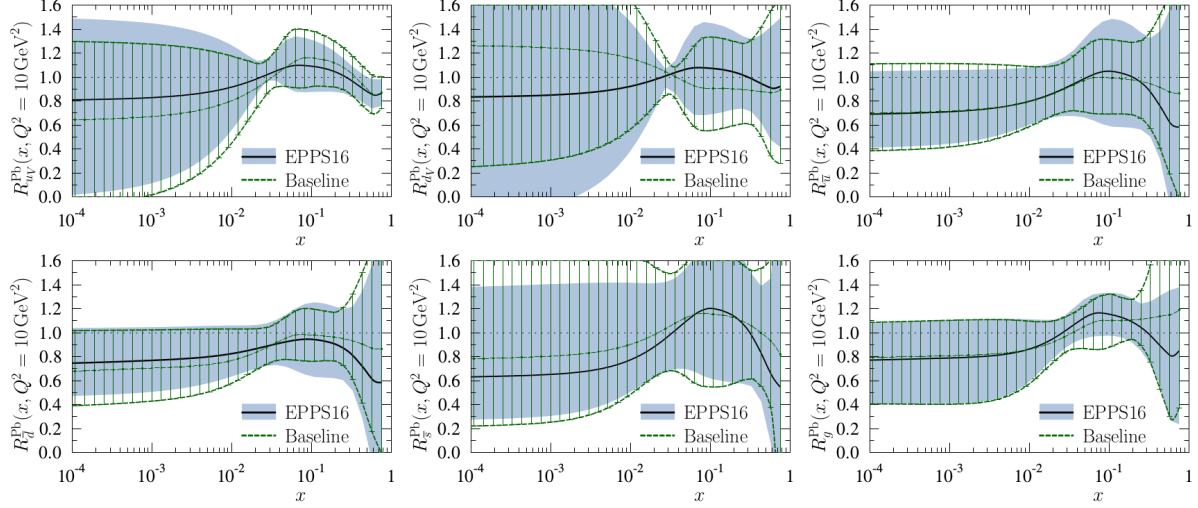


Figure 3.7: Results of the EPPS16 nuclear correction factor  $R^A$  for Pb ions at  $Q^2 = 10 \text{ GeV}^2$ , corresponding to: up valence quarks (top-left), down valence quarks (top-middle), up anti-quarks (top-right), down anti-quarks (bottom-left), strange anti-quarks (bottom-middle) and gluons (bottom-right). The black curve represents the central fit while the blue bands shows the total uncertainty of the PDF fit. The results are compared against a baseline made by performing the EPPS16 fits on the same datasets used for EPS09. Figures taken from Ref. [161].

$$xf_a^{p/A}(x, Q_0^2) = c_0 x^{c_1} (1-x)^{c_2} e^{c_3 x} (1 + e^{x_4 x})^{c_5} \\ \frac{\bar{d}(x, Q_0^2)}{\bar{u}(x, Q_0^2)} = c_0 x^{c_1} (1-x)^{c_2} + (1 + c_3 x)(1-x)^{c_4} \quad (3.15)$$

where  $f_a^{p/A}$  is the bound proton nPDF of a parton  $a$  in a nucleus A,  $\bar{d}$  and  $\bar{u}$  are the down and up anti-quark nPDFs, respectively,  $c_i$  are parameters, and the parametrisation scale  $Q_0$  is fixed at  $1.3 \text{ GeV}$ . The strange quark and anti-quark nPDFs are assumed to be the same. The  $A$ -dependence of the nPDFs is parametrised in nCTEQ15 using the coefficients  $c_i$ , according to:

$$c_i(A) = c_{i,0} + c_{i,1} (1 - A^{-c_{i,2}}) \quad (3.16)$$

The nCTEQ15 fits are performed using 16 free parameters. In addition, the nCTEQ15 treats the up and down valence quark PDFs independently but it assumes no flavour dependence for nuclear modifications of the up and down anti-quarks.

Figure 3.8 shows the nCTEQ15 results of the full nuclear lead PDFs  $f^{Pb}$  at  $Q = 10 \text{ GeV}$  compared to the results from the EPS09 and HKN07 [164] nPDFs. One can see that

at  $x \gtrsim 0.05$  the up and down valence quark nPDFs dominates while at  $x < 0.01$  the sea quarks and the gluons nPDFs become dominant.

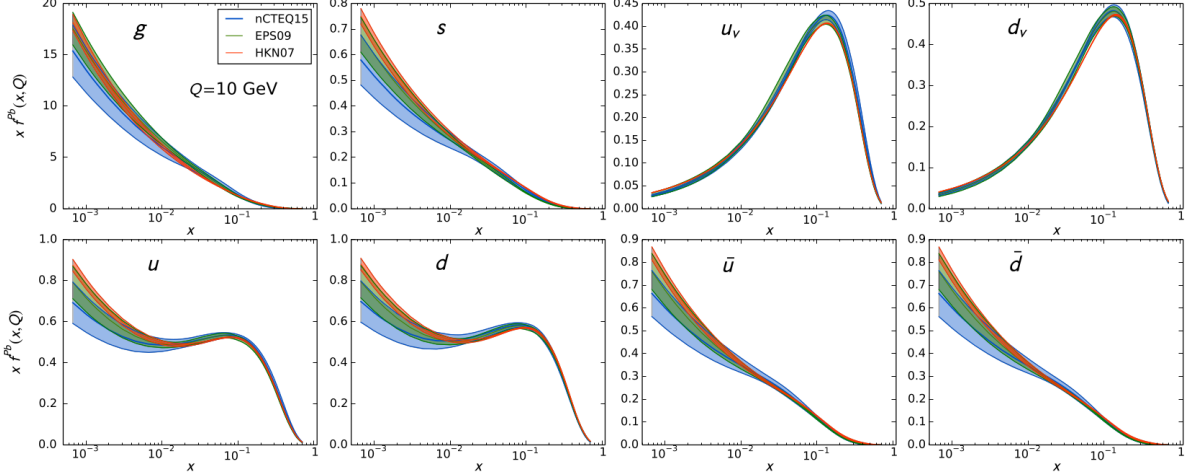


Figure 3.8: Results of the nCTEQ15 full nuclear PDFs for Pb ions  $f^{Pb}$  at  $Q = 10\text{ GeV}$  (blue curve with band), compared to the corresponding ones from EPS09 [159] (green curve with band) and HKN07 [164] (orange curve with band). The plots, in order from top-left to bottom-right, correspond to: gluons, strange quarks, up valence quarks, down valence quarks, up quarks, down quarks, up anti-quarks and down anti-quarks. Figures taken from Ref. [163].

A comparison between the results of the nCTEQ15 and EPPS16 nuclear modifications at  $Q = 100\text{ GeV}$  is shown in Figure 3.9. The nCTEQ15 central set expects more shadowing at low  $x$  than EPPS16 for the down valence quarks, while the opposite trend is observed for up valence quarks. Moreover, the uncertainties of the EPPS16 calculations are much larger than the nCTEQ15 ones because the EPPS16 uses more parameters to fit the nuclear modifications.

The main characteristics of the EPS09, EPPS16 and nCTEQ15 nuclear PDFs are summarized in Table 3.2.

### 3.1.5 Experimental results at LHC

Measurements of the weak boson production in heavy-ion collisions have been performed by the LHC experiments. The latest results have been derived from p-Pb collisions at  $\sqrt{s_{NN}} = 5.02\text{ TeV}$  and Pb-Pb collisions at  $\sqrt{s_{NN}} = 2.76\text{ TeV}$  and  $\sqrt{s_{NN}} = 5.02\text{ TeV}$ . This subsection gives a brief summary on some of the results.

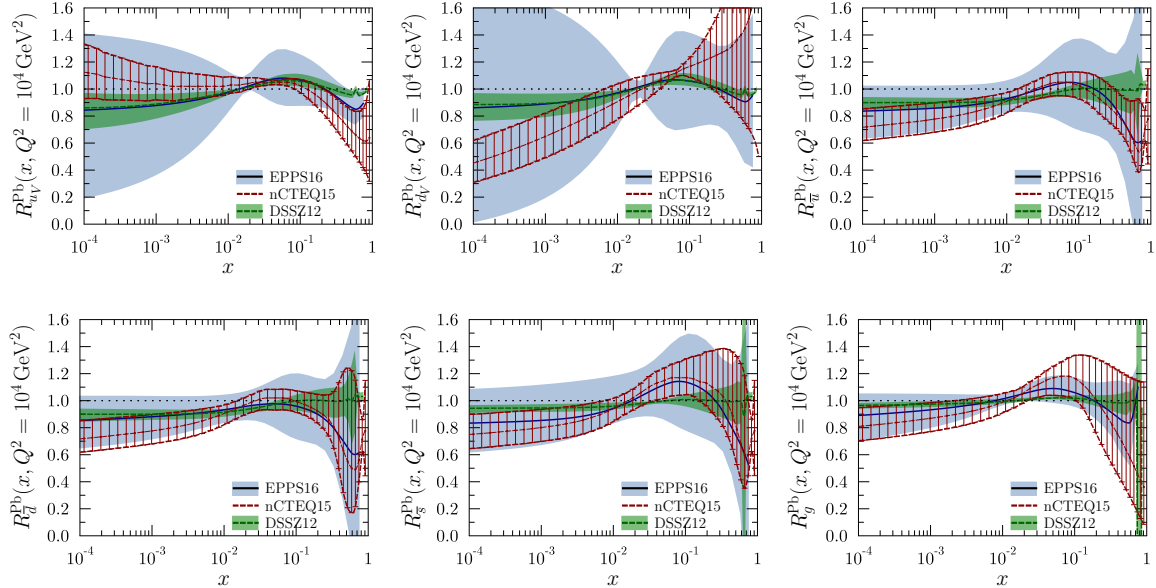


Figure 3.9: Comparison between the EPPS16 (blue curve with band), nCTEQ15 (red curves with hatching) and DSSZ12 (green curve with band) nuclear modifications performed at  $Q^2 = 10^4 \text{ GeV}^2$ , corresponding to: up valence quarks (top-left), down valence quarks (top-middle), up anti-quarks (top-right), down anti-quarks (bottom-left), strange anti-quarks (bottom-middle) and gluons (bottom-right). Figures provided by the EPPS16 authors.

**Pb-Pb results.** The CMS [165, 166] and ATLAS [167, 168] collaborations measured the W- and Z-boson production in Pb-Pb collisions at  $\sqrt{s_{\text{NN}}} = 2.76 \text{ TeV}$  in the lepton decay channel. The ATLAS and CMS measurements were performed in the mid-rapidity region ( $|y| < 2.5$ ). The results are in good agreement with NLO pQCD calculations with and without nuclear PDF corrections. Moreover, the centrality dependence of the weak boson yields is observed to scale with  $N_{\text{coll}}$ , within uncertainties. In the case of W boson, the lepton charge asymmetry of  $W^\pm$ , defined as  $(N_\ell^+ - N_\ell^-)/(N_\ell^+ + N_\ell^-)$ , is found to be different from the results in p-p collisions, but this is understood to be simply associated to the different number of protons and neutrons in the Pb nuclei, the isospin effect. The statistical precision of the results is not enough to provide significant constraints on the global fits to the PDFs.

Results from the ALICE collaboration extend the measurements on the production of Z bosons in Pb-Pb collisions at  $\sqrt{s_{\text{NN}}} = 5.20 \text{ TeV}$  [169] in the low Bjorken- $x$  forward rapidity region ( $2.5 < y < 4.0$ ), where more shadowing is expected. The measurements deviate significantly ( $\sim 3$  standard deviations) from calculations assuming only isospin

nPDF	EPS09	EPPS16	nCTEQ15
Order	NLO	NLO	NLO
Fit	nuclear modification	nuclear modification	nuclear PDF
Baseline PDF	CTEQ6	CT14	
Free parameters	15	20	17
Data points	929	1811	708
EMC DY dileptons in p-A	Yes	Yes	Yes
RHIC pions in d-A	Yes	Yes	Yes
SLAC $l^\pm$ -A DIS	Yes	Yes	Yes
CHORUS $\nu$ -A DIS	No	Yes	No
RHIC DY in $\pi$ -A	No	Yes	No
LHC dijets in pPb	No	Yes	No
LHC weak bosons in pPb	No	Yes	No

Table 3.2: Summary of the information of EPS09, EPPS16 and nCTEQ15 nuclear PDFs.

effects and agree with calculations including nuclear PDF corrections.

**p-Pb results.** The ATLAS collaboration has measured the Z-boson production in p-Pb collisions at  $\sqrt{s_{\text{NN}}} = 5.02 \text{ TeV}$  [170]. The Z-boson cross section as a function of the Z-boson rapidity determined in the centre-of-mass frame, is displayed in Figure 3.10. The results are better described by the PDF model calculations including nuclear modifications, although the free-proton PDF calculations are not excluded within the precision of the measurement.

The CMS and ALICE collaborations have published results on the production of W bosons in p-Pb collisions at  $\sqrt{s_{\text{NN}}} = 5.02 \text{ TeV}$  [171, 172]. The measurements of the W-boson production cross section performed by the ALICE collaboration [172], as a function of the lepton rapidity in the centre-of-mass frame, are shown in Figure 3.11. The ALICE results are compared to NLO calculations using the CT10 proton PDF and NNLO calculations using the FEWZ generator and the MSTW200 proton PDF, with and without EPS09 nuclear PDF corrections. The cross section results are found to be in good agreement with the NLO model calculations while NNLO calculations without nuclear PDF modifications slightly overestimate the measurement at forward lepton rapidity ( $2.03 < |y_{\text{cms}}| < 3.53$ ).

Finally, the W-boson measurements of CMS [171] are performed in the muon and electron decay channels as a function of the lepton pseudorapidity in the laboratory frame [171]. Figure 3.12 shows the measured cross sections for  $W^- \rightarrow \ell^- \bar{\nu}_\ell$  (left) and  $W^+ \rightarrow \ell^+ \nu_\ell$  (middle), and the lepton charge asymmetry (right), compared to the NLO

### 3.1. INTRODUCTION

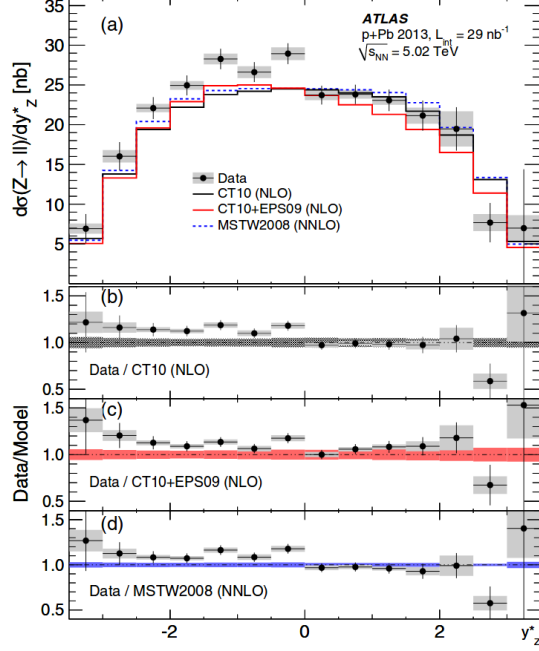


Figure 3.10: Distribution of the production cross section for  $Z \rightarrow \mu^+\mu^-$  measured in p-Pb collisions at  $\sqrt{s_{NN}} = 5.02$  TeV as a function of the Z-boson rapidity in the centre-of-mass frame. Figure taken from Ref. [170].

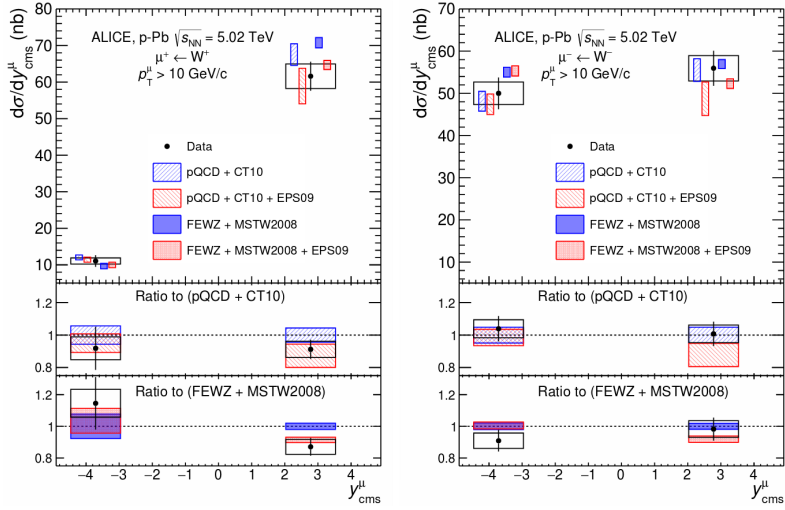


Figure 3.11: Distribution of the production cross section for  $W^- \rightarrow \mu^- \bar{\nu}_\mu$  (left) and  $W^+ \rightarrow \mu^+ \nu_\mu$  (right) measured in p-Pb collisions at  $\sqrt{s_{NN}} = 5.02$  TeV as a function of the muon rapidity in the centre-of-mass frame. Figures taken from Ref. [172].

pQCD calculations using the CT10 proton PDF with and without EPS09 nuclear corrections. Both theoretical calculations are found to be in good agreement with the measured

cross sections within uncertainties, except in the backward region ( $\eta_{\text{lab}} < -1.0$ ) for  $W^-$  bosons, where a small excess is seen in the results. The small deviation is also reflected in the measured lepton charge asymmetry, where the model calculations overestimate the data in the region  $-2.0 < \eta_{\text{lab}} < -1.0$ . It was suggested at the time that the small disagreement between the PDF calculations and the data could be due to different flavour dependence between the up and down quark PDFs [171].

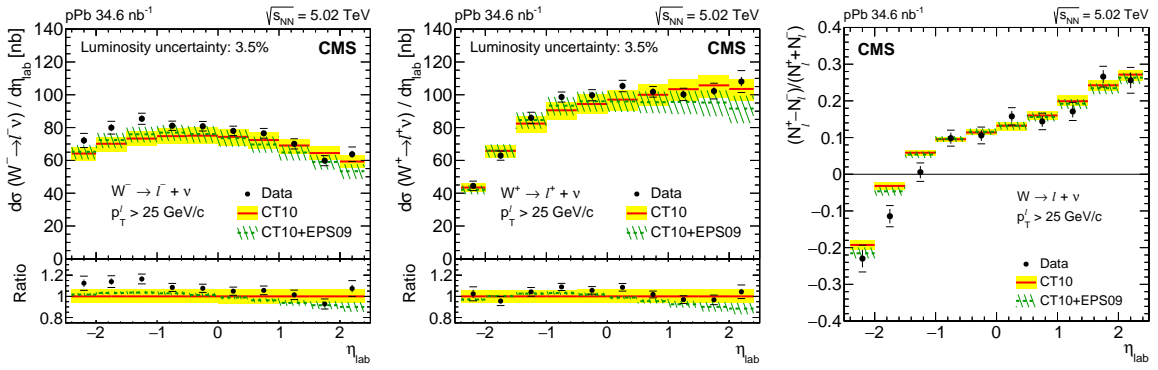


Figure 3.12: Distribution of the production cross section for  $W^- \rightarrow \ell^- \bar{\nu}_\ell$  (left) and  $W^+ \rightarrow \ell^+ \bar{\nu}_\ell$  (middle), and the lepton charge asymmetry (right) measured in p-Pb collisions at  $\sqrt{s_{\text{NN}}} = 5.02 \text{ TeV}$  as a function of the lepton pseudorapidity in the laboratory frame. The CT10 PDF calculations with EPS09 (green line) and without (red line) nuclear PDF corrections are included. The bottom panels present the ratio of the CT10+EPS09 (green line) and data (black points) normalised to the CT10 baseline. Figures taken from Ref. [171].

## 3.2 Analysis

In this section, the analysis of the W-boson production in p-Pb collisions at  $\sqrt{s_{\text{NN}}} = 8.16 \text{ TeV}$  is described. The measurement is performed in the  $W^\pm \rightarrow \mu^\pm \nu_\mu$  decay channel using data recorded with the CMS detector and the signal event yields are extracted from the missing transverse momentum  $p_T^{\text{miss}}$  distributions. The analysis is currently in the final stage of the internal collaboration review and will be submitted to a peer-review journal in the near future.

The dataset used is introduced in Section 3.2.1, the NLO simulations for the signal and background processes are listed in Section 3.2.2, and the event selection is described in Section 3.2.3. The corrections for the simulated weak boson  $p_T$  and the  $p_T^{\text{miss}}$  are explained in Section 3.2.4 and Section 3.2.5, respectively. The measurement of the signal efficiency is presented in Section 3.2.6 and the extraction of the signal event yields is

detailed in Section 3.2.7. The observables of the analysis are introduced in Section 3.2.8. In Section 3.2.9, the different sources of systematic uncertainties and the methods employed to estimate them are presented.

### 3.2.1 Dataset

The production of W bosons is measured in p-Pb collisions using data recorded by the CMS detector at the end of 2016. The dataset employed in this analysis is composed of events selected by the HLT trigger, requiring the presence of at least one identified muon candidate with  $p_T > 12$  GeV/ $c$ . The data were reconstructed with CMSSW 8.0.30 and thoroughly validated by the CMS collaboration. Only fractions of the dataset, recorded with all CMS subdetectors operating in optimal conditions, were processed. The total integrated luminosity of the recorded data corresponds to  $173.4$  nb $^{-1}$ , currently known within 3.5% [173].

The p-Pb data-taking period was divided in two parts, as explained in Section 2.1.5. In the first part of the p-Pb run (labelled as Ppb), the proton beam was circulating in the clockwise direction along the LHC ring, while in the second part (referred as pPb), the proton beam was circulating counter-clockwise. The integrated luminosity recorded in the Ppb and pPb runs was  $62.6$  nb $^{-1}$  and  $110.8$  nb $^{-1}$ , respectively.

Since the LHC dipole magnets apply the same magnetic rigidity (i.e. momentum-to-charge ratio) to both beams [174], the energy of the Pb beam is constrained by the energy of the proton beam  $E_p$ , and the number of nucleons ( $A_{\text{Pb}} = 208$ ) and electric charge ( $Z_{\text{Pb}} = 82$ ) of the Pb nucleus. During the entire p-Pb run, the energy of the proton beam was 6.50 TeV and as a result, the energy per nucleon  $E_{\text{Pb}}$  of the Pb beam was then:

$$E_{\text{Pb}} = \frac{Z_{\text{Pb}}}{A_{\text{Pb}}} \times E_p = 2.56 \text{ TeV} \quad (3.17)$$

In addition, the energy of the nucleon-nucleon collisions in the centre-of-mass (CM) frame can be derived in this case using:

$$\sqrt{s_{\text{NN}}} = 2 \sqrt{\frac{Z_{\text{Pb}}}{A_{\text{Pb}}} \times E_p} = 8.16 \text{ TeV} \quad (3.18)$$

Considering that the CMS detector is rapidity-symmetric with respect to the beam orientation, the pPb and Ppb samples are merged in order to maximize the statistics of the data. This is done by first flipping the sign of the pseudorapidity of particles from the Ppb sample measured in the laboratory frame, and then combining them with the

events from the pPb sample. The combined sample corresponds to p-Pb collisions with the proton always going toward positive pseudorapidity. From hereafter, all results in this analysis are derived using the combined pPb sample.

Due to the energy difference between the p-Pb colliding beams, the nucleon-pair CM frame is not at rest with respect to the laboratory frame. Massless particles emitted in the CM frame experience a constant longitudinal boost given by:

$$|\Delta\eta| = \frac{1}{2} \times \left| \ln \left( \frac{Z_{\text{Pb}}}{A_{\text{Pb}}} \right) \right| = 0.465 \quad (3.19)$$

As a consequence, the pseudorapidity measured in the CM frame ( $\eta_{\text{CM}}$ ) is derived from the one determined in the laboratory frame ( $\eta_{\text{lab}}$ ), in the following way:

$$\eta_{\text{CM}} = \eta_{\text{lab}} - 0.465 \quad (3.20)$$

### 3.2.2 Next-to-leading order simulations

Fully reconstructed Monte Carlo (MC) simulations are used to describe the W-boson signal, and the top-quark and electroweak background processes. The MC samples were generated at NLO using the PPositive Weight Hardest Emission Generator (POWHEG) version 2 [175, 176, 177]. To account for QCD and electroweak theory corrections, the POWHEG-BOX packages  $W_{\text{ew}}\text{-BMMNP}$  [178] and  $Z_{\text{ew}}\text{-BMMNPV}$  [179] were used to generate the  $pp \rightarrow W \rightarrow \ell\nu_\ell$  and  $pp \rightarrow Z/\gamma^* \rightarrow \ell^+\ell^-$  processes, respectively. The  $pp \rightarrow t\bar{t}$  was generated using the POWHEG-BOX package  $hqv$  [180], which is a heavy flavour quark generator at NLO QCD.

In order to simulate p-Pb collisions, I added to the POWHEG Fortran code a subroutine that modifies the PDFs of one of the incoming particles (referred as the Pb nucleus) by applying the EPPS16 nuclear correction factors derived for  $\text{Pb}^{82+}$  nuclei <sup>2</sup> [161], since the standard POWHEG framework only generates p-p collision events. In this case, the POWHEG event generation starts by evaluating the PDFs associated to both incoming particles (proton and Pb nucleus) using the NLO CT14 PDF set [153]. Afterwards, the PDFs corresponding to the Pb nucleus are modified with my subroutine, following the procedure defined in Ref. [161] and described in the following steps:

1. The EPPS16 nuclear correction factors  $R$  are applied to the PDFs computed by POWHEG, in the following way:

---

<sup>2</sup>The EPPS16 nuclear correction factors for each nuclei can be found in <https://www.jyu.fi/science/en/physics/research/highenergy/urhic/npdfs/epps16-nuclear-pdfs>

$$\begin{aligned}
 \hat{f}_p^d &= R_s^d f_p^{\bar{d}} + R_v^d (f_p^d - f_p^{\bar{d}}) & ; \quad \hat{f}_p^{\bar{d}} &= R_s^d f_p^d \\
 \hat{f}_p^u &= R_s^u f_p^{\bar{u}} + R_v^u (f_p^u - f_p^{\bar{u}}) & ; \quad \hat{f}_p^{\bar{u}} &= R_s^u f_p^u \\
 \hat{f}_p^x &= R_s^x f_p^x & ; \quad \hat{f}_p^{\bar{x}} &= R_s^x f_p^{\bar{x}} \quad \text{where } x = \{s, c, b\} \\
 \hat{f}_p^g &= R^g f_p^g
 \end{aligned} \tag{3.21}$$

where  $\hat{f}_p$  represent the PDFs of a proton bound in the Pb nucleus,  $f_p$  are the free proton PDFs obtained with NLO CT14, and  $R_s^x$ ,  $R_v^x$  and  $R^g$  are the EPPS16 nuclear correction factors for sea quarks, valence quarks and gluons, accordingly.

2. The bound neutron PDFs ( $\hat{f}_n$ ) are then derived from the bound proton PDFs, by interchanging the up and down (anti-)quark PDFs (isospin symmetry between protons and neutrons), according to:

$$\begin{aligned}
 \hat{f}_n^d &= \hat{f}_p^u & ; \quad \hat{f}_n^u &= \hat{f}_p^d \\
 \hat{f}_n^{\bar{d}} &= \hat{f}_p^{\bar{u}} & ; \quad \hat{f}_n^{\bar{u}} &= \hat{f}_p^{\bar{d}}
 \end{aligned} \tag{3.22}$$

and assuming the same PDFs ( $\hat{f}_n^i = \hat{f}_p^i$ ) for the other flavours.

3. The bound proton and neutron PDFs are combined to form the Pb-nucleus PDFs ( $f_{Pb}$ ), taking into account the number of protons ( $Z_{Pb}$ ) and neutrons ( $N_{Pb} = A_{Pb} - Z_{Pb}$ ) in the Pb nucleus, as done in:

$$\begin{aligned}
 f_{Pb}^d &= \left( \frac{Z_{Pb}}{A_{Pb}} \right) \hat{f}_p^d + \left( \frac{N_{Pb}}{A_{Pb}} \right) \hat{f}_n^d & ; \quad f_{Pb}^{\bar{d}} &= \left( \frac{Z_{Pb}}{A_{Pb}} \right) \hat{f}_p^{\bar{d}} + \left( \frac{N_{Pb}}{A_{Pb}} \right) \hat{f}_n^{\bar{d}} \\
 f_{Pb}^u &= \left( \frac{Z_{Pb}}{A_{Pb}} \right) \hat{f}_p^u + \left( \frac{N_{Pb}}{A_{Pb}} \right) \hat{f}_n^u & ; \quad f_{Pb}^{\bar{u}} &= \left( \frac{Z_{Pb}}{A_{Pb}} \right) \hat{f}_p^{\bar{u}} + \left( \frac{N_{Pb}}{A_{Pb}} \right) \hat{f}_n^{\bar{u}} \\
 f_{Pb}^i &= \hat{f}_p^i \quad \text{for other flavours}
 \end{aligned} \tag{3.23}$$

4. The PDFs originally derived by POWHEG are then replaced with the modified PDFs defined in Eq. (3.23), and the rest of the event generation is done with the standard POWHEG framework with no further changes.

The parton showering is performed by hadronizing the POWHEG events with PYTHIA 8.212 [181], using the CUETP8M1 underlying event (UE) tune [181, 182]. The full CMS detector response is simulated in all MC samples, based on GEANT4 [183], considering a realistic alignment and calibration of the beam spot and the different subdetectors

of CMS, tuned on data. The MC events are reconstructed with the standard CMS p-p reconstruction software used during 2016 data taking.

To consider a more realistic distribution of the underlying environment present in p-Pb collisions, the MC signal events were embedded in a minimum bias (i.e. inelastic hadronic interactions) sample generated with EPOS LHC [184], taking into account both p-Pb boost directions. The EPOS LHC MC samples were tuned to reproduce the global event properties of the p-Pb data such as the charged-hadron transverse momentum spectrum and the particle multiplicity [185]. The list of simulated samples and the cross sections used in this analysis are summarized in Table 3.3. The cross sections of the electroweak processes corresponds to the POWHEG NLO cross sections scaled by  $A_{\text{Pb}}$ , while the  $t\bar{t}$  cross section is taken from the inclusive cross section measured in pPb collisions at  $\sqrt{s_{\text{NN}}} = 8.16 \text{ TeV}$  by the CMS collaboration [186].

Process	Cross section [nb]	Generated events
$p\text{Pb} \rightarrow W^+ \rightarrow \mu^+ \nu_\mu$	1214	982714
$p\text{pb} \rightarrow W^+ \rightarrow \mu^+ \nu_\mu$	1214	981874
$p\text{Pb} \rightarrow W^- \rightarrow \mu^- \bar{\nu}_\mu$	1083	995726
$p\text{pb} \rightarrow W^- \rightarrow \mu^- \bar{\nu}_\mu$	1083	998908
$p\text{Pb} \rightarrow W^+ \rightarrow \bar{\tau} \nu_\tau$	1147	481125
$p\text{pb} \rightarrow W^+ \rightarrow \bar{\tau} \nu_\tau$	1147	500000
$p\text{Pb} \rightarrow W^- \rightarrow \tau \bar{\nu}_\tau$	1023	495450
$p\text{pb} \rightarrow W^- \rightarrow \tau \bar{\nu}_\tau$	1023	498092
$p\text{Pb} \rightarrow Z/\gamma^* \rightarrow \mu^+ \mu^-$	266	1000000
$p\text{pb} \rightarrow Z/\gamma^* \rightarrow \mu^+ \mu^-$	266	1000000
$p\text{pb} \rightarrow Z/\gamma^* \rightarrow \tau \bar{\tau}$	259	498444
$p\text{Pb} \rightarrow t\bar{t}$	$45 \pm 8$	99578
$p\text{pb} \rightarrow t\bar{t}$	$45 \pm 8$	100000

Table 3.3: Simulated NLO samples used for the W-boson measurement in p-Pb at 8.16 TeV. The listed cross sections are the POWHEG NLO cross sections scaled by  $A_{\text{Pb}} = 208$ , except for the  $t\bar{t}$  production cross section which is taken from the CMS measurement in p-Pb at 8.16 TeV [186].

The pPb and Pbp simulated samples are also combined in the same way as done for data, but the generated events are weighed before merging the samples by applying a global weight, according to their p-Pb boost direction, defined as:

$$w_{\text{MC}} = \frac{\sigma \times \mathcal{L}_{\text{data}}}{N_{\text{gen}}} \quad (3.24)$$

where  $\mathcal{L}_{\text{data}}$  corresponds to the integrated luminosity recorded in each proton-lead run ( $110.8 \text{ nb}^{-1}$  for pPb and  $62.6 \text{ nb}^{-1}$  for PbP),  $\sigma$  is the cross section associated to the simulated process (listed in Table 3.3) and  $N_{\text{gen}}$  is the total number of generated events. The global weighing is applied to ensure that each MC sample is normalised to the corresponding integrated luminosity of the data.

### 3.2.3 Event selection

The signal events, determined by the process  $W \rightarrow \mu\nu_\mu$ , are characterised by a high- $p_T$  muon and the presence of missing transverse momentum  $p_T^{\text{miss}}$ , originated from the undetected neutrino. Events with similar characteristics can be produced by other background processes, such as semi-leptonic decays of hadrons formed within jets or dilepton decays of Z bosons. This section explain the different selections implemented to suppress the background while keeping the signal.

#### 3.2.3.1 p-Pb global filter

In order to ensure that the samples are not contaminated by events not originating from the inelastic hadronic collisions, a standard p-Pb Global Event Filter (GEF) is applied. The different selections included in the p-Pb GEF are described below:

- Primary vertex filter: requires the presence of a primary vertex reconstructed from at least two tracks, within a longitudinal (transverse) distance of 25 cm (2 cm) of the nominal interaction point. This selection reduces the contamination from non-collision backgrounds, such as cosmic-ray muons or accelerator-induced particles.
- HF coincidence filter: requires at least one tower on each side of the interaction point in the Hadron-Forward calorimeter, with an energy deposit per tower of at least 3 GeV. This filter rejects events from electronic noise and beam-beam electromagnetic interactions.
- Beam-scraping filter: requires at least 25% of tracks in the event to be high quality tracks. This requirement is used to further suppress the contribution from beam-related backgrounds, such as beam-gas interactions and beam-halo events.

The impact of the GEF was checked both in data and simulation. Only 0.08% of events in data and 0.06% of events in the  $W \rightarrow \mu\nu_\mu$  simulation, passing all analysis selections summarized in Section 3.2.3.5, were removed by the filter.

### 3.2.3.2 Trigger

The events used in this analysis were selected online with the HLT trigger HLT\_PAL3Mu12. This trigger requires a fully reconstructed L3 muon with  $p_T > 12 \text{ GeV}/c$ . The HLT trigger was seeded with the L1 trigger path L1\_SingleMu7, which pass events with at least one L1 muon with  $p_T > 7 \text{ GeV}/c$ . It is to be noted that only muons of  $p_T$  greater than  $25 \text{ GeV}/c$  are considered in the offline analysis, and such trigger is extremely efficient for those.

A reconstructed muon is considered matched to the trigger, if it matches the L3 muon that fired the trigger. The matching criteria between the reconstructed muon and the L3 muon requires:

$$\Delta R(\mu_{\text{reco}}, \mu_{\text{HLT}}) = \sqrt{(\eta_{\text{reco}}^\mu - \eta_{\text{HLT}}^\mu)^2 + (\phi_{\text{reco}}^\mu - \phi_{\text{HLT}}^\mu)^2} < 0.1 \quad (3.25)$$

The  $\Delta R < 0.1$  matching criteria is a standard threshold commonly used in CMS analyses employing L3 muon triggers [112]. It has been selected taking into account the  $\eta$  and  $\phi$  resolutions of muon tracks reconstructed with the HLT L3 and offline muon algorithms.

### 3.2.3.3 Muon selection

Muon candidates are identified using a standard *tight* selection, optimised for muons with high  $p_T$ . The tight selection requires muon candidates to be reconstructed globally from hits in the muon stations and the tracker, be identified with the PF algorithm [114] and pass the following criteria:

- The muon track fit has at least a  $\chi^2$  per degree of freedom less than ten, ensuring a minimal fit quality.
- The muon track segments are matched to at least two muon stations, making the selection consistent with the muon trigger logic.
- The transverse impact parameter (longitudinal distance) of the muon track is consistent with the primary vertex within 2 mm (5 mm), to reduce the background from cosmic rays and muon decays in flight (e.g. from pion, kaon and heavy-flavour hadron decays).
- The muon track has at least one hit in the pixel detector to further suppress muons from decays in flight.

- The muon track includes hits in at least six inner-tracker layers to guarantee a good  $p_T$  measurement.

Apart from the *tight* identification criteria, muon candidates are also required to be isolated in order to reduce the proportion of muons coming from jets. Muons are considered isolated if the sum of the  $p_T$  of all PF-identified photons, charged hadrons and neutral hadrons, within a cone of  $\Delta R(\mu, \text{PF}) < 0.3$ , is less than 15% of the muon  $p_T^\mu$ . The muon isolation variable is thus defined as:

$$I^\mu = \left( \sum_{\substack{\Delta R < 0.3 \\ \text{charged hadrons}}} p_T + \sum_{\substack{\Delta R < 0.3 \\ \text{neutral hadrons}}} p_T + \sum_{\substack{\Delta R < 0.3 \\ \text{photons}}} p_T \right) / p_T^\mu \quad (3.26)$$

Finally, muon candidates are required to have  $p_T > 25 \text{ GeV}/c$  and be within  $|\eta_{\text{lab}}| < 2.4$ . If more than one muon is found with  $p_T > 25 \text{ GeV}/c$  and passing the identification criteria in a given event, then the corresponding muon with the highest  $p_T$  is used. This happens in 3% of events in data but are later suppressed down to 0.001% of events with the  $Z/\gamma^* \rightarrow \mu^+ \mu^-$  veto described in the next section.

### 3.2.3.4 $Z/\gamma^* \rightarrow \mu^+ \mu^-$ veto

A veto is applied to suppress the contribution from  $Z/\gamma^* \rightarrow \mu^+ \mu^-$  background events. This veto consists in removing events that contain at least two opposite-sign muons with  $p_T > 15 \text{ GeV}/c$ , each passing the muon identification and isolation criteria.

The probability that  $Z/\gamma^* \rightarrow \mu^+ \mu^-$  events survive the veto is checked using simulation. The denominator of the  $Z/\gamma^* \rightarrow \mu^+ \mu^-$  veto efficiency is filled with muons passing the signal selection criteria summarised in the next section, while the numerator is filled with the same muons as long as the event passes the  $Z/\gamma^* \rightarrow \mu^+ \mu^-$  veto. The simulated survival probability is shown in Figure 3.13. As can be observed, most of the  $Z/\gamma^* \rightarrow \mu^+ \mu^-$  events that survive the veto mainly contributes in the forward pseudorapidity region, where one of the muons from the  $Z/\gamma^*$ -boson decay escapes the detector.

### 3.2.3.5 Event selection summary

In summary, the signal selection consists of the detection of a high- $p_T$  muon, passing the identification criteria detailed in Section 3.2.3.3. The muon candidate is required to have  $p_T > 25 \text{ GeV}/c$ , be isolated and match the trigger (see Section 3.2.3.2). The events entering the signal region are also required to satisfy the p-Pb global event filter (Section 3.2.3.1) and the  $Z/\gamma^* \rightarrow \mu^+ \mu^-$  veto (Section 3.2.3.4).

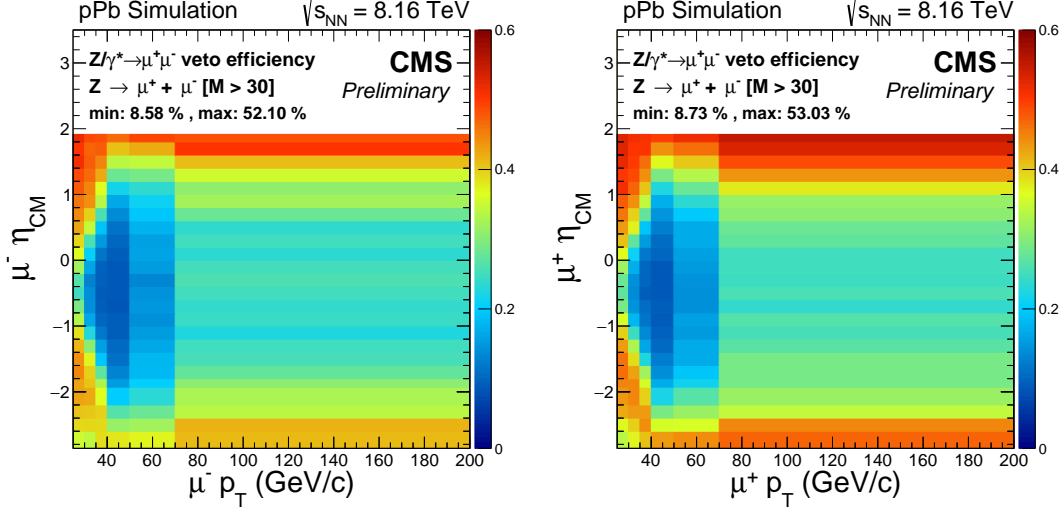


Figure 3.13: Survival probability of single muons from a  $Z/\gamma^* \rightarrow \mu^+\mu^-$  ( $M > 30 \text{ GeV}/c^2$ ) simulation, as a function of the muon  $\eta_{CM}^\mu$  and  $p_T^\mu$ , separated in negative (left) and positive (right) charged muons. Muons are required to have  $p_T > 25 \text{ GeV}/c$  and  $|\eta| < 2.4$ , match the trigger and pass the isolation and identification criteria.

The other signature of a  $W \rightarrow \nu\mu$  event is a high- $p_T$  neutrino, estimated through the  $p_T^{\text{miss}}$ . No explicit selection is applied on the missing transverse momentum. The  $p_T^{\text{miss}}$  is directly used to extract the event yields by fitting the signal and background components. Apart from the main signal sample, two more samples are used:

- $Z \rightarrow \mu^+\mu^-$  control sample: selects  $Z \rightarrow \mu^+\mu^-$  events by reverting the  $Z/\gamma^* \rightarrow \mu^+\mu^-$  veto and selecting  $\mu^+\mu^-$  pairs with invariant mass within the  $Z$ -boson mass window. Used to derive corrections for the weak boson  $p_T$  (Section 3.2.4) and the  $p_T^{\text{miss}}$  (Section 3.2.5).
- QCD jet control sample: selects non-isolated muon events by reverting the muon isolation cut. Used to determine the shape of the QCD jet background from data.

The conditions used to define the signal and control regions of interest are illustrated in Figure 3.14.

### 3.2.4 Correction for weak-boson transverse momentum

In a p-Pb collision at high energies, the partons can be described as moving collinearly with the proton or the Pb nucleus, contributing to the momentum only along the beam axis. As a result, at leading order,  $W$  and  $Z$  bosons are produced with no transverse

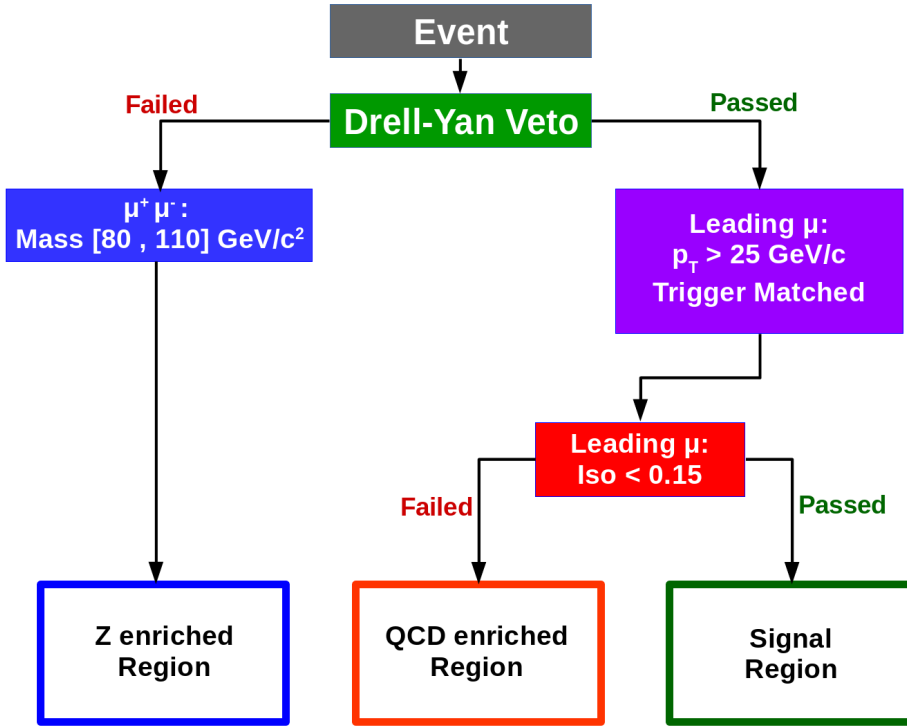


Figure 3.14: Flowchart illustrating the way the events are classified.

momentum. Higher order processes, such as NLO or next-to-NLO, can radiate quarks and gluons that recoil against the weak boson, which acquires transverse momentum in the process.

Since the simulations were produced using the POWHEG NLO generator, the absence of higher order contributions can lead to a mismodelling of the weak boson  $p_T$ , which can then affect the  $p_T$  distribution of the boson decay products (e.g. muon and neutrino). To check this, one can select  $Z \rightarrow \mu^+ \mu^-$  events and compare the  $p_T$  distribution of  $Z$  boson candidates from simulation and data.

The  $p_T$  distribution of  $Z$  bosons has been measured in an on-going CMS analysis of the Drell–Yan production in pPb collisions at 8.16 TeV<sup>3</sup>, which makes use of the same data and electroweak NLO simulations presented in this chapter. As part of the DY analysis, the measurement of the  $Z$ -boson  $p_T$  distribution in the dimuon mass region [60, 120]  $\text{GeV}/c^2$  was compared, after correcting for acceptance and efficiency, to the generated one from POWHEG and found to disagree by up to 20%. To correct for the disagreement, the ratio between the measured and simulated  $p_T$ -differential  $Z \rightarrow \mu^+ \mu^-$  cross sections

<sup>3</sup>The details of the CMS Drell–Yan analysis can be checked in the internal analysis website <http://cms.cern.ch/iCMS/analysisadmin/cadilines?line=HIN-18-003&tp=an&id=2036&ancode=HIN-18-003>

was parametrised as a function of the Z-boson  $p_T$ , resulting in:

$$w^Z(p_T) = \frac{\left(\frac{d\sigma[Z \rightarrow \mu^+ \mu^-]}{dp_T}\right)^{\text{data}}}{\left(\frac{d\sigma[Z \rightarrow \mu^+ \mu^-]}{dp_T}\right)^{\text{MC}}} = \frac{1}{1.19 - 0.37 \times p_T^{-0.37}} \quad (3.27)$$

and the generated Z-boson  $p_T$  distribution was then weighed per event using  $w^Z(p_T)$ .

Considering that Z and W bosons have similar production mechanisms and masses,  $w^Z(p_T)$  is also used to weigh, on an event-by-event basis, the generated W-boson  $p_T$  spectrum. The boson  $p_T$  weighing is applied to the POWHEG simulations of both signal ( $W \rightarrow \mu\nu_\mu$ ) and electroweak backgrounds ( $W \rightarrow \tau\nu_\tau$ ,  $Z/\gamma^* \rightarrow \mu^+ \mu^-$  and  $Z/\gamma^* \rightarrow \tau\bar{\tau}$ ).

The impact of the boson  $p_T$  weighing is checked on a W-boson enhanced sample in data and simulation, made by applying a requirement on the transverse mass, defined as  $M_T = \sqrt{p_T^\mu \cdot p_T^{\text{miss}} \cdot (1 - \cos(\Delta\theta))}$ , where  $\Delta\theta$  is the azimuthal angle between the  $\vec{p}_T^{\text{miss}}$  and muon  $\vec{p}_T^\mu$ . The events of the W-boson enhanced sample are selected from the signal region by requiring  $M_T > 60 \text{ GeV}/c$ , and the corresponding muon  $p_T$  distribution is then compared before and after applying the boson  $p_T$  weighing in Figure 3.15. The simulated muon  $p_T$  distribution is observed to describe better the data in the high- $p_T$  region ( $p_T^\mu > 40 \text{ GeV}/c$ ) after weighing the generated W-boson  $p_T$  distribution.

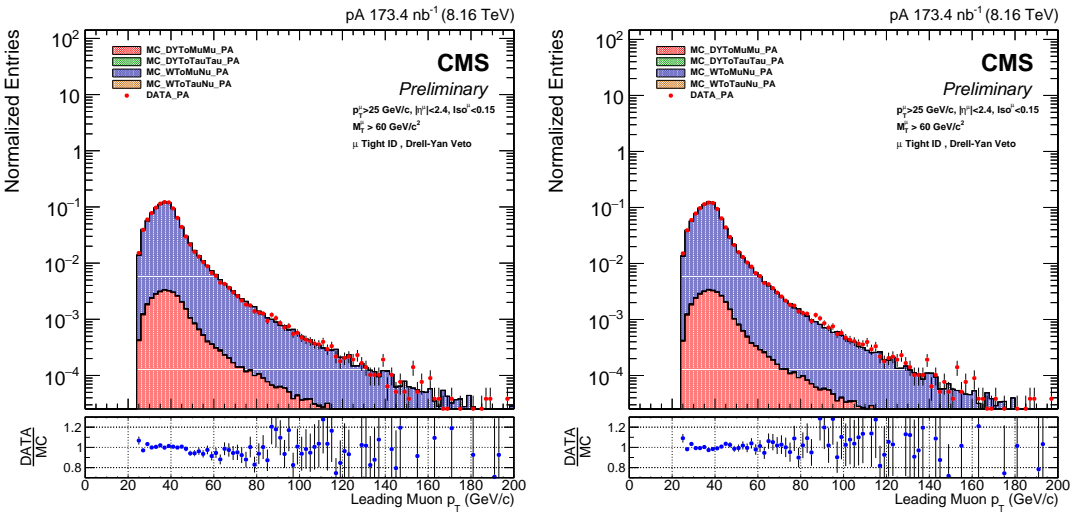


Figure 3.15: Muon  $p_T$  distribution extracted from the W-boson enhanced sample before (left) and after (right) applying the boson  $p_T$  weights. The red points correspond to data, while the blue and red filled areas correspond to events from the  $W \rightarrow \mu\nu_\mu$  and  $Z/\gamma^* \rightarrow \mu^+ \mu^-$  simulations, respectively. The bottom panels show the ratio of data over simulation.

### 3.2.5 Corrections for missing transverse momentum

Since the W-boson analysis relies on  $p_T^{\text{miss}}$  distributions from simulations to extract the signal, it is important that the simulated  $p_T^{\text{miss}}$  describes the data. To achieve this, the  $p_T$  distribution of the reconstructed particles, including those recoiling against the weak boson (referred as the recoil), have to be well modelled.

The  $p_T^{\text{miss}}$  vector derived from  $W \rightarrow \mu\nu_\mu$  events can be decomposed, according to Eq. (2.5), in two parts: the  $p_T$  vector of the muon candidate ( $\vec{p}_T^\mu$ ) and the  $p_T$  vector of the recoil ( $\vec{u}_T$ ), as defined in:

$$\vec{p}_T^{\text{miss}} = -(\vec{u}_T + \vec{p}_T^\mu) \quad (3.28)$$

The recoil  $\vec{u}_T$  is measured via the  $\vec{p}_T$  vectorial sum of all particles identified in an event with the PF algorithm *excluding* the muon from the W-boson decay, as given by:

$$\vec{u}_T = \left( \sum_{\text{particles}} \vec{p}_T \right) - \vec{p}_T^\mu \quad (3.29)$$

The recoil is a complex quantity that includes particles from the hard scattering that balance the W-boson  $p_T$  and from the underlying event (e.g. spectator parton interactions and multiple parton scatterings), as well as effects related to the detector (e.g. electronic noise,  $p_T$  resolution, reconstruction efficiency and acceptance) and the accelerator (e.g. beam-beam remnants). As a result, the recoil is difficult to simulate precisely in p-Pb collisions and the mismodelling of the recoil  $u_T$  can affect the signal extraction.

To improve the modelling of the  $p_T^{\text{miss}}$  in the signal region, the  $p_T^{\text{miss}}$  is corrected in two steps. First, the distribution of the simulated event activity measured as a function of the total energy deposited in the HF calorimeter (hereafter referred as the HF energy) is weighed to the level observed in data as detailed in Section 3.2.5.1. Afterwards, the simulated recoil is calibrated following the procedure described in Section 3.2.5.2.

#### 3.2.5.1 Event activity weighing

The muon isolation and the  $p_T^{\text{miss}}$  are computed by summing over particles produced in the event. As a consequence, any disagreement in the modelling of the event activity (EA) can impact the muon efficiency and the signal extraction. The disagreement between data and the POWHEG simulations embedded in EPOS LHC minimum bias events can be caused by the presence of hard probes such as W bosons, which bias the event activity towards higher particle multiplicity compared to minimum bias events.

To check if the event activity is well modelled in the simulations, the distribution of the number of tracks per event and the HF energy is compared between data and simulation. Since the W-boson sample contains a considerable fraction of background events, a  $Z \rightarrow \mu^+ \mu^-$  control sample is preferred to assess the difference between data and simulation, assuming that weak bosons are produced with similar event activity. The  $Z \rightarrow \mu^+ \mu^-$  events are selected by requiring a  $\mu^+ \mu^-$  pair within the invariant mass region  $80 < M_{\mu^+ \mu^-} < 110$  GeV/c $^2$  as detailed in Section 3.2.3.5. The data-simulation comparisons are shown in Figure 3.16, and it is observed that the simulated samples are indeed not able to reproduce the event activity present in p-Pb data.

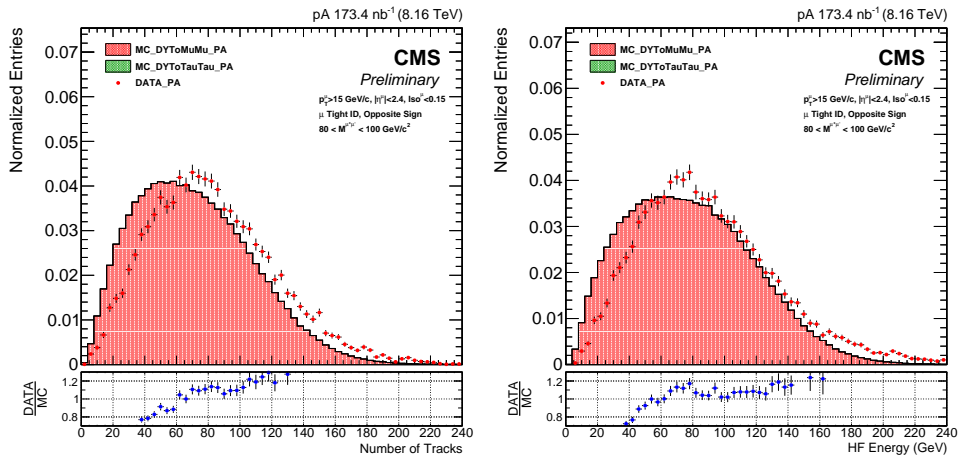


Figure 3.16: Distribution of the number of tracks per event (left) and the total energy deposited in the HF calorimeter (right) in  $Z \rightarrow \mu^+ \mu^-$  events. The red points and filled area correspond to data and  $Z/\gamma^* \rightarrow \mu^+ \mu^-$  simulation, respectively.

The modelling of the event activity is improved using a set of weights determined from the ratio of the number of  $Z \rightarrow \mu^+ \mu^-$  events extracted from data and simulation in different bins of HF energy ( $E_{\text{HF}}$ )<sup>4</sup>, as given by:

$$w^{\text{EA}}(E_{\text{HF}}) = \frac{N_{Z \rightarrow \mu^+ \mu^-}^{\text{data}}[E_{\text{HF}}]}{N_{Z \rightarrow \mu^+ \mu^-}^{\text{MC}}[E_{\text{HF}}]} \quad (3.30)$$

The  $w^{\text{EA}}(E_{\text{HF}})$  weights are used, event-by-event, to weigh the HF energy distribution of the electroweak and  $t\bar{t}$  simulations. Figure 3.17 illustrates how the HF energy weights improves the description of the data  $p_T^{\text{miss}}$  distribution by the simulation. The remaining

<sup>4</sup>The HF distribution is preferred over the track multiplicity because it is less biased by the signal itself. Nonetheless, a systematic uncertainty is assigned by instead weighing according to the track multiplicity distribution, as documented in Section 3.2.9.6.

level of disagreement in the  $p_T^{\text{miss}}$  is then corrected for by calibrating the simulated recoil as explained in the next section.

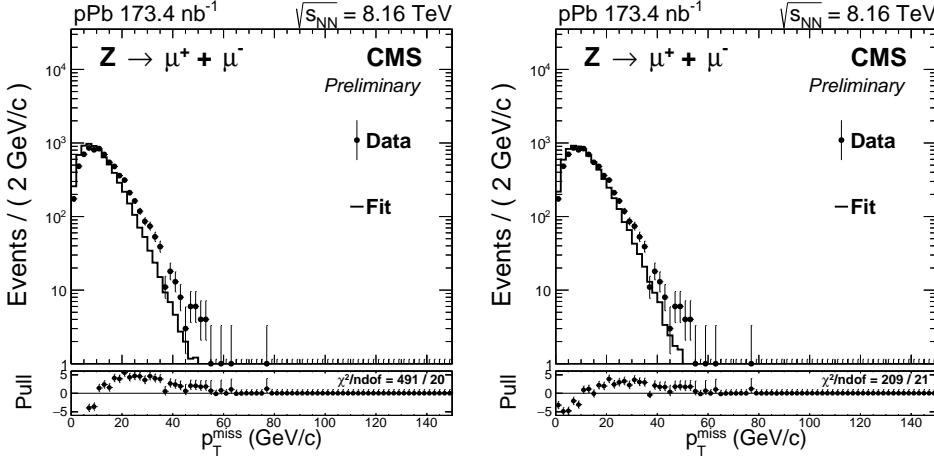


Figure 3.17: Comparison of the  $p_T^{\text{miss}}$  distribution in data and simulation for  $Z \rightarrow \mu^+ \mu^-$  events before (left) and after (right) applying the HF energy weights.

### 3.2.5.2 Recoil calibration

The recoil calibration procedure starts by measuring the recoil in  $Z \rightarrow \mu^+ \mu^-$  events in data and simulation, and then parametrise, in each sample, the components of the recoil  $\vec{u}_T$  with respect to the transverse momentum of the  $Z$  boson ( $q_T^Z$ ). Afterwards, these parametrisations are used to scale the  $\vec{u}_T$  components of each electroweak simulated event (W or Z boson), according to the boson  $p_T$ . By construction, the resulting average recoil distribution matches the corresponding one from data. Similar techniques used to calibrate the recoil have been documented in [115, 116, 187].

The  $Z \rightarrow \mu^+ \mu^-$  control sample employed to extract the recoil calibration is the same as the one used to derive the event activity weights described in the previous section. In addition, the HF energy and the generated  $Z$ -boson  $p_T$  distributions of the simulated control samples have been weighed accordingly.

**Extraction of the recoil scale and resolution.** Since there are no neutrinos produced in the initial hard scattering of  $Z \rightarrow \mu^+ \mu^-$  events, the  $p_T^{\text{miss}}$  spectrum can be used to directly measure the  $p_T^{\text{miss}}$  resolution. Figure 3.18 compares the  $p_T^{\text{miss}}$  spectra extracted from data and simulation in the  $Z \rightarrow \mu^+ \mu^-$  control sample. It is observed that the simulation does not properly describe the  $p_T^{\text{miss}}$  distribution measured in data.

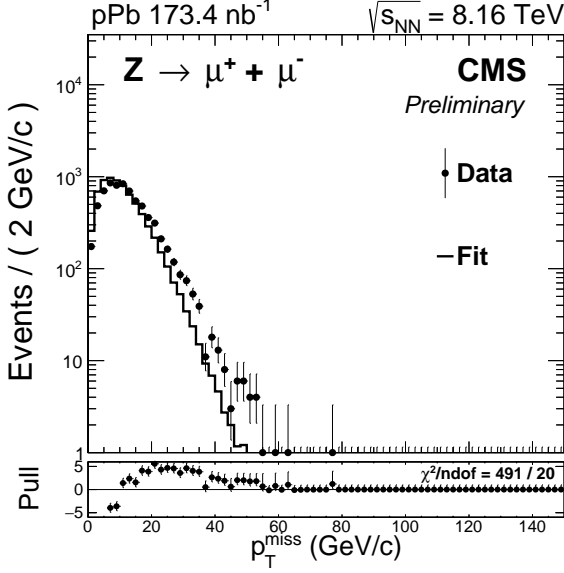


Figure 3.18: Distribution of the  $p_T^{\text{miss}}$  in data and simulation for  $Z \rightarrow \mu^+ \mu^-$  selected events.

In the case of  $Z \rightarrow \mu^+ \mu^-$  events, the recoil  $\vec{u}_T$  is measured by *subtracting* the  $p_T$  vector of the  $Z$ -boson candidate ( $\vec{q}_T^Z = \vec{p}_T^{\mu^+} + \vec{p}_T^{\mu^-}$ ) from the  $\vec{p}_T^{\text{miss}}$ , according to:

$$\vec{u}_T = -\vec{p}_T^{\text{miss}} - \vec{q}_T^Z \quad (3.31)$$

The recoil  $\vec{u}_T$  is then projected along the  $Z$ -boson  $\vec{q}_T^Z$  direction. The parallel and perpendicular components of  $\vec{u}_T$ , with respect to the  $\vec{q}_T^Z$ , are labelled as  $u_{\parallel}$  and  $u_{\perp}$ , respectively. Figure 3.19 shows the components of the recoil in  $Z \rightarrow \mu^+ \mu^-$  events.

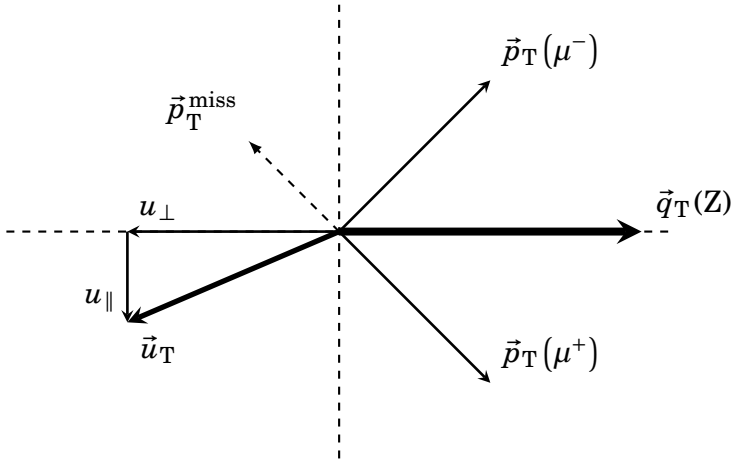


Figure 3.19: Definition and components of the recoil  $\vec{u}_T$  for  $Z \rightarrow \mu^+ \mu^-$  events.

The  $u_{\parallel}$  and  $u_{\perp}$  recoil components are evaluated event-by-event and sorted in 30 bins of  $q_T^Z$  defined within the range  $0 < q_T^Z < 140$  GeV/c. The distributions of  $u_{\parallel}$  and  $u_{\perp}$  from data and simulation are fitted separately in each  $q_T^Z$  bin with a weighed sum of two Gaussian functions, according to:

$$\begin{aligned} F(u_{\parallel}) &= N_{\parallel} \cdot \left( f_{\parallel} \cdot \exp \left[ \frac{(u_{\parallel} - \mu_{\parallel})^2}{2 \cdot \sigma_{\parallel,1}^2} \right] + (1 - f_{\parallel}) \cdot \exp \left[ \frac{(u_{\parallel} - \mu_{\parallel})^2}{2 \cdot \sigma_{\parallel,2}^2} \right] \right) \\ F(u_{\perp}) &= N_{\perp} \cdot \left( f_{\perp} \cdot \exp \left[ \frac{(u_{\perp} - \mu_{\perp})^2}{2 \cdot \sigma_{\perp,1}^2} \right] + (1 - f_{\perp}) \cdot \exp \left[ \frac{(u_{\perp} - \mu_{\perp})^2}{2 \cdot \sigma_{\perp,2}^2} \right] \right) \end{aligned} \quad (3.32)$$

where  $N_{\parallel(\perp)}$  corresponds to the number of events in each  $q_T^Z$  bin,  $f_{\parallel(\perp)}$  is the weight of the Gaussian components,  $\mu_{\parallel(\perp)}$  is the mean of the Gaussian functions, and  $\sigma_{\parallel(\perp),1}$  and  $\sigma_{\parallel(\perp),2}$  are the corresponding Gaussian widths. The parameters  $f_{\parallel}$  and  $f_{\perp}$  are fixed to:  $f_{\parallel} = f_{\perp} = 0.70$  in data and  $f_{\parallel} = f_{\perp} = 0.45$  in simulation, to obtain a better convergence of the fits. The other parameters are left free.

Examples of the distributions of the parallel and perpendicular recoil components are shown in Figure 3.20 for data and simulation. Also, the fits performed with the weighed combination of Gaussian functions and their pull distributions are presented.

**Parameterisation of the recoil scale.** The Gaussian mean parameter  $\mu_{\parallel}$  of the recoil parallel component is extracted in each  $q_T^Z$  bin by fitting the recoil  $u_{\parallel}$  distribution as shown in Figure 3.20. The profile of  $\mu_{\parallel}$  as a function of  $q_T^Z$  is then fitted using the following function:

$$\mu_{\parallel}(q_T^Z) = - \left( c_0 + c_1 q_T^Z \right) \left( \frac{1 + \text{Erf} \left[ \alpha \cdot (q_T^Z)^{\beta} \right]}{2} \right) \quad (3.33)$$

where  $c_0$ ,  $c_1$ ,  $\alpha$  and  $\beta$  are free parameters, and  $\text{Erf}(x)$  is the Gaussian error function. These fits are shown in Figure 3.21, where the sign of  $\mu_{\parallel}$  has been reversed to plot the results in the positive y-axis. The slope  $c_1$  and intercept  $c_0$  parameters are found to be  $c_1 \approx 0.9$  and  $c_0 < 1.0$  GeV/c, which means that the average  $u_{\parallel}$  is roughly 10% lower than  $q_T^Z$  and the contributions at  $q_T^Z = 0$  are negligible. The distributions of the average  $u_{\parallel}$  for data and simulation are observed to be in good agreement.

In the case of the perpendicular recoil component, the average  $u_{\perp}$  value should be zero based on momentum conservation. To check this, the profile of the Gaussian mean parameter  $\mu_{\perp}$  as a function of  $q_T^Z$  is fitted in data and simulation with a constant function:

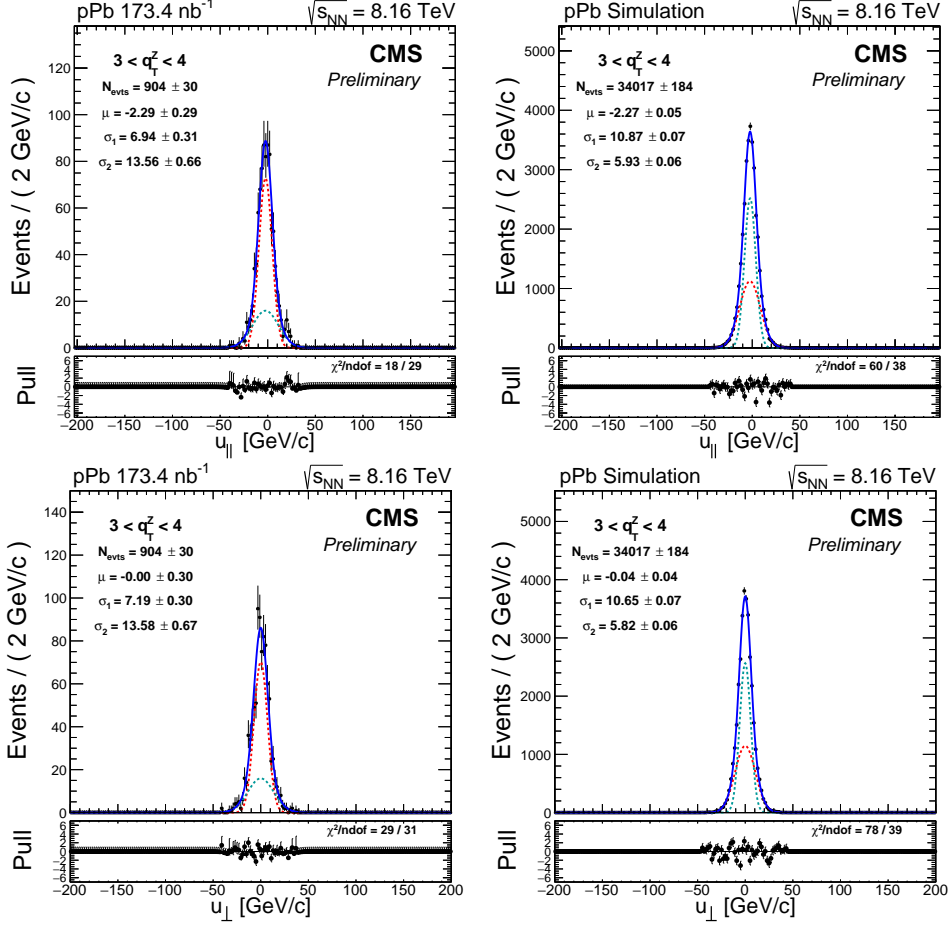


Figure 3.20: Distributions of the  $u_{\parallel}$  (top) and  $u_{\perp}$  (bottom) recoil components in data (left) and simulation (right). The fit function is based on a weighed sum of two Gaussian distributions as defined in Eq. (3.32). The solid black line represents the total fit function while the Gaussian components are depicted by the green and red dashed lines. The plots correspond to the  $q_T^Z$  bin  $[3, 4]$   $\text{GeV}/c$ .

$$\mu_{\perp}(q_T^Z) = c_0 \quad (3.34)$$

The outcome of the fits is shown in Figure 3.22. As expected, the  $\mu_{\perp}$  is found to be consistent with zero in simulation and data, showing that there is no bias that affects the average value of the recoil component perpendicular to  $\vec{q}_T^Z$ . From now on,  $\mu_{\perp}$  is fixed to zero.

**Parameterisation of the recoil resolution.** The two Gaussian width parameters ( $\sigma_{\parallel(\perp),1}$  and  $\sigma_{\parallel(\perp),2}$ ) of the parallel (perpendicular) component of the recoil are also ex-

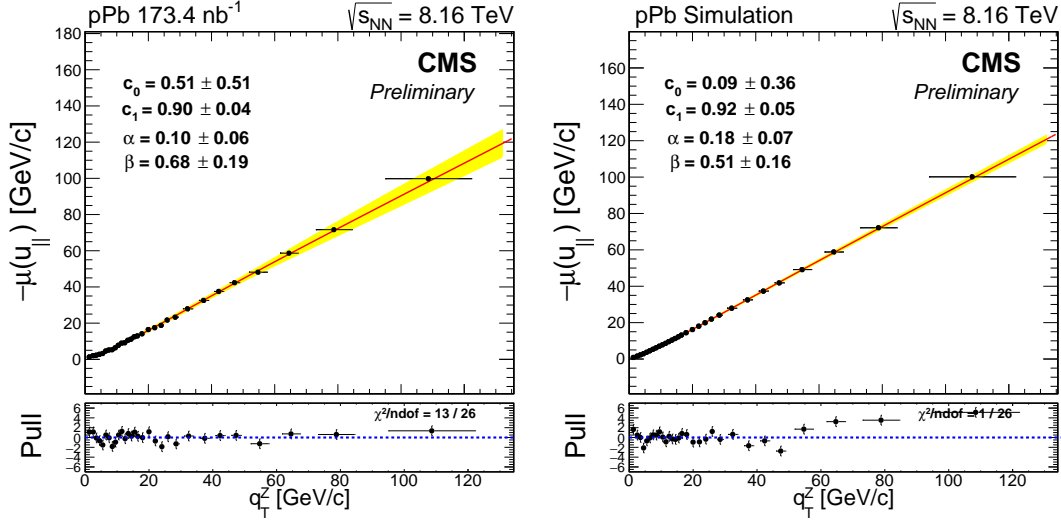


Figure 3.21: Fits of the profile of  $-\mu_{\parallel}$  as a function of  $q_T^Z$ . The results are derived from  $Z \rightarrow \mu^+ \mu^-$  events in data (left) and simulation (right). The yellow band represents the 68% error band of the fit.

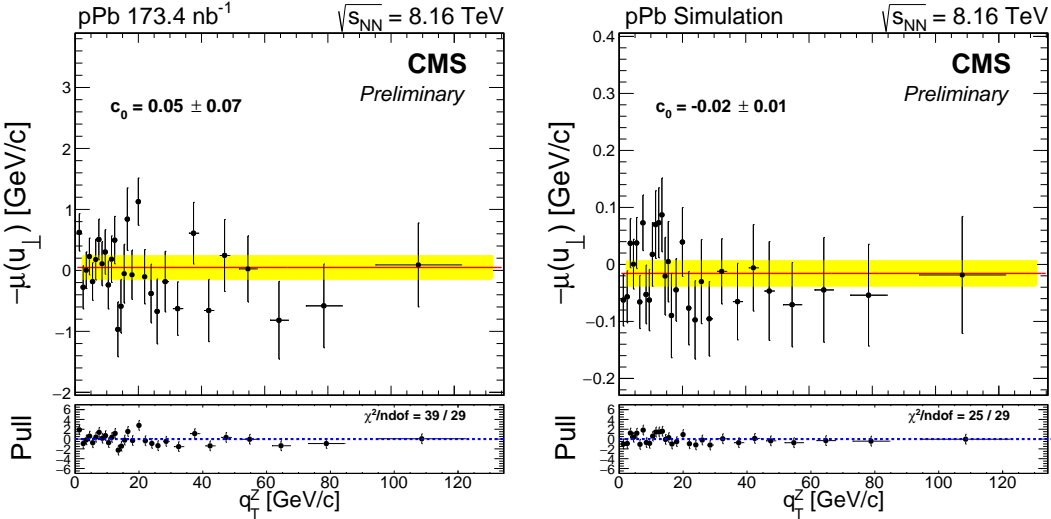


Figure 3.22: Fits of the profile of  $\mu_{\perp}$  as a function of  $q_T^Z$ . The results are derived from  $Z \rightarrow \mu^+ \mu^-$  events in data (left) and simulation (right). The yellow band represents the 68% error band of the fit.

tracted from the recoil fits for each  $q_T^Z$  bin. The  $\sigma_{\parallel(\perp),1}$  and  $\sigma_{\parallel(\perp),2}$  parameters of  $u_{\parallel}$  ( $u_{\perp}$ ) are parametrised as a function of  $q_T^Z$  using the following formula:

$$\sigma_{1,2}(q_T^Z) = \sqrt{s_0^2 + s_1^2 \cdot q_T^{\alpha}} \quad (3.35)$$

where  $s_0$ ,  $s_1$  and  $\alpha$  are free parameters. The results of the fits to the  $\sigma_1$  and  $\sigma_2$

profiles as a function of  $q_T^Z$  are presented in Figure 3.23 for  $u_{\parallel}$  and in Figure 3.24 for  $u_{\perp}$ . In addition, the profiles of the weighed average of the two Gaussian width parameters, given by:

$$\begin{aligned}\sigma_{\perp} &= f_{\perp} \cdot \sigma_{\perp,1} + (1 - f_{\perp}) \cdot \sigma_{\perp,2} \\ \sigma_{\parallel} &= f_{\parallel} \cdot \sigma_{\parallel,1} + (1 - f_{\parallel}) \cdot \sigma_{\parallel,2}\end{aligned}\quad (3.36)$$

are also fitted using Eq. (3.35) and the results are shown in Figure 3.23 and Figure 3.24.

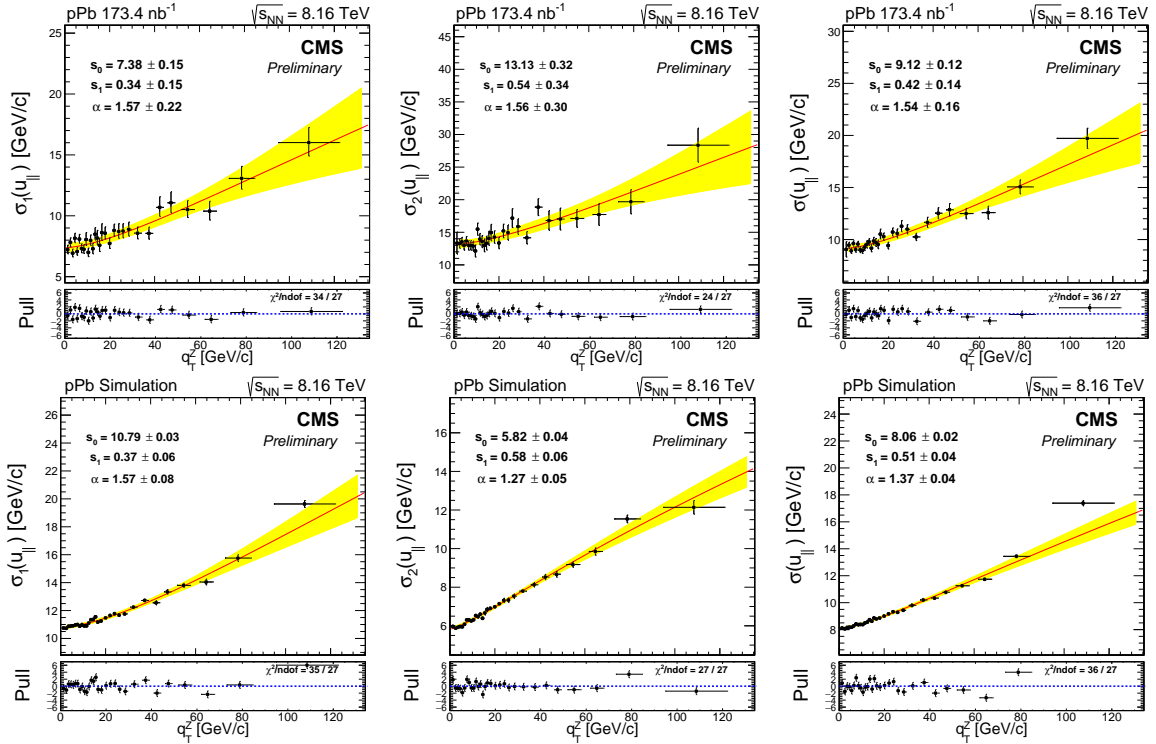


Figure 3.23: Fits to the profile of the  $\sigma_{\parallel,1}$  (left),  $\sigma_{\parallel,2}$  (middle) and weighed average  $\sigma_{\parallel}$  (right) values of the parallel recoil component as a function of  $q_T^Z$ . The results are derived from  $Z \rightarrow \mu^+ \mu^-$  events in data (top) and simulation (bottom).

It is observed in Figure 3.23 and 3.24, that the recoil resolution increases with  $q_T^Z$ . This is expected since high- $p_T$  Z bosons are produced in association with several jets from higher order processes, which contributes to the recoil resolution.

Also, the parameter  $s_0$  of the weighed average  $\sigma$ , which measures the recoil resolution at  $q_T^Z = 0$  GeV/c, is found to be larger in data than in simulation, which means that the modelling of the contributions not originating from the hard scattering (e.g. underlying

### 3.2. ANALYSIS

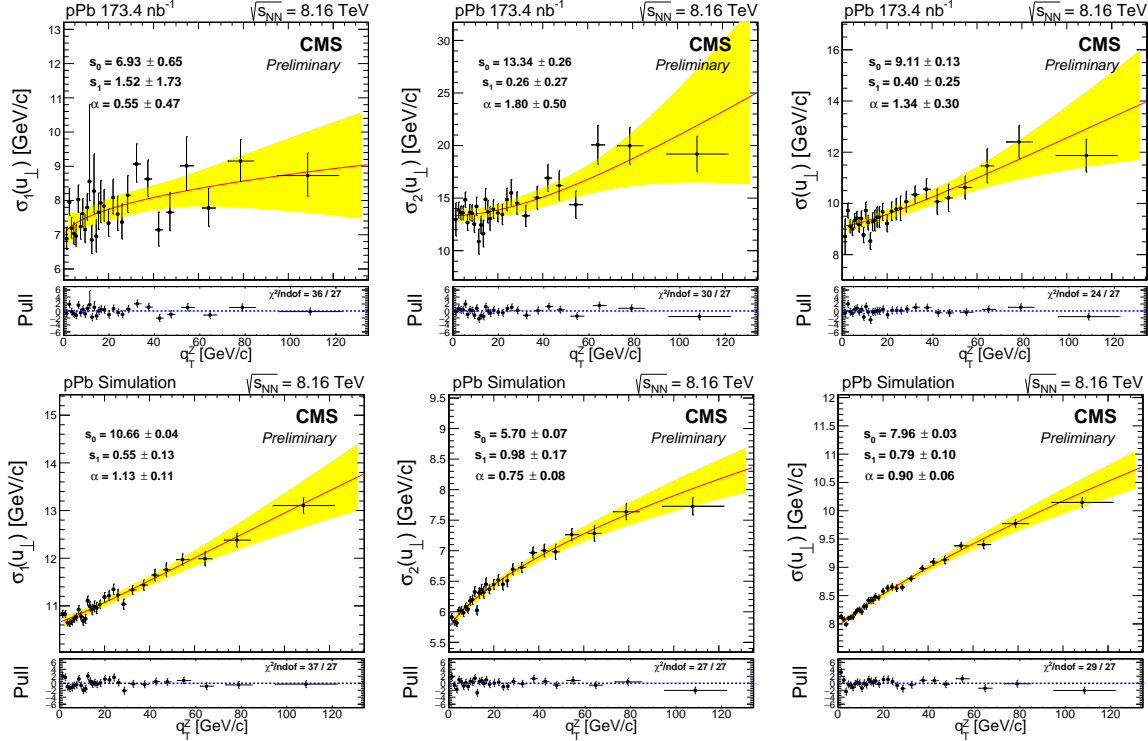


Figure 3.24: Fits for the  $\sigma_{\perp,1}$  (left),  $\sigma_{\perp,2}$  (middle) and weighed average  $\sigma_{\perp}$  (right) values of the recoil perpendicular component as a function of  $q_T$ . The results are derived from  $Z \rightarrow \mu^+ \mu^-$  events in data (top) and simulation (bottom).

events) are underestimated compared to data. In addition, the contributions to the recoil resolution at high  $q_T^Z$  are also larger in data than in simulation.

**Calibration of the simulated recoil.** The recoil corrections are applied to the following simulated processes:  $W \rightarrow \mu\nu_\mu$ ,  $Z/\gamma^* \rightarrow \mu^+ \mu^-$  and  $W \rightarrow \tau\nu_\tau$ . The simulated recoil distribution is calibrated using the parametric equations obtained in the previous sections for the Gaussian mean  $\mu(q_T)$  and weighed-average width  $\sigma(q_T)$ . These parametric equations are summarised below:

- Recoil parametric equations from data:

$$\begin{aligned} \mu_{\parallel}^{\text{data}}(q_T) &= (0.5 + 0.9 \cdot q_T) \left( \frac{1 + \text{Erf}[0.1 \cdot (q_T)^{0.7}]}{2} \right) \\ \sigma_{\parallel}^{\text{data}}(q_T) &= \sqrt{9.1^2 + 0.4^2 \cdot (q_T)^{1.5}} \\ \sigma_{\perp}^{\text{data}}(q_T) &= \sqrt{9.1^2 + 0.4^2 \cdot (q_T)^{1.3}} \end{aligned} \quad (3.37)$$

- Recoil parametric equations from simulation:

$$\begin{aligned}\mu_{\parallel}^{\text{MC}}(q_T) &= (0.1 + 0.9 \cdot q_T) \left( \frac{1 + \text{Erf}[0.2 \cdot (q_T)^{0.5}]}{2} \right) \\ \sigma_{\parallel}^{\text{MC}}(q_T) &= \sqrt{8.1^2 + 0.5^2 \cdot (q_T)^{1.4}} \\ \sigma_{\perp}^{\text{MC}}(q_T) &= \sqrt{8.0^2 + 0.8^2 \cdot (q_T)^{0.9}}\end{aligned}\quad (3.38)$$

The procedure to calibrate the simulated recoil starts by computing the  $p_T$  vector of the boson ( $\vec{q}_T$ ) and simulated recoil ( $\vec{u}_T^{\text{MC}}$ ). The boson  $\vec{q}_T$  is determined using the reconstructed muon information whenever possible, as described below:

- $W \rightarrow \mu\nu_\mu$ :  $\vec{q}_T$  is the  $\vec{p}_T$  sum of the reconstructed muon and generated neutrino.
- $W \rightarrow \tau\nu_\tau$ :  $\vec{q}_T$  is the generated  $W$  boson  $p_T$  vector.
- $Z/\gamma^* \rightarrow \mu^+ \mu^-$ : if one of the muons is not reconstructed, then  $\vec{q}_T$  is the  $\vec{p}_T$  sum of the reconstructed muon and the generated-only muon, otherwise  $\vec{q}_T$  is equal to the  $\vec{p}_T$  sum of both reconstructed muons ( $\vec{q}_T^{Z/\gamma^*}$ ).

The recoil  $\vec{u}_T^{\text{MC}}$  of the simulated event is derived by *removing* from the  $\vec{p}_T^{\text{miss}}$ , the reconstructed muons from the decay of the weak boson. In other words, for  $W \rightarrow \mu\nu_\mu$  events,  $Z/\gamma^* \rightarrow \mu^+ \mu^-$  events with only one reconstructed muon ( $Z/\gamma^* \rightarrow \mu$ ) and  $W \rightarrow \tau\nu_\tau$  events, the  $\vec{u}_T^{\text{MC}} = -\vec{p}_T^{\text{miss}} - \vec{p}_T^\mu$ , while for  $Z/\gamma^* \rightarrow \mu^+ \mu^-$  events with both muons reconstructed, the  $\vec{u}_T^{\text{MC}} = -\vec{p}_T^{\text{miss}} - \vec{q}_T^{Z/\gamma^*}$ .

Once the  $\vec{u}_T^{\text{MC}}$  and  $\vec{q}_T$  have been derived for a given event, the  $\vec{u}_T^{\text{MC}}$  is then separated in a component parallel ( $u_{\parallel}^{\text{MC}}$ ) and perpendicular ( $u_{\perp}^{\text{MC}}$ ) to the direction of  $\vec{q}_T$ . The simulated recoil components are then scaled event-by-event, according to:

$$\begin{aligned}u_{\parallel}^{\text{corr}} &= \left( u_{\parallel}^{\text{MC}} - \mu_{\parallel}^{\text{MC}}(q_T) \right) \cdot \left( \frac{\sigma_{\parallel}^{\text{data}}(q_T)}{\sigma_{\parallel}^{\text{MC}}(q_T)} \right) + \mu_{\parallel}^{\text{data}}(q_T) \\ u_{\perp}^{\text{corr}} &= u_{\perp}^{\text{MC}} \cdot \left( \frac{\mu_{\perp}^{\text{data}}(q_T)}{\sigma_{\perp}^{\text{MC}}(q_T)} \right)\end{aligned}\quad (3.39)$$

Afterwards, the corrected recoil  $\vec{u}_T^{\text{corr}}$  is propagated to the  $p_T^{\text{miss}}$  of the event, as follows:

- For  $W \rightarrow \mu\nu_\mu$ ,  $W \rightarrow \tau\nu_\tau$  and  $Z/\gamma^* \rightarrow \mu$  events:

$$p_T^{\text{miss}} = |u_T^{\text{corr}} + \vec{p}_T^\mu| \quad (3.40)$$

- For fully reconstructed  $Z/\gamma^* \rightarrow \mu^+ \mu^-$  events:

$$p_T^{\text{miss}} = \left| u_T^{\text{corr}} + \vec{q}_T^{Z/\gamma^*} \right| \quad (3.41)$$

As an alternative method used to determine the systematic uncertainty associated to the recoil calibration method, the simulated recoil components are smeared, instead of being scaled, by generating a random recoil component per event according to the following Gaussian distribution functions:

$$\begin{aligned} u_{\parallel}^{\text{corr}} &= \text{Gauss} \left( u_{\parallel} - \mu_{\parallel}^{\text{MC}}(q_T) + \mu_{\parallel}^{\text{data}}(q_T), \sqrt{\sigma_{\parallel}^{\text{data}}(q_T)^2 - \sigma_{\parallel}^{\text{MC}}(q_T)^2} \right) \\ u_{\perp}^{\text{corr}} &= \text{Gauss} \left( u_{\perp}, \sqrt{\sigma_{\perp}^{\text{data}}(q_T)^2 - \sigma_{\perp}^{\text{MC}}(q_T)^2} \right) \end{aligned} \quad (3.42)$$

**Closure test.** The recoil calibration is checked using the  $Z \rightarrow \mu^+ \mu^-$  control sample. The  $p_T^{\text{miss}}$  spectrum from data and the corrected one from simulation are shown in Figure 3.25. As can be observed, the agreement between data and simulation is significantly improved after applying the recoil calibration using the scaling method.

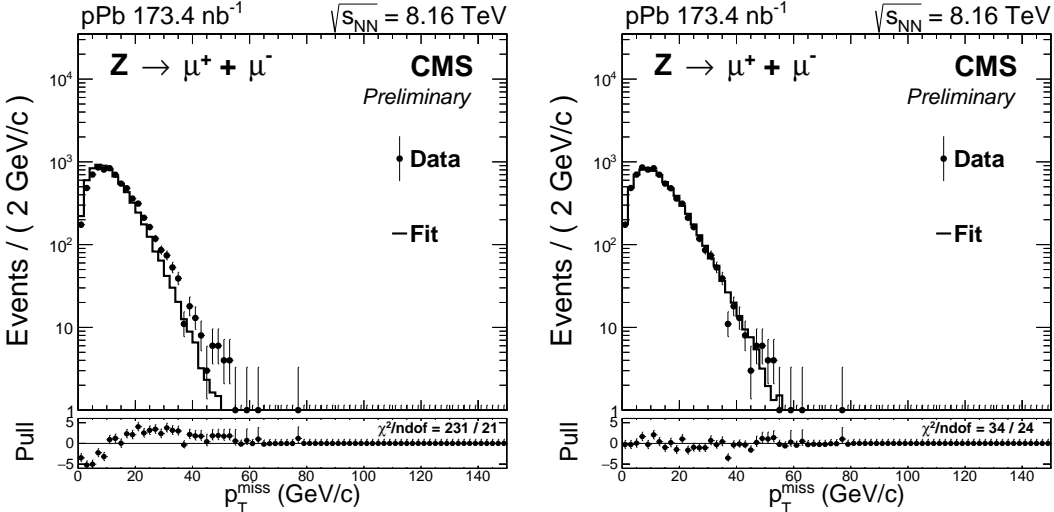


Figure 3.25: A comparison of the  $p_T^{\text{miss}}$  distribution from  $Z \rightarrow \mu^+ \mu^-$  events between data and simulation, before (left) and after (right) calibrating the simulated recoil. The distributions of the simulated HF energy and generated Z-boson  $p_T$  have been weighed.

**Impact of the recoil calibration in the signal region.** The  $p_T^{\text{miss}}$  distribution in the signal region is compared between data and the simulations. The fit to the data

is performed following the signal extraction procedure described in Section 3.2.7. The recoil corrections are applied to the electroweak simulations using both the nominal scaling method and the alternative smearing method, and the results are shown in Figure 3.26. Both the nominal and the alternative recoil calibrations improve significantly the agreement between the  $p_T^{\text{miss}}$  distribution extracted from data and simulations.

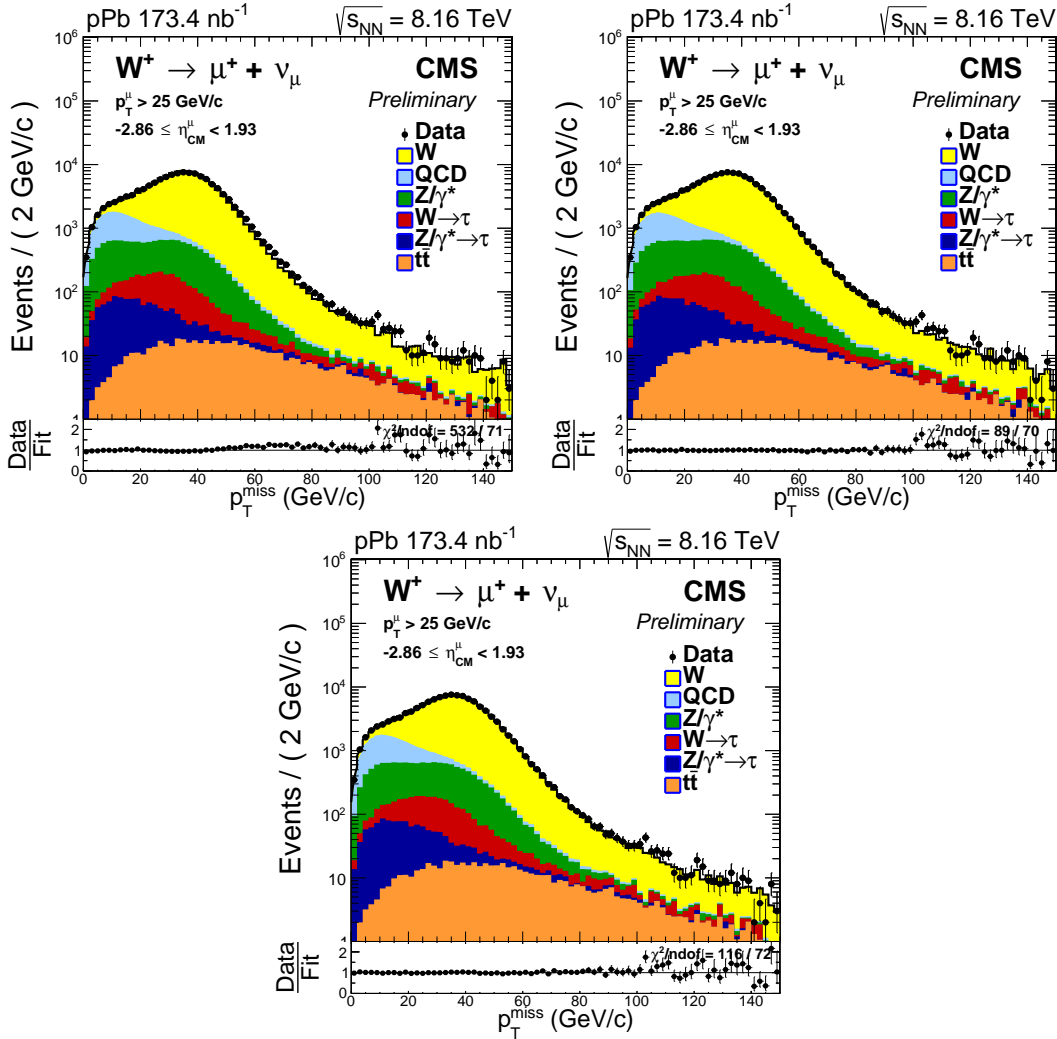


Figure 3.26: Comparison of the  $p_T^{\text{miss}}$  distribution in data and simulation for positive-charged muons in the  $\eta_{\text{CM}}^{\mu}$ -inclusive signal region. The results are shown before (top-left) and after (top-right) applying the recoil calibrations using the nominal scaling method. The result using the alternative smearing method (bottom) is also presented.

### 3.2.6 Signal efficiency

The  $W \rightarrow \mu\nu_\mu$  signal efficiency is defined as the probability for a muon with  $p_T > 25$  GeV/c and  $|\eta_{\text{lab}}^\mu| < 2.4$ , to be reconstructed and pass all the analysis selection criteria. The signal efficiency is obtained from simulation as detailed in Section 3.2.6.1 and then corrected using data-to-MC efficiency ratios derived with the tag-and-probe method as explained in Section 3.2.6.2.

#### 3.2.6.1 Simulated signal efficiency

The signal efficiency is estimated using the  $W \rightarrow \mu\nu_\mu$  simulations since they contain the full history of the signal events, including the generation and reconstruction of the particles. To improve the modelling of the event activity in p-Pb and the W-boson  $p_T$  spectrum, the distributions of the generated W-boson  $p_T$  and simulated HF energy are weighed per event as explained in Section 3.2.4 and Section 3.2.5.1, respectively.

A reconstructed muon is considered an offline muon if it satisfies the signal selection requirements. Among the selection criteria, an offline muon is required to satisfy the isolation and identification criteria defined in Section 3.2.3.3, match the trigger, have  $p_T^\mu > 25$  GeV/c and be within the CMS detector coverage  $|\eta_{\text{lab}}^\mu| < 2.4$ .

The signal efficiency of the simulated events is computed as the fraction of *generated* muons matched to an *offline* muon around a cone of  $\Delta R = \sqrt{\Delta\eta^2 + \Delta\phi^2} < 0.05$ . All generated muons are required to be within the analysis kinematic region ( $p_T^\mu > 25$  GeV/c and  $|\eta_{\text{lab}}^\mu| < 2.4$ ) and come from a W-boson decay. The signal efficiency of the pPb and Pbp  $W \rightarrow \mu\nu_\mu$  simulations is derived as a function of the generated muon  $\eta_{\text{lab}}^\mu$ , according to:

$$\epsilon_{\text{pPb(Pbp)}}^{\mu^\pm}(\eta_{\text{lab}}^\mu) = \left( \frac{N_{\text{off}}^{\mu^\pm}[\eta_{\text{lab}}^\mu]}{N_{\text{gen}, p_T > 25 \text{ GeV}/c}^{\mu^\pm}[\eta_{\text{lab}}^\mu]} \right)_{\text{pPb(Pbp)}} \quad (3.43)$$

where  $N_{\text{off}}$  and  $N_{\text{gen}}$  are the number of offline and generated muons, accordingly. A comparison of the signal efficiencies from the pPb and Pbp simulations is shown in Figure 3.27. A good agreement between the two samples is observed.

The signal efficiencies extracted from the pPb and Pbp  $W \rightarrow \mu\nu_\mu$  simulations are then combined in the centre-of-mass frame, and the final simulated signal efficiency  $\epsilon_{\text{MC}}^{\mu^\pm}$  is obtained as:

$$\epsilon_{\text{MC}}^{\mu^\pm}(\eta_{\text{CM}}^\mu) = \frac{\mathcal{L}_{\text{pPb}} \cdot \epsilon_{\text{pPb}}^{\mu^\pm}(\eta_{\text{CM}}^\mu) + \mathcal{L}_{\text{Pbp}} \cdot \epsilon_{\text{Pbp}}^{\mu^\pm}(\eta_{\text{CM}}^\mu)}{\mathcal{L}_{\text{pPb}} + \mathcal{L}_{\text{Pbp}}} \quad (3.44)$$

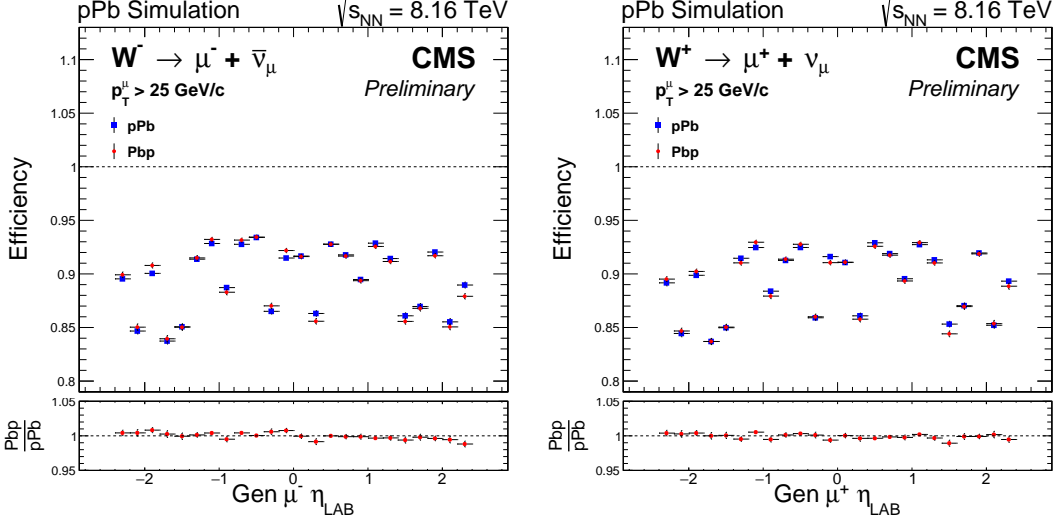


Figure 3.27: Comparison of the signal efficiency derived from the pPb and Ppb  $W \rightarrow \mu\nu_\mu$  simulations as a function of the generated muon  $\eta_{lab}$ , separated in negative (left) and positive (right) charged muons. The distributions of the simulated HF energy and generated W-boson  $p_T$  have been weighed. The bottom panel shows the ratio of Ppb over pPb signal efficiencies.

where  $\mathcal{L}_{pPb}$  and  $\mathcal{L}_{Ppb}$  are the recorded integrated luminosity of each p-Pb run. The results of the  $W \rightarrow \mu\nu_\mu$  efficiency, extracted from the simulations, are shown in Figure 3.28.

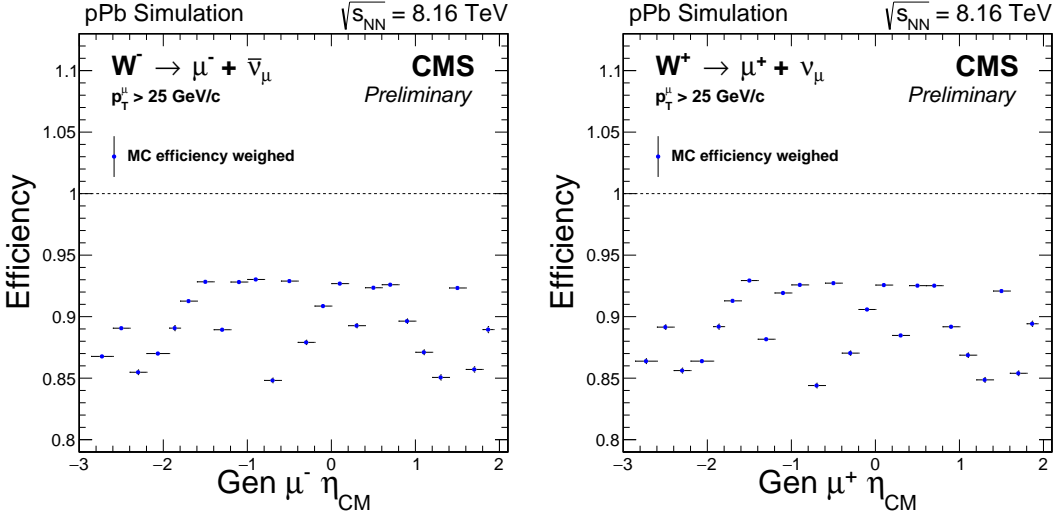


Figure 3.28: Simulated signal efficiency derived from the  $W \rightarrow \mu\nu_\mu$  NLO simulations as a function of the generated muon  $\eta_{CM}$ , separated in negative (left) and positive (right) charged muons. The distributions of the simulated HF energy and generated W-boson  $p_T$  have been weighed.

### 3.2.6.2 Corrected signal efficiency

The simulation of the CMS detector is very precise but still far from fully describing all the detector conditions observed in real data. In order to compensate for the imperfections in the simulation, a set of data-to-MC corrections provided by the CMS heavy-ion (HIN) group are used to improve the estimation of the signal efficiency. These corrections are derived from the ratio of efficiencies measured in data and simulation using the tag-and-probe (TnP) method.

The tag-and-probe method is a data-driven technique widely used to compute efficiencies of physical objects, such as muons, produced from the decay of known mass resonances (e.g. Z bosons). One advantage of the TnP method is that it can be applied to data and simulation, allowing to assess the possible differences between the data and simulated muon efficiencies. The TnP analysis performed in p-Pb collisions by the CMS HIN group is documented in the internal analysis note [188].

**Definition of the tag-and-probe efficiencies.** To study the different elements that enter in the reconstruction and selection of muons, the total muon efficiency is factorised in five different components, according to:

$$\epsilon^\mu = \epsilon_{\text{STA}} \cdot \epsilon_{\text{TRK}} \cdot \epsilon_{\text{ID}} \cdot \epsilon_{\text{Trig}} \cdot \epsilon_{\text{Iso}} \quad (3.45)$$

where each efficiency component is defined relative to the previous one, as described below:

- $\epsilon_{\text{STA}}$  : represents the standalone-muon (STA) reconstruction efficiency. It is probed by tracker tracks and is derived by matching the probe to a standalone muon.
- $\epsilon_{\text{trk}}$  : represents the global muon tracking efficiency. It is probed by standalone muons and is derived by matching the probe to a global muon.
- $\epsilon_{\text{ID}}$  : represents the muon identification efficiency. It is probed by global muons and is determined by requiring that the probe satisfies the tight identification criteria defined in Section 3.2.3.3.
- $\epsilon_{\text{trig}}$  : represents the muon trigger efficiency. It is probed by global muons passing the identification criteria, and is determined by requiring that the probe is matched to the muon trigger.

- $\epsilon_{\text{iso}}$  : represents the muon isolation efficiency. It is probed by global muons passing the identification criteria and matched to the trigger, and it is computed by requiring that the probe pass the muon isolation requirement ( $I^\mu < 0.15$ ).

**Extraction of the tag-and-probe efficiencies.** For high- $p_T$  muons ( $p_T > 15 \text{ GeV}/c$ ), the dimuon decay of Z bosons is used to create a clean sample. In each event, a high-quality muon, called the *tag*, is combined with the *probe* of the efficiency being measured, to form a tag-probe pair within the Z-boson mass window. The tag and the probe are required to have  $p_T > 15 \text{ GeV}/c$  and be inside the acceptance of CMS ( $|\eta_{\text{lab}}| < 2.4$ ). In addition, the tag is also required to satisfy the muon isolation and identification criteria, and be matched to the trigger.

The tag-probe pairs are separated into two samples depending on whether the probe pass the selection criteria under study. The efficiency is then determined by performing a simultaneous unbinned maximum likelihood fit to the tag-probe invariant mass distribution ( $m_{\text{TP}}$ ) for failing and passing probes. The  $Z \rightarrow \mu^+ \mu^-$  signal distributions are parametrised with a Voigt profile [189] and the background distributions with an exponential. The same procedure is performed for all efficiencies measured in data and simulation.

As an example, the fits to the tag-probe invariant mass distribution for passing and failing probes, used to measure the STA reconstruction efficiency, are shown in Figure 3.29.

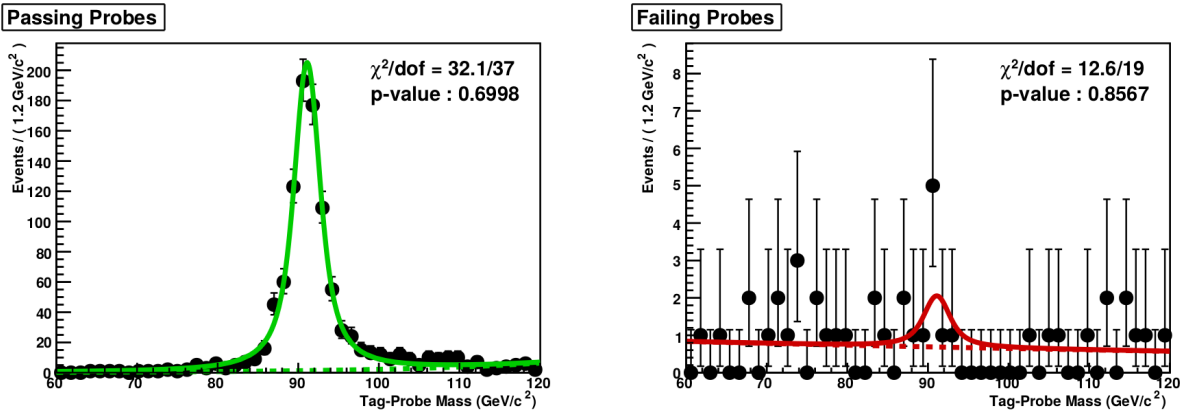


Figure 3.29: Fits to the tag-probe invariant mass distribution for passing (left) and failing (right) probes, used to measure the STA reconstruction efficiency. The results correspond to the probe kinematic region:  $|\eta_{\text{lab}}| < 2.4$  and  $50 < p_T < 80 \text{ GeV}/c$ . Figures taken from the internal analysis note [188].

**Results of the tag-and-probe efficiencies.** The STA reconstruction  $\epsilon_{\text{STA}}$  and global muon tracking  $\epsilon_{\text{trk}}$  efficiencies are found to agree between data and simulation within an uncertainty of 0.6% and < 0.1%, respectively, and no correction is required for the simulated  $W \rightarrow \mu\nu_\mu$  efficiency.

In the case of the muon identification  $\epsilon_{\text{ID}}$  and isolation  $\epsilon_{\text{iso}}$  efficiencies, the results obtained from simulation are observed to disagree with those from data, as shown in Figure 3.30. As a result, the efficiencies measured in data and simulation, as a function of the probed  $p_T$ , are fitted with: a linear function ( $f_{\text{ID}}(p_T) = a \cdot p_T + b$ ) for muon identification and a displaced error function ( $f_{\text{iso}}(p_T) = a \cdot \text{Erf}[(p_T - c)/b] + d$ ) for muon isolation. The fits to the efficiencies are performed in three regions of probe  $\eta_{\text{lab}}$ , corresponding to:  $|\eta_{\text{lab}}^\mu| < 1.2$ ,  $1.2 < |\eta_{\text{lab}}^\mu| < 2.1$  and  $2.1 < |\eta_{\text{lab}}^\mu| < 2.4$ . The ratios of the fitted functions extracted from the data and simulation efficiencies, for muon identification ( $w_{\text{ID}} = f_{\text{ID}}^{\text{data}}/f_{\text{ID}}^{\text{MC}}$ ) and for muon isolation ( $w_{\text{iso}} = f_{\text{iso}}^{\text{data}}/f_{\text{iso}}^{\text{MC}}$ ), are used as TnP corrections for the simulated  $W \rightarrow \mu\nu_\mu$  efficiency.

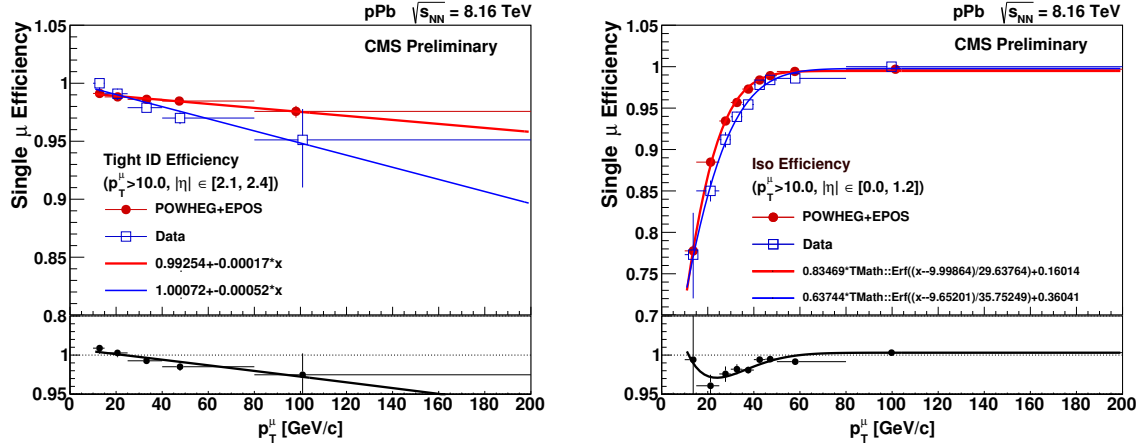


Figure 3.30: Muon identification (left) and isolation (right) efficiencies extracted from data (blue) and simulation (red) using the TnP method, as a function of the probe  $p_T$ . The bottom panels show the data-to-simulation efficiency ratio. The results of the fits to the efficiencies are also shown. Figures taken from the internal analysis note [188].

The muon trigger efficiency  $\epsilon_{\text{trig}}$  extracted from the simulation is seen to disagree with the results from data as a function of the probe  $\eta_{\text{lab}}$ , as presented in Figure 3.31. In this case, the ratio of the measured efficiency extracted from data and simulation ( $w_{\text{trig}} = \epsilon_{\text{ID}}^{\text{data}}/\epsilon_{\text{ID}}^{\text{MC}}$ ), in each bin of probe  $\eta_{\text{lab}}$ , is used to correct the simulated  $W \rightarrow \mu\nu_\mu$  efficiency.

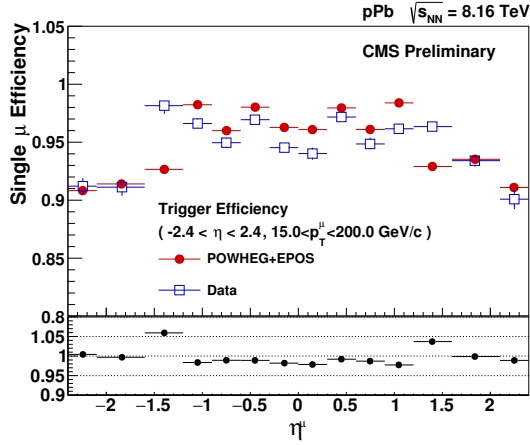


Figure 3.31: Muon trigger efficiency extracted from data (blue) and simulation (red) using the TnP method, as a function of the probe  $\eta_{\text{lab}}$ . The bottom panel shows the data-to-simulation efficiency ratio. Figure taken from the internal analysis note [188].

**Correction of the signal efficiency.** The simulated signal efficiency is recomputed by weighing the offline muon yield per event using the TnP corrections provided by the CMS HIN group, for muon identification  $w_{\text{ID}}$ , trigger  $w_{\text{trig}}$  and isolation  $w_{\text{iso}}$ , according to:

$$\epsilon_{\text{corr}}^{\mu^\pm} = \frac{\left[ \sum_{i=1}^{N_{\text{off}}^{\mu^\pm}} w_{\text{ID}}(p_T^\mu, |\eta_{\text{lab}}^\mu|) \cdot w_{\text{trig}}(\eta_{\text{lab}}) \cdot w_{\text{iso}}(p_T^\mu, |\eta_{\text{lab}}^\mu|) \right]}{N_{\text{gen}, p_T > 25 \text{ GeV}/c}^{\mu^\pm}} \quad (3.46)$$

where the TnP corrections are evaluated as a function of the offline muon  $p_T$  and  $\eta_{\text{lab}}$  in each event, and the sum is performed over the simulated signal events.

**Uncertainties of the tag-and-probe corrections.** The uncertainties associated to the TnP corrections are driven by the larger background and lower statistics present in data. As a result, only the uncertainties associated to the data efficiencies are propagated to the TnP corrections, while the simulation efficiencies are fixed. The statistical and systematic components of the TnP correction uncertainties are estimated by performing the following set of variations:

- (A) Statistical uncertainty for muon ID and isolation: estimated by generating a hundred sets of TnP corrections using pseudo-experiments. For each pseudo-

experiment, the data efficiency points are randomly varied based on a Gaussian distribution of width equal to the statistical uncertainty of the efficiency points.

- (B) Statistical uncertainty for muon trigger: estimated with two sets of TnP corrections, determined by varying the data efficiency points up and down according to their statistical uncertainty.
- (C) Systematic uncertainty of the efficiency extraction: derived by refitting the tag-probe invariant mass distributions after varying the signal and background functional forms, and by extending the range of the Z-boson mass window. These uncertainties are then propagated to the TnP corrections by varying the data efficiency points up and down by one standard deviation, producing two sets of TnP corrections.
- (D) Systematic uncertainty of the efficiency parametrisation for muon ID and isolation: estimated by using the ratio of the efficiency points from data and simulation ( $w = \epsilon^{\text{data}} / \epsilon^{\text{MC}}$ ), instead of the fitted efficiency curves.

In addition, an uncertainty of 0.34% is included to account for the impact of the different level of event activity present in data and simulation. This is derived by comparing the simulated muon isolation efficiency before and after applying the HF energy weighing. Moreover, the uncertainty of 0.6% is also added to account for possible mismodelling of the STA reconstruction efficiency, determined from the level of agreement between data and simulation.

The uncertainties of the TnP corrections are propagated to the signal efficiency in two ways:

- For the hundred TnP corrections described in (A): the signal efficiency is recomputed with each of the TnP corrections and the RMS of the hundred signal efficiencies obtained is then taken as the uncertainty on the signal efficiency.
- For the up and down variations used in (B), (C) and (D): the uncertainty on the signal efficiency is determined from the largest difference between applying the up or down varied TnP corrections and the nominal one.

The total uncertainty on the signal efficiency due to TnP corrections, is obtained by summing in quadrature the uncertainties from (A), (B), (C) and (D). The additional relative uncertainties of 0.34% and 0.6% are also included.

**Results of the signal efficiency correction.** The corrected signal efficiency is shown in Figure 3.32, including the uncertainties due to TnP correction.

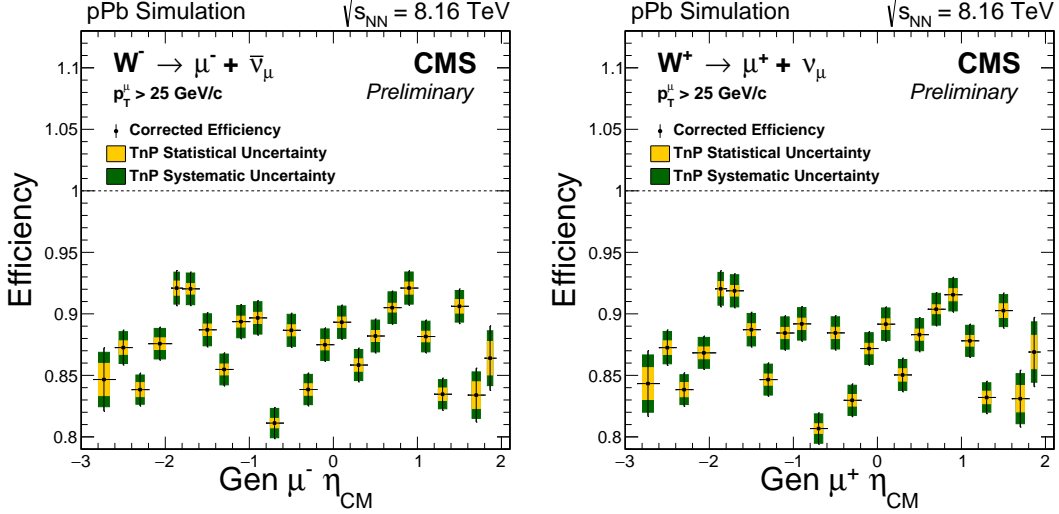


Figure 3.32: Corrected signal efficiency as a function of the generated muon  $\eta_{\text{CM}}$ , separated in negative (left) and positive (right) charged muons. The yellow and green boxes represents the uncertainty on the signal efficiency due to the TnP statistics and systematics, respectively.

The relative difference between the corrected and the simulated signal efficiencies ( $(\epsilon_{\text{corr}} - \epsilon_{\text{MC}})/\epsilon_{\text{MC}}$ ), is presented in Table 3.4 as a function of the generated  $\eta_{\text{CM}}$ . The largest variation due to the TnP corrections is found to be 4.7%.

### 3.2.7 Signal extraction

The signal and background event yields are extracted by fitting the  $p_{\text{T}}^{\text{miss}}$  distribution from data. The background events correspond to high- $p_{\text{T}}$  muons that satisfy the signal selection criteria and are not produced from a direct decay of a W boson. A brief description of the background sources considered in this analysis is given below:

- QCD jet: constitute high- $p_{\text{T}}$  muons produced from semi-leptonic decays of heavy-flavour hadrons formed within jets. Such muons are generally surrounded by a large hadronic activity and their contribution is significantly suppressed by selecting isolated muons ( $I^{\mu} < 0.15$ ). However, muons from hadron decays can sometimes pass the isolation criteria and thus, a small fraction of the QCD jet background remains in the signal region.

$\eta_{CM}^\mu$ Range	$\mu^- \frac{\epsilon_{corr} - \epsilon_{MC}}{\epsilon_{MC}} [\%]$	$\mu^+ \frac{\epsilon_{corr} - \epsilon_{MC}}{\epsilon_{MC}} [\%]$
-2.86 , -2.60	-2.4	-2.4
-2.60 , -2.40	-2.0	-2.1
-2.40 , -2.20	-1.9	-2.1
-2.20 , -1.93	0.7	0.5
-1.93 , -1.80	3.4	3.2
-1.80 , -1.60	0.8	0.6
-1.60 , -1.40	-4.4	-4.5
-1.40 , -1.20	-3.9	-4.0
-1.20 , -1.00	-3.7	-3.8
-1.00 , -0.80	-3.6	-3.7
-0.80 , -0.60	-4.4	-4.4
-0.60 , -0.40	-4.6	-4.6
-0.40 , -0.20	-4.6	-4.7
-0.20 , +0.00	-3.7	-3.8
+0.00 , +0.20	-3.6	-3.7
+0.20 , +0.40	-3.8	-3.9
+0.40 , +0.60	-4.5	-4.6
+0.60 , +0.80	-2.3	-2.3
+0.80 , +1.00	2.7	2.7
+1.00 , +1.20	1.2	1.1
+1.20 , +1.40	-1.9	-2.0
+1.40 , +1.60	-1.9	-2.0
+1.60 , +1.80	-2.7	-2.7
+1.80 , +1.93	-2.9	-2.8

Table 3.4: Relative difference between the corrected and simulated signal efficiencies as a function of the generated muon  $\eta_{CM}$ , separated in negative and positive charged muons.

- $Z/\gamma^* \rightarrow \mu^+ \mu^-$ : a high- $p_T$  muon produced from a Z-boson decay or Drell–Yan. The contribution from this process is suppressed by applying the  $Z/\gamma^* \rightarrow \mu^+ \mu^-$  veto, which excludes events containing at least one pair of well-identified isolated muons, each with  $p_T > 15$  GeV/c. The  $Z/\gamma^* \rightarrow \mu^+ \mu^-$  events, in which one of the two muons is produced outside of the CMS coverage ( $|\eta_{lab}| < 2.4$ ) or does not satisfy the muon selection criteria, survive the veto. Such events are expected to contribute more in the CMS endcap regions ( $|\eta| > 2.0$ ), where one of the muons from the  $Z/\gamma^* \rightarrow \mu^+ \mu^-$  decay escapes the detector producing a large  $p_T^{\text{miss}}$ .
- $t\bar{t} \rightarrow \mu\nu_\mu + X$ : a high- $p_T$  muon from semi-leptonic decays of top (anti-)quarks. The inclusive cross section of top-quark pair production in pPb at  $\sqrt{s_{\text{NN}}} = 8.16$  TeV, has

been measured by the CMS collaboration to be  $\sigma_{t\bar{t}} = 45 \pm 8$  nb [186]. The  $t\bar{t}$  process is expected to have a very small impact in the signal region due its small inclusive cross section and its branching ratio (13.4%) to muons [21].

- $W \rightarrow \tau\nu_\tau \rightarrow \mu\nu_\mu + X$ : consists of the leptonic decay of a  $W$  boson into a  $\tau$  lepton, which then decays into a high- $p_T$  muon.
- $Z/\gamma^* \rightarrow \tau\bar{\tau} \rightarrow \mu\nu_\mu + X$ : corresponds to a ditau decay of a  $Z$  boson or virtual photon, where one of the  $\tau$  leptons then decays into a high- $p_T$  muon.

The largest source of background in the signal region corresponds to QCD jets which represent approximately 18% of events in data. Among the electroweak background processes, the dominant one is the  $Z/\gamma^* \rightarrow \mu^+\mu^-$  background. The electroweak background amounts to roughly 12% of the events in the signal region, divided as:  $Z/\gamma^* \rightarrow \mu^+\mu^-$  (9%),  $W \rightarrow \tau\nu_\tau$  (2%) and  $Z/\gamma^* \rightarrow \tau\bar{\tau}$  (1%). The  $t\bar{t}$  background contributes roughly 0.5% of events. Other electroweak processes such as double boson decays ( $WW$ ,  $WZ$  and  $ZZ$ ) have been checked to contribute less than 0.03%, so they are not considered.

The shape of the QCD jet background is modelled using a functional form derived from data as explained in Section 3.2.7.1 and the shapes of the signal,  $t\bar{t}$  background and electroweak background are estimated using the  $p_T^{\text{miss}}$  distribution from simulations, as described in Section 3.2.7.2. Section 3.2.7.3 introduces the model used to extract the signal. The event yields obtained from the fits are presented in Section 3.2.7.4 and corrected for efficiency in Section 3.2.7.5.

### 3.2.7.1 Modelling of the QCD jet background

The QCD jet background cannot be simulated reliably in p-Pb collisions due to the imprecise knowledge of the production cross sections and nuclear modifications of hadrons, and the inaccurate modelling of the event activity. Thus, a data-driven approach is used to determine the  $p_T^{\text{miss}}$  distribution of the QCD jet background.

The overall procedure consists of the following steps: first the parametrisation of the QCD jet  $p_T^{\text{miss}}$  distribution in a region dominated by non-isolated muons, then the determination of the dependence of the QCD jet  $p_T^{\text{miss}}$  functional form with respect to the muon isolation and finally the extrapolation of the QCD jet  $p_T^{\text{miss}}$  functional form to low muon isolation values, namely in the signal region.

The  $p_T^{\text{miss}}$  distribution of the QCD jet background is parametrised by a modified Rayleigh distribution, defined as:

$$f_{\text{QCD}}(p_T^{\text{miss}}) = p_T^{\text{miss}} \cdot \exp \left( -\frac{(p_T^{\text{miss}})^2}{2(\sigma_0 + \sigma_1 \cdot p_T^{\text{miss}} + \sigma_2 \cdot (p_T^{\text{miss}})^2)^2} \right) \quad (3.47)$$

where  $\sigma_0$ ,  $\sigma_1$ , and  $\sigma_2$  are free parameters extracted by performing an unbinned maximum-likelihood fit to the  $p_T^{\text{miss}}$  distribution in a control sample from data. The events in the control sample are selected by applying all signal selection requirements, except the muon isolation cut. The fits are performed separately for positive and negative charged muon events.

To derive the muon isolation dependence of the QCD jet background parameters, the  $p_T^{\text{miss}}$  spectrum in the control sample is fitted with the QCD jet  $p_T^{\text{miss}}$  functional form, in five bins of the muon isolation variable with the following boundaries: [ 0.4 , 0.5 , 0.6 , 0.7 , 0.8 , 0.9 ]. Lower muon isolation values ( $I^\mu < 0.4$ ) are discarded, due to the large contamination from weak boson decays. The results of the QCD jet background fits, corresponding to the lowest and highest muon isolation regions, are shown in Figure 3.33.

The QCD background parameters  $\sigma_0$ ,  $\sigma_1$ , and  $\sigma_2$ , are extracted from the fits to the  $p_T^{\text{miss}}$  spectrum in each muon isolation bin, and their profile as a function of  $I^\mu$  is observed to be well described by a linear function, given by:

$$\sigma_i(I^\mu) = \hat{\sigma}_i + s_i \cdot I^\mu \quad (3.48)$$

where  $\hat{\sigma}_i$  and  $s_i$  are free parameters extracted separately for each QCD background parameter. The outcome of the linear fits is shown in Figure 3.34.

The  $\sigma_0$ ,  $\sigma_1$ , and  $\sigma_2$  parameters are extrapolated to the signal region (average muon isolation of 0.03) using the parametrisation as a function of  $I^\mu$  extracted from the linear fits. The values of the QCD background parameters derived from the extrapolation are presented in Table 3.5.

Parameter	QCD jet $\rightarrow \mu^-$	QCD jet $\rightarrow \mu^+$
$\sigma_0$	$14.6 \pm 0.2$	$14.7 \pm 0.2$
$\sigma_1$	$6.3 \pm 0.2$	$6.8 \pm 0.2$
$\sigma_2$	$0.5 \pm 0.2$	$0.5 \pm 0.1$

Table 3.5: QCD background parameters extrapolated to  $I^\mu = 0.03$ . The results are presented for positive and negative charged muons in the  $\eta_{\text{CM}}^\mu$ -inclusive range.

The QCD jet  $p_T^{\text{miss}}$  distribution is estimated separately for positive and negative charged muon events to account for possible differences between the  $\mu^+$  and  $\mu^-$  yields

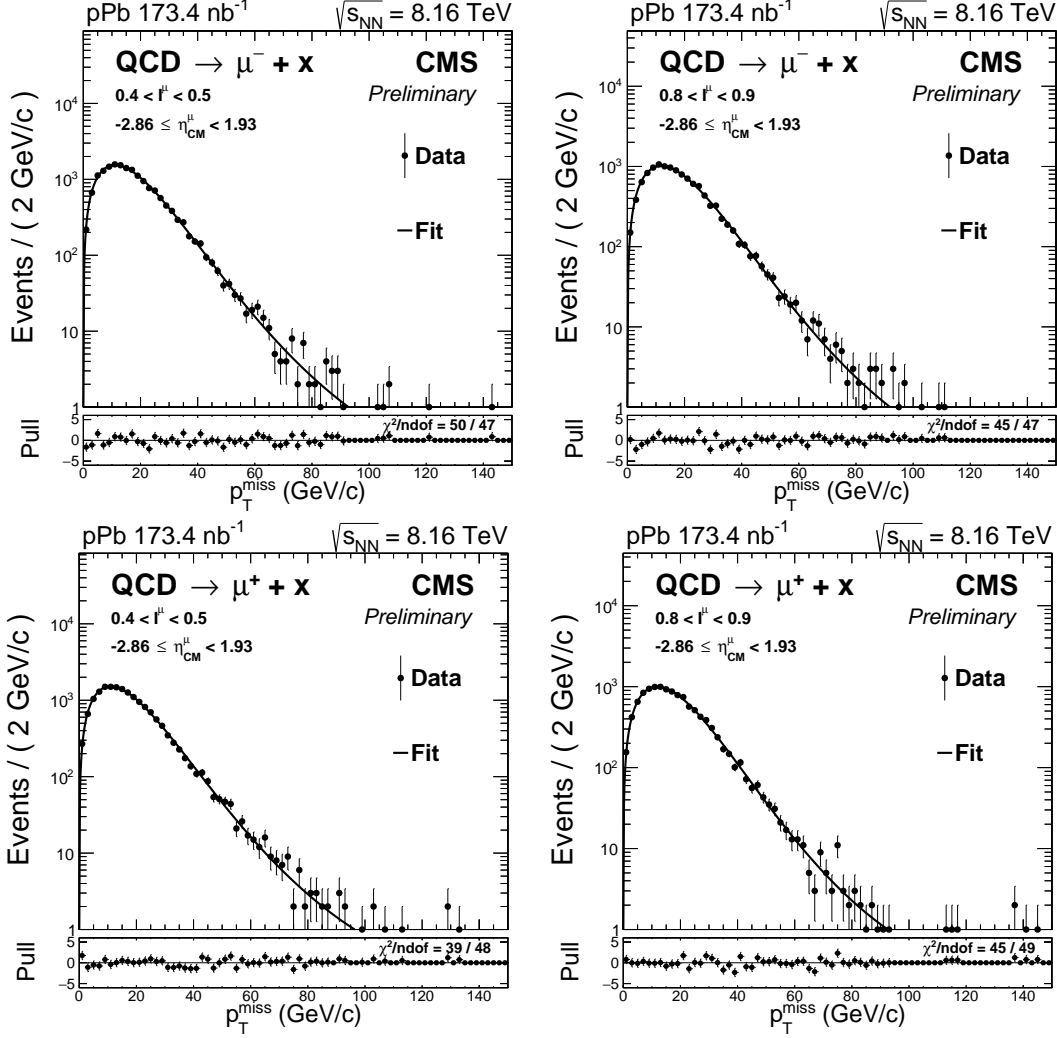


Figure 3.33: QCD jet background fits to the  $p_T^{\text{miss}}$  distribution in a control sample of non-isolated muon events corresponding to the muon isolation bins:  $0.4 < I^\mu < 0.5$  (left) and  $0.8 < I^\mu < 0.9$  (right). The results are shown for positive (top) and negative (bottom) charged muons separately.

arising from the detector response, acceptance and/or muon production from hadron decays. Although the differences are expected to be small, they are still computed separately to be conservative.

The dependence of the extrapolated  $p_T^{\text{miss}}$  functional form of the QCD jet background on the muon  $\eta_{\text{CM}}^\mu$  is checked by splitting the control sample in different  $\eta_{\text{CM}}^\mu$  bins, and then repeating the QCD jet shape extraction procedure for each  $\eta_{\text{CM}}^\mu$  bin. The results of the extrapolated values of  $\sigma_0$ ,  $\sigma_1$ , and  $\sigma_2$ , determined for each  $\eta_{\text{CM}}^\mu$  bin, are compared in Figure 3.35 to the results obtained in the  $\eta_{\text{CM}}^\mu$ -inclusive range.

### 3.2. ANALYSIS

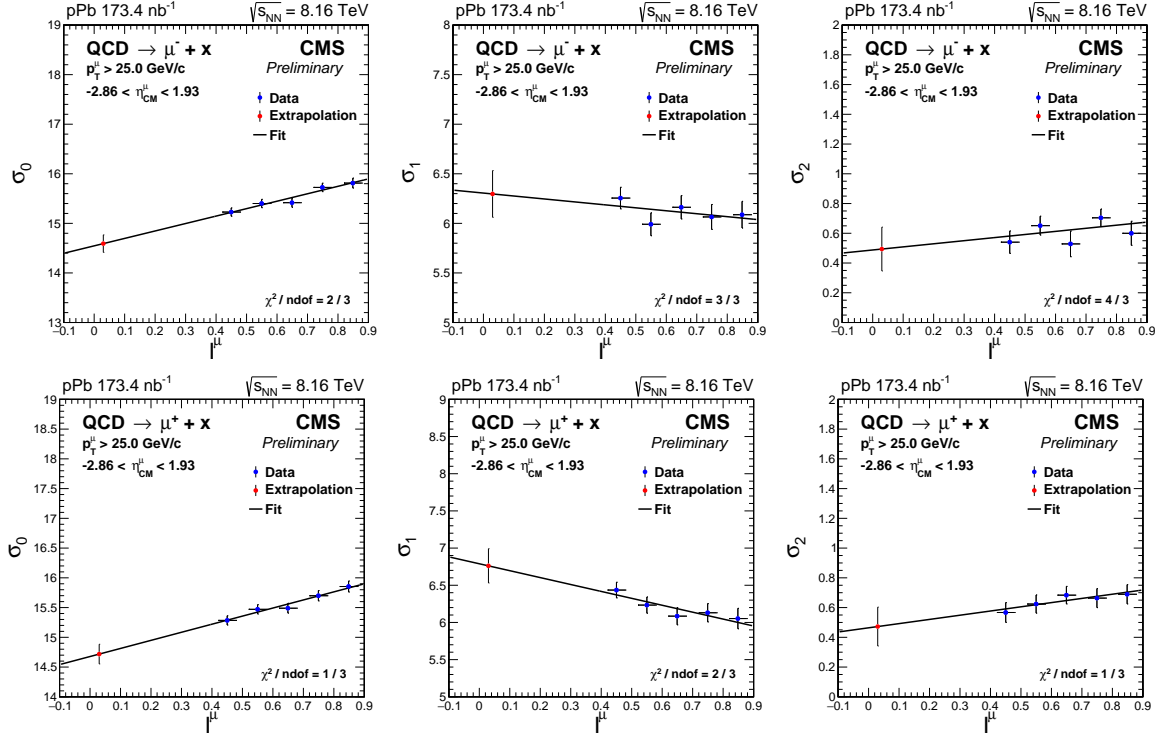


Figure 3.34: Linear fits to the profile of the QCD background parameters:  $\sigma_0$  (left),  $\sigma_1$  (middle) and  $\sigma_2$  (right), with respect to the muon isolation variable  $I^\mu$ . The results are shown for negative (top) and positive (bottom) charged muons in the  $\eta_{\text{CM}}^\mu$ -inclusive range. The red points represent the value obtained by linearly extrapolating to  $I^\mu = 0.03$ .

It is observed that the  $\sigma_0$ ,  $\sigma_1$ , and  $\sigma_2$  parameters, extrapolated to low muon isolation, do not vary significantly with respect to  $\eta_{\text{CM}}^\mu$  and are found to be consistent with the corresponding values obtained in the  $\eta_{\text{CM}}^\mu$ -inclusive range. As a result, the extrapolated parameters derived in the  $\eta_{\text{CM}}^\mu$ -inclusive range for  $\mu^+$  and  $\mu^-$ , are used to fix the QCD jet background shape when fitting the signal.

#### 3.2.7.2 Modelling of the signal, $t\bar{t}$ and electroweak backgrounds

The  $p_T^{\text{miss}}$  distribution of the signal, as well as the  $t\bar{t}$  and electroweak background events, are estimated using the corresponding POWHEG simulations mentioned in Section 3.2.2. The simulated events for each process are required to satisfy the signal selection criteria summarised in Section 3.2.3.5.

In order to improve the description of the data, several corrections are applied to the simulations. First, the simulated HF energy distribution is weighed as explained in Section 3.2.5.1. Then, the generated weak boson  $p_T$  distribution from the  $W \rightarrow \mu\nu_\mu$ ,  $W \rightarrow$

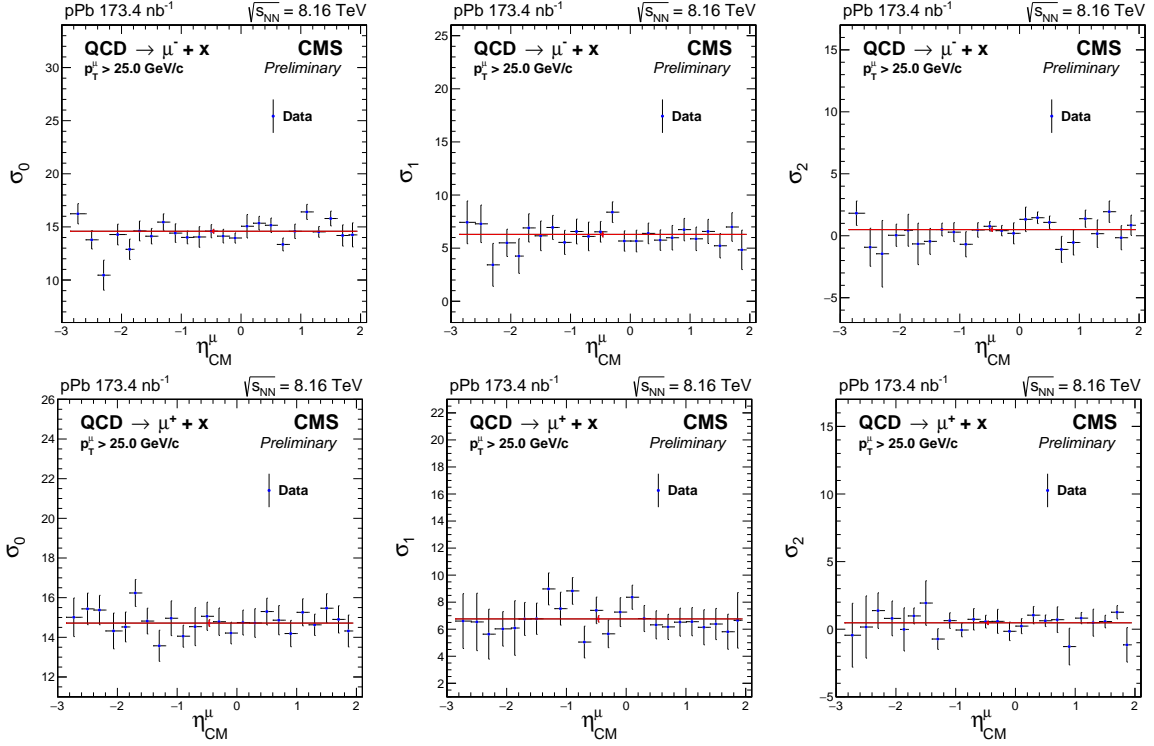


Figure 3.35: Muon  $\eta_{\text{CM}}^\mu$  dependence of  $\sigma_0$  (left),  $\sigma_1$  (middle) and  $\sigma_2$  (right) parameters extrapolated to  $I^\mu = 0.03$ . The results are shown for negative (top) and positive (bottom) charged muons. The red line corresponds to the QCD jet parameter extrapolated in the  $\eta_{\text{CM}}^\mu$ -inclusive range.

$\tau\nu_\tau$ ,  $Z/\gamma^* \rightarrow \mu^+\mu^-$  and  $Z/\gamma^* \rightarrow \tau\bar{\tau}$  simulations, is weighed as described in Section 3.2.4. And finally, the recoil of  $W \rightarrow \mu\nu_\mu$ ,  $W \rightarrow \tau\nu_\tau$  and  $Z/\gamma^* \rightarrow \mu^+\mu^-$  events is calibrated as detailed in Section 3.2.5.2, improving the agreement of the  $p_T^{\text{miss}}$  distribution between data and simulation.

Once the simulations have been corrected, the  $p_T^{\text{miss}}$  distribution of the signal,  $t\bar{t}$  background and electroweak background, are determined by building a template histogram of the simulated  $p_T^{\text{miss}}$  distribution (2 GeV/c bin width). These template histograms are then used in the fitting procedure describe in the next section.

### 3.2.7.3 Fit model

The number of  $W \rightarrow \mu\nu_\mu$  signal events is obtained by performing an unbinned maximum-likelihood fit of the observed  $p_T^{\text{miss}}$  distribution in different muon  $\eta_{\text{CM}}^\mu$  regions. The fits are done using a combination of template histograms and a functional form. The data analysis framework RooFit v3.60 [190] is used to make the fits.

The total fit model includes six contributions: the signal  $W \rightarrow \mu\nu_\mu$  template ( $\mathcal{T}_W$ ), the electroweak background templates  $Z/\gamma^* \rightarrow \mu^+\mu^-$  ( $\mathcal{T}_{Z\mu}$ ),  $W \rightarrow \tau\nu_\tau$  ( $\mathcal{T}_{W\tau}$ ) and  $Z/\gamma^* \rightarrow \tau\bar{\tau}$  ( $\mathcal{T}_{Z\tau}$ ), the  $t\bar{t}$  background template ( $\mathcal{T}_{t\bar{t}}$ ), and the QCD jet background functional form ( $\mathcal{F}_{QCD}$ ). The model used to fit the data is:

$$N_W \cdot (\mathcal{T}_W + r_{Z\mu} \cdot \mathcal{T}_{Z\mu} + r_{W\tau} \cdot \mathcal{T}_{W\tau} + r_{Z\tau} \cdot \mathcal{T}_{Z\tau} + r_{t\bar{t}} \cdot \mathcal{T}_{t\bar{t}}) + N_{QCD} \cdot \mathcal{F}_{QCD} \quad (3.49)$$

where  $N_W$  and  $N_{QCD}$  are the normalisation factors of the  $W \rightarrow \mu\nu_\mu$  signal and QCD jet background component,  $r_{t\bar{t}}$  represents the ratio of  $t\bar{t}$  background events over the number of signal events ( $N_{t\bar{t}}/N_W$ ), and  $r_{Z\mu}$ ,  $r_{Z\tau}$  and  $r_{W\tau}$  are the corresponding ratios for the  $Z/\gamma^* \rightarrow \mu^+\mu^-$ ,  $Z/\gamma^* \rightarrow \tau\bar{\tau}$  and  $W \rightarrow \tau\nu_\tau$  background processes, respectively.

The  $p_T^{\text{miss}}$  distributions of the signal,  $t\bar{t}$  background and electroweak background processes are defined based on template histograms extracted from simulations. Being very small and with a moderately discriminating shape, the electroweak and  $t\bar{t}$  background components cannot be directly and independently fitted on data. Instead, we take advantage that their nuclear modification should be small and close to the one of the  $W$ -boson signal. Thus, the ratios of  $Z/\gamma^* \rightarrow \mu^+\mu^-$ ,  $Z/\gamma^* \rightarrow \tau\bar{\tau}$ ,  $W \rightarrow \tau\nu_\tau$  and  $t\bar{t}$  events over the number of  $W \rightarrow \mu\nu_\mu$  events, are fixed to the results from simulations after having normalised all the MC samples to the recorded integrated luminosity of data as detailed in Section 3.2.2 and applied all analysis corrections and selection criteria.

The QCD jet background contribution is taken into account by means of a functional form depending on three parameters. For the fits to the  $p_T^{\text{miss}}$  distribution in the signal region, the  $\sigma_0$ ,  $\sigma_1$  and  $\sigma_2$  parameters are fixed to the extrapolated values mentioned in Table 3.5, and the normalisation is left free.

The  $p_T^{\text{miss}}$  distribution is fitted separately for  $W^+ \rightarrow \mu^+\nu_\mu$  and  $W^- \rightarrow \mu^-\bar{\nu}_\mu$  events. Only the signal ( $N_W$ ) and the QCD jet background ( $N_{QCD}$ ) normalisation factors are left free when fitting the signal region in data. The fits are done in the  $\eta_{CM}^\mu$ -inclusive range and in bins of muon  $\eta_{CM}^\mu$ . The results of the fits performed in the  $\eta_{CM}^\mu$ -inclusive range are shown in Figure 3.36 and those performed in the other muon  $\eta_{CM}^\mu$  bins are presented in Appendix B.

### 3.2.7.4 Extracted event yields

The results of the fits to the data in each of the different muon  $\eta_{CM}$  bins are summarized in Table 3.6 and Table 3.7 for  $W^- \rightarrow \mu^-\bar{\nu}_\mu$  and  $W^+ \rightarrow \mu^+\nu_\mu$  events, respectively.

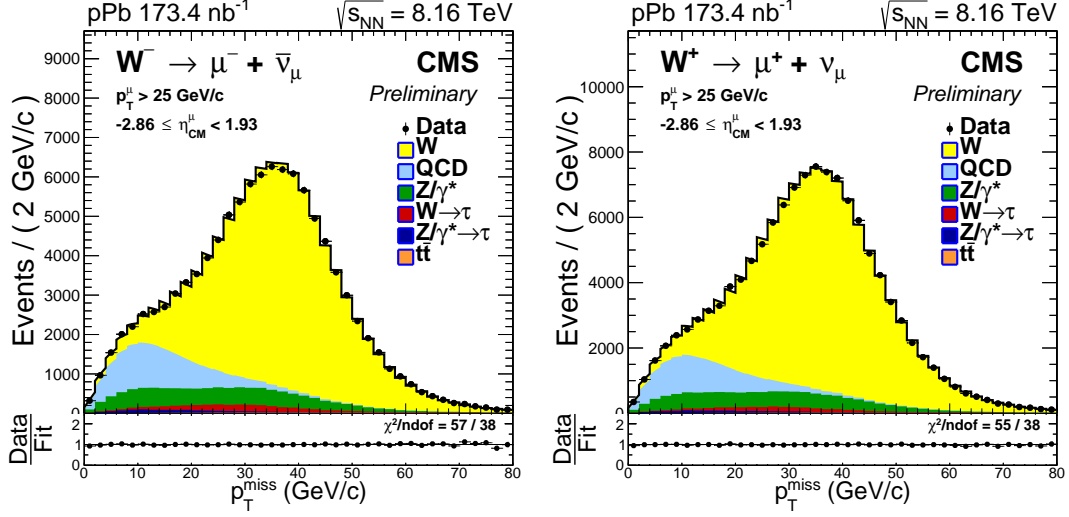


Figure 3.36: The  $p_T^{\text{miss}}$  distribution for  $W^- \rightarrow \mu^- \bar{\nu}_\mu$  (left) and  $W^+ \rightarrow \mu^+ \nu_\mu$  (right) events within the  $\eta_{\text{CM}}^\mu$ -inclusive range, shown in linear scale. Unbinned fits to the data (black points) are performed with six contributions, stacked from top to bottom:  $W \rightarrow \mu \nu_\mu$  (yellow), QCD jet (light blue),  $Z/\gamma^* \rightarrow \mu^+ \mu^-$  (green),  $W \rightarrow \tau \nu_\tau$  (red),  $Z/\gamma^* \rightarrow \tau \bar{\tau}$  (dark blue) and  $t\bar{t}$  (orange). The lower panel, on each figure, display the ratio of the measurements over the result of the fit. The Baker-Cousins [191]  $\chi^2$  test value over the number of degrees of freedom is also shown.

### 3.2.7.5 Corrected event yields

The signal event yields extracted from the fits are corrected by taking into account the efficiency of the detector, according to:

$$N_\mu^\pm(\eta_{\text{CM}}^\mu) = \frac{N_{\mu,\text{raw}}^\pm(\eta_{\text{CM}}^\mu)}{\epsilon_{\text{corr}}^\pm(\eta_{\text{CM}}^\mu)} \quad (3.50)$$

where  $N_{\mu,\text{raw}}$  is the number of signal events extracted from the fits,  $N_\mu$  is the number of signal events after correcting for efficiency and  $\epsilon_{\text{corr}}^\pm$  is the signal efficiency corrected with the TnP corrections. The statistical uncertainty of the corrected signal yields are computed based on error propagation with:

$$\delta N_\mu^\pm = \frac{\delta N_{\mu,\text{raw}}^\pm(\eta_{\text{CM}}^\mu)}{\epsilon_{\text{corr}}^\pm(\eta_{\text{CM}}^\mu)} \quad (3.51)$$

where  $\delta N_{\mu,\text{raw}}^\pm$  is the uncertainty of the signal event yield determined from the fits to the data. The results of the corrected signal event yields for each muon  $\eta_{\text{CM}}^\mu$  range are summarized in Table 3.8 and Table 3.9 for  $W^- \rightarrow \mu^- \bar{\nu}_\mu$  and  $W^+ \rightarrow \mu^+ \nu_\mu$  events, accordingly.

$\eta_{\text{CM}}^\mu$ Range	Total	Signal	$Z/\gamma^* \rightarrow \mu^+ \mu^-$	$W \rightarrow \tau \nu_\tau$	$Z/\gamma^* \rightarrow \tau \bar{\tau}$	$t\bar{t}$	QCD
-2.86 , -2.60	5210	$4041 \pm 65$	$560 \pm 9$	$135 \pm 2$	$45 \pm 1$	$3.1 \pm 0.1$	$427 \pm 40$
-2.60 , -2.40	4308	$3395 \pm 60$	$461 \pm 8$	$102 \pm 2$	$36 \pm 1$	$4.0 \pm 0.1$	$310 \pm 37$
-2.40 , -2.20	4273	$3276 \pm 59$	$449 \pm 8$	$100 \pm 2$	$36 \pm 1$	$5.9 \pm 0.1$	$407 \pm 38$
-2.20 , -1.93	6423	$4920 \pm 74$	$654 \pm 10$	$156 \pm 2$	$62 \pm 1$	$12.9 \pm 0.2$	$617 \pm 48$
-1.93 , -1.80	3140	$2419 \pm 52$	$303 \pm 6$	$79 \pm 2$	$28 \pm 1$	$8.4 \pm 0.2$	$302 \pm 34$
-1.80 , -1.60	4822	$3672 \pm 64$	$435 \pm 8$	$117 \pm 2$	$45 \pm 1$	$15.2 \pm 0.3$	$537 \pm 43$
-1.60 , -1.40	4727	$3631 \pm 64$	$390 \pm 7$	$117 \pm 2$	$39 \pm 1$	$18.8 \pm 0.3$	$533 \pm 43$
-1.40 , -1.20	4521	$3590 \pm 64$	$340 \pm 6$	$109 \pm 2$	$45 \pm 1$	$21.6 \pm 0.4$	$416 \pm 40$
-1.20 , -1.00	4626	$3666 \pm 65$	$306 \pm 5$	$118 \pm 2$	$48 \pm 1$	$25.2 \pm 0.4$	$463 \pm 42$
-1.00 , -0.80	4722	$3762 \pm 66$	$277 \pm 5$	$119 \pm 2$	$45 \pm 1$	$32 \pm 1$	$488 \pm 43$
-0.80 , -0.60	4198	$3425 \pm 63$	$238 \pm 4$	$102 \pm 2$	$46 \pm 1$	$32 \pm 1$	$355 \pm 39$
-0.60 , -0.40	4648	$3738 \pm 66$	$245 \pm 4$	$119 \pm 2$	$54 \pm 1$	$35 \pm 1$	$456 \pm 43$
-0.40 , -0.20	4344	$3478 \pm 64$	$226 \pm 4$	$111 \pm 2$	$50 \pm 1$	$36 \pm 1$	$443 \pm 41$
-0.20 , +0.00	4474	$3510 \pm 65$	$260 \pm 5$	$113 \pm 2$	$43 \pm 1$	$39 \pm 1$	$509 \pm 43$
+0.00 , +0.20	4643	$3654 \pm 65$	$309 \pm 6$	$114 \pm 2$	$47 \pm 1$	$42 \pm 1$	$477 \pm 43$
+0.20 , +0.40	4638	$3533 \pm 64$	$335 \pm 6$	$111 \pm 2$	$50 \pm 1$	$42 \pm 1$	$567 \pm 44$
+0.40 , +0.60	4718	$3528 \pm 63$	$390 \pm 7$	$114 \pm 2$	$46 \pm 1$	$39 \pm 1$	$601 \pm 44$
+0.60 , +0.80	4552	$3375 \pm 62$	$446 \pm 8$	$103 \pm 2$	$48 \pm 1$	$37 \pm 1$	$544 \pm 43$
+0.80 , +1.00	4637	$3325 \pm 61$	$489 \pm 9$	$103 \pm 2$	$43 \pm 1$	$37 \pm 1$	$640 \pm 44$
+1.00 , +1.20	4612	$3265 \pm 60$	$539 \pm 10$	$105 \pm 2$	$45 \pm 1$	$29 \pm 1$	$630 \pm 44$
+1.20 , +1.40	4053	$2769 \pm 55$	$517 \pm 10$	$78 \pm 2$	$38 \pm 1$	$23.8 \pm 0.5$	$627 \pm 42$
+1.40 , +1.60	4251	$2917 \pm 56$	$620 \pm 12$	$96 \pm 2$	$39 \pm 1$	$21.5 \pm 0.4$	$557 \pm 42$
+1.60 , +1.80	3844	$2506 \pm 51$	$611 \pm 12$	$78 \pm 2$	$35 \pm 1$	$15.4 \pm 0.3$	$599 \pm 41$
+1.80 , +1.93	2640	$1719 \pm 42$	$439 \pm 11$	$54 \pm 1$	$22 \pm 1$	$9.6 \pm 0.2$	$397 \pm 33$

Table 3.6: Event yields of  $W^- \rightarrow \mu^- \bar{\nu}_\mu$  and background processes, extracted from the fits to the  $p_T^{\text{miss}}$  distribution in each muon  $\eta_{\text{CM}}^\mu$  region. All analysis selection criteria are applied including the muon  $p_T > 25$  GeV/c. All uncertainties shown are statistical only.

### 3.2.8 Observables

The main motivation behind measuring the W-boson production in p-Pb collisions is to probe the nuclear modifications of the PDFs. To accomplish this, the efficiency-corrected  $W \rightarrow \mu \nu_\mu$  event yields are combined to measure three kinds of observables: cross sections, muon charge asymmetry and forward-backward ratios.

**$W \rightarrow \mu \nu_\mu$  cross sections.** The  $W^\pm \rightarrow \mu^\pm \nu_\mu$  differential cross sections are computed as a function of  $\eta_{\text{CM}}^\mu$ , according to:

$$\frac{d\sigma(W^\pm \rightarrow \mu^\pm \nu_\mu)}{d\eta_{\text{CM}}^\mu}(\eta_{\text{CM}}^\mu) = \frac{N_\mu^\pm(\eta_{\text{CM}}^\mu)}{\mathcal{L} \cdot \Delta\eta_{\text{CM}}^\mu} \quad (3.52)$$

$\eta_{\text{CM}}^\mu$ Range	Total	Signal	$Z/\gamma^* \rightarrow \mu^+ \mu^-$	$W \rightarrow \tau \nu_\tau$	$Z/\gamma^* \rightarrow \tau \bar{\tau}$	$t\bar{t}$	QCD
-2.86 , -2.60	4465	$3358 \pm 59$	$583 \pm 10$	$67 \pm 1$	$44 \pm 1$	$3.3 \pm 0.1$	$409 \pm 38$
-2.60 , -2.40	4234	$3247 \pm 58$	$526 \pm 9$	$65 \pm 1$	$35 \pm 1$	$4.2 \pm 0.1$	$358 \pm 36$
-2.40 , -2.20	4377	$3351 \pm 60$	$500 \pm 9$	$61 \pm 1$	$36 \pm 1$	$6.5 \pm 0.1$	$423 \pm 38$
-2.20 , -1.93	6847	$5257 \pm 76$	$714 \pm 10$	$101 \pm 1$	$53 \pm 1$	$14.3 \pm 0.2$	$706 \pm 49$
-1.93 , -1.80	3592	$2762 \pm 55$	$335 \pm 7$	$56 \pm 1$	$29 \pm 1$	$8.5 \pm 0.2$	$400 \pm 36$
-1.80 , -1.60	5421	$4299 \pm 69$	$488 \pm 8$	$94 \pm 2$	$50 \pm 1$	$16.0 \pm 0.3$	$471 \pm 43$
-1.60 , -1.40	5343	$4375 \pm 70$	$446 \pm 7$	$96 \pm 2$	$45 \pm 1$	$18.0 \pm 0.3$	$364 \pm 42$
-1.40 , -1.20	5129	$4182 \pm 69$	$375 \pm 6$	$98 \pm 2$	$41 \pm 1$	$23.4 \pm 0.4$	$405 \pm 43$
-1.20 , -1.00	5382	$4465 \pm 72$	$339 \pm 5$	$100 \pm 2$	$53 \pm 1$	$28.3 \pm 0.5$	$395 \pm 43$
-1.00 , -0.80	5467	$4485 \pm 73$	$306 \pm 5$	$100 \pm 2$	$50 \pm 1$	$32 \pm 1$	$491 \pm 45$
-0.80 , -0.60	4738	$3960 \pm 68$	$244 \pm 4$	$89 \pm 2$	$42 \pm 1$	$29 \pm 1$	$373 \pm 41$
-0.60 , -0.40	5349	$4435 \pm 73$	$255 \pm 4$	$99 \pm 2$	$49 \pm 1$	$38 \pm 1$	$473 \pm 45$
-0.40 , -0.20	5027	$4146 \pm 70$	$238 \pm 4$	$88 \pm 1$	$46 \pm 1$	$37 \pm 1$	$468 \pm 43$
-0.20 , +0.00	5161	$4269 \pm 71$	$268 \pm 4$	$99 \pm 2$	$45 \pm 1$	$39 \pm 1$	$439 \pm 43$
+0.00 , +0.20	5473	$4352 \pm 72$	$308 \pm 5$	$100 \pm 2$	$52 \pm 1$	$39 \pm 1$	$621 \pm 47$
+0.20 , +0.40	5175	$4179 \pm 70$	$337 \pm 6$	$99 \pm 2$	$48 \pm 1$	$37 \pm 1$	$475 \pm 44$
+0.40 , +0.60	5482	$4334 \pm 71$	$399 \pm 7$	$93 \pm 2$	$43 \pm 1$	$36 \pm 1$	$576 \pm 46$
+0.60 , +0.80	5722	$4469 \pm 72$	$469 \pm 8$	$99 \pm 2$	$51 \pm 1$	$38 \pm 1$	$595 \pm 47$
+0.80 , +1.00	6061	$4652 \pm 72$	$561 \pm 9$	$99 \pm 2$	$48 \pm 1$	$37 \pm 1$	$664 \pm 48$
+1.00 , +1.20	5814	$4404 \pm 70$	$595 \pm 9$	$102 \pm 2$	$41 \pm 1$	$33 \pm 1$	$639 \pm 47$
+1.20 , +1.40	5365	$4050 \pm 67$	$570 \pm 9$	$87 \pm 1$	$35 \pm 1$	$23.9 \pm 0.4$	$596 \pm 45$
+1.40 , +1.60	5768	$4308 \pm 68$	$674 \pm 11$	$92 \pm 1$	$39 \pm 1$	$21.5 \pm 0.3$	$633 \pm 46$
+1.60 , +1.80	5320	$3969 \pm 65$	$662 \pm 11$	$81 \pm 1$	$34 \pm 1$	$16.1 \pm 0.3$	$557 \pm 44$
+1.80 , +1.93	3600	$2654 \pm 53$	$450 \pm 9$	$63 \pm 1$	$19.8 \pm 0.4$	$9.3 \pm 0.2$	$404 \pm 36$

Table 3.7: Event yields of  $W^+ \rightarrow \mu^+ \nu_\mu$  and background processes, extracted from the fits to the  $p_T^{\text{miss}}$  distribution in each muon  $\eta_{\text{CM}}^\mu$  region. All analysis selection criteria are applied including the muon  $p_T > 25$  GeV/c. All uncertainties shown are statistical only.

where  $\mathcal{L} = 173.4 \pm 6.1$  nb $^{-1}$  is the recorded integrated luminosity,  $\Delta\eta_{\text{CM}}^\mu$  is the width of the  $\eta_{\text{CM}}^\mu$  range in which the measurement is performed and  $N_\mu(\eta_{\text{CM}}^\mu)$  is the number of signal events after correcting for efficiency.

**Muon charge asymmetry.** The muon charge asymmetry measures the difference between the event yields of the  $W^- \rightarrow \mu^- \bar{\nu}_\mu$  and  $W^+ \rightarrow \mu^+ \nu_\mu$  processes, which is sensitive to the number of protons and neutrons in the nucleus (isospin effect), and to the flavour dependence of the nuclear modifications of the PDFs. It is defined in the following way:

$$\mathcal{A}_\mu(\eta_{\text{CM}}^\mu) = \frac{N_\mu^+(\eta_{\text{CM}}^\mu) - N_\mu^-(\eta_{\text{CM}}^\mu)}{N_\mu^+(\eta_{\text{CM}}^\mu) + N_\mu^-(\eta_{\text{CM}}^\mu)} \quad (3.53)$$

where  $N_\mu^-$  and  $N_\mu^+$  represents the efficiency-corrected number of  $W^- \rightarrow \mu^- \bar{\nu}_\mu$  and

$\eta_{\text{CM}}^\mu$ Range	Extracted yield	Efficiency (%)	Corrected yield
-2.86 , -2.60	$4041 \pm 65$	$84.7 \pm 0.2$	$4773 \pm 77$
-2.60 , -2.40	$3395 \pm 60$	$87.3 \pm 0.2$	$3891 \pm 69$
-2.40 , -2.20	$3276 \pm 59$	$83.8 \pm 0.2$	$3907 \pm 71$
-2.20 , -1.93	$4920 \pm 74$	$87.6 \pm 0.2$	$5619 \pm 84$
-1.93 , -1.80	$2419 \pm 52$	$92.1 \pm 0.2$	$2627 \pm 56$
-1.80 , -1.60	$3672 \pm 64$	$92.0 \pm 0.1$	$3990 \pm 70$
-1.60 , -1.40	$3631 \pm 64$	$88.7 \pm 0.2$	$4093 \pm 72$
-1.40 , -1.20	$3590 \pm 64$	$85.5 \pm 0.2$	$4200 \pm 75$
-1.20 , -1.00	$3666 \pm 65$	$89.4 \pm 0.2$	$4102 \pm 73$
-1.00 , -0.80	$3762 \pm 66$	$89.7 \pm 0.2$	$4195 \pm 74$
-0.80 , -0.60	$3425 \pm 63$	$81.1 \pm 0.2$	$4222 \pm 78$
-0.60 , -0.40	$3738 \pm 66$	$88.7 \pm 0.2$	$4216 \pm 75$
-0.40 , -0.20	$3478 \pm 64$	$83.8 \pm 0.2$	$4148 \pm 76$
-0.20 , +0.00	$3510 \pm 65$	$87.5 \pm 0.2$	$4012 \pm 74$
+0.00 , +0.20	$3654 \pm 65$	$89.3 \pm 0.2$	$4091 \pm 73$
+0.20 , +0.40	$3533 \pm 64$	$85.8 \pm 0.2$	$4116 \pm 74$
+0.40 , +0.60	$3528 \pm 63$	$88.2 \pm 0.2$	$4000 \pm 72$
+0.60 , +0.80	$3375 \pm 62$	$90.5 \pm 0.2$	$3729 \pm 68$
+0.80 , +1.00	$3325 \pm 61$	$92.1 \pm 0.2$	$3610 \pm 66$
+1.00 , +1.20	$3265 \pm 60$	$88.2 \pm 0.2$	$3704 \pm 68$
+1.20 , +1.40	$2769 \pm 55$	$83.5 \pm 0.2$	$3318 \pm 65$
+1.40 , +1.60	$2917 \pm 56$	$90.6 \pm 0.2$	$3219 \pm 61$
+1.60 , +1.80	$2506 \pm 51$	$83.4 \pm 0.2$	$3005 \pm 61$
+1.80 , +1.93	$1719 \pm 42$	$86.4 \pm 0.3$	$1990 \pm 48$

Table 3.8: Corrected event yields of  $W^- \rightarrow \mu^- \bar{\nu}_\mu$ , given for each muon  $\eta_{\text{CM}}^\mu$  bin. All analysis selection criteria are applied including the muon  $p_T > 25$  GeV/c. The muon efficiency has been corrected by applying the tag-and-probe corrections, HF energy weights and vector boson  $p_T$  weights, event-by-event. All uncertainties shown are statistical only.

$W^+ \rightarrow \mu^+ \nu_\mu$  events, respectively.

**Forward-backward ratios.** To probe the modification of the PDFs between different pseudorapidity regions, the signal event yields measured in the forward region ( $\eta_{\text{CM}}^\mu > 0$ ) are combined with those measured in the backward region ( $\eta_{\text{CM}}^\mu < 0$ ), to derive forward-backward ratios. These ratios are computed separately for  $W^+ \rightarrow \mu^+ \nu_\mu$  and  $W^- \rightarrow \mu^- \bar{\nu}_\mu$  events in the following way:

$$R_{\text{FB}}^\pm(\eta_{\text{CM}}^\mu) = \frac{N_\mu^\pm(+\eta_{\text{CM}}^\mu)}{N_\mu^\pm(-\eta_{\text{CM}}^\mu)} \quad (3.54)$$

$\eta_{\text{CM}}^{\mu}$ Range	Extracted yield	Efficiency (%)	Corrected yield
-2.86 , -2.60	$3358 \pm 59$	$84.3 \pm 0.2$	$3982 \pm 70$
-2.60 , -2.40	$3247 \pm 58$	$87.3 \pm 0.2$	$3721 \pm 66$
-2.40 , -2.20	$3351 \pm 60$	$83.8 \pm 0.2$	$3997 \pm 71$
-2.20 , -1.93	$5257 \pm 76$	$86.8 \pm 0.2$	$6055 \pm 87$
-1.93 , -1.80	$2762 \pm 55$	$92.0 \pm 0.2$	$3001 \pm 60$
-1.80 , -1.60	$4299 \pm 69$	$91.9 \pm 0.1$	$4679 \pm 75$
-1.60 , -1.40	$4375 \pm 70$	$88.7 \pm 0.2$	$4931 \pm 79$
-1.40 , -1.20	$4182 \pm 69$	$84.7 \pm 0.2$	$4940 \pm 82$
-1.20 , -1.00	$4465 \pm 72$	$88.4 \pm 0.2$	$5049 \pm 81$
-1.00 , -0.80	$4485 \pm 73$	$89.2 \pm 0.2$	$5029 \pm 82$
-0.80 , -0.60	$3960 \pm 68$	$80.7 \pm 0.2$	$4908 \pm 85$
-0.60 , -0.40	$4435 \pm 73$	$88.5 \pm 0.2$	$5015 \pm 83$
-0.40 , -0.20	$4146 \pm 70$	$83.0 \pm 0.2$	$4996 \pm 85$
-0.20 , +0.00	$4269 \pm 71$	$87.2 \pm 0.2$	$4897 \pm 81$
+0.00 , +0.20	$4352 \pm 72$	$89.2 \pm 0.2$	$4881 \pm 81$
+0.20 , +0.40	$4179 \pm 70$	$85.0 \pm 0.2$	$4915 \pm 82$
+0.40 , +0.60	$4334 \pm 71$	$88.3 \pm 0.2$	$4908 \pm 81$
+0.60 , +0.80	$4469 \pm 72$	$90.4 \pm 0.2$	$4944 \pm 79$
+0.80 , +1.00	$4652 \pm 72$	$91.6 \pm 0.2$	$5081 \pm 79$
+1.00 , +1.20	$4404 \pm 70$	$87.8 \pm 0.2$	$5016 \pm 80$
+1.20 , +1.40	$4050 \pm 67$	$83.2 \pm 0.2$	$4867 \pm 80$
+1.40 , +1.60	$4308 \pm 68$	$90.3 \pm 0.2$	$4773 \pm 76$
+1.60 , +1.80	$3969 \pm 65$	$83.1 \pm 0.2$	$4776 \pm 78$
+1.80 , +1.93	$2654 \pm 53$	$86.9 \pm 0.2$	$3054 \pm 61$

Table 3.9: Corrected event yields of  $W^+ \rightarrow \mu^+ \nu_{\mu}$ , given for each muon  $\eta_{\text{CM}}^{\mu}$ . All analysis selection criteria are applied including the muon  $p_T > 25$  GeV/c. The muon efficiency has been corrected by applying the tag-and-probe corrections, HF energy weights and vector boson  $p_T$  weights, event-by-event. All uncertainties shown are statistical only.

A forward-backward ratio is also derived for all  $W \rightarrow \mu \nu_{\mu}$  events, by combining the yields of the  $W^- \rightarrow \mu^- \bar{\nu}_{\mu}$  and  $W^+ \rightarrow \mu^+ \nu_{\mu}$  processes, according to:

$$R_{\text{FB}}(\eta_{\text{CM}}^{\mu}) = \frac{N_{\mu}^{+}(+\eta_{\text{CM}}^{\mu}) + N_{\mu}^{-}(+\eta_{\text{CM}}^{\mu})}{N_{\mu}^{+}(-\eta_{\text{CM}}^{\mu}) + N_{\mu}^{-}(-\eta_{\text{CM}}^{\mu})} \quad (3.55)$$

### 3.2.9 Systematic uncertainties

This section presents the different sources and the procedure employed to determine the systematic uncertainties in the measurement of the W-boson production in p-Pb

collisions.

### 3.2.9.1 Luminosity

The recorded integrated luminosity of the 2016 p-Pb data sample is  $173.4 \text{ nb}^{-1}$ , and is known with a precision of 3.5% [173]. Since the integrated luminosity cancels in forward-backward ratios and in the muon charge asymmetry, it only affects the measurement of the  $W \rightarrow \mu\nu_\mu$  differential cross sections. In this case, this 3.5% systematic uncertainty is global and the bin-to-bin correlation is 100%. This uncertainty is the dominant one on the  $W \rightarrow \mu\nu_\mu$  differential cross sections.

### 3.2.9.2 Signal efficiency

The dominant systematic uncertainties on the forward-backward ratios and muon charge asymmetry are due to the estimation of the signal efficiency. Since the signal efficiencies are computed from simulations and corrected using the TnP corrections, two sources of systematic uncertainties are considered. The first one corresponds to the theoretical modelling of the simulated signal, which takes into account the uncertainty on the nuclear PDFs and the impact of the renormalisation and factorisation scales. The second source corresponds to the TnP correction uncertainties, which derive from the  $Z \rightarrow \mu^+ \mu^-$  control sample used to extract the TnP data efficiencies.

**Theoretical modelling.** The NLO model used to generate the simulations can impact the measurement of the signal efficiencies. The main sources of theoretical uncertainties include the choice of the nuclear parton distribution functions (EPPS16+CT14), and the renormalisation and factorisation scales.

Since the PDFs are not calculable from first principles but are determined experimentally, in particular by the measurements reported here, the inclusion of any PDF introduces an additional systematic uncertainty. Thus, it is important to determine the impact of a change of PDF on the signal efficiencies. The procedure to derive the theoretical uncertainties of the PDF variations consists of reweighing the simulations event-by-event using weights derived from POWHEG after applying various PDF sets. The PDF sets are accessed through the LHAPDF6 [192] framework and consist of 56 CT14 PDFs and 40 EPPS16 nuclear corrections. Once the simulations are reweighed with each PDF set, the efficiencies are recomputed and used to recalculate all the observables. The nPDF uncertainty is determined by combining the EPPS16+CT14 PDF variations of the observables using the Hessian approach, as recommended by the EPPS16 authors [161].

Moreover, the uncertainty due to the renormalisation ( $\mu_R$ ) and factorisation ( $\mu_F$ ) scales is computed by varying these two scales in POWHEG using the following six combinations:

$$\left( \frac{\mu_R}{M_W}, \frac{\mu_F}{M_W} \right) = [ (0.5, 0.5), (1.0, 0.5), (0.5, 1.0), (1.0, 2.0), (2.0, 1.0), (2.0, 2.0) ]$$

The simulations are reweighted event-by-event using the POWHEG weights produced with each set of scales, then the efficiencies are recomputed and the observables are recalculated for each varied efficiency. The variations on the observables are combined by taking the envelope (i.e. the maximum variation in each  $\eta_{\text{CM}}^\mu$  range).

The systematic uncertainties from the PDF and scale variations are summed in quadrature, and amount to 0.1%. Thus, the theoretical uncertainties have negligible impact on the signal efficiencies.

**Tag-and-probe corrections.** The main source of systematic uncertainty in the measurement of the signal efficiency arises from the application of the TnP corrections. As mentioned in Section 3.2.6.2, the statistical and systematic uncertainties of the TnP corrections are derived from the muon identification, isolation and trigger efficiencies measured in data.

It is crucial to consider the correlation between the different TnP uncertainties as a function of muon pseudorapidity and its charge, since they could cancel in the forward-backward ratios and muon charge asymmetry. The statistical TnP variations are uncorrelated between the different  $\eta_{\text{lab}}$  ranges in which they were derived. The systematic TnP variations are considered to be fully correlated as a function of muon charge since the detector response is the same for muons and anti-muons, and uncorrelated between the different  $\eta_{\text{CM}}$  ranges (spanning different detectors).

To compute the uncertainties, the muon charge asymmetry and the forward-backward ratios are recalculated for each efficiency derived by varying the TnP corrections. The TnP uncertainties are then determined by taking the difference between the value obtained with the varied TnP correction and its nominal value, combining the uncertainties as explained in Section 3.2.6.2. If the source of TnP correction is correlated in muon charge or pseudorapidity, the corresponding signal yields are varied at the same time. Moreover, for the  $W^\pm$  differential cross sections, the statistical and systematic TnP uncertainties are calculated by propagating the uncertainties on the corrected signal efficiency.

The largest systematic uncertainty due to the TnP corrections amounts to 3.2% and the dominant TnP uncertainties are derived from the TnP systematic variations of the

muon isolation (2.5%) and trigger (1.1%) components. The TnP systematic uncertainties on the muon isolation and trigger efficiency mainly arise from varying the background functional form used to fit the tag-probe invariant mass distribution, which lacks of statistics.

### 3.2.9.3 QCD jet background

The systematic uncertainty in the QCD jet background originates from the uncertainty in the modelling of the QCD jet  $p_T^{\text{miss}}$  distribution in the signal region. The nominal procedure consists in fixing the parameters of the modified Rayleigh distribution from the fits extrapolated from data as explained in Section 3.2.7.1. In order to estimate the uncertainty of the mismodelling of the  $p_T^{\text{miss}}$  distribution of the QCD jet background, both the parameters and the functional form are varied.

**QCD jet background parameters.** The first source of systematic uncertainty reflects the possible mismodelling of the QCD jet background shape due to the  $\eta_{\text{CM}}^\mu$  dependence of the QCD background parameters. In order to check this, the parameters of the nominal QCD jet model are set free but constrained to be near their nominal values by using a Gaussian penalty. The width of the penalty Gaussian function is fixed, for a given QCD background parameter, to the root mean square (RMS) of the set of extrapolated results along all  $\eta_{\text{CM}}^\mu$  ranges, shown in Figure 3.35. The RMS values used in the Gaussian penalty for the  $\sigma_0$ ,  $\sigma_1$  and  $\sigma_2$  parameters are presented in Table 3.10. The difference between the number of signal events extracted from the Gaussian-constrained fits and the nominal fits is taken as the systematic uncertainty, which is then propagated to all observables. This source of uncertainty is considered to be fully uncorrelated since the  $p_T^{\text{miss}}$  distribution in each  $\eta_{\text{CM}}^\mu$  range is fitted separately.

Parameter	RMS	
	QCD jet $\rightarrow \mu^-$	QCD jet $\rightarrow \mu^+$
$\sigma_0$	1.0	0.5
$\sigma_1$	0.9	0.9
$\sigma_2$	0.7	0.6

Table 3.10: The RMS of the set of QCD background parameters extrapolated along all  $\eta_{\text{CM}}^\mu$  regions.

Another systematic variation consists of changing the muon isolation point used to extrapolate the QCD background parameters. In the nominal case, the isolation point of

0.03 is determined from the average muon isolation value in data within the signal region. As an alternative case, the muon isolation distribution is checked in a QCD PYTHIA simulated sample satisfying the signal selection criteria, and the average isolation value is determined to be approximately 0.08. As a result, the QCD background parameters are recomputed by extrapolating them to an isolation point of  $I^\mu = 0.08$ , and the fits are redone by fixing the QCD background parameters to the extrapolated values in the  $\eta_{\text{CM}}^\mu$ -inclusive range as in the nominal case. The difference between the number of signal events extracted from the fits using the varied QCD background shape and the nominal results is taken as the systematic uncertainty. This uncertainty is propagated to all observables. The QCD background parameters extrapolated to  $I^\mu = 0.08$  are listed in Table 3.11. Since the result in each  $\eta_{\text{CM}}^\mu$  range varies independently, the uncertainty is considered to be fully uncorrelated.

Parameter	$QCD \rightarrow \mu^-$	$QCD \rightarrow \mu^+$
$\sigma_0$	14.67	14.79
$\sigma_1$	6.28	6.71
$\sigma_2$	0.50	0.49

Table 3.11: QCD shape parameters extrapolated to the average muon isolation point  $I^\mu = 0.08$ .

The systematic uncertainty associated to the  $\eta_{\text{CM}}^\mu$  dependence of the QCD background parameters amounts to 1.1%, while the uncertainty corresponding to the change of extrapolation point represents 0.2%.

**QCD jet background functional form.** To assign a systematic uncertainty due to the assumed functional form for modelling the QCD jet background  $p_T^{\text{miss}}$  distribution, a different model is used. The alternative  $p_T^{\text{miss}}$  functional form employed, taken from Ref.[171], is given by:

$$f_{\text{QCD}}(p_T^{\text{miss}}) = (p_T^{\text{miss}} + x_0)^\alpha \cdot \exp\left(\beta \cdot \sqrt{p_T^{\text{miss}} + x_0}\right) \quad (3.56)$$

The extrapolation procedure explained in Section 3.2.7.1 is redone using the alternative model. All the fits are remade using the alternative QCD background functional form fixed to the parameters extrapolated in the  $\eta_{\text{CM}}^\mu$ -inclusive range. The difference between the number of signal events measured using the alternative QCD background model and the nominal results is taken as the systematic uncertainty due to mismodelling of the

QCD jet background shape. This systematic uncertainty is propagated to all observables and amounts to 0.6%. The bin-to-bin correlation is taken to be fully uncorrelated.

### 3.2.9.4 Electroweak and $t\bar{t}$ backgrounds

The  $t\bar{t}$  background and the different sources of electroweak background are described using template histograms derived from simulations. The simulated samples are scaled to the recorded integrated luminosity of data using the NLO POWHEG cross sections for the electroweak processes and the CMS measured cross section for the  $t\bar{t}$  production. Since for each these background sources, the ratio of background over signal events is fixed to simulation when performing the fits, a systematic uncertainty is assigned to each source by varying up and down their cross sections as explained below. The systematic uncertainty in each  $\eta_{CM}^\mu$  range is derived by taking the maximum difference between the nominal and the up/down variations. The bin-to-bin correlations in muon charge and pseudorapidity are considered correlated since the total cross section is used to normalise all simulated events.

**$Z/\gamma^* \rightarrow \mu^+ \mu^-$  background.** The uncertainty on the ratio of  $Z/W$  total cross sections is estimated using the Monte Carlo for FeMtobarn processes (MCFM) program [193] at NLO with the CT14+EPPS16 nuclear PDFs. A relative uncertainty of 0.8% for  $Z/W^-$  and 1.3% for  $Z/W^+$  cross-section ratios is determined with MCFM taking into account the PDF uncertainties. Since the cross sections in the muon channel depend on the branching ratio associated to each process, their uncertainty has to also be taken into account. The values of the branching ratios correspond to  $BR(Z \rightarrow \mu^+ \mu^-) = (3.366 \pm 0.007)\%$  and  $BR(W \rightarrow \mu \nu_\mu) = (10.63 \pm 0.15)\%$  [21], which gives a relative uncertainty on the ratio of  $Z/W$  branching ratios of 1.4%. Summing in quadrature the MCFM uncertainties with the ones derived from the branching ratios, one gets a total relative uncertainty for  $Z/W^+$  of 1.6% and for  $Z/W^-$  of 1.9%. To be conservative the systematic variation is fixed to 2% overall. The systematic uncertainty on the  $W$ -boson yield is then determined by varying the  $Z/\gamma^* \rightarrow \mu^+ \mu^-$  cross section by 2% up and down when performing the fits, yielding a change of 0.3% in the measured  $W \rightarrow \mu \nu_\mu$  cross sections.

**$Z/\gamma^* \rightarrow \tau\bar{\tau}$  background.** The uncertainty on the ratio of  $Z/\gamma^* \rightarrow \tau\bar{\tau}$  background over signal events is considered to be the same as the 2% uncertainty determined for the  $Z/\gamma^* \rightarrow \mu^+ \mu^-$  background. Hence, the  $Z/\gamma^* \rightarrow \tau\bar{\tau}$  cross section is varied by 2% up and

down when performing the fits. The impact of this systematic uncertainty is negligible and modifies the  $W \rightarrow \mu\nu_\mu$  cross sections by 0.01%.

**$W \rightarrow \tau\nu_\tau$  background.** The values of the  $W$ -boson leptonic branching ratios correspond to  $\text{BR}(W \rightarrow \mu\nu_\mu) = (10.63 \pm 0.15)\%$  and  $\text{BR}(W \rightarrow \tau\nu_\tau) = (11.38 \pm 0.21)\%$  [21], which gives a relative uncertainty on the ratio of  $W \rightarrow \tau\nu_\tau$  over  $W \rightarrow \mu\nu_\mu$  cross sections of 2.3%. Thus, the systematic uncertainty is estimated by varying the ratio of  $W \rightarrow \tau\nu_\tau$  to signal events up and down by  $\pm 2.3\%$ . The impact of this systematic uncertainty on the  $W \rightarrow \mu\nu_\mu$  cross sections is found to be 0.04%.

**$t\bar{t}$  background.** The  $t\bar{t}$  simulation is normalized using the CMS measured total cross section  $\sigma_{t\bar{t}} = 45 \pm 8 \text{ nb}$  [186]. The systematic related to the  $t\bar{t}$  background normalization is computed by varying up and down the  $t\bar{t}$  cross section by its measured relative uncertainty ( $\pm 18\%$ ). This systematic uncertainty amounts to 0.2%.

### 3.2.9.5 Weak boson $p_T$

The modelling of the weak boson  $p_T$  in the signal and electroweak background simulations is corrected by weighing event-by-event the generated weak boson  $p_T$  distribution following the procedure described in Section 3.2.4. To determine the impact of the modelling of the weak boson  $p_T$ , the boson  $p_T$  corrections are removed and both the efficiency and the fits to the  $p_T^{\text{miss}}$  distribution are remade. The systematic uncertainty is determined in each  $\eta_{\text{CM}}^\mu$  range from the difference between the nominal results and the results obtained without weighing the generated boson  $p_T$  distribution. This uncertainty amounts to 0.5% and it is considered to be correlated with respect to muon charge and pseudorapidity.

### 3.2.9.6 Event activity

The modelling of the event activity present in p-Pb collisions is improved by weighing the distribution of the total HF energy, as explained in Section 3.2.5.1. The event activity is also correlated with other global variables, such as the number of tracks per event. Since the pseudorapidity coverages of the tracker ( $|\eta| < 2.5$ ) and the HF calorimeter ( $3.0 < |\eta| < 5.4$ ) are different, the HF energy and the track multiplicity are sensitive to different kinematic regions of the event activity. Thus, the systematic uncertainty on the modelling of the event activity is determined by weighing instead the distribution of the simulated track multiplicity following the same procedure as the one used for the

HF energy. The fits to the  $p_T^{\text{miss}}$  distribution and the signal efficiency are recomputed after weighing the simulated track multiplicity distribution. The difference between the varied and nominal observables is assigned as the systematic uncertainty in each muon  $\eta_{\text{CM}}^\mu$  range. This uncertainty is considered correlated in muon charge and pseudorapidity, and it amounts to 0.6%.

### 3.2.9.7 Recoil calibration

The uncertainties due to the recoil calibration are of different nature: statistical and systematic. The statistical component arises from the uncertainties associated to the recoil scale and resolution derived from the fits to the recoil distributions from data. The systematic components arise from the following sources:

- The recoil calibration method employed to correct the simulated  $p_T^{\text{miss}}$  distribution;
- The choice of functional form used to fit the recoil distributions in each  $q_T^Z$  range;
- The parametrisation of the  $q_T$  dependence of the recoil scale and resolution.

**Statistical component.** In order to estimate the uncertainty associated to the recoil resolution, the weighed average Gaussian widths of the perpendicular and parallel recoil components, defined in Eq. (3.36), are randomly smeared in each  $q_T^Z$  range using a Gaussian distribution centred on the parameter value and with a width equal to the parameter uncertainty. The  $q_T$  dependence is parametrised again using the nominal functions presented in Eq. (3.35). The procedure is repeated a hundred times, and the recoil calibrations are applied to the simulated  $p_T^{\text{miss}}$  distributions, redoing the measurements every time. The RMS of the number of signal events extracted from the fits using each variation of the recoil calibration, is used to determine the statistical uncertainty of the recoil calibration. This uncertainty is propagated to all observables and amounts to 0.09%. It is considered fully uncorrelated.

**Systematic components.** The fit function used to parametrise the  $q_T$  dependence of the recoil scale and resolution, is varied in both data and simulation to determine the associated uncertainty. Instead of using the nominal functions for the Gaussian mean (Eq. (3.33)) and Gaussian widths (Eq. (3.35)), a second order polynomial is used to parametrise the Gaussian parameters with respect to  $q_T^Z$ . The varied recoil calibration is applied to the simulated  $p_T^{\text{miss}}$  distributions, which are then used to extract the signal from the data. The difference between the observables measured using the varied

recoil calibration and the nominal observables, in each  $\eta_{\text{CM}}^\mu$ , is assigned as a systematic uncertainty.

The uncertainty on the shape of the recoil distributions in each  $q_T^Z$  range is estimated by varying the recoil fit model. Instead of using a sum of two Gaussian functions, the recoil distributions are parametrised with a sum of a Breit-Wigner and a Gaussian distribution, in both data and simulation (varied at the same time). The resulting  $q_T$  dependence of the recoil scale and resolution is determined following the nominal procedure and the measurements are performed again. The systematic uncertainty is determined as the variation between the observables derived with the varied recoil calibration and the nominal ones.

Moreover, the uncertainty associated to the method used to apply the recoil calibration is determined by smearing the recoil distributions as described in Eq. (3.42), instead of scaling them as done in the nominal case. The difference between the varied and nominal observables in each  $\eta_{\text{CM}}^\mu$  is assigned as a systematic uncertainty.

The largest source of systematic uncertainty in this case is the one associated to the shape of the recoil distribution, which amounts to 0.3%. The uncertainty related to the recoil calibration represents 0.2%, while the uncertainty corresponding to the  $q_T$  dependence of the recoil scale and resolution is determined to be 0.06%. These uncertainties are considered correlated both in muon charge and pseudorapidity.

### 3.2.9.8 W-boson POWHEG BOX

The  $W \rightarrow \mu\nu_\mu$  simulations were generated using the POWHEG-BOX package `W_ew-BMMNP` [178], in which electroweak NLO corrections are implemented. In order to assess the impact of these NLO corrections on the final results, the  $W \rightarrow \mu\nu_\mu$  simulations were remade instead using the standard POWHEG-BOX package `W` [194], which does not include electroweak NLO corrections, following the same procedure described in Section 3.2.2.

To determine the systematic uncertainty, the signal efficiencies and the template histograms for the signal were recomputed using the  $W \rightarrow \mu\nu_\mu$  simulations without electroweak NLO corrections. Then, the fits to the  $p_T^{\text{miss}}$  distribution in data were performed again, and the difference between the observables measured using the varied signal templates and the nominal results is assigned as a systematic uncertainty in each  $\eta_{\text{CM}}^\mu$  range. This uncertainty amounts to 0.9% and it is considered to be fully correlated.

### 3.2.9.9 Summary of systematic uncertainties

The largest systematic uncertainty for each category among all  $\eta_{\text{CM}}^\mu$  ranges is summarised in Table 3.12. The systematic uncertainties are shown for each observable, including the  $W \rightarrow \mu\nu_\mu$  cross sections, muon charge asymmetry and the forward-backward ratios. The uncertainties presented for the cross sections are relative while those for the forward-backward ratios and the muon charge asymmetry are absolute.

Systematic Variation	$\sigma(W^- \rightarrow \mu^-\bar{\nu}_\mu)$ [%]	$\sigma(W^+ \rightarrow \mu^+\nu_\mu)$ [%]	$R_{\text{FB}}^-$	$R_{\text{FB}}^+$	$R_{\text{FB}}$	$\mathcal{A}_\mu$
Luminosity	3.5	3.5	0.000	0.000	0.000	0.000
Signal efficiency	3.0	3.2	0.026	0.037	0.030	0.011
QCD jet background	1.2	0.7	0.016	0.007	0.009	0.006
Electroweak and tt backgrounds	0.4	0.3	0.002	0.001	0.001	0.000
Weak boson $p_T$	0.5	0.4	0.001	0.001	0.001	0.001
Event activity	0.6	0.4	0.002	0.002	0.001	0.002
Recoil calibration	0.2	0.3	0.002	0.004	0.002	0.002
W-boson POWHEG-BOX	0.9	0.5	0.007	0.004	0.006	0.003
Total systematic uncertainty	4.8	4.8	0.030	0.038	0.031	0.013
Statistical uncertainty	2.4	2.0	0.026	0.029	0.019	0.015

Table 3.12: Maximum uncertainty of the measured observables determined for each category. The uncertainties of the  $W \rightarrow \mu\nu_\mu$  differential cross sections are relative while for the forward-backward ratios and muon charge asymmetry they are absolute.

The uncertainties of the measurements are shown in Figure 3.37 as a function of  $\eta_{\text{CM}}^\mu$ . They are observed to be similar between the different  $\eta_{\text{CM}}^\mu$  ranges, except for the most backward and forward regions, which are driven by the systematic uncertainty on the signal efficiency. It is also seen that the systematic uncertainties dominate on the  $W^\pm \rightarrow \mu^\pm\nu_\mu$  differential cross sections and the forward-backward ratios in all  $\eta_{\text{CM}}^\mu$  ranges. In the case of the muon charge asymmetry, most of the systematic uncertainties are found to be suppressed due to the correlations in muon charge, and as a result, the statistical uncertainties dominate in most of the  $\eta_{\text{CM}}^\mu$  ranges.

### 3.2.9.10 Covariance matrix

The covariance matrices of the  $W \rightarrow \mu\nu_\mu$  differential cross sections, the forward-backward ratios and the muon charge asymmetry are computed by taking into account the measurements extracted in each  $\eta_{\text{CM}}^\mu$  range. In the case of the  $W^\pm \rightarrow \mu^\pm\nu_\mu$  differential cross sections and the  $W^\pm \rightarrow \mu^\pm\nu_\mu$  forward-backward ratios, the matrices are made of 48x48 entries (24 muon  $\eta_{\text{CM}}^\mu$  ranges times two muon charge measurements), while for the muon charge asymmetry and the charge-summed forward-backward ratio, only 24x24 entries are considered.

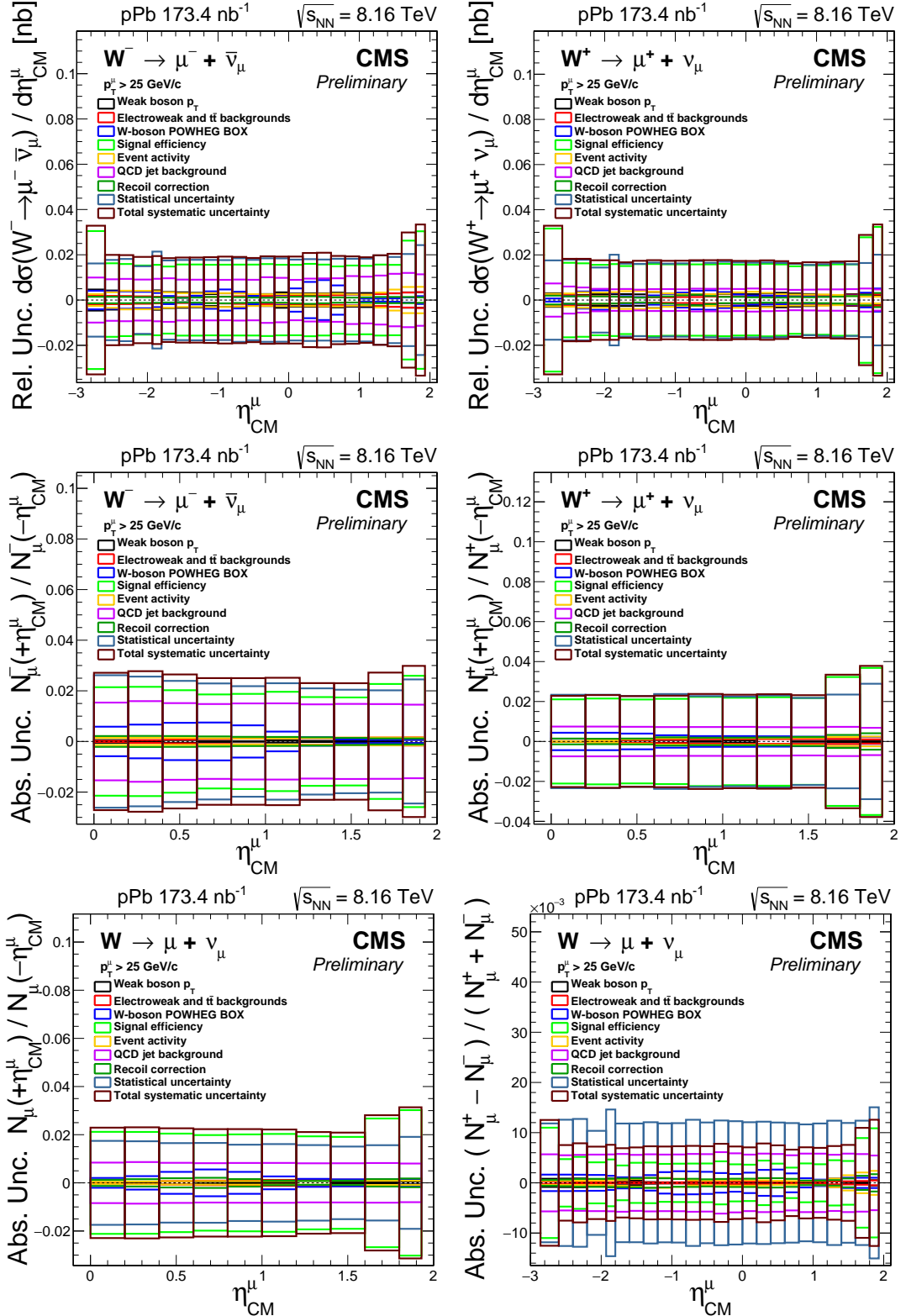


Figure 3.37: Uncertainty corresponding to each category with respect to  $\eta_{\text{CM}}$ . The plots are divided as:  $W^- \rightarrow \mu^- \bar{\nu}_\mu$  (top-left) and  $W^+ \rightarrow \mu^+ \nu_\mu$  (top-right) cross sections,  $W^- \rightarrow \mu^- \bar{\nu}_\mu$  (middle-left) and  $W^+ \rightarrow \mu^+ \nu_\mu$  (middle-right)  $R_{\text{FB}}$ , and the charge-summed  $R_{\text{FB}}$  (bottom-left) and muon charge asymmetry (bottom-right). The uncertainties of the cross sections are relative while for the  $R_{\text{FB}}$  and muon charge asymmetry are absolute. The luminosity uncertainty is not included.

For a given  $(i, j)$  entry of the covariance matrix, the covariance is calculated as the uncertainty in bin  $i$  times the uncertainty in bin  $j$ . If the uncertainty is uncorrelated, the off-diagonal elements are set to zero. The total covariance matrix of each observable is determined by summing the covariance matrix of the statistical uncertainty together with the covariance matrices of all the systematic uncertainties.

The covariance matrix of the statistical uncertainty corresponds to a fully diagonal matrix where each  $(i, i)$  element in the diagonal is the square of the statistical uncertainty of bin  $i$ . On the other hand, the covariance matrix of each systematic uncertainty is computed by taking into account the bin-to-bin correlations in muon charge and pseudorapidity.

The total correlation matrix of each observable is derived from the total covariance matrix, using the following formula:

$$\text{corr}(i, j) = \frac{\text{cov}(i, j)}{\sqrt{\text{cov}(i, i) \times \text{cov}(j, j)}} \quad (3.57)$$

The corresponding correlation matrices are shown in Figure 3.38. The black lines are used to distinguish the different bins in muon charge, which are ordered in a given plot from top to bottom as: Minus-Minus, Minus-Plus, Plus-Minus and Plus-Plus. The large correlation observed in the  $W \rightarrow \mu\nu_\mu$  differential cross sections arises from the luminosity uncertainty. On the other hand, the TnP corrections for muon isolation and identification are applied in wide  $|\eta_{\text{lab}}|$  intervals which justify the anti-correlation observed with respect to  $\eta_{\text{CM}}$  in the muon charge asymmetry.

### 3.3 Results

This section presents the analysis results of the W-boson production in pPb collisions at  $\sqrt{s_{\text{NN}}} = 8.16 \text{ TeV}$ . The W-boson yields are extracted in the muon kinematic region defined by  $p_T^\mu > 25 \text{ GeV}/c$  and  $|\eta_{\text{lab}}^\mu| < 2.4$ . The  $W \rightarrow \mu\nu_\mu$  differential cross sections, the muon charge asymmetry, and the forward-backward ratios are measured as a function of muon  $\eta_{\text{CM}}^\mu$ . The measurements are compared to PDF calculations with and without including nuclear modifications.

#### 3.3.1 W-boson production in p-Pb at 8.16 TeV

The  $W^\pm \rightarrow \mu^\pm \nu_\mu$  differential cross sections are derived using Eq. (3.52). The results of the differential cross sections of  $W^+ \rightarrow \mu^+ \nu_\mu$  and  $W^- \rightarrow \mu^- \bar{\nu}_\mu$  are shown as a function muon

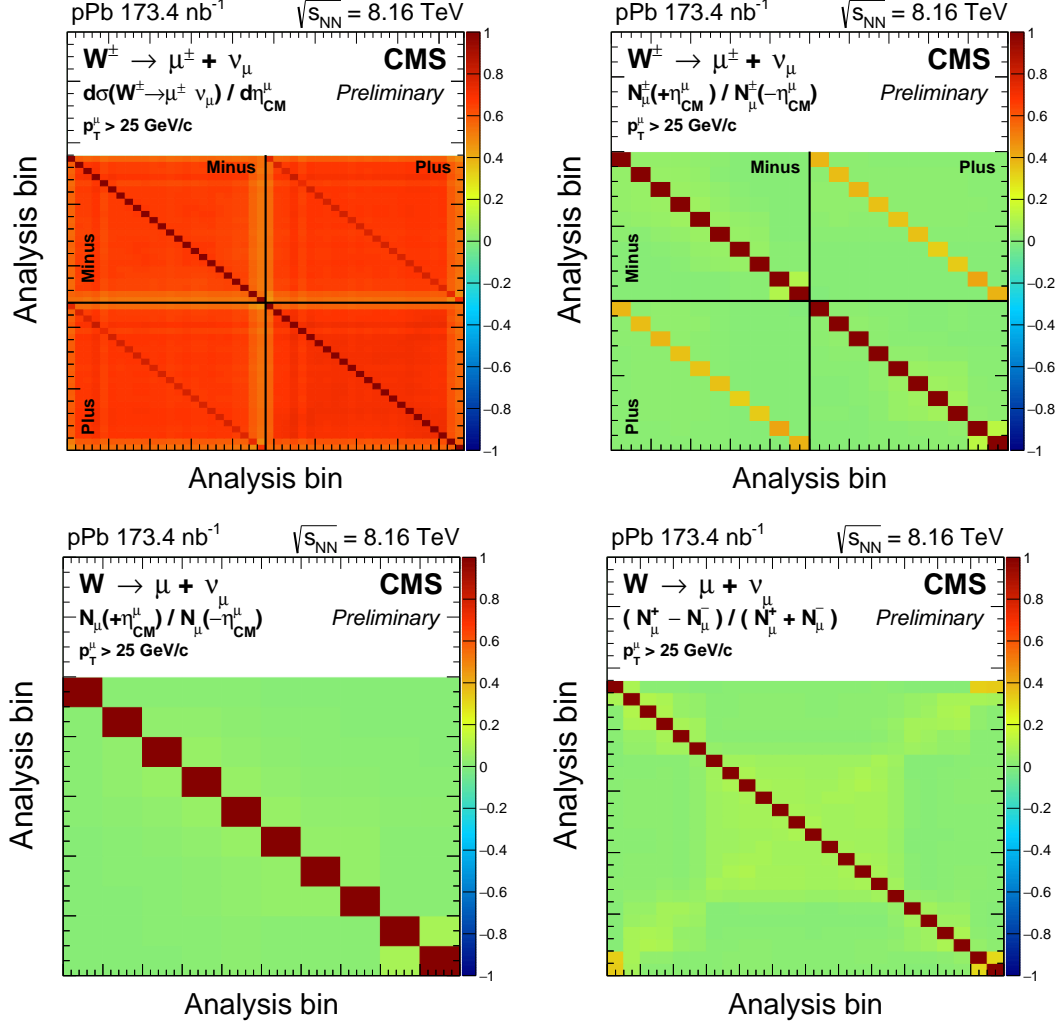


Figure 3.38: Correlation matrices for:  $\text{W}^\pm$  cross section (top-left),  $\text{W}^\pm R_{FB}$  (top-right), charge-inclusive  $R_{FB}$  (bottom-left), and charge asymmetry (bottom-right). The lines in the top plots are used to separate the different muon charge bins.

$\eta_\text{CM}^\mu$  in Figure 3.39. The vertical error bars represent the statistical uncertainties from the number of  $\text{W} \rightarrow \mu\nu_\mu$  events measured in each  $\eta_\text{CM}^\mu$  range, while the brackets show the statistical and total systematic uncertainties summed in quadrature. The global integrated luminosity uncertainty of 3.5% [173] is not shown in the figures.

The opposite trend seen between the  $\text{W}^+ \rightarrow \mu^+\nu_\mu$  and  $\text{W}^- \rightarrow \mu^-\bar{\nu}_\mu$  differential cross sections as a function of  $\eta_\text{CM}^\mu$  is expected from parity violation of the electroweak interaction. The  $\text{W}^+$  bosons decay to a right-handed anti-muon boosted in the opposite direction, while the  $\text{W}^-$  bosons decay to a left-handed muon along the direction of the  $\text{W}^-$  boson.

The muon charge asymmetry is determined from the efficiency-corrected signal event

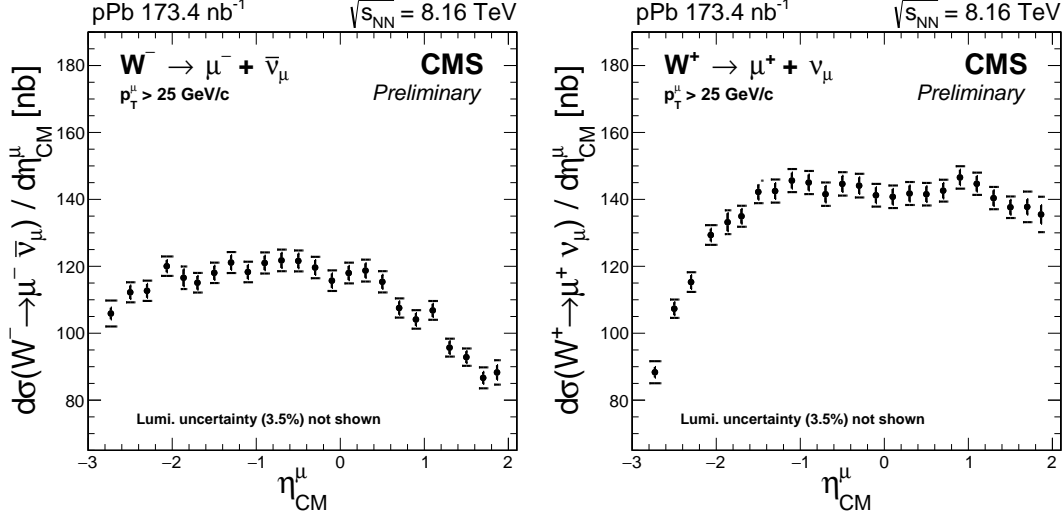


Figure 3.39: Differential production cross sections for  $W^+ \rightarrow \mu^+ \nu_\mu$  (left) and  $W^- \rightarrow \mu^- \bar{\nu}_\mu$  (right), as a function of the muon pseudorapidity in the center-of-mass frame. The brackets represent the statistical and systematic uncertainties summed in quadrature, while the error bars show the statistical uncertainties only. The global luminosity uncertainty of 3.5% [173] is not shown.

yields using Eq. (3.53). The measured muon charge asymmetry is shown in Figure 3.40 as a function muon  $\eta_{CM}^\mu$ .

The  $W^+ \rightarrow \mu^+ \nu_\mu$  and  $W^- \rightarrow \mu^- \bar{\nu}_\mu$  forward-backward ratios are computed using Eq. (3.54), while the charge-summed forward-backward ratio is determined using Eq. (3.55). As mentioned in Section 3.2.1, the forward region ( $\eta_{CM}^\mu > 0$ ) is defined on the proton-going direction while the backward region corresponds to the Pb-going direction. The results of the muon forward-backward ratios are shown in Figure 3.41.

### 3.3.2 Comparison with theoretical models

The measurements of the  $W$ -boson production in p-Pb collisions at 8.16 TeV are compared to three NLO PDF calculations. In all three PDF calculations, the isospin effect is taking into account for the Pb nucleus. A description of each PDF model is provided below:

- CT14: this model assumes no nuclear modifications and uses the NLO CT14 proton PDF for both the incoming proton and Pb-ion.
- CT14+EPPS16: this PDF model employs the CT14 PDF for the incoming proton and apply the EPPS16 nuclear corrections on the CT14 PDF for the incoming Pb-ion.

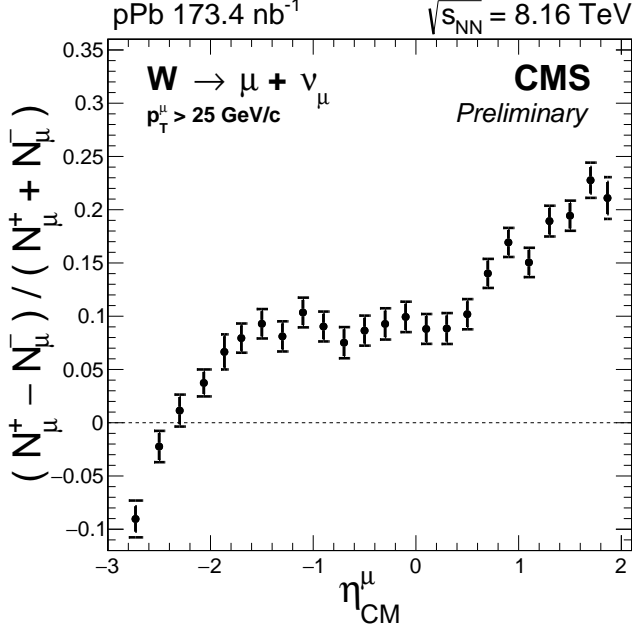


Figure 3.40: Muon charge asymmetry as a function of the muon pseudorapidity in the center-of-mass frame. The brackets represent the statistical and systematic uncertainties summed in quadrature, while the error bars show the statistical uncertainties only.

- CT14+nCTEQ15: this PDF model makes use of the CT14 PDF for the incoming proton and the nCTEQ15 nuclear PDF for the incoming Pb-ion.

The results of the PDF models are derived using the parton-level Monte Carlo program MCFM [193]. The comparison between the PDF calculations and the data are shown in Figure 3.42 for the  $W \rightarrow \mu\nu_\mu$  differential cross sections, in Figure 3.43 for the muon charge asymmetry and in Figure 3.44 for the forward-backward ratios. In all figures, the results of the CT14 PDF model calculations are shown using continuous lines, while the CT14+EPPS16 and CT14+nCTEQ15, are shown with green and brown dashed lines, respectively.

As can be seen in Figure 3.42, the  $W \rightarrow \mu\nu_\mu$  cross section measurements at forward rapidity favour the PDF calculations including nuclear modifications, while at backward rapidity all three PDF calculations are in good agreement with the data. Moreover, in the case of the muon charge asymmetry shown in Figure 3.43, the results of the theory calculations derived using the CT14 proton PDF only, and those including the EPPS16 nuclear modifications, are in good agreement with the measurements, while the nCTEQ15 nPDF calculations expect a slightly larger muon charge asymmetry in the most backward  $\eta_\text{CM}^\mu$  range. Finally, from the ratios of the signal event yields at forward-

### 3.3. RESULTS

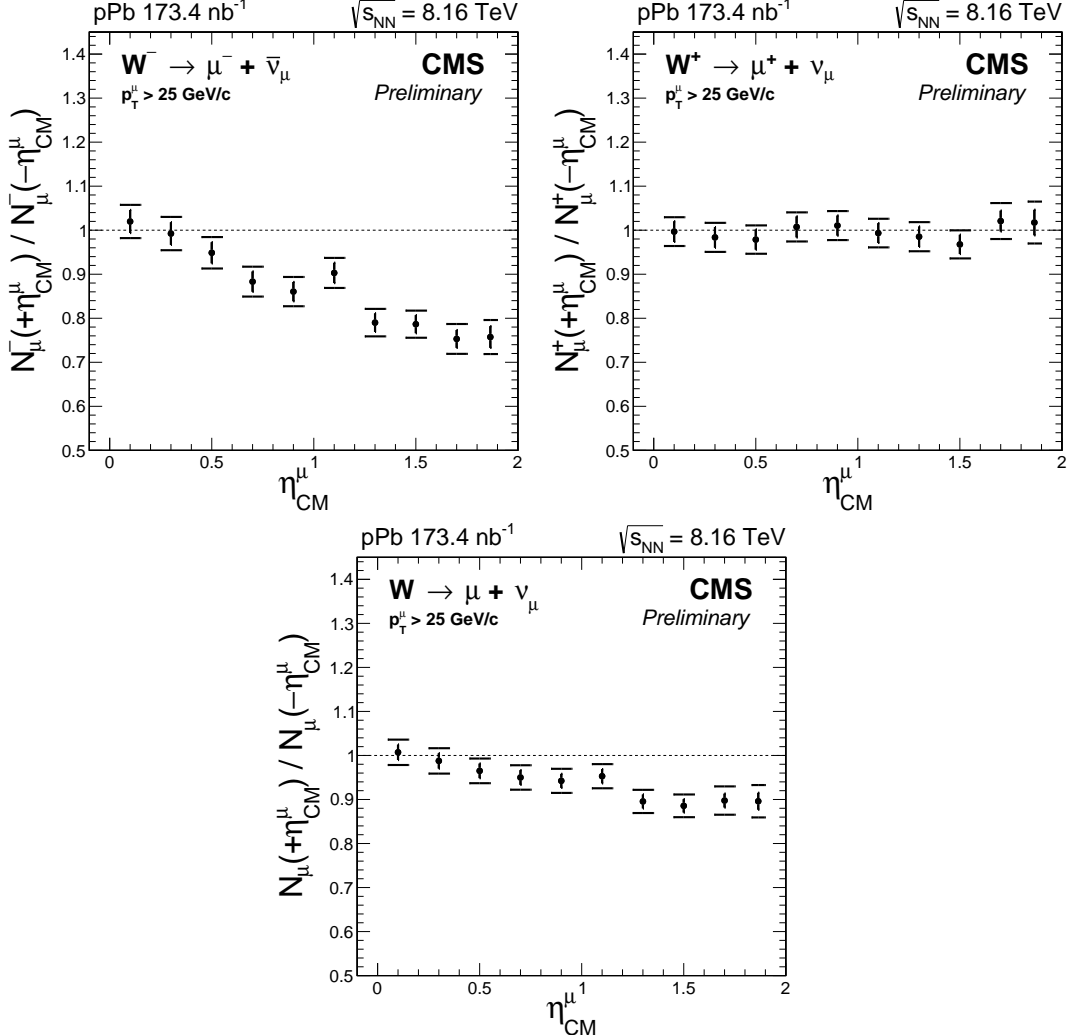


Figure 3.41: Forward-backward ratios, for the positive (top-left), negative (top-right) and all (bottom) charged muons. The brackets represent the statistical and systematic uncertainties summed in quadrature, while the error bars show the statistical uncertainties only.

over-backward  $\eta_{\text{CM}}^{\mu}$  displayed in Figure 3.44, the nuclear PDF calculations describe much better the data compared to the free-nucleon PDF calculation.

In order to quantify the level of agreement between each PDF calculation and the measurements of the W-boson production in p-Pb collisions, a  $\chi^2$  test is performed according to:

$$\chi^2 = \sum_i \sum_j \left[ (t(i) - d(i)) \cdot (\text{COV}_{\text{data}} + \text{COV}_{\text{theory}})^{-1} [i, j] \cdot (t(j) - d(j)) \right] \quad (3.58)$$

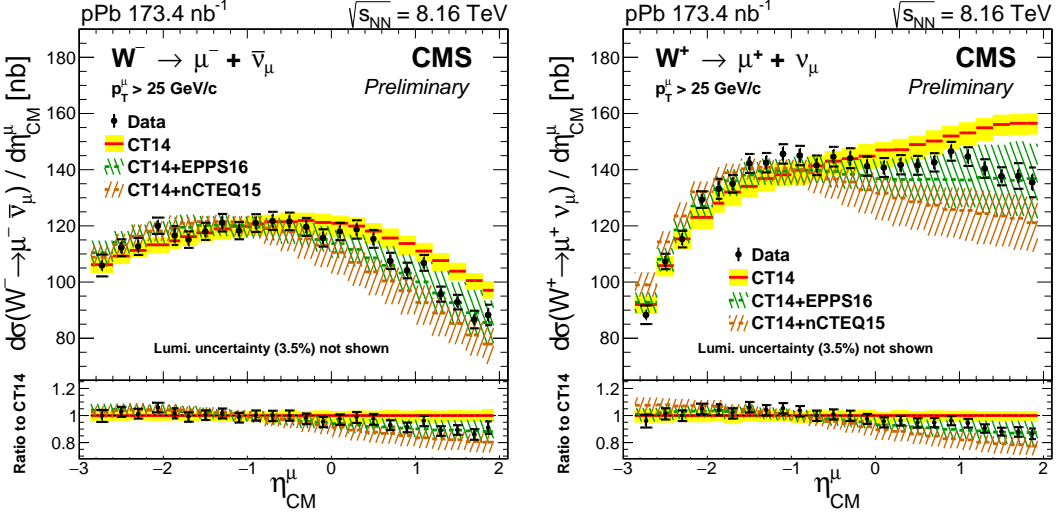


Figure 3.42: Differential cross sections for  $W^+ \rightarrow \mu^+ \nu_\mu$  (left) and  $W^- \rightarrow \mu^- \bar{\nu}_\mu$  (right), as a function of the muon  $\eta_{CM}^\mu$ . Errors bars represent the statistical uncertainties, while the brackets represent the statistical and systematic uncertainties summed in quadrature. The global luminosity uncertainty of 3.5% is not displayed. Theoretical predictions with (CT14+EPPS16 shown in dashed green line and CT14+nCTEQ15 shown in dashed brown line) and without (CT14, solid red line) PDF nuclear modifications are also shown, with the uncertainty bands. All theory uncertainty bands include the PDF uncertainties.

where  $t(i)$  is the value of the observable derived from the PDF calculation in bin  $i$ ,  $d(j)$  is the value of the observable measured in data in bin  $j$ , and  $(\text{COV}_{\text{data}} + \text{COV}_{\text{theory}})^{-1}$  is the inverse of the sum of the covariance matrices extracted from the data and PDF calculations. This approach takes into account the bin-to-bin correlations in both muon charge and pseudorapidity.

The outcome of the  $\chi^2$  statistical test derived using the CT14 PDF, CT14+EPPS16 nPDF and CT14+nCTEQ15 nPDF calculations are summarized in Table 3.13. The results of the CT14 PDF calculations are significantly disfavoured by the measurements, while the PDF calculations including nuclear modifications are in good agreement. In addition, the measurements tend to favour the nPDF calculations of the CT14+EPPS16 model over the ones from the CT14+nCTEQ15 model.

Considering the smaller size of the uncertainties of the measurements compared to those from the PDF models, the measurements have the potential to constrain the parametrisations of the EPPS16 nuclear modifications and the nCTEQ15 nuclear PDFs.

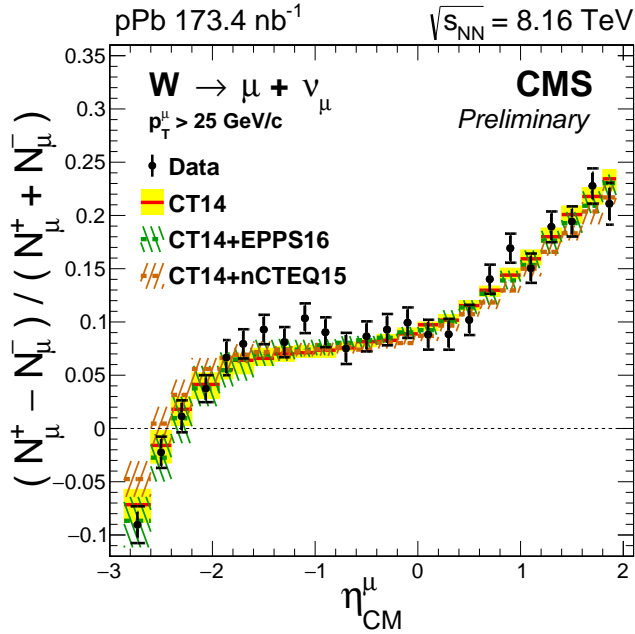


Figure 3.43: Muon charge asymmetry of  $W \rightarrow \mu\nu_\mu$ , given for each muon  $\eta_{CM}^\mu$  range. Errors bars represent the statistical uncertainties, while the brackets represent the statistical and systematic uncertainties summed in quadrature. Theoretical predictions with (CT14+EPPS16 shown in dashed green line and CT14+nCTEQ15 shown in dashed brown line) and without (CT14, solid red line) PDF nuclear modifications are also shown, with the uncertainty bands. All theory uncertainty bands include the PDF uncertainties.

Observable	CT14			CT14+EPPS16			CT14+nCTEQ15		
	$\chi^2$	ndf	Prob.(%)	$\chi^2$	ndf	Prob.(%)	$\chi^2$	ndf	Prob.(%)
$d\sigma(W^\pm \rightarrow \mu^\pm \nu_\mu) / d\eta_{CM}^\mu$	135	48	$3 \times 10^{-8}$	32	48	96	40	48	79
$(N_\mu^+ - N_\mu^-) / (N_\mu^+ + N_\mu^-)$	23	24	54	18	24	80	29	24	23
$N_\mu^\pm (+\eta_{CM}^\mu) / N_\mu^\pm (-\eta_{CM}^\mu)$	98	20	$3 \times 10^{-10}$	11	20	95	14	20	83
$N_\mu (+\eta_{CM}^\mu) / N_\mu (-\eta_{CM}^\mu)$	87	10	$2 \times 10^{-12}$	3	10	99	5	10	90

Table 3.13: Results of the  $\chi^2$  statistical test between the measurements and the theory calculations from the CT14 PDF, CT14+EPPS16 nPDF and CT14+nCTEQ15 nPDF models. The value of the  $\chi^2$ , the number of degrees of freedom (ndf) and the  $\chi^2$  probability (Prob.), are presented for the  $W^\pm \rightarrow \mu^\pm \nu_\mu$  differential cross sections, the muon charge asymmetry, the  $W^\pm \rightarrow \mu^\pm \nu_\mu$  forward-backward ratios, and the charge-summed forward-backward ratio, respectively.

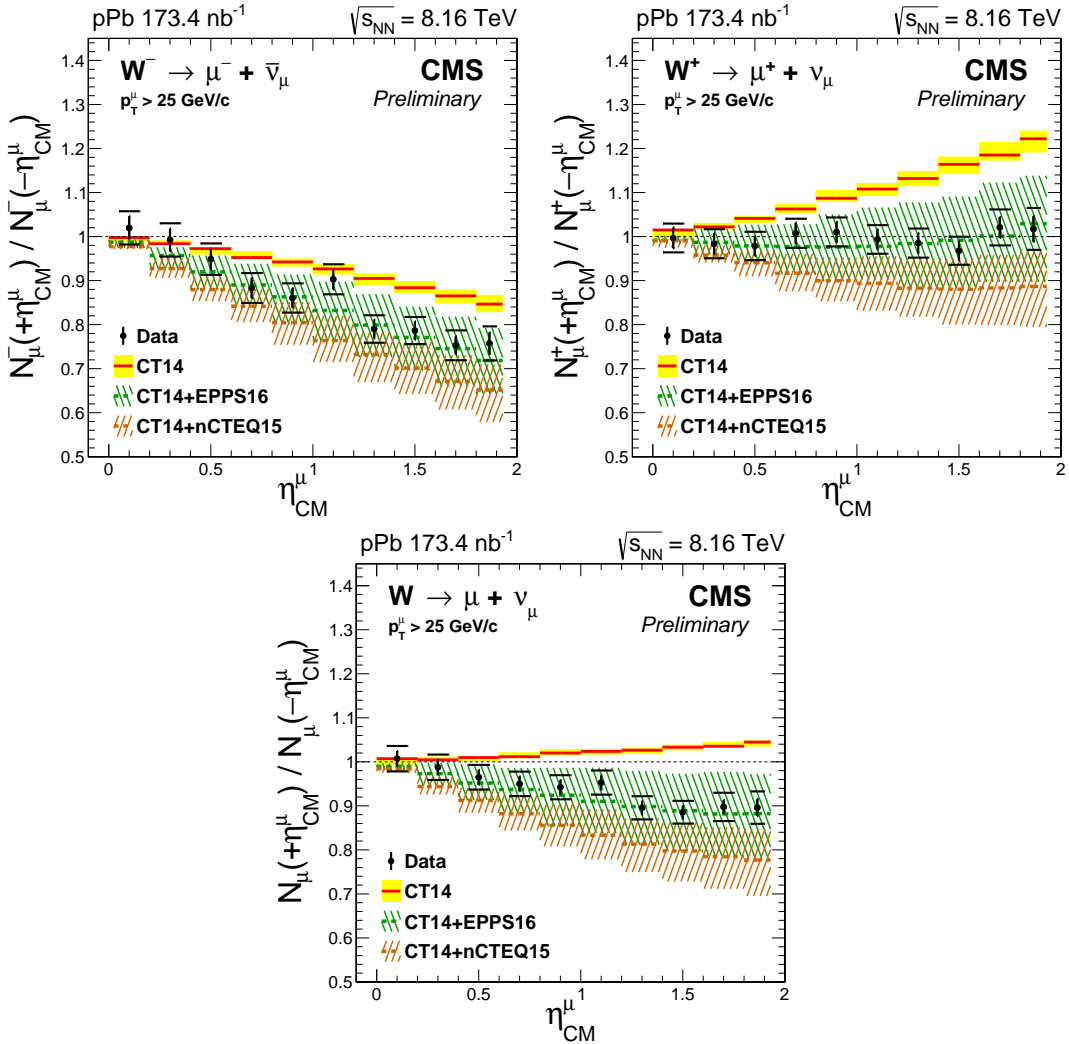


Figure 3.44: Forward-backward ratio of  $W \rightarrow \mu\nu_\mu$ , given for each muon  $\eta_{CM}^\mu$  range separated in negative (top-left), positive (top-right) and all (bottom) charged muons. Errors bars represent the statistical uncertainties, while the brackets represent the statistical and systematic uncertainties summed in quadrature. Theoretical predictions with (CT14+EPPS16 shown in dashed green line and CT14+nCTEQ15 shown in dashed brown line) and without (CT14, solid red line) PDF nuclear modifications are also shown, with the uncertainty bands include the PDF uncertainties.

## CHARMONIUM PRODUCTION IN LEAD-LEAD COLLISIONS

This chapter reports the measurement of the production of  $J/\psi$  and  $\psi(2S)$  mesons in lead-lead (Pb-Pb) collisions compared to p-p collisions at  $\sqrt{s_{\text{NN}}} = 5.02 \text{ TeV}$ . The physics of charmonia in heavy-ion collisions is briefly introduced in Section 4.1. The  $J/\psi$  and  $\psi(2S)$  meson analyses are then described in detail in Section 4.2. Section 4.3 presents the results of the prompt and nonprompt  $J/\psi$ -meson production, and the nuclear modification of prompt  $\psi(2S)$  mesons relative to  $J/\psi$  mesons.

### 4.1 Introduction

This section provides an introduction to the physics of charmonia in hadronic and heavy-ion collisions. The basic properties of charmonium states are detailed in Section 4.1.1, followed by a brief description of different models of charmonium hadroproduction in Section 4.1.2. A short overview of some nuclear matter effects that can impact the measurement of charmonium production in heavy-ion collisions is presented in Section 4.1.3, as well as the current understanding of their role in the past measurements.

#### 4.1.1 Spectrum of charmonium states

Charmonia are bound states of a charm quark and anti-quark. They are part of the family of quarkonium mesons, briefly introduced in Section 1.2.4.4. The first observation of a charmonium state was published in 1974, by the collaborations lead by Burton Richter

at SLAC [134] and Sam Ting at BNL [133]. Both experiments found a narrow resonance in the  $e^+e^-$  and  $\mu^+\mu^-$  decay channels with an invariant mass of  $m \approx 3.1$  GeV/ $c^2$ , which was named J by Sam Ting and  $\psi$  by Burton Richter, thus later referred as the  $J/\psi$  meson.

Following a non-relativistic approach, by solving the Schrödinger equation using a  $c\bar{c}$  potential model as mentioned in Section 1.2.4.4, the charmonium states can be classified according to the total spin  $S$ , orbital angular momentum  $L$  and total angular momentum  $J$  of the  $c\bar{c}$  system. Depending on the spin of the  $c\bar{c}$  pair, charmonia can either be singlet ( $S = 0$ ) or triplet ( $S = 1$ ). The charmonium states are typically labelled using the notation  $n^{2S+1}L_J$ , where  $n$  is the principal quantum number. By convention, the charmonium states with values  $L = 0, 1, 2, \dots$  are denoted as S, P, D .... In this notation, the  $J/\psi$  meson ( $n = 1, S = 1, J = 1$ ) represents the S-wave ground state  $1^3S_1$ , while the  $\psi(2S)$  meson ( $n = 2, S = 1, J = 1$ ) corresponds to its first excited state  $2^3S_1$ . The mass of charmonium states increases with  $n$ , being larger for higher excited states. Table 4.1 summarises the mass and width of some charmonium states.

Charmonium state	$n^{2S+1}L_J$	Width [ MeV/ $c^2$ ]	Mass [ MeV/ $c^2$ ]
$\eta_c(1S)$	$1^1S_0$	$32.1 \pm 0.9$	$2983.9 \pm 0.5$
$J/\psi$	$1^3S_1$	$0.0929 \pm 0.0028$	$3096.900 \pm 0.006$
$h_c$	$1^1P_1$	$0.70 \pm 0.36$	$3525.38 \pm 0.11$
$\chi_{c0}$	$1^3P_0$	$10.5 \pm 0.8$	$3414.71 \pm 0.30$
$\chi_{c1}$	$1^3P_1$	$0.88 \pm 0.05$	$3510.67 \pm 0.05$
$\chi_{c2}$	$1^3P_2$	$2.00 \pm 0.11$	$3556.17 \pm 0.07$
$\eta_c(2S)$	$2^1S_0$	$11.3^{+3.2}_{-2.9}$	$3637.6 \pm 1.2$
$\psi(2S)$	$2^3S_1$	$0.294 \pm 0.008$	$3686.097 \pm 0.010$

Table 4.1: The width and mass of charmonium states below the  $D\bar{D}$ -meson pair mass. Information taken from Ref. [21].

The branching ratios for charmonium decays depend on the mass of the bound state. On the one hand, charmonium states with masses above two times the D-meson mass ( $m_D$ ), that is 3.73 GeV/ $c^2$ , preferentially decays to open-charm hadrons (i.e. with non-zero charm quantum numbers, such as D mesons or charmed baryons), favoured by the Okuba-Zweig-Iizuka (OZI) rule [195, 196, 197]. On the other hand, charmonium states with masses below  $2m_D$ , decays radiatively (e.g.  $\chi_c \rightarrow J/\psi + \gamma$ ) or hadronically (e.g.  $\psi(2S) \rightarrow J/\psi + 2\pi$ ) to lower mass charmonium states or light hadrons, and also electromagnetically to lepton pairs. As a result, charmonium states below the  $D\bar{D}$  threshold appear as mass peaks in the dilepton invariant mass distribution, while those above do not. The different charmonium decays to lower mass charmonia are shown in Figure 4.1 and the main

branching ratios for decays of  $J/\psi$  and  $\psi(2S)$  mesons are presented in Table 4.2.

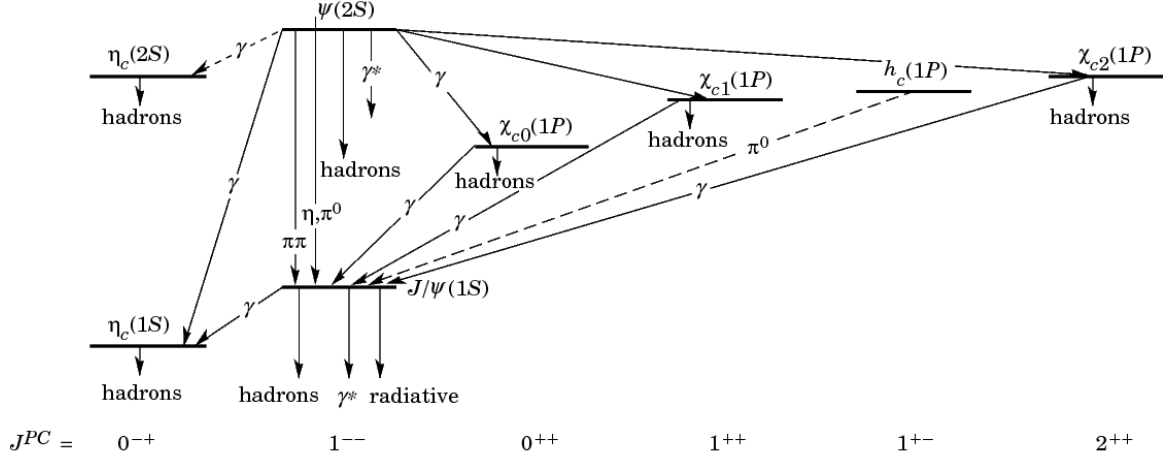


Figure 4.1: Illustration of the different charmonium decays to lower mass charmonium states. The dashed (solid) lines represent radiative (hadronic) decays. Figure taken from Ref. [198].

Charmonium	Branching ratio [%]		
	$\mu^+ \mu^-$	$e^+ e^-$	hadrons
$J/\psi$	$5.961 \pm 0.033$	$5.971 \pm 0.032$	$87.7 \pm 0.5$
$\psi(2S)$	$0.80 \pm 0.06$	$0.793 \pm 0.017$	$97.86 \pm 0.13$

Table 4.2: Branching ratios for decays of  $J/\psi$  and  $\psi(2S)$  mesons. Information taken from Ref. [21].

### 4.1.2 Hadroproduction of charmonia

Charmonia can be produced from various sources including: the initial hard scattering (direct), decays of higher mass charmonium states (feed-down), or weak decays of hadrons containing bottom quarks. Directly produced charmonium states or those from feed-down contributions are known as *prompt*, while charmonium states from b-hadron decays are called *nonprompt*. A brief introduction to some of the models used to describe the production of charmonia in hadron collisions are presented in the following sub-sections.

#### 4.1.2.1 Colour singlet model

The Colour Singlet Model (CSM) was first proposed in 1975 by Martin Einhorn and Stephen Ellis [199, 200], to describe the hadroproduction of  $\eta_c$  mesons. It assumes that

the quantum numbers of the  $c\bar{c}$  pairs do not change between their production and subsequent hadronisation into charmonia. As a consequence, the  $c\bar{c}$  pair has the same angular momentum, spin and colour charge as the charmonium state it eventually forms and since all hadrons are colour singlets, the CSM requires the  $c\bar{c}$  pair to be produced in a colour singlet state. The model also considers charmonia as non-relativistic bound states, neglecting the relative momentum of the charm quarks inside the charmonium [201]. Under these conditions, the probability that a colour-singlet  $c\bar{c}$  pair becomes a charmonium state is proportional to the square of the  $c\bar{c}$  wave function and its derivatives, evaluated at the origin in position space. The inclusive cross section of the production of a S-wave charmonium state  $\Psi$  in collisions of hadrons  $h_A$  and  $h_B$ , is given in the CSM by [202]:

$$\sigma^{\text{CSM}}[h_A h_B \rightarrow \Psi + X] = \sigma[h_A h_B \rightarrow c\bar{c}_{[1]} + X] \cdot |\psi_{c\bar{c}}(0)|^2 \quad (4.1)$$

where  $\sigma[h_A h_B \rightarrow c\bar{c}_{[1]} + X]$  is the hadroproduction cross section of a colour-singlet  $c\bar{c}$  pair, and  $\psi_{c\bar{c}}$  is the corresponding  $c\bar{c}$  wave function. The main advantage of the CSM is that it becomes fully predictive once the magnitudes of the  $c\bar{c}$  wave functions are fixed, since it does not contain any other free parameters. The  $|\psi_{c\bar{c}}(0)|^2$  can be determined from experimental measurements of charmonium decay widths or using potential models of the  $c\bar{c}$  system [203].

The CSM has been able to describe the bulk production of charmonia at RHIC [204], but it significantly underestimates the  $p_T$ -differential cross section of prompt charmonia measured in  $p\bar{p}$  collisions at Tevatron [205]. Moreover, the model suffers from infrared divergences when extending the calculations to charmonium states with nonzero orbital angular momentum (e.g.  $\chi_c$  meson) [206]. However, the inclusion of NLO and NNLO corrections in  $\alpha_s$  improves the agreement with the experimental results [203].

#### 4.1.2.2 Colour evaporation model

The Colour Evaporation Model (CEM) is an alternative model of charmonium production, introduced by Harald Fritz [207] and Francis Halzen [208] in 1977. Contrary to the CSM, the CEM allows the quantum states of the  $c\bar{c}$  pair to change during its evolution. In the CEM, a charmonium state can be produced from any  $c\bar{c}$  pair with an invariant mass between the threshold to create a charm-quark pair  $2m_c$  and the one to produce the lightest pair of open-charm hadrons  $2m_D$  (i.e. D-meson pair). The CEM does not impose any constraints on the colour charge of the  $c\bar{c}$  pair in order to form a charmonium state, and instead assumes that the colour state of the  $c\bar{c}$  pair is neutralised via soft gluon interactions with the collision-induced medium after its production (this process

is called colour evaporation). In addition, the interaction with the medium is assumed to randomise the spin and angular-momentum states of the  $c\bar{c}$  pairs, making the CEM insensitive to the polarization of charmonia. The probability that  $c\bar{c}$  pairs, with an invariant mass below  $2m_D$ , hadronise into a charmonium state is represented by a fraction  $F_\psi$ , which is assumed to be constant and universal (i.e. does not depend on the  $c\bar{c}$  kinematics or the hard process) [206]. In the CEM, the hadronic cross section for the production of a charmonium state  $\psi$  is defined as:

$$\sigma^{\text{CEM}}[h_A h_B \rightarrow \psi + X] = F_\psi \int_{2m_c}^{2m_D} dm_{c\bar{c}} \frac{d\sigma[h_A h_B \rightarrow c\bar{c} + X]}{dm_{c\bar{c}}} \quad (4.2)$$

where  $m_{c\bar{c}}$  is the invariant mass of the  $c\bar{c}$  pair, and  $\sigma[h_A h_B \rightarrow c\bar{c} + X]$  is the hadronic cross section of the production of  $c\bar{c}$  pairs, averaged over all spin, angular-momentum and colour-charge states. The only free parameters of the CEM are the fractions  $F_\psi$ , which are constrained with experimental data. The description of the  $p_T$  distribution of charmonia requires to consider contributions from at least NLO, which includes  $c\bar{c}$ -pair production associated with gluons or light (anti-)quarks [209].

The CEM has been successful at describing the overall hadronic production of charmonium states [210], but it fails to explain the differences observed between the hadroproduction and photoproduction measurements [206], and the relative production rates between the  $\chi_{c1}$  and  $\chi_{c2}$  states measured at Tevatron [211] and LHC [212]. Recent developments have lead to an improved version of the CEM [213], which attempts to describe the  $p_T$ -dependence of charmonium polarization by sorting the states based on their spin.

#### 4.1.2.3 Nonrelativistic QCD

NonRelativistic QCD (NRQCD) is an effective quantum field theory formulated in 1992 by Geoffrey Bodwin, Eric Braaten and Peter Lepage [214], in an attempt to cure the infrared divergences present in the CSM calculations of P-wave charmonium states. The production and decay of charmonia involves large momentum scales, such as the charm-quark mass ( $m_c = 1.29 \text{ GeV}/c^2$ ) or the parton momentum scales during the hard scattering, which are much larger than  $\Lambda_{\text{QCD}} \approx 255 \text{ MeV}$ . As a result, the  $\alpha_s$  value associated to the formation of  $c\bar{c}$  pairs are small enough ( $\alpha_s(m_c) \approx 0.25$ ) for perturbation theory to be applied. However, the hadronisation of  $c\bar{c}$  pairs to charmonium states involves low-momentum processes which are inherently nonperturbative [206].

The NRQCD formalism makes use of perturbative calculation techniques by separating the high-momentum (short-distance) perturbative effects ( $c\bar{c}$ -pair production) from

the low-momentum (long-distance) nonperturbative effects (charmonium formation), in a process called factorisation. The NRQCD factorisation approach matches the derivations from full QCD at momentum scales less than  $m_c v_c$ , where  $v_c$  is the mean velocity of bound charm quarks in the charmonium CM frame. Since  $v_c$  is low for charmonia ( $v_c^2 \approx 0.3$ ), the NRQCD calculations are simplified by applying nonrelativistic approximations [206]. The inclusive cross section for the production of a charmonium state  $\psi$  with  $p_T \geq m_c$ , from collisions of hadrons  $h_A$  and  $h_B$ , is determined in NRQCD by:

$$\sigma^{\text{NRQCD}} [h_A h_B \rightarrow \psi + X] = \sum_n \sigma [h_A h_B \rightarrow c\bar{c}_{[n]} + X] (\mu_\Lambda) \cdot \langle \mathcal{O}_n^\psi \rangle \quad (4.3)$$

where  $\mu_\Lambda$  is an ultraviolet cutoff parameter. The nonperturbative coefficient  $\langle \mathcal{O}_n^\psi \rangle$ , called Long-Distance Matrix Element (LDME), is the vacuum expectation value of the NRQCD four-fermion operator  $\mathcal{O}_n^\psi$  and defines the probability for a  $c\bar{c}$  pair in a given quantum state  $n$  to evolve into a charmonium state  $\psi$ . The LDMEs contain the nonperturbative components related to the hadronisation of the  $c\bar{c}$  pairs into charmonia. These matrix elements are process independent and can be constrained by fitting experimental data [206]. Moreover, the perturbative coefficient  $\sigma [h_A h_B \rightarrow c\bar{c}_{[n]} + X]$  represents the hadronic cross section for the production of  $c\bar{c}$  pairs in a quantum state  $n$  and can be computed using pQCD. One important remark of NRQCD is that the  $c\bar{c}$  pairs are not required to be produced with the same spin, angular momentum and colour charge as the charmonium states that they eventually hadronise to. As a consequence, the  $c\bar{c}$  pairs can either be produced in a colour-singlet or colour-octet state [206]. Examples of Feynman diagrams involved in the production of  $J/\psi$  mesons from colour-singlet or colour-octet  $c\bar{c}$  pairs are shown in Figure 4.2.

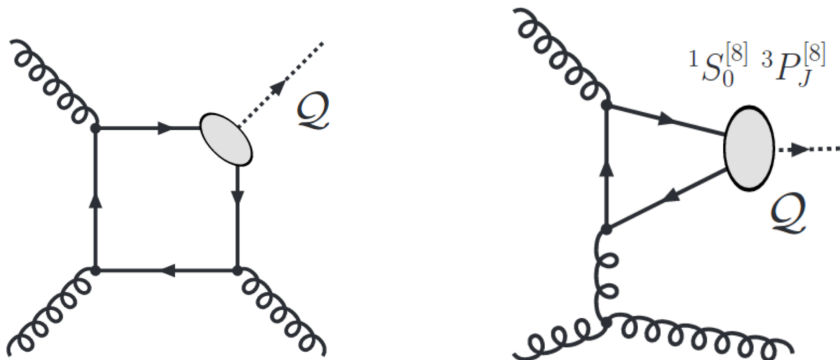


Figure 4.2: Illustration of a colour-singlet (left) and colour-octet (right) Feynman diagram, at leading order ( $\alpha_s^3$ ), that contribute to the production of quarkonium states. Diagrams taken from Ref. [215].

In practice, the sum over the quantum states shown in Eq. (4.3) is expanded in terms of  $v_c$  and  $\alpha_s$ . The infinite number of independent matrix elements is then reduced to a finite set of LDMEs by truncating the sum up to a given order in  $v_c$  and making use of spin symmetry relations between charmonium states. At leading order in  $v_c$ , the S-wave charmonium multiplets (e.g.  $J/\psi$  and  $\eta_c$ ) are described by four LDMEs (one colour singlet and three colour octets) [206], and the CSM can then be recovered by keeping only the colour-singlet term.

NRQCD has been very successful at describing the hadroproduction yield of charmonia at Tevatron, RHIC and LHC [216, 217, 218, 219]. However, it fails to describe the  $J/\psi$ -meson polarization results in hadronic collisions at the Tevatron [220] and LHC [221]. In addition, recent measurements of prompt  $J/\psi$  mesons in jets produced in p-p collisions at  $\sqrt{s} = 5.02 \text{ TeV}$  [222, 223], have shown significant deviations from the NRQCD calculations derived with the PYTHIA event generator.

#### 4.1.2.4 Charmonium production from b-hadron decays

The decay of b hadrons constitute an important contribution to the production of charmonia. Bottom quarks are copiously produced at the LHC, mainly through the gluon fusion process ( $g + g \rightarrow b + \bar{b} + X$ ). They hadronise to B mesons and b baryons (e.g.  $\Lambda_b$  and  $\Sigma_b$  baryons), which can then decay weakly into charmonia as shown in Figure 4.3. The branching ratios for inclusive decays of b hadrons ( $h_b$ ) into charmonia,  $BR(h_b \rightarrow \psi + X)$ , have been determined by combining the measurements of b baryons and B mesons, performed at LHC, LEP, Tevatron and Sp $\bar{p}$ S, and are listed in Table 4.3.

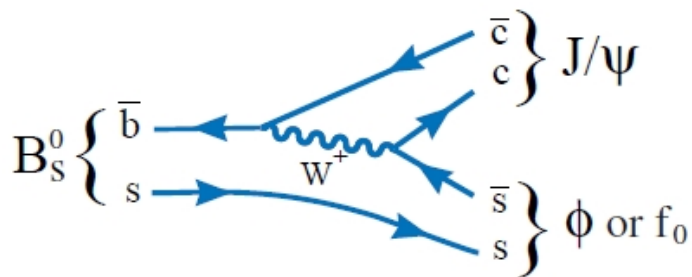


Figure 4.3: Feynman diagram of a  $B_s^0$  decay to  $J/\psi$  meson. Diagram taken from Ref. [224].

The inclusive cross section of charmonium production from b-hadron decays in p-p collisions is described by:

Charmonium state	Branching ratio [%]
$\eta_c(1S)$	$4.5 \pm 1.9$
$J/\psi$	$1.16 \pm 0.10$
$\chi_{c0}$	$1.5 \pm 0.6$
$\chi_{c1}$	$1.4 \pm 0.4$
$\chi_{c2}$	$0.62 \pm 0.29$
$\psi(2S)$	$0.286 \pm 0.028$

Table 4.3: Branching ratios for inclusive charmonium decays of b-hadron mixtures ( $B^\pm/B^0/B_s^0$ /b-baryon) determined from measurements at LHC, LEP, Tevatron and SppS. Information taken from Ref. [21].

$$\sigma [pp \rightarrow b + X \rightarrow \psi + X'] = \sum_{j=b \text{ hadrons}} \sigma [pp \rightarrow b + X] \otimes D(b \rightarrow h_b^j) \cdot BR(h_b^j \rightarrow \psi + X) \quad (4.4)$$

where  $\sigma[pp \rightarrow b + X]$  is the total production cross section of bottom quarks in p-p collisions and  $D(b \rightarrow h_b^j)$  is a fragmentation function (FF), which describes the probability that a bottom quark hadronises into a b hadron  $h_b^j$  with a fraction  $z$  of its momentum ( $p_{h_b} = z \cdot p_b$ ). The FFs are considered universal and can be extracted by fitting experimental data. The bottom-quark fragmentation fractions for different b hadrons have been measured at LEP and Tevatron, and the results are shown in Table 4.4.

b hadron	Fragmentation fraction [%]	
	$Z \rightarrow b\bar{b}$	$p\bar{p} \rightarrow b\bar{b} + X$
$B^+$	$41.5 \pm 0.8$	$32.4 \pm 2.1$
$B^0$	$41.5 \pm 0.8$	$32.4 \pm 2.1$
$B_s^0$	$8.8 \pm 1.3$	$10.1 \pm 1.5$
b baryons	$8.9 \pm 1.2$	$21.8 \pm 4.7$

Table 4.4: Fragmentation fractions of bottom quarks into b hadrons measured at Tevatron in  $p\bar{p}$  collisions at  $\sqrt{s} = 1.96$  TeV and at LEP in  $Z \rightarrow b\bar{b}$  decays. Information taken from Ref. [21].

### 4.1.3 Charmonia in heavy-ion collisions

The observed yields of charmonia are modified in heavy-ion collisions by an interplay of different effects that can take place in the initial or final state of the collision. The effects that originate from the nuclear environment are often called cold nuclear matter (CNM) effects, while those that are caused by the hot and dense medium formed in the collision, the QGP, are known as hot nuclear matter (HNM) effects.

### 4.1.3.1 Cold nuclear matter effects

Understanding the impact of the cold nuclear matter effects is crucial to be able to characterise the hot medium produced in heavy-ion collisions. The charmonium production can be affected by several CNM effects, such as nuclear absorption, gluon shadowing, energy loss and Cronin effect.

**Nuclear absorption.** After the  $c\bar{c}$  pairs are formed, they will then travel across the nucleus. While crossing the nuclear medium, the  $c\bar{c}$  pair may scatter with the target nucleons. After successive interactions, the  $c\bar{c}$  pair can end up breaking up and the charm quarks then hadronise into open-charm mesons. This process is known as nuclear absorption. The probability that the  $c\bar{c}$  pair survives the nuclear interactions is determined using a Glauber model approach, given by [202]:

$$S_{\text{abs}} = \int d^2 b \int dz \cdot \rho_A(b, z) \cdot \exp \left[ - \int_z^{\text{inf}} dz' \cdot \rho_A(b, z') \cdot \sigma_{\text{abs}}(z' - z) \right] \quad (4.5)$$

where  $b$  is the impact parameter of the collision,  $\rho_A$  is the density profile of the nucleus,  $z$  is the position of the  $c\bar{c}$  pair production vertex along the beam direction, and  $\sigma_{\text{abs}}$  is an effective cross section used to characterise the nuclear absorption.

To determine the impact of the nuclear absorption on the production of charmonia, it is useful to compare the collision time ( $\tau_{\text{coll}}$ ) to the typical time needed to form a charmonium state ( $\tau_\psi$ ). The collision time is defined as the time it takes for two Lorentz-contracted nuclei to cross, given by  $\tau_{\text{coll}} = 2R/\gamma_{\text{CM}}$  [225], where  $\gamma_{\text{CM}} = \sqrt{s_{\text{NN}}}/m_p$  is the beam Lorentz  $\gamma$  factor in the CM frame,  $m_p = 938$  MeV/c<sup>2</sup> is the proton mass and  $R$  is the radius of the nuclei ( $\approx 6.62$  fm for a Pb nucleus [226]). Considering Pb-Pb collisions at  $\sqrt{s_{\text{NN}}} = 5.02$  TeV, the collision time is less than 0.003 fm/c which is much smaller than the formation time of charmonia ( $\tau_\psi \sim 0.4$  fm/c) [202]. As a consequence, the charmonium suppression due to nuclear absorption is expected to be negligible at the LHC.

**Gluon shadowing.** At the LHC, the dominant production mode of  $c\bar{c}$  pairs is the gluon fusion process ( $g + g \rightarrow \psi + X$ ), due to the large amount of gluons produced at high energies. As a result, the charmonium production is sensitive to the nuclear modifications of the gluon PDFs in heavy-ion collisions. The momentum fraction  $x$  of the two colliding partons, involved in the hard scattering, depends at leading order on the charmonium mass  $m_\psi$ , the energy per nucleon  $\sqrt{s_{\text{NN}}}$  and the charmonium rapidity  $y$ , according to  $x = m_\psi \cdot e^{\pm y} / \sqrt{s_{\text{NN}}}$ . In Pb-Pb collisions at  $\sqrt{s_{\text{NN}}} = 5.02$  TeV, the  $x$ -range probed by the production of charmonia in the CMS rapidity coverage ( $|y| < 2.4$ ) is  $x < 10^{-2}$ , which

corresponds to the shadowing region as illustrated in Figure 3.6. The EPPS16 and nCTEQ15 nuclear modifications of the gluon PDFs, evaluated at  $Q = 3.16\text{GeV}$ , are shown in Figure 4.4. The central value points to a depletion of the gluon nuclear PDFs of the order of 20% at  $x < 10^{-2}$ , which should lead to a suppression of the charmonium production. However, the nuclear PDFs are currently not constrained enough to provide precise calculations of the impact of gluon shadowing at low  $x$ .

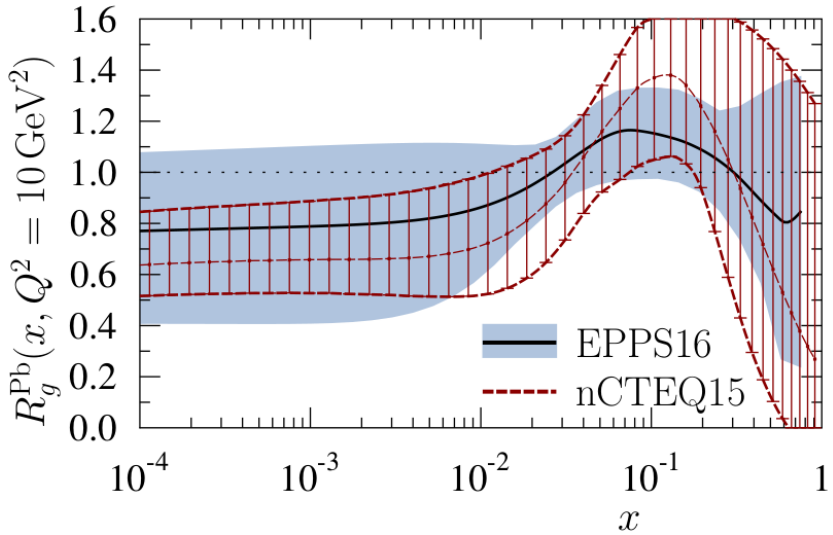


Figure 4.4: Gluon nuclear PDF modification factor determined with EPPS16 (black curve with blue band) and nCTEQ15 (red curves with hatching) nPDF calculations at  $Q^2 = 10\text{GeV}^2$ . Figure taken from Ref. [161].

**Energy loss and Cronin effect.** When high-energy partons traverse the nuclear medium, they lose energy through gluon radiation induced by multiple scatterings in the target nucleus, before or after the hard interaction. It has been proposed by Arleo *et al.* [227, 228, 229], that if the formation length of the radiated gluon is much larger than the size of the nucleus, the gluon radiation becomes coherent (i.e. the radiated gluon would see the nucleus as a whole). The coherent energy loss is proportional to the energy of the incident particle and it effectively decreases the rapidity of the hard particle.

Moreover, as high-energy partons undergo elastic scatterings in the nucleus, they gain transverse momentum in the process. As a consequence, the average partonic  $\langle p_T^2 \rangle$  (known as  $p_T$ -broadening) increases proportionally to the number of scattering centres encountered in the medium. These leads to an enhancement of the particle yields at intermediate  $p_T$  ( $< 10\text{ GeV}/c$ ). This effect was discovered in 1974 by Cronin *et al.*, in proton-tungsten collisions [230], and it is known as the Cronin effect.

## 4.1. INTRODUCTION

The ALICE collaboration has measured the nuclear modification factor of  $J/\psi$  mesons in p-Pb collisions at  $\sqrt{s_{NN}} = 5.02$  TeV [231]. The results are shown in Figure 4.5 as a function of  $p_T$  and compared to theory calculations including energy loss with (light green band) and without (dark green band) EPS09 nuclear PDFs. The theory calculations considering energy loss and gluon shadowing are found to be consistent with the measurements at  $p_T > 2$  GeV/c, while those with only energy loss effects overestimate the results in the central and forward rapidity regions. Regarding the low  $p_T$  and forward region, the theory calculations expect a larger suppression of  $J/\psi$  mesons than what is observed in the measurements.

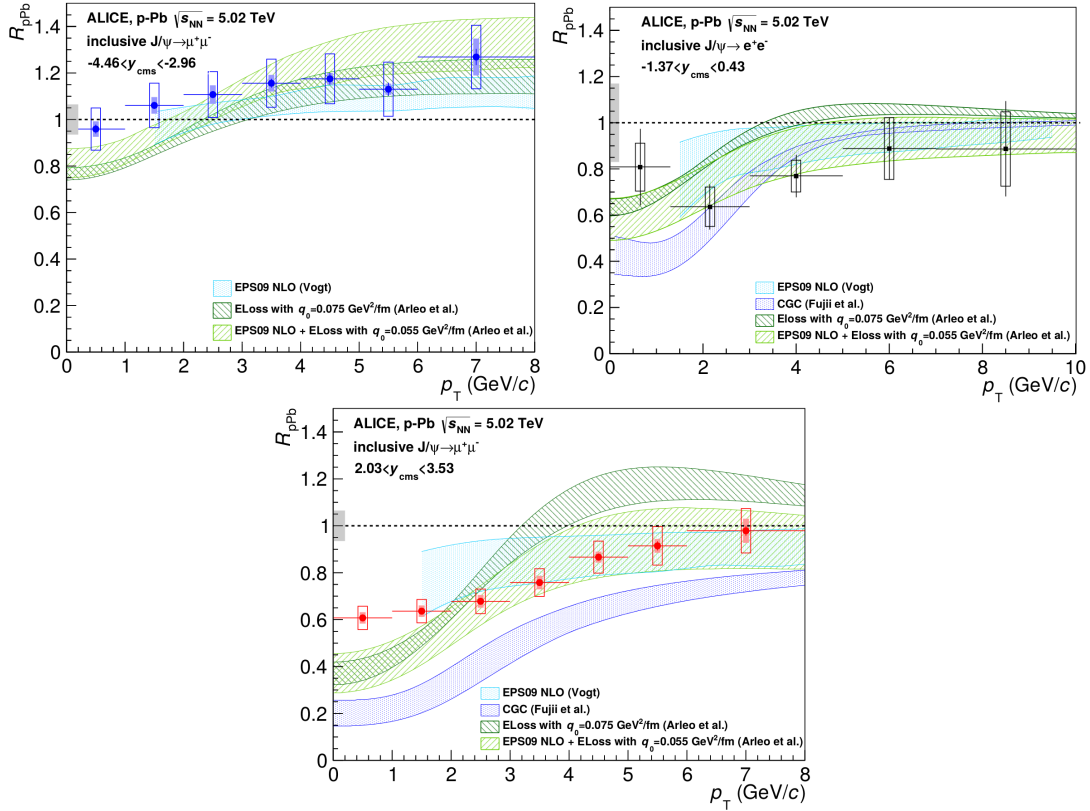


Figure 4.5: Nuclear modification factor of  $J/\psi$  mesons as a function of  $p_T$  in the backward (top-left), mid (top-right) and forward (bottom) rapidity regions. The bars (boxes) represent the statistical (systematic) uncertainties, while the gray box at unity indicate the size of the global uncertainty. The results are compared to nPDF (EPS09), energy loss (Arleo et al), and gluon saturation (CGC) calculations. Figure taken from Ref. [231].

### 4.1.3.2 Hot nuclear matter effects

Charmonia are considered important probes of the QGP since they are produced in the initial hard scattering and experience the full evolution of the medium. The presence of the deconfined medium is expected to dissociate the charmonium states through a process called colour-charge screening, which can occur sequentially depending on the medium temperature and the charmonium binding energies. In addition, the large abundance of charm quarks at the LHC can lead to a recombination of uncorrelated charm quarks, enhancing the charmonium yields.

**Colour-charge screening.** In the presence of the QGP, the binding potential of charmonia is screened by the colour charges of the surrounding quarks in the medium. This mechanism was first proposed in 1986 by Matsui and Satz [79]. The colour-charge screening is described through a Debye screening radius  $r_D(T) \propto 1/T$ , which decreases for larger temperatures  $T$  of the medium. If the Debye screening radius becomes smaller than the radius of a given charmonium state, the charm quarks are no longer able to maintain the bound state and the  $c\bar{c}$  pair dissociates. The  $c\bar{c}$  binding potential  $V_{c\bar{c}}$ , including the colour-charge screening effect, can be expressed as:

$$V_{c\bar{c}}(r, T) = -\frac{a}{r} \exp\left[\frac{-r}{r_D(T)}\right] + b \cdot r_D(T) \left(1 - \exp\left[\frac{-r}{r_D(T)}\right]\right) \quad (4.6)$$

where if  $r_D \rightarrow \infty$  (i.e. no screening,  $T = 0$ ), one recovers the Cornell potential shown in Eq. (1.17). On the other hand, if  $r_D \rightarrow 0$ , the  $c\bar{c}$  binding potential becomes zero and the charm quarks are no longer confined. At the hadronisation stage, the deconfined charm quarks predominantly bind with light quarks, forming open-charm mesons and reducing the charmonium yields in the process.

Since the charmonium radius increases for higher excited states, as shown in Table 4.5, it is expected that  $\psi(2S)$  mesons will dissociate at lower medium temperatures compared to  $J/\psi$  mesons, leading to a sequential suppression pattern. This effect can be quantified by comparing the nuclear modification factor of  $\psi(2S)$  mesons to the one of  $J/\psi$  mesons.

**Charmonium regeneration.** The charm-quark total cross section is large at the LHC, leading to an abundant production of charm and anti-charm quarks (up to 200  $c\bar{c}$  pairs in a central Pb-Pb collision [87]), which may combine to produce charmonium states. This additional source of charmonium production is expected to enhance the nuclear modification factor of charmonia. Since the thermal production of charm quarks (i.e.

Charmonium state	Binding energy [GeV]	Radius [fm]
$J/\psi$	0.64	0.25
$\chi_c(1P)$	0.20	0.36
$\psi(2S)$	0.05	0.45

Table 4.5: Binding energy and radius of  $J/\psi$ ,  $\chi_c(1P)$  and  $\psi(2S)$  mesons. Information taken from Ref. [202].

produced in the medium) is negligible, due to their large mass, the recombined  $c\bar{c}$  pairs are mainly formed by charm quarks produced in the hard scattering. This recombination mechanism, commonly known as charmonium regeneration, can be described using a statistical model [232, 85], where the charm quarks are recombined during the hadronisation stage. Alternatively, the regeneration of charmonia can also be described using transport models [233], where the charmonium states are continuously dissociating and regenerating throughout the evolution of the QGP. Since the uncorrelated charm quarks are required to be close in phase space, to be able to form a charmonium state, the regeneration mechanism mainly plays a role at low charmonium  $p_T$  and narrow rapidities.

#### 4.1.3.3 Current understanding

The suppression and regeneration of quarkonia, as a possible signature of the QGP, were briefly discussed in Section 1.2.4.4. As was mentioned there, an anomalous suppression of  $J/\psi$  and  $\psi(2S)$  mesons in central collisions was already observed at SPS at  $\sqrt{s_{NN}} = 17.3 \text{ GeV}$  [82, 234], which could not be explained considering only CNM effects. Later, measurements performed at RHIC at  $\sqrt{s_{NN}} = 200 \text{ GeV}$  [84] showed similar levels of  $J/\psi$ -meson suppression at mid-rapidity and stronger suppression at forward rapidity. Two explanations were proposed to describe the results at RHIC: the first one suggested that contributions from regenerated  $J/\psi$  mesons could accommodate the agreement observed between RHIC and SPS, while the second one was able to describe the differences seen between forward and mid-rapidity taking into account nPDF effects and nuclear absorption.

The production of  $J/\psi$  mesons has been measured at the LHC in Pb-Pb collisions at  $\sqrt{s_{NN}} = 2.76 \text{ TeV}$ . The general feature observed among the different LHC experiments is a strong suppression of charmonia ( $R_{AA} << 1$ ) in central collisions consistent with colour-charge screening. In addition, the ALICE collaboration has reported a weaker suppression of  $J/\psi$  mesons in particular at low  $p_T$  compared to RHIC measurements [88],

which has been attributed to  $J/\psi$ -meson regeneration. Measurements in p-Pb collisions have also been performed at the LHC, which are found to be consistent with calculations including nuclear modifications of the PDFs and/or energy loss. However, the exact contributions of the various hot and cold nuclear matter effects are difficult to assess, specially due to the large uncertainties on the gluon nuclear PDFs and the limited statistical precision of the data. As a result, more precise and differential measurements are needed, both to constrain the models and to disentangle the different contributions that play a role in heavy-ion collisions.

As for bottomonia, measuring the excited states could bring important information. The CMS collaboration has reported the nuclear modification of  $\psi(2S)$  mesons relative to  $J/\psi$  mesons in Pb-Pb collisions at  $\sqrt{s_{\text{NN}}} = 2.76 \text{ TeV}$  [235]. The results of the double ratio of  $\psi(2S)$  over  $J/\psi$  yields,  $(N_{\psi(2S)}/N_{J/\psi})_{\text{PbPb}}/(N_{\psi(2S)}/N_{J/\psi})_{\text{pp}}$ , are presented as a function of  $\langle N_{\text{part}} \rangle$  in Figure 4.6. The  $\psi(2S)$  mesons are observed to be more suppressed than  $J/\psi$  mesons at high  $p_T$  ( $> 6.5 \text{ GeV}/c$ ) in the mid-rapidity region, consistent with the sequential suppression scenario. On the contrary, in the forward rapidity region and moderate  $p_T$  range ( $3 < p_T < 30 \text{ GeV}/c$ ), the  $\psi(2S)$  mesons are found to be less suppressed than  $J/\psi$  mesons in the most central Pb-Pb collisions, which was unexpected at the time and still not fully understood. However, a similar measurement performed by the ALICE collaboration in central Pb-Pb collisions [236], extending down to  $p_T = 0 \text{ GeV}/c$ , points to a larger  $\psi(2S)$ -meson suppression than for  $J/\psi$  mesons. Transport model calculations [237] have attempted to explain the results by arguing that  $\psi(2S)$  and  $J/\psi$  mesons are regenerated at different stages of the QGP evolution, leading to possible weaker overall suppression of  $\psi(2S)$  relative to  $J/\psi$  mesons, depending on the region of phase space they probe.

The measurements of the charmonium production in Pb-Pb collisions at  $\sqrt{s_{\text{NN}}} = 5.02 \text{ TeV}$ , presented in the following sections, benefits from a larger integrated luminosity ( $\times 2$ ) and higher energy compared to the Pb-Pb measurements at  $\sqrt{s_{\text{NN}}} = 2.76 \text{ TeV}$ . This allows to extend the  $p_T$  reach of the measurements, increase the precision of the results and perform more differential studies.

## 4.2 Analysis

In this section, two related analyses of the charmonium production in p-p and Pb-Pb collisions at  $\sqrt{s_{\text{NN}}} = 5.02 \text{ TeV}$ , are described. The measurements are performed in the  $\mu^+ \mu^-$  decay channel using data recorded with the CMS detector. In both of the analy-

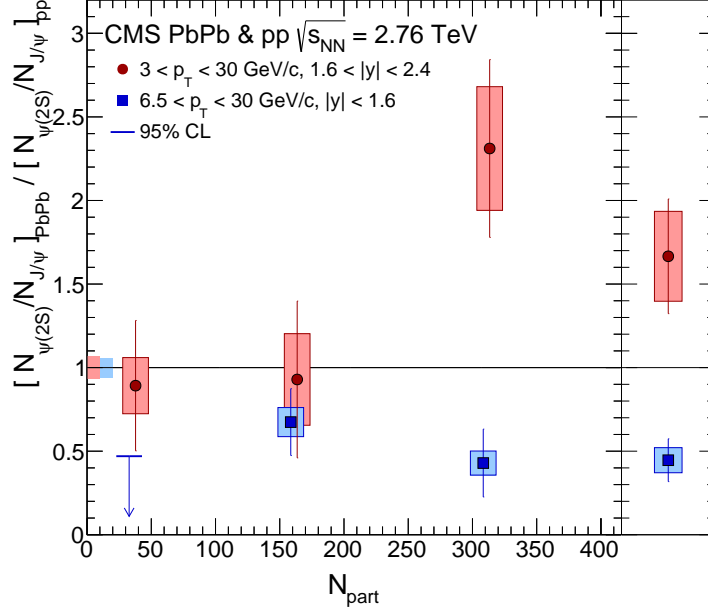


Figure 4.6: Double ratio of  $\psi(2S)$  over  $J/\psi$  yields as a function of  $\langle N_{\text{part}} \rangle$ , in the mid-rapidity (blue squares) and forward rapidity (red circles) regions. The results integrated in centrality are shown at the rightmost edge. The bars (boxes) represents the statistical (systematic) uncertainties, while the boxes at unity indicate the uncertainties on the p-p measurements. Figure taken from Ref. [235].

ses, I made significant contributions in the signal extraction, acceptance studies and determination of the systematic uncertainties related to the fitting procedure.

The first analysis [7] studies the modification of the prompt and nonprompt  $J/\psi$  meson production in Pb-Pb compared to p-p collisions at the same energy. To accomplish this, the nuclear modification factor of  $J/\psi$  mesons is measured in different collision centrality bins, and  $J/\psi$ -meson  $p_T$  and rapidity ( $y$ ) ranges. The second analysis [6] probes the nuclear modification of  $\psi(2S)$  mesons relative to  $J/\psi$  mesons, by measuring the double ratio of  $\psi(2S)$  over  $J/\psi$  yields in Pb-Pb relative to p-p collisions, defined as:

$$\rho^{\psi(2S)/J/\psi} = \frac{(N_{\psi(2S)}/N_{J/\psi})_{\text{PbPb}}}{(N_{\psi(2S)}/N_{J/\psi})_{\text{pp}}} \quad (4.7)$$

One advantage of measuring the double ratio of charmonium yields is that the acceptance and efficiency of the two charmonium states cancel in the ratio due their similar masses and production mechanisms. For this reason, as well as the limited statistics of the  $\psi(2S)$  mesons compared to  $J/\psi$  mesons, the second analysis was published first and relatively fast after the data was taken, while the first analysis was more

elaborate and required more time to complete.

The p-p and Pb-Pb datasets employed are introduced in Section 4.2.1, while the charmonium simulations are listed in Section 4.2.2 and the event selection is presented in Section 4.2.3. The procedure used to extract the prompt and nonprompt  $J/\psi$ -meson yields is explained in Section 4.2.4 and the extraction of the single ratios of  $\psi(2S)$  over  $J/\psi$  meson yields is detailed in Section 4.2.5. The charmonium efficiency and acceptance are derived in Section 4.2.6. Section 4.2.7 and Section 4.2.8 report the systematic uncertainties associated to the measurement of the  $J/\psi$ -meson yields and the double ratio of charmonium yields, respectively.

### 4.2.1 Dataset

The measurement of the nuclear modification of  $\psi(2S)$  and  $J/\psi$  mesons is performed using data recorded in 2015 by the CMS detector, in p-p and Pb-Pb collisions at  $\sqrt{s_{\text{NN}}} = 5.02 \text{ TeV}$ . The main datasets employed in the analyses, called *DoubleMu0* for p-p and *HIONiaDoubleMu0* for Pb-Pb, consist of events selected by the CMS trigger system, requiring the presence of at least two L1 muon candidates. An additional dataset selecting also L1 double muon events, referred as *HIONiaPeripheral30100*, is employed to measure the charmonium production in peripheral Pb-Pb collisions (centrality range 30 – 100%), since it accumulated more integrated luminosity than HIONiaDoubleMu0<sup>1</sup>.

The p-p and Pb-Pb datasets were reconstructed with CMSSW 7.5.8, making use of the standard p-p and heavy-ion specific reconstruction algorithms employed during the data-taking period, respectively. After a meticulous check of the quality of the data by the CMS collaboration, the content of the datasets were filtered excluding events in which the tracker or the muon system were not operating in proper conditions. The total integrated luminosity of the data samples is presented in Table 4.6.

System	Primary dataset	Integrated luminosity
Pb-Pb	HIONiaDoubleMu0	$351 \mu\text{b}^{-1}$
Pb-Pb	HIONiaPeripheral30100	$464 \mu\text{b}^{-1}$
p-p	DoubleMu0	$28 \text{ pb}^{-1}$

Table 4.6: Total integrated luminosity of each dataset used in the analysis of the charmonium nuclear modification in p-p and Pb-Pb collisions at  $\sqrt{s_{\text{NN}}} = 5.02 \text{ TeV}$ .

---

<sup>1</sup>The data rate of HIONiaDoubleMu0 was reduced during part of the Pb-Pb run because it exceeded the bandwidth threshold of the Tier-0 computing centre.

### 4.2.2 Charmonium simulations

The production of  $\psi(2S)$  and  $J/\psi$  mesons is described using fully reconstructed Monte-Carlo simulated samples. The simulations were made separately for charmonia produced directly from the hard scattering (prompt  $J/\psi$  and  $\psi(2S)$  mesons), and for  $J/\psi$  mesons produced from the decay of b hadrons (nonprompt  $J/\psi$  mesons), for both p-p and Pb-Pb collisions. The prompt  $\psi(2S)$  and  $J/\psi$  events were generated with PYTHIA 8.209 [181], which models the charmonium production using NRQCD. Regarding the nonprompt  $J/\psi$  sample, the b hadrons ( $B^\pm, B^0, \bar{B}^0, B_s^0, \bar{B}_s^0$  mesons) were decayed with the EVTGEN v1.3 [238] package interfaced to PYTHIA 8.209. The CUETP8M1 underlying event PYTHIA tune [239, 182] was used in all samples.

Moreover, the underlying environment present in Pb-Pb collisions was first simulated with HYDJET 1.9 [240] and then embedded to each PYTHIA signal event, by matching the position of the simulated interaction vertex. The full CMS detector response was simulated in all charmonium simulations, based on GEANT4 [183], and the p-p and Pb-Pb simulated collision events were reconstructed with the corresponding reconstruction algorithms used during 2015 data taking.

In addition, the Pb-Pb simulations were produced in several ranges of charmonium or B-meson  $p_T$ , in order to have similar statistics available in each  $p_T$  range. As a result,  $w_{p_T}$  weights are used for each meson  $p_T$  range to combine the different Pb-Pb simulations and form a continuous  $p_T$  spectrum.

Finally, in order to match the centrality distribution of the signal simulations to what is observed in data, each Pb-Pb event is weighed by the average  $N_{\text{coll}}$  corresponding to the centrality range of the simulated collision. The differences between the data and simulated centrality distributions are due to the fact that the signal events were embedded into minimum bias HYDJET events equally distributed in centrality, while the production of charmonium in data is biased towards more central collisions (i.e. scales with  $N_{\text{coll}}$ ). Thus, in summary, each Pb-Pb charmonium simulated event is weighed by:

$$w_{\text{MC}} = N_{\text{gen}}^{gen} \frac{w_{p_T} \cdot N_{\text{coll}}}{\sum_{i=1}^{N_{\text{gen}}^{gen}} (w_{p_T}^i \cdot N_{\text{coll}}^i)} \quad (4.8)$$

where the weights are normalised so that their sum is effectively equal to the number of generated events. The list of charmonium simulations are summarized in Table 4.7.

Process	Generator	Criteria	Acceptance	Events
$\text{PbPb} \rightarrow J/\psi \rightarrow \mu^+ \mu^-$	PYTHIA +HYDJET	$J/\psi p_T[0,3] \text{ GeV}/c$	$2.5 \times 10^{-1}$	150659
		$J/\psi p_T[3,6] \text{ GeV}/c$	$1.7 \times 10^{-1}$	3842575
		$J/\psi p_T[6,9] \text{ GeV}/c$	$2.0 \times 10^{-2}$	2268977
		$J/\psi p_T[9,12] \text{ GeV}/c$	$4.0 \times 10^{-3}$	168628
		$J/\psi p_T[12,15] \text{ GeV}/c$	$1.2 \times 10^{-3}$	155793
		$J/\psi p_T[15,30] \text{ GeV}/c$	$7.2 \times 10^{-4}$	104729
$\text{PbPb} \rightarrow \psi(2S) \rightarrow \mu^+ \mu^-$	PYTHIA +HYDJET	$J/\psi p_T[30,\infty] \text{ GeV}/c$	$3.3 \times 10^{-5}$	47059
		$\psi(2S) p_T[0,3] \text{ GeV}/c$	$2.4 \times 10^{-1}$	96623
		$\psi(2S) p_T[3,6] \text{ GeV}/c$	$2.1 \times 10^{-1}$	89880
		$\psi(2S) p_T[6,9] \text{ GeV}/c$	$3.1 \times 10^{-2}$	98836
		$\psi(2S) p_T[9,12] \text{ GeV}/c$	$6.4 \times 10^{-3}$	102038
		$\psi(2S) p_T[12,15] \text{ GeV}/c$	$2.0 \times 10^{-3}$	94370
$\text{PbPb} \rightarrow B \rightarrow J/\psi \rightarrow \mu^+ \mu^-$	EVTGEN +PYTHIA +HYDJET	$\psi(2S) p_T[15,\infty] \text{ GeV}/c$	$1.2 \times 10^{-3}$	49857
		$B p_T[0,3] \text{ GeV}/c$	$2.7 \times 10^{-1}$	140257
		$B p_T[3,6] \text{ GeV}/c$	$1.5 \times 10^{-1}$	5192754
		$B p_T[6,9] \text{ GeV}/c$	$5.0 \times 10^{-2}$	1786414
		$B p_T[9,12] \text{ GeV}/c$	$1.0 \times 10^{-3}$	165143
		$B p_T[12,15] \text{ GeV}/c$	$3.6 \times 10^{-3}$	141064
$\text{pp} \rightarrow J/\psi \rightarrow \mu^+ \mu^-$	PYTHIA	$B p_T[15,30] \text{ GeV}/c$	$2.1 \times 10^{-3}$	107742
		$B p_T[30,\infty] \text{ GeV}/c$	$1.4 \times 10^{-4}$	41803
			1.0	60830490
			1.0	60830490
$\text{pp} \rightarrow B \rightarrow J/\psi \rightarrow \mu^+ \mu^-$	PYTHIA		1.0	69652510

Table 4.7: Simulations used in the analysis of the charmonium production in Pb-Pb and p-p collisions at 5.02 TeV.

### 4.2.3 Event selection

The charmonium candidates are reconstructed in the dimuon decay channel (i.e.  $J/\psi \rightarrow \mu^+ \mu^-$  and  $\psi(2S) \rightarrow \mu^+ \mu^-$ ), by pairing opposite-charge muons. Since the  $J/\psi$  and  $\psi(2S)$  masses are small ( $m_{J/\psi} = 3.097 \text{ GeV}/c^2$  and  $m_{\psi(2S)} = 3.686 \text{ GeV}/c^2$ ), the signal events are dominated by the presence of low  $p_T$  muons ( $\langle p_T^\mu \rangle \sim 1.6 \text{ GeV}/c$ ), contrary to the W-boson analysis reported in Chapter 3. The selection used to identify the charmonium events is detailed in this section.

#### 4.2.3.1 Minimum bias event selection

The p-p and Pb-Pb minimum bias events are selected by applying a global event filter (GEF) offline to suppress the background events not originating from the inelastic hadronic scattering. The GEF for p-p collision events consists of the following filters:

- Beam-Scraping filter: Requires at least 25% of tracks in the event to be high quality tracks.
- Primary Vertex filter: Requires a primary vertex reconstructed from at least two tracks, within a longitudinal (transverse) distance of 25 cm (2 cm) of the IP.

In the case of Pb-Pb collisions, since the projectiles are more charged (82 protons per Pb ion), the background contribution from electromagnetic interactions between Pb beams is significantly enhanced, and as a result a tighter event selection is applied including the following filters:

- HF coincidence filter: requires at least three towers on each side of the interaction point in the HF calorimeter, with an energy deposit per tower of at least 3 GeV. This filter rejects events from electronic noise and beam-beam electromagnetic interactions.
- Cluster compatibility filter: rejects beam-scraping events (i.e. muons produced when the beam particles hit the LHC collimators), by requiring that the shape of the silicon pixel clusters are compatible with tracks originating from the primary vertex.

The Pb-Pb collision events are also required to contain at least one reconstructed primary vertex as done for p-p data. The efficiency of the GEF in Pb-Pb minimum bias events has been determined to be  $99\pm2\%$ . This efficiency can surpass 100% due to the remaining contamination of non-hadronic collisions in the sample. The number of Pb-Pb minimum bias events passing the GEF corresponds to  $N_{\text{MB}} = 2.34 \times 10^9$  for HIONiaDoubleMu0 and  $N_{\text{MB}} = 3.09 \times 10^9$  for HIONiaPeripheral30100.

#### 4.2.3.2 Trigger

The events used in the analysis of the charmonium production in p-p and Pb-Pb collisions were selected by the trigger called HLT\_HIL1DoubleMu0, which requires the presence

of two L1 muons (with no muon  $p_T$  requirement) in coincidence with a bunch crossing identified by the BPTX detectors (to suppress contributions from cosmic-ray muons).

In addition, events derived from the dimuon peripheral dataset HIOniaPeripheral30100 were selected by the trigger HLT\_HIL1DoubleMu0\_2HF\_Cent30100, which requires, in addition to the HLT\_HIL1DoubleMu0 trigger conditions, a signal in coincidence on both sides of the HF detector and a total energy deposit in the HF calorimeters consistent with a collision centrality between 30% and 100%.

To make sure that each muon employed in the analysis is associated to an online muon that fired the dimuon triggers, the reconstructed muons are required to be matched to the corresponding L1 muons within a  $\eta$ - $\phi$  cone defined as:

$$\Delta R(\mu_{\text{reco}}, \mu_{\text{L1}}) = \sqrt{(\eta_{\text{reco}} - \eta_{\text{L1}})^2 + (\phi_{\text{reco}} - \phi_{\text{L1}})^2} < 0.3 \quad (4.9)$$

The standard  $\Delta R < 0.3$  threshold is employed in CMS analyses using L1 muon triggers [106]. Since L1 muons are reconstructed only in the muon stations, their position ( $\eta, \phi$ ) resolution is worse than for HLT L3 muons (which includes also the inner-tracker information). As a consequence, a wider  $\Delta R$  matching criteria is utilised for L1 muons compared to the one used in the W-boson analysis ( $\Delta R < 0.1$ ).

#### 4.2.3.3 Centrality determination in Pb-Pb collisions

The centrality percentiles of Pb-Pb collisions are derived by sampling the distribution of the total energy deposited in the HF calorimeters in bins of 0.5% of the total hadronic cross section. The HF energy distribution is determined in minimum-bias events (i.e. requiring a bunch crossing and a coincidence between signals from the  $-z$  and  $+z$  sides of the HF calorimeters) passing the GEF. The yield as a function of the HF energy is then corrected for the efficiency of the minimum-bias trigger and the GEF selection. Figure 4.7 presents the distribution of the total HF energy in Pb-Pb collisions separated in centrality classes.

Figure 4.8 shows the centrality distribution of the dimuon triggered Pb-Pb dataset. The selection of hard-probe processes, such as the production of charmonium states, bias the centrality distribution towards central collisions.

The centrality percentiles are associated with the average geometrical quantities of the collision (e.g.  $N_{\text{part}}$  and  $T_{\text{AA}}$ ) using a Glauber MC model as explained in Section 1.2.2. The centrality intervals used in Pb-Pb collisions and the corresponding average  $N_{\text{part}}$  and  $T_{\text{AA}}$  values are presented in Table 4.8.

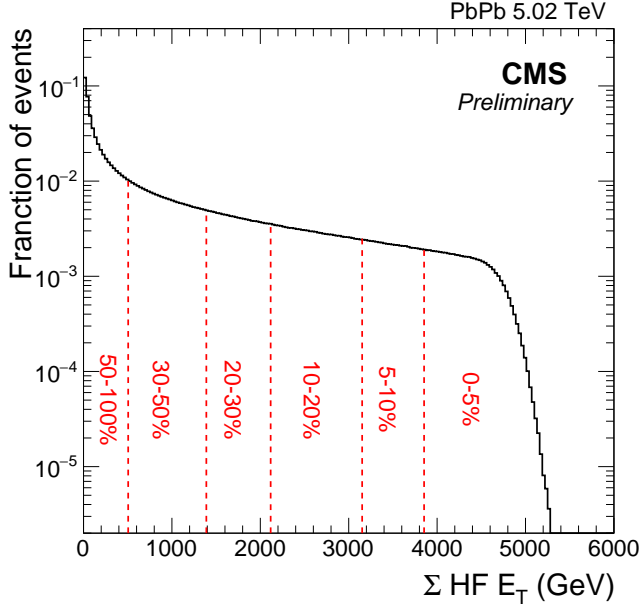


Figure 4.7: Distribution of the total energy deposited in the HF calorimeters in Pb-Pb collisions at 5.02 TeV, for minimum-bias events passing the GEF selection. The different centrality classes are shown. Figure taken from the internal analysis note [241].

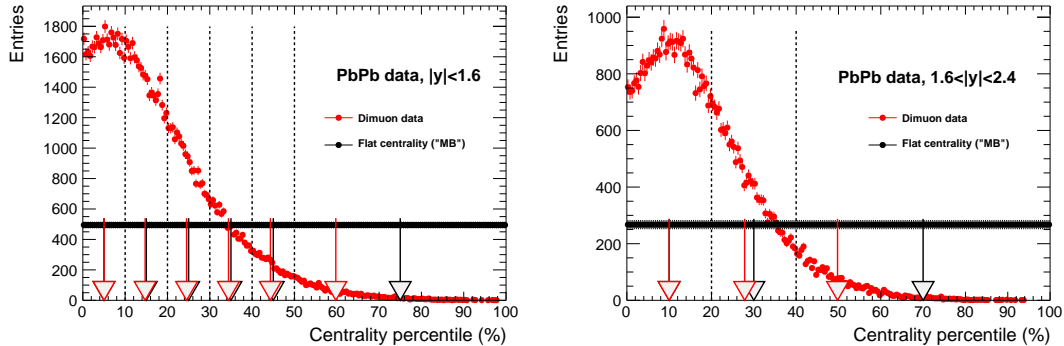


Figure 4.8: Centrality distribution of  $\mu^+ \mu^-$  events in Pb-Pb collisions passing the GEF cuts (red), with  $2.2 < M_{\mu^+ \mu^-} < 4.5$   $\text{GeV}/c^2$ , for  $|y| < 1.6$  (left) and  $1.6 < |y| < 2.4$  (right). The distribution of the minimum-bias sample, flat by definition, is shown in black. The limits of the centrality bins used for the  $\psi(2S)$  analysis are shown as vertical dashed lines, with the most central (peripheral) range on the right (left). The average centrality in each centrality range is also shown as an arrow, in red and black for the dimuon and minimum-bias datasets, respectively.

#### 4.2.3.4 Muon selection

Muon candidates are identified using a *soft* selection. Contrary to the muon selection criteria used in the W-boson analysis, which was optimised for high- $p_T$  muons, the

Centrality range [%]	$\langle T_{AA} \rangle$	$\langle N_{\text{part}} \rangle$
0 - 100	$5.61+0.16-0.19$	$114.0+2.6-2.6$
0 - 5	$25.98+0.47-0.77$	$384.3+1.8-2.0$
5 - 10	$20.46+0.38-0.60$	$333.3+3.0-3.2$
10 - 15	$16.11+0.35-0.50$	$285.4+3.5-3.7$
15 - 20	$12.60+0.32-0.43$	$242.9+3.8-3.9$
20 - 25	$9.80+0.31-0.37$	$205.7+3.9-4.1$
25 - 30	$7.52+0.29-0.32$	$172.7+4.0-4.0$
30 - 35	$5.71+0.27-0.27$	$144.1+4.0-4.0$
35 - 40	$4.25+0.23-0.24$	$118.7+4.0-4.0$
40 - 45	$3.10+0.19-0.19$	$96.51+3.8-3.8$
45 - 50	$2.22+0.16-0.16$	$77.4+3.7-3.6$
50 - 60	$1.30+0.12-0.12$	$53.9+3.2-3.1$
60 - 70	$0.57+0.07-0.06$	$30.6+2.6-2.4$
70 - 100	$0.11+0.02-0.01$	$8.3+1.0-0.6$
0 - 10	$23.22+0.43-0.69$	$358.8+2.4-2.6$
10 - 20	$14.35+0.33-0.45$	$264.2+3.6-3.8$
20 - 30	$8.66+0.29-0.33$	$189.2+4.0-4.1$
30 - 40	$4.98+0.24-0.24$	$131.4+4.0-4.0$
40 - 50	$2.66+0.18-0.17$	$87.0+3.7-4.3$
50 - 100	$0.44+0.05-0.03$	$21.9+1.8-1.0$
10 - 30	$11.51+0.30-0.39$	$226.7+3.7-3.9$
30 - 100	$1.41+0.09-0.06$	$46.8+2.4-1.2$
0 - 20	$18.79+0.37-0.56$	$311.5+2.9-3.1$
20 - 40	$6.82+0.26-0.28$	$160.3+4.0-4.0$
40 - 100	$0.81+0.07-0.05$	$32.7+2.1-1.1$

Table 4.8: Values of the centrality-integrated number of participants  $\langle N_{\text{part}} \rangle$  and nuclear overlap factor  $\langle T_{AA} \rangle$ , determined in the different collision centrality ranges used in the analysis. Information taken from the internal analysis note [241].

*soft* selection has been designed to be highly efficient for muons with low transverse momentum ( $p_T < 10$  GeV/c). The *soft* selection requires muon candidates to pass the following criteria:

- The muon track is identified both by the tracker-muon and the global-muon algorithms.
- The tracker track extrapolated to the muon system is matched with at least one muon segment within a distance less than  $3\sigma$  along the  $x$  and  $y$  coordinates. Muon

segments are excluded if they have a better match with other tracker tracks.

- The muon track includes hits in more than five inner-tracker layers, ensuring a good  $p_T$  measurement.
- The muon track has measurements in at least one pixel layer to suppress muons from decays in flight.
- The transverse impact parameter (longitudinal distance) of the muon track is consistent with the primary vertex within 0.3 cm (20 cm), to reduce the background from cosmic-ray muons.

#### 4.2.3.5 Muon kinematic cut

The single muon kinematic selection is optimised, using the  $J/\psi$ -meson simulated samples, by requiring (in different muon  $p_T - \eta$  bins) that the number of muon candidates passing the trigger, reconstruction and identification algorithms is more than 10% of the number of generated muons. The muon kinematic cuts are described in Eq. (4.10) and shown in Figure 4.9.

$$\begin{aligned} p_T^\mu &> 3.5 \text{ GeV}/c & \text{for } |\eta^\mu| < 1.2 \\ p_T^\mu &> (5.77 - 1.89 \times |\eta^\mu|) \text{ GeV}/c & \text{for } 1.2 \leq |\eta^\mu| < 2.1 \\ p_T^\mu &> 1.8 \text{ GeV}/c & \text{for } 2.1 \leq |\eta^\mu| < 2.4 \end{aligned} \quad (4.10)$$

#### 4.2.3.6 Charmonium selection

The  $J/\psi \rightarrow \mu^+ \mu^-$  and  $\psi(2S) \rightarrow \mu^+ \mu^-$  candidate selection consists of the detection of two low- $p_T$  muons of opposite electric charge, each passing all identification criteria explained in Section 4.2.3.4, the kinematic cuts detailed in Section 4.2.3.5, and the trigger matching condition mentioned in Section 4.2.3.2. Moreover, each dimuon candidate is required to have a  $\chi^2$  probability larger than 1% that the two muons derive from a common vertex. This selection is used in most CMS quarkonium analyses to remove a large fraction of background events while keeping, by construction, 99% of signal events (two muons coming from the same vertex).

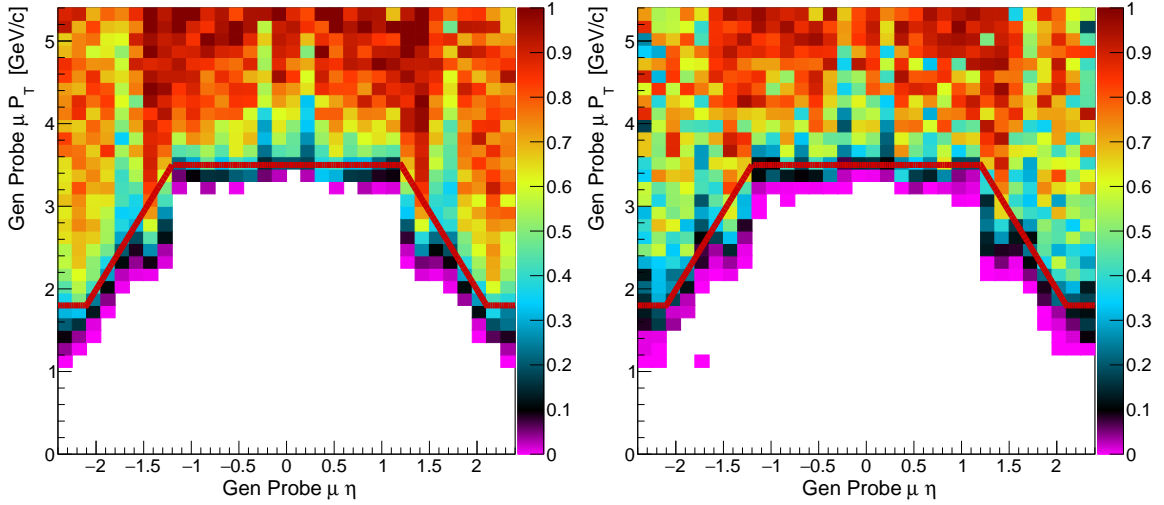


Figure 4.9: Distribution of the ratio of the number of reconstructed, identified and triggered muons over the number of generated muons, as a function of muon  $p_T$  and  $\eta$ . The results are derived from the prompt  $J/\psi$  simulations corresponding to p-p (left) and Pb-Pb (right) collisions. The red line represents the single muon kinematic cuts.

#### 4.2.4 Extraction of prompt and nonprompt $J/\psi$ mesons

This section describes the procedure used to extract the yields of prompt and nonprompt  $J/\psi \rightarrow \mu^+ \mu^-$  candidates in p-p and Pb-Pb collision data. Considering the large lifetime of b hadrons ( $\tau_B \sim 1.5$  ps), the prompt and nonprompt  $J/\psi$  mesons are distinguished by virtue of the pseudoproper-decay length  $\ell_{J/\psi}$ , determined from the displacement between the primary collision and secondary  $\mu^+ \mu^-$  vertices, as detailed in Section 4.2.4.1.

The  $J/\psi$ -meson yields are extracted by performing a two-dimensional unbinned-maximum likelihood fit to the  $\mu^+ \mu^-$  invariant mass ( $m^{\mu\mu}$ ) and  $\ell_{J/\psi}$  distributions (hereafter referred as 2D fit), performed with the RooFit framework [190]. The expression of the total functional form  $F(m^{\mu\mu}, \ell_{J/\psi})$ , used in the 2D fit, is defined as:

$$F(m^{\mu\mu}, \ell_{J/\psi}) = \sum_{i=J/\psi, \text{bkg}} N_i \cdot M_i(m^{\mu\mu}) \cdot D_i(\ell_{J/\psi}) \otimes R_i(\ell_{J/\psi}) \quad (4.11)$$

where  $\otimes$  represents a convolution with respect to the  $\ell_{J/\psi}$  variable,  $N_{J/\psi}$  is the number of inclusive  $J/\psi$  mesons (i.e. including prompt and nonprompt  $J/\psi$  mesons),  $N_{\text{bkg}}$  is the number of background dimuons,  $R_{J/\psi}$  ( $R_{\text{bkg}}$ ) represents the  $\ell_{J/\psi}$  resolution of signal (background) dimuons, and  $M_i$  and  $D_i$  are the  $m^{\mu\mu}$  and  $\ell_{J/\psi}$  functional forms for each event source, respectively.

The 2D fits are done in four rapidity intervals corresponding to 0-0.6, 0.6-1.2, 1.2-1.8 and 1.8-2.4. In the most forward rapidity region ( $1.8 < |y^{\mu\mu}| < 2.4$ ), the  $\text{J}/\psi$ -meson yields are extracted down to 3  $\text{GeV}/c$ , while in the other rapidity regions ( $|y^{\mu\mu}| < 1.8$ ) they are extracted down to 6.5  $\text{GeV}/c$ , reflecting the CMS detector acceptance. The signal extraction is also performed in several centrality bins with the following boundaries: [0, 5, 10, 15, 20, 25, 30, 35, 40, 45, 50, 60, 70, 100%] at  $|y^{\mu\mu}| < 2.4$  and [0, 10, 20, 30, 40, 50, 100%] in each of the rapidity intervals. The full set of analysis bins used in the  $\text{J}/\psi$ -meson analysis is listed in Appendix C.

Due to the complexity of the 2D functional form and the limited statistics to fully constrain all its parameters at the same time, the 2D fits are performed in four sequential steps:

1. The  $m^{\mu\mu}$  shape of the signal is parametrised using a weighed sum of two Crystal Ball functions, while the background is described with a Chebyshev function (Section 4.2.4.2). The  $m^{\mu\mu}$  functional form is fitted on data and the corresponding parameters are fixed in this step.
2. The shape of the  $\ell_{\text{J}/\psi}$  resolution is determined from data by fitting the  $\ell_{\text{J}/\psi} < 0$  distribution with a weighed sum of three Gaussian distributions, taking into account the  $\ell_{\text{J}/\psi}$  uncertainty in each event (Section 4.2.4.3).
3. The  $\ell_{\text{J}/\psi}$  true lineshape of the nonprompt  $\text{J}/\psi$  mesons is parametrised with an exponential function, while the nonprompt component of the background is parametrised with a weighed sum of three exponential functions (Section 4.2.4.4). The  $\ell_{\text{J}/\psi}$  functional form, derived by convolving the  $\ell_{\text{J}/\psi}$  true lineshape with the  $\ell_{\text{J}/\psi}$  resolution model, is fitted on data and the parameters of the  $\ell_{\text{J}/\psi}$  true lineshapes are constrained in this step.
4. The  $\ell_{\text{J}/\psi}$  and  $m^{\mu\mu}$  distributions in data are fitted with the 2D functional form  $F(m^{\mu\mu}, \ell_{\text{J}/\psi})$  (Section 4.2.4.5), and the prompt and nonprompt  $\text{J}/\psi$  meson yields are extracted (Section 4.2.4.6).

A detailed description of each step is provided in Sections 4.2.4.2 to 4.2.4.5. An example of the 2D fit results projected along the  $m^{\mu\mu}$  and  $\ell_{\text{J}/\psi}$  variables are shown in Figure 4.10, extracted from Pb-Pb collision data.

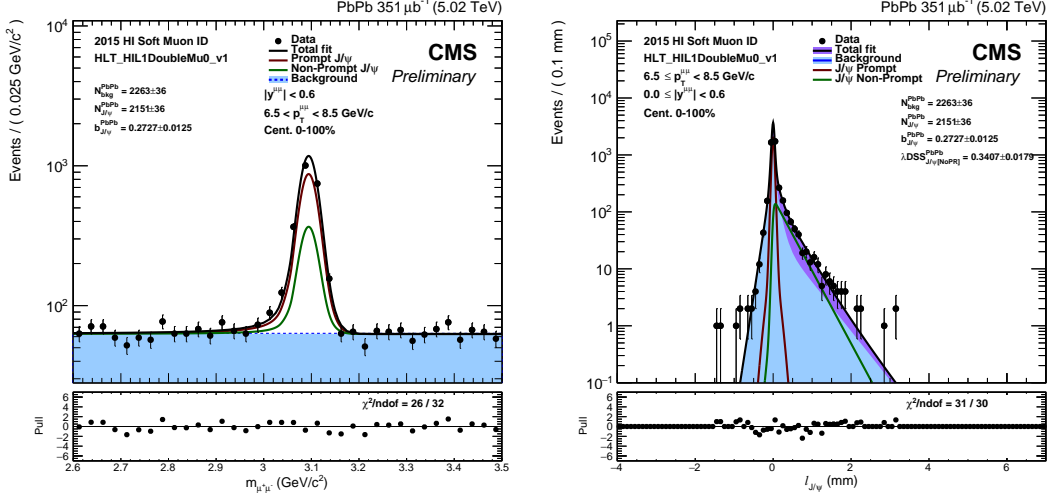


Figure 4.10: Results of the 2D fits performed on Pb-Pb data, projected onto the dimuon invariant mass (left) and pseudoproper-decay length (right) variables.

#### 4.2.4.1 Definition of pseudoproper-decay length

The pseudoproper-decay length  $\ell_{J/\psi}$  of  $\mu^+\mu^-$  candidates, used to estimate the b-hadron decay length, is defined as:

$$\ell_{J/\psi} = m_{J/\psi} \cdot \frac{\vec{p}^{\mu\mu} \cdot \vec{r}}{(p^{\mu\mu})^2} \quad (4.12)$$

where  $m_{J/\psi} = 3.0969$  GeV/c<sup>2</sup> is the mass of the  $J/\psi$  meson [21],  $\vec{p}^{\mu\mu}$  is the dimuon momentum vector and  $\vec{r}$  is the displacement vector between the position of the primary collision vertex and the dimuon vertex.

The primary collision vertex is reconstructed by fitting the position, along the beam axis, of all tracks produced promptly within a radius of 5 cm from the interaction region, while the secondary  $\mu^+\mu^-$  vertex is determined by extrapolating the position of closest approach between the two muon tracks. The vertex fit is performed using an adaptive vertex fitting algorithm [242, 243], which determines the best estimate of the vertex parameters, including its position and covariance matrix [244].

The uncertainty associated to the  $\ell_{J/\psi}$  measurement, referred as  $\sigma_\ell$ , is computed as:

$$\sigma_\ell = \sqrt{m_{J/\psi} \cdot \frac{\vec{p}^{\mu\mu} \cdot S \cdot \vec{p}^{\mu\mu}}{(p^{\mu\mu})^2}} \quad (4.13)$$

where  $S$  is the sum of the covariance matrices associated to the primary collision and  $\mu^+\mu^-$  vertex fits. The pseudoproper-decay length is measured in the CMS detector with a

resolution of  $35\text{ }\mu\text{m}$ , allowing to resolve the decay vertex of b hadrons.

#### 4.2.4.2 Dimuon invariant mass parametrisation

The inclusive  $\text{J}/\psi$  meson and background yields are extracted by fitting the  $m^{\mu\mu}$  distribution in the dimuon invariant mass region  $2.6 < m^{\mu\mu} < 3.5 \text{ GeV}/c^2$ . The main source of background in this mass region derives from pairs of uncorrelated muons produced from leptonic decays of kaons and pions, and semi-leptonic decays of heavy-flavour hadrons. These uncorrelated muon pairs are combined forming a continuous  $m^{\mu\mu}$  distribution (i.e. combinatorial background). On the contrary, the  $\text{J}/\psi$  mesons decay to correlated muon pairs producing a narrow peak (i.e. resonance) in the  $m^{\mu\mu}$  spectrum around  $m^{\mu\mu} \approx 3.09 \text{ GeV}/c^2$ . As a consequence, different functional forms are used to model the signal and background  $m^{\mu\mu}$  shapes.

**Parametrisation of the  $\text{J}/\psi$ -meson invariant mass shape.** The  $m^{\mu\mu}$  distribution of inclusive  $\text{J}/\psi$  mesons is modelled with a weighed sum of two Crystal Ball (CB) functions. The Crystal Ball function consists of a Gaussian core and a power-law tail. The Gaussian core is parametrised with a width  $\sigma_{\text{CB}}$  and a mean  $m_{\text{J}/\psi}$ , while the power-law tail is parametrised by an exponent  $n_{\text{J}/\psi}$  that accounts for energy loss due to final-state photon radiation and a parameter  $\alpha_{\text{J}/\psi}$  that determines the transition point between the Gaussian and the power-law functions, as defined in:

$$\text{CB}(m) = \begin{cases} \frac{1}{\sqrt{2\pi}\sigma_{\text{CB}}} \exp\left[-\frac{1}{2}\left(\frac{m-m_{\text{J}/\psi}}{\sigma_{\text{CB}}}\right)^2\right], & \text{if } \left(\frac{m-m_{\text{J}/\psi}}{\sigma_{\text{CB}}}\right) > -\alpha_{\text{J}/\psi} \\ \frac{1}{\sqrt{2\pi}\sigma_{\text{CB}}} \exp\left[-\frac{|\alpha_{\text{J}/\psi}|^2}{2}\right] \left(\frac{n_{\text{J}/\psi}}{|\alpha_{\text{J}/\psi}|}\right)^{n_{\text{J}/\psi}} \left(\frac{n_{\text{J}/\psi}}{|\alpha_{\text{J}/\psi}|} - |\alpha_{\text{J}/\psi}| - \frac{m-m_{\text{J}/\psi}}{\sigma_{\text{CB}}}\right)^{-n_{\text{J}/\psi}}, & \text{if } \left(\frac{m-m_{\text{J}/\psi}}{\sigma_{\text{CB}}}\right) \leq -\alpha_{\text{J}/\psi} \end{cases} \quad (4.14)$$

The total  $m^{\mu\mu}$  functional form of the signal is then given by:

$$M_{\text{J}/\psi}(m^{\mu\mu}) = f_{\text{J}/\psi} \cdot \text{CB}_1(m^{\mu\mu}) + (1 - f_{\text{J}/\psi}) \cdot \text{CB}_2(m^{\mu\mu}) \quad (4.15)$$

where the two Crystal Ball functions are defined with common mean  $m_{\text{J}/\psi}$  and tail parameters  $\alpha_{\text{J}/\psi}$  and  $n_{\text{J}/\psi}$ , and the two CB widths are constrained such that  $\sigma_{\text{CB},2} \geq \sigma_{\text{CB},1}$ .

The Crystal Ball parameters are optimised by fitting the prompt  $\text{J}/\psi$ -meson simulations. An example of such fits in Pb-Pb collisions is shown in Figure 4.11. On the one hand, the parameters are found to be consistent within different collision systems and

also as a function of collision centrality and dimuon  $p_T$ . On the other hand, the fits performed in the inclusive dimuon rapidity region ( $|y^{\mu\mu}| < 2.4$ ) are different from those done in differential  $y^{\mu\mu}$  regions. As a result, different sets of parameters are used for the differential and integrated rapidity regions, extracted from the p-p and Pb-Pb prompt  $J/\psi$ -meson simulations. The set of parameters for the differential rapidity regions are determined from the corresponding rapidity-averaged values.

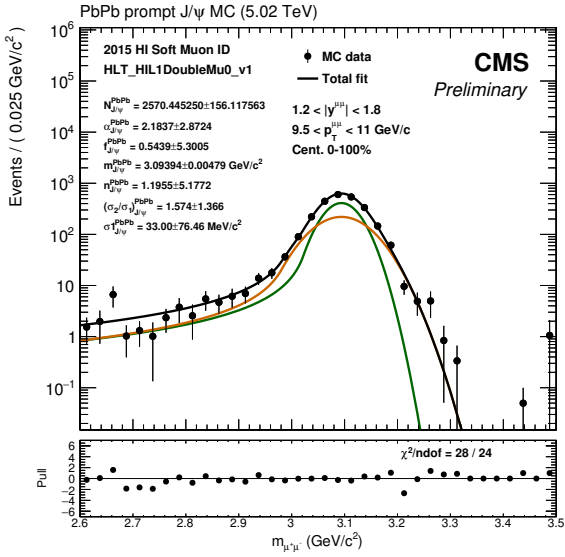


Figure 4.11: Fit to the  $\mu^+\mu^-$  invariant mass distribution in Pb-Pb simulation derived at  $9.5 < p_T < 11$  GeV/c in the rapidity region  $1.2 < |y| < 1.8$ . The black line represents the total fit model while the green and orange lines represent the shape of each CB component.

When fitting the  $m^{\mu\mu}$  distribution in p-p and Pb-Pb collision data, the tail parameters  $\alpha_{J/\psi}$  and  $n_{J/\psi}$  are fixed to the values extracted from simulation, while the ratio of CB widths ( $\sigma_{CB,2}/\sigma_{CB,1}$ ) is also fixed to simulation only when fitting the Pb-Pb data. This is done because the data samples do not provide sufficient constraining power to reliably estimate the CB tail parameters. The set of parameters left free in both p-p and Pb-Pb data fits are  $f_{J/\psi}$ ,  $m_{J/\psi}$  and  $\sigma_{CB,1}$ , while  $\sigma_{CB,2}$  is left free only in the p-p data fits. The signal shape parameters extracted from simulations are summarised in Table 4.9.

**Parametrisation of the background invariant mass shape.** The  $m^{\mu\mu}$  distribution of background dimuons is described with a Chebyshev function of order  $N$ , defined as:

Rapidity region	$f_{J/\psi}$	$\alpha_{J/\psi}$	$n_{J/\psi}$	$\sigma_{CB,2}/\sigma_{CB,1}$
Differential	0.78	<b>2.10</b>	<b>1.35</b>	<b>1.68</b>
$ y  < 2.4$	0.58	<b>1.94</b>	<b>1.64</b>	<b>2.06</b>

Table 4.9: Parameters extracted from the prompt  $J/\psi$ -meson simulation and used to constrain the double Crystal Ball functions in each differential and integrated rapidity region. The parameters fixed to simulation in both Pb-Pb and p-p data fits are shown in bold blue colour, while those fixed to simulation only on Pb-Pb data are displayed in bold red colour. The  $f_{J/\psi}$  values from simulation are only used for the initialisation step in the data fits.

$$M_{\text{bkg}}^N(m^{\mu\mu}) = \sum_{i=0}^N c_i T_i(m^{\mu\mu}) \quad (4.16)$$

where  $T_i$  is a Chebyshev polynomial of order  $i$  and  $c_i$  is the corresponding fit parameter. The Chebyshev polynomials are determined using the following recurrence relation [245]:

$$T_0(m) = 1 \quad ; \quad T_1(m) = m \quad ; \quad T_{i+1}(m) = 2mT_i(m) - T_{i-1}(m) \quad (4.17)$$

The main advantage of using a Chebyshev function is that the fit parameters  $c_i$  are uncorrelated with each other, improving the convergence of the dimuon invariant mass fits. The order of the background  $m^{\mu\mu}$  model is varied between 0 and 6, and the best order for each analysis bin is chosen by performing a Log-Likelihood Ratio (LLR) test. The LLR test compares the resulting minimised Negative Log-Likelihood (NLL) of a Chebyshev fit of order  $N$  to the NLL of a Chebyshev fit of order  $N + 1$  and  $N + 2$  (two subsequent orders are needed to account for the change between odd and even polynomials).

The difference between the NLL values derived from the fits using a Chebyshev polynomial of order  $N$  and  $M > N$ , is proportional to a  $\chi^2$  distribution with  $2(M - N)$  number of degrees of freedom, in particular:

$$\chi^2_{N \rightarrow N+1} = 2 \cdot (\text{NLL}_N - \text{NLL}_{N+1}) \quad ; \quad \chi^2_{N \rightarrow N+2} = 2 \cdot (\text{NLL}_N - \text{NLL}_{N+2}) \quad (4.18)$$

For a given Chebyshev function of order  $N$ , the next order is considered to fit the data significantly better if the  $\chi^2$  probabilities associated to the  $N + 1$  or  $N + 2$  orders are less than 5%. Thus, if in a given analysis bin, the next order does not significantly improve the quality of the fit, then the current order of the Chebyshev function is chosen. As an example, Table 4.10 summarises the results of the LLR test performed in Pb-Pb

data for dimuons within  $0.6 < |y^{\mu\mu}| < 1.2$  and  $9.5 \leq p_T^{\mu\mu} < 11$  GeV/c, which in this case the first order is chosen since  $p(\chi^2_{1-2}, 2)$  and  $p(\chi^2_{1-3}, 4)$  are larger than 5%.

M	NLL	$p(N=0)$	$p(N=1)$	$p(N=2)$	$p(N=3)$	$p(N=4)$
0	-28534.76					
1	-28537.94	4.2%				
2	-28538.08	15.6%	<b>86.8%</b>			
3	-28538.44	28.9%	<b>90.9%</b>	69.8%		
4	-28538.82	42.3%	94.1%	83.3%	68.8%	
5	-28538.93	59.7%	98.2%	94.6%	91.4%	89.4%
6	-28539.40	67.9%	98.3%	95.5%	92.7%	88.2%

Table 4.10: Results of the LLR test used to determine the order of the Chebyshev function for the background  $\mu^+ \mu^-$  invariant mass fitted in Pb-Pb data within  $0.6 < |y^{\mu\mu}| < 1.2$  and  $9.5 \leq p_T^{\mu\mu} < 11$  GeV/c. The LLR test results of which the  $\chi^2$  probability determined for two consecutive orders ( $M = N + 1$  and  $M = N + 2$ ) are higher than 5% are highlighted in bold.

Another example is given in Figure 4.12, where the fits to the dimuon invariant mass distribution in Pb-Pb and p-p collision data have been performed using a first order and second order Chebyshev function, respectively. Among all the analysis bins, the orders of the Chebyshev function selected by the LLR tests are not larger than first order in Pb-Pb fits and third order in p-p fits.

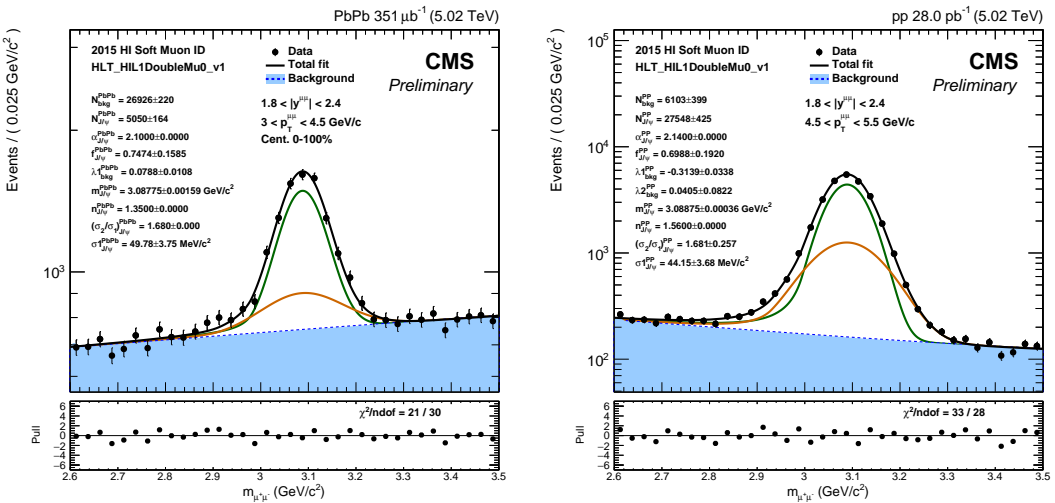


Figure 4.12: Results of the fits to the  $\mu^+ \mu^-$  invariant mass distribution in Pb-Pb (left) and p-p (right) data. The black line represents the total fit model while the blue filled area represents the fitted background shape.

#### 4.2.4.3 Pseudoproper-decay length resolution

The  $\ell_{J/\psi}$  resolution function depends on the measurement of the dimuon momentum and its vertex position, and as a result, it is affected by the  $\ell_{J/\psi}$  uncertainty ( $\sigma_\ell$ ) of each event. In addition, since the  $\sigma_\ell$  depends on the  $p_T$  and rapidity of dimuon candidates, the  $\sigma_\ell$  distribution may differ between background and signal dimuons. In order to take into account the  $\ell_{J/\psi}$  uncertainty in each event, the  $\ell_{J/\psi}$  resolution of signal and background dimuons is modelled with:

$$R_{J/\psi(\text{bkg})}(\ell_{J/\psi}) = \int d\sigma_\ell R(\ell_{J/\psi}|\sigma_\ell) \cdot \mathcal{P}_{J/\psi(\text{bkg})}(\sigma_\ell) \quad (4.19)$$

where  $R(\ell_{J/\psi}|\sigma_\ell)$  is the functional form of the  $\ell_{J/\psi}$  resolution depending on  $\sigma_\ell$ , and  $\mathcal{P}_{J/\psi(\text{bkg})}(\sigma_\ell)$  represents the signal (background)  $\sigma_\ell$  distribution.

Using this approach, the  $\ell_{J/\psi}$  resolution is adjusted for each event to the measured  $\ell_{J/\psi}$  uncertainty weighed by the corresponding  $\sigma_\ell$  distribution for signal and background dimuons. The parametrisation of the  $\ell_{J/\psi}$  resolution and the determination of the  $\sigma_\ell$  distributions are detailed as follows.

**Extraction of the  $\sigma_\ell$  distribution.** The distribution of  $\sigma_\ell$  is described using a template histogram determined from data. The corresponding  $\sigma_\ell$  distributions for signal and background dimuons are extracted using the statistical technique called *sPlot* [246].

The *sPlot* technique can be applied to a multivariate data sample made of a combination of several sources of events (e.g. signal and background), where each event is described by a set of variables divided in two categories. The first category consists of discriminating variables whose distributions are known for each source of events, while the second category corresponds to a set of variables, called control variables, whose distributions for some sources are unknown. The *sPlot* technique allows to reconstruct the distribution of the control variables for each source, by weighing the events with the so-called *sWeights*, computed with the information of the discriminating variables.

In the  $J/\psi$  meson analysis, the  $\mu^+ \mu^-$  invariant mass is used as discriminating variable in order to determine the signal and background distributions of  $\sigma_\ell$ . The corresponding *sWeights* are derived using the  $m^{\mu\mu}$  functional forms of each source ( $M_{J/\psi}$  and  $M_{\text{bkg}}$ ), obtained in Section 4.2.4.2, in the following way:

$${}_s\mathcal{W}_i(m^{\mu\mu}) = \frac{\sum_{j=\{\text{J}/\psi, \text{bkg}\}} V_{i,j} \cdot M_j(m^{\mu\mu})}{\sum_{j=\{\text{J}/\psi, \text{bkg}\}} N_j \cdot M_j(m^{\mu\mu})} \quad , \quad \text{for } i = \text{J}/\psi, \text{bkg} \quad (4.20)$$

where  $N_j$  is the number of dimuon events from source  $j$ , and  $V_{i,j}$  is the element of the covariance matrix associated to the  $i^{\text{th}}$  and  $j^{\text{th}}$  sources ( $i,j = \text{J}/\psi$  and background). The covariance matrix of each source is computed by inverting the following matrix:

$$V_{i,j}^{-1} = \frac{M_i(m_{\mu\mu}) \cdot M_j(m_{\mu\mu})}{\sum_{i=\{\text{J}/\psi, \text{bkg}\}} N_i \cdot M_i(m_{\mu\mu})} \quad (4.21)$$

Once determined, the  $s\mathcal{W}_{\text{J}/\psi}$  and  $s\mathcal{W}_{\text{bkg}}$  weights are then applied to each event to create a signal-like and a background-like dataset. Each dataset is subsequently projected onto the  $\sigma_\ell$  variable, to extract the signal and background  $\sigma_\ell$  distributions and form  $\sigma_\ell$  template histograms for each source. An example of a  $\sigma_\ell$  distribution in p-p and Pb-Pb collision data is presented in Figure 4.13.

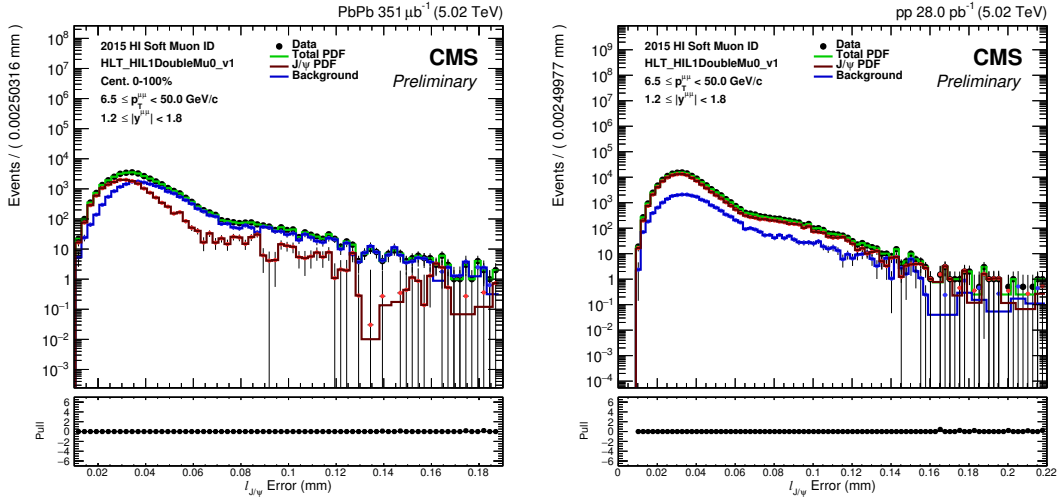


Figure 4.13: Distributions of the  $\sigma_\ell$  for signal (red line), background (blue line) and all (green line) dimuons, extracted from Pb-Pb (left) and p-p (right) data. The bottom panel shows the ratio between the data and the total template histogram extracted using the sPlot technique.

**Parametrisation of the  $\ell_{\text{J}/\psi}$  resolution.** The  $\ell_{\text{J}/\psi}$  resolution is parametrised in data from the negative tail of the  $\ell_{\text{J}/\psi}$  signal distribution, which is due to resolution. Since both signal and background dimuons can have negative  $\ell_{\text{J}/\psi}$  values, the contribution from each source is separated using the *sPlot* technique, as was done for the  $\sigma_\ell$  distribution in the previous part. The resulting  $\ell_{\text{J}/\psi} < 0$  distribution, derived from the *sPlot* signal-like dataset, is then fitted with a weighed sum of three Gaussian functions, defined as:

$$R(\ell_{J/\psi} | \sigma_\ell) = \frac{f_1^r}{s_1^r \sigma_\ell \sqrt{2\pi}} \exp \left[ \frac{1}{2} \left( \frac{\ell_{J/\psi}}{s_1^r \sigma_\ell} \right)^2 \right] + (1 - f_1^r) \left[ \frac{f_2^r}{s_2^r \sigma_\ell \sqrt{2\pi}} \exp \left[ \frac{1}{2} \left( \frac{\ell_{J/\psi}}{s_2^r \sigma_\ell} \right)^2 \right] + \frac{(1 - f_2^r)}{s_3^r \sigma_\ell \sqrt{2\pi}} \exp \left[ \frac{1}{2} \left( \frac{\ell_{J/\psi}}{s_3^r \sigma_\ell} \right)^2 \right] \right] \quad (4.22)$$

where  $s^r$  are scale factors that account for deviations from the measured  $\ell_{J/\psi}$  uncertainties, and  $f^r$  are the weights of the Gaussian components. The  $s^r$  and  $f^r$  parameters are left free in the fits to the data. The Gaussian mean values have been checked to be consistent with zero, and are fixed to zero in the fits. The scale factors  $s_i^r$  are constrained such that  $s_3^r \geq s_2^r \geq s_1^r$ .

Two examples of  $\ell_{J/\psi}$  resolution fits for p-p and Pb-Pb data are given in Figure 4.14 plotted as a function of  $\ell_{J/\psi}/\sigma_\ell$ .

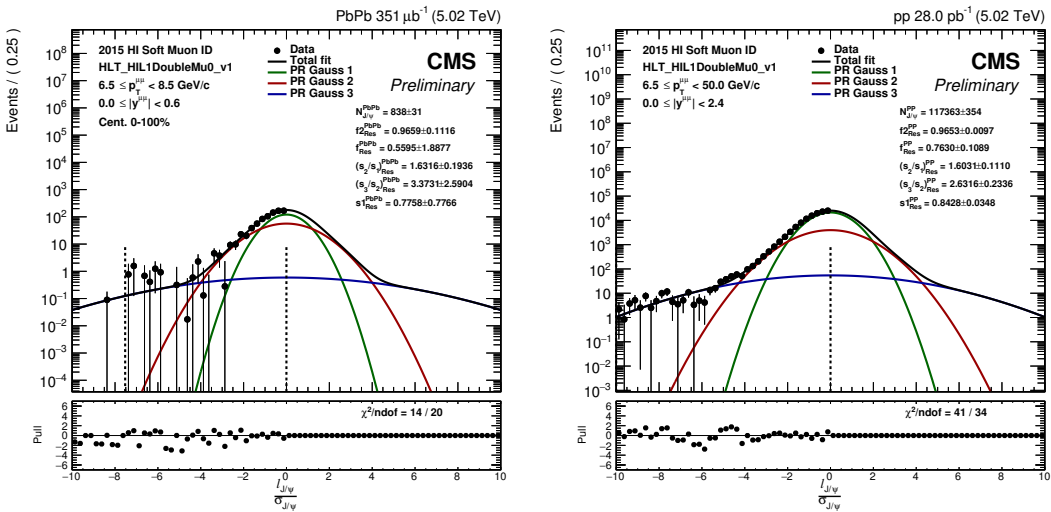


Figure 4.14: Results of the  $\ell_{J/\psi}$  resolution fits for signal dimuons in data. The results are presented as a function of  $\ell_{J/\psi}/\sigma_\ell$  and the dashed lines represent the fitted range.

#### 4.2.4.4 Pseudopropor-decay length parametrisation

The  $\ell_{J/\psi}$  distribution of  $J/\psi \rightarrow \mu^+ \mu^-$  events is separated in two components: prompt and nonprompt  $J/\psi$  mesons. In the case of background dimuons, the description of the  $\ell_{J/\psi}$  distribution is also separated in a prompt and nonprompt component. On the one hand, the prompt background component represents  $\mu^+ \mu^-$  pairs from background events whose dimuon vertex is consistent with the primary collision vertex, such as low mass Drell-

Yan events. On the other hand, the nonprompt background components are made of uncorrelated muons faking a displaced vertex.

**Parametrisation of the  $\ell_{J/\psi}$  true lineshape of  $J/\psi$  mesons.** The  $\ell_{J/\psi}$  true lineshape of prompt  $J/\psi$  mesons is described with a Dirac delta function ( $\delta(\ell_{J/\psi})$ ) and the one for nonprompt  $J/\psi$  mesons is modelled with an exponential function. The signal  $\ell_{J/\psi}$  true functional form is then given by:

$$D_{J/\psi}(\ell_{J/\psi}) = b_{J/\psi} \cdot \exp(-|\lambda_B| \cdot \ell_{J/\psi}) + (1 - b_{J/\psi}) \cdot \delta(\ell_{J/\psi}) \quad (4.23)$$

where  $b_{J/\psi}$  is the fraction of nonprompt  $J/\psi$  mesons and  $\lambda_B$  represents the average decay length of b hadrons. The  $\lambda_B$  parameter is initialised, when performing the 2D fits on data, to the value obtained by fitting the generated  $\ell_{J/\psi}$  distribution of the nonprompt  $J/\psi$  simulation.

Examples of fits to the generated  $\ell_{J/\psi}$  distribution of nonprompt  $J/\psi$  simulations are shown in Figure 4.15 for Pb-Pb and p-p data (the  $\lambda_B$  parameter is labelled in the plots as  $\lambda_{\text{DSS}}$ <sup>2</sup>).

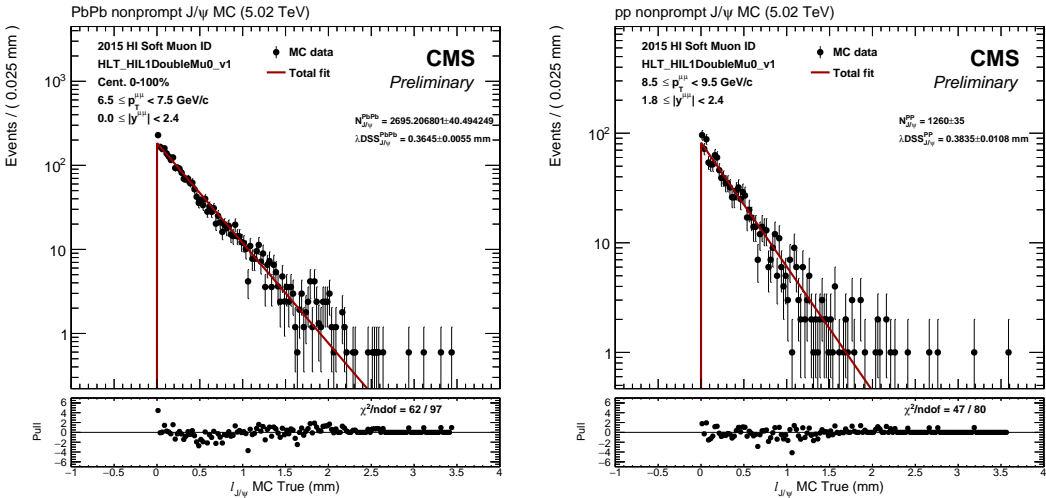


Figure 4.15: Fits to the  $\ell_{J/\psi}$  distribution of generated nonprompt  $J/\psi \rightarrow \mu^+ \mu^-$  events in Pb-Pb (left) and p-p (right) simulations. The fitted value for  $\lambda_B = \lambda_{\text{DSS}}$  is shown.

**Parametrisation of the background  $\ell_{J/\psi}$  true lineshape.** The nonprompt component of the background  $\ell_{J/\psi}$  true lineshape is described with a weighed sum of three

<sup>2</sup>The initial DSS stands for Decays on Single Side.

## 4.2. ANALYSIS

exponential functions, while the prompt component is described with a Dirac delta function. The full background  $\ell_{J/\psi}$  true model is defined as:

$$D_{\text{bkg}}(\ell_{J/\psi}) = b_{\text{bkg}} \cdot \{ f_{\text{DL}} [f_{\text{SS}} \cdot \exp(-|\lambda_{\text{SS}}| \cdot \ell_{J/\psi}) + (1 - f_{\text{SS}}) \cdot \exp(|\lambda_{\text{F}}| \cdot \ell_{J/\psi})] \\ + (1 - f_{\text{DL}}) \cdot \exp(-|\lambda_{\text{DS}}| |\ell_{J/\psi}|) \} \\ + (1 - b_{\text{bkg}}) \cdot \delta(\ell_{J/\psi}) \quad (4.24)$$

where  $b_{\text{bkg}}$  is the fraction of nonprompt background dimuons,  $f_{\text{DL}}$  and  $f_{\text{SS}}$  are the weights of the exponential functions, and  $\lambda_{\text{SS}}$ ,  $\lambda_{\text{F}}$  and  $\lambda_{\text{DS}}$  are the exponential parameters associated to the single sided ( $\ell_{J/\psi} > 0$ ), flipped ( $\ell_{J/\psi} < 0$ ) and double sided (symmetric  $\ell_{J/\psi}$ ) exponential decay models, respectively.

The  $\ell_{J/\psi}$  true lineshape of the background is parametrised in data by fitting the  $\ell_{J/\psi}$  distribution of the background-like data sample derived with the *sPlot* technique. The model used to fit the data is given by:

$$F_{\text{bkg}}(\ell_{J/\psi}) = N_{\text{bkg}} \cdot D_{\text{bkg}}(\ell_{J/\psi}) \otimes R_{\text{bkg}}(\ell_{J/\psi}) \quad (4.25)$$

where the  $\ell_{J/\psi}$  resolution parameters have been fixed to data as detailed in Section 4.2.4.3, and only the  $N_{\text{bkg}}$  and the  $D_{\text{bkg}}$  parameters ( $\lambda$ ,  $f$  and  $b_{\text{bkg}}$ ) are left free. Examples of fits to the  $\ell_{J/\psi}$  distribution of background dimuons are shown in Figure 4.16 for p-p and Pb-Pb data.

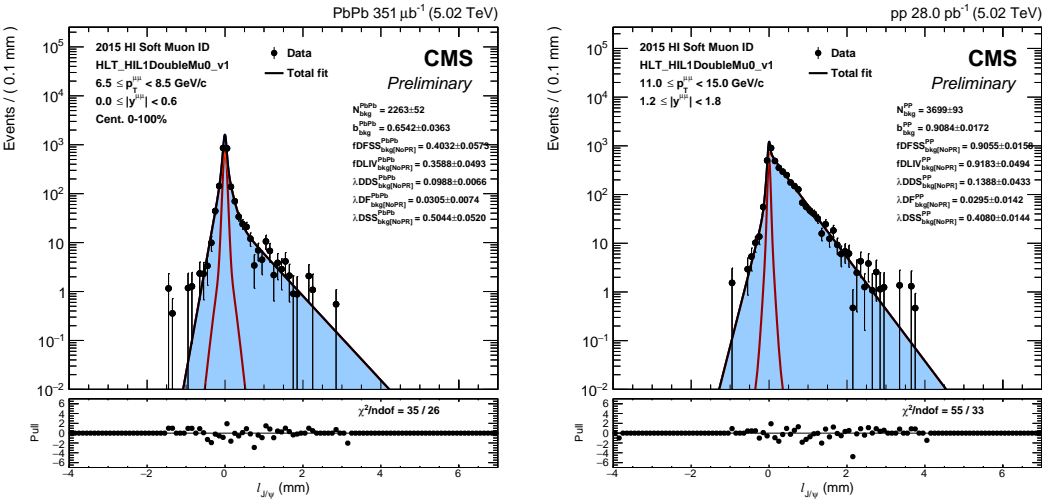


Figure 4.16: Fits to the  $\ell_{J/\psi}$  distribution of background events in Pb-Pb (left) and p-p (right) collision data.

#### 4.2.4.5 Two-dimensional fit to the $m^{\mu\mu}$ and $\ell_{J/\psi}$ distributions

The 2D fits to the  $m^{\mu\mu}$  and  $\ell_{J/\psi}$  distributions represent the last step in the procedure to extract the  $J/\psi$ -meson yields. The parameters used in the 2D fit model are fixed as explained in the previous sections, except for the average decay length of b hadrons  $\lambda_B$ , the fraction of nonprompt  $J/\psi$ -mesons  $b_{J/\psi}$ , the inclusive  $J/\psi$ -meson yield  $N_{J/\psi}$ , and the background yield  $N_{bkg}$ . Figure 4.10 shows an example of 2D fit extracted from Pb-Pb collision data.

#### 4.2.4.6 Prompt and nonprompt $J/\psi$ meson yields

Finally, the yields of the prompt ( $N_{J/\psi}^P$ ) and nonprompt ( $N_{J/\psi}^{NP}$ )  $J/\psi$  mesons are simply derived from the number of inclusive  $J/\psi$  mesons  $N_{J/\psi}$  and the fraction of nonprompt  $J/\psi$  mesons  $b_{J/\psi}$ , according to:

$$\begin{aligned} N_{J/\psi}^P &= (1 - b_{J/\psi}) \cdot N_{J/\psi} \\ N_{J/\psi}^{NP} &= b_{J/\psi} \cdot N_{J/\psi} \end{aligned} \tag{4.26}$$

and the corresponding statistical uncertainty are computed using error propagation and taking into account the correlation between  $b_{J/\psi}$  and  $N_{J/\psi}$ , determined from the 2D fits.

### 4.2.5 Extraction of prompt $\psi(2S)/J/\psi$ ratio

This section explains the steps followed to measure the ratio of prompt  $\psi(2S)$  over  $J/\psi$  meson yields, in p-p and Pb-Pb collisions. In this case, due to the low amount of  $\psi(2S)$  mesons present in Pb-Pb collisions, it is not possible to perform a 2D fit to the  $m^{\mu\mu}$  and  $\ell_{J/\psi}$  distributions, and an alternative procedure is used instead to measure the prompt charmonium yields.

In order to extract the yields of prompt charmonia, the dimuons are required to pass a  $\ell_{J/\psi}$  selection that rejects dimuons with  $\ell_{J/\psi}$  values above a given threshold. The  $\ell_{J/\psi}$  selection threshold is optimized using simulations as detailed in Section 4.2.5.1, keeping 90% of prompt charmonia while rejecting more than 80% of nonprompt charmonia. Then, the  $\psi(2S)$ -to- $J/\psi$  yields ratio is extracted from data by fitting the  $m^{\mu\mu}$  distribution of dimuons passing the  $\ell_{J/\psi}$  selection, as explained in Section 4.2.5.2. And finally, the ratio of prompt  $\psi(2S)$  over  $J/\psi$  meson yields is determined by subtracting the remaining nonprompt charmonia passing the  $\ell_{J/\psi}$  selection, as described in Section 4.2.5.3.

Due to the more limited  $\psi(2S)$ -meson statistics, the extraction of the ratios of  $\psi(2S)$  over  $J/\psi$  meson yields is performed in wider bins compared to the  $J/\psi$ -meson analysis. In this case, the fits are performed in two kinematic regions: mid-rapidity ( $0 < |y^{\mu\mu}| < 1.6$ ,  $p_T^{\mu\mu} > 6.5$  GeV/c) and forward rapidity ( $1.6 < |y^{\mu\mu}| < 2.4$ ,  $p_T^{\mu\mu} > 3$  GeV/c). The lower  $p_T^{\mu\mu}$  thresholds in each rapidity region reflect the acceptance of the detector. The measurements are also extracted in different  $p_T^{\mu\mu}$  intervals with boundaries: [6.5, 9, 12, 15, 20, 30] GeV/c at mid-rapidity and [3, 6.5, 12, 30] GeV/c at forward rapidity, and in different centrality bins corresponding to: 0-10, 10-20, 20-30, 30-40, 40-50 and 50-100% at mid-rapidity, and 0-20, 20-40 and 40-100% at forward rapidity. The analysis bins used in the  $\psi(2S)$ -to- $J/\psi$  double ratio analysis are summarised in Table C.4.

#### 4.2.5.1 Definition of the $\ell_{J/\psi}$ selection for prompt charmonia

The threshold of the  $\ell_{J/\psi}$  selection is tuned using prompt  $J/\psi$  simulations, by requiring that the fraction of prompt  $J/\psi$  mesons that pass the selection is 90%, in each analysis bin. The simulated  $\ell_{J/\psi}$  distributions of prompt and nonprompt signal dimuons in the forward rapidity region, and the corresponding  $\ell_{J/\psi}$  selection threshold, are shown in Figure 4.17.

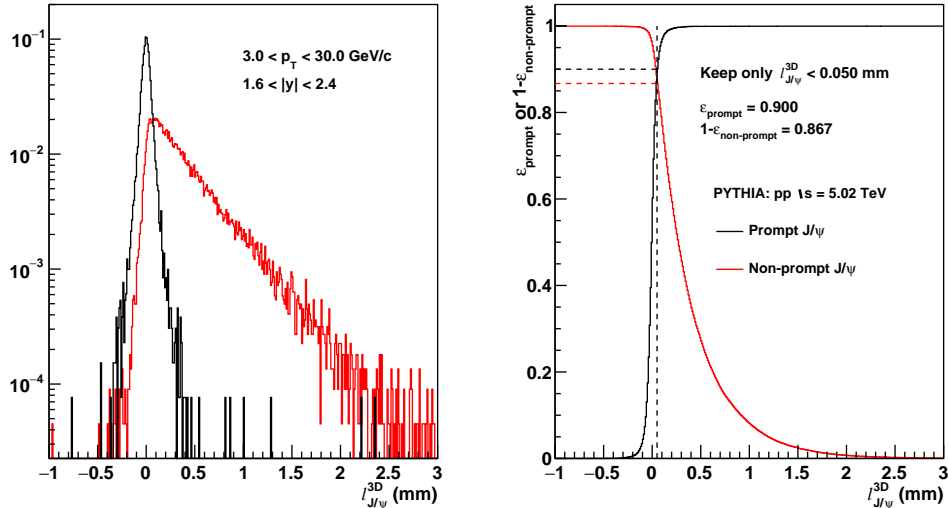


Figure 4.17: Distribution of  $\ell_{J/\psi}$  (left) in the p-p simulations of prompt and nonprompt  $J/\psi$  mesons, and an illustration (right) of the way the  $\ell_{J/\psi}$  selection threshold is chosen. The results corresponds to the mid-rapidity region  $|y^{\mu\mu}| < 1.6$ .

The  $\ell_{J/\psi}$  selection thresholds extracted from the simulations are found to be consistent

between the different collision systems and centrality bins, but they vary between different dimuon  $p_T$  and rapidity regions. As a result, the thresholds are extracted in several  $p_T^{\mu\mu}$  regions at mid- and forward rapidity. Then, the profile of the  $\ell_{J/\psi}$  selection thresholds ( $l_P$ ) with respect of  $p_T^{\mu\mu}$  is fitted separately for each rapidity region, with the following function:

$$l_P(p_T^{\mu\mu}) = a + \frac{b}{p_T^{\mu\mu}} \quad (4.27)$$

where  $a$  and  $b$  are free parameters. Figure 4.18 displays the fit results of the  $l_P$  profile as a function of  $p_T^{\mu\mu}$  in the two rapidity regions<sup>3</sup>. The  $\ell_{J/\psi}$  selection, derived from the fits as a function of  $p_T^{\mu\mu}$ , is summarised in:

$$\ell_{J/\psi}[\text{mm}] < \begin{cases} 0.012 + (0.23/p_T^{\mu\mu} [\text{GeV}/c]), & \text{if } |y^{\mu\mu}| \leq 1.6 \\ 0.014 + (0.28/p_T^{\mu\mu} [\text{GeV}/c]), & \text{if } |y^{\mu\mu}| > 1.6 \end{cases} \quad (4.28)$$

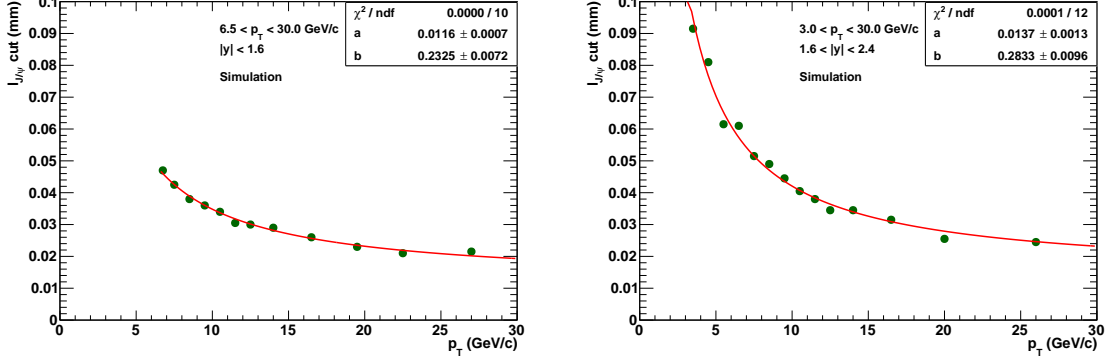


Figure 4.18: Profile of the  $\ell_{J/\psi}$  selection thresholds (green points) with respect to  $p_T^{\mu\mu}$ , extracted from the  $J/\psi$  simulations in the mid-rapidity (left) and forward rapidity (right) regions. The fitted functions (red lines) are also displayed and the values of their parameters are shown in the box.

The efficiencies of passing the  $\ell_{J/\psi}$  selection, as a function of  $p_T^{\mu\mu}$ , are presented in Figure 4.19. By construction, the  $\ell_{J/\psi}$  selection efficiencies of prompt  $J/\psi$  mesons are close

<sup>3</sup>It is unfortunate that the small statistical uncertainties arising from the large MC statistics were not taken into account in these fits. However, this procedure only provides a working point which is used consistently across the analysis (to compute the efficiency, extract the signal, etc.) and hence should not carry an uncertainty of statistical nature. The systematic uncertainty linked to the procedure itself is described in Section 4.2.8.

to 90%, while it is observed to be more efficient for prompt  $\psi(2S)$  mesons, due to the slightly higher momentum of the muons. However, the difference between the prompt  $J/\psi$  and  $\psi(2S)$  efficiencies are found to be similar in p-p and Pb-Pb simulations. The efficiency for nonprompt  $J/\psi$  mesons, leading to a contamination from this component, is seen to increase when going towards lower  $p_T^{\mu\mu}$  values reaching up to 20%. These efficiencies are used in Section 4.2.5.3 to subtract the nonprompt charmonium contamination from the measured ratios of  $\psi(2S)$  over  $J/\psi$  mesons.

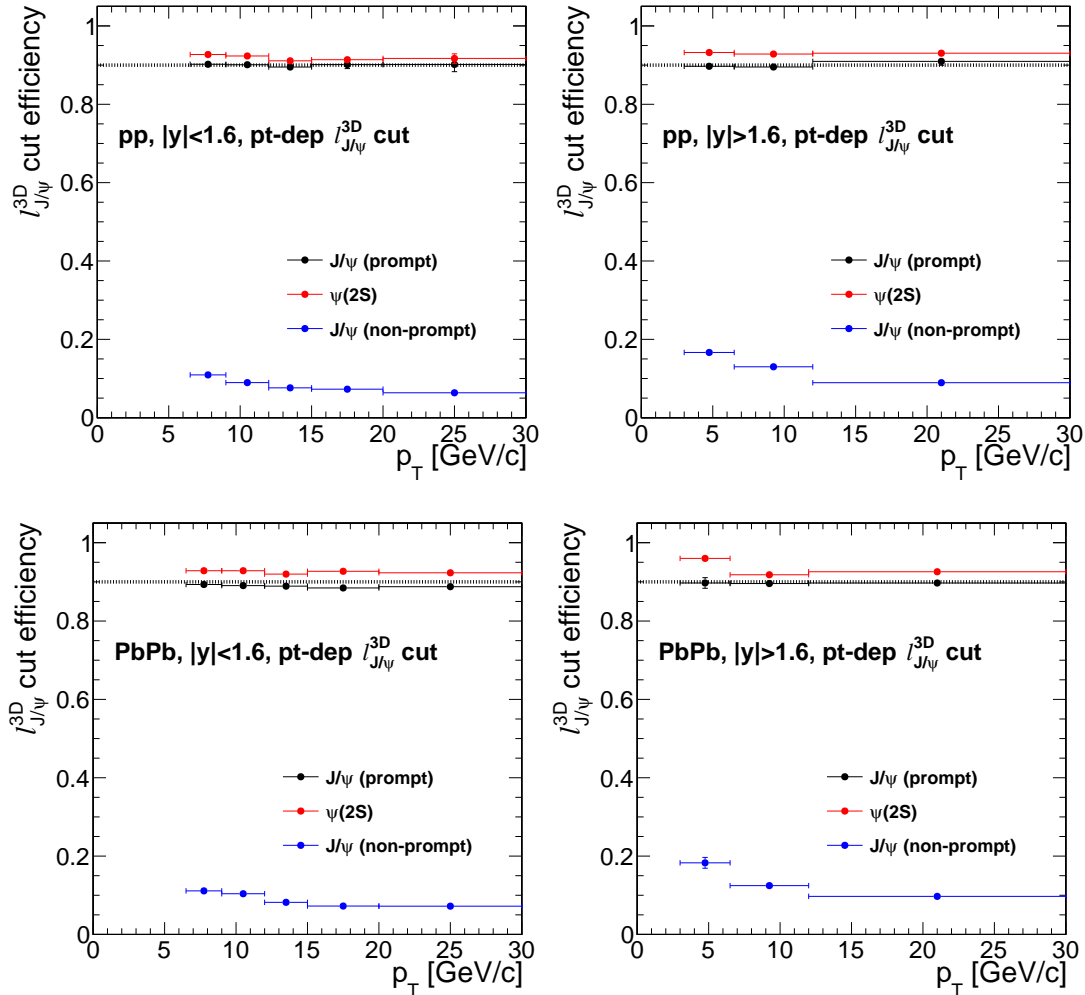


Figure 4.19: Efficiency of passing the  $\ell_{J/\psi}$  selection as a function of  $p_T^{\mu\mu}$  for prompt  $J/\psi$  (black points), prompt  $\psi(2S)$  (red points) and nonprompt  $J/\psi$  (blue points) mesons. The results are extracted from p-p (top) and Pb-Pb (bottom) simulations in the mid-rapidity (left) and forward rapidity (right) regions.

#### 4.2.5.2 Fits to the dimuon invariant mass distribution

The ratio of  $\psi(2\text{S})$  over  $\text{J}/\psi$  meson yields is extracted separately in p-p and Pb-Pb collisions by performing an unbinned maximum-likelihood fit to the  $m^{\mu\mu}$  distribution within the region  $2.2 < m_{\mu^+\mu^-} < 4.5 \text{ GeV}/c^2$ . The total fit model used is defined as:

$$F(m^{\mu\mu}) = N_{\text{J}/\psi} \cdot [M_{\text{J}/\psi}(m^{\mu\mu}) + R_\psi \cdot M_{\psi(2\text{S})}(m^{\mu\mu})] + N_{\text{bkg}} \cdot M_{\text{bkg}}(m^{\mu\mu}) \quad (4.29)$$

where  $R_\psi$  is the  $\psi(2\text{S})$ -to- $\text{J}/\psi$  yields ratio,  $N_{\text{J}/\psi}$  ( $N_{\text{bkg}}$ ) is the number of  $\text{J}/\psi$  meson (background) events, and  $M_i$  represents the  $m^{\mu\mu}$  functional form for each source of events.

The parametrisation of the signal and background  $m^{\mu\mu}$  distributions follows the same strategy used in Section 4.2.4.2. The shapes of  $\text{J}/\psi$  and  $\psi(2\text{S})$  mesons are described using a weighed sum of two Crystal Ball (CB) functions with common mean. Since the statistics in data is not enough for a reliable fit of the  $\psi(2\text{S})$  mass peak, the  $\psi(2\text{S})$  CB parameters are constrained to the  $\text{J}/\psi$  ones. The following criteria are used to constrain the  $\psi(2\text{S})$  CB parameters when performing the data fits:

- The tail parameters are taken to be the same between the  $\text{J}/\psi$  and  $\psi(2\text{S})$  CB functions ( $\alpha_{\psi(2\text{S})} = \alpha_{\text{J}/\psi}$ ,  $n_{\psi(2\text{S})} = n_{\text{J}/\psi}$ ).
- The weight of the  $\psi(2\text{S})$  CB components is fixed to the  $\text{J}/\psi$  CB weight ( $f_{\psi(2\text{S})} = f_{\text{J}/\psi}$ ).
- The  $\psi(2\text{S})$  CB mean parameter is fixed to the  $\text{J}/\psi$  CB mean multiplied by the mass ratio of  $\psi(2\text{S})$  over  $\text{J}/\psi$  mesons ( $m_{\psi(2\text{S})}/m_{\text{J}/\psi} = 1.1902$ ) [21].
- The two width parameters of the  $\psi(2\text{S})$  CB function are fixed to the corresponding  $\text{J}/\psi$  CB widths scaled by the  $\psi(2\text{S})$  to  $\text{J}/\psi$  mass ratio ( $\sigma_{\text{CB},i}^{\psi(2\text{S})} = (m_{\psi(2\text{S})}/m_{\text{J}/\psi}) \cdot \sigma_{\text{CB},i}^{\text{J}/\psi}$ ).

The  $\text{J}/\psi$  CB parameters are tuned using the prompt  $\text{J}/\psi$  simulations after applying the  $\ell_{\text{J}/\psi}$  selection defined in the previous section. The parameter values extracted from the p-p and Pb-Pb simulations are found to be in good agreement, and thus, the results obtained from the p-p simulation are used. The nominal values of the CB parameters are presented in Table 4.11, where those that appear in bold are fixed when performing the fits to  $m^{\mu\mu}$  distribution in data. The parameters that are left free in the data fits are: the weight of the CB components  $f_{\text{J}/\psi}$ , the mean parameter  $m_{\text{J}/\psi}$ , the width parameter  $\sigma_{\text{CB},1}^{\text{J}/\psi}$ , the number of  $\text{J}/\psi$  mesons  $N_{\text{J}/\psi}$ , and the ratio of  $\psi(2\text{S})$  over  $\text{J}/\psi$  meson yields  $R_\psi$ . When fitting the p-p data, the width parameter  $\sigma_{\text{CB},2}$  is also left free.

## 4.2. ANALYSIS

$y^{\mu\mu}$	$p_T^{\mu\mu}$ [GeV/c]	$f_{J/\psi}$	$\alpha_{J/\psi}$	$n_{J/\psi}$	$\sigma_{CB,2}/\sigma_{CB,1}$
0–1.6	6.5–30.0	0.71	<b>1.87</b>	<b>1.76</b>	1.94
1.6–2.4	3.0–30.0	0.82	<b>2.18</b>	<b>1.46</b>	1.79

Table 4.11: Parameters extracted for the double Crystal Ball function from the prompt  $J/\psi$ -meson p-p simulation after applying the  $\ell_{J/\psi}$  selection. The values shown correspond to the  $p_T$ -centrality integrated fits. The CB parameters fixed to simulation when performing the data fits are shown in bold font.

In the case of the background, the  $m^{\mu\mu}$  shape is modelled using a Chebyshev function of order  $N$ , where the order for each analysis bin is defined using a LLR test as performed in Section 4.2.4.2. The selected background Chebyshev functions are of first or second order.

The results of the fits to the  $m^{\mu\mu}$  distribution in Pb-Pb and p-p collisions, performed in the  $p_T$ -centrality-inclusive region at mid-rapidity after applying the  $\ell_{J/\psi}$  selection, are shown in Figure 4.20.

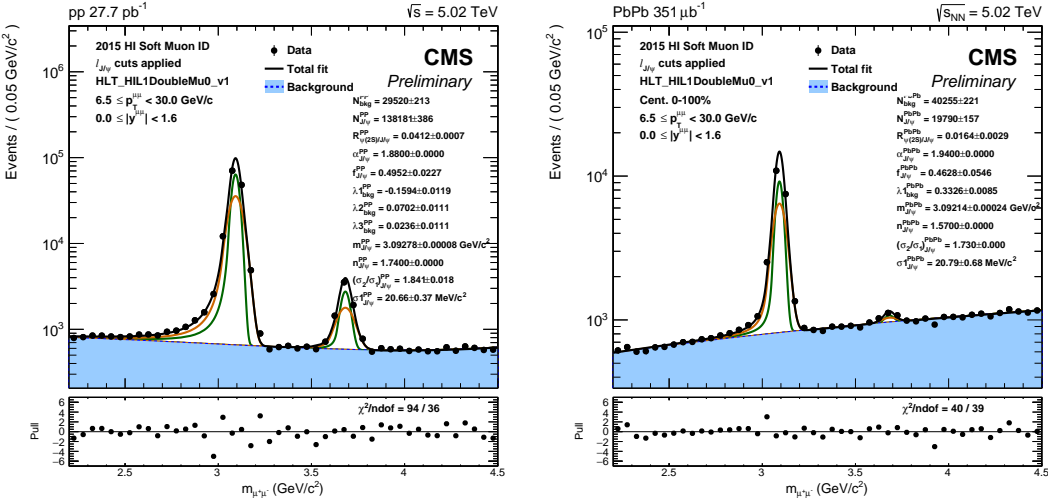


Figure 4.20: Fits to the  $m^{\mu\mu}$  distribution in p-p (left) and Pb-Pb (right) collisions. The results correspond to dimuon events derived in  $p_T$ -centrality-inclusive region at mid-rapidity after applying the  $\ell_{J/\psi}$  selection. The black line represents the total fit model while the blue filled area represents the fitted background shape.

### 4.2.5.3 Correction for nonprompt charmonium contamination

Since the main goal of the analysis is to measure the ratio of prompt  $\psi(2S)$  over  $J/\psi$  meson yields, it is important to correct for the amount of nonprompt charmonia that

remains after selecting dimuons with low  $\ell_{J/\psi}$ , even though they represent a small fraction of the sample. In order to do this, four categories of events are considered as illustrated in Figure 4.21, which are:

- (A): Prompt charmonia passing the  $\ell_{J/\psi}$  selection.
- (B): Nonprompt charmonia passing the  $\ell_{J/\psi}$  selection.
- (C): Prompt charmonia failing the  $\ell_{J/\psi}$  selection.
- (D): Nonprompt charmonia failing the  $\ell_{J/\psi}$  selection.

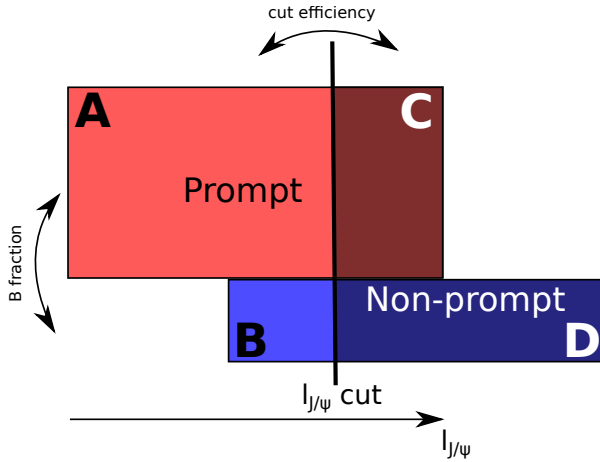


Figure 4.21: Definition of the different categories of events considered for the subtraction of nonprompt charmonia.

Based on the categories presented in Figure 4.21, the objective is to extract the number of *prompt*  $\psi$  ( $\psi(2S)$  or  $J/\psi$ ) mesons defined in the region  $A + C$ . The number of charmonia in the region  $A + B$  (labelled as *pass*) is extracted from the  $m^{\mu\mu}$  fits after selecting dimuons passing the  $\ell_{J/\psi}$  selection. Furthermore, the charmonium yields in the region  $C + D$  (referred as *fail*) are simply measured by inverting the  $\ell_{J/\psi}$  selection (i.e. selecting dimuons with high  $\ell_{J/\psi}$ ) and redoing the fits to the  $m^{\mu\mu}$  spectrum following the same procedure used in the previous section.

Using the  $\ell_{J/\psi}$  selection efficiencies estimated from the prompt ( $\epsilon_\psi^P$ ) and nonprompt ( $\epsilon_\psi^{NP}$ ) charmonium simulations, and the charmonium yields extracted from the  $m^{\mu\mu}$  fits after applying the  $\ell_{J/\psi}$  selection ( $N_\psi^{\text{pass}}$ ) and inverting it ( $N_\psi^{\text{fail}}$ ), one can derive the following equation:

$$N_\psi^{\text{pass}} = \left[ \epsilon_\psi^P \cdot f_\psi^P + \epsilon_\psi^{\text{NP}} \cdot (1 - f_\psi^P) \right] \cdot N_\psi^{\text{tot}} \quad (4.30)$$

where  $f_\psi^P$  is the fraction of prompt charmonia and  $N_\psi^{\text{tot}}$  is the total amount of  $\psi$  mesons (i.e.  $N_\psi^{\text{tot}} = N_\psi^{\text{pass}} + N_\psi^{\text{fail}}$ ). One can then deduce from Eq. (4.30) the number of prompt charmonia, given by:

$$N_\psi^P = f_\psi^P \cdot N_\psi^{\text{tot}} = \frac{N_\psi^{\text{pass}} - \epsilon_\psi^{\text{NP}} \cdot N_\psi^{\text{tot}}}{\epsilon_\psi^P - \epsilon_\psi^{\text{NP}}} \quad (4.31)$$

The ratios of prompt  $\psi(2S)$  over  $J/\psi$  meson yields are then determined for p-p and Pb-Pb collisions, according to:

$$R_\psi^P = \frac{N_{\psi(2S)}^P}{N_{J/\psi}^P} \quad (4.32)$$

The largest relative difference between the ratios of charmonium yields extracted from the  $m^{\mu\mu}$  distribution of dimuons passing the  $\ell_{J/\psi}$  selection ( $R_\psi^{\text{pass}}$ ) and the ratios of prompt charmonium yields ( $R_\psi^P$ ), is found to be 6% for p-p data and 18% for Pb-Pb data. Regarding the double ratio, the largest relative difference is 16%.

### 4.2.6 Charmonium acceptance and efficiency

This section presents the standard procedure used to estimate the charmonium acceptance and efficiency based on simulations. In order to improve the modelling of the  $p_T$  and rapidity spectra of charmonia, the kinematic distribution of the simulated dimuons are weighed as explained in Section 4.2.6.1. Afterwards, the  $J/\psi$  meson acceptance and efficiency are determined from simulations as described in Section 4.2.6.2 and Section 4.2.6.3, respectively. Then, the  $J/\psi$  meson efficiency is corrected using data-to-simulation efficiency ratios derived with the tag-and-probe method as detailed in Section 4.2.6.4. Finally, the double ratio of prompt  $\psi(2S)$  over  $J/\psi$  meson efficiencies in Pb-Pb relative to p-p collisions are checked to be consistent with unity in Section 4.2.6.5.

#### 4.2.6.1 Correction for charmonium $p_T$ and rapidity

The detector acceptance and efficiency depends on the  $p_T$  and rapidity distributions of the detected particles. In order to derive reliable estimations from charmonium simulations, it is important to ensure that the kinematic distributions of charmonia are as close as possible to that of real data.

To accomplish this, a weight is assigned to each simulated dimuon according to their  $y^{\mu\mu}$  and  $p_T^{\mu\mu}$ . This weight is obtained from the ratio of the  $J/\psi$ -meson  $p_T$  spectrum measured in data over the one derived from simulation, in the different rapidity regions used in the  $J/\psi$ -meson analysis. The number of observed prompt and nonprompt  $J/\psi$  mesons extracted from the 2D fits to the  $m^{\mu\mu}$  and  $\ell_{J/\psi}$  distributions in data, described in Section 4.2.4, are compared to the corresponding ones measured in the prompt and nonprompt  $J/\psi \rightarrow \mu^+ \mu^-$  simulations, respectively. The  $p_T^{\mu\mu}$  distributions in each rapidity region are normalised to the number of observed  $J/\psi$  mesons (prompt or nonprompt) in the inclusive region ( $|y^{\mu\mu}| < 2.4$  and  $3.0 < p_T^{\mu\mu} < 50$  GeV/c). The  $J/\psi$ -meson kinematic weights are then defined as:

$$w^{J/\psi}(p_T^{\mu\mu}, y^{\mu\mu}) = \frac{\frac{1}{N_{\text{data}}^{\mu\mu}} \frac{d^2 N_{\text{data}}^{\mu\mu}}{dp_T^{\mu\mu} dy^{\mu\mu}}(p_T^{\mu\mu}, y^{\mu\mu})}{\frac{1}{N_{\text{MC}}^{\mu\mu}} \frac{d^2 N_{\text{MC}}^{\mu\mu}}{dp_T^{\mu\mu} dy^{\mu\mu}}(p_T^{\mu\mu}, y^{\mu\mu})} \quad (4.33)$$

where  $N_{\text{data}}^{\mu\mu}$  and  $N_{\text{MC}}^{\mu\mu}$  are the number of  $J/\psi$  mesons measured in the inclusive region in data and simulation, respectively. The  $J/\psi$ -meson kinematic weights determined as a function of  $p_T^{\mu\mu}$ , in the mid-rapidity region, are presented in Figure 4.22. They are found to vary between 0.4 and 1.6 depending on  $p_T^{\mu\mu}$  and  $y^{\mu\mu}$ .

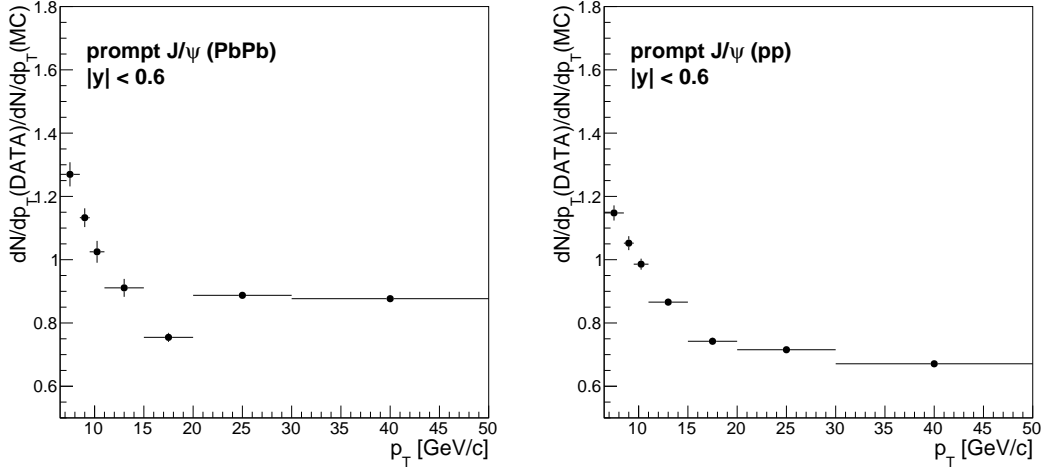


Figure 4.22: Data-to-simulation ratios of the prompt  $J/\psi$ -meson  $p_T$  distribution measured in the  $|y^{\mu\mu}| < 0.6$  rapidity region, in Pb-Pb (left) and p-p (right) collisions.

### 4.2.6.2 Acceptance of $\text{J}/\psi$ mesons

The  $\text{J}/\psi$ -meson acceptance is estimated using the p-p simulations. It is defined as the fraction of generated  $\mu^+\mu^-$  pairs from  $\text{J}/\psi$ -meson decays, with each muon satisfying the kinematic selection (labelled as *in CMS*) listed in Section 4.2.3.5. The modelling of the  $p_{\text{T}}$  and rapidity of prompt and nonprompt  $\text{J}/\psi$  mesons is improved by weighing each generated dimuon, based on their  $p_{\text{T}}^{\mu\mu}$  and  $y^{\mu\mu}$  values, using the  $\text{J}/\psi$ -meson kinematic weights  $w^{\text{J}/\psi}$  defined in the previous section. The  $\text{J}/\psi$ -meson acceptance ( $\mathcal{A}_{\text{J}/\psi}$ ) is determined as a function of the generated dimuon  $p_{\text{T}}$  and rapidity, according to:

$$\mathcal{A}_{\text{J}/\psi}(p_{\text{T}}^{\mu\mu}, y^{\mu\mu}) = \frac{N_{\text{gen},\mu \text{ in CMS}}^{\text{J}/\psi \rightarrow \mu^+\mu^-}(p_{\text{T}}^{\mu\mu}, y^{\mu\mu})}{N_{\text{gen}}^{\text{J}/\psi \rightarrow \mu^+\mu^-}(p_{\text{T}}^{\mu\mu}, y^{\mu\mu})} \quad (4.34)$$

where  $N_{\text{gen}}^{\text{J}/\psi \rightarrow \mu^+\mu^-}(p_{\text{T}}^{\mu\mu}, y^{\mu\mu})$  is the number of generated dimuons in a given  $p_{\text{T}}^{\mu\mu}$  and  $y^{\mu\mu}$  range, and  $N_{\text{gen},\mu \text{ in CMS}}^{\text{J}/\psi \rightarrow \mu^+\mu^-}(p_{\text{T}}^{\mu\mu}, y^{\mu\mu})$  represents the number of those satisfying the muon kinematic selection.

The  $\text{J}/\psi$ -meson acceptance derived from the prompt  $\text{J}/\psi$  simulations is presented in Figure 4.23. The trend observed as a function of dimuon  $p_{\text{T}}$  and rapidity is caused by the CMS muon kinematic coverage.  $\text{J}/\psi$  mesons produced in the forward region or at higher  $p_{\text{T}}$  are more likely to decay to muons that reach the CMS muon stations than those produced at mid-rapidity or lower  $p_{\text{T}}$ .

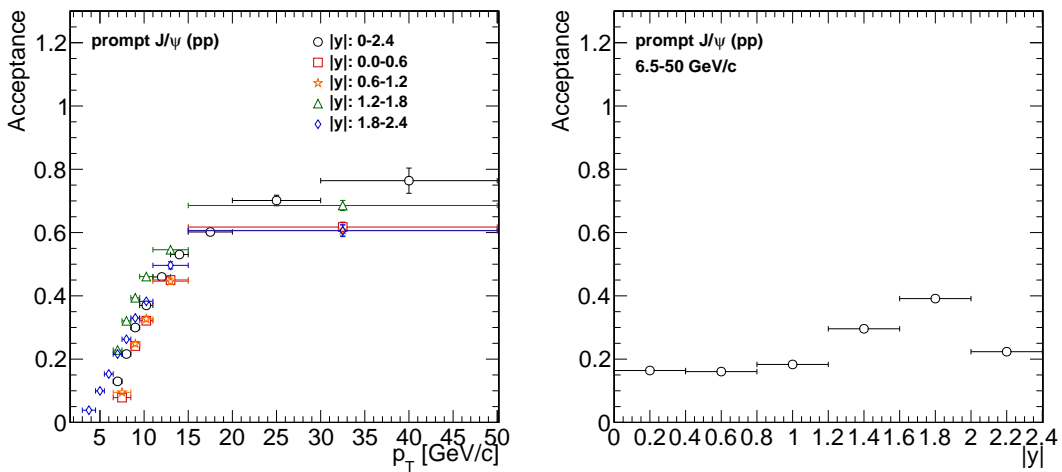


Figure 4.23: Acceptance of prompt  $\text{J}/\psi$  mesons, estimated from simulations, as a function of  $p_{\text{T}}^{\mu\mu}$  (left) and  $y^{\mu\mu}$  (right). The error bars represent the statistical uncertainties.

#### 4.2.6.3 Efficiency of $\text{J}/\psi$ mesons

The  $\text{J}/\psi \rightarrow \mu^+ \mu^-$  simulations are used to measure the efficiency of prompt and nonprompt  $\text{J}/\psi$  mesons, in p-p and Pb-Pb collisions. In this case, a reconstructed  $\mu^+ \mu^-$  pair satisfying the charmonium selection requirements, detailed in Sections 4.2.3.4 to 4.2.3.6, is referred to as a dimuon candidate in the following. Among these selection criteria, each reconstructed muon is required to satisfy the muon kinematic selection and identification criteria, and match the trigger. Also, the two muon tracks of the dimuon candidate are required to derive from a common vertex with  $\chi^2$  probability larger than 1%.

The  $\text{J}/\psi$ -meson efficiency is defined as the fraction of generated  $\mu^+ \mu^-$  pairs in the acceptance that can be matched to a dimuon candidate, with each generated muon satisfying the kinematic selection. The matching between a generated dimuon and a dimuon candidate is performed by requiring that each generated and reconstructed muon of same charge are within  $\Delta R(\mu_{\text{gen}}, \mu_{\text{reco}}) < 0.03$ . The  $p_{\text{T}}$  and rapidity spectra of the dimuon candidates and generated dimuons are weighed per event with the  $w^{\text{J}/\psi}$  kinematic weights, as was done in the previous section. The  $\text{J}/\psi$ -meson efficiency ( $\epsilon_{\text{J}/\psi}$ ) is computed as a function of the dimuon  $p_{\text{T}}$  and rapidity, according to:

$$\epsilon_{\text{J}/\psi}(p_{\text{T}}^{\mu\mu}, y^{\mu\mu}) = \frac{N_{\text{candidate}}^{\text{J}/\psi \rightarrow \mu^+ \mu^-}(p_{\text{T}}^{\mu\mu}, y^{\mu\mu})}{N_{\text{gen, } \mu \text{ in CMS}}^{\text{J}/\psi \rightarrow \mu^+ \mu^-}(p_{\text{T}}^{\mu\mu}, y^{\mu\mu})} \quad (4.35)$$

where  $N_{\text{candidate}}^{\text{J}/\psi \rightarrow \mu^+ \mu^-}$  and  $N_{\text{gen, } \mu \text{ in CMS}}^{\text{J}/\psi \rightarrow \mu^+ \mu^-}$  are the number of dimuon candidates and generated dimuons within the kinematic acceptance of the analysis, accordingly.

#### 4.2.6.4 Efficiency of $\text{J}/\psi$ mesons corrected with the tag-and-probe method

In order to take into account possible discrepancies between the muon efficiencies in simulation and those in data, the  $\text{J}/\psi$ -meson efficiencies are corrected with a set of data-to-simulation corrections provided by the CMS HIN group and derived using the tag-and-probe method. This collective work, to which I only participated marginally, is documented in an internal analysis note [247].

The TnP corrections for Pb-Pb and p-p efficiencies are computed following a procedure similar to the one used for p-Pb collisions, which is described in detail in Section 3.2.6.2. The main difference is that it addresses lower muon momentum. To provide these muons, a sample of  $\text{J}/\psi$  mesons is used instead of Z bosons. Thus, the TnP corrections are extracted from the prompt  $\text{J}/\psi \rightarrow \mu^+ \mu^-$  simulations and from a data sample of single muon events selected with the HLT trigger. The TnP method is used to measure

the standalone-muon reconstruction, tracking, identification and trigger efficiencies in data and simulation. Apart from the different muon identification and trigger criteria, these TnP efficiencies are probed in the same way as done for p-Pb collisions. The TnP efficiencies are extracted by fitting the tag-probe invariant mass distribution, within the  $J/\psi$  mass region ( $2.6 < m^{\mu\mu} < 3.5 \text{ GeV}/c^2$ ), for probes passing and failing the criteria of each efficiency under study.

After comparing the TnP efficiencies extracted from data and simulation, it is found that the muon simulated efficiencies for standalone-muon reconstruction, tracking and identification, are in good agreement with the data efficiencies. However, the trigger efficiencies are observed to disagree between simulation and data both in p-p and Pb-Pb collisions, as shown in Figure 4.24. As a result, only the simulated trigger efficiency requires a correction.

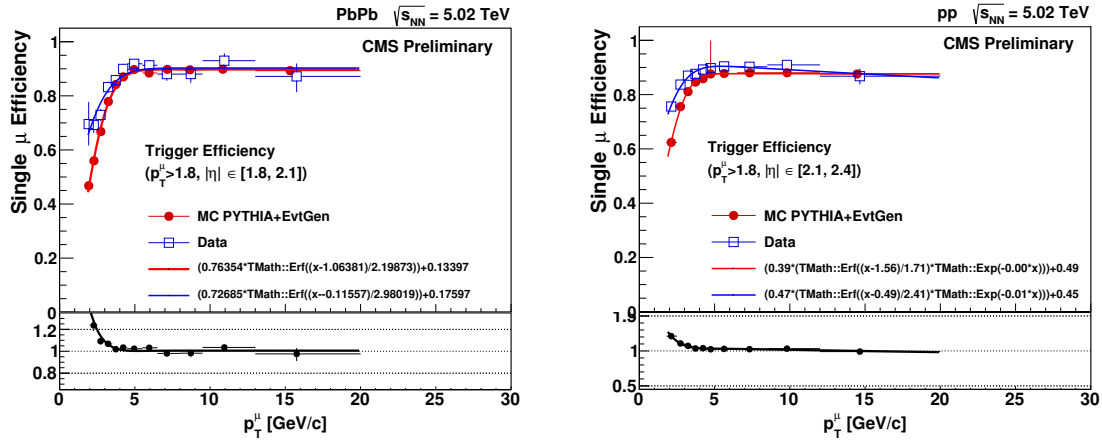


Figure 4.24: Muon trigger efficiencies as a function of the probe  $p_T$ . The efficiencies are extracted, using the TnP method, from data (blue) and simulation (red) in Pb-Pb collisions at  $1.8 < |\eta^\mu| < 2.1$  (left) and p-p collisions at  $2.1 < |\eta^\mu| < 2.4$  (right). The bottom panels show the data-to-simulation efficiency ratio. The results of the fits to the efficiencies are also shown. Figures taken from the internal analysis note [247].

The muon trigger efficiencies are measured with respect to the probe  $p_T$ , in four  $|\eta|$  regions with boundaries: [0.0, 1.2, 1.8, 2.1, 2.4]. The  $p_T$  dependence in each  $|\eta|$  region is parametrised with a function of the form  $f_{\text{trig}}(p_T) = c_1 \cdot \text{Erf}[(p_T - c_2)/c_3] \cdot \exp[c_4 \cdot p_T] + c_5$ , where Erf is the error function and  $c_i$  are free parameters. The TnP-correction weight for the trigger efficiency is then derived from the ratio of the fitted functions, extracted from data and simulation, as a function of probe  $p_T$  in each  $|\eta|$  region, given by:

$$w_{\text{trig}}(p_T, |\eta|) = \left[ \frac{f_{\text{trig}}^{\text{data}}(p_T)}{f_{\text{trig}}^{\text{MC}}(p_T)} \right] (|\eta|) \quad (4.36)$$

To apply the TnP corrections, the  $J/\psi$ -meson efficiency is recomputed by weighing each dimuon candidate with the TnP-correction weights for each muon to trigger, according to:

$$\epsilon_{J/\psi} = \frac{\left[ \sum_{i=1}^{N_{\text{candidate}}^{J/\psi \rightarrow \mu^+ \mu^-}} w_{\text{trig}}(p_T^{\mu,+}, |\eta^{\mu,+}|) \cdot w_{\text{trig}}(p_T^{\mu,-}, |\eta^{\mu,-}|) \right]}{N_{\text{gen, } \mu \text{ in CMS}}^{J/\psi \rightarrow \mu^+ \mu^-}} \quad (4.37)$$

where  $p_T^{\mu,+(\mu,-)}$  is the transverse momentum of positive (negative) charged muons, and  $\eta^{\mu,+(\mu,-)}$  is the corresponding pseudorapidity.

In the worst case, for  $3 < p_T^{\mu\mu} < 4.5$   $\text{GeV}/c$ , the TnP correction increases the  $J/\psi$ -meson efficiency by a factor of 1.35 (from 31% to 42%) and 1.38 (from 16% to 22%) in p-p and Pb-Pb collisions, respectively. This is mostly due to a bad emulation of the L1 trigger at low  $p_T$  in the simulation, proving the importance of the data-driven efficiency correction. The effect decreases with  $p_T$  ending up with corrections of less than 4% for  $p_T > 10$   $\text{GeV}/c$ . The corrected  $J/\psi$ -meson efficiencies are shown for p-p and Pb-Pb simulated events in Figure 4.25 and Figure 4.26, respectively.

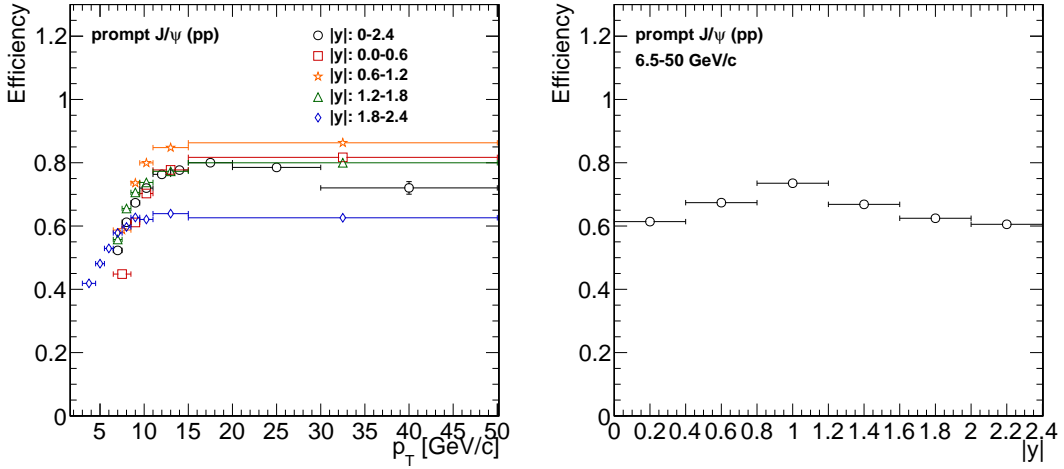


Figure 4.25: Corrected efficiencies of prompt  $J/\psi$  mesons measured in p-p collisions. Left: as a function of  $p_T^{\mu\mu}$  in different rapidity regions. Right: as function of rapidity. The error bars represent statistical uncertainties.

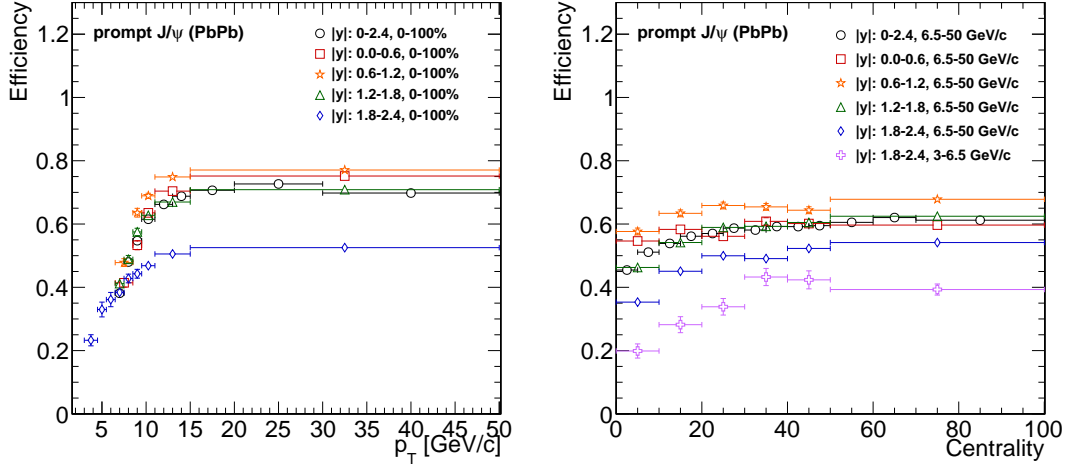


Figure 4.26: Corrected efficiencies of prompt  $J/\psi$  mesons measured in Pb-Pb collisions, as a function of  $p_T^{\mu\mu}$  (left) and centrality (right), in different rapidity regions. The error bars represent statistical uncertainties.

#### 4.2.6.5 Double ratio of prompt $\psi(2S)/J/\psi$ efficiencies

Since the prompt  $\psi(2S)$  and  $J/\psi$  mesons have similar masses and production mechanisms, it is expected that their efficiencies cancel at first order when measuring the double ratio of prompt charmonium yields in Pb-Pb relative to p-p collisions. In order to check this, the efficiency of  $\psi(2S)$  mesons ( $\epsilon_{\psi(2S)}$ ) is estimated from the prompt  $\psi(2S) \rightarrow \mu^+ \mu^-$  simulation, following the same procedure used to determine the  $J/\psi$  meson efficiency, described in the previous sections.

The prompt  $\psi(2S)$  and  $J/\psi$  meson efficiencies are computed in p-p and Pb-Pb collisions, including the  $\ell_{J/\psi}$  selection defined in Section 4.2.5, and the double ratio of prompt charmonium efficiencies is then computed as:

$$\chi^{\psi(2S)/J/\psi} = \frac{\left(\epsilon_{\psi(2S)} / \epsilon_{J/\psi}\right)_{\text{PbPb}}}{\left(\epsilon_{\psi(2S)} / \epsilon_{J/\psi}\right)_{\text{pp}}} \quad (4.38)$$

The results of the double ratio of prompt charmonium efficiencies are presented in Figure 4.27. It is observed that the  $\chi^{\psi(2S)/J/\psi}$  is consistent with unity overall as expected. Thus, the measurements of the double ratio of prompt charmonium yields do not require to be corrected for detector efficiency, and the difference with respect to unity is assigned as a systematic uncertainty as detailed in Section 4.2.8.2.

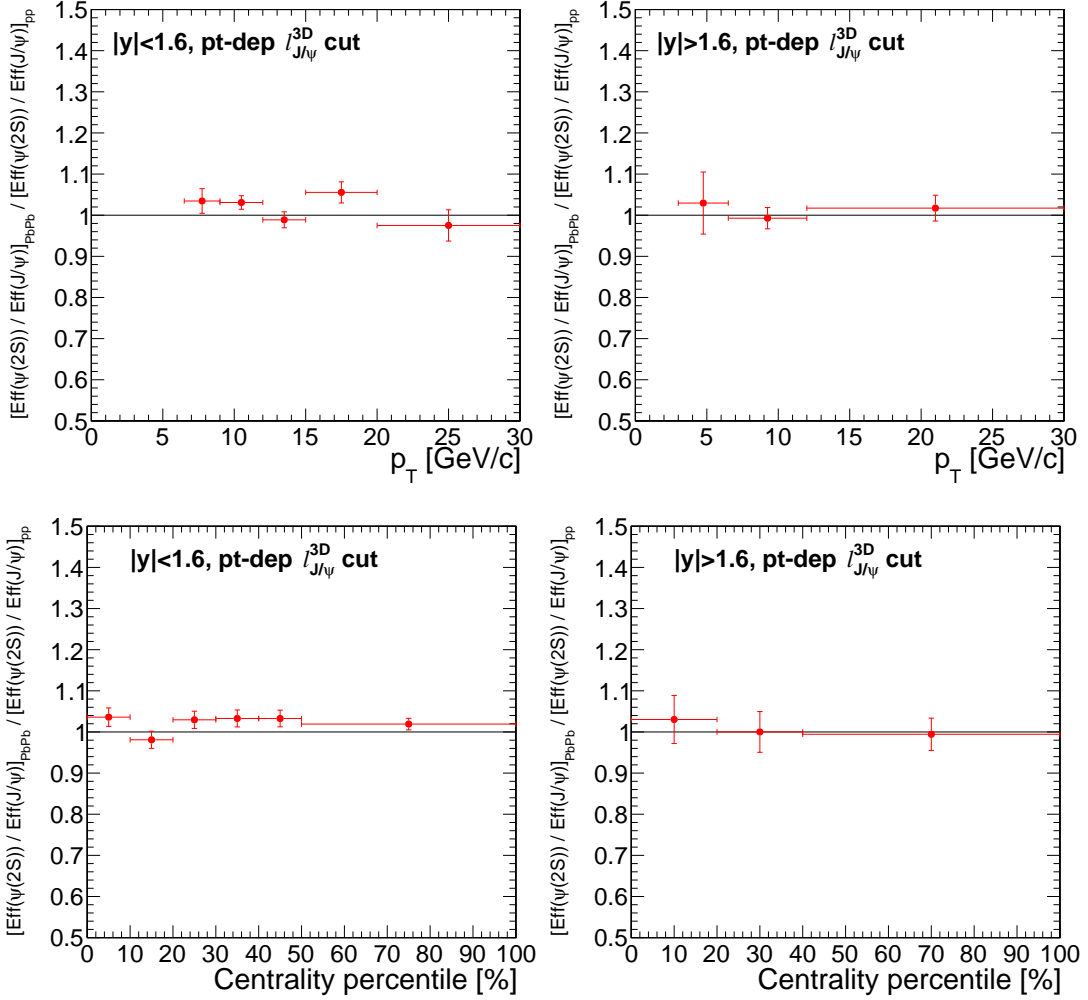


Figure 4.27: Double ratios of prompt charmonium efficiencies as a function of  $p_T^{\mu\mu}$  (top) and centrality (bottom), in the rapidity regions:  $|y^{\mu\mu}| < 1.6$  (left) and  $|y^{\mu\mu}| > 1.6$  (right). The error bars represent statistical uncertainties.

#### 4.2.7 Systematic uncertainties of $J/\psi$ -meson yields

This section describes the procedure used to derive the systematic uncertainties associated to the measurement of the prompt and nonprompt  $J/\psi$ -meson yields. The different sources of systematic uncertainties arise from: the parametrisation of the dimuon invariant mass and pseudoproper-decay length distributions used to extract the signal, and the estimation of the efficiency of  $J/\psi$  mesons. In this case, the leading systematic uncertainty of the  $J/\psi$ -meson measurements in p-p and Pb-Pb collisions correspond to the TnP efficiency corrections and the  $\ell_{J/\psi}$  parametrisation, respectively. When describing

each systematic source, the corresponding largest relative uncertainty is mentioned.

#### 4.2.7.1 Uncertainty on the dimuon invariant mass parametrisation

The uncertainty associated to the modelling of the  $m^{\mu\mu}$  distribution arises from the parametrisation of the signal and background invariant mass shape. It is determined by varying the different components of the  $m^{\mu\mu}$  functional form and redoing the 2D data fits, while using the nominal  $\ell_{J/\psi}$  functional form.

**Parametrisation of the  $J/\psi$ -meson invariant mass distribution.** In order to estimate the systematic uncertainty associated to the choice of the  $J/\psi$ -meson invariant mass shape, two variations are performed:

- **Variation of the  $J/\psi$ -meson invariant mass parameters:** the parameters fixed to simulation (i.e. the tail parameters  $\alpha_{J/\psi}$  and  $n_{J/\psi}$ , and the ratio of CB widths) are released and the data fits are repeated. To improve the convergence of the fits, a set of Gaussian penalty functions, centred in the nominal value of the corresponding parameters, are added to constrain their range of variation.

The range of variation of  $\alpha_{J/\psi}$ ,  $n_{J/\psi}$  and the ratio of CB widths is determined from data by redoing the  $m^{\mu\mu}$  fits, leaving only one parameter free at the time while the other parameters are fixed to their nominal values. The RMS of the difference between the parameter value extracted from the data fit and the nominal one is computed including the results from different  $p_T^{\mu\mu}$  and centrality intervals within each rapidity region, and the largest RMS obtained among the different rapidity regions is taken as the width of the corresponding Gaussian penalty function. The RMS is defined here as:

$$\text{RMS} = \sqrt{\frac{1}{\sum_i 1/(\sigma_{\text{data}}^i)^2} \cdot \sum_i \frac{(\text{par}_{\text{MC}} - \text{par}_{\text{data}}^i)^2}{(\sigma_{\text{data}}^i)^2}} \quad (4.39)$$

where the sum runs over different  $p_T$  and centrality bins in the same rapidity region,  $\text{par}_{\text{data}}^i$  and  $\sigma_{\text{data}}^i$  is the value and uncertainty of the parameter extracted from the data fit in a given analysis bin  $i$ , respectively, and  $\text{par}_{\text{MC}}$  is the corresponding nominal value derived from simulation. The width of the Gaussian penalty functions of each CB parameter is presented, relative to the nominal parameter value, in Table 4.12.

System	$\alpha_{J/\psi}$ [%]	$n_{J/\psi}$ [%]	$\sigma_{CB,2}/\sigma_{CB,1}$ [%]
p-p	16	21	
Pb-Pb	21	54	30

Table 4.12: Relative width used in the Gaussian penalty functions for the tail parameters  $\alpha_{J/\psi}$  and  $n_{J/\psi}$ , and the ratio of CB widths. The Gaussian width is shown relative to the nominal parameter value.

The  $n_{J/\psi}$  parameter presents the largest relative width due to the lack of statistics in data, especially in Pb-Pb collisions, to effectively constrain its value. Nonetheless, it is to be noted that the tails contribute to a very small fraction of the signal events as seen in Figure 4.11. Thus, variations of the CB tail parameters do not impact significantly the signal yields extracted from data.

The systematic uncertainty associated to the determination of the signal mass parameters from simulations is estimated by performing the data fits with the Gaussian penalty functions, and the difference between the varied  $J/\psi$ -meson yields and the nominal results is taken as the uncertainty.

- **Variation of the  $J/\psi$ -meson invariant mass model:** the functional form of the signal invariant mass shape is changed from the nominal double Crystal Ball function to a Crystal Ball plus a Gaussian function (with common mean parameters), defined as:

$$M_{J/\psi}(m_{\mu^+\mu^-}) = f_{J/\psi} \cdot \text{CB}(m^{\mu\mu}) + (1 - f_{J/\psi}) \cdot \text{Gauss}(m^{\mu\mu}) \quad (4.40)$$

As in the nominal case, the parameters of the alternative signal  $m^{\mu\mu}$  model are tuned from fits to the  $J/\psi$ -meson simulations, and the tail parameters  $\alpha_{J/\psi}$  and  $n_{J/\psi}$  are fixed to simulation in both p-p and Pb-Pb data fits, while the ratio of CB over Gaussian widths ( $\sigma_{CB}/\sigma_G$ ) is fixed only in the Pb-Pb data fits.

The systematic uncertainty on the signal shape parametrisation is then determined from the quadratic sum of the uncertainties obtained from varying the invariant mass parameters and the shape model. The corresponding uncertainty for prompt and non-prompt  $J/\psi$  mesons amounts to 1.2% (2.7%) and 2.4% (2.7%), in p-p (Pb-Pb) collisions, respectively.

**Parametrisation of the background invariant mass shape.** In the case of the background invariant mass parametrisation, three variations are performed to derive the corresponding systematic uncertainty, given by:

- **Variation of the LLR test threshold:** the  $\chi^2$  probability threshold is increased from the nominal value (5%) to 10% and reduced to 2.5%, and the LLR tests are repeated for each threshold. The background models selected from each LLR test are then used to redo the 2D fits.
- **Variation of the dimuon invariant mass fitting range:** the range of the  $m^{\mu\mu}$  distribution used in the 2D fits is changed from 2.6-3.5 GeV/c<sup>2</sup> to 2.6-3.4 GeV/c<sup>2</sup>. The 2D fits are then remade using the same orders of Chebyshev functions as used in the nominal fits.
- **Variation of the background invariant mass model:** the background  $m^{\mu\mu}$  functional form is changed from the nominal Chebyshev function to an exponential of a Chebyshev function, defined as:

$$M_{\text{bkg}}^N(m^{\mu\mu}) = \exp \left[ \sum_{i=0}^N c_i T_i(m^{\mu\mu}) \right] \quad (4.41)$$

where  $T$  are Chebyshev polynomials and  $c$  are free parameters. As in the nominal analysis, the  $m^{\mu\mu}$  distribution in data is fitted using the alternative background model with orders between 0 and 6, and the LLR test is employed with a 5% threshold to decide the best order in each analysis bin.

The uncertainty associated to each systematic variation is determined by computing the deviation of the measured prompt and nonprompt J/ $\psi$ -meson yields from the nominal results. In the case of the two variations done for the LLR test threshold, the maximum deviation between the two variations is taken for each J/ $\psi$ -meson yield. The systematic uncertainties of the different sources are combined by adding them in quadrature. The combined uncertainty amounts to 0.6% (3.0%) for prompt J/ $\psi$  mesons and 1.6% (2.9%) for nonprompt J/ $\psi$  mesons, in p-p (Pb-Pb) collisions.

#### 4.2.7.2 Uncertainty on the pseudoproper-decay length parametrisation

The different systematic variations performed for the pseudoproper-decay length parametrisation are summarised as follows:

1. Modelling of the  $\sigma_\ell$  distribution: replace the nominal signal and background  $\sigma_\ell$  templates in the 2D fits with the template of the total  $\sigma_\ell$  distribution.
2. Parametrisation of the  $\ell_{J/\psi}$  resolution: parametrise the  $\ell_{J/\psi}$  resolution model using the simulated sample of prompt  $J/\psi$  mesons instead of data.
3. Parametrisation of the nonprompt  $J/\psi$ -meson  $\ell_{J/\psi}$  shape: replace the exponential  $\ell_{J/\psi}$  model used to describe nonprompt  $J/\psi$  mesons in the 2D fits with a template of the  $\ell_{J/\psi}$  distribution derived from simulation.
4. Parametrisation of the background  $\ell_{J/\psi}$  shape: use a template of the  $\ell_{J/\psi}$  distribution from the background-like dataset derived with  $sPlot$ , instead of a functional form.

The method and result of these four sources are detailed below, and the resulting uncertainties are summed in quadrature with the other systematic sources.

**Modelling of the  $\sigma_\ell$  distribution.** To estimate the uncertainty associated to the use of the signal and background  $\sigma_\ell$  template histograms, derived from the  $sPlot$  background- and signal-like datasets, the template histograms of the signal and background are made instead using the full  $\sigma_\ell$  distribution and the 2D fits are remade. The difference between the varied and nominal  $J/\psi$  meson yields is taken as the systematic uncertainty, which amounts to 0.6% (6.3%) for prompt  $J/\psi$  mesons and 2.1% (4.2%) for nonprompt  $J/\psi$  mesons, in p-p (Pb-Pb) collisions.

**Parametrisation of the  $\ell_{J/\psi}$  resolution.** The systematic uncertainty due to the parametrisation of the  $\ell_{J/\psi}$  resolution is estimated by extracting the  $\ell_{J/\psi}$  resolution parameters from  $J/\psi$ -meson simulations instead of the data. The  $\ell_{J/\psi}$  resolution parameters are extracted from simulated samples of prompt  $J/\psi$  mesons by fitting the nominal  $\ell_{J/\psi}$  resolution model (weighed sum of three Gaussians) to the simulated  $\ell_{J/\psi}$  distribution. The varied  $\ell_{J/\psi}$  resolution parameters are then used to remake the 2D fits and the uncertainty is derived from the difference between the varied  $J/\psi$ -meson yields and the nominal ones. This systematic uncertainty amounts in p-p (Pb-Pb) collisions to 1.5% (4.7%) for prompt  $J/\psi$  mesons and 5.3% (9.6%) for nonprompt  $J/\psi$  mesons.

**Parametrisation of the nonprompt  $J/\psi$ -meson  $\ell_{J/\psi}$  shape.** The systematic uncertainty associated to the modelling of the  $\ell_{J/\psi}$  distribution of nonprompt  $J/\psi$  mesons is computed by replacing the nominal signal functional form (convolution of exponential

decay with  $\ell_{J/\psi}$  resolution model) with an unbinned template of the reconstructed  $\ell_{J/\psi}$  distribution derived from simulation of nonprompt  $J/\psi$  mesons. The  $\ell_{J/\psi}$  templates are made using a kernel estimation technique [248], implemented in the RooFit framework, which parametrises the distribution of a given variable by superimposing a Gaussian function to each data point. The uncertainty is then determined from the difference between the varied signal yields and the nominal results, and reaches up to 0.8% (3.4%) for prompt  $J/\psi$  mesons and 2.1% (12.1%) for nonprompt  $J/\psi$  mesons, in p-p (Pb-Pb) collisions.

**Parametrisation of the background  $\ell_{J/\psi}$  shape.** The systematic uncertainty related to the choice of background  $\ell_{J/\psi}$  model is determined by replacing the nominal background functional form (three exponential decay functions convolved with the  $\ell_{J/\psi}$  resolution model) with an unbinned template. The template is built from the  $\ell_{J/\psi}$  distribution of the `sPlot` background-like dataset employed in Section 4.2.4.4, using the RooFit kernel estimation technique. This uncertainty contributes in p-p (Pb-Pb) collisions up to 0.5% (10%) for prompt  $J/\psi$  mesons and 1.2% (22.3%) for nonprompt  $J/\psi$  mesons.

#### 4.2.7.3 Uncertainty on the $J/\psi$ -meson efficiency

There are two main sources of systematics that affect the measurement of the  $J/\psi$ -meson efficiencies: the TnP-correction weights used to correct the simulated efficiencies and the charmonium  $p_T^{\mu\mu} \cdot y^{\mu\mu}$  weights applied to improve the modelling of the  $J/\psi$ -meson  $p_T$  and rapidity. Among these two, the largest uncertainty is obtained from the TnP corrections, which is dominated by the uncertainty on the extraction of the standalone-muon reconstruction efficiency in data.

**Tag-and-probe correction.** The uncertainty associated to the TnP correction derives from the measurement of the TnP data efficiency of muon identification, trigger, tracking and standalone-muon reconstruction.

Regarding the tracking efficiency, an overall systematic uncertainty is determined from the largest difference found between data and simulation, which corresponds to a relative uncertainty on the  $J/\psi$ -meson yields measured in p-p and Pb-Pb collisions of 1.0% and 2.4%, respectively. On the other hand, for the standalone-muon reconstruction, trigger and muon identification, the uncertainties of the TnP-correction weights are separated in a statistical and systematic component. The statistical component of the TnP-correction uncertainty is evaluated by producing a hundred sets of TnP-correction weights, where each point is randomly generated using a Gaussian distribution spread

according to its statistical uncertainty. The hundred sets of TnP-correction weights are then used to recompute the  $J/\psi$ -meson efficiencies and the corresponding systematic uncertainty is estimated by computing the RMS of the hundred variations of the prompt and nonprompt  $J/\psi$ -meson efficiencies. The systematic component of the TnP-correction uncertainty is propagated using two sets of TnP-correction weights generated by shifting all points up and down, according to the systematic uncertainty of each point (derived by varying the settings of the TnP invariant mass fits). The  $J/\psi$ -meson efficiencies are then corrected with each set of TnP-correction weights and the maximum deviation of the two varied efficiencies with respect to the nominal one is taken as the systematic uncertainty on the efficiency of prompt and nonprompt  $J/\psi$  mesons.

The statistical component of the TnP uncertainty represents 1.5% (4.6%) for the p-p (Pb-Pb) efficiencies. Regarding the systematic components of the TnP uncertainty, the largest uncertainty is obtained from the standalone-muon reconstruction efficiency, which corresponds to 9.6%, while the TnP-correction uncertainties associated to the trigger and muon identification efficiencies in p-p (Pb-Pb) collisions amounts to 0.5% (5.2%) and to 1.1% (3.3%), respectively.

**Charmonium transverse momentum and rapidity weighing.** The simulated samples of  $J/\psi$  mesons are weighed as a function of dimuon  $p_T$  and rapidity, to match the  $p_T$  spectrum of prompt and nonprompt  $J/\psi$  mesons observed in data in four rapidity regions. In order to estimate the uncertainty of the weighing procedure, a hundred sets of weights are randomly generated using a Gaussian distribution for each  $p_T^{\mu\mu}$ - $y^{\mu\mu}$  interval, where the Gaussian width is fixed to the uncertainty of the corresponding dimuon kinematic weight. The simulations are reweighed with each set of generated dimuon kinematic weights and then used to recompute the efficiencies of prompt and nonprompt  $J/\psi$  mesons. The corresponding systematic uncertainty is then determined from the RMS of the hundred varied efficiencies compared to the nominal efficiency for prompt and nonprompt  $J/\psi$  mesons. In this case, the largest relative uncertainty on the p-p (Pb-Pb)  $J/\psi$ -meson efficiencies corresponds to 0.2% (1.8%).

#### 4.2.8 Systematic uncertainties on the $\psi(2S)/J/\psi$ ratio

This section is dedicated to the systematic uncertainties that contributes in the measurement of the  $(N_{\psi(2S)}/N_{J/\psi})_{\text{PbPb}}/(N_{\psi(2S)}/N_{J/\psi})_{\text{pp}}$  double ratio. Three sources of systematics are accounted for: the parametrisation of the dimuon invariant mass used in the signal

extraction, the degree of cancellation of the charmonium efficiencies in the double ratio and the subtraction of the nonprompt charmonium component.

#### 4.2.8.1 Uncertainty on the dimuon invariant mass parametrisation

A large part of the method used to determine the uncertainty on the signal and background  $m^{\mu\mu}$  shape parametrisation is common to the one used for the prompt and nonprompt  $J/\psi$  meson yields, presented in Section 4.2.7.1. Indeed, the  $\psi(2S)$ -to- $J/\psi$  double ratio analysis was performed first and was less demanding in terms of systematic uncertainties, due to the limited  $\psi(2S)$  statistics. However, it served as a basis for the  $J/\psi$ -meson yield analysis and all the sources considered here were kept.

The functional forms of the  $J/\psi$ -meson,  $\psi(2S)$ -meson and background invariant mass shape are varied accordingly and the fits to data are remade. The nominal background shape is used when varying the signal functional form and vice versa. The variations performed on the signal functional forms includes:

- varying the CB parameters fixed to simulation ( $\alpha_{J/\psi}$ ,  $n_{J/\psi}$  and  $\sigma_{CB,2}/\sigma_{CB,1}$ ) in the following way:
  1. setting  $\alpha_{J/\psi}$  free while keeping  $n_{J/\psi}$  (and  $\sigma_{CB,2}/\sigma_{CB,1}$  in Pb-Pb fits) fixed to simulation;
  2. setting  $n_{J/\psi}$  free while keeping  $\alpha_{J/\psi}$  fixed (only done for p-p data since the Pb-Pb data fits did not converge);
  3. fixing the CB parameters to their corresponding values derived from the prompt  $\psi(2S)$ -meson simulation, instead of the  $J/\psi$ -meson simulation.
- changing the signal shape model by using a Gaussian plus a Crystal Ball function (with common mean), instead of the nominal double Crystal Ball function. The alternative model parameters are tuned and fixed in the same way as done for the nominal model;

In the case of the background functional form, the following variations are done:

- the fitted dimuon invariant mass range is changed to 2.2-4.2  $\text{GeV}/c^2$ , instead of 2.2-4.5  $\text{GeV}/c^2$ ;
- the background shape model is changed to an exponential of a Chebyshev function, instead of the nominal Chebyshev function. The LLR tests are remade to determine the best order of the exponent in each analysis bin;

- the LLR test selection criteria is changed by varying the  $\chi^2$ -probability threshold to 10% and 2.5%, instead of nominal 5%.

For each source of uncertainty (choice of signal and background models), the maximum difference between the  $(N_{\psi(2S)}/N_{J/\psi})$  ratio extracted from the varied data fits and the nominal results defines the uncertainty on the single ratio of charmonium yields. This procedure is performed separately for p-p and Pb-Pb collisions, and the corresponding uncertainties on the single ratios are then propagated to the double ratio.

The largest relative uncertainty on the  $(N_{\psi(2S)}/N_{J/\psi})$  ratio from the signal parametrisation derives from changing the signal shape model and corresponds to 1.9% (18.5%) in p-p (Pb-Pb) collisions. In the case of the background parametrisation, the largest relative uncertainty arises from the LLR test (5.3%) in p-p data and from changing the background shape model (37.3%) in Pb-Pb data.

#### 4.2.8.2 Uncertainty on the cancellation of the double ratio of efficiencies

The cancellation of the double ratio of  $\psi(2S)$  over  $J/\psi$  meson efficiencies is verified up to a finite degree of precision determined by the statistical precision of the simulations and the modelling of the charmonium kinematic spectra. In this case, the following sources of systematic uncertainties are taken into account:

- the statistical uncertainty of the double ratio of efficiencies extracted from the simulated samples (i.e. the error bars in Figure 4.27);
- the difference between unity and the value of the double ratio of efficiencies computed after weighing per-event the simulated dimuon  $p_T$  spectrum to the corresponding charmonium  $p_T$  distribution observed in data (the charmonium  $p_T$  spectrum in data is extracted from the nominal fits);
- the spread of the double ratio of efficiencies determined with MC studies, considering the range of  $p_T$  spectra compatible with the Pb-Pb and p-p data. This is done by generating a hundred random  $p_T$  distributions of the charmonium  $p_T$  spectrum extracted from the nominal data fits, where each data point is randomised following a Gaussian distribution with mean and width equal to the nominal value and statistical uncertainty, respectively. Then the simulated dimuon  $p_T$  spectrum is weighed, event-by-event, to match each of the generated random  $p_T$  distributions, and in each case, the double ratio of efficiencies is computed. The RMS of the one hundred efficiency double ratio values is taken as the systematic uncertainty.

These three sources of uncertainties are summed in quadrature. In this case, the largest relative uncertainty on the double ratio of charmonium yields amounts to 20%.

#### 4.2.8.3 Uncertainty on the subtraction of nonprompt charmonia

The nominal method used to subtract the nonprompt charmonium contamination relies on simulations to determine the expected fraction of prompt and nonprompt charmonia passing and failing the  $\ell_{J/\psi}$  selection. To determine the uncertainty on this procedure, a set of 2D fits are employed using the same procedure employed in Ref. [249], which is similar to the one presented in this chapter.

The 2D fits are performed in two dimuon invariant mass ranges: 2.2-3.5 GeV/ $c^2$  and 3.3-4.4 GeV/ $c^2$ . The first one is used to extract the fraction of nonprompt  $J/\psi$  mesons in p-p and Pb-Pb data, while the second range is used to derive the nonprompt  $\psi(2S)$  meson fraction from p-p data only. The prompt charmonium yields are then computed using the nonprompt charmonium fractions extracted from the 2D fits ( $f_\psi^{\text{NP},\text{2D}}$ ), as given by:

$$N_\psi^{\text{P},\text{2D}} = \left(1 - f_\psi^{\text{NP},\text{2D}}\right) N_\psi^{\text{tot}} \quad (4.42)$$

where  $N_\psi^{\text{tot}}$  is the total number of charmonia extracted from the nominal fits.

In the case of  $\psi(2S)$  mesons in Pb-Pb collisions, the number of prompt  $\psi(2S)$  mesons is derived according to:

$$N_{\psi(2S),\text{PbPb}}^{\text{P},\text{2D}} = N_{\psi(2S),\text{PbPb}}^{\text{P},\text{nominal}} \times \left( \frac{N_{\psi(2S),\text{pp}}^{\text{P},\text{2D}}}{N_{\psi(2S),\text{pp}}^{\text{P},\text{nominal}}} \right) \quad (4.43)$$

where  $N_{\psi(2S)}^{\text{P},\text{nominal}}$  is the number of prompt  $\psi(2S)$  mesons determined in the nominal case, as presented in Section 4.2.5.3.

The double ratio is then recomputed using the prompt charmonium yields derived from Eq. (4.42) and Eq. (4.43). The difference between the double ratio of charmonium yields when accounting for the nonprompt charmonium contamination using the nominal method and using 2D fits, is taken as a systematic uncertainty. The largest relative uncertainty is found to be 17.7%.

## 4.3 Results

This section presents the measurements of the charmonium production in Pb-Pb and p-p collisions at  $\sqrt{s_{\text{NN}}} = 5.02 \text{ TeV}$ . The results of the nonprompt fraction of  $J/\psi$  mesons are shown in Section 4.3.1. In Section 4.3.2, the measurements of the normalised cross sections of  $J/\psi$ -meson production in p-p and Pb-Pb collisions, are reported. The nuclear modification factor of  $J/\psi$  mesons and the double ratio of prompt  $\psi(2S)$  over  $J/\psi$  meson yields are presented in Section 4.3.3 and Section 4.3.4, respectively.

### 4.3.1 Nonprompt fraction of $J/\psi$ mesons

The fraction of  $J/\psi$  mesons coming from b-hadron decays is measured in p-p and Pb-Pb collisions at  $\sqrt{s_{\text{NN}}} = 5.02 \text{ TeV}$ , for different dimuon rapidity and  $p_T$  intervals. The nonprompt  $J/\psi$ -meson fraction is extracted by performing 2D fits to the  $m^{\mu\mu}$  and  $\ell_{J/\psi}$  distributions in data. The extracted fractions are corrected for detector acceptance and efficiency, in each analysis bin and collision system, according to:

$$b_{J/\psi} = b_{J/\psi}^{\text{raw}} \left( \frac{(\mathcal{A}_{J/\psi} \times \epsilon_{J/\psi})^P}{b_{J/\psi}^{\text{raw}} (\mathcal{A}_{J/\psi} \times \epsilon_{J/\psi})^P + (1 - b_{J/\psi}^{\text{raw}}) (\mathcal{A}_{J/\psi} \times \epsilon_{J/\psi})^{\text{NP}}} \right) \quad (4.44)$$

where  $b_{J/\psi}^{\text{raw}}$  is the nonprompt  $J/\psi$ -meson fraction determined from the data fits, and  $(\mathcal{A}_{J/\psi} \times \epsilon_{J/\psi})^P$  and  $(\mathcal{A}_{J/\psi} \times \epsilon_{J/\psi})^{\text{NP}}$  are the acceptance times efficiency factors for prompt and nonprompt  $J/\psi$  mesons, respectively. The systematic uncertainty of the acceptance and efficiency corrections, and the statistical uncertainty from the 2D fits, are propagated to the measured nonprompt  $J/\psi$ -meson fraction.

Figure 4.28 shows the  $b_{J/\psi}$  results as a function of dimuon  $p_T$  and rapidity, measured in p-p and Pb-Pb collisions. The nonprompt fraction of  $J/\psi$  mesons is observed to not vary significantly with respect to rapidity. However, it depends strongly on  $p_T^{\mu\mu}$ , increasing from  $\sim 0.2$  at  $p_T^{\mu\mu} \approx 6.5 \text{ GeV}/c$  to  $\sim 0.6$  at  $p_T^{\mu\mu} > 30 \text{ GeV}/c$ . The  $b_{J/\psi}$  measurements are also seen to be slightly larger in Pb-Pb compared to p-p collisions at  $p_T^{\mu\mu} < 20 \text{ GeV}/c$ . Considering the significant  $b_{J/\psi}$  fraction measured at high  $p_T$ , these results reaffirm the need to distinguish the contributions from prompt and nonprompt  $J/\psi$  mesons, in order to disentangle the hot nuclear matter effects that impact the production of charmonia and b hadrons.

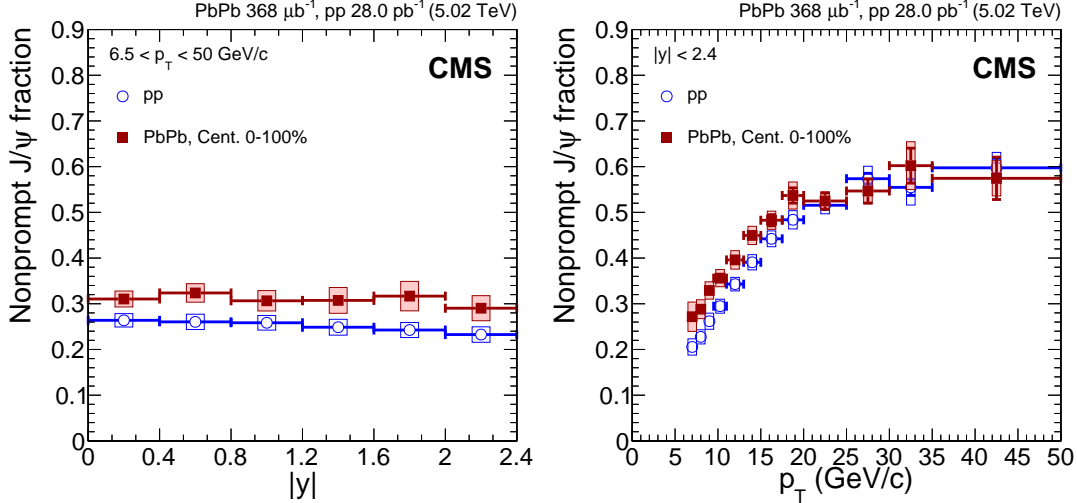


Figure 4.28: Nonprompt fraction of  $J/\psi$  mesons measured in p-p and Pb-Pb collisions, as a function of dimuon rapidity (left) and  $p_T$  (right). The boxes (bars) represent the systematic (statistical) uncertainties. Figures published in Ref. [7].

### 4.3.2 Cross section of prompt and nonprompt $J/\psi$ mesons

The  $J/\psi$ -meson production cross sections are derived from the measured number of prompt and nonprompt  $J/\psi$  mesons as:

$$N_{J/\psi} = \frac{N_{J/\psi}^{\text{raw}}}{(\mathcal{A}_{J/\psi} \times \epsilon_{J/\psi})} \quad (4.45)$$

where  $N_{J/\psi}^{\text{raw}}$  is the number of prompt or nonprompt  $J/\psi$  mesons extracted from the 2D fits to the  $m^{\mu\mu}$  and  $\ell_{J/\psi}$  distributions in data, and  $\epsilon_{J/\psi}$  and  $\mathcal{A}_{J/\psi}$  are the corresponding  $J/\psi$ -meson efficiency and acceptance, respectively. In the case of p-p collisions, the production cross section of prompt and nonprompt  $J/\psi$  mesons decaying into  $\mu^+\mu^-$  is computed as follows:

$$B(J/\psi \rightarrow \mu^+\mu^-) \frac{d^2\sigma_{J/\psi}^{\text{pp}}}{dp_T^{\mu\mu} dy^{\mu\mu}} = \frac{1}{\mathcal{L}_{\text{pp}}} \left( \frac{N_{J/\psi}^{\text{pp}}}{\Delta p_T^{\mu\mu} \Delta y^{\mu\mu}} \right) \quad (4.46)$$

where  $B$  represents the branching ratio of  $J/\psi \rightarrow \mu^+\mu^-$  decays,  $N_{J/\psi}^{\text{pp}}$  is the number of prompt or nonprompt  $J/\psi$  mesons measured in p-p collisions,  $\mathcal{L}_{\text{pp}} = 28.0 \pm 0.6 \text{ pb}^{-1}$  is the recorded integrated luminosity of the p-p data sample, and  $\Delta p_T^{\mu\mu}$  and  $\Delta y^{\mu\mu}$  are the widths of the dimuon  $p_T$  and rapidity intervals in which the measurement is performed.

In order to directly compare the Pb-Pb measurements with those from p-p collisions, the  $J/\psi \rightarrow \mu^+\mu^-$  cross section in Pb-Pb collisions is presented in the following way:

$$B(J/\psi \rightarrow \mu^+ \mu^-) \frac{d^2\sigma_{J/\psi}^{\text{PbPb}}}{dp_T^{\mu\mu} dy^{\mu\mu}} = \frac{1}{\langle T_{\text{AA}} \rangle \cdot N_{\text{MB}}} \left( \frac{N_{J/\psi}^{\text{pp}}}{\Delta p_T^{\mu\mu} \Delta y^{\mu\mu}} \right) \quad (4.47)$$

where  $N_{\text{MB}} = (2.37 \pm 0.05) \times 10^9$  represents the efficiency-corrected number of minimum bias events sampled by the analysis trigger and  $\langle T_{\text{AA}} \rangle = 5.61^{+0.16}_{-0.19}$  is the nuclear-overlap function integrated over the 0 – 100% centrality range. The centrality-integrated  $T_{\text{AA}}$  is equal to  $A^2/\sigma_{\text{PbPb}}^{\text{inel}}$ , where  $A = 208$  is the atomic number of Pb ions and  $\sigma_{\text{PbPb}}^{\text{inel}} = N_{\text{MB}}/\mathcal{L}_{\text{PbPb}}$  is the total PbPb inelastic cross section.

The systematic uncertainties that impact the measurement of the prompt and non-prompt  $J/\psi \rightarrow \mu^+ \mu^-$  cross sections in p-p and Pb-Pb collisions are:

- The uncertainty on the  $J/\psi$ -meson extraction. It is associated to the parametrisation of the dimuon  $m^{\mu\mu}$  and  $\ell_{J/\psi}$  distributions, and it is determined by varying the different components of the 2D fit model as described in Sections 4.2.7.1 and 4.2.7.2.
- The uncertainty on the efficiency estimation. It includes the uncertainties due to the TnP corrections applied to the efficiency, the  $J/\psi$ -meson  $p_T$  and rapidity weighing applied to the simulated dimuons, and the statistics of the simulated samples, as detailed in Section 4.2.7.3.
- The uncertainty on the measurement of the number of minimum bias events  $N_{\text{MB}}$  probed by the dimuon trigger, which corresponds to 2%.
- The uncertainty on the p-p integrated luminosity. It has been derived by the CMS collaboration and corresponds to 2.3% [250].
- The uncertainty on the  $\langle T_{\text{AA}} \rangle$  computation. The  $\langle T_{\text{AA}} \rangle$  relative asymmetric uncertainty in the centrality range 0 – 100% is  $[-3.4\%, +2.8\%]$ .

The global uncertainties (i.e. the same across all measurements) of the  $J/\psi$ -meson cross sections correspond to: the p-p integrated luminosity uncertainty of 2.3% for p-p collisions, and the  $\langle T_{\text{AA}} \rangle$  and  $N_{\text{MB}}$  uncertainties, which quadrature sums to a relative asymmetric uncertainty of  $[-3.9\%, +3.4\%]$ , for Pb-Pb collisions.

The results of the  $J/\psi$ -meson cross sections, measured in p-p and Pb-Pb collisions are presented in Figure 4.29. The  $J/\psi$ -meson cross sections decrease rapidly towards higher  $p_T^{\mu\mu}$  values, with the same trend between prompt and nonprompt  $J/\psi$  mesons, and between both collision systems. The measurements as a function of rapidity are seen to

decrease when approaching the forward region ( $|y^{\mu\mu}| > 1.2$ ), and similar trends are also observed between the different measurements.

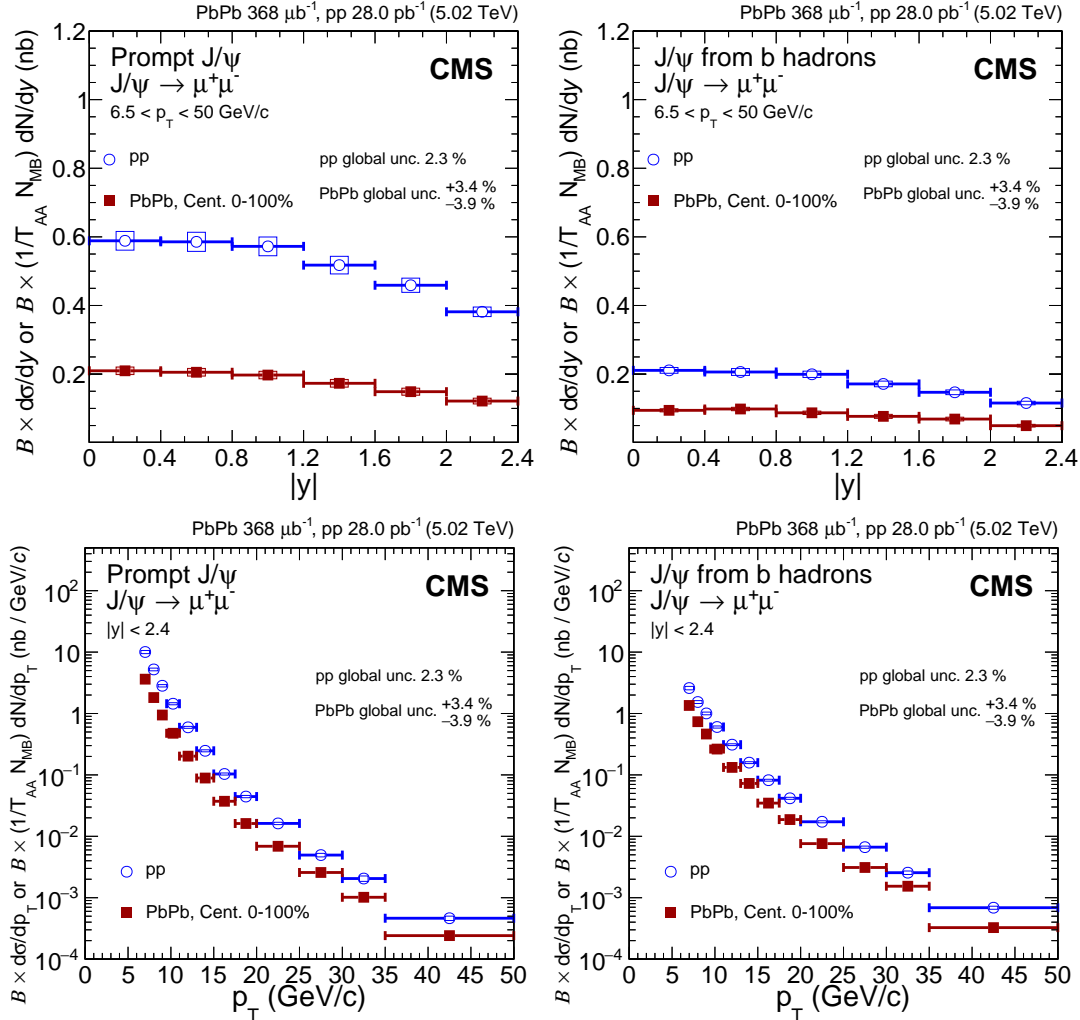


Figure 4.29: Differential cross section of the production of prompt (left) and nonprompt (right)  $J/\psi$  mesons decaying into  $\mu^+\mu^-$ , as a function of dimuon rapidity (top) and  $p_T$  (bottom) in p-p (blue open circles) and Pb-Pb (red squares) collisions. The boxes (bars) represent the systematic (statistical) uncertainties. The global relative uncertainties are written in the plots. Figures published in Ref. [7].

### 4.3.3 Nuclear modification factor of $J/\psi$ mesons

The modification of the prompt and nonprompt production of  $J/\psi$  mesons in Pb-Pb collisions is studied by measuring the nuclear modification factor, computed from the ratio

of PbPb-to-pp cross sections presented in the previous section. The nuclear modification factor of  $J/\psi$  mesons is defined as:

$$R_{AA}^{J/\psi} = \left( \frac{d^2\sigma_{J/\psi}^{PbPb}/dp_T^{\mu\mu} dy^{\mu\mu}}{d^2\sigma_{J/\psi}^{pp}/dp_T^{\mu\mu} dy^{\mu\mu}} \right) = \frac{\mathcal{L}_{pp}}{\langle T_{AA} \rangle \cdot N_{MB} \cdot \Delta_{cent}} \left( \frac{N_{J/\psi}^{PbPb}}{N_{J/\psi}^{pp}} \right) \quad (4.48)$$

where  $\Delta_{cent}$  is the fraction of the total hadronic inelastic cross section sampled in the measured centrality range (e.g. 0.3 for 70–100%). The measurements of the  $J/\psi$ -meson nuclear modification factor are performed as a function of the dimuon  $p_T$ , rapidity and the average number of participants  $\langle N_{part} \rangle$ .

The global uncertainties that enter in the measurement of the nuclear modification factor depend on which variable is used to bin the data. On the one hand, if the results are measured differentially in centrality, the global uncertainties include the statistical and systematic uncertainty of the  $J/\psi$ -meson cross section in p-p collisions, and the  $N_{MB}$  uncertainty of the Pb-Pb data. On the other hand, if the measurements are performed in different  $p_T^{\mu\mu}$  or  $y^{\mu\mu}$  intervals, then the global uncertainty includes the p-p integrated luminosity uncertainty, the Pb-Pb  $N_{MB}$  uncertainty and the uncertainty on the  $\langle T_{AA} \rangle$  corresponding to the centrality range probed. The  $\langle T_{AA} \rangle$  uncertainties are found to vary from 2% in central Pb-Pb collisions to 16% in the most peripheral ones, as presented in Table 4.8.

#### 4.3.3.1 Prompt $J/\psi$ -meson $R_{AA}$

The  $R_{AA}$  results as a function of  $p_T^{\mu\mu}$ , rapidity and  $\langle N_{part} \rangle$  are shown in Figure 4.30. The measurements are compared with the CMS results derived at  $\sqrt{s_{NN}} = 2.76$  TeV and found to be in agreement within uncertainties.

The prompt  $J/\psi$ -meson  $R_{AA}$  is less than unity in all measurements, which means that prompt  $J/\psi$  mesons are suppressed in Pb-Pb collisions. It is observed that the dependence on  $p_T^{\mu\mu}$  is mostly flat at  $p_T^{\mu\mu} > 6.5$  GeV/c, except in the highest  $p_T$  intervals ( $p_T^{\mu\mu} > 20$  GeV/c), where the prompt  $J/\psi$ -meson suppression is seen to be weaker. Moreover, the prompt  $J/\psi$  mesons are more suppressed toward central collisions, which is consistent with the picture of colour-screening due to the QGP.

Double-differential results as a function of  $p_T^{\mu\mu}$  and  $\langle N_{part} \rangle$  are displayed in Figure 4.31. The  $p_T^{\mu\mu}$  dependence is presented for the mid- ( $|y^{\mu\mu}| < 0.6$ ) and most forward ( $2.0 < |y^{\mu\mu}| < 2.4$ ) rapidity regions, while the measurements as a function of  $\langle N_{part} \rangle$  are shown in two dimuon  $p_T$  intervals:  $3 < p_T^{\mu\mu} < 6.5$  GeV/c and  $6.5 < p_T^{\mu\mu} < 50$  GeV/c, at for-

### 4.3. RESULTS

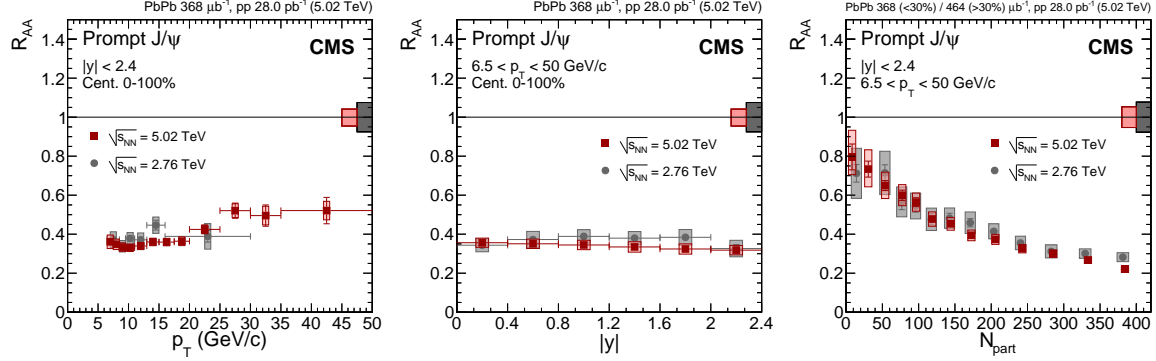


Figure 4.30: Nuclear modification factor of prompt  $J/\psi$  mesons measured at  $\sqrt{s_{NN}} = 2.76 \text{ TeV}$  [249] (grey circles) and  $\sqrt{s_{NN}} = 5.02 \text{ TeV}$  [7] (red squares), as a function of dimuon  $p_T$  (left), rapidity (middle) and  $\langle N_{\text{part}} \rangle$  (right). The boxes (bars) represent the systematic (statistical) uncertainties. The size of the global relative uncertainties are depicted in the boxes plotted at  $R_{\text{AA}} = 1$ . Figures published in Ref. [7].

ward rapidity. An indication of less suppression is seen in central collisions ( $\langle N_{\text{part}} \rangle > 200$ , corresponding to 0-30% centrality) for lower  $p_T^{\mu\mu}$  values ( $3.0 < p_T^{\mu\mu} < 6.5 \text{ GeV}/c$ ). Such reduction in the  $J/\psi$ -meson suppression could be caused by possible contributions from regenerated charmonia due to the hot medium.

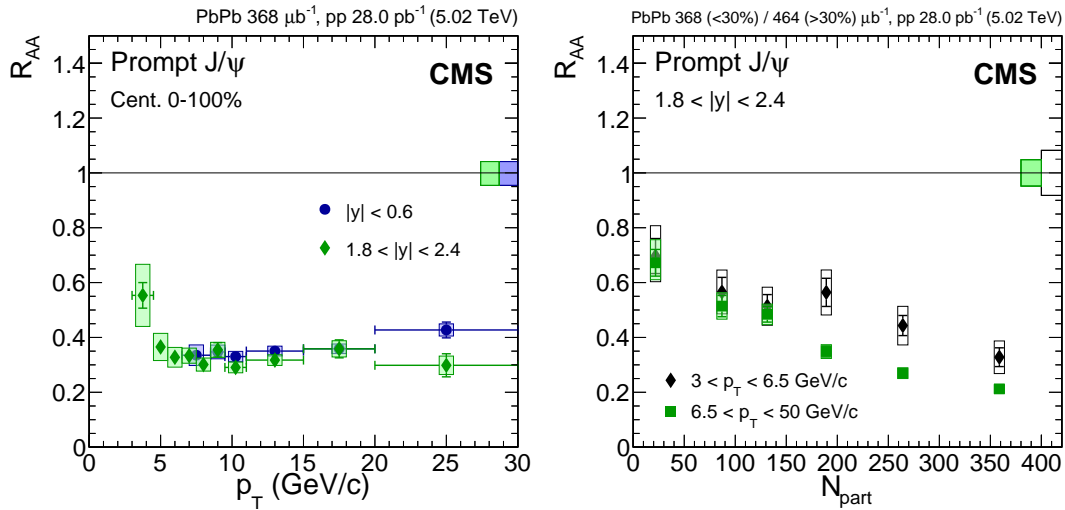


Figure 4.31: Nuclear modification factor of prompt  $J/\psi$  mesons. Left: as a function of  $p_T^{\mu\mu}$  in the mid- and most forward rapidity regions. Right: as a function of  $\langle N_{\text{part}} \rangle$  at  $3 < p_T^{\mu\mu} < 6.5 \text{ GeV}/c$  and  $6.5 < p_T^{\mu\mu} < 50 \text{ GeV}/c$ , in the  $1.8 < |y^{\mu\mu}| < 2.4$  rapidity region. The boxes (bars) represent the systematic (statistical) uncertainties. The size of the global relative uncertainties are depicted in the boxes plotted at  $R_{\text{AA}} = 1$ . Figures published in Ref. [7].

### 4.3.3.2 Nonprompt $J/\psi$ -meson $R_{AA}$

The suppression of b hadrons is probed by the nuclear modification factor of nonprompt  $J/\psi$  mesons. The nonprompt  $J/\psi$ -meson results as a function of  $p_T$ , rapidity and  $\langle N_{\text{part}} \rangle$  are compared to the corresponding ones obtained at  $\sqrt{s_{\text{NN}}} = 2.76 \text{ TeV}$  in Figure 4.32. The measurements at both collision energies are also found to be in good overall agreement.

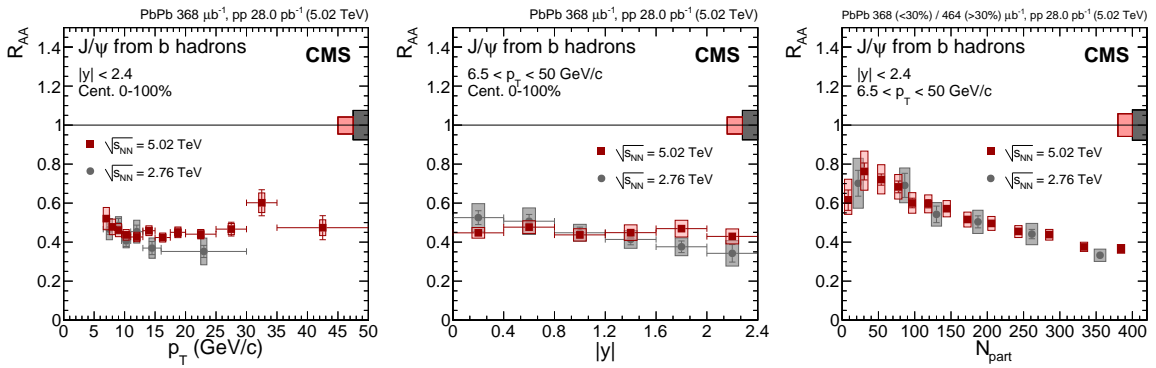


Figure 4.32: Nuclear modification factor of nonprompt  $J/\psi$  mesons measured at  $\sqrt{s_{\text{NN}}} = 2.76 \text{ TeV}$  [249] (grey circles) and  $\sqrt{s_{\text{NN}}} = 5.02 \text{ TeV}$  [7] (red squares), as a function of dimuon  $p_T$  (left), rapidity (middle) and  $\langle N_{\text{part}} \rangle$  (right). The boxes (bars) represent the systematic (statistical) uncertainties. The size of the global relative uncertainties are depicted in the boxes plotted at  $R_{AA} = 1$ . Figures published in Ref. [7].

The b hadrons are suppressed in all measurements and the nonprompt  $J/\psi$ -meson  $R_{AA}$  decreases towards high  $p_T^{\mu\mu}$  reaching a value of  $R_{AA} \approx 0.4$ . The suppression is observed to not vary significantly with respect to rapidity. In addition, the suppression of b hadrons becomes stronger for more central collisions. The nonprompt  $J/\psi$ -meson nuclear modification factor varies from  $R_{AA} \approx 0.7$  in the most peripheral centrality bin (50 – 100%) to  $R_{AA} \approx 0.4$  for the most central Pb-Pb collisions (0 – 10%).

In Figure 4.33, the  $R_{AA}$  of nonprompt  $J/\psi$  mesons is presented as a function of  $p_T^{\mu\mu}$  in the mid- and forward rapidity regions (left), and  $\langle N_{\text{part}} \rangle$  in two  $p_T^{\mu\mu}$  intervals (right). A hint of stronger suppression is seen in the highest  $p_T$  interval ( $6.5 < p_T^{\mu\mu} < 50 \text{ GeV}/c$ ) as a function of  $\langle N_{\text{part}} \rangle$ , which could originate from parton energy loss (i.e. jet quenching) of bottom quarks in the QGP medium as detailed in Section 1.2.4.3. More differential studies can be found in Ref. [7].

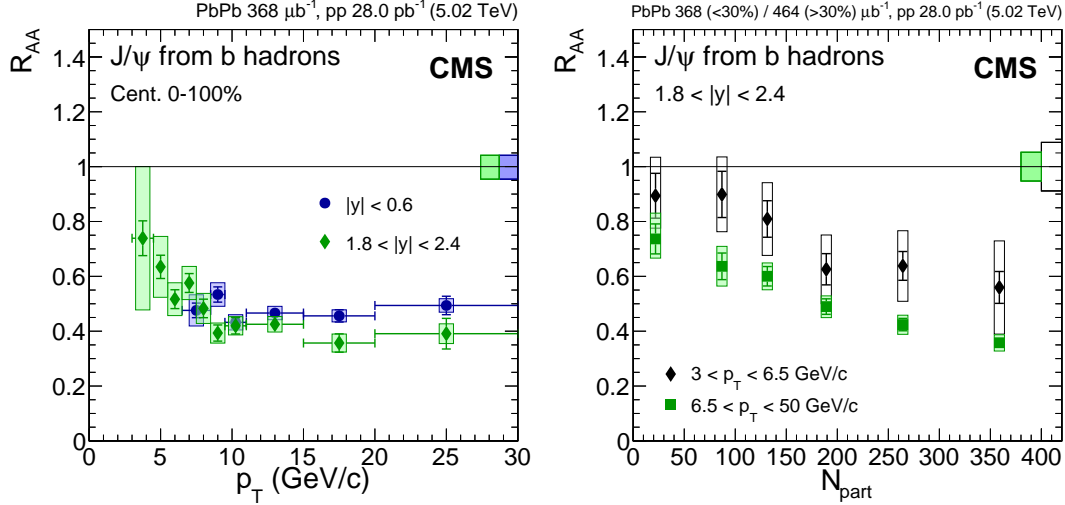


Figure 4.33: Nuclear modification factor of nonprompt  $J/\psi$  mesons. Left: as a function of  $p_T^{\mu\mu}$  in the mid- and most forward rapidity regions. Right: as a function of  $\langle N_{part} \rangle$  in two  $p_T^{\mu\mu}$  intervals at forward rapidity. The boxes (bars) represent the systematic (statistical) uncertainties. The size of the global relative uncertainties are depicted in the boxes plotted at  $R_{AA} = 1$ . Figures published in Ref. [7].

#### 4.3.4 Double ratio of prompt $\psi(2S)$ /J/ $\psi$ yields

The double ratio of prompt  $\psi(2S)$  over  $J/\psi$  meson yields,  $(N_{\psi(2S)}/N_{J/\psi})_{\text{PbPb}}/(N_{\psi(2S)}/N_{J/\psi})_{\text{pp}}$ , is derived from the  $\psi(2S)$ -to- $J/\psi$  yields ratios measured in p-p and Pb-Pb collisions, as detailed in Section 4.2.5. The systematic uncertainties that affects the measurement of the double ratio of prompt charmonium yields are:

- The uncertainty on the extraction of the  $\psi(2S)$ -to- $J/\psi$  yields ratios, derived from the parametrisation of the  $m^{\mu\mu}$  distribution in p-p and Pb-Pb collisions. This uncertainty is found to be less than 0.02 (0.11) from the p-p (Pb-Pb) data fits.
- The uncertainty on the cancellation of the prompt charmonium efficiencies. This uncertainty is seen to vary between 0.01 and 0.05, except at  $3 < p_T^{\mu\mu} < 6.5$  GeV/c, where it seen to be 0.10.
- The uncertainty on the subtraction of the nonprompt charmonium contamination, which is less than 0.07.

The results of the  $(N_{\psi(2S)}/N_{J/\psi})_{\text{PbPb}}/(N_{\psi(2S)}/N_{J/\psi})_{\text{pp}}$ , as a function of  $p_T^{\mu\mu}$ , are presented in Figure 4.34. Since the values of the double ratios of prompt charmonium yields and the prompt  $J/\psi$ -meson  $R_{AA}$  are below unity in all measurements, the prompt  $\psi(2S)$  mesons

are more suppressed than the prompt  $J/\psi$  mesons in Pb-Pb collisions. This is consistent with a sequential suppression of charmonia in the QGP. The results at mid- and forward rapidity regions are compatible within uncertainties, and no significant dependence is seen as a function of  $p_T^{\mu\mu}$ .

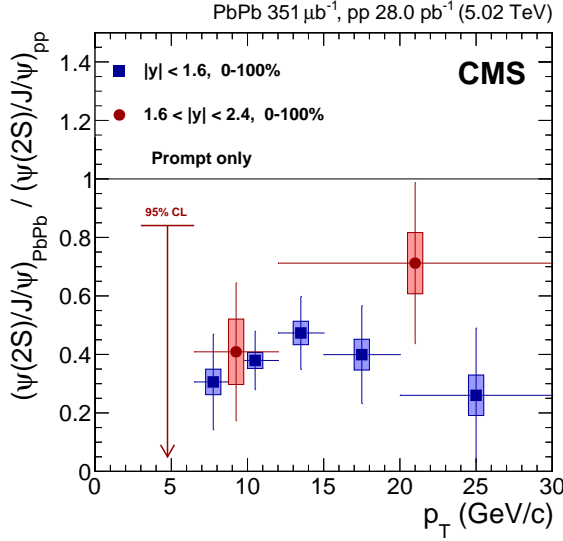


Figure 4.34: Double ratio of prompt  $\psi(2S)$  over  $J/\psi$  meson yields as a function of the dimuon  $p_T$ , at  $|y^{\mu\mu}| < 1.6$  (squares) and  $1.6 < |y^{\mu\mu}| < 2.4$  (circles). The horizontal lines denotes the widths of the  $p_T$  intervals. The bars (boxes) represent the statistical (systematic) uncertainties, while the arrows indicate the 95% CL interval where the measurement is consistent with zero. Figure published in Ref. [6].

The measurements of the double ratio of prompt charmonium yields are also performed for different centrality intervals, as shown in terms of  $\langle N_{\text{part}} \rangle$  in Figure 4.35, separately for mid-rapidity (left) and forward rapidity (right). The results do not exhibit a clear dependence with respect to  $\langle N_{\text{part}} \rangle$ . Moreover, the double ratios measured in the 20 – 100% centrality range at forward rapidity and the most central collisions (0 – 20%) at mid-rapidity, are consistent with zero. The results at  $\sqrt{s_{\text{NN}}} = 5.02 \text{ TeV}$  are compared with the previous CMS measurement at  $\sqrt{s_{\text{NN}}} = 2.76 \text{ TeV}$ . On the one hand, the results with respect to  $\langle N_{\text{part}} \rangle$  at both energies are observed to be compatible in the mid-rapidity region at  $6.5 < p_T^{\mu\mu} < 30 \text{ GeV}/c$ . On the other hand, the measurements extending to lower  $p_T^{\mu\mu}$  intervals ( $3 < p_T^{\mu\mu} < 30$ ) in the forward rapidity region are strongly reduced at  $\sqrt{s_{\text{NN}}} = 5.02 \text{ TeV}$  compared to  $\sqrt{s_{\text{NN}}} = 2.76 \text{ TeV}$ , and the enhancement present at  $\sqrt{s_{\text{NN}}} = 2.76 \text{ TeV}$  for the most central collisions is not seen at  $\sqrt{s_{\text{NN}}} = 5.02 \text{ TeV}$ . The difference in the centrality-integrated interval, between  $\sqrt{s_{\text{NN}}} = 2.76 \text{ TeV}$  and  $\sqrt{s_{\text{NN}}} = 5.02 \text{ TeV}$ , corresponds to roughly 3 standard deviations.

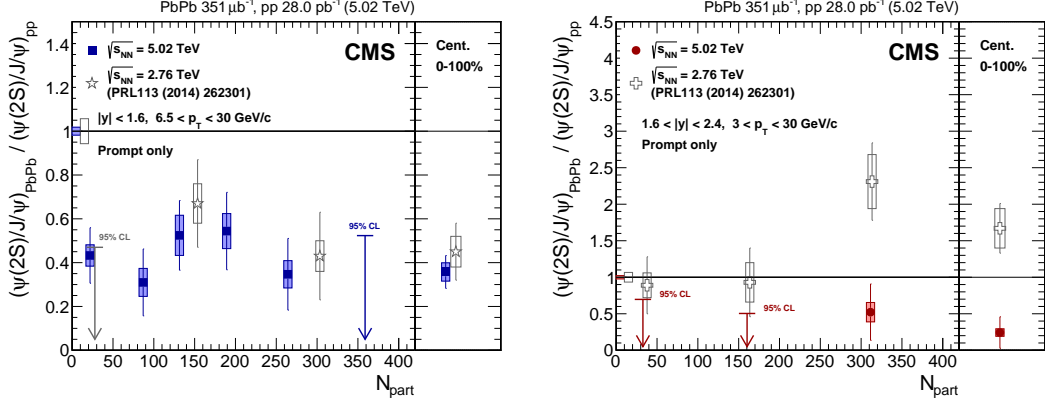


Figure 4.35: Comparison of the double ratio of prompt  $\psi(2S)$  over  $J/\psi$  meson yields measured at  $\sqrt{s_{NN}} = 2.76 \text{ TeV}$  [235] (open markers) and  $\sqrt{s_{NN}} = 5.02 \text{ TeV}$  [6] (solid markers), as a function of  $\langle N_{\text{part}} \rangle$  at  $|y^{\mu\mu}| < 1.6$  (left) and  $1.6 < |y^{\mu\mu}| < 2.4$  (right). The bars (boxes) represent the statistical (systematic) uncertainties, while the arrows indicate the 95% CL interval where the measurement is consistent with zero. Figures published in Ref. [6].

### 4.3.5 Discussion

Currently, no theory predictions have been compared to the measurements of  $J/\psi$ -meson  $R_{AA}$  at  $\sqrt{s_{NN}} = 5.02 \text{ TeV}$  presented in this chapter. Nonetheless, the prompt  $J/\psi$ -meson results obtained at  $\sqrt{s_{NN}} = 2.76 \text{ TeV}$ , which are found to be in good agreement with the current measurements, are well described by transport model calculations performed by Rapp and Xiao [251], mixing suppression and regeneration effects.

The main novelty of the current 5.02 TeV analysis is to reach higher  $p_T$  ranges, above 30  $\text{GeV}/c$ , thanks to the increase in beam luminosity and energy. Figure 4.36 shows a comparison of the  $R_{AA}$  distribution of prompt  $J/\psi$  and  $D^0$  mesons [252] (left), and of nonprompt  $J/\psi$  meson,  $D^0$  mesons and light hadrons [253] (right). The prompt charmonium and  $D^0$ -meson  $R_{AA}$  results are found to be compatible, in particular for  $p_T > 15 \text{ GeV}/c$ , where the  $R_{AA}$  is rising as  $p_T$  grows. This rise is understood in the context of jet quenching: more and more energetic partons lose a smaller fraction of their energy. Ultimately,  $R_{AA}$  reach unity for very high- $p_T$  light hadrons. This suggests that energy loss should play a role for  $J/\psi$  mesons, as for any other hadron. Logically, high- $p_T$  prompt  $J/\psi$  mesons must partly arise from the fragmentation of gluons or color-octet quarkonium states, which are subject to energy loss effects induced by the QGP medium, while nonprompt  $J/\psi$  mesons reflects the energy loss of b quarks.

A model-independent analysis performed by Arleo in Ref. [254], considering only radiative parton energy loss, exhibits a universal trend in the  $R_{AA}$  spectrum of hadrons

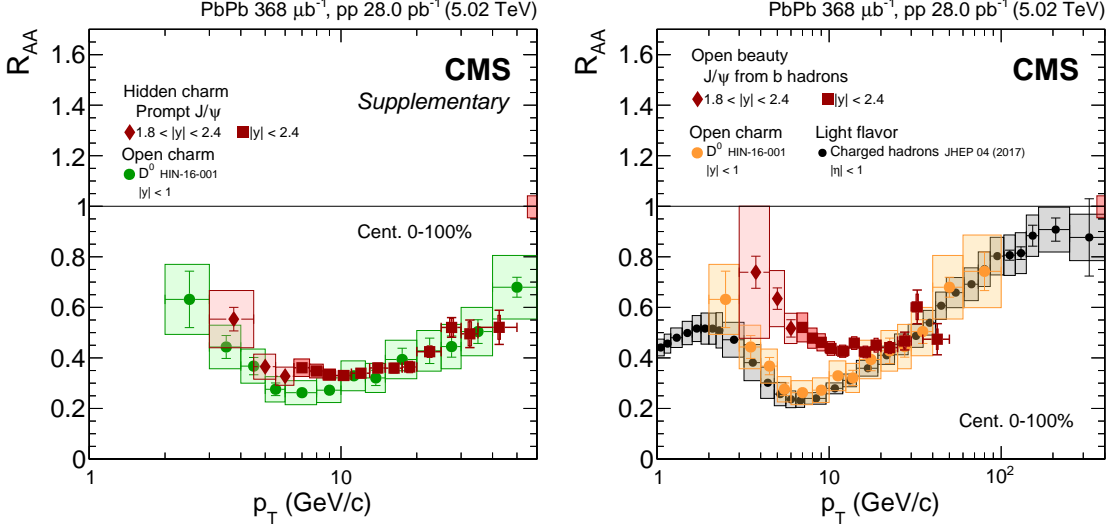


Figure 4.36: Distribution of the nuclear modification factor of different hadron species as a function of  $p_T$  in Pb-Pb collisions at  $\sqrt{s_{NN}} = 5.02\text{ TeV}$ . Left: for prompt  $J/\psi$  mesons (red markers) and  $D^0$  mesons [252] (green points). Right: for nonprompt  $J/\psi$  mesons (red markers),  $D^0$  mesons [252] (orange points) and light charged hadrons [253] (black points). The boxes (bars) represent the systematic (statistical) uncertainties. The size of the global relative uncertainties are depicted in the box plotted at  $R_{AA} = 1$ .

(including  $J/\psi$  and  $D$  mesons) at  $p_T > 10 \text{ GeV}/c$ , consistent with the CMS measurements. Thus, the results presented here reaffirms the need to further include parton energy loss in the theoretical description of the  $J/\psi$  meson production in Pb-Pb collisions, as long as they are not integrated over  $p_T$ .

On the  $\psi(2S)$  front, a possible interpretation of the double ratio results is provided by Rapp and Du in Ref. [255], using a transport model approach. The model calculations are compared to the double ratio measurements in Figure 4.37. According to the authors, the enhancement observed at  $\sqrt{s_{NN}} = 2.76\text{ TeV}$  could be a signature of sequential regeneration of charmonia. They propose that  $\psi(2S)$  mesons are regenerated later in the medium evolution, where the larger collective flow shifts their transverse momentum to  $p_T > 3 \text{ GeV}/c$ , while the  $J/\psi$  mesons are mainly regenerated earlier at lower  $p_T$  [237]. However, at higher collision energies, the  $p_T$  spectrum of the regenerated  $J/\psi$  mesons is shifted to  $p_T > 3 \text{ GeV}/c$  due to the increase in transverse flow, leading to the suppression pattern observed at  $\sqrt{s_{NN}} = 5.02\text{ TeV}$ .

Future Pb-Pb runs, such as the 5.02 TeV one that will take place at the end of 2018, will provide higher statistics. This will allow to measure more precisely and differentially the yields of  $\psi(2S)$  mesons and extend the charmonium  $p_T$  reach to even higher values,

### 4.3. RESULTS

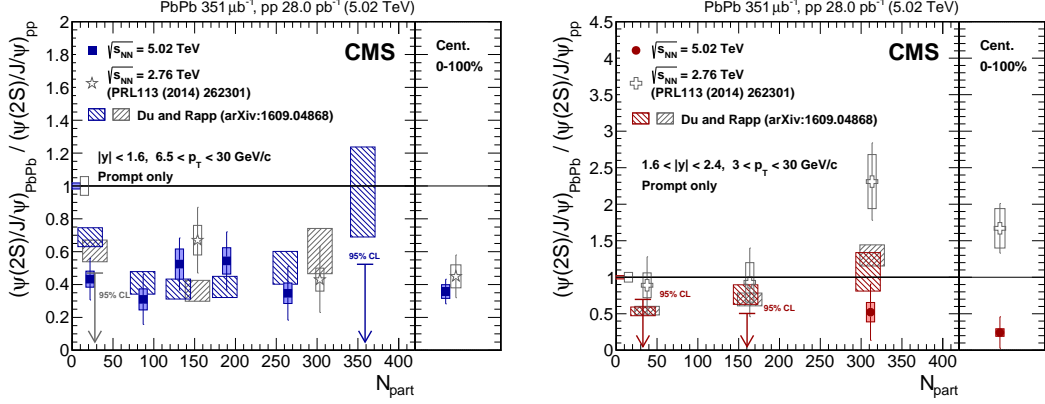


Figure 4.37: Double ratio of prompt  $\psi(2S)$  over  $J/\psi$  meson yields measured at  $\sqrt{s_{NN}} = 2.76 \text{ TeV}$  [235] (open markers) and  $\sqrt{s_{NN}} = 5.02 \text{ TeV}$  (solid markers), as a function of  $\langle N_{\text{part}} \rangle$  at  $|y^{\mu\mu}| < 1.6$  (left) and  $1.6 < |y^{\mu\mu}| < 2.4$  (right). The bars (boxes) represent the statistical (systematic) uncertainties, while the arrows indicate the 95% CL interval where the measurement is consistent with zero. The results of the Rapp and Du model [237] at 2.76 TeV (white boxes) and 5.02 TeV (red and blue boxes) are also shown.

which will be crucial to disentangle the nuclear matter effects that impact charmonia in heavy-ion collisions.



## CONCLUSION

The understanding of the cold nuclear matter effects, arising from the sole presence of nuclei, is crucial in order to characterise the quark-gluon plasma (QGP) produced in heavy-ion collisions. Among these effects, one that impacts the production of particles formed in the initial hard scattering is the nuclear modification of the parton distribution functions (PDF). Due to the non-perturbative behaviour of the strong interactions, the PDFs can not be determined theoretically and instead are parametrised using experimental data. Weak bosons provide good measurements of the PDF modifications in nuclear collisions since they do not interact strongly with the medium. Thanks to the high collision energy available at the Large Hadron Collider (LHC), it has become possible to measure the production of weak bosons in heavy-ion collisions. The LHC collaborations have studied the weak boson production in p-Pb at  $\sqrt{s_{\text{NN}}} = 5.02 \text{ TeV}$ , where hints of nuclear modifications of the PDFs were observed in the forward rapidity region, although the free-proton PDF calculations were also consistent with the measurements within the statistical precision of the data.

In the scope of this thesis, I measured the W-boson production in p-Pb collisions at  $\sqrt{s_{\text{NN}}} = 8.16 \text{ TeV}$  with the Compact Muon Solenoid detector and required the systematic uncertainties to be largely decreased. Compared to previous measurements at  $\sqrt{s_{\text{NN}}} = 5.02 \text{ TeV}$ , the analysis benefits from an increased W-boson statistics due to the higher beam energy and integrated luminosity. The measured W-boson production is found to be in good agreement with the EPPS16 and nCTEQ15 nuclear PDF sets. On the other hand, the W-boson measurements significantly disfavoured the CT14 free-proton PDF calculations, revealing unambiguously the presence of nuclear modifications in the production of electroweak bosons, for the first time. Considering the smaller size of the measured uncertainties, compared to the model calculations, the W-boson measurements have the potential to constrain the parametrisations of the quark nuclear PDFs.

The hot nuclear matter effects caused by the QGP are probed in this thesis through the study of the charmonium production in heavy-ion collisions. Two related analyses were presented in the second part of the manuscript: the production of prompt and

nonprompt  $J/\psi$  mesons, and the nuclear modification of  $\psi(2S)$  mesons relative to  $J/\psi$  mesons, in Pb-Pb collisions at  $\sqrt{s_{NN}} = 5.02\text{ TeV}$ .

Prompt and nonprompt  $J/\psi$  mesons are found to be suppressed in all measurements. Their nuclear modification factor ( $R_{AA}$ ) is observed to depend on centrality, being more suppressed towards more central collisions, while no significant dependence on rapidity is seen. On the one hand, an indication of weaker suppression is observed for prompt  $J/\psi$  mesons, in the lowest transverse momentum ( $p_T$ ) interval ( $3 < p_T < 6.5 \text{ GeV}/c$ ) and most central collisions (0-30%), which may originate from  $J/\psi$  regeneration. Also, for the first time, a hint of less suppression of prompt  $J/\psi$  mesons is seen in the highest  $p_T$  range ( $p_T > 25 \text{ GeV}/c$ ) compared to the intermediate  $p_T$  range ( $6.5 < p_T < 25 \text{ GeV}/c$ ), which may reflect the energy loss of initial partons fragmenting into  $J/\psi$  mesons. On the other hand, the nonprompt  $J/\psi$ -meson suppression is seen to be more pronounced at high  $p_T$ , likely caused by jet quenching of bottom quarks. In the overlapping range, the measured  $J/\psi$ -meson  $R_{AA}$  is compatible with previous measurements at  $\sqrt{s_{NN}} = 2.76\text{ TeV}$ .

The measurement of the  $(N_{\psi(2S)}/N_{J/\psi})_{\text{PbPb}}/(N_{\psi(2S)}/N_{J/\psi})_{\text{pp}}$  double ratio in Pb-Pb at  $\sqrt{s_{NN}} = 5.02\text{ TeV}$  shows that the  $\psi(2S)$  mesons are more suppressed than  $J/\psi$  mesons, which is consistent with the sequential suppression of charmonia in the QGP. Comparisons with measurements at  $\sqrt{s_{NN}} = 2.76\text{ TeV}$  show a good agreement of the double ratio at high  $p_T$  in the mid-rapidity region. On the contrary, extending the  $p_T$  range down to  $3 \text{ GeV}/c$  in the forward rapidity region shows a stronger reduction of the double ratio at  $\sqrt{s_{NN}} = 5.02\text{ TeV}$  compared to  $\sqrt{s_{NN}} = 2.76\text{ TeV}$ , where the two measurements deviate by almost 3 standard deviations in the centrality-integrated interval. A sequential regeneration of charmonia has been suggested to explain the double ratio results at both collision energies.



## RÉSUMÉ EN FRANÇAIS

### Chapitre 1 : Physique nucléaire des hautes énergies

Les progrès réalisés par la communauté scientifique au cours du siècle dernier ont repoussé les limites de notre compréhension du monde subatomique et ont conduit à la formulation d'une des théories de la physique les plus abouties, le modèle standard (SM) des particules. Le SM est un cadre théorique qui décrit les propriétés des particules élémentaires et leurs interactions. Les particules élémentaires sont soit des fermions, soit des bosons.

Les fermions sont des particules de spin demi-entier qui se comportent selon les statistiques de Fermi-Dirac. Ils sont classés en deux catégories : les leptons et les quarks. Il existe six leptons organisés en trois *générations* : l'électron ( $e^-$ ) et le neutrino électronique ( $\nu_e$ ), le muon ( $\mu^-$ ) et le neutrino muonique ( $\nu_\mu$ ), et le tau ( $\tau^-$ ) et le neutrino tauique ( $\nu_\tau$ ). Dans le cas des quarks, il existe six *savateurs* couplées également en trois générations : up (u) et down (d), charm (c) et strange (s), top (t) et bottom (b).

Les interactions entre les fermions sont décrites dans le SM par trois interactions fondamentales : la force électromagnétique, la force nucléaire forte et la interaction faible. Chaque interaction fondamentale est médiée par l'échange de bosons, qui sont des particules de spin entier qui suivent les statistiques de Bose-Einstein. Les interactions électromagnétiques entre les particules avec une charge électrique sont médiées par des photons. Les interactions faibles peuvent agir sur tous les fermions et sont médiées par les bosons vecteurs  $W^+$ ,  $W^-$  et  $Z$ . Les interactions fortes sont médiées par les gluons et

sont décrites par la théorie de la chromodynamique quantique (QCD).

La chromodynamique quantique est une théorie de champ quantique non abélienne reposant sur le groupe de symétrie de jauge SU(3). Les principaux objets de la QCD sont les quarks qui portent une charge de couleur et les gluons qui portent une charge de couleur et une charge d'anti-couleur. La force des interactions fortes est paramétrée par la constante de couplage  $\alpha_s$ , qui dépend de l'échelle d'énergie  $Q$ . Aux faibles énergies, le couplage fort augmente, confinant les partons (i.e. les quarks et les gluons) dans des hadrons, tandis qu'à des énergies plus élevées, le couplage fort diminue, ce qui conduit à la liberté asymptotique des partons (les partons apparaissent comme ponctuels et libres quand on interagit sur un hadron à grande énergie). Les hadrons composés de trois (anti-)quarks sont appelés (anti-)baryons, alors que ceux composés d'un quark et d'un anti-quark sont appelés des mésons.

La production de particules lors de collisions hadroniques dépend de l'évolution des partons à l'intérieur des hadrons. Le contenu partonique des hadrons peut être étudié via les fonctions de distribution de parton (PDF), qui représentent la probabilité qu'un parton porte une fraction donnée  $x$  (également appelée Bjorken  $x$ ) de la quantité de mouvement totale du hadron. Selon le théorème de factorisation de la QCD, la section efficace d'un processus donné peut être scindée en une section efficace partonique multipliée par la PDF de chaque hadron entrant. D'une part, la section efficace partonique peut être calculée à l'aide de la méthode QCD perturbative et ne dépend pas des hadrons en collision. D'autre part, les PDF ne peuvent pas être calculés à partir des premiers principes en raison de la nature non perturbative de la QCD, mais ils peuvent être déterminés à partir d'ajustements globaux reposant sur des données expérimentales, car les PDF sont indépendants du processus de diffusion initial.

La matière nucléaire normale existe dans la nature à basse température et à densité baryonique relativement élevée. Cependant, à des températures ou des densités d'énergie suffisamment élevées, la matière subit une transition de phase vers un état où les quarks et les gluons sont libérés, le plasma de quarks et de gluons (QGP). Pour recréer le QGP en laboratoire, des collisions de noyaux (ions lourds) sont pratiquées dans des accélérateurs à haute énergie.

La formation et les caractéristiques de QGP dans les collisions noyau-noyau dépendent du nombre de nucléons en collision. Pour étudier la dynamique de l'environnement nucléaire, les collisions d'ions lourds sont classées en fonction de leur centralité. Experimentalement, les classes de centralité sont définies en mesurant l'énergie déposée dans des détecteurs souvent positionnés vers l'avant. Le nombre moyen de nucléons

---

participant à la collision ( $\langle N_{\text{part}} \rangle$ ) et le nombre de collisions binaires nucléon-nucléon ( $\langle N_{\text{coll}} \rangle$ ) sont déterminés, pour chaque classe de centralité, en simulant les collisions de nucléons à l'aide d'un modèle de Monte Carlo (MC) Glauber.

Le QGP ne peut pas être observé directement de manière expérimentale, car il n'existe que pour une très courte période. Néanmoins, le QGP peut être étudié indirectement en mesurant la manière dont les particules (et donc le milieu) produits lors de la collision sont modifiés par la présence du QGP. De nombreuses signatures expérimentales ont été utilisées pour évaluer les différentes propriétés du QGP, telles que l'augmentation de la production de quarks étranges, la suppression des quarkonia, l'atténuation de l'énergie des jets, les anisotropies dans la distribution azimutale des particules (flux elliptique), entre autres. Le mécanisme de production de chaque sonde expérimentale dépend de l'échelle du processus. Les signatures produites dans des processus impliquant un fort transfert d'impulsion sont appelées sondes dures, tandis que celles produites à faible transfert d'impulsion sont appelées sondes douces.

La majorité des particules produites lors de collisions d'ions lourds sont molles. Ces sondes douces sont utilisées pour étudier l'évolution thermique et hydrodynamique du milieu. Les rendements de production de particules molles varient progressivement avec  $N_{\text{part}}$ . La production des hadrons étranges et le flux elliptique sont deux exemples de sondes douces. D'autre part, des sondes dures sont produites à partir des diffusions dures parton-parton pendant la phase initiale de la collision. Les sondes dures sont des outils idéaux pour étudier la structure du système car elles sont produites de manière théoriquement contrôlée et suffisamment tôt pour traverser le QGP. Le nombre de particules dures produites est proportionnel à  $N_{\text{coll}}$ . Certaines des principales sondes dures utilisées pour étudier le milieu nucléaire incluent les bosons électrofaibles, les quarkonia et les jets.

L'environnement présent dans un noyau peut affecter la production de particules produites lors de collisions d'ions lourds, y compris en l'absence de QGP. La mesure de particules électrofaibles qui n'interagissent pas avec le QGP (photons, bosons Z et W) permet d'étudier la modification nucléaire des PDF. Les PDF des noyaux sont des informations cruciales pour les prédictions théoriques des collisionneurs d'ions lourds ; leur détermination précise à l'aide de données expérimentales est indispensable pour quantifier l'état initial des réactions noyau-noyau.

## Chapitre 2 : Montage expérimental

Le grand collisionneur de hadrons (LHC) du CERN est actuellement le plus grand et le plus puissant accélérateur de particules au monde. Il est installé dans un tunnel souterrain de 26,7 km de circonférence, situé aussi profond que 175 m sous la frontière franco-suisse. Le LHC est capable d'accélérer et de faire entrer en collision des faisceaux de protons ou d'ions lourds (par exemple des noyaux de plomb). Les premières collisions noyau-noyau au LHC ont eu lieu en 2010 avec des faisceaux de plomb à 2,76 TeV. Depuis lors, le LHC est entré en collision avec différentes configurations impliquant des ions, notamment p-Pb à 2,76 TeV (2013), Pb-Pb à 5,02 TeV (2015), p-Pb à 8,16 TeV (2016), Xe-Xe à 5,44 TeV (2017) et à la fin de 2018, le LHC prévoit de fournir un plus grand ensemble de collisions Pb-Pb à 5,02 TeV.

Le Compact Muon Solenoid (CMS) est un détecteur de particules polyvalent logé dans une caverne souterraine au point d'interaction (IP) 5 du LHC. Le détecteur CMS est composé d'un tonneau situé dans la zone de rapidité centrale, fermé par deux disques, un de chaque côté de l'IP, formant un détecteur cylindrique hermétique. Il est constitué de quatre systèmes de sous-détecteurs principaux : le trajectographe en silicium, le calorimètre électromagnétique (ECAL), le calorimètre hadronique (HCAL) et les chambres à muons. Un aimant solénoïdal supraconducteur, placé dans le tonneau, engendre un champ magnétique de 3,8 T. Le trajectographe, l'ECAL et le HCAL sont situés dans le volume de l'électroaimant, tandis que les détecteurs de muons sont placés à l'extérieur, entre les couches de la culasse à retour de flux, ce qui limite le flux magnétique.

Le système de trajectographie interne est conçu pour mesurer la trajectoire des particules et reconstruire la position du vertex de l'interaction primaire et des désintégrations secondaires. Il est composé d'un détecteur de pixels et d'un détecteur au silicium à micropistes. L'ECAL est un calorimètre homogène hermétique composé de tungstate de plomb ( $\text{PbWO}_4$ ) et conçu pour mesurer l'énergie des électrons et des photons. Le HCAL est un calorimètre hermétique à échantillonnage constitué de dalles en scintillateur plastique, intercalées avec des plaques, qui吸orbe l'énergie des hadrons. Le système de trajectographie des muons mesure l'impulsion et la charge des muons dans la région efficace  $|\eta| < 2,4$ , utilisant trois types de technologies gazeuses : les tubes à dérive (DT), les chambres à pistes cathodiques (CSC) et les chambres à plaques résistives (RPC).

Dans les conditions de conception du LHC, les deux faisceaux traversent chaque IP toutes les 25 ns, ce qui correspond à une fréquence de 40 MHz. Une fois qu'une collision est enregistrée par le détecteur CMS, tous les canaux du détecteur sont lus et les données

---

sont envoyées au centre de calcul du CERN (Tier-0). Toutefois, le débit de traitement de Tier-0 est limité par les performances de ses processeurs et sa capacité de stockage, et doit être maintenu au-dessous de 1 kHz. Pour atteindre cet objectif, l'expérience CMS a mis en place un système de déclenchement à deux niveaux. Le premier niveau, appelé déclencheur de niveau 1 (L1), réduit le taux de collision à un taux de sortie de 100 kHz, en filtrant les événements à l'aide de processeurs dédiés. Le niveau de déclenchement suivant, appelé déclencheur de haut niveau (HLT), est exécuté dans un *cluster* d'ordinateurs situé dans la caverne de l'expérience CMS. Les algorithmes logiciels du HLT réduisent le débit de données jusqu'à la limite requise par le Tier-0.

Une fois qu'un événement est sélectionné par le HLT, les informations du détecteur sont transférées au centre de calcul Tier-0 et traitées dans le cadre logiciel de CMS. Les algorithmes de reconstruction commencent par créer les *hits*, les segments et les clusters mesurés dans chacun des sous-détecteurs CMS, et traitent ensuite les informations du détecteur pour former des objets physiques tels que des particules chargées, des muons, des électrons, des photons et des jets. Les candidats muons sont reconstruits dans CMS en utilisant les informations du système de trajectographie interne et du système de muons.

Comme les neutrinos ne peuvent pas être détectés, leur présence est déduite du déséquilibre global d'impulsion des particules dans le plan transverse, connu sous le nom d'impulsion transverse manquante ( $p_T^{\text{miss}}$ ). La  $p_T^{\text{miss}}$  est définie comme la norme de vecteur  $\vec{p}_T^{\text{miss}}$ , qui représente la somme vectorielle inverse de l'impulsion transverse de toutes les particules identifiées par le détecteur CMS dans un événement.

## Chapitre 3 : La production de bosons W dans les collisions p-Pb

Ce chapitre décrit la mesure de la production de bosons W dans des collisions proton-plomb à une énergie dans le centre de masse (CM) de nucléon-nucléon  $\sqrt{s_{\text{NN}}} = 8,16 \text{ TeV}$  avec le détecteur CMS. La production inclusive de bosons W est mesurée par le canal de décroissance muonique, représenté par le processus  $p\text{Pb} \rightarrow W + X \rightarrow \mu + \nu_\mu + X$ . Puisque la masse du boson W est grande ( $M_W = 80,385 \text{ GeV}/c^2$ ), les bosons W se forment pendant les diffusions dures initiales entre les partons du proton entrant et ceux des nucléons liés dans l'ion Pb.

Les bosons W sont principalement produits dans les collisions pPb par les interactions entre les quarks de valence et les anti-quarks de la mer du proton et des nucléons. Le

mode de production dominant des bosons  $W^+$  correspond à l'annihilation des quarks up et anti-quarks down ( $u\bar{d} \rightarrow W^+$ ), tandis que pour des bosons  $W^-$  il s'agit de l'annihilation des quarks down avec des anti-quarks up ( $d\bar{u} \rightarrow W^-$ ). Les contributions suivantes proviennent de  $c\bar{s}$  et  $s\bar{c}$ , tandis que les autres contributions quark-antiquark sont supprimées en fonction des éléments non diagonaux de la matrice CKM de couplages des quarks. Par conséquent, la section efficace du boson  $W$  mesuré dans les données p-Pb, est principalement sensible aux PDF nucléaires (nPDF) des quarks et des anti-quarks légers.

Dans les collisions d'ions lourds, les PDF des protons et des neutrons liés dans un noyau sont modifiées par la présence de l'environnement nucléaire. Les PDF sont supprimées pour des fractions d'impulsion  $x \lesssim 0,1$  (ombrage ou *shadowing*) et augmentées à  $0,1 \lesssim x \lesssim 0,3$  (*anti-shadowing*) en raison des interactions multiples entre les partons des différents nucléons. Ils peuvent également être supprimés à  $0,3 \lesssim x \lesssim 0,7$  (effet EMC) en raison de modifications de la structure des nucléons et considérablement renforcés à  $x > 0,7$  (effet de mouvement de Fermi) résultant du mouvement des nucléons. Les derniers paramétrages des PDF nucléaires sont les ensembles EPPS16 et nCTEQ15.

La production de bosons  $W$  est mesurée dans des collisions p-Pb à l'aide de données enregistrées par le détecteur CMS à la fin de 2016. L'ensemble de données utilisé dans cette analyse est composé d'événements sélectionnés par le déclencheur HLT, nécessitant la présence d'au moins un candidat muon identifié avec  $p_T > 12$  GeV/c. La luminosité totale intégrée des données enregistrées correspond à  $173,4$  nb $^{-1}$ , actuellement connue à 3,5% près.

Pendant la période de prise de données, les directions des faisceaux de proton et de plomb ont été permutees après la collecte d'une luminosité intégrée de 62,6 nb $^{-1}$ . Les énergies du faisceau étaient de 6,5 TeV pour les protons et de 2,56 TeV par nucléon pour les noyaux de plomb. Par convention, le côté vers lequel pointe le proton (Pb-) définit la région positive (négative) de pseudo-rapidité  $\eta$ , appelée direction avant (arrière). En raison du système de collision asymétrique, les particules sans masse produites dans le référentiel du centre de masse nucléon-nucléon à une pseudo-rapidité  $\eta_{CM}$  sont reconstruites à  $\eta_{lab} = \eta_{CM} - 0.465$  dans le cadre de laboratoire. Les mesures du boson  $W^\pm$  présentées dans cette thèse sont exprimées en termes de la pseudorapidité du muon dans le référentiel du CM,  $\eta_{CM}^\mu$ .

Les événements de signal, déterminés par le processus  $W^\pm \rightarrow \mu^\pm \nu_\mu$ , sont caractérisés par la présence d'un muon isolé de haut  $p_T$ , et d'une importante  $p_T^{\text{miss}}$ . Pour améliorer la pureté du signal, la région efficace de l'analyse a été limitée aux muons de  $p_T > 25$  GeV/c avec  $|\eta_{lab}^\mu| < 2,4$ . Les muons sont sélectionnés en appliquant un critère de sélection

---

standard et doivent être isolés de l'activité hadronique à proximité afin de réduire le bruit de fond dû aux désintégrations semi-muoniques de hadrons formés au sein de jets (appelé fond de jet QCD). Le paramètre d'isolation du muon ( $I^\mu$ ) est défini comme la somme des  $p_T$  de tous les photons, hadrons chargés et hadrons neutres, reconstruits dans un cône de rayon  $\Delta R = 0,3$  autour du candidat muon. Un muon est considéré isolé si  $I^\mu$  est inférieur à 15% du  $p_T$  du muon. Pour supprimer davantage les événements d'arrière-plan provenant des désintégrations muoniques de bosons Z ou de photons virtuels (Drell–Yan), les événements contenant au moins deux muons isolés de charges opposées, chaque muon ayant  $p_T^\mu > 15 \text{ GeV}/c$ , sont enlevés.

Les sources de fond produisant des muons de haut  $p_T$  qui satisfont aux critères de sélection de l'analyse sont estimées à l'aide de simulations de Monte Carlo (MC), à l'exception du fond de jet QCD, décrit à l'aide d'une technique fondée sur les données. La distribution de  $p_T^{\text{miss}}$  du fond de jet QCD est modélisée par une distribution de Rayleigh modifiée qui est paramétrée sur un échantillon de muons réels et non isolés, et extrapolée à la région de signal de muons isolés.

Les échantillons simulés ont été engendrés au NLO à l'aide du générateur POWHEG v2. La simulation des collisions pPb est effectuée à l'aide de l'ensemble de PDF CT14 corrigé par les facteurs de modification nucléaire EPPS16. Les densités de partons des protons et des neutrons sont mises à l'échelle en fonction de la masse et du numéro atomique des isotopes de plomb. Les gerbes partoniques sont simulées en hadronisant les événements POWHEG avec PYTHIA 8.212, à l'aide de l'ajustement d'événement sous-jacent CUETP8M1. La réponse complète du détecteur CMS est simulée dans tous les échantillons MC, sur la base de GEANT4, en considérant un alignement et un étalonnage réalistes des différents sous-détecteurs. Pour envisager une distribution plus réaliste de l'environnement sous-jacent présent dans les collisions p-Pb, les événements de signal MC ont été incorporés dans un échantillon à biais minimal (i.e. interactions inélastiques hadroniques) généré avec EPOS LHC, en tenant compte des deux directions de collisions p-Pb.

Afin d'améliorer l'accord entre les simulations électrofaibles et les données, la distribution du  $p_T$  du boson faible est pondérée à l'aide d'une fonction dépendant de  $p_T$  dérivée du rapport des distributions du  $p_T$  du boson Z dans les événements  $Z \rightarrow \mu^+ \mu^-$  des données et de la simulation. De plus, les événements pPb sont pondérés en faisant correspondre la distribution d'énergie simulée reconstruite dans les calorimètres hadroniques avant à celle observée dans les données d'un échantillon  $Z/\gamma^* \rightarrow \mu^+ \mu^-$ . Enfin, le recul simulé des bosons W et Z, défini comme la somme vectorielle des  $p_T$  de toutes les particules

reconstruites à l'exclusion des produits de désintégration du boson faible, est calibré de manière à ce que sa distribution moyenne corresponde à celle des données.

Le nombre d'événements de signal  $W \rightarrow \mu\nu_\mu$  est obtenu en effectuant un ajustement de vraisemblance maximale de la distribution  $p_T^{\text{miss}}$  observée dans différentes régions de  $\eta_{\text{CM}}^\mu$ . Le modèle d'ajustement total comprend six contributions : le modèle du signal  $W \rightarrow \mu\nu_\mu$ , les modèles des processus des fonds  $Z/\gamma^* \rightarrow \mu^+\mu^-$ ,  $W \rightarrow \tau\nu_\tau$ ,  $Z/\gamma^* \rightarrow \tau\bar{\tau}$  et  $t\bar{t}$ , et la forme fonctionnelle du fond de jet QCD.

Les sections efficaces pour les désintégrations  $W^\pm \rightarrow \mu^\pm\nu_\mu$  mesurées dans les collisions p-Pb à 8,16 TeV sont comparées aux calculs PDF NLO utilisant les PDF des nucléons CT14, y compris les modifications nucléaires données par les ensembles EPP16 et nCTEQ15. Les mesures à rapidité positive favorisent les calculs qui incluent les modifications nucléaires, tandis que les trois calculs à rapidité négative sont en bon accord avec les données.

Les taux des muons chargés positivement et négativement ( $N_\mu$ ) sont ensuite combinés pour mesurer les rapports avant-arrière  $N_\mu(+\eta_{\text{CM}}^\mu)/N_\mu(-\eta_{\text{CM}}^\mu)$ . Les résultats sont en bon accord avec les calculs de PDF nucléaire EPPS16 et nCTEQ15. Par ailleurs, les mesures de boson W contredisent de manière significative les calculs fondés sur les PDF de nucléons nus CT14, révélant sans ambiguïté la présence de modifications nucléaires dans la production de bosons électrofaibles, pour la première fois. Compte tenu de la taille des incertitudes mesurées, plus petite que celles du modèle, les mesures de boson W imposent des contraintes fortes sur les paramétrages des PDF nucléaires des quarks et des anti-quarks.

## Chapitre 4 : Production des charmonia dans les collisions Pb-Pb

Les charmonia sont des états liés d'un quark charm et d'un anti-quark charm. Les charmonia peuvent être produits à partir de diverses sources, notamment : la diffusion dure initiale (directe), les désintégrations d'états charmonium de masse supérieure (feed-down) ou les désintégrations faibles de hadrons contenant des quarks bottom. Les états charmonium produits directement ou provenant de contributions de feed-down sont appelés *prompt*, alors que les états charmonium issus de désintégrations de hadron b sont appelés *nonprompt*.

Les taux des charmonia observés sont modifiés dans les collisions d'ions lourds par un jeu d'effets différents pouvant se produire dans l'état initial ou final de la collision. Les

---

effets provenant de l'environnement nucléaire sont souvent appelés effets de la matière nucléaire froide (CNM), tandis que ceux causés par le milieu chaud et dense formé lors de la collision, le QGP, sont appelés effets de la matière nucléaire chaude (HNM). La compréhension de l'impact des effets de la matière nucléaire froide est cruciale pour pouvoir caractériser le milieu chaud produit lors de collisions d'ions lourds. La production des charmonia peut être affectée par plusieurs effets CNM, tels que l'absorption nucléaire, l'ombrage des gluons, la perte d'énergie et l'effet Cronin.

Les charmonia sont considérés comme des sondes importantes du QGP car ils sont produits lors de la diffusion dure initiale et subissent toute l'évolution du milieu. On s'attend à ce que la présence du milieu déconfiné dissocie les états du charmonium grâce à un processus appelé écrantage de la charge de couleur, qui peut se produire de manière séquentielle en fonction des énergies de liaison du charmonium. De plus, la grande abondance de quarks charm au LHC peut conduire à une recombinaison de quarks charm non corrélés, augmentant ainsi la production des charmonia.

La production de mésons  $J/\psi$  a été mesurée au LHC lors de collisions Pb-Pb à  $\sqrt{s_{NN}} = 2,76$  TeV. La caractéristique générale observée parmi les différentes expériences du LHC est une forte suppression du charmonia lors de collisions centrales en cohérence avec l'écrantage de la charge de couleur. De plus, la collaboration ALICE a signalé une suppression plus faible des mésons  $J/\psi$ , en particulier à faible  $p_T$ , par rapport aux mesures au RHIC, ce qui a été attribué à la régénération du méson  $J/\psi$ . Des mesures dans des collisions p-Pb ont également été effectuées au LHC, qui se sont révélées cohérentes avec les calculs incluant les modifications nucléaires des PDF et/ou les pertes d'énergie. Cependant, les contributions exactes des divers effets de la matière nucléaire à chaud et à froid sont difficiles à évaluer, en particulier en raison des grandes incertitudes sur les PDF nucléaires du gluon et de la précision statistique limitée des données. En conséquence, des mesures plus précises et différentielles sont nécessaires, à la fois pour contraindre les modèles et pour démêler les différentes contributions qui jouent un rôle dans les collisions d'ions lourds.

Dans ce chapitre, deux analyses associées de la production des charmonia dans les collisions p-p et Pb-Pb à  $\sqrt{s_{NN}} = 5,02$  TeV sont décrites. La première analyse étudie la modification de la production prompte et non-prompte des mésons  $J/\psi$  dans Pb-Pb par rapport aux collisions de p-p à la même énergie. Pour ce faire, le facteur de modification nucléaire ( $R_{AA}$ ) des mésons  $J/\psi$  est mesuré dans différentes classes de centralité de collision et intervalles de cinématique du méson  $J/\psi$ . La deuxième analyse porte sur la modification nucléaire des mésons  $\psi(2S)$  par rapport aux mésons  $J/\psi$ , en mesurant

---

## APPENDIX A. RÉSUMÉ EN FRANÇAIS

le double rapport des taux de  $\psi(2S)$  sur  $J/\psi$  dans Pb-Pb par rapport aux collisions p-p, définies comme  $(N_{\psi(2S)}/N_{J/\psi})_{\text{PbPb}}/(N_{\psi(2S)}/N_{J/\psi})_{\text{pp}}$ .

Les candidats charmonium sont reconstruits dans le canal de désintégration en deux muons (i.e.  $J/\psi \rightarrow \mu^+ \mu^-$  et  $\psi(2S) \rightarrow \mu^+ \mu^-$ ), en appariant des muons de charge opposée. Puisque les masses  $J/\psi$  et  $\psi(2S)$  sont petites ( $m_{J/\psi} = 3,097 \text{ GeV}/c^2$  et  $m_{\psi(2S)} = 3,686 \text{ GeV}/c^2$ ), les événements de signal sont dominés par la présence de muons de faible  $p_T$  ( $\langle p_T^\mu \rangle \sim 1.6 \text{ GeV}/c$ ), contrairement à l'analyse des bosons W présentée au chapitre 3. Les événements de fond sont supprimés en exigeant que chaque candidat double muon ait une probabilité  $\chi^2$  supérieure à 1% que les deux muons dérivent d'un vertex commun.

Les taux des mésons  $J/\psi$  prompts et non prompts sont extraits en effectuant un ajustement de vraisemblance maximum à deux dimensions des distributions de masse invariante de  $\mu^+ \mu^-$  ( $m^{\mu\mu}$ ) et de longueur de la désintégration de pseudo-proper ( $\ell_{J/\psi}$ ). Le  $\ell_{J/\psi}$  des candidats  $\mu^+ \mu^-$  est définie comme  $\ell_{J/\psi} = m_{J/\psi} \cdot (\vec{p}^{\mu\mu} \cdot \vec{r}) / ((p^{\mu\mu})^2)$ , où  $m_{J/\psi} = 3.0969 \text{ GeV}/c^2$  est la masse du méson  $J/\psi$ ,  $\vec{p}^{\mu\mu}$  est le vecteur d'impulsion du double muon et  $\vec{r}$  est le vecteur de déplacement entre la position du vertex de collision principal et le vertex du double muon.

Pour extraire les taux des mésons  $\psi(2S)$  prompts, les doubles muons doivent passer une sélection sur  $\ell_{J/\psi}$  qui rejette les dimuons avec des valeurs de  $\ell_{J/\psi}$  supérieures à un seuil donné. Le seuil de sélection sur  $\ell_{J/\psi}$  est optimisé à l'aide de simulations, en conservant 90% des charmonia prompts tout en rejetant plus de 80% des charmonia non prompts. Le rapport des taux des mésons  $\psi(2S)$  sur  $J/\psi$  est extrait des données en ajustant la distribution du  $m^{\mu\mu}$  des doubles muons passant la sélection sur  $\ell_{J/\psi}$ , et le rapport des taux des mésons  $\psi(2S)$  prompt sur  $J/\psi$  prompt est déterminé par soustraction du charmonia non prompts qui passe la sélection sur  $\ell_{J/\psi}$ .

La production de mésons  $J/\psi$  prompts et non prompts s'avère supprimée dans toutes les mesures. On observe que le facteur de modification nucléaire  $R_{AA}$  des mésons  $J/\psi$  dépend de la centralité, étant davantage supprimé pour les collisions plus centrales, alors qu'aucune dépendance significative en la rapidité n'est observée. D'une part, on observe une indication de suppression plus faible pour les mésons  $J/\psi$  prompts, dans l'intervalle d'impulsion transverse le plus bas ( $3 < p_T < 6.5 \text{ GeV}/c$ ) et la plupart des collisions centrales (0-30%), pouvant provenir de la régénération des mésons  $J/\psi$ . En revanche, la suppression des mésons  $J/\psi$  non prompts semble être plus prononcée à haute  $p_T$ , probablement à cause de l'atténuation des jets (jet *quenching*) des quarks bottom. Dans la plage de chevauchement, le  $R_{AA}$  des mésons  $J/\psi$  mesuré est compatible avec les mesures précédentes à  $\sqrt{s_{NN}} = 2,76 \text{ TeV}$ .

---

Les résultats des  $R_{AA}$  des charmonia prompts sont compatibles à ceux des mésons  $D^0$ , en particulier à  $p_T > 15 \text{ GeV}/c$ , où  $R_{AA}$  augmente avec  $p_T$ . Cette augmentation est comprise dans le contexte de l'atténuation des jets. Ceci suggère que la perte d'énergie devrait jouer un rôle important pour les mésons  $J/\psi$ , comme pour tout autre hadron. Les mésons  $J/\psi$  prompts à haut  $p_T$  doivent provenir en partie de la fragmentation des gluons ou des états de quarkonium de couleur-octet, qui sont soumis aux effets de perte d'énergie induits par le milieu QGP.

La mesure du double rapport  $(N_{\psi(2S)}/N_{J/\psi})_{\text{Pb-Pb}}/(N_{\psi(2S)}/N_{J/\psi})_{\text{pp}}$  dans Pb-Pb à  $\sqrt{s_{NN}} = 5,02 \text{ TeV}$  montre que les mésons  $\psi(2S)$  sont plus supprimés que les mésons  $J/\psi$ , ce qui est compatible avec le scénario de suppression séquentielle des charmonia dans le QGP. Les comparaisons avec les mesures à  $\sqrt{s_{NN}} = 2,76 \text{ TeV}$  montrent un bon accord du double rapport à haut  $p_T$  dans la région de mid-rapidité. Au contraire, l'extension de la plage de  $p_T$  jusqu'à  $3 \text{ GeV}/c$  dans la région de rapidité vers l'avant montre une réduction plus importante du double rapport à  $\sqrt{s_{NN}} = 5,02 \text{ TeV}$  par rapport à  $\sqrt{s_{NN}} = 2,76 \text{ TeV}$ . Une régénération séquentielle du charmonia a été suggérée pour expliquer les résultats du double rapport aux deux énergies de collision.





## RESULTS OF THE FITS FOR THE W BOSON ANALYSIS

The results of the fits to the  $p_T^{\text{miss}}$  distribution in data are shown in Figure B.1 for  $W^- \rightarrow \mu^- \bar{\nu}_\mu$  events, in Figure B.2 for  $W^+ \rightarrow \mu^+ \nu_\mu$  events, and in Figure B.3 for the  $\eta_{\text{CM}}^\mu$ -inclusive range.

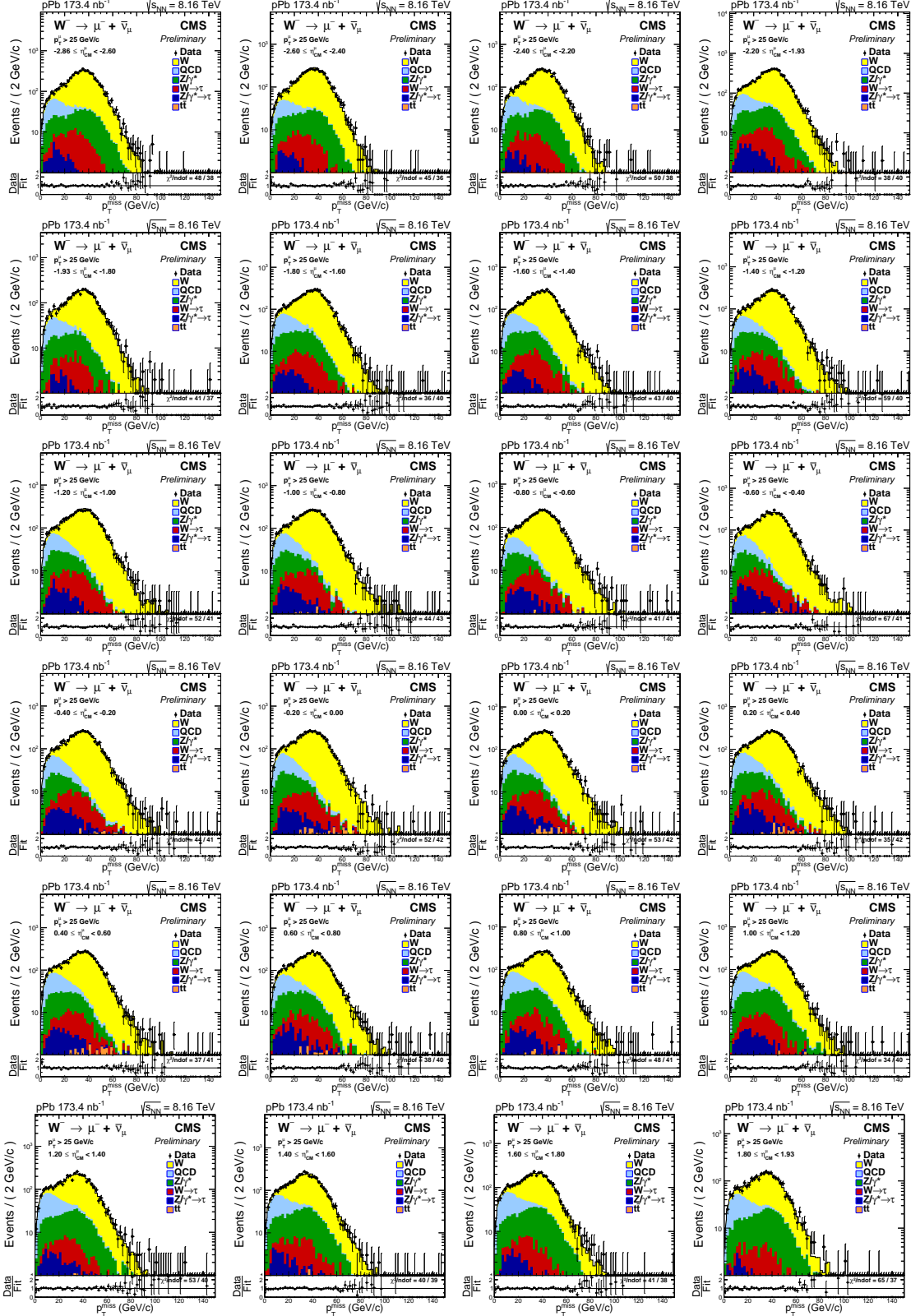


Figure B.1: The  $p_T^{\text{miss}}$  distribution for  $W^- \rightarrow \mu^- \bar{\nu}_\mu$  events within each fitted  $\eta_{\text{CM}}^\mu$  range, shown in logarithmic scale. Unbinned fits to the data (black points) are performed with six contributions, stacked from top to bottom:  $W^+ \rightarrow \mu^+ \nu_\mu$  (yellow), QCD multijet (light blue),  $Z/\gamma^* \rightarrow \mu^+ \mu^-$  (green),  $W^+ \rightarrow \bar{\tau} \nu_\tau$  (red),  $Z/\gamma^* \rightarrow \tau \bar{\tau}$  (dark blue) and  $t\bar{t}$  (orange). Error bars represent statistical uncertainties. The lower panels display the data divided by the result of the fit, for each  $\eta_{\text{CM}}^\mu$  range. The Baker-Cousins [191]  $\chi^2$  test value over the number of degrees of freedom is also shown.

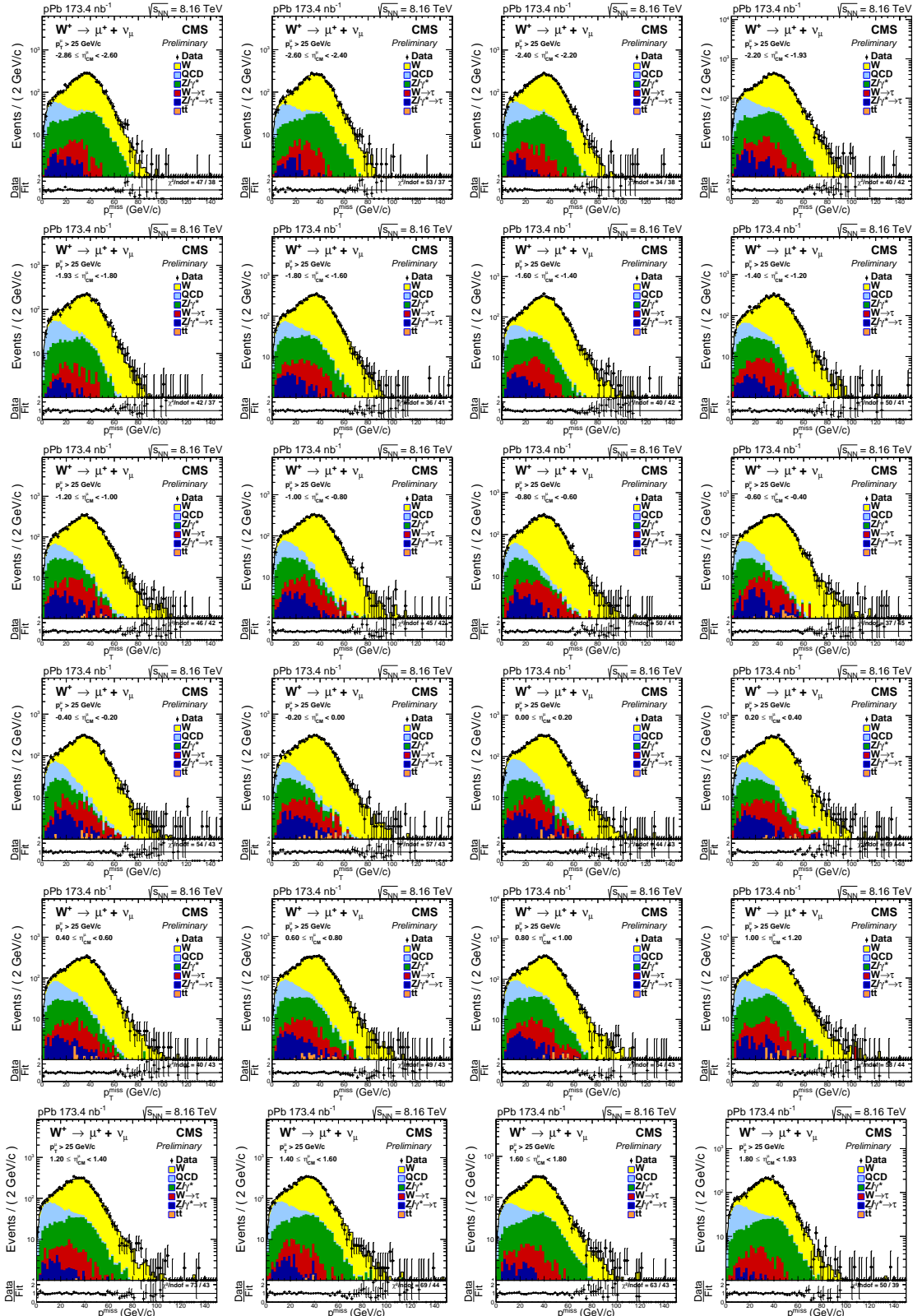


Figure B.2: The  $p_T^{\text{miss}}$  distribution for  $W^+ \rightarrow \mu^+ \nu_\mu$  events within each fitted  $\eta_{\text{CM}}^\mu$  range, shown in logarithmic scale. Unbinned fits to the data (black points) are performed with six contributions, stacked from top to bottom:  $W^+ \rightarrow \mu^+ \nu_\mu$  (yellow), QCD multijet (light blue),  $Z/\gamma^* \rightarrow \mu^+ \mu^-$  (green),  $W^+ \rightarrow \bar{\tau} \nu_\tau$  (red),  $Z/\gamma^* \rightarrow \tau \bar{\tau}$  (dark blue) and  $t\bar{t}$  (orange). Error bars represent statistical uncertainties. The lower panels display the data divided by the result of the fit, for each  $\eta_{\text{CM}}^\mu$  range. The Baker-Cousins [191]  $\chi^2$  test value over the number of degrees of freedom is also shown.

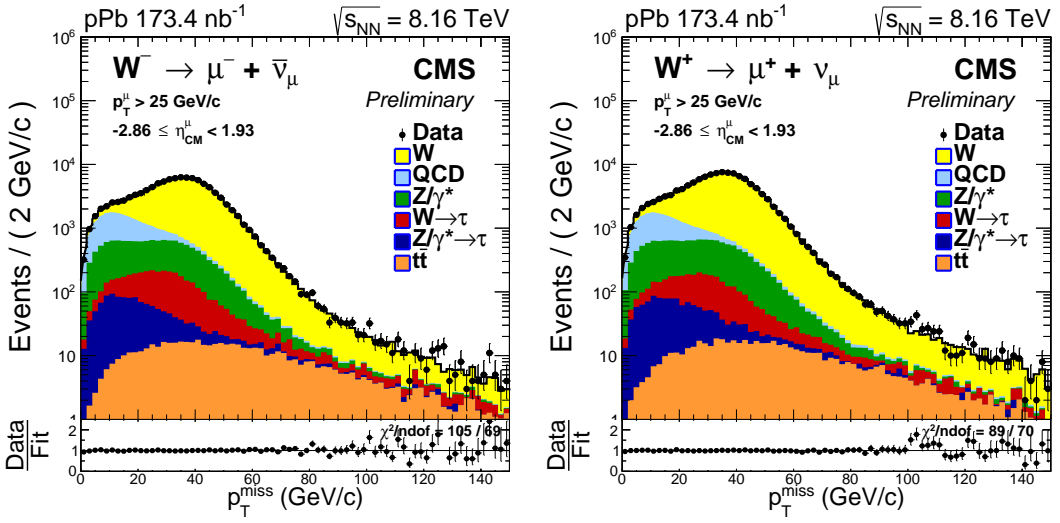


Figure B.3: The  $p_T^{\text{miss}}$  distribution for  $W^- \rightarrow \mu^- \bar{\nu}_\mu$  (left) and  $W^+ \rightarrow \mu^+ \nu_\mu$  (right) events within the  $\eta_{CM}^\mu$ -inclusive range, shown in logarithmic scale. Unbinned fits to the data (black points) are performed with six contributions, stacked from top to bottom:  $W \rightarrow \mu \nu_\mu$  (yellow), QCD multijet (light blue),  $Z/\gamma^* \rightarrow \mu^+ \mu^-$  (green),  $W \rightarrow \tau \nu_\tau$  (red),  $Z/\gamma^* \rightarrow \tau \bar{\tau}$  (dark blue) and  $t\bar{t}$  (orange). Error bars represent statistical uncertainties. The lower panels display the data divided by the result of the fit, for each  $\eta_{CM}^\mu$  range. The Baker-Cousins [191]  $\chi^2$  test value over the number of degrees of freedom is also shown.



## ANALYSIS BINS USED IN THE CHARMONIA ANALYSES

This appendix summarises the different bins in which the  $J/\psi$ -meson  $R_{AA}$  and  $\psi(2S)$ -to- $J/\psi$  double ratio analyses are performed. The binning used for the measurement of the  $J/\psi$ -meson  $R_{AA}$  as a function of centrality is listed in Table C.1, while the one used as a function of dimuon  $p_T$  in different rapidity and centrality intervals is presented in Table C.2 and Table C.3, respectively. Regarding the measurement of the double ratio of charmonium yields, the different analysis bins are summarised in Table C.4.

$ y $	$p_T$ [GeV/c]	Centrality [%]	Pb-Pb dataset
[0.0,0.6]	[6.5,50.0]	0-10	HIONiaDoubleMu0
	[6.5,50.0]	10-20	HIONiaDoubleMu0
	[6.5,50.0]	20-30	HIONiaDoubleMu0
	[6.5,50.0]	30-40	HIONiaPeripheral30100
	[6.5,50.0]	40-50	HIONiaPeripheral30100
	[6.5,50.0]	50-100	HIONiaPeripheral30100
[0.6,1.2]	[6.5,50.0]	0-10	HIONiaDoubleMu0
	[6.5,50.0]	10-20	HIONiaDoubleMu0
	[6.5,50.0]	20-30	HIONiaDoubleMu0
	[6.5,50.0]	30-40	HIONiaPeripheral30100
	[6.5,50.0]	40-50	HIONiaPeripheral30100
	[6.5,50.0]	50-100	HIONiaPeripheral30100
[1.2,1.8]	[6.5,50.0]	0-10	HIONiaDoubleMu0
	[6.5,50.0]	10-20	HIONiaDoubleMu0
	[6.5,50.0]	20-30	HIONiaDoubleMu0
	[6.5,50.0]	30-40	HIONiaPeripheral30100
	[6.5,50.0]	40-50	HIONiaPeripheral30100
	[6.5,50.0]	50-100	HIONiaPeripheral30100
[1.8,2.4]	[3.0,6.5]	0-10	HIONiaDoubleMu0
	[3.0,6.5]	10-20	HIONiaDoubleMu0
	[3.0,6.5]	20-30	HIONiaDoubleMu0
	[3.0,6.5]	30-40	HIONiaPeripheral30100
	[3.0,6.5]	40-50	HIONiaPeripheral30100
	[3.0,6.5]	50-100	HIONiaPeripheral30100
[1.8,2.4]	[6.5,50.0]	0-10	HIONiaDoubleMu0
	[6.5,50.0]	10-20	HIONiaDoubleMu0
	[6.5,50.0]	20-30	HIONiaDoubleMu0
	[6.5,50.0]	30-40	HIONiaPeripheral30100
	[6.5,50.0]	40-50	HIONiaPeripheral30100
	[6.5,50.0]	50-100	HIONiaPeripheral30100
[0.0,2.4]	[6.5,50.0]	0-5	HIONiaDoubleMu0
	[6.5,50.0]	5-10	HIONiaDoubleMu0
	[6.5,50.0]	10-15	HIONiaDoubleMu0
	[6.5,50.0]	15-20	HIONiaDoubleMu0
	[6.5,50.0]	20-25	HIONiaDoubleMu0
	[6.5,50.0]	25-30	HIONiaDoubleMu0
	[6.5,50.0]	30-35	HIONiaPeripheral30100
	[6.5,50.0]	35-40	HIONiaPeripheral30100
	[6.5,50.0]	40-45	HIONiaPeripheral30100
	[6.5,50.0]	45-50	HIONiaPeripheral30100
	[6.5,50.0]	50-60	HIONiaPeripheral30100
	[6.5,50.0]	60-70	HIONiaPeripheral30100
	[6.5,50.0]	70-100	HIONiaPeripheral30100

Table C.1: Summary of the bin boundaries used in the  $J/\psi$ -meson  $R_{AA}$  analysis as a function of centrality for different rapidity regions.

$ y $	$p_T$ [GeV/c]	Centrality [%]	Pb-Pb dataset
[0.0, 0.6]	[6.5, 8.5]	0-10	HIONiaDoubleMu0
[0.0, 0.6]	[8.5, 9.5]	10-20	HIONiaDoubleMu0
[0.0, 0.6]	[9.5, 11.0]	20-30	HIONiaDoubleMu0
[0.0, 0.6]	[11.0, 15.0]	30-40	HIONiaDoubleMu0
[0.0, 0.6]	[15.0, 50.0]	40-50	HIONiaDoubleMu0
[0.6, 1.2]	[6.5, 8.5]	0-100	HIONiaDoubleMu0
[0.6, 1.2]	[8.5, 9.5]	0-100	HIONiaDoubleMu0
[0.6, 1.2]	[9.5, 11.0]	0-100	HIONiaDoubleMu0
[0.6, 1.2]	[11.0, 15.0]	0-100	HIONiaDoubleMu0
[0.6, 1.2]	[15.0, 50.0]	0-100	HIONiaDoubleMu0
[1.2, 1.6]	[6.5, 7.5]	0-100	HIONiaDoubleMu0
[1.2, 1.6]	[7.5, 8.5]	0-100	HIONiaDoubleMu0
[1.2, 1.6]	[8.5, 9.5]	0-100	HIONiaDoubleMu0
[1.2, 1.6]	[9.5, 11.0]	0-100	HIONiaDoubleMu0
[1.2, 1.6]	[11.0, 15.0]	0-100	HIONiaDoubleMu0
[1.2, 1.6]	[15.0, 50.0]	0-100	HIONiaDoubleMu0
[1.6, 2.4]	[3.0, 4.5]	0-100	HIONiaDoubleMu0
[1.6, 2.4]	[4.5, 5.5]	0-100	HIONiaDoubleMu0
[1.6, 2.4]	[5.5, 6.5]	0-100	HIONiaDoubleMu0
[1.6, 2.4]	[6.5, 7.5]	0-100	HIONiaDoubleMu0
[1.6, 2.4]	[7.5, 8.5]	0-100	HIONiaDoubleMu0
[1.6, 2.4]	[8.5, 9.5]	0-100	HIONiaDoubleMu0
[1.6, 2.4]	[9.5, 11.0]	0-100	HIONiaDoubleMu0
[1.6, 2.4]	[11.0, 15.0]	0-100	HIONiaDoubleMu0
[1.6, 2.4]	[15.0, 50.0]	0-100	HIONiaDoubleMu0
[0.0, 2.4]	[6.5, 7.5]	0-100	HIONiaDoubleMu0
[0.0, 2.4]	[7.5, 8.5]	0-100	HIONiaDoubleMu0
[0.0, 2.4]	[8.5, 9.5]	0-100	HIONiaDoubleMu0
[0.0, 2.4]	[9.5, 11.0]	0-100	HIONiaDoubleMu0
[0.0, 2.4]	[11.0, 13.0]	0-100	HIONiaDoubleMu0
[0.0, 2.4]	[13.0, 15.0]	0-100	HIONiaDoubleMu0
[0.0, 2.4]	[15.0, 20.0]	0-100	HIONiaDoubleMu0
[0.0, 2.4]	[20.0, 30.0]	0-100	HIONiaDoubleMu0
[0.0, 2.4]	[30.0, 50.0]	0-100	HIONiaDoubleMu0

Table C.2: Summary of the bin boundaries used in the  $J/\psi$ -meson  $R_{AA}$  analysis as a function of  $p_T$  for different rapidity regions.

$ y $	$p_T$ [GeV/c]	Centrality [%]	Pb-Pb dataset
[0.0,2.4]	[6.5, 7.5]	0-10	HIONiaDoubleMu0
[0.0,2.4]	[7.5, 8.5]	0-10	HIONiaDoubleMu0
[0.0,2.4]	[8.5, 9.5]	0-10	HIONiaDoubleMu0
[0.0,2.4]	[9.5, 11.0]	0-10	HIONiaDoubleMu0
[0.0,2.4]	[11.0, 13.0]	0-10	HIONiaDoubleMu0
[0.0,2.4]	[13.0, 15.0]	0-10	HIONiaDoubleMu0
[0.0,2.4]	[15.0, 20.0]	0-10	HIONiaDoubleMu0
[0.0,2.4]	[20.0, 50.0]	0-10	HIONiaDoubleMu0
[0.0,2.4]	[6.5, 7.5]	10-30	HIONiaDoubleMu0
[0.0,2.4]	[7.5, 8.5]	10-30	HIONiaDoubleMu0
[0.0,2.4]	[8.5, 9.5]	10-30	HIONiaDoubleMu0
[0.0,2.4]	[9.5, 11.0]	10-30	HIONiaDoubleMu0
[0.0,2.4]	[11.0, 13.0]	10-30	HIONiaDoubleMu0
[0.0,2.4]	[13.0, 15.0]	10-30	HIONiaDoubleMu0
[0.0,2.4]	[15.0, 20.0]	10-30	HIONiaDoubleMu0
[0.0,2.4]	[20.0, 50.0]	10-30	HIONiaDoubleMu0
[0.0,2.4]	[6.5, 7.5]	30-100	HIONiaPeripheral30100
[0.0,2.4]	[7.5, 8.5]	30-100	HIONiaPeripheral30100
[0.0,2.4]	[8.5, 9.5]	30-100	HIONiaPeripheral30100
[0.0,2.4]	[9.5, 11.0]	30-100	HIONiaPeripheral30100
[0.0,2.4]	[11.0, 13.0]	30-100	HIONiaPeripheral30100
[0.0,2.4]	[13.0, 15.0]	30-100	HIONiaPeripheral30100
[0.0,2.4]	[15.0, 20.0]	30-100	HIONiaPeripheral30100
[0.0,2.4]	[20.0, 50.0]	30-100	HIONiaPeripheral30100

Table C.3: Summary of the bin boundaries used in the  $J/\psi$ -meson  $R_{AA}$  analysis as a function of  $p_T$  for different centrality intervals.

$ y $	$p_T$ [GeV/c ]	Centrality [%]	Pb-Pb dataset
[0,1.6]	[6.5,30]	0-10	HIONiaDoubleMu0
[0,1.6]	[6.5,30]	10-20	HIONiaDoubleMu0
[0,1.6]	[6.5,30]	20-30	HIONiaDoubleMu0
[0,1.6]	[6.5,30]	30-40	HIONiaPeripheral30100
[0,1.6]	[6.5,30]	40-50	HIONiaPeripheral30100
[0,1.6]	[6.5,30]	50-100	HIONiaPeripheral30100
[1.6,2.4]	[3,30]	0-20	HIONiaDoubleMu0
[1.6,2.4]	[3,30]	20-40	HIONiaDoubleMu0
[1.6,2.4]	[3,30]	40-100	HIONiaPeripheral30100
[0,1.6]	[6.5,9]	0-100	HIONiaDoubleMu0
[0,1.6]	[9,12]	0-100	HIONiaDoubleMu0
[0,1.6]	[12,15]	0-100	HIONiaDoubleMu0
[0,1.6]	[15,20]	0-100	HIONiaDoubleMu0
[0,1.6]	[20,30]	0-100	HIONiaDoubleMu0
[1.6,2.4]	[3,6.5]	0-100	HIONiaDoubleMu0
[1.6,2.4]	[6.5,12]	0-100	HIONiaDoubleMu0
[1.6,2.4]	[12,30]	0-100	HIONiaDoubleMu0

Table C.4: Summary of the bin boundaries used in the  $\psi(2S)$ -to- $J/\psi$  double ratio analysis.



## BIBLIOGRAPHY

- [1] **CMS** Collaboration, S. Chatrchyan *et al.*, “The CMS Experiment at the CERN LHC”, *Journal of Instrumentation* **3** (2008), no. 8, P08004. [[Cited on pages 1, 38, 41, 44, 45, 46, 47, 53, 273, and 274.](#)]
- [2] M. Benedikt, P. Collier, V. Mertens, J. Poole, and K. Schindl, “LHC Design Report. 3. The LHC injector chain”, CERN, Geneva, 2004. [[Cited on page 1.](#)]
- [3] A. G. Stahl Leiton, “nPDF studies with electroweak bosons in pPb collisions at 8.16 TeV with the CMS detector”. XXVII International Conference on Ultrarelativistic Nucleus-Nucleus Collisions (Quark Matter 2018): Venice, Italy, May 14-19, 2018. [[Cited on page 2.](#)]
- [4] A. G. Stahl Leiton, “nPDF studies with electroweak bosons in pPb collisions with the CMS detector”. XXXIX International Conference on High Energy Physics (ICHEP 2018): Seoul, Korea, July 4-11, 2018. [[Cited on page 2.](#)]
- [5] CMS Collaboration, “Constraints on nuclear parton distributions from W boson production in pPb collisions at  $\sqrt{s_{\text{NN}}} = 8.16 \text{ TeV}$ ”, Tech. Rep. CMS-PAS-HIN-17-007, CERN, Geneva, 2018. [[Cited on page 2.](#)]
- [6] **CMS** Collaboration, A. M. Sirunyan *et al.*, “Relative Modification of Prompt  $\psi(2S)$  and  $J/\psi$  Yields from pp to PbPb Collisions at  $\sqrt{s_{\text{NN}}} = 5.02 \text{ TeV}$ ”, *Physical Review Letters* **118** (2017), no. 16, 162301, arXiv:1611.01438. [[Cited on pages 2, 159, 212, 213, and 283.](#)]
- [7] **CMS** Collaboration, A. M. Sirunyan *et al.*, “Measurement of prompt and nonprompt charmonium suppression in PbPb collisions at 5.02 TeV”, *European Physical Journal C* **78** (2018), no. 6, 509, arXiv:1712.08959. [[Cited on pages 2, 159, 205, 207, 209, 210, 211, 282, and 283.](#)]
- [8] A. G. Stahl, “Charmonium production in pp, pPb and PbPb collisions with CMS”, in “Proceedings, Hot Quarks 2016: Workshop for Young Scientists on the Physics

## BIBLIOGRAPHY

---

- of Ultrarelativistic Nucleus-Nucleus Collisions (HQ2016): South Padre Island, Texas, September 12-17, 2016”, vol. 832, p. 012031. *Journal of Physics: Conference Series*, 2017. [[Cited on page 2.](#)]
- [9] A. G. Stahl Leiton, “Charmonium production in pPb and PbPb collisions at 5.02 TeV with CMS”, in “Proceedings, 2017 European Physical Society Conference on High Energy Physics (EPS-HEP 2017): Venice, Italy, July 5-12, 2017”, p. 196. *Proceedings of Science*, 2017. [[Cited on page 2.](#)]
- [10] E. Fermi, “Sulla quantizzazione del gas perfetto monoatomico”, *Rendiconti Lincei* **3** (1926) 145. [[Cited on page 4.](#)]
- [11] P. A. M. Dirac, “On the theory of quantum mechanics”, *Proceedings of the Royal Society of London A: Mathematical, Physical and Engineering Sciences* **112** (1926), no. 762, 661. [[Cited on page 4.](#)]
- [12] W. Pauli, “Über den Zusammenhang des Abschlusses der Elektronengruppen im Atom mit der Komplexstruktur der Spektren”, *Zeitschrift für Physik* **31** (1925) 765. [[Cited on page 4.](#)]
- [13] S. N. Bose, “Plancks Gesetz und Lichtquantenhypothese”, *Zeitschrift für Physik* **26** (1924) 178. [[Cited on page 4.](#)]
- [14] A. Einstein, “Quantentheorie des einatomigen idealen Gases. Zweite Abhandlung”, *Sitzungsberichte der Preussischen Akademie der Wissenschaften* **1** (1925) 3. [[Cited on page 4.](#)]
- [15] **Belle** Collaboration, A. Bondar *et al.*, “Observation of two charged bottomonium-like resonances in Y(5S) decays”, *Physical Review Letters* **108** (2012), no. 6, 122001, arXiv:1110.2251. [[Cited on page 5.](#)]
- [16] **LHCb** Collaboration, R. Aaij *et al.*, “Observation of  $J/\psi p$  Resonances Consistent with Pentaquark States in  $\Lambda_b^0 \rightarrow J/\psi K^- p$  Decays”, *Physical Review Letters* **115** (2015) 072001, arXiv:1507.03414. [[Cited on page 5.](#)]
- [17] P. W. Higgs, “Broken Symmetries and the Masses of Gauge Bosons”, *Physical Review Letters* **13** (1964) 367. [[Cited on pages 5, 68, and 69.](#)]
- [18] F. Englert and R. Brout, “Broken Symmetry and the Mass of Gauge Vector Mesons”, *Physical Review Letters* **13** (1964) 321. [[Cited on pages 5, 68, and 69.](#)]

- [19] **CMS** Collaboration, S. Chatrchyan *et al.*, “Observation of a new boson at a mass of 125 GeV with the CMS experiment at the LHC”, *Physics Letters B* **716** (2012) 30, arXiv:1207.7235. [[Cited on pages 5 and 68.](#)]
- [20] **ATLAS** Collaboration, G. Aad *et al.*, “Observation of a new particle in the search for the Standard Model Higgs boson with the ATLAS detector at the LHC”, *Physics Letters B* **716** (2012) 1, arXiv:1207.7214. [[Cited on pages 5 and 68.](#)]
- [21] **Particle Data Group** Collaboration, C. Patrignani *et al.*, “Review of Particle Physics”, *Physical Review D* **98** (2018) 030001. [[Cited on pages 6, 8, 9, 70, 71, 72, 116, 131, 132, 146, 147, 152, 170, 184, 267, 268, and 271.](#)]
- [22] M. Gell-Mann, “The Eightfold Way: A Theory of strong interaction symmetry”, tech. rep., California Institute of Technology Laboratory, 1961. [[Cited on page 5.](#)]
- [23] Y. Ne’eman, “Derivation of strong interactions from a gauge invariance”, *Nuclear Physics* **26** (1961) 222, [,34(1961)]. [[Cited on page 5.](#)]
- [24] M. Gell-Mann, “A Schematic Model of Baryons and Mesons”, *Physics Letters* **8** (1964) 214. [[Cited on page 5.](#)]
- [25] G. Zweig, “An SU(3) model for strong interaction symmetry and its breaking. Version 2”, *Developments in the Quark Theory of Hadrons* **1** (1964) 22. [[Cited on page 5.](#)]
- [26] O. W. Greenberg, “Spin and Unitary Spin Independence in a Paraquark Model of Baryons and Mesons”, *Physical Review Letters* **13** (1964) 598. [[Cited on page 5.](#)]
- [27] H. Fritzsch, M. Gell-Mann, and H. Leutwyler, “Advantages of the Color Octet Gluon Picture”, *Physics Letters B* **47** (1973) 365. [[Cited on page 5.](#)]
- [28] G. ’t Hooft and M. J. G. Veltman, “Regularization and Renormalization of Gauge Fields”, *Nuclear Physics B* **44** (1972) 189. [[Cited on page 7.](#)]
- [29] J. L. Kneur and A. Neveu, “ $\Lambda_{\overline{\text{MS}}}$  from Renormalization Group Optimized Perturbation”, *Physical Review D* **85** (2012) 014005, arXiv:1108.3501. [[Cited on pages 8 and 14.](#)]
- [30] D. J. Gross and F. Wilczek, “Ultraviolet Behavior of Nonabelian Gauge Theories”, *Physical Review Letters* **30** (1973) 1343, [,271(1973)]. [[Cited on page 8.](#)]

## BIBLIOGRAPHY

---

- [31] H. D. Politzer, “Reliable Perturbative Results for Strong Interactions?”, *Physical Review Letters* **30** (1973) 1346, [,274(1973)]. [[Cited on page 8.](#)]
- [32] L. V. P. R. de Broglie, “Recherches sur la théorie des quanta”, *Annales de Physique* **10** (1925), no. 3, 22. [[Cited on page 9.](#)]
- [33] M. N. Chernodub, “Background magnetic field stabilizes QCD string against breaking”, arXiv:1001.0570. [[Cited on pages 10 and 271.](#)]
- [34] J. D. Bjorken, “Current Algebra at Small Distances”, in “Proceedings, 41st International School of Physics “Enrico Fermi”: Varenna, Italy, July 17-29, 1967”, p. 55. New York: Academic Press, 1968. [[Cited on page 10.](#)]
- [35] J. C. Collins, D. E. Soper, and G. F. Sterman, “Factorization of Hard Processes in QCD”, *Advanced Series on Directions in High Energy Physics* **5** (1989) 1, arXiv:hep-ph/0409313. [[Cited on page 11.](#)]
- [36] G. Altarelli and G. Parisi, “Asymptotic Freedom in Parton Language”, *Nuclear Physics B* **126** (1977) 298. [[Cited on page 11.](#)]
- [37] Y. L. Dokshitzer, “Calculation of the Structure Functions for Deep Inelastic Scattering and e+ e- Annihilation by Perturbation Theory in Quantum Chromodynamics.”, *Soviet Physics Journal of Experimental and Theoretical Physics* **46** (1977) 641. [[Cited on page 11.](#)]
- [38] V. N. Gribov and L. N. Lipatov, “Deep inelastic ep scattering in perturbation theory”, *Soviet Journal of Nuclear Physics* **15** (1972) 438. [[Cited on page 11.](#)]
- [39] **ZEUS** Collaboration, S. Chekanov *et al.*, “A ZEUS next-to-leading-order QCD analysis of data on deep inelastic scattering”, *Physical Review D* **67** (2003) 012007, arXiv:hep-ex/0208023. [[Cited on pages 12, 13, and 271.](#)]
- [40] R. Hagedorn, “Statistical thermodynamics of strong interactions at high energies”, *Nuovo cimento, supplemento* **3** (1965) 147. [[Cited on page 14.](#)]
- [41] C. Ratti, “Lattice QCD and heavy ion collisions: a review of recent progress”, *Reports on Progress in Physics* **81** (2018), no. 8, 084301, arXiv:1804.07810. [[Cited on page 14.](#)]

- [42] O. Kaczmarek, “Lattice QCD results on soft and hard probes of strongly interacting matter”, *Nuclear Physics A* **967** (2017) 137, arXiv:1705.10682. [[Cited on page 14.](#)]
- [43] N. R. Council, “nuclear physics: Exploring the heart of matter”, The National Academies Press, Washington, DC, 2013. [[Cited on pages 15, 18, and 271.](#)]
- [44] M. G. Alford, A. Schmitt, K. Rajagopal, and T. Schäfer, “Color superconductivity in dense quark matter”, *Reviews of Modern Physics* **80** (2008) 1455, arXiv:0709.4635. [[Cited on page 14.](#)]
- [45] H.-T. Ding, “Recent lattice QCD results and phase diagram of strongly interacting matter”, *Nuclear Physics A* **931** (2014) 52, arXiv:1408.5236. [[Cited on page 14.](#)]
- [46] A. Bazavov *et al.*, “Equation of state and QCD transition at finite temperature”, *Physical Review D* **80** (2009) 014504, arXiv:0903.4379. [[Cited on page 14.](#)]
- [47] W. Scheid, H. Müller, and W. Greiner, “Nuclear Shock Waves in Heavy-Ion Collisions”, *Physical Review Letters* **32** (1974) 741. [[Cited on page 15.](#)]
- [48] E. J. Lofgren, “Accelerator Division Annual Reports, 1 july 1972 12/31/1974”, Tech. Rep. LBL-3835, Lawrence Berkeley National Laboratory, United States, 1975. [[Cited on page 16.](#)]
- [49] V. R. Pandharipande, D. Pines, and R. A. Smith, “Neutron star structure: theory, observation, and speculation.”, *Astrophysical Journal* **208** (1976) 550. [[Cited on page 16.](#)]
- [50] T. L. Ainsworth, E. Baron, G. E. Brown, J. Cooperstein, and M. Prakash, “Equation of State of Dense Nuclear Matter”, *Nuclear Physics A* **464** (1987) 740. [[Cited on page 16.](#)]
- [51] CERN, “New State of Matter created at CERN”, 2000. [Online; accessed June 11, 2018]. [[Cited on page 16.](#)]
- [52] W. F., “Run overview of the Relativistic Heavy Ion collider”, 2000. [Online; accessed July 28, 2018]. [[Cited on page 17.](#)]
- [53] **BRAHMS** Collaboration, I. Arsene *et al.*, “Quark gluon plasma and color glass condensate at RHIC? The Perspective from the BRAHMS experiment”, *Nuclear Physics A* **757** (2005) 1, arXiv:nucl-ex/0410020. [[Cited on page 17.](#)]

## BIBLIOGRAPHY

---

- [54] **PHENIX** Collaboration, K. Adcox *et al.*, “Formation of dense partonic matter in relativistic nucleus-nucleus collisions at RHIC: Experimental evaluation by the PHENIX collaboration”, *Nuclear Physics A* **757** (2005) 184, arXiv:nucl-ex/0410003. [[Cited on page 17.](#)]
- [55] **STAR** Collaboration, J. Adams *et al.*, “Experimental and theoretical challenges in the search for the quark gluon plasma: The STAR Collaboration’s critical assessment of the evidence from RHIC collisions”, *Nuclear Physics A* **757** (2005) 102, arXiv:nucl-ex/0501009. [[Cited on page 17.](#)]
- [56] B. B. Back *et al.*, “The PHOBOS perspective on discoveries at RHIC”, *Nuclear Physics A* **757** (2005) 28, arXiv:nucl-ex/0410022. [[Cited on page 17.](#)]
- [57] M. L. Miller, K. Reygers, S. J. Sanders, and P. Steinberg, “Glauber modeling in high energy nuclear collisions”, *Annual Review of Nuclear and Particle Science* **57** (2007) 205, arXiv:nucl-ex/0701025. [[Cited on pages 18 and 19.](#)]
- [58] U. W. Heinz, “The Strongly coupled quark-gluon plasma created at RHIC”, *Journal of Physics A: Mathematical and Theoretical* **42** (2009) 214003, arXiv:0810.5529. [[Cited on pages 22 and 271.](#)]
- [59] R. Snellings, “Elliptic Flow: A Brief Review”, *New Journal of Physics* **13** (2011) 055008, arXiv:1102.3010. [[Cited on pages 22 and 23.](#)]
- [60] P. Kovtun, D. T. Son, and A. O. Starinets, “Viscosity in Strongly Interacting Quantum Field Theories from Black Hole Physics”, *Physical Review Letters* **94** (2005) 111601, arXiv:hep-th/0405231. [[Cited on page 23.](#)]
- [61] J.-Y. Ollitrault, “Relativistic hydrodynamics for heavy-ion collisions”, *European Journal of Physics* **29** (2008) 275, arXiv:0708.2433. [[Cited on page 23.](#)]
- [62] P. Braun-Munzinger and J. Stachel, “The quest for the quark-gluon plasma”, *Nature* **448** (2007) 302. [[Cited on pages 23, 24, and 271.](#)]
- [63] **CMS** Collaboration, V. Khachatryan *et al.*, “Observation of Long-Range Near-Side Angular Correlations in Proton-Proton Collisions at the LHC”, *Journal of High Energy Physics* **09** (2010) 091, arXiv:1009.4122. [[Cited on pages 23, 25, and 272.](#)]
- [64] **PHOBOS** Collaboration, B. Alver *et al.*, “System size dependence of cluster properties from two-particle angular correlations in Cu+Cu and Au+Au collisions

- at  $\sqrt{s_{NN}} = 200$  GeV”, *Physical Review C* **81** (2010) 024904, arXiv:0812.1172. [Cited on page 24.]
- [65] J. Rafelski and R. Hagedorn, “From Hadron Gas to Quark Matter II”, in “Proceedings of International Symposium on Statistical Mechanics of Quarks and Hadrons: Bielefeld, Germany, August 24-31, 1980”, p. 253. 1980. [Cited on page 25.]
- [66] A. Capella, “Strangeness enhancement in heavy ion collisions”, *Physics Letters B* **364** (1995) 175, arXiv:hep-ph/9501331. [Cited on pages 25 and 26.]
- [67] K. Safarik, “Strangeness production at CERN SPS”, *Journal of Physics G: Nuclear and Particle Physics* **27** (2001), no. 3, 579. [Cited on page 25.]
- [68] **NA49** Collaboration, A. Mischke *et al.*, “Lambda production in central Pb + Pb collisions at CERN SPS energies”, *Journal of Physics G: Nuclear and Particle Physics* **28** (2002) 1761, arXiv:nucl-ex/0201012. [Cited on page 25.]
- [69] **STAR** Collaboration, B. I. Abelev *et al.*, “Enhanced strange baryon production in Au+Au collisions compared to p+p at  $\sqrt{s_{NN}} = 200$  GeV”, *Physical Review C* **77** (2008) 044908, arXiv:0705.2511. [Cited on pages 25, 26, and 272.]
- [70] **ALICE** Collaboration, J. Adam *et al.*, “Enhanced production of multi-strange hadrons in high-multiplicity proton-proton collisions”, *Nature Physics* **13** (2017) 535, arXiv:1606.07424. [Cited on pages 26 and 272.]
- [71] M. Cacciari, G. P. Salam, and G. Soyez, “The Anti-k(t) jet clustering algorithm”, *Journal of High Energy Physics* **4** (2008) 063, arXiv:0802.1189. [Cited on page 27.]
- [72] J. D. Bjorken, “Energy Loss of Energetic Partons in Quark - Gluon Plasma: Possible Extinction of High  $p_T$  Jets in Hadron-Hadron Collisions”, 1982. [Cited on page 27.]
- [73] A. P. S. . A. Stonebraker, “Sketch of jet production in proton-proton and heavy-ion collisions”, 2014. [Online; accessed June 8, 2018]. [Cited on pages 27 and 272.]
- [74] **PHENIX** Collaboration, A. Adare *et al.*, “Centrality dependence of low-momentum direct-photon production in Au+Au collisions at  $\sqrt{s_{NN}} = 200$  GeV”, *Physical Review C* **91** (2015), no. 6, 064904, arXiv:1405.3940. [Cited on page 28.]

## BIBLIOGRAPHY

---

- [75] B. Betz, “Jet Quenching in Heavy-Ion Collisions - The Transition Era from RHIC to LHC”, *The European Physical Journal A* **48** (2012) 164, arXiv:1211.5897. [Cited on pages 29 and 272.]
- [76] **ATLAS** Collaboration, G. Aad *et al.*, “Observation of a Centrality-Dependent Dijet Asymmetry in Lead-Lead Collisions at  $\sqrt{s_{NN}} = 2.76$  TeV with the ATLAS Detector at the LHC”, *Physical Review Letters* **105** (2010) 252303, arXiv:1011.6182. [Cited on pages 28, 30, and 272.]
- [77] **CMS** Collaboration, S. Chatrchyan *et al.*, “Observation and studies of jet quenching in PbPb collisions at nucleon-nucleon center-of-mass energy  $\sqrt{s_{NN}} = 2.76$  TeV”, *Physical Review C* **84** (2011) 024906, arXiv:1102.1957. [Cited on page 28.]
- [78] H. S. Chung, J. Lee, and D. Kang, “Cornell Potential Parameters for S-wave Heavy Quarkonia”, *Journal of the Korean Physical Society* **52** (2008) 1151, arXiv:0803.3116. [Cited on page 29.]
- [79] T. Matsui and H. Satz, “ $J/\psi$  Suppression by Quark-Gluon Plasma Formation”, *Physics Letters B* **178** (1986) 416. [Cited on pages 30 and 156.]
- [80] **CMS** Collaboration, A. M. Sirunyan *et al.*, “Suppression of Excited  $\Upsilon$  States Relative to the Ground State in Pb-Pb Collisions at  $\sqrt{s_{NN}} = 5.02\text{TeV}$ ”, *Physical Review Letters* **120** (2018), no. 14, 142301, arXiv:1706.05984. [Cited on pages 30, 31, and 272.]
- [81] **LHCb** Collaboration, R. Aaij *et al.*, “Study of  $\chi_b$  meson production in p p collisions at  $\sqrt{s} = 7$  and 8 TeV and observation of the decay  $\chi_b(3P) \rightarrow \Upsilon(3S)\gamma$ ”, *European Physical Journal C* **74** (2014), no. 10, 3092, arXiv:1407.7734. [Cited on page 31.]
- [82] **NA50** Collaboration, M. C. Abreu *et al.*, “Anomalous  $J/\psi$  suppression in Pb-Pb interactions at 158 GeV/c per nucleon”, *Physics Letters B* **410** (1997) 337. [Cited on pages 31 and 157.]
- [83] **NA50** Collaboration, B. Alessandro *et al.*, “A New measurement of  $J/\psi$  suppression in Pb-Pb collisions at 158-GeV per nucleon”, *European Physical Journal C* **39** (2005) 335, arXiv:hep-ex/0412036. [Cited on page 31.]
- [84] **PHENIX** Collaboration, A. Adare *et al.*, “ $J/\psi$  Production vs Centrality, Transverse Momentum, and Rapidity in Au+Au Collisions at  $\sqrt{s_{NN}} = 200$  GeV”,

*Physical Review Letters* **98** (2007) 232301, arXiv:nucl-ex/0611020. [Cited on pages 31 and 157.]

- [85] P. Braun-Munzinger and J. Stachel, “(Non)thermal aspects of charmonium production and a new look at  $J/\psi$  suppression”, *Physics Letters B* **490** (2000) 196, arXiv:nucl-th/0007059. [Cited on pages 32 and 157.]
- [86] L. Yan, P. Zhuang, and N. Xu, “ $J/\psi$  Production in Quark-Gluon Plasma”, *Physical Review Letters* **97** (2006) 232301, arXiv:nucl-th/0608010. [Cited on page 32.]
- [87] R. Vogt, “Systematics of heavy quark production at RHIC”, arXiv:hep-ph/0203151. [Cited on pages 32 and 156.]
- [88] **ALICE** Collaboration, B. B. Abelev *et al.*, “Centrality, rapidity and transverse momentum dependence of  $J/\psi$  suppression in Pb-Pb collisions at  $\sqrt{s_{NN}} = 2.76$  TeV”, *Physics Letters B* **734** (2014) 314, arXiv:1311.0214. [Cited on pages 32, 33, 157, and 273.]
- [89] **CMS** Collaboration, S. Chatrchyan *et al.*, “Study of Z production in PbPb and pp collisions at  $\sqrt{s_{NN}} = 2.76$  TeV in the dimuon and dielectron decay channels”, *Journal of High Energy Physics* **03** (2015) 022, arXiv:1410.4825. [Cited on pages 33, 34, and 273.]
- [90] A. del Rosso, “Particle kickers. Aiguiller les particules”, Jun 2014. [Cited on pages 38 and 273.]
- [91] **ALICE** Collaboration, K. Aamodt *et al.*, “The ALICE experiment at the CERN LHC”, *Journal of Instrumentation* **3** (2008), no. 8, P08002. [Cited on page 37.]
- [92] **ATLAS** Collaboration, G. Aad *et al.*, “The ATLAS Experiment at the CERN Large Hadron Collider”, *Journal of Instrumentation* **3** (2008), no. 8, P08003. [Cited on page 38.]
- [93] **LHCb** Collaboration, A. A. Alves, Jr. *et al.*, “The LHCb Detector at the LHC”, *Journal of Instrumentation* **3** (2008), no. 8, P08005. [Cited on page 38.]
- [94] J. Jowett *et al.*, “The 2015 Heavy-Ion Run of the LHC”, in “Proceedings, 7th International Particle Accelerator Conference (IPAC 2016): Busan, Korea, May 8-13, 2016”. Joint Accelerator Conferences Website Publishing, paper TUPMW027, 2016. [Cited on pages 40, 41, and 273.]

## BIBLIOGRAPHY

---

- [95] J. Jowett *et al.*, “The 2016 Proton-Nucleus Run of the LHC”, in “Proceedings, 8th International Particle Accelerator Conference (IPAC 2017): Copenhagen, Denmark, May 14-19, 2017”. Joint Accelerator Conferences Website Publishing, paper TUPVA014, 2017. [[Cited on pages 42 and 273.](#)]
- [96] J. M. Jowett, “Colliding Heavy Ions in the LHC”, in “Proceedings, 9th International Particle Accelerator Conference (IPAC 2018): Vancouver, BC, Canada, April 29 - May 4, 2018”, p. 584. Joint Accelerator Conferences Website Publishing, paper TUXGBD2, 2018. [[Cited on pages 42 and 267.](#)]
- [97] T. Sakuma and T. McCauley, “Detector and Event Visualization with SketchUp at the CMS Experiment”, *Journal of Physics: Conference Series* **513** (2014), no. 2, 022032. [[Cited on pages 43 and 273.](#)]
- [98] C. Battilana, “The CMS muon system: status and upgrades for LHC Run-2 and performance of muon reconstruction with 13 TeV data”, *Journal of Instrumentation* **12** (2017) C01048. [[Cited on page 44.](#)]
- [99] **CMS** Collaboration, J. Mans, J. Anderson, B. Dahmes, P. de Barbaro, J. Freeman, T. Grassi, E. Hazen, J. Mans, R. Ruchti, I. Schimdt, *et al.*, “CMS Technical Design Report for the Phase 1 Upgrade of the Hadron Calorimeter”, 2012. [[Cited on pages 44, 49, and 273.](#)]
- [100] **CMS** Collaboration, A. Tapper and D. Acosta, “CMS Technical Design Report for the Level-1 Trigger Upgrade”, tech. rep., CERN, 2013. [[Cited on pages 45 and 56.](#)]
- [101] **CMS** Collaboration, A. Benaglia, “The CMS ECAL performance with examples”, *Journal of Instrumentation* **9** (2014) C02008. [[Cited on pages 47 and 273.](#)]
- [102] G. Abbiendi, “The CMS muon system in Run2: preparation, status and first results”, *Proceedings of Science* **234** (2016) 237. [[Cited on pages 51 and 273.](#)]
- [103] **CMS** Collaboration, S. Chatrchyan *et al.*, “Performance of the CMS Drift Tube Chambers with Cosmic Rays”, *Journal of Instrumentation* **5** (2010), no. 3, P03015. [[Cited on pages 52 and 274.](#)]
- [104] M. Abbrescia *et al.*, “Beam test results on double-gap resistive plate chambers proposed for CMS experiment”, *Nuclear Instruments and Methods in Physics Research Section A: Accelerators, Spectrometers, Detectors and Associated Equipment* **414** (1998), no. 2, 135. [[Cited on pages 53 and 274.](#)]

- [105] CMS Collaboration, “Resistive Plate Chambers”, 2011. [Online; accessed July 7, 2018]. [[Cited on pages 53 and 274.](#)]
- [106] CMS Collaboration, V. Khachatryan *et al.*, “The CMS trigger system”, *Journal of Instrumentation* **12** (2017), no. 1, P01020. [[Cited on pages 54, 55, and 164.](#)]
- [107] J. J. Brooke, D. G. Cussans, R. Frazier, G. Heath, D. Machin, and D. Newbold, “Hardware and Firmware for the CMS Global Calorimeter Trigger”, in “Proceedings, 9th Workshop on Electronics for LHC Experiments, Amsterdam, The Netherlands, 29 Sep - 3 Oct 2003”, p. 226. 2003. [[Cited on pages 55 and 274.](#)]
- [108] A. Zabi *et al.*, “Triggering on electrons, jets and tau leptons with the CMS upgraded calorimeter trigger for the LHC RUN II”, *Journal of Instrumentation* **11** (2016), no. 2, C02008. [[Cited on page 57.](#)]
- [109] J. Fulcher, J. Lingemann, D. Rabady, T. Reis, and H. Sakulin, “The New Global Muon Trigger of the CMS Experiment”, *IEEE Transactions on Nuclear Science* **64** (2017), no. 6, 1467. [[Cited on page 57.](#)]
- [110] J.-M. André *et al.*, “Performance of the new DAQ system of the CMS experiment for run-2”, in “Proceedings, 2016 IEEE-NPSS Real Time Conference (RT): Padua, Italy, June 6-10, 2016”, p. 1. 2016. [[Cited on page 58.](#)]
- [111] R. Frühwirth, “Application of Kalman filtering to track and vertex fitting”, *Nuclear Instruments and Methods in Physics Research Section A: Accelerators, Spectrometers, Detectors and Associated Equipment* **262** (1987), no. 2, 444. [[Cited on pages 59 and 60.](#)]
- [112] CMS Collaboration, A. M. Sirunyan *et al.*, “Performance of the CMS muon detector and muon reconstruction with proton-proton collisions at  $\sqrt{s} = 13$  TeV”, *Journal of Instrumentation* **13** (2018), no. 6, P06015. [[Cited on pages 60 and 90.](#)]
- [113] D. Barney, “CMS Detector Slice”, CMS Collection., Jan 2016, unpublished. [[Cited on pages 61 and 274.](#)]
- [114] CMS Collaboration, A. M. Sirunyan *et al.*, “Particle-flow reconstruction and global event description with the CMS detector”, *Journal of Instrumentation* **12** (2017), no. 10, P10003, arXiv:1706.04965. [[Cited on pages 63 and 90.](#)]

## BIBLIOGRAPHY

---

- [115] CMS Collaboration, “Performance of missing transverse momentum in pp collisions at  $\sqrt{s}=13$  TeV using the CMS detector”, Tech. Rep. CMS-PAS-JME-17-001, CERN, Geneva, 2018. [[Cited on pages 63 and 97.](#)]
- [116] CMS Collaboration, V. Khachatryan *et al.*, “Performance of the CMS missing transverse momentum reconstruction in pp data at  $\sqrt{s} = 8$  TeV”, *Journal of Instrumentation* **10** (2015), no. 2, P02006. [[Cited on pages 63 and 97.](#)]
- [117] E. Rutherford, “Uranium Radiation and the Electrical conduction Produced by it”, *Philosophical Magazine* **47** (1899) 109. [[Cited on page 66.](#)]
- [118] J. Chadwick, “Intensitätsverteilung im magnetischen Spektrum von  $\beta$ -Strahlen von Radium B+C”, *Verhandlungen der deutschen physikalischen Gesellschaft* **16** (1914) 383. [[Cited on page 66.](#)]
- [119] J. Chadwick and C. D. Ellis, “A Preliminary Investigation of the Intensity Distribution in the  $\beta$ -Ray Spectra of Radium B and C”, *Proceedings of the Cambridge Philosophical Society* **21** (1922) 274. [[Cited on page 66.](#)]
- [120] W. Pauli, “Fünf Arbeiten zum Ausschliessungsprinzip und zum Neutrino”, Wissenschaftliche Buchgesellschaft, [Abt. Verlag], 1977. [[Cited on page 66.](#)]
- [121] K. Winter, “Neutrino physics”, Cambridge University Press, 1991. [[Cited on page 66.](#)]
- [122] J. Chadwick, “Possible Existence of a Neutron”, *Nature* **129** (1932) 312. [[Cited on page 66.](#)]
- [123] E. Fermi, “Collected Papers of Enrico Fermi”, University of Chicago Press, 1965. [[Cited on page 66.](#)]
- [124] E. Fermi, “Versuch einer Theorie der  $\beta$ -Strahlen. I”, *Zeitschrift für Physik* **88** (1934) 161. [[Cited on page 66.](#)]
- [125] T. D. Lee and C. N. Yang, “Question of Parity Conservation in Weak Interactions”, *Physical Review* **104** (1956) 254. [[Cited on pages 66 and 67.](#)]
- [126] C. S. Wu, E. Ambler, R. W. Hayward, D. D. Hoppes, and R. P. Hudson, “Experimental Test of Parity Conservation in Beta Decay”, *Physical Review* **105** (1957) 1413. [[Cited on page 67.](#)]

- [127] M. Goldhaber, L. Grodzins, and A. W. Sunyar, “Helicity of Neutrinos”, *Physical Review* **109** (1958) 1015. [[Cited on page 67.](#)]
- [128] E. C. G. Sudarshan and R. E. Marshak, “Origin of the Universal V-A theory”, *American Institute of Physics Conference Proceedings* **300** (1994) 110, [,0001(1984)]. [[Cited on page 67.](#)]
- [129] J. H. Christenson, J. W. Cronin, V. L. Fitch, and R. Turlay, “Evidence for the  $2\pi$  Decay of the  $K_2^0$  Meson”, *Physical Review Letters* **13** (1964) 138. [[Cited on page 67.](#)]
- [130] M. Kobayashi and T. Maskawa, “CP Violation in the Renormalizable Theory of Weak Interaction”, *Progress of Theoretical Physics* **49** (1973) 652. [[Cited on page 67.](#)]
- [131] N. Cabibbo, “Unitary Symmetry and Leptonic Decays”, *Physical Review Letters* **10** (1963) 531, [,648(1963)]. [[Cited on page 67.](#)]
- [132] S. L. Glashow, J. Iliopoulos, and L. Maiani, “Weak Interactions with Lepton-Hadron Symmetry”, *Physical Review D* **2** (1970) 1285. [[Cited on page 67.](#)]
- [133] **E598** Collaboration, J. J. Aubert *et al.*, “Experimental Observation of a Heavy Particle  $J$ ”, *Physical Review Letters* **33** (1974) 1404. [[Cited on pages 67 and 146.](#)]
- [134] **SLAC-SP-017** Collaboration, J. E. Augustin *et al.*, “Discovery of a Narrow Resonance in  $e^+e^-$  Annihilation”, *Physical Review Letters* **33** (1974) 1406. [[Cited on pages 67 and 146.](#)]
- [135] S. W. Herb *et al.*, “Observation of a Dimuon Resonance at 9.5 GeV in 400-GeV Proton-Nucleus Collisions”, *Physical Review Letters* **39** (1977) 252. [[Cited on page 67.](#)]
- [136] **CDF** Collaboration, F. Abe *et al.*, “Observation of top quark production in  $\bar{p}p$  collisions”, *Physical Review Letters* **74** (1995) 2626, arXiv:hep-ex/9503002. [[Cited on page 67.](#)]
- [137] P. A. M. Dirac, “The Principles of Quantum Mechanics”, Clarendon Press, 1930. [[Cited on page 67.](#)]
- [138] S. L. Glashow, “The renormalizability of vector meson interactions”, *Nuclear Physics* **10** (1959) 107. [[Cited on pages 67 and 69.](#)]

## BIBLIOGRAPHY

---

- [139] S. Weinberg, “A Model of Leptons”, *Physical Review Letters* **19** (1967) 1264. [Cited on pages 67 and 69.]
- [140] A. Salam and J. C. Ward, “Weak and Electromagnetic Interactions”, *Nuovo Cimento* **11** (1959) 568. [Cited on pages 67 and 69.]
- [141] G. t. Hooft, “Renormalizable Lagrangians for massive Yang-Mills fields”, *Nuclear Physics B* **35** (1971) 167. [Cited on page 68.]
- [142] G. t. Hooft and M. Veltman, “Regularization and renormalization of gauge fields”, *Nuclear Physics B* **44** (1972) 189. [Cited on page 68.]
- [143] **Gargamelle Neutrino** Collaboration, F. J. Hasert *et al.*, “Observation of Neutrino Like Interactions without Muon or Electron in the Gargamelle Neutrino Experiment”, *Nuclear Physics B* **73** (1974) 1. [Cited on page 68.]
- [144] C. Rubbia, P. McIntyre, and D. Cline, *Producing Massive Neutral Intermediate Vector Bosons with Existing Accelerators*, p. 683. Vieweg+Teubner Verlag, Wiesbaden, 1977. [Cited on page 68.]
- [145] S. van der Meer, “Stochastic damping of betatron oscillations in the ISR”, Tech. Rep. CERN-ISR-PO-72-31. ISR-PO-72-31, CERN, Geneva, Aug 1972. [Cited on page 68.]
- [146] G. Arnison *et al.*, “Experimental observation of isolated large transverse energy electrons with associated missing energy at  $\sqrt{s} = 540 \text{ GeV}$ ”, *Physics Letters B* **122** (1983) 103. [Cited on page 68.]
- [147] M. Banner *et al.*, “Observation of single isolated electrons of high transverse momentum in events with missing transverse energy at the CERN pp collider”, *Physics Letters B* **122** (1983) 476. [Cited on page 68.]
- [148] **UA1** Collaboration, G. Arnison *et al.*, “Experimental observation of lepton pairs of invariant mass around  $95 \text{ GeV}/c^2$  at the CERN SPS collider”, *Physics Letters B* **126** (1983) 398, [,7.55(1983)]. [Cited on page 68.]
- [149] **UA2** Collaboration, P. Bagnaia *et al.*, “Evidence for  $Z^0 \rightarrow e^+e^-$  at the CERN  $\bar{p}p$  Collider”, *Physics Letters B* **129** (1983) 130, [,7.69(1983)]. [Cited on page 68.]
- [150] S. Myers, “The LEP Collider, from design to approval and commissioning”, CERN, Geneva, 1991. Delivered at CERN, 26 Nov 1990. [Cited on page 68.]

- [151] **DØ Collaboration** Collaboration, V. M. Abazov *et al.*, “Improved  $W$  boson mass measurement with the DØ detector”, *Physical Review D* **66** Jul (2002) 012001. [[Cited on page 68.](#)]
- [152] R. R. Wilson, “The Tevatron”, *Physics Today* **30** (1977) 23. [[Cited on page 68.](#)]
- [153] S. Dulat, T.-J. Hou, J. Gao, M. Guzzi, J. Huston, P. Nadolsky, J. Pumplin, C. Schmidt, D. Stump, and C. P. Yuan, “New parton distribution functions from a global analysis of quantum chromodynamics”, *Physical Review D* **93** (2016) 033006, arXiv:1506.07443. [[Cited on pages 74, 75, 86, and 274.](#)]
- [154] **European Muon** Collaboration, J. J. Aubert *et al.*, “The ratio of the nucleon structure functions  $F_2^N$  for iron and deuterium”, *Physics Letters B* **123** (1983) 275–278. [[Cited on page 76.](#)]
- [155] **European Muon** Collaboration, M. Arneodo *et al.*, “Shadowing in Deep Inelastic Muon Scattering from Nuclear Targets”, *Physics Letters B* **211** (1988) 493. [[Cited on page 76.](#)]
- [156] H. Paukkunen, “Nuclear PDFs in the beginning of the LHC era”, *Nuclear Physics A* **926** (2014) 24, arXiv:1401.2345. [[Cited on pages 76 and 274.](#)]
- [157] K. J. Eskola, V. J. Kolhinen, and C. A. Salgado, “The Scale dependent nuclear effects in parton distributions for practical applications”, *European Physical Journal C* **9** (1999) 61, arXiv:hep-ph/9807297. [[Cited on page 77.](#)]
- [158] K. J. Eskola, H. Paukkunen, and C. A. Salgado, “An Improved global analysis of nuclear parton distribution functions including RHIC data”, *Journal of High Energy Physics* **07** (2008) 102, arXiv:0802.0139. [[Cited on page 77.](#)]
- [159] K. J. Eskola, H. Paukkunen, and C. A. Salgado, “EPS09: A New Generation of NLO and LO Nuclear Parton Distribution Functions”, *Journal of High Energy Physics* **04** (2009) 065, arXiv:0902.4154. [[Cited on pages 77, 80, and 275.](#)]
- [160] D. de Florian, R. Sassot, P. Zurita, and M. Stratmann, “Global Analysis of Nuclear Parton Distributions”, *Physical Review D* **85** (2012) 074028, arXiv:1112.6324. [[Cited on page 77.](#)]
- [161] K. J. Eskola, P. Paakkinen, H. Paukkunen, and C. A. Salgado, “EPPS16: Nuclear parton distributions with LHC data”, *European Physical Journal C* **77** (2017) 163, arXiv:1612.05741. [[Cited on pages 77, 79, 86, 127, 154, 274, and 279.](#)]

## BIBLIOGRAPHY

---

- [162] **CMS** Collaboration, A. M. Sirunyan *et al.*, “Constraining gluon distributions in nuclei using dijets in proton-proton and proton-lead collisions at  $\sqrt{s_{\text{NN}}} = 5.02 \text{ TeV}$ ”, *Physical Review Letters* **121** (2018), no. 6, 062002, arXiv:1805.04736. [[Cited on page 77.](#)]
- [163] K. Kovarik *et al.*, “nCTEQ15 - Global analysis of nuclear parton distributions with uncertainties in the CTEQ framework”, *Physical Review D* **93** (2016), no. 8, 085037, arXiv:1509.00792. [[Cited on pages 78, 80, and 275.](#)]
- [164] M. Hirai, S. Kumano, and T. H. Nagai, “Determination of nuclear parton distribution functions and their uncertainties in next-to-leading order”, *Physical Review C* **76** (2007) 065207, arXiv:0709.3038. [[Cited on pages 79, 80, and 275.](#)]
- [165] **CMS** Collaboration, S. Chatrchyan *et al.*, “Study of W boson production in PbPb and  $p p$  collisions at  $\sqrt{s_{\text{NN}}} = 2.76 \text{ TeV}$ ”, *Physics Letters B* **715** (2012) 66, arXiv:1205.6334. [[Cited on page 81.](#)]
- [166] **CMS** Collaboration, S. Chatrchyan *et al.*, “Study of Z boson production in PbPb collisions at  $\sqrt{s_{\text{NN}}} = 2.76 \text{ TeV}$ ”, *Physical Review Letters* **106** (2011) 212301, arXiv:1102.5435. [[Cited on page 81.](#)]
- [167] **ATLAS** Collaboration, G. Aad *et al.*, “Measurement of the production and lepton charge asymmetry of W bosons in Pb+Pb collisions at  $\sqrt{s_{\text{NN}}} = 2.76 \text{ TeV}$  with the ATLAS detector”, *European Physical Journal C* **75** (2015), no. 1, 23, arXiv:1408.4674. [[Cited on page 81.](#)]
- [168] **ATLAS** Collaboration, G. Aad *et al.*, “Measurement of Z boson Production in Pb+Pb Collisions at  $\sqrt{s_{\text{NN}}} = 2.76 \text{ TeV}$  with the ATLAS Detector”, *Physical Review Letters* **110** (2013), no. 2, 022301, arXiv:1210.6486. [[Cited on page 81.](#)]
- [169] **ALICE** Collaboration, S. Acharya *et al.*, “Measurement of  $Z^0$ -boson production at large rapidities in Pb-Pb collisions at  $\sqrt{s_{\text{NN}}} = 5.02 \text{ TeV}$ ”, *Physics Letters B* **780** (2018) 372, arXiv:1711.10753. [[Cited on page 81.](#)]
- [170] **ATLAS** Collaboration, G. Aad *et al.*, “Z boson production in p+Pb collisions at  $\sqrt{s_{\text{NN}}} = 5.02 \text{ TeV}$  measured with the ATLAS detector”, *Physical Review C* **92** (2015), no. 4, 044915, arXiv:1507.06232. [[Cited on pages 82, 83, and 275.](#)]

- [171] CMS Collaboration, V. Khachatryan *et al.*, “Study of W boson production in pPb collisions at  $\sqrt{s_{\text{NN}}} = 5.02$  TeV”, *Physics Letters B* **750** (2015) 565, arXiv:1503.05825. [[Cited on pages 82, 84, 130, and 275.](#)]
- [172] ALICE Collaboration, J. Adam *et al.*, “W and Z boson production in p-Pb collisions at  $\sqrt{s_{\text{NN}}} = 5.02$  TeV”, *Journal of High Energy Physics* **02** (2017) 077, arXiv:1611.03002. [[Cited on pages 82, 83, and 275.](#)]
- [173] CMS Collaboration, “CMS luminosity measurement using 2016 proton-nucleus collisions at nucleon-nucleon center-of-mass energy of 8.16 TeV”, Tech. Rep. CMS-PAS-LUM-17-002, CERN, Geneva, 2018. [[Cited on pages 85, 127, 138, 139, and 278.](#)]
- [174] C. A. Salgado *et al.*, “Proton-Nucleus Collisions at the LHC: Scientific Opportunities and Requirements”, *Journal of Physics G: Nuclear and Particle Physics* **39** (2012), no. 1, 015010, arXiv:1105.3919. [[Cited on page 85.](#)]
- [175] S. Frixione, P. Nason, and C. Oleari, “Matching NLO QCD computations with Parton Shower simulations: the POWHEG method”, *Journal of High Energy Physics* **11** (2007) 070, arXiv:0709.2092. [[Cited on page 86.](#)]
- [176] P. Nason, “A New method for combining NLO QCD with shower Monte Carlo algorithms”, *Journal of High Energy Physics* **11** (2004) 040, arXiv:hep-ph/0409146. [[Cited on page 86.](#)]
- [177] S. Alioli, P. Nason, C. Oleari, and E. Re, “A general framework for implementing NLO calculations in shower Monte Carlo programs: the POWHEG BOX”, *Journal of High Energy Physics* **06** (2010) 043, arXiv:1002.2581. [[Cited on page 86.](#)]
- [178] L. Barze, G. Montagna, P. Nason, O. Nicrosini, and F. Piccinini, “Implementation of electroweak corrections in the POWHEG BOX: single W production”, *Journal of High Energy Physics* **04** (2012) 037, arXiv:1202.0465. [[Cited on pages 86 and 134.](#)]
- [179] L. Barze, G. Montagna, P. Nason, O. Nicrosini, F. Piccinini, and A. Vicini, “Neutral-current Drell–Yan with combined QCD and electroweak corrections in the POWHEG BOX”, *European Physical Journal C* **73** (2013) 2474, arXiv:1302.4606. [[Cited on page 86.](#)]

## BIBLIOGRAPHY

---

- [180] S. Frixione, P. Nason, and G. Ridolfi, “A positive-weight next-to-leading-order Monte Carlo for heavy flavour hadroproduction”, *Journal of High Energy Physics* **09** (2007) 126, arXiv:0707.3088. [[Cited on page 86.](#)]
- [181] T. Sjöstrand, S. Ask, J. R. Christiansen, R. Corke, N. Desai, P. Ilten, S. Mrenna, S. Prestel, C. O. Rasmussen, and P. Z. Skands, “An Introduction to PYTHIA 8.2”, *Computer Physics Communications* **191** (2015) 159, arXiv:1410.3012. [[Cited on pages 87 and 161.](#)]
- [182] **CMS** Collaboration, S. Chatrchyan *et al.*, “Study of the underlying event at forward rapidity in pp collisions at  $\sqrt{s} = 0.9, 2.76,$  and  $7 \text{ TeV}$ ”, *Journal of High Energy Physics* **04** (2013) 072, arXiv:1302.2394. [[Cited on pages 87 and 161.](#)]
- [183] **GEANT4** Collaboration, S. Agostinelli *et al.*, “GEANT4: A Simulation toolkit”, *Nuclear Instruments and Methods in Physics Research Section A: Accelerators, Spectrometers, Detectors and Associated Equipment* **506** (2003) 250. [[Cited on pages 87 and 161.](#)]
- [184] T. Pierog, I. Karpenko, J. M. Katzy, E. Yatsenko, and K. Werner, “EPOS LHC: Test of collective hadronization with data measured at the CERN Large Hadron Collider”, *Physical Review C* **92** (2015) 034906, arXiv:1306.0121. [[Cited on page 88.](#)]
- [185] **CMS** Collaboration, A. M. Sirunyan *et al.*, “Pseudorapidity distributions of charged hadrons in proton-lead collisions at  $\sqrt{s_{\text{NN}}} = 5.02$  and  $8.16 \text{ TeV}$ ”, *Journal of High Energy Physics* **01** (2018) 045, arXiv:1710.09355. [[Cited on page 88.](#)]
- [186] **CMS** Collaboration, A. M. Sirunyan *et al.*, “Observation of top quark production in proton-nucleus collisions”, *Physical Review Letters* **119** (2017) 242001, arXiv:1709.07411. [[Cited on pages 88, 116, 132, and 267.](#)]
- [187] **D0** Collaboration, V. M. Abazov *et al.*, “A Novel method for modeling the recoil in W boson events at hadron collider”, *Nuclear Instruments and Methods in Physics Research Section A: Accelerators, Spectrometers, Detectors and Associated Equipment* **609** (2009) 250, arXiv:0907.3713. [[Cited on page 97.](#)]
- [188] CMS Collaboration, “Muon performance studies in 2016 pPb data”, Tech. Rep. CMS-HIN-AN-17-137, CERN, Geneva, 2017. [[Cited on pages 109, 110, 111, 112, and 277.](#)]

- [189] B. H. Armstrong, “Spectrum line profiles: The Voigt function”, *Journal of Quantitative Spectroscopy and Radiative Transfer* **7** (1967) 61. [[Cited on page 110.](#)]
- [190] W. Verkerke and D. P. Kirkby, “The RooFit toolkit for data modeling”, in “Proceedings, Statistical Problems in Particle Physics, Astrophysics and Cosmology (PHYSTAT 05): Oxford, UK, September 12-15, 2005”, p. 186. 2003. arXiv:physics/0306116. [[Cited on pages 120 and 168.](#)]
- [191] S. Baker and R. D. Cousins, “Clarification of the Use of Chi Square and Likelihood Functions in Fits to Histograms”, *Nuclear Instruments and Methods in Physics Research* **221** (1984) 437. [[Cited on pages 122, 232, 233, 234, 278, 284, and 285.](#)]
- [192] A. Buckley, J. Ferrando, S. Lloyd, K. Nordström, B. Page, M. Rüfenacht, M. Schönherr, and G. Watt, “LHAPDF6: parton density access in the LHC precision era”, *European Physical Journal C* **75** (2015) 132, arXiv:1412.7420. [[Cited on page 127.](#)]
- [193] R. Boughezal, J. M. Campbell, R. K. Ellis, C. Focke, W. Giele, X. Liu, F. Petriello, and C. Williams, “Color singlet production at NNLO in MCFM”, *European Physical Journal C* **77** (2017) 7, arXiv:1605.08011. [[Cited on pages 131 and 140.](#)]
- [194] S. Alioli, P. Nason, C. Oleari, and E. Re, “NLO vector-boson production matched with shower in POWHEG”, *Journal of High Energy Physics* **07** (2008) 060, arXiv:0805.4802. [[Cited on page 134.](#)]
- [195] S. Okubo, “ $\varphi$ -meson and unitary symmetry model”, *Physics Letters* **5** (1963) 165. [[Cited on page 146.](#)]
- [196] G. Zweig, “An SU(3) model for strong interaction symmetry and its breaking. Version 2”, in “Developments in the Quark Theory of Hadrons”, D. Lichtenberg and S. P. Rosen, eds., vol. 1, p. 22. Hadronic Press, Nonantum, MA, 1964. [[Cited on page 146.](#)]
- [197] J. Iizuka, “Systematics and phenomenology of meson family”, *Progress of Theoretical Physics Supplement* **37** (1966) 21. [[Cited on page 146.](#)]
- [198] J.-M. Richard, “An introduction to the quark model”, in “Ferrara International School Niccolo Cabeo 2012: Hadronic spectroscopy Ferrara, Italy, May 21-26, 2012”. 2012. arXiv:1205.4326. [[Cited on pages 147 and 279.](#)]

## BIBLIOGRAPHY

---

- [199] M. B. Einhorn and S. D. Ellis, “Hadronic Production of the New Resonances: Are Gluons Important?”, *Physical Review Letters* **34** (1975) 1190–1193. [[Cited on page 147.](#)]
- [200] M. B. Einhorn and S. D. Ellis, “Hadronic production of the new resonances: Probing gluon distributions”, *Physical Review D* **12** (1975) 2007. [[Cited on page 147.](#)]
- [201] C.-H. Chang, “Hadronic production of  $J/\psi$  associated with a gluon”, *Nuclear Physics B* **172** (1980) 425. [[Cited on page 148.](#)]
- [202] A. Andronic *et al.*, “Heavy-flavour and quarkonium production in the LHC era: from proton-proton to heavy-ion collisions”, *European Physical Journal C* **76** (2016), no. 3, 107, arXiv:1506.03981. [[Cited on pages 148, 153, 157, and 269.](#)]
- [203] J. P. Lansberg, “ $J/\psi$ ,  $\psi'$  and  $\Upsilon$  production at hadron colliders: A Review”, *International Journal of Modern Physics A* **21** (2006) 3857, arXiv:hep-ph/0602091. [[Cited on page 148.](#)]
- [204] S. J. Brodsky and J.-P. Lansberg, “Heavy-quarkonium production in high energy proton-proton collisions at RHIC”, *Physical Review D* **81** (2010) 051502, arXiv:0908.0754. [[Cited on page 148.](#)]
- [205] **CDF** Collaboration, F. Abe *et al.*, “Production of  $J/\psi$  mesons from  $\chi_c$  meson decays in  $p\bar{p}$  collisions at  $\sqrt{s} = 1.8$  TeV”, *Physical Review Letters* **79** (1997) 578. [[Cited on page 148.](#)]
- [206] **Quarkonium Working Group** Collaboration, N. Brambilla *et al.*, “Heavy quarkonium physics”, arXiv:hep-ph/0412158. [[Cited on pages 148, 149, 150, and 151.](#)]
- [207] H. Fritzsch, “Producing heavy quark flavors in hadronic collisions: A test of quantum chromodynamics”, *Physics Letters B* **67** (1977) 217. [[Cited on page 148.](#)]
- [208] F. Halzen, “CVC for gluons and hadroproduction of quark flavours”, *Physics Letters B* **69** (1977) 105. [[Cited on page 148.](#)]
- [209] R. Gavai, D. Kharzeev, H. Satz, G. A. Schuler, K. Sridhar, and R. Vogt, “Quarkonium production in hadronic collisions”, *International Journal of Modern Physics A* **10** (1995) 3043, arXiv:hep-ph/9502270. [[Cited on page 149.](#)]

- [210] J. F. Amundson, O. J. P. Eboli, E. M. Gregores, and F. Halzen, “Quantitative tests of color evaporation: charmonium production”, *Physics Letters B* **390** (1997) 323, arXiv:hep-ph/9605295. [[Cited on page 149.](#)]
- [211] **CDF** Collaboration, A. Abulencia *et al.*, “Measurement of  $\sigma_{\chi_{c2}} \mathcal{B}(\chi_{c2} \rightarrow J/\psi \gamma)/\sigma_{\chi_{c1}} \mathcal{B}(\chi_{c1} \rightarrow J/\psi \gamma)$  in  $p\bar{p}$  collisions at  $\sqrt{s} = 1.96$  TeV”, *Physical Review Letters* **98** (2007) 232001, arXiv:hep-ex/0703028. [[Cited on page 149.](#)]
- [212] **CMS** Collaboration, S. Chatrchyan *et al.*, “Measurement of the relative prompt production rate of  $\chi_{c2}$  and  $\chi_{c1}$  in pp collisions at  $\sqrt{s} = 7$  TeV”, *European Physical Journal C* **72** (2012) 2251, arXiv:1210.0875. [[Cited on page 149.](#)]
- [213] V. Cheung and R. Vogt, “Polarized Heavy Quarkonium Production in the Color Evaporation Model”, *Physical Review D* **95** (2017), no. 7, 074021, arXiv:1702.07809. [[Cited on page 149.](#)]
- [214] G. T. Bodwin, E. Braaten, and G. P. Lepage, “Rigorous QCD Predictions for Decays of P-Wave Quarkonia”, in “The Fermilab Meeting DPF 92. Proceedings, 7th Meeting of the American Physical Society, Division of Particles and Fields, Batavia, USA, November 10-14, 1992. Vol. 1, 2”, p. 1063. 1992. arXiv:hep-ph/9211253. [[Cited on page 149.](#)]
- [215] J. P. Lansberg, “On the mechanisms of heavy-quarkonium hadroproduction”, *European Physical Journal C* **61** (2009) 693, arXiv:0811.4005. [[Cited on pages 150 and 279.](#)]
- [216] **ATLAS** Collaboration, G. Aad *et al.*, “Measurement of the differential cross-sections of prompt and non-prompt production of  $J/\psi$  and  $\psi(2S)$  in  $pp$  collisions at  $\sqrt{s} = 7$  and 8 TeV with the ATLAS detector”, *European Physical Journal C* **76** (2016), no. 5, 283, arXiv:1512.03657. [[Cited on page 151.](#)]
- [217] B. Paul, M. Mandal, P. Roy, and S. Chattapadhyay, “Systematic study of charmonium production in p-p collisions at LHC energies”, *Journal of Physics G: Nuclear and Particle Physics* **42** (2015), no. 6, 065101, arXiv:1411.6783. [[Cited on page 151.](#)]
- [218] R. Sharma and I. Vitev, “High transverse momentum quarkonium production and dissociation in heavy ion collisions”, *Physical Review C* **87** (2013), no. 4, 044905, arXiv:1203.0329. [[Cited on page 151.](#)]

## BIBLIOGRAPHY

---

- [219] Y.-Q. Ma and R. Venugopalan, “Comprehensive Description of  $J/\psi$  Production in Proton-Proton Collisions at Collider Energies”, *Physical Review Letters* **113** (2014), no. 19, 192301, arXiv:1408.4075. [[Cited on page 151.](#)]
- [220] Z. Sun and H.-F. Zhang, “Reconciling charmonium production and polarization data in the midrapidity region at hadron colliders within the nonrelativistic QCD framework”, *Chinese Physics C* **42** (2018), no. 4, 043104, arXiv:1505.02675. [[Cited on page 151.](#)]
- [221] H. S. Shao, H. Han, Y. Q. Ma, C. Meng, Y. J. Zhang, and K. T. Chao, “Yields and polarizations of prompt  $J/\psi$  and  $\psi(2S)$  production in hadronic collisions”, *Journal of High Energy Physics* **05** (2015) 103, arXiv:1411.3300. [[Cited on page 151.](#)]
- [222] CMS Collaboration, “Production of prompt and nonprompt  $J/\psi$  mesons in jets in pp collisions at  $\sqrt{s} = 5.02$  TeV”, Tech. Rep. CMS-PAS-HIN-18-012, CERN, Geneva, 2018. [[Cited on page 151.](#)]
- [223] LHCb Collaboration, R. Aaij *et al.*, “Study of  $J/\psi$  Production in Jets”, *Physical Review Letters* **118** (2017), no. 19, 192001, arXiv:1701.05116. [[Cited on page 151.](#)]
- [224] LHCb Collaboration, R. Aaij *et al.*, “First observation of  $B_s^0 \rightarrow J/\psi f_0(980)$  decays”, *Physics Letters B* **698** (2011) 115, arXiv:1102.0206. [[Cited on pages 151 and 279.](#)]
- [225] P. Braun-Munzinger and J. Stachel, “Charmonium from Statistical Hadronization of Heavy Quarks: A Probe for Deconfinement in the Quark-Gluon Plasma”, *Landolt-Bornstein* **23** (2010) 424, arXiv:0901.2500. [[Cited on page 153.](#)]
- [226] B. Alver, M. Baker, C. Loizides, and P. Steinberg, “The PHOBOS Glauber Monte Carlo”, arXiv:0805.4411. [[Cited on page 153.](#)]
- [227] F. Arleo, S. Peigné, and T. Sami, “Revisiting scaling properties of medium-induced gluon radiation”, *Physical Review D* **83** (2011) 114036, arXiv:1006.0818. [[Cited on page 154.](#)]
- [228] F. Arleo and S. Peigné, “Heavy-quarkonium suppression in p-A collisions from parton energy loss in cold QCD matter”, *Journal of High Energy Physics* **3** (2013) 122, arXiv:1212.0434. [[Cited on page 154.](#)]

- [229] S. Peigné, F. Arleo, and R. Kolevatov, “Coherent medium-induced gluon radiation in hard forward  $1 \rightarrow 1$  partonic processes”, *Physical Review D* **93** (2016) 014006, arXiv:1402.1671. [[Cited on page 154.](#)]
- [230] J. W. Cronin, H. J. Frisch, M. J. Shochet, J. P. Boymond, R. Mermod, P. A. Piroue, and R. L. Sumner, “Production of hadrons with large transverse momentum at 200, 300, and 400 GeV”, *Physical Review D* **11** (1975) 3105. [[Cited on page 154.](#)]
- [231] **ALICE** Collaboration, J. Adam *et al.*, “Rapidity and transverse-momentum dependence of the inclusive  $J/\psi$  nuclear modification factor in p-Pb collisions at  $\sqrt{s_{NN}} = 5.02$  TeV”, *Journal of High Energy Physics* **06** (2015) 055, arXiv:1503.07179. [[Cited on pages 155 and 280.](#)]
- [232] P. Braun-Munzinger and J. Stachel, “Charmonium from Statistical Hadronization of Heavy Quarks: A Probe for Deconfinement in the Quark-Gluon Plasma”, *Landolt-Börnstein* **23** (2010) 424, arXiv:0901.2500. [[Cited on page 157.](#)]
- [233] L. Grandchamp, R. Rapp, and G. E. Brown, “In-Medium Effects on Charmonium Production in Heavy-Ion Collisions”, *Physical Review Letters* **92** (2004) 212301, arXiv:hep-ph/0306077. [[Cited on page 157.](#)]
- [234] **NA50** Collaboration, B. Alessandro *et al.*, “ $\psi'$  production in Pb-Pb collisions at 158 GeV/nucleon”, *European Physical Journal C* **49** (2007) 559, arXiv:nucl-ex/0612013. [[Cited on page 157.](#)]
- [235] **CMS** Collaboration, V. Khachatryan *et al.*, “Measurement of Prompt  $\psi(2S) \rightarrow J/\psi$  Yield Ratios in Pb-Pb and p-p Collisions at  $\sqrt{s_{NN}} = 2.76$  TeV”, *Physical Review Letters* **113** (2014), no. 26, 262301, arXiv:1410.1804. [[Cited on pages 158, 159, 213, 215, 280, 283, and 284.](#)]
- [236] **ALICE** Collaboration, J. Adam *et al.*, “Differential studies of inclusive  $J/\psi$  and  $\psi(2S)$  production at forward rapidity in Pb-Pb collisions at  $\sqrt{s_{NN}} = 2.76$  TeV”, *Journal of High Energy Physics* **05** (2016) 179, arXiv:1506.08804. [[Cited on page 158.](#)]
- [237] X. Du and R. Rapp, “Sequential Regeneration of Charmonia in Heavy-Ion Collisions”, *Nuclear Physics A* **943** (2015) 147, arXiv:1504.00670. [[Cited on pages 158, 214, 215, and 284.](#)]

## BIBLIOGRAPHY

---

- [238] D. J. Lange, “The EvtGen particle decay simulation package”, *Nuclear Instruments and Methods in Physics Research Section A: Accelerators, Spectrometers, Detectors and Associated Equipment* **462** (2001) 152. [[Cited on page 161.](#)]
- [239] **CMS** Collaboration, V. Khachatryan *et al.*, “Event generator tunes obtained from underlying event and multiparton scattering measurements”, *European Physical Journal C* **76** (2016), no. 3, 155, arXiv:1512.00815. [[Cited on page 161.](#)]
- [240] I. P. Lokhtin and A. M. Snigirev, “A Model of jet quenching in ultrarelativistic heavy ion collisions and high  $p_T$  hadron spectra at RHIC”, *European Physical Journal C* **45** (2006) 211, arXiv:hep-ph/0506189. [[Cited on page 161.](#)]
- [241] CMS Collaboration, “Centrality and Event Plane reconstruction for PbPb collisions at 5 TeV in 2015”, Tech. Rep. CMS-HIN-AN-15-080, CERN, Geneva, 2015. [[Cited on pages 165, 166, 269, and 280.](#)]
- [242] T. Speer, K. Prokofiev, R. Frühwirth, W. Waltenberger, and P. Vanlaer, “Vertex Fitting in the CMS Tracker”, Tech. Rep. CMS-NOTE-2006-032, CERN, Geneva, Feb 2006. [[Cited on page 170.](#)]
- [243] R. Frühwirth, W. Waltenberger, and P. Vanlaer, “Adaptive vertex fitting”, *Journal of Physics G: Nuclear and Particle Physics* **34** (2007) 343. [[Cited on page 170.](#)]
- [244] **CMS** Collaboration, S. Chatrchyan *et al.*, “Description and performance of track and primary-vertex reconstruction with the CMS tracker”, *Journal of Instrumentation* **9** (2014), no. 10, P10009, arXiv:1405.6569. [[Cited on page 170.](#)]
- [245] J. C. Mason and D. C. Handscomb, “Chebyshev Polynomials”, CRC Press, 2002. [[Cited on page 173.](#)]
- [246] M. Pivk and F. R. Le Diberder, “ $\hat{\text{Plot}}$ : A Statistical tool to unfold data distributions”, *Nuclear Instruments and Methods in Physics Research Section A: Accelerators, Spectrometers, Detectors and Associated Equipment* **555** (2005) 356, arXiv:physics/0402083. [[Cited on page 175.](#)]
- [247] CMS Collaboration, “Muon performance studies in 2015 5.02 TeV pp and PbPb Data”, Tech. Rep. CMS-HIN-AN-16-048, CERN, Geneva, 2016. [[Cited on pages 190, 191, and 282.](#)]
- [248] K. S. Cranmer, “Kernel estimation in high-energy physics”, *Computer Physics Communications* **136** (2001) 198, arXiv:hep-ex/0011057. [[Cited on page 199.](#)]

- [249] CMS Collaboration, V. Khachatryan *et al.*, “Suppression and azimuthal anisotropy of prompt and nonprompt J/ $\psi$  production in PbPb collisions at  $\sqrt{s_{\text{NN}}} = 2.76$  TeV”, *European Physical Journal C* **77** (2017), no. 4, 252, arXiv:1610.00613. [[Cited on pages 203, 209, 210, 282, and 283.](#)]
- [250] CMS Collaboration, “CMS Luminosity Calibration for the pp Reference Run at  $\sqrt{s} = 5.02$  TeV”, Tech. Rep. CMS-PAS-LUM-16-001, CERN, Geneva, 2016. [[Cited on page 206.](#)]
- [251] X. Zhao and R. Rapp, “Medium Modifications and Production of Charmonia at LHC”, *Nuclear Physics A* **859** (2011) 114, arXiv:1102.2194. [[Cited on page 213.](#)]
- [252] CMS Collaboration, A. M. Sirunyan *et al.*, “Nuclear modification factor of D<sup>0</sup> mesons in PbPb collisions at  $\sqrt{s_{\text{NN}}} = 5.02$  TeV”, *Physics Letters B* **782** (2018) 474, arXiv:1708.04962. [[Cited on pages 213, 214, and 284.](#)]
- [253] CMS Collaboration, V. Khachatryan *et al.*, “Charged-particle nuclear modification factors in PbPb and pPb collisions at  $\sqrt{s_{\text{NN}}} = 5.02$  TeV”, *Journal of High Energy Physics* **4** (2017) 039, arXiv:1611.01664. [[Cited on pages 213, 214, and 284.](#)]
- [254] F. Arleo, “Quenching of Hadron Spectra in Heavy Ion Collisions at the LHC”, *Physical Review Letters* **119** (2017), no. 6, 062302, arXiv:1703.10852. [[Cited on page 213.](#)]
- [255] X. Du and R. Rapp, “ $\psi(2S)$  Production at the LHC”, *Journal of Physics: Conference Series* **779** (2017) 012042, arXiv:1609.04868. [[Cited on page 214.](#)]



## LIST OF TABLES

1.1 Basic properties of quarks, leptons and bosons from the SM. The table includes the mass, electric charge, spin and type of interactions of each particle. The values are taken from Ref. [21]. . . . .	6
2.1 LHC beam parameters during the highest luminosity physics fills. The luminosity values are averages for CMS. Information extracted from Ref. [96]. . . . .	42
3.1 Experimental values of the mass, width and branching fractions of weak bosons extracted from the PDG [21]. . . . .	71
3.2 Summary of the information of EPS09, EPPS16 and nCTEQ15 nuclear PDFs. . . . .	82
3.3 Simulated NLO samples used for the W-boson measurement in p-Pb at 8.16 TeV. The listed cross sections are the POWHEG NLO cross sections scaled by $A_{\text{Pb}} = 208$ , except for the $t\bar{t}$ production cross section which is taken from the CMS measurement in p-Pb at 8.16 TeV [186]. . . . .	88
3.4 Relative difference between the corrected and simulated signal efficiencies as a function of the generated muon $\eta_{\text{CM}}$ , separated in negative and positive charged muons. . . . .	115
3.5 QCD background parameters extrapolated to $I^\mu = 0.03$ . The results are presented for positive and negative charged muons in the $\eta_{\text{CM}}^\mu$ -inclusive range. . . . .	117
3.6 Event yields of $W^- \rightarrow \mu^- \bar{\nu}_\mu$ and background processes, extracted from the fits to the $p_T^{\text{miss}}$ distribution in each muon $\eta_{\text{CM}}^\mu$ region. All analysis selection criteria are applied including the muon $p_T > 25$ GeV/c. All uncertainties shown are statistical only. . . . .	123
3.7 Event yields of $W^+ \rightarrow \mu^+ \nu_\mu$ and background processes, extracted from the fits to the $p_T^{\text{miss}}$ distribution in each muon $\eta_{\text{CM}}^\mu$ region. All analysis selection criteria are applied including the muon $p_T > 25$ GeV/c. All uncertainties shown are statistical only. . . . .	124

---

3.8 Corrected event yields of $W^- \rightarrow \mu^- \bar{\nu}_\mu$ , given for each muon $\eta_{CM}^\mu$ bin. All analysis selection criteria are applied including the muon $p_T > 25$ GeV/c. The muon efficiency has been corrected by applying the tag-and-probe corrections, HF energy weights and vector boson $p_T$ weights, event-by-event. All uncertainties shown are statistical only. . . . .	125
3.9 Corrected event yields of $W^+ \rightarrow \mu^+ \nu_\mu$ , given for each muon $\eta_{CM}^\mu$ . All analysis selection criteria are applied including the muon $p_T > 25$ GeV/c. The muon efficiency has been corrected by applying the tag-and-probe corrections, HF energy weights and vector boson $p_T$ weights, event-by-event. All uncertainties shown are statistical only. . . . .	126
3.10 The RMS of the set of QCD background parameters extrapolated along all $\eta_{CM}^\mu$ regions. . . . .	129
3.11 QCD shape parameters extrapolated to the average muon isolation point $I^\mu = 0.08$ . . . . .	130
3.12 Maximum uncertainty of the measured observables determined for each category. The uncertainties of the $W \rightarrow \mu \nu_\mu$ differential cross sections are relative while for the forward-backward ratios and muon charge asymmetry they are absolute. . . . .	135
3.13 Results of the $\chi^2$ statistical test between the measurements and the theory calculations from the CT14 PDF, CT14+EPPS16 nPDF and CT14+nCTEQ15 nPDF models. The value of the $\chi^2$ , the number of degrees of freedom (ndf) and the $\chi^2$ probability (Prob.), are presented for the $W^\pm \rightarrow \mu^\pm \nu_\mu$ differential cross sections, the muon charge asymmetry, the $W^\pm \rightarrow \mu^\pm \nu_\mu$ forward-backward ratios, and the charge-summed forward-backward ratio, respectively. . . . .	143
4.1 The width and mass of charmonium states below the $D\bar{D}$ -meson pair mass. Information taken from Ref. [21]. . . . .	146
4.2 Branching ratios for decays of $J/\psi$ and $\psi(2S)$ mesons. Information taken from Ref. [21]. . . . .	147
4.3 Branching ratios for inclusive charmonium decays of b-hadron mixtures ( $B^\pm/B^0/B_s^0/b$ -baryon) determined from measurements at LHC, LEP, Tevatron and SppS. Information taken from Ref. [21]. . . . .	152
4.4 Fragmentation fractions of bottom quarks into b hadrons measured at Tevatron in $p\bar{p}$ collisions at $\sqrt{s} = 1.96$ TeV and at LEP in $Z \rightarrow b\bar{b}$ decays. Information taken from Ref. [21]. . . . .	152

4.5 Binding energy and radius of $J/\psi$ , $\chi_c(1P)$ and $\psi(2S)$ mesons. Information taken from Ref. [202]. . . . .	157
4.6 Total integrated luminosity of each dataset used in the analysis of the charmonium nuclear modification in p-p and Pb-Pb collisions at $\sqrt{s_{\text{NN}}} = 5.02 \text{ TeV}$ . . . . .	160
4.7 Simulations used in the analysis of the charmonium production in Pb-Pb and p-p collisions at 5.02 TeV. . . . .	162
4.8 Values of the centrality-integrated number of participants $\langle N_{\text{part}} \rangle$ and nuclear overlap factor $\langle T_{\text{AA}} \rangle$ , determined in the different collision centrality ranges used in the analysis. Information taken from the internal analysis note [241]. . . . .	166
4.9 Parameters extracted from the prompt $J/\psi$ -meson simulation and used to constrain the double Crystal Ball functions in each differential and integrated rapidity region. The parameters fixed to simulation in both Pb-Pb and p-p data fits are shown in bold blue colour, while those fixed to simulation only on Pb-Pb data are displayed in bold red colour. The $f_{J/\psi}$ values from simulation are only used for the initialisation step in the data fits. . . . .	173
4.10 Results of the LLR test used to determine the order of the Chebyshev function for the background $\mu^+ \mu^-$ invariant mass fitted in Pb-Pb data within $0.6 <  y^{\mu\mu}  < 1.2$ and $9.5 \leq p_T^{\mu\mu} < 11 \text{ GeV}/c$ . The LLR test results of which the $\chi^2$ probability determined for two consecutive orders ( $M = N + 1$ and $M = N + 2$ ) are higher than 5% are highlighted in bold. . . . .	174
4.11 Parameters extracted for the double Crystal Ball function from the prompt $J/\psi$ -meson p-p simulation after applying the $\ell_{J/\psi}$ selection. The values shown correspond to the $p_T$ -centrality integrated fits. The CB parameters fixed to simulation when performing the data fits are shown in bold font. . . . .	185
4.12 Relative width used in the Gaussian penalty functions for the tail parameters $\alpha_{J/\psi}$ and $n_{J/\psi}$ , and the ratio of CB widths. The Gaussian width is shown relative to the nominal parameter value. . . . .	196
C.1 Summary of the bin boundaries used in the $J/\psi$ -meson $R_{\text{AA}}$ analysis as a function of centrality for different rapidity regions. . . . .	
236	
C.2 Summary of the bin boundaries used in the $J/\psi$ -meson $R_{\text{AA}}$ analysis as a function of $p_T$ for different rapidity regions. . . . .	
237	
C.3 Summary of the bin boundaries used in the $J/\psi$ -meson $R_{\text{AA}}$ analysis as a function of $p_T$ for different centrality intervals. . . . .	
238	
C.4 Summary of the bin boundaries used in the $\psi(2S)$ -to- $J/\psi$ double ratio analysis.	
239	



## LIST OF FIGURES

1.1	Feynman diagrams of the QCD vertices for quark-gluon coupling (left), triple-gluon self-coupling (middle) and quadri-gluon self-coupling (right). . . . .	7
1.2	Feynman diagrams of 1-loop contributions to pQCD. . . . .	8
1.3	Summary of measurements of $\alpha_s$ as a function of the energy scale $Q$ . Figure taken from Ref. [21]. . . . .	9
1.4	Sketch of the gluon string breaking between a quark $Q$ and an anti-quark $\bar{Q}$ due to $q\bar{q}$ pair creation. Figure taken from Ref. [33]. . . . .	10
1.5	Feynman diagram of deep inelastic scattering of electrons against protons. .	12
1.6	Next-to-leading order QCD fits to the ZEUS $F_2$ structure function data from 1996, 1997 and proton fixed-target at HERA. The error bands of the fit represent the total experimental uncertainty from both correlated and uncorrelated sources. Figure taken from Ref. [39]. . . . .	13
1.7	Feynman diagram of the Drell-Yan process. . . . .	13
1.8	Sketch of the QCD phase diagram for nuclear matter. The solid lines show the phase boundaries and the solid circle represents the critical point. Figure taken from Ref. [43]. . . . .	15
1.9	Illustration of two nucleus with impact parameter $b$ before (left) and after (right) colliding. Figure taken from Ref. [43]. . . . .	18
1.10	Schematic representation of the optical Glauber model geometry. . . . .	19
1.11	Sketch of the evolution of a relativistic heavy-ion collision. . . . .	20
1.12	Sketch of the elliptic flow produced in non-central heavy-ion collisions. Figure taken from Ref. [58]. . . . .	22
1.13	Elliptic flow distribution of as a function of transverse momentum for $\pi^\pm$ mesons, $K_s^0$ mesons, antiprotons and $\Lambda$ baryons measured by STAR collaboration in Au-Au collisions at $\sqrt{s_{NN}} = 200$ GeV. The results are compared with relativistic hydrodynamic calculations. Figure taken from Ref. [62]. . . . .	24

- 1.14 3D display of the  $\Delta\eta$ - $\Delta\phi$  correlation function between two charged particles with  $1 \text{ GeV}/c < p_T < 3 \text{ GeV}/c$ , measured by the CMS collaboration in high multiplicity ( $N \geq 110$ ) p-p collisions at  $\sqrt{s} = 7 \text{ TeV}$ . Figure taken from Ref. [63]. . . . . 25
- 1.15 Left: Distribution of the yield of inclusive protons and strange baryons, measured by the STAR collaboration in Au-Au collisions at  $\sqrt{s_{NN}} = 200 \text{ GeV}$  (solid symbols) and by the NA57 collaboration in Pb-Pb collisions at  $\sqrt{s_{NN}} = 17.3 \text{ GeV}$  (empty symbols), relative to the corresponding yield in p-p (at RHIC) or p-Be (at SPS) collisions scaled by  $N_{\text{part}}$ . Figure from Ref. [69]. Right: Distribution of the  $p_T$ -integrated yield ratios of strange hadrons to pions as a function of the average charged-particle multiplicity measured in  $|\eta| < 0.5$  by the ALICE collaboration in p-p, p-Pb and Pb-Pb collisions at  $\sqrt{s} = 7 \text{ TeV}$ ,  $\sqrt{s_{NN}} = 5.02 \text{ TeV}$  and  $\sqrt{s_{NN}} = 2.76 \text{ TeV}$ , respectively. Figure from Ref. [70]. . . . . 26
- 1.16 Sketch of the production mechanism of two jets in proton-proton (top) and heavy-ions (bottom) collisions. Figure taken from Ref. [73]. . . . . 27
- 1.17 Distribution of the nuclear modification factor  $R_{AA}$  of direct photons, pions,  $\eta$  mesons and charged hadrons, measured at RHIC in central Au-Au collisions at  $\sqrt{s_{NN}} = 200 \text{ GeV}$  as a function of  $p_T$ . Theoretical predictions of radiative parton energy loss are also included. Figure taken from Ref. [75]. . . . . 29
- 1.18 Dijet asymmetry measured by the ATLAS collaboration in lead-lead collisions at  $\sqrt{s_{NN}} = 2.76 \text{ TeV}$  (points) and proton-proton collisions at  $\sqrt{s} = 7 \text{ TeV}$  (open circles). The top panel shows the dijet asymmetry distributions and unquenched HIJING with superimposed PYTHIA dijets (solid yellow histograms), as a function of collision centrality. The bottom panel shows the distribution of the azimuthal angle between the two jets  $\Delta\phi$ , for data and HIJING+PYTHIA, also as a function of centrality. Figure taken from Ref. [76]. . . . . 30
- 1.19 Dimuon invariant mass distribution measured by the CMS collaboration in Pb-Pb collisions at  $\sqrt{s_{NN}} = 5.02 \text{ TeV}$ . The total fit (solid blue line), the background component (dot-dashed blue line) and the individual  $\Upsilon(1S)$ ,  $\Upsilon(2S)$  and  $\Upsilon(3S)$  mass peaks (dotted gray lines) are shown. The dashed red line represents the p-p signal shapes added on top of the Pb-Pb background and normalised to the  $\Upsilon(1S)$  mass peak in Pb-Pb. Figure taken from Ref. [80]. . . . . 31

1.20 Nuclear modification factor of $J/\psi$ meson as a function of transverse momentum measured by the ALICE collaboration in the 0% – 20% most central Pb-Pb collisions at $\sqrt{s_{\text{NN}}} = 2.76$ TeV compared to results from the PHENIX collaboration measured in the 0% – 20% most central Au-Au collisions at $\sqrt{s_{\text{NN}}} = 200$ GeV. Figure taken from Ref. [88]. . . . .	33
1.21 Nuclear modification factor $R_{\text{AA}}$ of $Z \rightarrow e^+e^-$ (blue squares) and $Z \rightarrow \mu^+\mu^-$ (red circles) events as a function of $N_{\text{part}}$ measured by the CMS collaboration in Pb-Pb collisions at $\sqrt{s_{\text{NN}}} = 2.76$ TeV. The open points represent the centrality-integrated $R_{\text{AA}}$ and the vertical lines (boxes) correspond to statistical (systematic) uncertainties. Figure taken from Ref. [89]. . . . .	34
2.1 Schematic diagram of the LHC injection chain for protons and Pb nuclei. The proton and Pb ion trajectories are indicated with red and blue arrows, accordingly. The location of each LHC detector is also included. . . . .	36
2.2 Schematic diagram of the LHC layout. Figure taken from Ref. [90]. . . . .	38
2.3 Integrated nucleon-pair luminosity delivered by the LHC to each experiment during Pb-Pb collisions at $\sqrt{s_{\text{NN}}} = 5.02$ TeV. The integrated luminosity of p-Pb collisions at $\sqrt{s_{\text{NN}}} = 5.02$ TeV and Pb-Pb collisions at $\sqrt{s_{\text{NN}}} = 2.76$ TeV are included for comparison. Figure taken from Ref. [94]. . . . .	41
2.4 Integrated proton-nucleus luminosity delivered by the LHC to each experiment during p-Pb collisions at $\sqrt{s_{\text{NN}}} = 8.16$ TeV (solid lines). The integrated luminosity of p-Pb collisions at $\sqrt{s_{\text{NN}}} = 5.02$ TeV (dashed lines) is included for comparison. Figure taken from Ref. [95]. . . . .	42
2.5 Cutaway view of the CMS detector in its configuration used during 2015 and 2016. Labels and basic details of each subdetector are included. [97] . . . . .	43
2.6 Schematic diagram of the coordinate system used in the CMS experiment. . .	45
2.7 View of the CMS tracker in the $r$ - $z$ plane. Each line represents a detector module. Figure taken from Ref. [1]. . . . .	46
2.8 Schematic layout [1] (left) of the CMS electromagnetic calorimeter, and its corresponding one-quarter geometric view [101] (right). . . . .	47
2.9 Geometric view of one quarter of the CMS detector, displaying the subdetectors of the hadron calorimeter: HB, HE, HF and HO. Figure taken from Ref. [99].	49
2.10 Geometric view of one quadrant the CMS detector in the $r$ - $z$ plane. Each chamber of the muon system is shown in blue (RPC), green (CSC) and orange (DT). Figure taken from Ref. [102]. . . . .	51

2.11 Schematic layout of a DT cell (left) and a DT chamber (right). Figures taken from [103]. . . . .	52
2.12 Schematic layout of a CSC. Figure taken from [1]. . . . .	53
2.13 Cross section view (left) [104] and exploded view (right) [105] of a RPC module. . . . .	53
2.14 Diagram of the legacy L1 trigger of CMS. Figure taken from Ref. [107]. . . . .	55
2.15 Diagram of the CMS L1 trigger used in 2016. . . . .	57
2.16 Cross section view of the CMS detector showing how particles interact in the CMS. The different types of muon tracks are indicated by boxes. Figure taken from Ref. [113]. . . . .	61
 3.1 Feynman diagrams of the decay modes of $W^+$ (left), $W^-$ (middle) and $Z$ (right) bosons to fermions. . . . .	71
3.2 Leading order Feynman diagram of $W$ boson production to final state leptons, from a collision between an incoming proton ( $p$ ) and a bound nucleon ( $a$ ) in a $Pb$ nucleus. . . . .	72
3.3 Next-to-leading order Feynman diagrams of $W$ boson partonic production to final state leptons. . . . .	73
3.4 Schematic diagram of the production of $W^-$ (left) and $W^+$ (right) bosons to muonic decays. The black arrows represent the particle direction of motion whereas the blue arrows correspond to its spin. The spin of the $W^\pm$ boson points in the direction of the anti-quark. . . . .	74
3.5 Results of the CT14 proton PDFs at NNLO derived at $Q = 2\text{ GeV}$ (left) and $Q = 100\text{ GeV}$ (right). Figures taken from Ref. [153]. . . . .	75
3.6 Illustration of the different nuclear PDF effects. Figure taken from Ref. [156]. . . . .	76
3.7 Results of the EPPS16 nuclear correction factor $R^A$ for $Pb$ ions at $Q^2 = 10\text{ GeV}^2$ , corresponding to: up valence quarks (top-left), down valence quarks (top-middle), up anti-quarks (top-right), down anti-quarks (bottom-left), strange anti-quarks (bottom-middle) and gluons (bottom-right). The black curve represents the central fit while the blue bands shows the total uncertainty of the PDF fit. The results are compared against a baseline made by performing the EPPS16 fits on the same datasets used for EPS09. Figures taken from Ref. [161]. . . . .	79

3.8 Results of the nCTEQ15 full nuclear PDFs for Pb ions $f^{\text{Pb}}$ at $Q = 10 \text{ GeV}$ (blue curve with band), compared to the corresponding ones from EPS09 [159] (green curve with band) and HKN07 [164] (orange curve with band). The plots, in order from top-left to bottom-right, correspond to: gluons, strange quarks, up valence quarks, down valence quarks, up quarks, down quarks, up anti-quarks and down anti-quarks. Figures taken from Ref. [163]. . . . .	80
3.9 Comparison between the EPPS16 (blue curve with band), nCTEQ15 (red curves with hatching) and DSSZ12 (green curve with band) nuclear modifications performed at $Q^2 = 10^4 \text{ GeV}^2$ , corresponding to: up valence quarks (top-left), down valence quarks (top-middle), up anti-quarks (top-right), down anti-quarks (bottom-left), strange anti-quarks (bottom-middle) and gluons (bottom-right). Figures provided by the EPPS16 authors. . . . .	81
3.10 Distribution of the production cross section for $Z \rightarrow \mu^+ \mu^-$ measured in p-Pb collisions at $\sqrt{s_{\text{NN}}} = 5.02 \text{ TeV}$ as a function of the Z-boson rapidity in the centre-of-mass frame. Figure taken from Ref. [170]. . . . .	83
3.11 Distribution of the production cross section for $W^- \rightarrow \mu^- \bar{\nu}_\mu$ (left) and $W^+ \rightarrow \mu^+ \nu_\mu$ (right) measured in p-Pb collisions at $\sqrt{s_{\text{NN}}} = 5.02 \text{ TeV}$ as a function of the muon rapidity in the centre-of-mass frame. Figures taken from Ref. [172].	83
3.12 Distribution of the production cross section for $W^- \rightarrow \ell^- \bar{\nu}_\ell$ (left) and $W^+ \rightarrow \ell^+ \nu_\ell$ (middle), and the lepton charge asymmetry (right) measured in p-Pb collisions at $\sqrt{s_{\text{NN}}} = 5.02 \text{ TeV}$ as a function of the lepton pseudorapidity in the laboratory frame. The CT10 PDF calculations with EPS09 (green line) and without (red line) nuclear PDF corrections are included. The bottom panels present the ratio of the CT10+EPS09 (green line) and data (black points) normalised to the CT10 baseline. Figures taken from Ref. [171]. . . . .	84
3.13 Survival probability of single muons from a $Z/\gamma^* \rightarrow \mu^+ \mu^-$ ( $M > 30 \text{ GeV}/c^2$ ) simulation, as a function of the muon $\eta_{\text{CM}}^\mu$ and $p_T^\mu$ , separated in negative (left) and positive (right) charged muons. Muons are required to have $p_T > 25 \text{ GeV}/c$ and $ \eta  < 2.4$ , match the trigger and pass the isolation and identification criteria.	92
3.14 Flowchart illustrating the way the events are classified. . . . .	93
3.15 Muon $p_T$ distribution extracted from the W-boson enhanced sample before (left) and after (right) applying the boson $p_T$ weights. The red points correspond to data, while the blue and red filled areas correspond to events from the $W \rightarrow \mu \nu_\mu$ and $Z/\gamma^* \rightarrow \mu^+ \mu^-$ simulations, respectively. The bottom panels show the ratio of data over simulation. . . . .	94

3.16 Distribution of the number of tracks per event (left) and the total energy deposited in the HF calorimeter (right) in $Z \rightarrow \mu^+ \mu^-$ events. The red points and filled area correspond to data and $Z/\gamma^* \rightarrow \mu^+ \mu^-$ simulation, respectively.	96
3.17 Comparison of the $p_T^{\text{miss}}$ distribution in data and simulation for $Z \rightarrow \mu^+ \mu^-$ events before (left) and after (right) applying the HF energy weights. . . . .	97
3.18 Distribution of the $p_T^{\text{miss}}$ in data and simulation for $Z \rightarrow \mu^+ \mu^-$ selected events.	98
3.19 Definition and components of the recoil $\vec{u}_T$ for $Z \rightarrow \mu^+ \mu^-$ events. . . . .	98
3.20 Distributions of the $u_{\parallel}$ (top) and $u_{\perp}$ (bottom) recoil components in data (left) and simulation (right). The fit function is based on a weighed sum of two Gaussian distributions as defined in Eq. (3.32). The solid black line represents the total fit function while the Gaussian components are depicted by the green and red dashed lines. The plots correspond to the $q_T^Z$ bin [3, 4] GeV/c. . . . .	100
3.21 Fits of the profile of $-\mu_{\parallel}$ as a function of $q_T^Z$ . The results are derived from $Z \rightarrow \mu^+ \mu^-$ events in data (left) and simulation (right). The yellow band represents the 68% error band of the fit. . . . .	101
3.22 Fits of the profile of $\mu_{\perp}$ as a function of $q_T^Z$ . The results are derived from $Z \rightarrow \mu^+ \mu^-$ events in data (left) and simulation (right). The yellow band represents the 68% error band of the fit. . . . .	101
3.23 Fits to the profile of the $\sigma_{\parallel,1}$ (left), $\sigma_{\parallel,2}$ (middle) and weighed average $\sigma_{\parallel}$ (right) values of the parallel recoil component as a function of $q_T^Z$ . The results are derived from $Z \rightarrow \mu^+ \mu^-$ events in data (top) and simulation (bottom). . . . .	102
3.24 Fits for the $\sigma_{\perp,1}$ (left), $\sigma_{\perp,2}$ (middle) and weighed average $\sigma_{\perp}$ (right) values of the recoil perpendicular component as a function of $q_T$ . The results are derived from $Z \rightarrow \mu^+ \mu^-$ events in data (top) and simulation (bottom). . . . .	103
3.25 A comparison of the $p_T^{\text{miss}}$ distribution from $Z \rightarrow \mu^+ \mu^-$ events between data and simulation, before (left) and after (right) calibrating the simulated recoil. The distributions of the simulated HF energy and generated Z-boson $p_T$ have been weighed. . . . .	105
3.26 Comparison of the $p_T^{\text{miss}}$ distribution in data and simulation for positive-charged muons in the $\eta_{\text{CM}}^{\mu}$ -inclusive signal region. The results are shown before (top-left) and after (top-right) applying the recoil calibrations using the nominal scaling method. The result using the alternative smearing method (bottom) is also presented. . . . .	106

---

3.27 Comparison of the signal efficiency derived from the pPb and Pbp $W \rightarrow \mu\nu_\mu$ simulations as a function of the generated muon $\eta_{\text{lab}}$ , separated in negative (left) and positive (right) charged muons. The distributions of the simulated HF energy and generated W-boson $p_T$ have been weighed. The bottom panel shows the ratio of Pbp over pPb signal efficiencies. . . . .	108
3.28 Simulated signal efficiency derived from the $W \rightarrow \mu\nu_\mu$ NLO simulations as a function of the generated muon $\eta_{\text{CM}}$ , separated in negative (left) and positive (right) charged muons. The distributions of the simulated HF energy and generated W-boson $p_T$ have been weighed. . . . .	108
3.29 Fits to the tag-probe invariant mass distribution for passing (left) and failing (right) probes, used to measure the STA reconstruction efficiency. The results correspond to the probe kinematic region: $ \eta_{\text{lab}}  < 2.4$ and $50 < p_T < 80$ GeV/c. Figures taken from the internal analysis note [188]. . . . .	110
3.30 Muon identification (left) and isolation (right) efficiencies extracted from data (blue) and simulation (red) using the TnP method, as a function of the probe $p_T$ . The bottom panels show the data-to-simulation efficiency ratio. The results of the fits to the efficiencies are also shown. Figures taken from the internal analysis note [188]. . . . .	111
3.31 Muon trigger efficiency extracted from data (blue) and simulation (red) using the TnP method, as a function of the probe $\eta_{\text{lab}}$ . The bottom panel shows the data-to-simulation efficiency ratio. Figure taken from the internal analysis note [188]. . . . .	112
3.32 Corrected signal efficiency as a function of the generated muon $\eta_{\text{CM}}$ , separated in negative (left) and positive (right) charged muons. The yellow and green boxes represents the uncertainty on the signal efficiency due to the TnP statistics and systematics, respectively. . . . .	114
3.33 QCD jet background fits to the $p_T^{\text{miss}}$ distribution in a control sample of non-isolated muon events corresponding to the muon isolation bins: $0.4 < I^\mu < 0.5$ (left) and $0.8 < I^\mu < 0.9$ (right). The results are shown for positive (top) and negative (bottom) charged muons separately. . . . .	118
3.34 Linear fits to the profile of the QCD background parameters: $\sigma_0$ (left), $\sigma_1$ (middle) and $\sigma_2$ (right), with respect to the muon isolation variable $I^\mu$ . The results are shown for negative (top) and positive (bottom) charged muons in the $\eta_{\text{CM}}^\mu$ -inclusive range. The red points represents the value obtained by linearly extrapolating to $I^\mu = 0.03$ . . . . .	119

3.35 Muon $\eta_{\text{CM}}^\mu$ dependence of $\sigma_0$ (left), $\sigma_1$ (middle) and $\sigma_2$ (right) parameters extrapolated to $I^\mu = 0.03$ . The results are shown for negative (top) and positive (bottom) charged muons. The red line corresponds to the QCD jet parameter extrapolated in the $\eta_{\text{CM}}^\mu$ -inclusive range. . . . .	120
3.36 The $p_T^{\text{miss}}$ distribution for $W^- \rightarrow \mu^- \bar{\nu}_\mu$ (left) and $W^+ \rightarrow \mu^+ \nu_\mu$ (right) events within the $\eta_{\text{CM}}^\mu$ -inclusive range, shown in linear scale. Unbinned fits to the data (black points) are performed with six contributions, stacked from top to bottom: $W \rightarrow \mu \nu_\mu$ (yellow), QCD jet (light blue), $Z/\gamma^* \rightarrow \mu^+ \mu^-$ (green), $W \rightarrow \tau \nu_\tau$ (red), $Z/\gamma^* \rightarrow \tau \bar{\tau}$ (dark blue) and $t\bar{t}$ (orange). The lower panel, on each figure, display the ratio of the measurements over the result of the fit. The Baker-Cousins [191] $\chi^2$ test value over the number of degrees of freedom is also shown. . . . .	122
3.37 Uncertainty corresponding to each category with respect to $\eta_{\text{CM}}$ . The plots are divided as: $W^- \rightarrow \mu^- \bar{\nu}_\mu$ (top-left) and $W^+ \rightarrow \mu^+ \nu_\mu$ (top-right) cross sections, $W^- \rightarrow \mu^- \bar{\nu}_\mu$ (middle-left) and $W^+ \rightarrow \mu^+ \nu_\mu$ (middle-right) $R_{FB}$ , and the charge-summed $R_{FB}$ (bottom-left) and muon charge asymmetry (bottom-right). The uncertainties of the cross sections are relative while for the $R_{FB}$ and muon charge asymmetry are absolute. The luminosity uncertainty is not included. .	136
3.38 Correlation matrices for: $W^\pm$ cross section (top-left) , $W^\pm R_{FB}$ (top-right) , charge-inclusive $R_{FB}$ (bottom-left) , and charge asymmetry (bottom-right). The lines in the top plots are used to separate the different muon charge bins.	138
3.39 Differential production cross sections for $W^+ \rightarrow \mu^+ \nu_\mu$ (left) and $W^- \rightarrow \mu^- \bar{\nu}_\mu$ (right), as a function of the muon pseudorapidity in the center-of-mass frame. The brackets represent the statistical and systematic uncertainties summed in quadrature, while the error bars show the statistical uncertainties only. The global luminosity uncertainty of 3.5% [173] is not shown. . . . .	139
3.40 Muon charge asymmetry as a function of the muon pseudorapidity in the center-of-mass frame. The brackets represent the statistical and systematic uncertainties summed in quadrature, while the error bars show the statistical uncertainties only. . . . .	140
3.41 Forward-backward ratios, for the positive (top-left), negative (top-right) and all (bottom) charged muons. The brackets represent the statistical and systematic uncertainties summed in quadrature, while the error bars show the statistical uncertainties only. . . . .	141

3.42 Differential cross sections for $W^+ \rightarrow \mu^+ \nu_\mu$ (left) and $W^- \rightarrow \mu^- \bar{\nu}_\mu$ (right), as a function of the muon $\eta_{CM}^\mu$ . Errors bars represent the statistical uncertainties, while the brackets represent the statistical and systematic uncertainties summed in quadrature. The global luminosity uncertainty of 3.5% is not displayed. Theoretical predictions with (CT14+EPPS16 shown in dashed green line and CT14+nCTEQ15 shown in dashed brown line) and without (CT14, solid red line) PDF nuclear modifications are also shown, with the uncertainty bands. All theory uncertainty bands include the PDF uncertainties. . . . .	142
3.43 Muon charge asymmetry of $W \rightarrow \mu \nu_\mu$ , given for each muon $\eta_{CM}^\mu$ range. Errors bars represent the statistical uncertainties, while the brackets represent the statistical and systematic uncertainties summed in quadrature. Theoretical predictions with (CT14+EPPS16 shown in dashed green line and CT14+nCTEQ15 shown in dashed brown line) and without (CT14, solid red line) PDF nuclear modifications are also shown, with the uncertainty bands. All theory uncertainty bands include the PDF uncertainties. . . . .	143
3.44 Forward-backward ratio of $W \rightarrow \mu \nu_\mu$ , given for each muon $\eta_{CM}^\mu$ range separated in negative (top-left), positive (top-right) and all (bottom) charged muons. Errors bars represent the statistical uncertainties, while the brackets represent the statistical and systematic uncertainties summed in quadrature. Theoretical predictions with (CT14+EPPS16 shown in dashed green line and CT14+nCTEQ15 shown in dashed brown line) and without (CT14, solid red line) PDF nuclear modifications are also shown, with the uncertainty bands. All theory uncertainty bands include the PDF uncertainties. . . . .	144
4.1 Illustration of the different charmonium decays to lower mass charmonium states. The dashed (solid) lines represent radiative (hadronic) decays. Figure taken from Ref. [198]. . . . .	147
4.2 Illustration of a colour-singlet (left) and colour-octet (right) Feynman diagram, at leading order ( $\alpha_s^3$ ), that contribute to the production of quarkonium states. Diagrams taken from Ref. [215]. . . . .	150
4.3 Feynman diagram of a $B_s^0$ decay to $J/\psi$ meson. Diagram taken from Ref. [224].	151
4.4 Gluon nuclear PDF modification factor determined with EPPS16 (black curve with blue band) and nCTEQ15 (red curves with hatching) nPDF calculations at $Q^2 = 10 \text{ GeV}^2$ . Figure taken from Ref. [161]. . . . .	154

4.5 Nuclear modification factor of $\text{J}/\psi$ mesons as a function of $p_{\text{T}}$ in the backward (top-left), mid (top-right) and forward (bottom) rapidity regions. The bars (boxes) represent the statistical (systematic) uncertainties, while the gray box at unity indicate the size of the global uncertainty. The results are compared to nPDF (EPS09), energy loss (Arleo et al), and gluon saturation (CGC) calculations. Figure taken from Ref. [231]. . . . .	155
4.6 Double ratio of $\psi(2\text{S})$ over $\text{J}/\psi$ yields as a function of $\langle N_{\text{part}} \rangle$ , in the mid-rapidity (blue squares) and forward rapidity (red circles) regions. The results integrated in centrality are shown at the rightmost edge. The bars (boxes) represents the statistical (systematic) uncertainties, while the boxes at unity indicate the uncertainties on the p-p measurements. Figure taken from Ref. [235]. . . . .	159
4.7 Distribution of the total energy deposited in the HF calorimeters in Pb-Pb collisions at 5.02 TeV, for minimum-bias events passing the GEF selection. The different centrality classes are shown. Figure taken from the internal analysis note [241]. . . . .	165
4.8 Centrality distribution of $\mu^+ \mu^-$ events in Pb-Pb collisions passing the GEF cuts (red), with $2.2 < M_{\mu^+ \mu^-} < 4.5 \text{ GeV}/c^2$ , for $ y  < 1.6$ (left) and $1.6 <  y  < 2.4$ (right). The distribution of the minimum-bias sample, flat by definition, is shown in black. The limits of the centrality bins used for the $\psi(2\text{S})$ analysis are shown as vertical dashed lines, with the most central (peripheral) range on the right (left). The average centrality in each centrality range is also shown as an arrow, in red and black for the dimuon and minimum-bias datasets, respectively. . . . .	165
4.9 Distribution of the ratio of the number of reconstructed, identified and triggered muons over the number of generated muons, as a function of muon $p_{\text{T}}$ and $\eta$ . The results are derived from the prompt $\text{J}/\psi$ simulations corresponding to p-p (left) and Pb-Pb (right) collisions. The red line represents the single muon kinematic cuts. . . . .	168
4.10 Results of the 2D fits performed on Pb-Pb data, projected onto the dimuon invariant mass (left) and pseudoproper-decay length (right) variables. . . . .	170
4.11 Fit to the $\mu^+ \mu^-$ invariant mass distribution in Pb-Pb simulation derived at $9.5 < p_{\text{T}} < 11 \text{ GeV}/c$ in the rapidity region $1.2 <  y  < 1.8$ . The black line represents the total fit model while the green and orange lines represent the shape of each CB component. . . . .	172

4.12 Results of the fits to the $\mu^+ \mu^-$ invariant mass distribution in Pb-Pb (left) and p-p (right) data. The black line represents the total fit model while the blue filled area represents the fitted background shape. . . . .	174
4.13 Distributions of the $\sigma_\ell$ for signal (red line), background (blue line) and all (green line) dimuons, extracted from Pb-Pb (left) and p-p (right) data. The bottom panel shows the ratio between the data and the total template histogram extracted using the sPlot technique. . . . .	176
4.14 Results of the $\ell_{J/\psi}$ resolution fits for signal dimuons in data. The results are presented as a function of $\ell_{J/\psi}/\sigma_\ell$ and the dashed lines represent the fitted range. . . . .	177
4.15 Fits to the $\ell_{J/\psi}$ distribution of generated nonprompt $J/\psi \rightarrow \mu^+ \mu^-$ events in Pb-Pb (left) and p-p (right) simulations. The fitted value for $\lambda_B = \lambda_{DSS}$ is shown. . . . .	178
4.16 Fits to the $\ell_{J/\psi}$ distribution of background events in Pb-Pb (left) and p-p (right) collision data. . . . .	179
4.17 Distribution of $\ell_{J/\psi}$ (left) in the p-p simulations of prompt and nonprompt $J/\psi$ mesons, and an illustration (right) of the way the $\ell_{J/\psi}$ selection threshold is chosen. The results corresponds to the mid-rapidity region $ y^{\mu\mu}  < 1.6$ . . . . .	181
4.18 Profile of the $\ell_{J/\psi}$ selection thresholds (green points) with respect to $p_T^{\mu\mu}$ , extracted from the $J/\psi$ simulations in the mid-rapidity (left) and forward rapidity (right) regions. The fitted functions (red lines) are also displayed and the values of their parameters are shown in the box. . . . .	182
4.19 Efficiency of passing the $\ell_{J/\psi}$ selection as a function of $p_T^{\mu\mu}$ for prompt $J/\psi$ (black points), prompt $\psi(2S)$ (red points) and nonprompt $J/\psi$ (blue points) mesons. The results are extracted from p-p (top) and Pb-Pb (bottom) simulations in the mid-rapidity (left) and forward rapidity (right) regions. . . . .	183
4.20 Fits to the $m^{\mu\mu}$ distribution in p-p (left) and Pb-Pb (right) collisions. The results correspond to dimuon events derived in $p_T$ -centrality-inclusive region at mid-rapidity after applying the $\ell_{J/\psi}$ selection. The black line represents the total fit model while the blue filled area represents the fitted background shape. . . . .	185
4.21 Definition of the different categories of events considered for the subtraction of nonprompt charmonia. . . . .	186
4.22 Data-to-simulation ratios of the prompt $J/\psi$ -meson $p_T$ distribution measured in the $ y^{\mu\mu}  < 0.6$ rapidity region, in Pb-Pb (left) and p-p (right) collisions. . . . .	188
4.23 Acceptance of prompt $J/\psi$ mesons, estimated from simulations, as a function of $p_T^{\mu\mu}$ (left) and $y^{\mu\mu}$ (right). The error bars represents the statistical uncertainties. . . . .	189

4.24 Muon trigger efficiencies as a function of the probe $p_T$ . The efficiencies are extracted, using the TnP method, from data (blue) and simulation (red) in Pb-Pb collisions at $1.8 <  \eta^\mu  < 2.1$ (left) and p-p collisions at $2.1 <  \eta^\mu  < 2.4$ (right). The bottom panels show the data-to-simulation efficiency ratio. The results of the fits to the efficiencies are also shown. Figures taken from the internal analysis note [247]. . . . .	191
4.25 Corrected efficiencies of prompt $J/\psi$ mesons measured in p-p collisions. Left: as a function of $p_T^{\mu\mu}$ in different rapidity regions. Right: as function of rapidity. The error bars represent statistical uncertainties. . . . .	192
4.26 Corrected efficiencies of prompt $J/\psi$ mesons measured in Pb-Pb collisions, as a function of $p_T^{\mu\mu}$ (left) and centrality (right), in different rapidity regions. The error bars represent statistical uncertainties. . . . .	193
4.27 Double ratios of prompt charmonium efficiencies as a function of $p_T^{\mu\mu}$ (top) and centrality (bottom), in the rapidity regions: $ y^{\mu\mu}  < 1.6$ (left) and $ y^{\mu\mu}  > 1.6$ (right). The error bars represent statistical uncertainties. . . . .	194
4.28 Nonprompt fraction of $J/\psi$ mesons measured in p-p and Pb-Pb collisions, as a function of dimuon rapidity (left) and $p_T$ (right). The boxes (bars) represent the systematic (statistical) uncertainties. Figures published in Ref. [7]. . . . .	205
4.29 Differential cross section of the production of prompt (left) and nonprompt (right) $J/\psi$ mesons decaying into $\mu^+ \mu^-$ , as a function of dimuon rapidity (top) and $p_T$ (bottom) in p-p (blue open circles) and Pb-Pb (red squares) collisions. The boxes (bars) represent the systematic (statistical) uncertainties. The global relative uncertainties are written in the plots. Figures published in Ref. [7]. . . . .	207
4.30 Nuclear modification factor of prompt $J/\psi$ mesons measured at $\sqrt{s_{NN}} = 2.76 \text{ TeV}$ [249] (grey circles) and $\sqrt{s_{NN}} = 5.02 \text{ TeV}$ [7] (red squares), as a function of dimuon $p_T$ (left), rapidity (middle) and $\langle N_{\text{part}} \rangle$ (right). The boxes (bars) represent the systematic (statistical) uncertainties. The size of the global relative uncertainties are depicted in the boxes plotted at $R_{AA} = 1$ . Figures published in Ref. [7]. . . . .	209

4.31 Nuclear modification factor of prompt $J/\psi$ mesons. Left: as a function of $p_T^{\mu\mu}$ in the mid- and most forward rapidity regions. Right: as a function of $\langle N_{\text{part}} \rangle$ at $3 < p_T^{\mu\mu} < 6.5 \text{ GeV}/c$ and $6.5 < p_T^{\mu\mu} < 50 \text{ GeV}/c$ , in the $1.8 <  y^{\mu\mu}  < 2.4$ rapidity region. The boxes (bars) represent the systematic (statistical) uncertainties. The size of the global relative uncertainties are depicted in the boxes plotted at $R_{\text{AA}} = 1$ . Figures published in Ref. [7]. . . . .	209
4.32 Nuclear modification factor of nonprompt $J/\psi$ mesons measured at $\sqrt{s_{\text{NN}}} = 2.76 \text{ TeV}$ [249] (grey circles) and $\sqrt{s_{\text{NN}}} = 5.02 \text{ TeV}$ [7] (red squares), as a function of dimuon $p_T$ (left), rapidity (middle) and $\langle N_{\text{part}} \rangle$ (right). The boxes (bars) represent the systematic (statistical) uncertainties. The size of the global relative uncertainties are depicted in the boxes plotted at $R_{\text{AA}} = 1$ . Figures published in Ref. [7]. . . . .	210
4.33 Nuclear modification factor of nonprompt $J/\psi$ mesons. Left: as a function of $p_T^{\mu\mu}$ in the mid- and most forward rapidity regions. Right: as a function of $\langle N_{\text{part}} \rangle$ in two $p_T^{\mu\mu}$ intervals at forward rapidity. The boxes (bars) represent the systematic (statistical) uncertainties. The size of the global relative uncertainties are depicted in the boxes plotted at $R_{\text{AA}} = 1$ . Figures published in Ref. [7]. . . . .	211
4.34 Double ratio of prompt $\psi(2S)$ over $J/\psi$ meson yields as a function of the dimuon $p_T$ , at $ y^{\mu\mu}  < 1.6$ (squares) and $1.6 <  y^{\mu\mu}  < 2.4$ (circles). The horizontal lines denotes the widths of the $p_T$ intervals. The bars (boxes) represent the statistical (systematic) uncertainties, while the arrows indicate the 95% CL interval where the measurement is consistent with zero. Figure published in Ref. [6]. . . . .	212
4.35 Comparison of the double ratio of prompt $\psi(2S)$ over $J/\psi$ meson yields measured at $\sqrt{s_{\text{NN}}} = 2.76 \text{ TeV}$ [235] (open markers) and $\sqrt{s_{\text{NN}}} = 5.02 \text{ TeV}$ [6] (solid markers), as a function of $\langle N_{\text{part}} \rangle$ at $ y^{\mu\mu}  < 1.6$ (left) and $1.6 <  y^{\mu\mu}  < 2.4$ (right). The bars (boxes) represent the statistical (systematic) uncertainties, while the arrows indicate the 95% CL interval where the measurement is consistent with zero. Figures published in Ref. [6]. . . . .	213

4.36 Distribution of the nuclear modification factor of different hadron species as a function of $p_T$ in Pb-Pb collisions at $\sqrt{s_{NN}} = 5.02\text{ TeV}$ . Left: for prompt $J/\psi$ mesons (red markers) and $D^0$ mesons [252] (green points). Right: for non-prompt $J/\psi$ mesons (red markers), $D^0$ mesons [252] (orange points) and light charged hadrons [253] (black points). The boxes (bars) represent the systematic (statistical) uncertainties. The size of the global relative uncertainties are depicted in the box plotted at $R_{AA} = 1$ . . . . .	214
4.37 Double ratio of prompt $\psi(2S)$ over $J/\psi$ meson yields measured at $\sqrt{s_{NN}} = 2.76\text{ TeV}$ [235] (open markers) and $\sqrt{s_{NN}} = 5.02\text{ TeV}$ (solid markers), as a function of $\langle N_{\text{part}} \rangle$ at $ y^{\mu\mu}  < 1.6$ (left) and $1.6 <  y^{\mu\mu}  < 2.4$ (right). The bars (boxes) represent the statistical (systematic) uncertainties, while the arrows indicate the 95% CL interval where the measurement is consistent with zero. The results of the Rapp and Du model [237] at 2.76 TeV (white boxes) and 5.02 TeV (red and blue boxes) are also shown. . . . .	215
B.1 The $p_T^{\text{miss}}$ distribution for $W^- \rightarrow \mu^- \bar{\nu}_\mu$ events within each fitted $\eta_{\text{CM}}^\mu$ range, shown in logarithmic scale. Unbinned fits to the data (black points) are performed with six contributions, stacked from top to bottom: $W^+ \rightarrow \mu^+ \nu_\mu$ (yellow), QCD multijet (light blue), $Z/\gamma^* \rightarrow \mu^+ \mu^-$ (green), $W^+ \rightarrow \bar{\tau} \nu_\tau$ (red), $Z/\gamma^* \rightarrow \tau \bar{\tau}$ (dark blue) and $t\bar{t}$ (orange). Error bars represent statistical uncertainties. The lower panels display the data divided by the result of the fit, for each $\eta_{\text{CM}}^\mu$ range. The Baker-Cousins [191] $\chi^2$ test value over the number of degrees of freedom is also shown. . . . .	232
B.2 The $p_T^{\text{miss}}$ distribution for $W^+ \rightarrow \mu^+ \nu_\mu$ events within each fitted $\eta_{\text{CM}}^\mu$ range, shown in logarithmic scale. Unbinned fits to the data (black points) are performed with six contributions, stacked from top to bottom: $W^+ \rightarrow \mu^+ \nu_\mu$ (yellow), QCD multijet (light blue), $Z/\gamma^* \rightarrow \mu^+ \mu^-$ (green), $W^+ \rightarrow \bar{\tau} \nu_\tau$ (red), $Z/\gamma^* \rightarrow \tau \bar{\tau}$ (dark blue) and $t\bar{t}$ (orange). Error bars represent statistical uncertainties. The lower panels display the data divided by the result of the fit, for each $\eta_{\text{CM}}^\mu$ range. The Baker-Cousins [191] $\chi^2$ test value over the number of degrees of freedom is also shown. . . . .	233

**FIGURE** **Page**





**Titre :** Mesure des bosons W en p-Pb à 8.16 TeV et des charmonia en Pb-Pb à 5.02 TeV avec le détecteur CMS au LHC.

**Mots clés :** Boson W, charmonia, physique des ions lourds, plasma de quarks et de gluons, CMS

**Résumé :** Les collisions d'ions lourds à haute énergie du grand collisionneur de hadrons, permettent d'étudier les propriétés de la matière nucléaire et de produire l'état chaud et dense de la matière déconfinée connu sous le nom de plasma de quarks et de gluons (QGP). Afin d'étudier les effets dus à la matière nucléaire dans les collisions d'ions lourds, la production de deux sondes dures importantes est étudiée dans cette thèse: les bosons W et les charmonia (mésons  $J/\psi$  et  $\psi(2S)$ ).

Les effets de la matière nucléaire froide, associés à la modification nucléaire des fonctions de distribution des partons (PDF), peuvent être caractérisés en étudiant la formation des bosons W dans les collisions d'ions lourds. En effet, la production des bosons W est déterminée par la diffusion dure initiale, puisque ces bosons n'interagissent pas fortement avec le milieu induit par la collision. L'analyse de la production des bosons W dans les collisions p-Pb à  $\sqrt{s_{NN}} = 8,16$  TeV avec le détecteur CMS est présentée dans la première partie de cette thèse. Les résultats sont en bon accord avec les calculs des PDFs incluant les modifications nucléaires, alors qu'ils excluent significativement l'hypothèse de nucléons libres, pour des fractions d'impulsion  $x$  petite. Puisque les mesures sont plus précises que les calculs des modèles, les résultats des bosons W ont le potentiel de contraindre les paramétrisations des PDF nucléaires, ce qui pourrait améliorer notre compréhension des effets des PDF sur d'autres sondes dures, comme les charmonia.

La production des charmonia est sensible à la formation et à l'évolution du milieu forte interaction formé lors de collisions d'ions lourds, en faisant ainsi une excellente sonde du QGP. La suppression ou l'augmentation des différents états du charmonium sont considérées comme des signatures de la présence du QGP. Dans cette thèse, la production prompte et non-prompte des mésons  $J/\psi$  est mesurée dans des collisions Pb-Pb à  $\sqrt{s_{NN}} = 5,02$  TeV. De plus, la modification des mésons  $\psi(2S)$  par rapport aux mésons  $J/\psi$  est mesurée pour le même système de collision. Le facteur de modification nucléaire des charmonia est déterminé en fonction de la centralité, de la rapidité et de l'impulsion transverse  $p_T$ . La production des mésons  $J/\psi$  prompts est supprimée dans les collisions Pb-Pb par rapport aux collisions p-p normalisés par le nombre de collisions binaires, bien qu'une suppression plus faible soit observée à  $3 < p_T < 6,5$  GeV/c dans les collisions Pb-Pb centrales. La production des quarks b, sondés par les charmonia non prompts, est également supprimée dans toute la région cinématique mesurée, et une plus faible suppression est observée à haut  $p_T$ . En ce qui concerne les mésons  $\psi(2S)$ , ils se révèlent plus fortement supprimés que les mésons  $J/\psi$  dans les collisions Pb-Pb.

**Title :** Measurement of W bosons in p-Pb at 8.16 TeV and of charmonia in Pb-Pb at 5.02 TeV with the CMS detector at the LHC

**Keywords :** W boson, charmonia, heavy-ion physics, quark-gluon plasma, CMS

**Abstract :** Heavy ions are collided at high energies at the Large Hadron Collider, allowing to study the properties of nuclear matter and to produce the hot and dense state of deconfined matter known as the Quark-Gluon Plasma (QGP). In order to probe the nuclear matter effects present in heavy-ion collisions, the production of two important hard probes is studied in this thesis: W bosons and charmonia ( $J/\psi$  and  $\psi(2S)$  mesons).

The cold nuclear matter effects, associated to the nuclear modification of the parton distribution functions (PDFs), can be characterised by studying the formation of W bosons in heavy-ion collisions. The production of W bosons represents an important tool to assess the PDF modifications, which impact the initial hard scattering, since these bosons do not interact strongly with the collision-induced medium. The analysis of the W-boson production in p-Pb collisions at  $\sqrt{s_{NN}} = 8,16$  TeV with the CMS detector is presented in the first part of this thesis. The results are in good agreement with PDF calculations including nuclear modifications, while they strongly disfavour the free-nucleon hypothesis at small momentum fractions  $x$ . Since the measurements are more precise than the model calculations, the W-boson results have the potential to constrain the nuclear PDF parametrisations, which could eventually improve our understanding of the PDF effects on other hard probes, such as charmonia.

The production of charmonia is sensitive to the formation and evolution of the strongly-interacting medium formed in heavy-ion collisions, thus making of it an excellent probe of the QGP. The suppression or enhancement of the different charmonium states is considered a signature of the presence of the QGP. In this thesis, the production of prompt and nonprompt  $J/\psi$  mesons is measured in Pb-Pb collisions at  $\sqrt{s_{NN}} = 5,02$  TeV. In addition, the modification of the  $\psi(2S)$  mesons relative to  $J/\psi$  mesons is reported for the same collision system. The nuclear modification factor of charmonia is determined as a function of centrality, rapidity and transverse momentum  $p_T$ . The production of prompt  $J/\psi$  mesons is suppressed in Pb-Pb collisions compared to binary-scaled p-p collisions, although a weaker suppression is observed at  $3 < p_T < 6,5$  GeV/c in central Pb-Pb collisions. The production of b quarks, probed by the nonprompt charmonia, are also suppressed over the full kinematic region measured, and a reduced suppression is observed at high  $p_T$ . Regarding the  $\psi(2S)$  mesons, they are found to be more strongly suppressed than  $J/\psi$  mesons in Pb-Pb collisions.



**LIST OF FIGURES**

---